ABSTRACT

Title of Dissertation:	CUCURBIT[N]URIL FUNCTIONALIZATION AND INCORPORATION INTO METAL-ORGANIC ASSEMBLIES
	Kimberly G. Brady, Doctor of Philosophy, 2021
Dissertation directed by:	Professor Lyle Isaacs, Department of Chemistry and Biochemistry

Molecular containers have been widely studied due to their unique ability to recognize guest molecules. Host compounds have been used in various applications including sensing, separations, and the development of smart materials due to these binding properties. The curcurbit[n]uril (CB[n]) family of macrocyclic containers are known for their high binding affinities and selectivities towards guest molecules in water. Altercation to the size and shape of the CB[n] cavity or addition of functional groups might expand potential applications.

Chapter 1 introduces supramolecular chemistry, specifically that of molecular containers. A review of CB[n] chemistry describes their exceptional binding properties and potential usage. However, poor water solubility limits the biological applications of CB[n]. The development of acyclic CB[n] and incorporation of cyclic CB[n] into metal-organic polyhedra (MOP) are described to enhance the potential biomedical properties of these containers.

Chapter 2 describes the extension of the glycoluril backbone of the acyclic CB[n]. The synthesis of the conformationally mobile S-shaped glycoluril pentamer building block and two new acyclic CB[n] receptors **P1** and **P2** are reported. In the presence of guests, **P2** adapts its conformation to form 1:1 **P2**·guest complexes. The binding free energy pays the energetic price for conformer selection. This energetically unfavorable conformer selection results in significantly decreased K_a values of **P1** and **P2** compared to **Tet1** and **Tet2**.

Chapter 3 presents the self-assembly of rigid-rod dipyridine ligand **III-1** with $M(en)(NO_3)_2$ (M = Pd, Pt) to afford triangular (**III-3**, **III-5**) and square (**III-4**, **III-6**) supramolecular coordination complexes. The binding affinity of **III-1** towards CB[n]-type containers result in the formation of triangular [4]molecular necklaces ([4]MNs, **III-7** – **III-10**) either by one-pot or post complexation approaches as evidence by ^{1}H NMR, DOSY NMR, and ESI-MS.

Chapter 4 investigates the self-assembly of three iron-based metal-organic polyhedra systems (**IV-6, IV-12,** and **IV-17**). CB[7] can be mechanically interlocked onto the edges of the scaffolds during the self-assembly process to yield MOPs **IV-7**, **IV-13**, and **IV-18** as evident by ^{1}H and DOSY NMR. Full saturation of the edges could not be achieved due to the slippage of the CB[n] units during the self-assembly process.

CUCURBIT[N]URIL FUNCTIONALIZATION AND INCORPORATION INTO METAL-ORGANIC ASSEMBLIES

by

Kimberly Grace Brady

Dissertation submitted to the Faculty of the Graduate School of the
University of Maryland, College Park, in partial fulfillment
of the requirements for the degree of
Doctor of Philosophy
2021

Advisory Committee:
Professor Lyle Isaacs, Chair
Professor Jeffery Davis
Professor Daniel Falvey
Professor Myles Poulin
Professor Volker Briken, Dean's Representative

© Copyright by
Kimberly Grace Brady
2021

Dedication

To my parents Frank and Tess Brady. Thank you for always encouraging me to follow my dreams.

Acknowledgements

First, I would like to thank my Ph.D. advisor, Professor Lyle Isaacs, for his guidance over the years. While my projects did not always go the way we planned, I have learned how to think critically about difficult problems and how to find ways to overcome those challenges. I have learned so much about chemistry from him and how to be a successful scientist. I am very grateful for his time and mentorship.

I would also like to thank the current and former Isaacs group members for all their support during my time at the University of Maryland. Thank you for teaching me the proper laboratory techniques, helping me troubleshoot experiments, asking difficult questions, and for all the support and encouragement. I would especially like to thank Dr. Soumen Samanta who helped me with my first project in the Isaacs group and taught me about metal-organic polyhedra. I would also like to thank Dr. Steven Murkli who started the graduate school journey with me. Thank you for listening to my endless practice presentations and giving me advice.

Lastly, I would like to thank my friends and family. Thank you for always believing in me and encouraging me to get my Ph.D. Special thanks to my mom and dad for always picking up the phone when I called and my friends from Saint Michael's college and the University of Maryland for helping celebrate every milestone and cheering me on the entire way.

Table of Contents

List of Tables

Chapter 2

Chapter 4

List of Figures

Chapter 1

Chapter 2

Figure II-2. NMR spectra recorded (800 MHz, 30 °C, DMSO-d_6) for **II-3a**: a) ^{1}H NMR spectrum. Selective 1D NOE recorded for **II-3a** with irradiation of: b) H_k, c) H_m, d) H_l, e) H_j, and f) H_i.

Figure II-3. ^{1}H NMR spectra recorded (400 MHz, DMSO-d_6, RT) for: a) **P1**, and b) **P2**. X = ^{13}C satellite.

Figure II-4. Representations of the different conformational isomers of **P1** that occur by flipping at the S-shaped methylene bridges.

Figure II-5. a) Chemical structures of **TriMe** and **TriH** with the definition of the terminal $H_3C\bullet\bullet\bullet CH_3$ distance d_{MM} and the global twist of glycoluril ribbon represented by a pseudo-dihedral angle τ_2. B) Top and c) front views of the geometries of the F1, F2, F3 conformers optimized at the B97-3c level of theory in implicit water (the back view is available in Figure II-S102).

Figure II-6. Structures of a) **P2'** (top line) and b) **P2'•II-8** (bottom line) in the F1, F2, and F3 folds obtained at the B97-3c level of theory in implicit water (see Figures II-S103 – II-S106 for other views and structures for **P1'** and **P1'•II-8**).

Figure II-7. a) Plot of the chemical shift of H_m of **P2** as a function of [**P2**]. The solid line represents the best non-linear fitting of the data to a two-fold self-association model (K_s = 189 ± 27 M^{-1}). B) Two representations of the selected snapshot from MD simulation of **P2**-F1•**P2**-F1. Solubilizing groups were removed for clarity. Ensembles of overlapping snapshots for **P2**-F1•**P2**-F1 and **P2**-F2•**P2**-F2, including solubilizing groups, are provided in Figures II-S107 and II-S108.

List of Schemes

Chapter 1

Chapter 2

Chapter 4

List of Charts

Chapter 3

List of Abbreviations

1D NOE	one-dimensional nuclear overhauser effect
^{1}H NMR	proton nuclear magnetic resonance
2D NMR	two-dimensional nuclear magnetic resonance
^{13}C NMR	carbon 13 nuclear magnetic resonance
Ac_2O	acetic anhydride
aq.	aqueous
$(Boc)_2O$	di-tert-butyl decarbonate
CB[n]	cucurbit[n]uril
CD_3CN	deuterated acetonitrile
CH_2Cl_2	dichloromethane
CH_3CN	acetonitrile
COSY	homonuclear correlation spectroscopy
D	diffusion coefficient
d	doublet
d	days
D_2O	deuterium oxide
DCM	dichloromethane
DFT	density functional theory
DMF	dimethylformamide
DMSO	dimethyl sulfoxide
DOSY	diffusion order spectroscopy
en	ethylenediamine

EPR	enhanced permeation and retention
Et_2O	diethyl ether
EtOH	ethanol
ESI-MS	electrospray ionization mass spectrometry
equiv.	equivalent
$FeSO_4$	iron (II) sulfate
$Fe(OTf)_2$	iron (II) triflate
H	hydrogen
h	hour
H_2O_2	hydrogen peroxide
H_2SO_4	sulfuric acid
HCl	hydrochloric acid
HMBC	heteronuclear multiple-bond correlation spectroscopy
HP	hydroxypropyl
HSQC	heteronuclear single quantum coherence spectroscopy
hυ	energy
Hz	hertz
i-CB[n]	inverted cucurbit[n]uril
ITC	isothermal titration calorimetry
J	coupling constant
K	kelvin
$K_2S_2O_8$	potassium persulfate
K_2SO_4	potassium sulfate

K_a	acid dissociation constant
kcal/mol	kilocalories per mole
KI	potassium iodide
K_s	self-association constant
$LiNTf_2$	lithium triflimide
M	molar
m	multiplet
M^{-1}	inverse molar
M+	molecular ion
M.p.	melting point
m/z	mass to charge ratio
m^2/s	meters squared per second
Me	methyl
MHz	megahertz
$MeSO_3H$	methanesulfonic acid
mM	millimolar
MIM	mechanically interlocked molecule
MOF	metal-organic framework
MOP	metal-organic polyhedra
MV	methyl viologen
[n]MN	[n]molecular necklace
NH_4PF_6	ammonium hexafluorophosphate
nm	nanometer

NaH_2PO_4	monosodium phosphate
$NaNO_3$	sodium nitrate
NTf_2	triflimide
p	para
PEG	polyethylene glycol
PF_6	hexafluorophosphate
pKa	negative base-10 logarithm of the acid dissociation constant
ppm	parts per million
RT	room temperature
SCC	supramolecular coordination complex
SMD	solvation model based on density
SOF	supramolecular organic framework
TFA	trifluoroacetic acid
UV/Vis	ultraviolet/ visible
Å	angstrom
β	beta
Δ	delta
Δδ	change in chemical shift
ΔH	change in enthalpy
Λ	lambda
λ	wavelength
λ_{max}	maximum wavelength
μM	micromolar

μm	micrometer
π	pi
Φ	quantum yield

Chapter 1: From Molecules to Supramolecular Structures

1.1 Introduction to Molecular Recognition

Pioneering research from the 1960s done by Pedersen,[1] Lehn,[2] and Cram[3] led to the discovery of various compounds (e.g., crown ethers, cryptands, and spherands) which could recognize complementary small molecules through non-covalent interactions. These kinetically reversible interactions which include hydrogen bonding, electrostatic, ion-dipole, $\pi - \pi$, and van der Waals interactions are the basis for the field of supramolecular chemistry. This domain is interested in interactions and connections "beyond the molecule" (Figure I-1).[4] It seeks to mimic the ability of nature to assemble simple molecular precursors into intricate assemblies. Nature can create these larger, more complex systems using functionalized biological building blocks that allow them to interact in a deliberate manner. Organic chemists have used this fundamental principle to build synthetic systems and materials in a similar fashion.

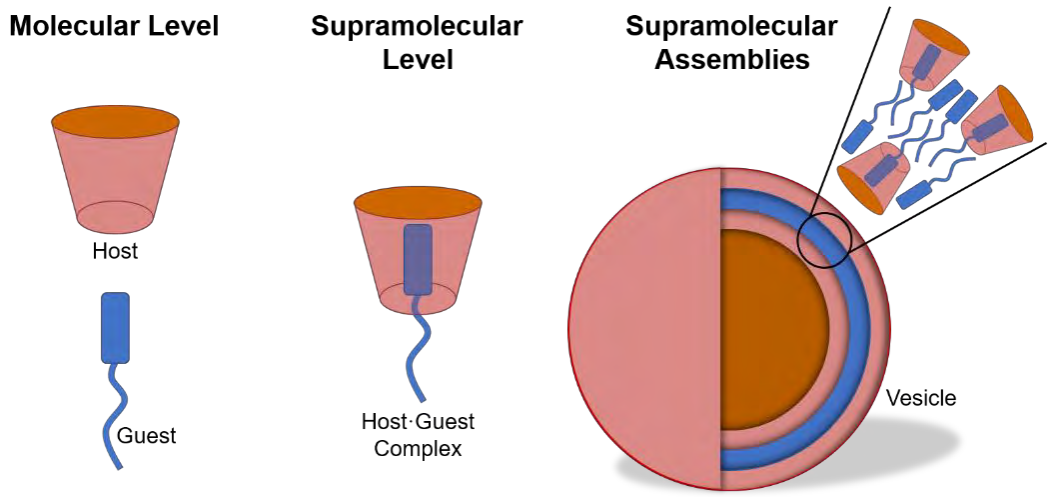

Figure I-1. Illustration of the concept behind supramolecular chemistry: arranging molecules into larger structures and assemblies through non-covalent interactions.

Supramolecular chemistry uses three main types of non-covalent interactions: (i) hydrogen bonding motifs; (ii) processes utilizing other non-covalent interactions (ion-dipole, ion-ion, van der Walls, hydrophobic interactions, etc.); and (iii) the use of strong directional metal-ligand bonds for assembly.[5-12] In each classification, building blocks self-organize to form hierarchical structures with different physicochemical properties. These systems are designed to assemble towards a thermodynamic minimum, however by tuning the reaction parameters, the equilibrium can shift towards a desired product. In the subsequent sections and chapters, I will describe work utilizing the latter two categories, with a focus on the synthesis of novel molecular containers and metal-organic polygons and polyhedra.

1.2 Introduction to Molecular Containers

The work done by Lehn, Cram, and Pedersen was awarded the Nobel prize in Chemistry in 1987. Their molecular hosts were able to imitate biological receptors using non-covalent interactions to bind small ionic guests with high selectivity. Their groundwork ignited the field of supramolecular chemistry and sparked the design and use of synthetic molecular containers. Since the development of the host receptors by these three Nobel laureates, more complex molecular containers containing hydrophobic cavities have been established (Figure I-2).[13-17]

Just like their macroscopic brethren, molecular containers hold and protect cargo from their surrounding environment; the major difference being that these containers do so at the molecular level. Molecular containers provide ideal structures for molecular recognition by internalized guest molecules based on their size, shape, and functional groups. Encapsulation can stabilize and alter the physical and chemical properties of a

guest molecule. Changes in pK_a, conformation, solubility, and optical properties can be achieved through cavity binding.[12, 18-25] These unique host·guest properties have been utilized in a variety of different applications. Advances with molecular containers can be seen in fields such as catalysis, development of molecular machines and chemical sensors, separation techniques, and the formulation, delivery, and sequestration of biologically active drugs.[9, 26-34]

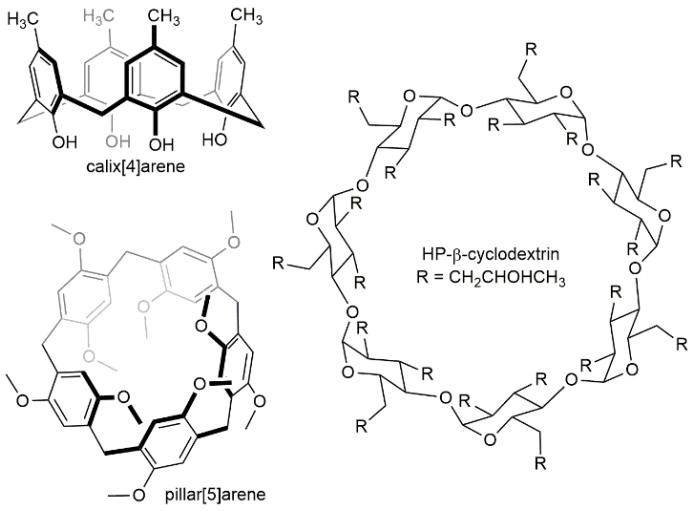

Figure I-2. Chemical structures of various molecular containers.

A popular class of molecular containers used for industrial applications is cyclodextrins.[35] These macrocycles are composed of linked dextrose units. In fact, the commercially available air freshener, Febreze®, contains HP-β-cyclodextrin as its active ingredient to encapsulate malodorous compounds and eliminate their smells.[36] This family of macrocycles has also been used to improve the solubility and stability of insoluble drug molecules.[37] Formulation of drug molecules with Capisol®, a polyanion β-cyclodextrin, has enabled the approval of several medicines (e.g., Nexterone®, Abilify®, Geodon®, and VFend®) by the Food and Drug Administration.[38] The high popularity of this container

arises from it being inexpensive to make, commercially available, easy to functionalize, and soluble in a variety of solvents. However, despite these many favorable characteristics, cyclodextrins only display modest binding affinities (K_a around 10^2 – 10^4 M^{-1}) and selectivities.[13, 35] A plethora of research is currently being done to develop other types of containers with better molecular recognition properties.[39-43]

1.3 The Cucurbit[n]uril Family of Molecular Containers

In 1905, Behrend and co-workers first published the synthesis of the condensation reaction between glycoluril and formaldehyde in concentrated HCl.[44] It was not until 1981 that the product was crystallized to observe the macrocyclic structure containing six glycoluril units bridged by twelve methylene units.[45] Cucurbit[6]uril (CB[6]), as the new compound came to be known, was the first member discovered in this family named after its resemblance to a pumpkin. Modification to the original procedure done by Kim[46] and Day[47, 48] in the early 2000s, yielded other various sized cucurbit[n]uril (CB[n]) members (Figure I-3a).

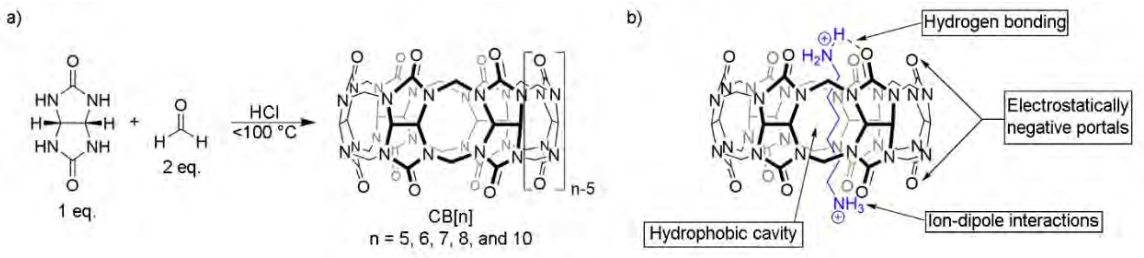

Figure I-3. a) Synthesis and structure of CB[n] and b) molecular recognition properties of CB[6] with hexane-1,4-diammonium chloride.

Popularity in the use of CB[n] increased rapidly due to their high binding affinities and selectivies toward cationic organic and inorganic molecules, specifically towards

dicationic alkyl diammonium guests in water (K_a commonly 10^6 M^{-1}; K_a up to 10^{17} M^{-1}).[27, 49-53] These improved molecular recognition properties emanate from the unique structural features of CB[n] (Figure 1-3b). [54, 55] The two electrostatically negative ureidyl carbonyl portals lining the top and bottom of the containers are excellent sites for hydrogen-bonding and ion-dipole interactions. These portals additionally provide entry of alkyl and aryl moieties into the hydrophobic cavity formed by the C-shaped glycoluril units. The structural rigidity of CB[n]s regulates the selectivity and binding capacity of guests based on the size of the container.[56] Also, the favorable displacement of entrapped high energy water from the cavity drives these higher binding affinities through enthalpic and entropic gains.

Cavity size plays a crucial role in determining what guests can bind to CB[n] and by which binding mode (Figure I-4).[57, 58] CB[5], the smallest member of the CB[n] family, only has a 2.4 Å portal diameter. Its small internal cavity limits its ability to form *inclusion* complexes with most molecules. Therefore, many species form *exclusion* complexes by binding to its electrostatically negative portals. As the number of glycoluril units increases, the ability of the container to bind a wider range of guest compounds expands. Addition of one glycoluril unit, to yield CB[6], causes the portal diameter to increase by 1.5 Å. This growth allows for the inclusion of aliphatic chain guests and exclusion complexes with alkali and alkaline earth cations. Bulkier guests, such as aromatic and adamantyl species, can begin to enter the cavity of CB[7] with a 5.4 Å portal diameter. More unique binding possibilities arise with the use of CB[8]; with a diameter of 6.9 Å, two guest molecules can enter the cavity simultaneously forming either 1:2 homoternary or 1:1:1 heteroternary

complexes (Figure I-4). The wider scope of guests and alternative binding capabilities make the use of CB[7] and CB[8] more attractive for various applications.[39, 59]

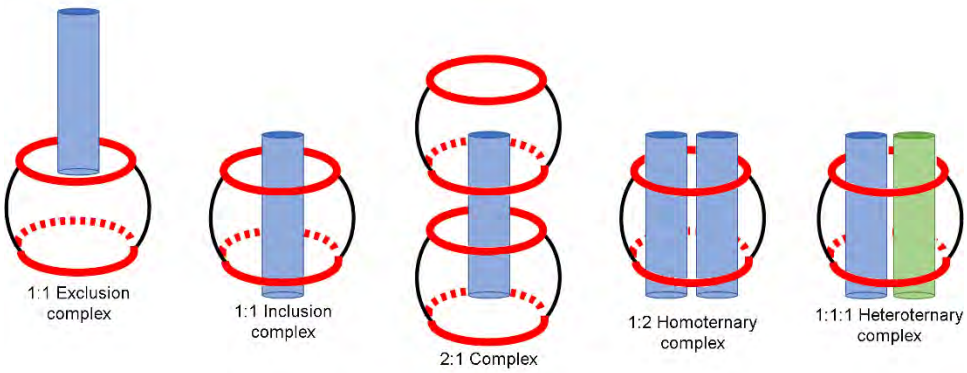

Figure I-4. Modes of guest binding towards CB[n] hosts.

CB[n]s have been employed in many applications including separation, transport, sensing, catalysis, drug delivery, and incorporation into molecular machines.[19, 27, 39, 59-67] However, CB[n] hosts are insoluble in organic solvents and are only weakly soluble in water (CB[5] and CB[7] = 20 – 30 mM; CB[6] = 0.018 mM; CB[8] < 0.01 mM).[53] This is especially detrimental for their potential use in biological applications. Altercation in the size and shape of the CB[n] cavity or the addition of functional groups could expand the biomedical use of CB[n] through enhancement of certain properties such as improved water solubility or higher binding constants.

1.4 Functionalization of Cucurbit[n]urils

Extensive research has been done to functionalize the internal and external surfaces of CB[n] molecular containers. Early work attempted modification through the homomeric cyclization of derivatized glycoluril units. Stoddart and co-workers were the first to successfully add methyl groups to the exterior equator of CB[n] by reacting

dimethylglycoluril with formaldehyde in 1992 to form decamethylcucurbit[5]uril (Me_{10}CB[5]).[68] In 2001, Kim and co-workers created more soluble CB[5] and CB[6] derivatives using cyclohexanoglycoluril as the monomer.[69] The synthesized hosts (Cy_6CB[6] and Cy_5CB[5]) display increased solubility in water (≈ 2 x 10^{-1} M) and other common solvents such as methanol, DMF, and DMSO (≤ 3 x 10^{-2} M). However, modification of CB[n] through this method primarily forms macrocycles with 5 or 6 glycoluril units which possess smaller and less useful cavities. The preference for CB[5] and CB[6] sized macrocycles is due to the more sever 1,5-diaxial steric interactions between substituents on neighboring glycoluril units in larger CB[n], therefore disfavoring their formation.

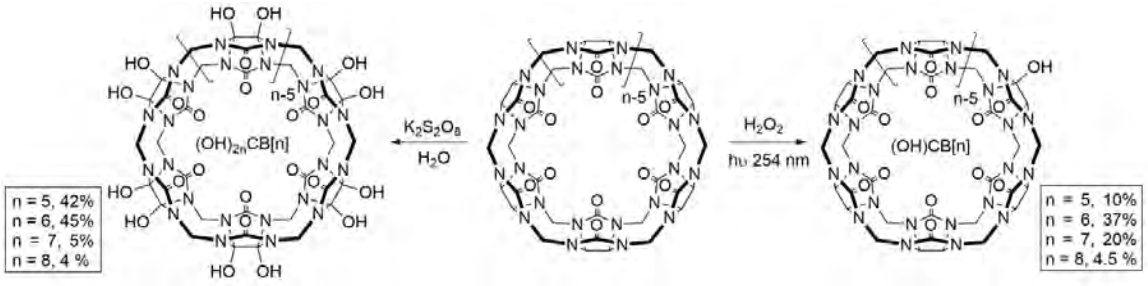

Scheme I-1. Synthesis of per- and mono-hydroxylated CB[n].

To increase the yields of functionalized CB[n], researchers began direct functionalization of pre-formed containers. The Kim group made the breakthrough of obtaining larger modified hosts by treating CB[5] – CB[8] with $K_2S_2O_8$ in water to produce per-hydroxylated $(HO)_{2n}$CB[n] species (Scheme I-1 *left*) through a radical oxidation reaction. While CB[7] and CB[8] derivatives were obtained, their poor yields of < 5% for CB[8] are believed to result from the limited solubility of starting materials as well as the instability of the per-hydroxylated products. However, the modification increased the

solubility of $(HO)_{12}$CB[6] in DMSO and DMF which allowed for subsequent derivatization yielding $(allyloxy)_{12}$CB[6]. CB[n] derivatives now could be attached to silica gel and used in chromatographic applications.[70] Direct photochemical mono-hydroxylation of CB[5] – CB[8] under mild reaction conditions (Scheme I-1 *right*) provided better control of subsequent functionalization.[71]

An alternative way to produce regioselective functionality of CB[n]s is through a building block approach. Work by the Isaacs group and others to yield methylene bridged glycoluril oligomers of desirable lengths made this method possible.[72, 73] The hexamer, which has potential in forming mono-functionalized CB[6] derivatives, was obtained through templation of *p*-xylylenediamine (PXDA, **I-3**) with glycoluril under the condensation reaction conditions with HCl and formaldehyde (Scheme I-2 *top*).[74] Reacting the hexamer with various functionalized starting materials, provides a variety of new containers with precise amounts of functional groups attached. More interestingly, when reacting **I-5** with functionalized cyclic bisetherglycoluril units (**I-6** or **I-7**), larger modified CB[n] were formed (Scheme I-2 *bottom*).[75, 76] These larger derivatized CB[n] have enhanced water solubility making them more attractive for biomedical applications such as drug solubilization, targeted drug delivery, and biological imaging.[77-79]

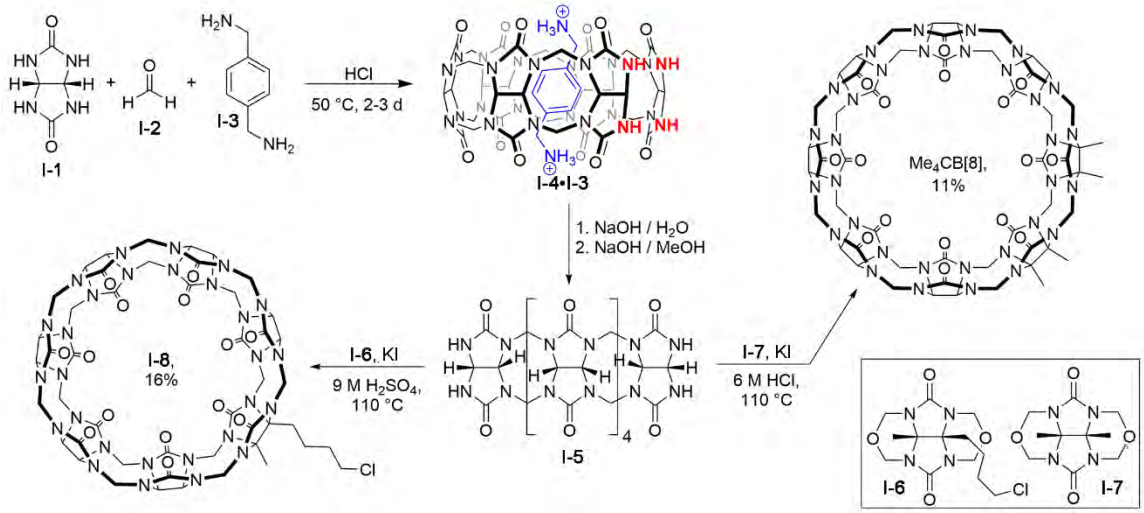

Scheme I-2. Templated synthesis of hexamer and building-block synthesis of monofunctionalized CB[7], **I-8**, and **Me$_4$CB[8]**.

While new functionalities can be achieved resulting in new CB[n] derivatives with higher solubilities and new possible applications, the yields for many of these modified CB[n] reactions, especially for the larger sized containers, are only modest at best. This difficulty to produce functionalized CB[n] containers along with their inherently poor water solubility has been a hurdle which many research groups continue to try to resolve.

1.5 Development of Acyclic Cucurbit[n]urils

The development of CB[n] like analogues, to combat the problems associated with the parent cyclic containers, has led to the discovery of hemicucurbit[n]urils,[80] bambus[n]urils[81] as well as other derivatives. The Isaacs group addressed the difficulty of modification and inherently poor solubility by developing a class of acyclic CB[n]-type receptors.[82, 83] These C-shaped containers are synthesized from a building block approach where glycoluril dimer (**I-9**) undergoes a condensation reaction with dimethylglycoluril cyclobisether (**I-10**) to produce glycoluril tetramer **I-11** (Scheme I-3). Functional groups

can be incorporated through the addition of modified aromatic walls (e.g., **I-12** or **I-13**).[83-88] These aromatic walls help to promote π–π interactions with guests, while their sulfonate functionalized arms dramatically enhance water solubility. The C-shape allows these new containers to have more flexible glycoluril backbones, while retaining their hydrophobic cavity, which allows for encapsulation of a wider range of differently sized guests.

Two acyclic CB[n]-type receptors, **Motor1** (with sulfonated *o*-xylylene walls) and **Motor2** (with sulfonated naphthalene walls), have high potential in numerous biomedical applications.[82, 89-91] **Motor1** has increased water solubility (346 mM) which is more than 10-fold higher than the most soluble macrocyclic CB[n] (CB[7] 20 – 30 mM). **Motor1** and **Motor2** can bind dialkyl, adamantyl, and aryl ammonium guests with K_a values of 10^5 – 10^9 M^{-1} (comparable to CB[6] and CB[7]).[92] **Motor1** and **Motor2** are also highly effective in enhancing the solubility of insoluble active pharmaceutical ingredients such as Paclitaxel, as well as acting as *in vivo* reversal agents for neuromuscular block.[82, 93] These containers exhibit low *in vitro* toxicity in human liver, kidney, and monocyte cell lines allowing for their potential *in vivo* use.[82] Sequestration of drugs of abuse can be exemplified in the reversal of the hyperlocomotive effect of methamphetamine performed with rats with **Motor1** and **Motor2**.[91] While lots of research has gone into finding additional potential biomedical applications, there has been a growing interest in how different aromatic walls,[94] length of the glycoluril backbone,[73] and various functionalized arms[92] affect the binding properties of these acyclic CB[n] containers.

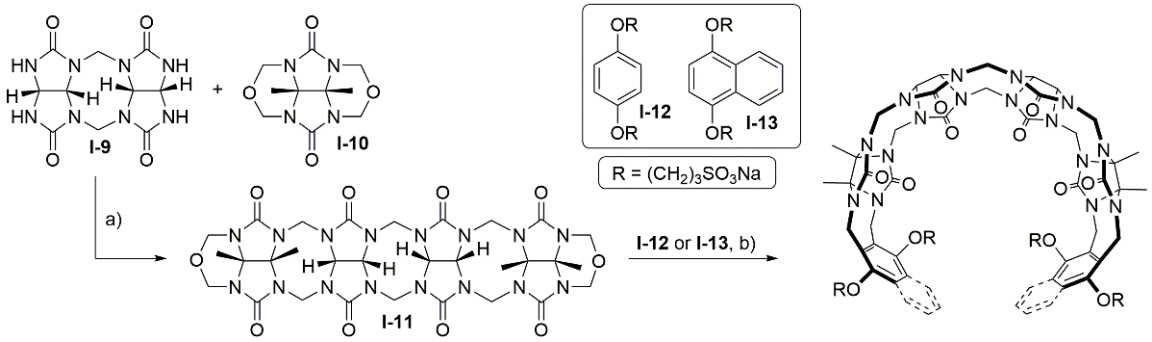

Scheme I-3. Building block synthesis of acyclic CB[*n*] hosts **Motor1** (*o*-xylylene walls) and **Motor2** (naphthalene walls) through glycoluril tetramer precursor (**I-11**). Conditions: a) $MeSO_3H$, 50 °C, 36%; b) **I-12** or **I-13**, Ac_2O, TFA, 70 °C, **Motor1**: 40%; **Motor2**: 30%. R = $(CH_2)_3SO_3Na$.

1.6 Self-Assembly Using Metal-Organic Coordination

Self-assembly has become a powerful strategy to spontaneously produce organized structures from an initial disordered state, a method routinely found in nature. This process involves molecules adopting defined arrangements directed by non-covalent interactions (i.e., ion-ion, ion-dipole, and π–π stacking) between complementary functional groups. In recent years, self-assembly utilizing metal-ligand coordination has been a growing technique to create larger, well-defined architectures.[5, 9-12, 95-100] The more predictable nature of the metal-ligand coordination sphere allows for greater control over the design of these two- and three-dimensional structures.

Discrete metal-organic assemblies are formed from metal-ligand, donor-acceptor interactions with bond energies between 15 – 50 kcal/mol. These connections are stronger than those of other non-covalent interactions (0.5 – 10 kcal/mol) but weaker than covalent bonds (60 – 120 kcal/mol) which allows for kinetic reversibility and self-correction.[5] Transition metals are routinely used as directing acceptor units with preferred coordination

geometries. Main group metals are less attractive due to their less predictable coordination preferences. When the metals are complexed with organic ligands, namely neutral N-donor ligands, highly charged complexes are formed which enhances aqueous solubility and their potential to act as hosts and containers.[101]

The use of well-defined building blocks leads to the formation of highly predictable, thermodynamically favored architectures (Figure I-5).[102] Since the self-assembly process is under thermodynamic control, the formation of discrete assemblies is able to overcome the kinetically unfavorable macrocyclization process at the expense of increased angle strain. Entropy also drives the assembly of these discrete structures to minimize the number of components used compared to larger polymeric species.[5]

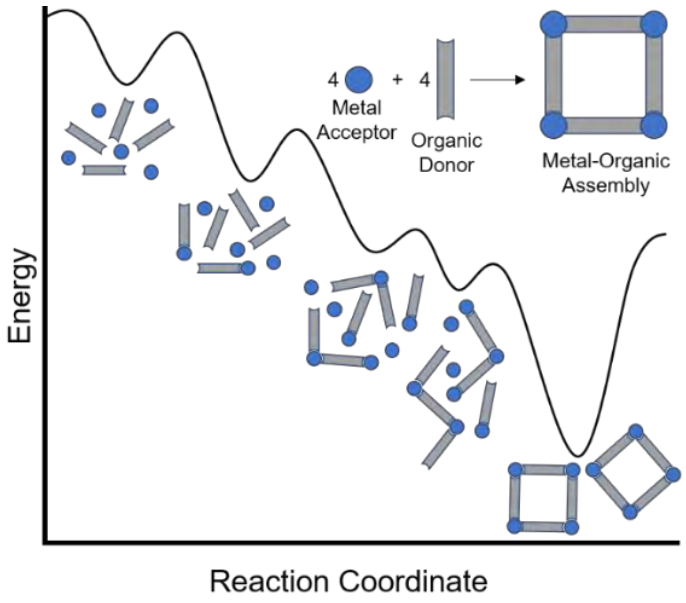

Figure I-5. Coordination-driven self-assembly. The system will reach the thermodynamically most stable product after going through various kinetic intermediates due to the reversibility of metal-ligand bonds.

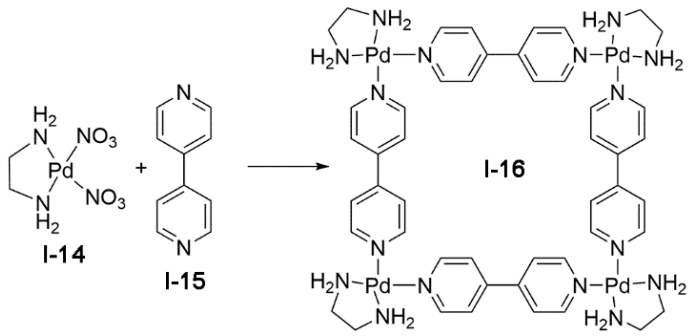

Scheme I-4. Directional-bonding coordination-driven self-assembly of the Fujita square.

Research by Stang,[103-105] Fujita,[106-108] Raymond,[109, 110] and others pioneered the high yielding strategy of directional-bonding coordination-driven self-assembly for the synthesis of supramolecular architectures with desired shape, size, and physical properties.[5, 9, 111] This approach uses structurally rigid precursors with predefined complementary angles at appropriate stoichiometric ratios. The organic donor ligands are usually highly directional bis(pyridine) units while metals are partially coordinatively unsaturated transition metals. Fujita used this approach to produce molecular squares consisting of linear (180°) bipyridine ligands with ethylenediamine palladium (or platinum) nitrate, containing coordination angle preferences of ligands to be 90° of each other (Scheme I-4).[106, 112] The rational design behind this strategy allowed scientists to create a wide variety of of 2- and 3- dimensional structures by using complementary building blocks (Figure I-6).[5] By adjusting the angle of one of the components, a variety of different shaped metal-organic structures can be formulated.

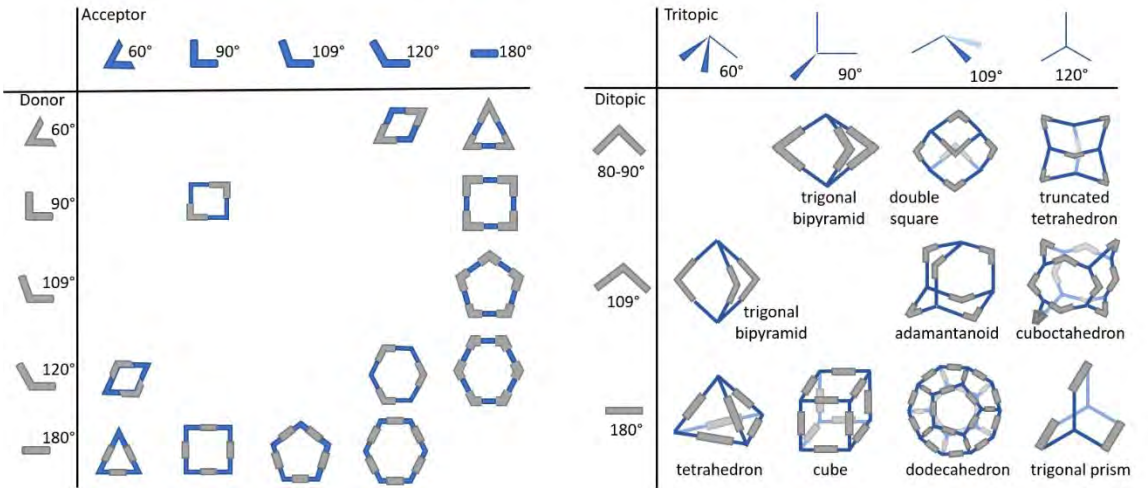

Figure I-6. The influence different angled building blocks play in the resultant self-assembled metal-organic architectures. a) Combination of building blocks to different shaped metal-organic polygons. b) Combination of di- and tritopic building blocks for metal-organic polyhedra. Adapted with permission from Chakrabarty, R.; Mukherjee, P. S.; Stang, P. J. *Chem. Rev.* **2011**, *111*, 6810-6918. Copyright 2011 American Chemical Society.

An alternative strategy to coordination-driven self-assembly of metal-organic structures is by using the symmetry-interaction approach.[113] In this method, multibranched chelating ligands with rigid backbones are mixed with uncapped metal centers. Chelation of ligands to metal centers provides a stronger overall binding strength compared to monodentate ligands. The symmetry and orientation of coordination drives the formation of the desired structure and helps deter formation of oligomers and polymers. Several discrete platonic solids, having faces consisting of only single regular polygons, such as tetrahedra have been synthesized using this method. The Nitschke group has published a large body of work utilizing this method to prepare iron based M_4L_6 tetrahedra through dynamic covalent and coordination bonds (Scheme I-5).[96, 114-119]

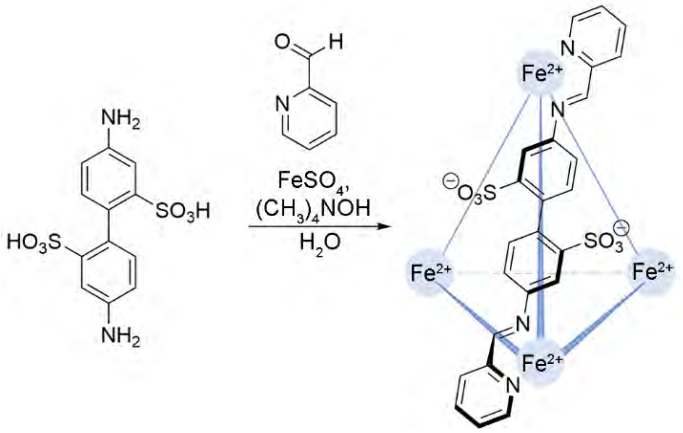

Scheme I-5. Coordination-driven self-assembly of iron based M_4L_6 tetrahedra cage synthesized by the Nitschke group utilizing the symmetry-interaction approach.

Several other conceptual methods for designing metal-organic 2- and 3-dimensional structures have been developed including paneling, weak-link, and dimetallic building block approaches.[113] Through these tactics, more complex systems including Archimedean solids – containing faces consisting of 2 or more regular polygons with precise control over geometry – have been synthesized. The defined shapes and cavities of these easily assembled architectures have led to their versatile use in several applications such as catalysis, sensing, and separations.[10-12, 96, 97, 120-125] A strategic combination of metal-organic architectures with other functional systems could yield multi-component systems with great potential as smart materials and supramolecular devices.

1.7 Incorporation of Molecular Containers into Metal-Organic Assemblies

Imitating the ability of nature to form highly sophisticated systems, such as cells which are comprised of organelles functioning synchronously, has been a major goal in supramolecular chemistry. One way to approach this goal is through the combination of smaller substructures producing multi-component systems. Synthetic chemists have come

closer to reaching this goal with the development of molecular switches and motors. In 2016, Jean-Pierre Sauvage,[126] Sir J. Fraser Stoddart,[127] and Bernard L. Feringa[128] were awarded the Nobel prize in chemistry for their design and synthesis of molecular machines. These systems consist of smaller subunits which function together with the capability of performing work. While these synthetic machines are still in their infancy, research continues to progress towards more complex systems with the potential to perform more difficult tasks such as molecular cars[129] and peptide synthesizers.[130]

One area of research where multi-component systems could improve efficacy is within drug delivery systems. The merger of different subunits could lead to structures which display stimuli responsive release of guests, the ability to target drugs to specific tissues, interesting photophysical properties for sensing, and improved solubilities. CB[n] hold great promise as an additional component due to their ability to improve the bioavailability of drugs inside their cavities. Incorporating these containers into larger, multi-component systems, allows for the further enhancement with new desirable properties.

Nanoparticle drug delivery is a technique seen prominently throughout the literature.[131-135] These materials are comparable in size to biomolecules and organelles, which helps to facilitate the drug delivery process. This size range causes longer circulation in the blood stream, better uptake by cells, and higher accumulation in cancer cells due to the enhanced permeability and retention (EPR) effect.[136-138] One issue that arises with this type of technology is the regulation of the size distribution during nanoparticle formation. Using metal-organic coordination-driven self-assembly might be a way to resolve this

dilemma to allow for better control over the structure including shape, distribution of functional groups, and particle size.

In 2016, the Isaacs group developed a metal-organic polyhedron (MOP) capped with CB[n]s (Scheme I-6) for drug delivery purposes.[139] They found that a doxorubicin prodrug which displays anti-cancer activity could be loaded onto the MOP through hetero-ternary complex formation with non-covalently attached CB[8]. This doxorubicin MOP was found to be 10-fold more cytotoxic towards HeLa cancer cells than equimolar quantities of the pro-drug alone. This enhanced cytotoxicity can be traced to the improved cellular uptake of the larger system, illustrating the potency of this new platform for drug delivery. The plug-and-play nature of this type of MOP provides an effective strategy for incorporating additional functionalities,[140] such as targeting groups and dye molecules for theranostic applications.

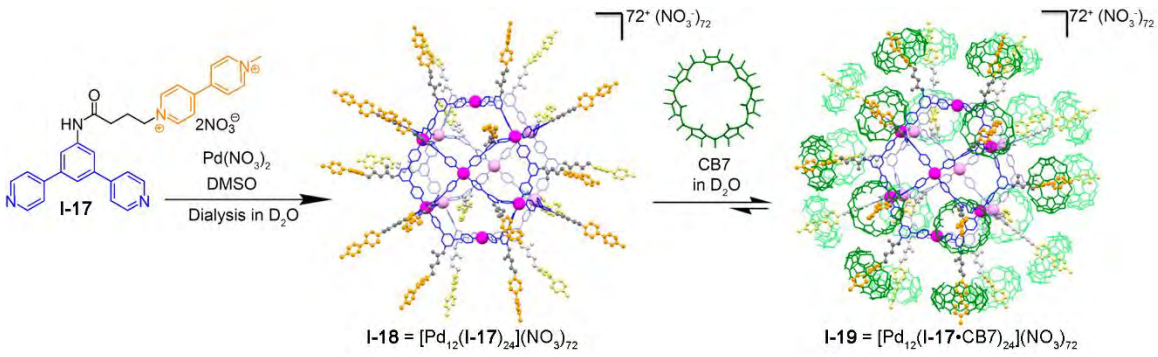

Scheme I-6. Self-assembly of MOP **I-18** in DMSO and noncovalent capping with CB[7] to yield MOP **I-19** in D_2O. Adapted with permission from Samanta, S.; Mondelet, D.; Briken, V.; Isaacs, L. *J. Am. Chem. Soc.* **2016**, *138*, 14488-14496. Copyright 2016 American Chemical Society.

1.8 Summary and Conclusions

Supramolecular chemistry studies the use of non-covalent interactions to assemble simple molecular precursors into intricate structures based on complexation between complementary functional groups. The development of molecular containers, which act as chemical receptors, is a major area in supramolecular chemistry due to their ability to manipulate the pK_a, conformation, solubility, and optical properties of a guest through cavity binding. CB[n] are a highly utilized family of molecular containers due to their high selectivity and binding affinity towards alkyl diammonium compounds. The CB[n] family has been used in various applications such as sensing, separation techniques, and in the development of molecular machines. However, the inherently poor water solubility of these cyclic members as well as the difficulty to functionalize has led to the synthesis of other glycoluril-based hosts, such as acyclic CB[n] members. These acyclic members have flexible backbones and functionalized aromatic walls allowing for the encapsulation of a wider range of guests and well as a greater ease to of chemical modification. Sulfonated arms increase the water solubility permitting for their use as solubilizers of insoluble active pharmaceutical ingredients and in drug sequestration applications. Ongoing research is being conducted to see how functionalization of different subunits (i.e., length of backbone and functionalized walls and arms) affect the binding properties of these acyclic containers. In chapter 2, I will discuss the work I have done in extending the glycoluril backbone and how it affects the ability of the container to bind to common CB[n] guest molecules.

Subsequently, in Chapters 3 and 4 I will describe the development of metal-organic assemblies with mechanically interlocked CB[n] units. Incorporation of CB[n]s into a multi-component system is an alternative way to create advanced materials. Using the

supramolecular concept of metal-ligand coordination-driven self-assembly, highly organized structures which feature mechanically interlocked molecular containers were built with high specificity. These nano-sized materials have potential as drug delivery vehicles due to their comparable size to biomolecules and organelles. Hopefully the introduction of CB[n] into MOPs might allow for higher payloads, stimuli-responsive release of drugs, and unique photophysical properties for biosensing.

Chapter 2: Conformationally Mobile Acyclic Cucurbit[n]uril-Type Receptors Derived from an S-shaped Methylene Bridged Glycoluril Pentamer

The work presented in the chapter was taken from Brady, K.G.; Gilberg, L.; Sigwalt, D.; Bistany-Riebman, J.; Murkli, S.; Klemm, J.; Kulhánek, P.; Šindelář, V.; Isaacs, L. *Supramol. Chem.* **2020**, *32*, 479-494.

K.G.B. was responsible for NMR binding studies of **P1** and **P2** with common CB[n] binding guests, 1D NOE studies on hosts and **II-3a**, and job plots. L.G. developed the synthesis of **P1** and **P2** hosts. D.S. preformed solubilization studies with insoluble drug compounds. J. B-R. helped synthesize **P1** and **P2** and attempted ITC studies with common CB[n] binding guests. S.M. and J.K. preformed ITC binding studies with **Tet2** and common CB[n] binding guests. P.K. did the computational studies.

2.1 Introduction

Over the past two decades, there have been great advances in the preparation of members of the cucurbit[n]uril (n = 5, 6, 7, 8, 10, 13-15, Figure II-1) family of molecular container compounds.[46-48, 141, 142] The defining features of CB[n] molecular containers are their two symmetry equivalent ureidyl carbonyl portals which are highly electrostatically negative and their central hydrophobic cavity.[45, 54, 56] Given these structural features, CB[n] are excellent hosts for hydrophobic (di)ammonium ions which often bind with K_a values in the $10^6 – 10^9$ M^{-1} range and in select cases with K_a values exceeding 10^{12} M^{-1} in aqueous solution.[50-52, 143, 144] The high affinity of macrocyclic CB[n]•guest complexes has been

traced to the presence of high energy waters in the cavity of CB[n] that are released upon complexation.[55, 145, 146] CB[n] hosts are also quite selective and large differences in K_a values are seen upon application of suitable stimuli (e.g. pH, electrochemical, photochemical).[63, 147-149] Accordingly, CB[n] have emerged as an outstanding platform for the development of functional supramolecular systems including chemical sensors, molecular machines, supramolecular polymers and materials, and drug delivery systems.[19, 39, 59, 63, 150] In recent years, the development of methods to prepare per- and mono-functionalized CB[n] hosts have allowed their strategic merger with polymers, solid phases, surfaces, nanoparticles, targeting ligands, antibodies, and fluorophores which has further extended their applicability in the chemical, biological, and biomedical arenas.[140, 151-160]

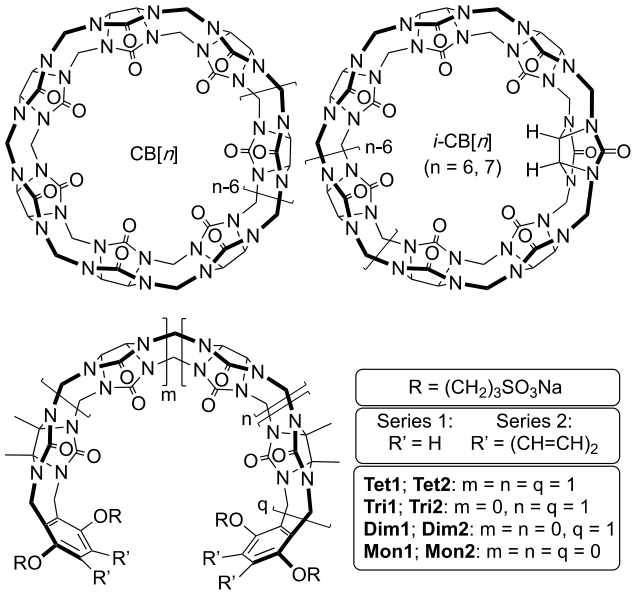

Figure II-1. Chemical structures of CB[*n*], *i*-CB[*n*] with one inverted glycoluril unit, and acyclic CB[*n*]-type receptors.

Over the years, the Isaacs and Šindelář groups have been very interested in the mechanism of CB[n] formation, especially the formation of the S-shaped and C-shaped diastereomeric methylene bridged glycoluril dimers.[161-165] The S-shaped forms are kinetic products whereas the C-shaped forms are the thermodynamic products which eventually lead to macrocyclic CB[n] by cyclooligomerization.[166] Inverted CB[n] (*i*-CB[n], Figure II-1) have also been isolated;[167] *i*-CB[n] feature a pair of methine H-atoms pointing into the CB[n] cavity and possess a pair of adjacent S-shaped units. The binding affinity of *i*-CB[n] (n = 6, 7) toward typical hydrophobic ammonium ions are weaker than the corresponding diastereomeric CB[n].[167] More recently, we have described the preparation of a class of receptors that feature a central glycoluril oligomer that is capped with two terminal aromatic walls (e.g. **Tet1** and **Tet2**, Figure II-1).[83, 168] By virtue of their glycoluril oligomer backbone, these receptors are preorganized into a C-shape and retain the essential binding features of the CB[n] family (e.g. tight and selective recognition of hydrophobic (di)cations). Accordingly, these hosts are referred to as acyclic CB[n]-type receptors. Numerous variants have been created, by us and others, that differ in the nature of the central glycoluril oligomer, the terminal aromatic walls, and the appended solubilizing groups.[83-88] Of the acyclic CB[n] based on glycoluril tetramer prepared to date, **Tet1** and **Tet2** have been used extensively because of their high binding affinity which has enabled their function as solubilizing excipients for insoluble drugs and as *in vivo* sequestration agents for neuromuscular blockers (e.g. rocuronium and vecuronium)[89, 90, 169] and drugs of abuse such as methamphetamine.[91] Host **Tet1** has displayed excellent biocompatibility according to the usual *in vitro* (e.g. cell death and metabolic activity, mutagenicity, lack of hERG ion channel inhibition) and *in vivo* (e.g. maximum tolerated dose, blood gases, blood

pH, mean arterial pressure) assays.[83] The group of Prof. Ruibing Wang has used macrocyclic CB[7] as a sequestering agent in related applications.[170] Previously, we have prepared and studied the molecular recognition properties of analogues of **Tet1** and **Tet2** based on central glycoluril monomer, dimer, and trimer (**Mon1** – **Tri1** and **Mon2** – **Tri2**).[73] We found that **Mon1** – **Tri1** and **Mon2** – **Tri2** do not function well as solubilizing agents for insoluble drugs due to their smaller cavities which result in lower binding constants. Accordingly, we wondered whether acyclic CB[n]-type receptors that feature an extended glycoluril oligomer (e.g. pentamer) might display higher binding affinity toward their guests than **Tet1** and **Tet2** and therefore function as superior sequestration agents. In this chapter, we describe the synthesis of pentamer derived acyclic CB[n] hosts **P1** and **P2** and investigations of their molecular recognition properties.

2.2 Results and Discussion

This results and discussion section is organized as follows. First, we describe the design, synthesis, and characterization of hosts **P1** and **P2**. Second, we measure the solubility of **P1** and **P2** in water. Third, we performed ^{1}H NMR titrations to determine the K_a values of **P1** and **P2** toward guests **II-6** – **II-11**. Finally, we discuss the trends in K_a values of **P1** and **P2** toward their guests using **Tet1** and **Tet2** as comparators and rationalize the observed changes based on molecular modelling studies.

2.2.1 Goal of the Study

The initial goal of this study was to determine the impact of the extension of the glycoluril oligomer backbone from tetramer (e.g. **Tet1** and **Tet2**) to pentamer on the molecular recognition properties toward typical cationic guests. In the process, however,

we uncovered that the synthesized pentamer hosts **P1** and **P2** feature two S-shaped units that endow them with conformational flexibility. Accordingly, we expanded our study to include the influence of conformational isomerism on guest binding.

2.2.2 Synthesis and Characterization of Pentamer Bis(Cyclic Ether) II-3a and Hosts P1 and P2

To prepare acyclic CB[n]-type hosts derived from glycoluril pentamer, we took advantage of a building block approach that relies on the double electrophilic aromatic substitution reaction between a central glycoluril oligomer and a dialkoxy aromatic wall. The condensation of glycoluril (**II-1**) with dimethylglycoluril bis(cyclic ether) (**II-2**) which was conducted at lower temperature (90% aq. $MeSO_3H$, 8-12 ˚C) in order to control the oligomerization process gave a complex crude reaction mixture from which we could isolate a single methylene bridged glycoluril pentamer (**II-3**) in gram scale batches (Scheme II-1). The ES-MS spectrum of **II-3** confirms its molecular formula ($C_{38}H_{46}N_{20}O_{12}$) and that it is composed of two equivalents of **II-1** and three equivalents of **II-2**. Because the substituents on the convex face of adjacent glycoluril rings may point in the same or opposite directions (e.g. C-shaped or S-shaped units), there are 10 possible diastereomers of **II-3**. The four diastereomers (**II-3a** – **II-3d**) depicted in Scheme II-1 are C_{2v}-symmetric whereas the six diastereomers that are not shown are C_s-symmetric. The ^{1}H NMR spectrum of **II-3** recorded in DMSO-d_6 shows three distinct resonances for the methyl groups (H_k – H_m), three pairs of doublets for the diastereotopic methylene bridges (H_c – H_h), and a pair of doublets for the glycoluril methines (H_i and H_j). Similarly, the ^{13}C NMR spectrum of **II-3** in DMSO-d_6 displays a total of 14 resonances which is only consistent with a C_{2v}-symmetric structure. Compound **II-3c** corresponds to the desired

glycoluril pentamer that consists of all C-shaped subunits. In contrast, **II-3a** and **II-3b** contain 2 S-shaped and 2 C-shaped segments whereas **II-3d** possesses 4 S-shaped segments. Given the known thermodynamic preference for the C-shaped diastereomers,[161-163, 165] we initially presumed that we had isolated **II-3c** and subsequently proceeded to create the pentamer derived hosts. It was only later, after observing the poor molecular recognition properties of **P1** and **P2** that we discovered that in reality we had isolated **II-3a**. The relative stereochemistry of **II-3a**, **P1**, and **P2** were fully assigned by a combination of ^{1}H, ^{13}C, selective 1D NOE, and 2D NMR experiments (Supporting Information). In brief, once the ^{1}H NMR has been fully assigned, we can use the selective 1D NOE experiments to step from the cyclic ether termini of **II-3a** toward the center determining relative stereochemistry at each step along the way. As shown in Figure II-2, H_c, H_d, and $(CH_3)_l$ show NOEs when $(CH_3)_k$ is irradiated. The resonance for $(CH_3)_l$ shows NOEs to H_e, H_f, and most importantly H_i which establishes the C-shaped relative stereochemistry of the terminal pairs of glycolurils. Proton H_i is coupled to and shows a NOE to the adjacent H_j. Irradiation of H_j shows a main NOE to H_j and very small NOEs to H_g and H_h but does not show a NOE to $(CH_3)_m$ which establishes that the central glycoluril is connected to its neighbors by S-shaped stereochemistry. The identity of H_g and H_h as adjacent to the central glycoluril was confirmed by HMBC cross peaks from H_g and H_h to the central $O{=}C_y$ which is a half-intensity resonance. From our previous studies of methylene bridged glycoluril dimers we know that the CH_2-bridges involved in S-shaped connections have smaller $^{3}J_{HCH}$ coupling constants that those involved in C-shaped connections (≈13.6 Hz vs. ≈16.0 Hz).[161-163, 165, 171] The observed coupling constant between H_g and H_h ($^{3}J_{HCH}$ = 13.7 Hz) of **II-3a** further supports the depicted diastereomer.

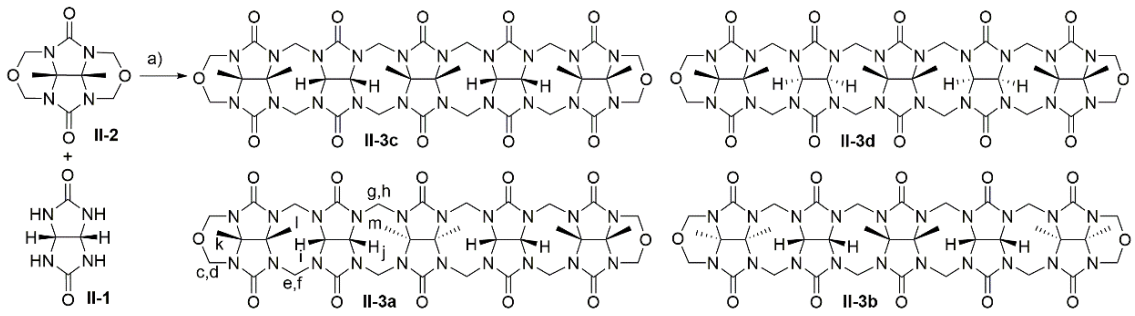

Scheme II-1. Synthesis of methylene bridged glycoluril pentamer **II-3a**. Compounds **II-3b** – **II-3d** were not isolated. Conditions: a) 90% aq. $MeSO_3H$, 8-12 ˚C (2 h) then RT (2 h), 5%.

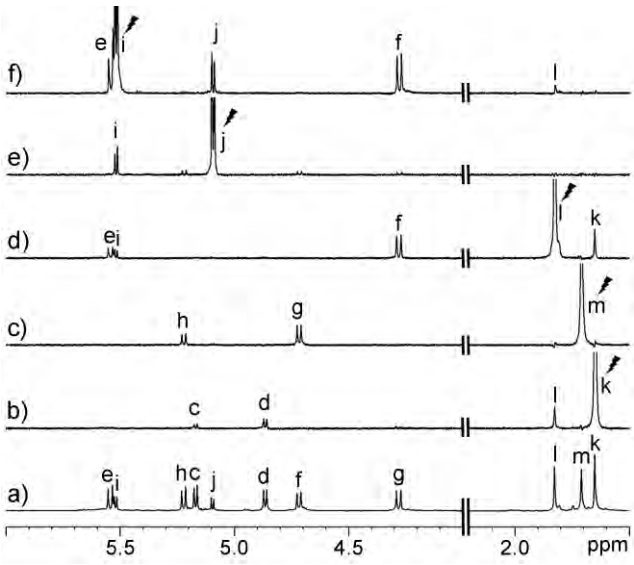

Figure II-2. NMR spectra recorded (800 MHz, 30 °C, DMSO-d_6) for **II-3a**: a) ^{1}H NMR spectrum. Selective 1D NOE recorded for **II-3a** with irradiation of: b) H_k, c) H_m, d) H_l, e) H_j, and f) H_i.

The sulfonated dialkoxy benzene and dialkoxy naphthalene sidewalls (**II-4** and **II-5**) required to synthesize hosts **P1** and **P2** were available from previous studies.[82] As shown in Scheme II-2, the attachment of walls **II-4** and **II-5** to pentamer **II-3a** was conducted under acidic conditions (TFA, 75 ˚C) in the presence of Ac_2O to increase reactivity[172] to

deliver **P1** (22%) and **P2** (27%) after purification by trituration with hot water (**P1**) and by precipitation from water (**P2**). Hosts **P1** and **P2** were characterized by spectroscopic means. The high resolution electrospray ionization mass spectra for **P1** displayed an ion at *m/z* 547.8031 ($[M-4Na+H]^{3-}$, calculated for $C_{62}H_{75}N_{20}O_{26}S_4$ 547.8020) whereas **P2** displayed an ion at *m/z* 872.2222 ($[M-4Na+2H]^{2-}$, calculated for $C_{70}H_{80}N_{20}O_{26}S_4$ 872.2223) which establish the molecular formulas required of **P1** and **P2**. Figure II-3 shows the ^{1}H NMR spectra recorded for **P1** and **P2** in DMSO-d_6. As expected, host **P1** exhibits a singlet for the four symmetry equivalent H_a protons, three resonances for the methyl groups (H_k, H_l, H_m), a pair of doublets for the equatorial methine protons (H_i and H_j), three pairs of doublets for the bridging methylene groups (H_c – H_h) in the required 4:4:4:4:4:4 ratio, and three resonances for the $O(CH_2)_3SO_3Na$ sidearms expected for a C_{2v}-symmetric structure (Figure II-3a). Figure II-3b shows the fully assigned ^{1}H NMR spectrum for **P2** which displays a similar pattern of resonances in accord with C_{2v}-symmetry. The ^{13}C NMR spectra recorded for **P1** (**P2**) display 20 (22) resonances (Supporting Information, Figures II-S10 and II-S21) in accord with the 20 (22) resonances expected based on C_{2v}-symmetry. As described above for **3a**, the relative stereochemistry of the glycoluril units of **P1** and **P2** was established based on the combined inference of ^{1}H, ^{13}C, COSY, HSQC, HMBC, and NOE experiments (Supporting Information). After having firmly established the constitutions and relative stereochemistry of **P1** and **P2** we moved on to determine their inherent solubility in aqueous solution. For this purpose, samples of **P1** and **P2** were weighed on a microbalance and then dissolved at room temperature in the smallest amount of D_2O possible with the aid of sonication; obtained solubility of **P1** (≈ 9 mM) and **P2** (≈11

mM) was then calculated in the standard way using the known mass, molecular weight, and volume.

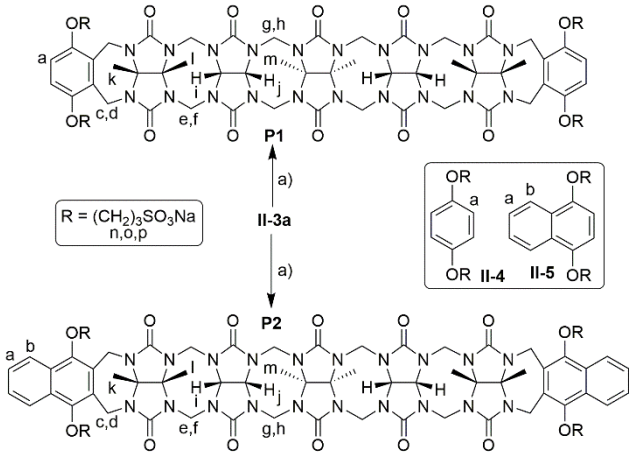

Scheme II-2. Synthesis of acyclic CB[*n*]-type receptors **P1** and **P2**. Conditions: a) **II-4** or **II-5**, Ac_2O, TFA, 75 °C, **P1**: 22%; **P2**: 27%.

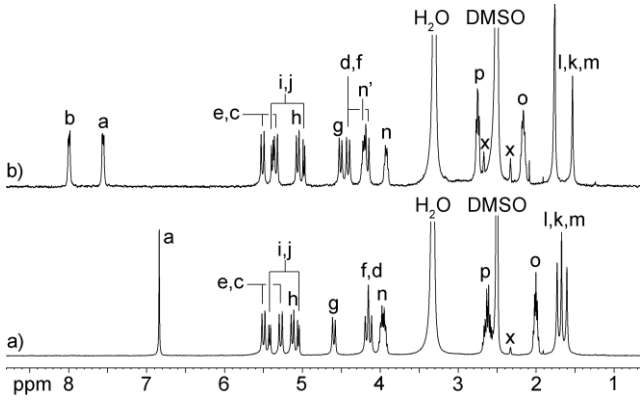

Figure II-33. ^{1}H NMR spectra recorded (400 MHz, DMSO-d_6, RT) for: a) **P1**, and b) **P2**. x = ^{13}C satellite.

2.2.3 Conformational Properties of Pentamer Derived Hosts P1 and P2

The chemical structures of **II-3a** and hosts **P1** and **P2** contain two S-shaped connections between adjacent glycolurils (e.g. the substituents at the equator of the glycoluril units are on opposite sides of the oligomer chain). From previous work, we know that each S-shaped segment can adopt two different conformations where the substituents on the convex face of one glycoluril point toward the concavity of the other glycoluril and vice versa.[161-163, 165, 171] Accordingly, there are three distinct conformations for compounds **II-3a**, **P1**, and **P2**; Figure II-4 depicts the three conformers (folds) of **P1** which we refer to as **P1**-F1, **P1**-F2, and **P1**-F3. From previous work, we also know that symmetrical S-shaped methylene bridged glycoluril dimers bearing H-atoms[165] or CO_2Et groups[161-163, 171] on their convex face undergo fast conformational exchange processes between the two chemically equivalent and isoenergetic S-shaped conformations such that the H-atoms on the bridging CH_2-groups are rendered chemically equivalent and appear as a singlet in the ^{1}H NMR spectrum. Finally, the sharp ^{1}H NMR spectra observed (Figure II-3) for **P1** and **P2** display the number of resonances expected for C_{2v}-symmetric **P1**-F1 or **P1**-F3 but not for C_s-symmetric **P1**-F2. This result indicates that **P1** (**P2**) is either fixed in the **P1**-F1 or **P1**-F3 (**P2**-F1 or **P2**-F3) folded form or is undergoing fast conversion between all three conformers on the chemical shift timescale. Experimentally, no significant changes in the ^{1}H NMR of **P2** were observed upon cooling to 10 °C in D_2O. It should be noted that **P1**-F1 features two terminal molecular clip-like clefts[173-175] shaped by one aromatic wall, whereas **P1**-F3 possesses a potential cavity that is reminiscent of *i*-CB[n]. The flexibility of sidearms in **P1**-F3 does not forbid induced cavity formation upon guest binding.

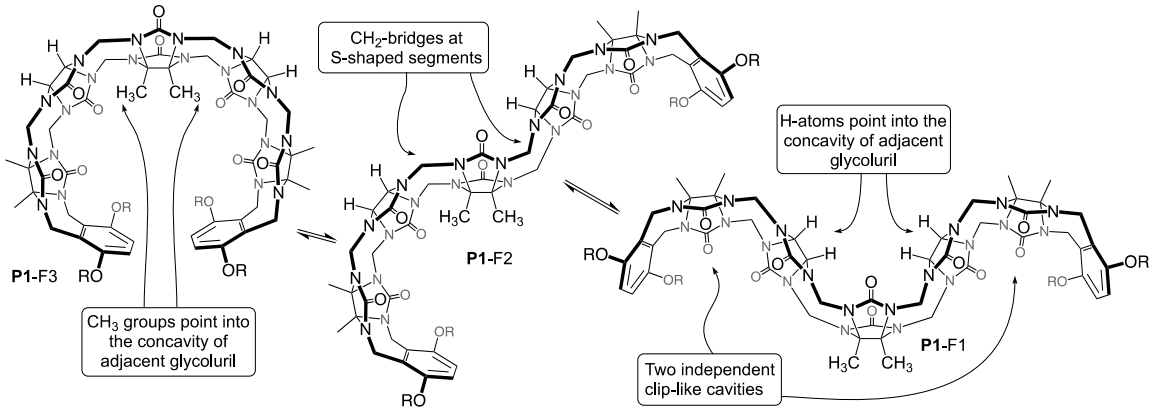

Figure II-4. Representations of the different conformational isomers of **P1** that occur by flipping at the S-shaped methylene bridges.

To gain insights into the relative populations of the different conformational states, computational methods using DFT were employed. To decipher the structural features of the methylene bridged glycoluril pentamer containing an inverted glycoluril unit, model systems comprising the glycoluril trimers **TriMe** and **TriH** (Figure II-5) were investigated. Based on our benchmarking of computational methods (Supporting Information, Tables II-S7, II-S8, II-S9, II-S10, II-S11), we employed the low-cost method B97-3c for geometry optimization and the accurate hybrid DFT functional PBE0 corrected for dispersion interactions (D3BJ) for final energy consideration. Both geometry and final energy calculations were performed in an implicit water environment provided by the SMD model. This model offers both polar and non-polar contributions to the solvation energies, and it is thus suitable for consideration of thermochemistry. The relative conformer stabilities obtained at the PBE0-D3BJ-SMD/def2-TZVPP//B97-3c-SMD level of theory are given in Table II-1 (Supporting Information, Tables II-S12 and II-S13 contain detailed data). For **TriH**, the three forms were of nearly equal relative energy (**TriH**-F3: 0.0 kcal mol^{-1}; **TriH**-

F2: 0.2 kcal mol^{-1}; **TriH**-F1: 0.6 kcal mol^{-1}) as expected based on literature precedent for the corresponding glycoluril dimers. In sharp contrast, for **TriMe**, the three folded forms are predicted to be of very different energies (**TriMe**-F3: 5.1 kcal mol^{-1}; **TriMe**-F2: 3.5 kcal mol^{-1}; **TriMe**-F1: 0.0 kcal mol^{-1}). The lower stabilities of the F2 and F3 conformers of **TriMe** is caused by solvent and internal contributions, but the data obtained in vacuum (Supporting Information) indicate that steric factors also make a significant contribution. We believe that the steric bulk of the methyl groups on the central glycoluril of **TriMe** effectively dictates that the molecule folds into the **TriMe**-F1 form to avoid placing the Me-groups into the concavity of the adjacent glycoluril rings. Several aspects of the geometries of the different folded structures of **TriMe** and **TriH** are noteworthy. For example, a comparison of the terminal $H_3C{\bullet\bullet\bullet}CH_3$ distance d_{MM} for **TriH**-F1 is 9.231 Å, whereas the corresponding distance for **TriMe**-F1 is 8.978 Å. The shorter d_{MM} distance in **TriMe** arises from the increased curvature of the glycoluril trimer due to the presence of the methyl groups on the concave face. In contrast, the $H_3C{\bullet\bullet\bullet}CH_3$ distance for **TriH**-F3 is 9.724 Å, whereas the corresponding length for **TriMe**-F3 is increased to 13.841 Å. Rather than deforming by changing the curvature of the glycoluril trimer as observed for F1, the F3 folded form of **TriMe** releases the tension by an end-to-end twisting of the glycoluril trimer unit. This twisting was observed computationally for all structures. We quantified the twist by two dihedral angles, τ_1 and τ_2, describing the local (on the inverted glycoluril) and the global twist of glycoluril ribbon (Supporting Information, Tables II-S11 and II-S13; τ_2 is defined in Figure II-5a). Due to the aforementioned steric factors, the global twist was found to be more pronounced for **TriMe**-F3 ($\tau_2 = 57.7°$) than for **TriH**-F3 ($\tau_2 = 0.2°$).

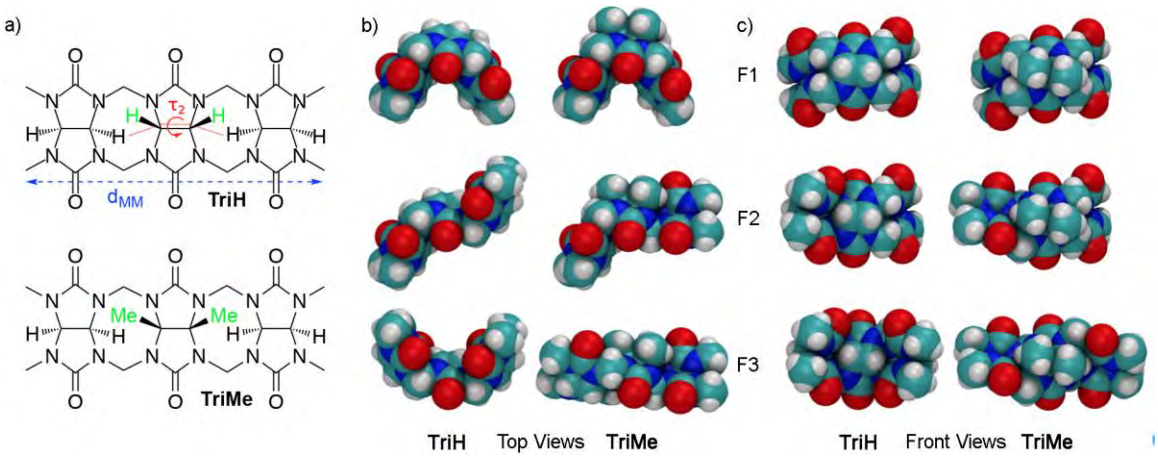

Figure II-5. a) Chemical structures of **TriMe** and **TriH** with the definition of the terminal $H_3C\bullet\bullet\bullet CH_3$ distance d_{MM} and the global twist of glycoluril ribbon represented by a pseudo-dihedral angle τ_2. b) Top and c) front views of the geometries of the F1, F2, F3 conformers optimized at the B97-3c level of theory in implicit water (the back view is available in Figure II-S102).

Table II-1. Relative conformer stabilities (E_r) for the investigated systems obtained at the PBE0-D3BJ/def2-TZVPP//B97-3c level of theory in the SMD model of implicit water. The relative energies E_r include contributions from the potential energy, as well as polar and non-polar solvation energies. Due to computational complexity, thermal contributions (vibration, rotation, and translation energies and entropies) were neglected. For each system, the most stable conformer has zero energy. All values are in kcal mol^{-1}.

	TriH	**TriMe**	**P1'**	**P2'**	**P1'·8**	**P2'·8**
Conf	**E_r**	**E_r**	**E_r**	**E_r**	**E_r**	**E_r**
F1	0.57	0.00	0.00	2.34	1.49	0.00
F2	0.22	3.45	3.05	4.11	2.87	2.98
F3	0.00	5.11	4.01	0.00	0.00	1.36

The use of glycoluril substituents as a conformational control element in this context is new.[176, 177] Our intention is to use **P1** or **P2** as a host for alkylammonium ions via its F3 folded form, which will require us to pay an energetic penalty to bias the conformational ensemble toward the **P1**-F3 or **P2**-F3 folded forms. Of course, the energetics of the F1 – F3 folded forms of **P1** and **P2** will be modified by the presence of the additional glycolurils and terminal aromatic rings which may bias the conformational ensemble toward the F3 form due to π–π interactions. To get at these questions, computational methods were employed. We used simplified models of **P1** and **P2** with removed solubilizing groups; these models are labeled as **P1'** and **P2'**. By this simplification, we tried to avoid possible problems with a not well-defined conformational preference of the flanking $O(CH_2)_3SO_3^-$ groups and the presence of negative charge (-4), which could be problematic for reliable DFT quantum chemical calculations. The computations of **P1'** and **P2'** were performed with the same methodology used for **TriMe** and **TriH** and the calculated relative conformational stabilities of **P1'** and **P2'** are provided in Table II-1. In the case of **P1'**, calculations revealed conformational preferences very similar to **TriMe**. This indicates that the conformational preferences are mainly dictated by the presence of the double S-shaped central glycoluril rather than the aromatic sidewalls. Interactions between the aromatic side walls of **P1'** and the central methyl groups (**P1'**-F2) or with the second aromatic sidewall (π–π stacking, **P1'**-F3) were observed, but these interactions are not large enough to counterbalance other effects such as solvation (see Table II-S15 for energy decomposition). In the case of **P2'**, the difference between the F1 and F2 (+1.8 kcal mol^{-1}) forms is similar to that of **P1'** (+3.1 kcal mol^{-1}) or TriMe (+3.5 kcal mol^{-1}), but the **P2'**-F3 form is the lowest energy conformational form.

Figure II-6 shows the minimized geometries of the **P2'**-F1, **P2'**-F2, and **P2'**-F3 conformations of host **P2'**; an analogous figure is given for **P1'** in the Supporting Information (Figure II-S103). In contrast to the idealized C_{2v}-symmetric line bond structures shown above in Figure II-4, we observe more compact conformations for **P2'**-F2 and **P2'**-F3, presumably due to the van der Waals interactions between the central Me-groups of **P2'** and the aromatic sidewall(s) in these conformations. For **P2'**-F3 (Figure II-6a), we additionally observe offset π–π interactions between the faces of the naphthalene sidewalls. These interactions are responsible for the overall preference for F3 (0.0 kcal mol^{-1}) over F2 (4.1 kcal mol^{-1}) and F1 (2.3 kcal mol^{-1}). For guest binding to occur within **P2'**-F3, the disruption of these intramolecular non-covalent interactions must be counterbalanced by stronger host•guest non-covalent interactions. For critical assessment of the obtained results two additional contributions must be mentioned which are not available in our calculations. The first is the absence of thermal motions (mainly entropy) in the calculated energies. It can be expected that F3 will have lower entropy than F1 because its compact structure will limit movements of its aromatic walls (Figure II-S107 shows the dynamic behavior of aromatic walls in **P2•P2** dimer). This effect will decrease the stability of the F3 conformer relative to F1. Second, destabilizing electrostatic interactions between the negatively charged solubilizing groups would be expected to be larger for **P2**-F3 than for **P2**-F1.

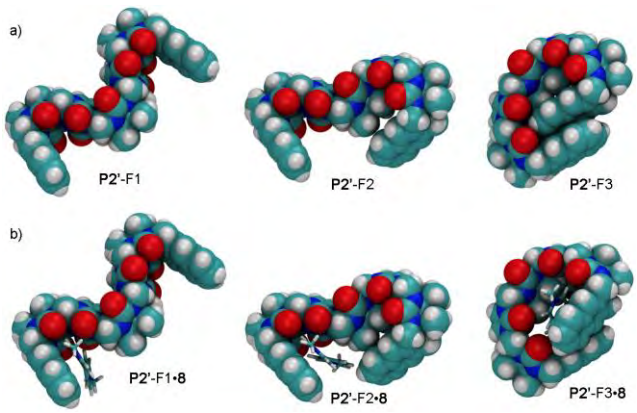

Figure II-6. Structures of a) **P2'** (top line) and b) **P2'•II-8** (bottom line) in the F1, F2, and F3 folds obtained at the B97-3c level of theory in implicit water (see Figures II-S103 - II-S106 for other views and structures for **P1'** and **P1'•II-8**).

2.2.4 Self-Association Studies Performed for P1 and P2

As a prelude to the planned host•guest binding studies, we investigated the self-association properties of **P1** and **P2** to ensure that the measured K_a values would not be influenced by host self-association.[17] Accordingly, we prepared solutions of **P1** and **P2** at their maximal solubility in D_2O and measured their ^1H NMR spectra as a function of [**P1**] or [**P2**] down to 0.12 mM. We did not observe any significant changes in the chemical shifts for **P1** over the 9 mM – 0.12 mM concentration range which indicates that **P1** does not undergo significant self-association (Supporting Information, Figure II-S24). Figure II-7a shows the chemical shift of H_m as a function of [**P2**]. We fitted the change in chemical shift to a two-fold self-association model[178, 179] which allowed us to extract the self-association constant of **P2** (K_s = 189 ± 27 M^{-1}). Because chemical exchange is fast on the NMR time scale, it is not possible to obtain precise information about the geometry of **P2•P2** from the NMR experiments. Accordingly, we performed molecular modelling; Figure II-7b shows a representative snapshot of the **P2**-F1•**P2**-F1 dimer from a 1 μs long

molecular dynamics simulation which is consistent with the observed upfield shifting of the H_a and H_b resonances of the aromatic sidewall and the resonance for $(CH_3)_m$ upon dimerization. The geometry of **P2•P2** depicted in Figure II-7b is reminiscent of the geometry of dimeric molecular clips prepared by the Nolte and Isaacs groups which feature the aromatic sidewall of one molecule penetrating into the cleft of the opposing molecule and vice versa.[173-175] We also attempted to model the dimer from the **P2**-F2 form. However, soon after the start, both flanking side arms underwent conformation change into F1 (see Figure II-S108).

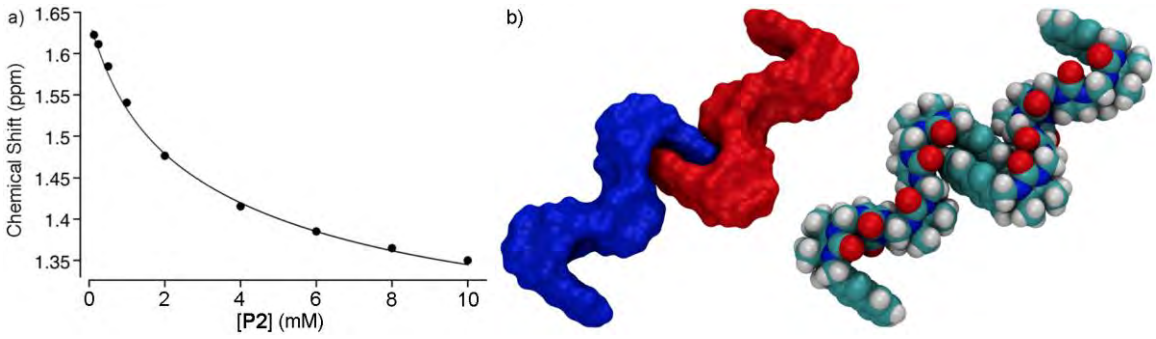

Figure II-7. a) Plot of the chemical shift of H_m of **P2** as a function of [**P2**]. The solid line represents the best non-linear fitting of the data to a two-fold self-association model (K_s = 189 ± 27 M^{-1}). b) Two representations of the selected snapshot from MD simulation of **P2**-F1•**P2**-F1. Solubilizing groups were removed for clarity. Ensembles of overlapping snapshots for **P2**-F1•**P2**-F1 and **P2**-F2•**P2**-F2, including solubilizing groups, are provided in Figures II-S107 and II-S108.

2.2.5 Attempted Use of P1 and P2 as Solubilizing Excipients for Insoluble Drugs

Given our previous work on the use of acyclic CB[n]-type receptors as solubilizing excipients for insoluble drugs,[180] we initially tested the solubilization abilities of **P1** and

P2 toward a small panel of insoluble drugs (paclitaxel, fenofibrate, itraconazole, tamoxifen and ethynylestradiol, Figure II-8). For this purpose, we separately prepared 7 mM solutions of **P1** and **P2** in 20 mM sodium phosphate buffered D_2O and dispensed the solution into a series of vials to which an excess of insoluble drug was added. After mixing overnight (16 h), the insolubles were removed by filtration through a 0.45 μm polyethersulfone membrane filter and the solution and a known volume of a solution of trimesic acid (1 mM) was transferred to an NMR tube for analysis. No drug solubilization was detected by ^{1}H NMR indicating that **P1** and **P2** are not promising candidates as solubilizing excipients for insoluble drugs.

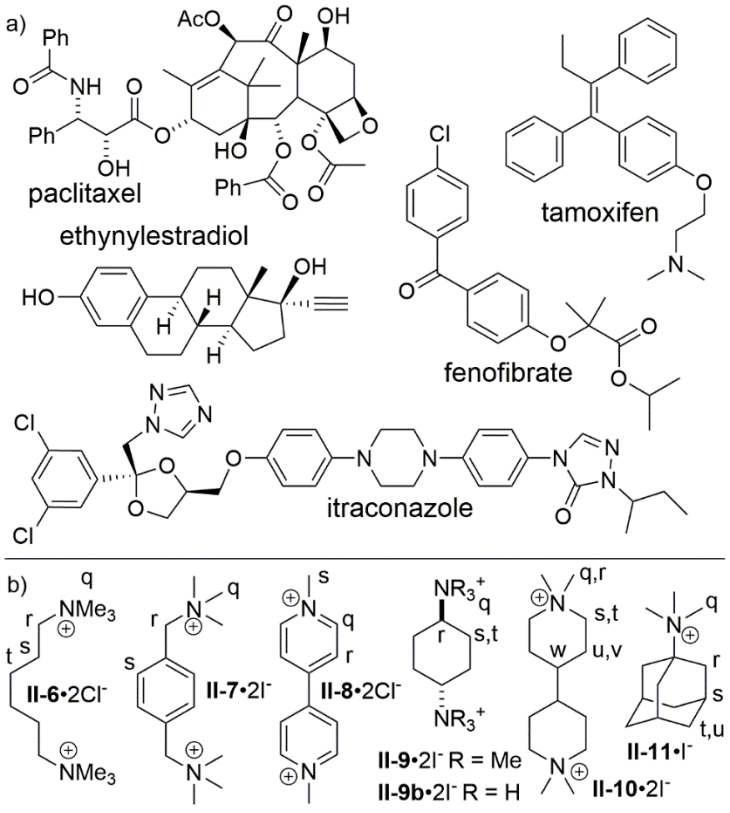

Figure II-8. Structures of: a) insoluble drugs, and b) (di)cationic guests **II-6** – **II-11** used in this study.

2.2.6 Qualitative ^{1}H NMR Investigations of Host•Guest Recognition

In order to understand the poor solubilizing ability of **P1** and **P2** we decided to perform qualitative host•guest binding studies at 1:1 and 1:2 host:guest ratios. Initially, we attempted to prepare solutions of host **P1** (1 mM) and guests **II-7**, **II-9**, and **II-10** ($\geq$ 2 mM) and observed the formation of precipitates indicating the poor solubility of the complexes. Similar observations were made for solutions of host **P2** (2 mM) and guests **II-7** – **II-9**. These problems can be avoided by working at lower concentrations of hosts **P1** and **P2** (e.g. 0.3 mM). It is not possible to reach saturation due to the low binding affinity for host•guest complexes of **P1** and **P2** (*vide infra*) and therefore experimentally observable complexation induced changes in chemical shift are small particularly for **P1**. For example, Figures II-9a-c show the ^{1}H NMR spectra recorded for **II-8** (0.3 mM) and 1:1 and 1:2 mixtures of **P1** and **II-8** which exhibit upfield shifts of $\leq$ 0.2 ppm under these conditions. In contrast, Figure II-10a-c shows the ^{1}H NMR spectra recorded for **II-8** (1.0 mM) and 1:1 and 1:2 mixtures of **P2** and **II-8**. Clear upfield shifting of the aromatic H-atoms (H_q and H_r) of **II-8** upon complexation suggest the formation of a complex where the aromatic rings of guest **II-8** are located inside rather than on the exterior of host **P2**. The guest exchange processes were fast on the ^{1}H NMR chemical shift timescale which is expected when the host•guest complexes are relatively weak. The Supporting Information (Figures II-S26 – II-S43) shows the analogous ^{1}H NMR spectra recorded for guests **II-7 – II-11** and hosts **P1** and **P2** which suggests the complexation of the central hydrophobic regions of guests **II-7** – **II-11** inside hosts **P1** and **P2** potentially in their **P1**-F3 and **P2**-F3 conformations.

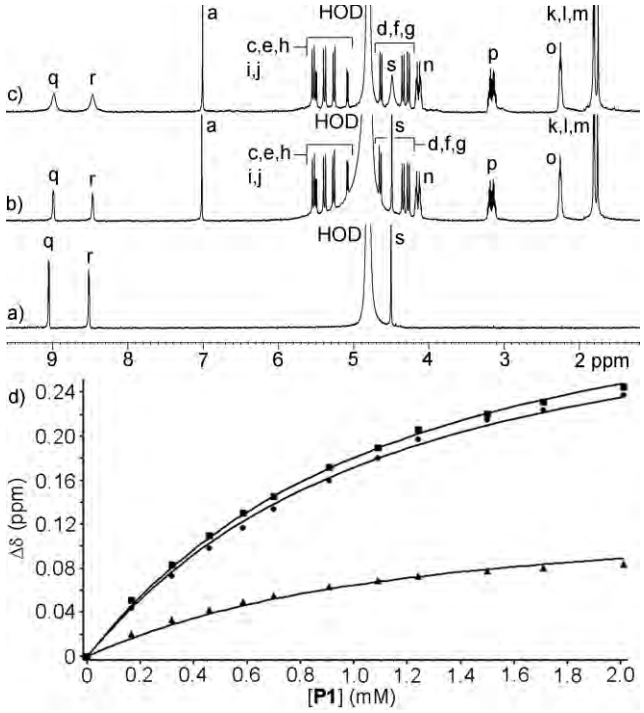

Figure II-9. ^{1}H NMR spectra recorded (600 MHz, D_2O, RT) for: a) **II-8** (0.3 mM), b) a 1:1 mixture of **P1** (0.3 mM) and **II-8** (0.3 mM), and c) a 1:2 mixture of **P1** (0.3 mM) and **II-8** (0.6 mM). d) Plot of the absolute value of the change in chemical shifts of H_q (■), H_r (•), and H_s (▲) during the titration of **II-8** (0.3 mM) with **P1** (0 – 2.01 mM) in D_2O.

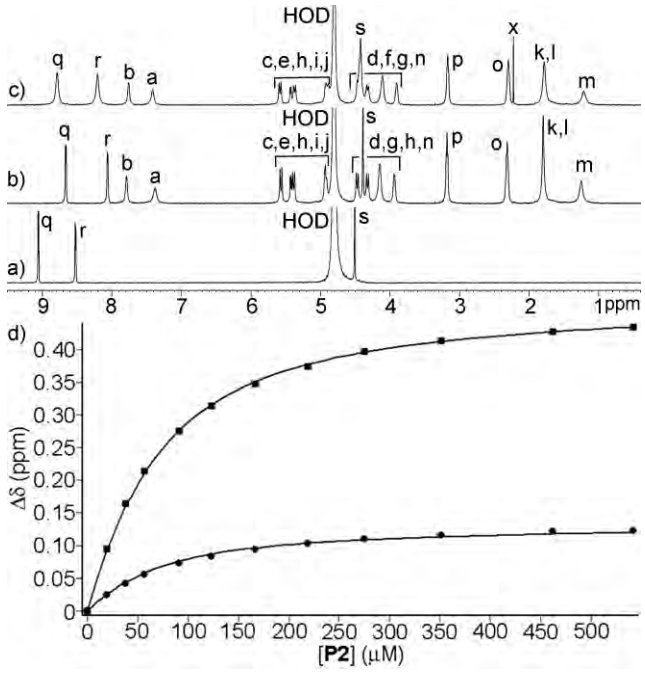

Figure II-10. ^{1}H NMR spectra recorded (600 MHz, D_2O, RT) for: a) **II-8** (1.0 mM), b) a 1:1 mixture of **P2** (1.0 mM) and **II-8** (1.0 mM), and c) a 1:2 mixture of **P2** (1.0 mM) and **II-8** (2.0 mM). d) Plot of the absolute value of the change in chemical shifts of H_q (■) and H_s (•) during the titration of **II-8** (0.04 mM) with **P2** (0 – 0.541 mM) in D_2O.

2.2.7 Measurement of the Host•Guest Binding Constants

Initially, we attempted to measure the K_a values for the host•guest complexes by isothermal titration calorimetry (ITC). Unfortunately, under our usual conditions (20 mM sodium phosphate buffer, pH 7.4) very little heat was evolved and the data could not be fitted to a standard 1:1 binding model. Accordingly, we turned to ^{1}H NMR titrations. The titration of **II-8** (0.06 mM) with **P2** (0 – 0.96 mM) conducted in 20 mM sodium phosphate buffer (pH 7.4) again resulted in only very small changes in chemical shift of **II-8** which made clear that **P1** and **P2** were poor hosts. Therefore, we changed the medium to the less competitive unbuffered D_2O for determination of K_a values for **P1** and **P2**. Figure II-9d

shows the change in chemical shift of (H_q, H_r, and H_s) of a fixed concentration of guest **II-8** (0.3 mM) upon titration with host **P1** (0 – 2.01 mM); the solid line represents the best fitting of the data to a 1:1 binding model implemented within Scientist^{TM} (Supporting Information) with K_a = 1100 ± 50 M^{-1}. Similarly, Figure II-10d shows the change in chemical shifts (H_q, H_s) of a fixed concentration of guest **II-8** (0.04 mM) recorded during the titration with host **P2** (0 – 541 μM). The solid line in figure II-10d represents the best non-linear least squares fit of the data to a binding model that takes into account the self-association of **P2** along with the 1:1 host:guest binding (Supporting Information) with K_a = 19800 ± 400 M^{-1}. Related titrations were performed for hosts **P1** and **P2** with guests **II-7** – **II-11** and are presented in the Supporting Information. The K_a values are collected in Table II-2. From the fitting of ^{1}H NMR titrations data curves (Supporting Information) we were also able to extract the limiting chemical shifts of the **P1**•guest and **P2**•guest complexes and calculate the complexation induced changes in chemical shift (Δδ, Table II-3). A perusal of Table II-3 reveals that for the naphthalene walled hosts, the complexation induced changes in chemical shifts (Δδ) of guests are significantly larger for **Tet2** than for **P2**. Similarly, between the benzene walled hosts, the Δδ values are larger for **Tet1** than for **P1**. These disparities suggest that the geometry of the **P1**•guest and **P2**•guest complexes are not directly analogous to those of **Tet1** and **Tet2**. Accordingly, we wondered whether these weak binding processes might simply reflect electrostatic and hydrophobic interaction between the guest and the *outside* of the aromatic walls of the host or potentially to one of the clip-like cavities of **P1**-F1 or **P2**-F1. To test this possibility, we performed titrations between guests **II-6** – **II-11** and aromatic sidewalls **II-4** and **II-5** (Supporting Information). No changes in chemical shift were observed for mixtures of

benzene derived wall **II-4** and guests **II-6** – **II-11**; accordingly, no K_a values or $\Delta\delta$ values are reported in Tables II-2 and II-3 for wall **II-4**. For naphthalene wall **II-5** we did observe changes in chemical shift upon titration with guests **II-6** – **II-11**; we fitted those changes to a 1:1 binding model to obtain K_a values and $\Delta\delta$ values (Tables II-2 and II-3). The K_a values for the complexation between wall **II-5** and **II-6** – **II-11** are 6.7 – 23.6-fold weaker than between host **P2** and **II-6** – **II-11** and the $\Delta\delta$ values (Table II-3) are much smaller for **II-5** than for **P2**. Based on this data we exclude the possibility that guests **II-6** – **II-11** simply bind to the exterior face of the aromatic sidewalls of host **P2**. The 1:1 stoichiometry of the **P2**•guest complexes were confirmed for guests **II-6**, **II-7**, and **II-10** by constructing Job plots (Supporting Information Figures II-S51 – II-S55). The 1:1 stoichiometry suggests that the guest•**P2** complexes exist as the guest•**P2**-F3 conformer. For the very weak complexes between **P1** and guests **II-6** – **II-11** the Job plots were inconclusive with no clear maxima. The utility of Job plots has been called into question, especially for weak complexes studied under dilute conditions.[181] In addition to the $\Delta\delta$ values for the guest upon complexation, we also monitored the changes in **P2** chemical shift upon complexation with **II-6** – **II-11** (Supporting Information) and generally observe upfield shifts for H_g ($\approx$ 0.3 ppm) and H_h ($\approx$ 0.1 ppm) and a slight downfield shift ($\leq$ 0.1 ppm) for H_e upon complexation. H_g and H_h are the diastereotopic protons on the methylene bridges involved in the S-shaped connections at the center of **P2**. The chemical shifts of the diastereotopic methylene bridges of CB[n] type hosts resonate at quite different chemical shifts due to the anisotropic effects of the ureidyl C=O group with the H-atoms nearer the lone pairs on oxygen appearing substantially downfield of those pointing away from the C=O groups. Accordingly, the significant upfield movement of H_g and H_h upon binding provides

additional support for our conclusion that **P2** undergoes conformation change upon binding to yield the **P2**-F3•guest complexes.

Table II- 2. Binding constants (K_a, M^{-1}) measured for the different container•guest complexes.

	P1[a,e]	**P2**[a,e]	**II-5**[a,e]	**Tet1**[f]	**Tet2**[f]
II-6	3.87 ± 0.12 x 10^2	7.71 ± 0.22 x 10^3	5.46 ± 0.46 x 10^2	8.93 ± 0.33 x 10^{7b}	4.59 ± 0.09 x 10^{8c}
II-7	1.40 ± 0.03 x 10^3	1.76 ± 0.05 x 10^4	7.47 ± 2.14 x 10^2	1.78 ± 0.07 x 10^{8b}	2.69 ± 0.09 x 10^{9c}
II-8	1.10 ± 0.05 x 10^3	1.98 ± 0.04 x 10^4	1.94 ± 0.13 x 10^3	4.69 ± 0.22 x 10^{8b}	2.14 ± 0.09 x 10^{9c}
II-9	9.00 ± 0.40 x 10^2	4.17 ± 0.08 x 10^3	6.21 ± 0.64 x 10^2	2.25 ± 0.08 x 10^{7b}	2.76 ± 0.15 x 10^{9c}
II-10	1.08 ± 0.05 x 10^3	5.12 ± 0.12 x 10^3	5.40 ± 0.58 x 10^2	3.09 ± 0.24 x 10^{6d}	1.30 ± 0.03 x 10^{10c}
II-11	3.75 ± 0.24 x 10^2	1.95 ± 0.10 x 10^3	2.70 ± 0.83 x 10^2	1.70 ± 0.05 x 10^{7b}	7.09 ± 0.21 x 10^{8c}

[a] Measured by ^{1}H NMR titration. [b] Lit. values.[92] Measured by ITC competition assay using butan-1-amine as competitor in cell. [c] Measured by ITC competition assay using **II-9b** as competitor in cell. [d] Measured by direct ITC titration. [e] Measured in D_2O at RT. [f] Measured in 20 mM NaH_2PO_4 buffered H_2O (pH 7.4) at 298 K).

Table II- 3. Complexation induced changes in chemical shifts (Δδ) of guests obtained from the non-linear data fitting of the titration data for **P1**, **P2**, and wall **II-5** or directly from the ^{1}H NMR spectra for the tight binding complexes of **Tet1** and **Tet2**. For atom lettering see Figure II-8.

Guest	Host	H_q Δδ	H_r Δδ	H_s Δδ	H_t Δδ	H_u Δδ	H_v Δδ	H_w Δδ
II-6	**Tet2**	0.50	1.17	1.37	1.32			
II-6	**II-5**	0.07	0.10	0.11	0.11			
II-6	**P2**	0.04	0.41	0.59	0.97			
II-6	**Tet1**	0.11	0.78	1.09	1.38			
II-6	**P1**	0.12	0.43	0.38	0.78			
II-7	**Tet2**	0.66	0.36	1.61				
II-7	**II-5**	0.07	0.16	0.15				
II-7	**P2**	0.18	0.34	0.76				
II-7	**Tet1**	0.17	0.72	1.27				
II-7	**P1**	0.08	0.17	0.29				
II-8	**Tet2**	1.05	1.56	0.30				
II-8	**II-5**	0.13	0.16	0.06				
II-8	**P2**	0.48	0.57	0.13				
II-8	**Tet1**	1.08	0.81	0.20				
II-8	**P1**	0.37	0.35	0.14				
II-9	**Tet2**	0.89	2.06	1.38	1.64			
II-9	**II-5**	0.05	0.20	0.11	0.12			
II-9	**P2**	0.16	0.50	0.41	0.53			
II-9	**Tet1**	0.88	0.81	0.91	1.08			
II-9	**P1**	0.27	0.79	0.62	0.67			
II-10	**Tet2**	0.34	0.77	1.02	1.28	1.44	1.47	1.09
II-10	**II-5**	0.07	0.10	0.16	0.18	0.19	0.20	0.24
II-10	**P2**	0.12	0.19	0.27	0.42	0.59	0.60	0.78
II-10	**Tet1**	0.25	0.45	0.60	0.77	0.96	0.89	1.17
II-10	**P1**	0.19	0.18	0.37	0.41	0.59	0.54	0.69
II-11	**Tet2**	0.42	1.62	1.90	1.16	1.5		
II-11	**II-5**	0.08	0.11	0.07	0.06	0.07		
II-11	**P2**	0.18	0.51	0.55	0.35	0.60		
II-11	**Tet1**	0.29	1.22	1.14	0.73	1.28		
II-11	**P1**	0.27	0.77	0.74	0.48	0.79		

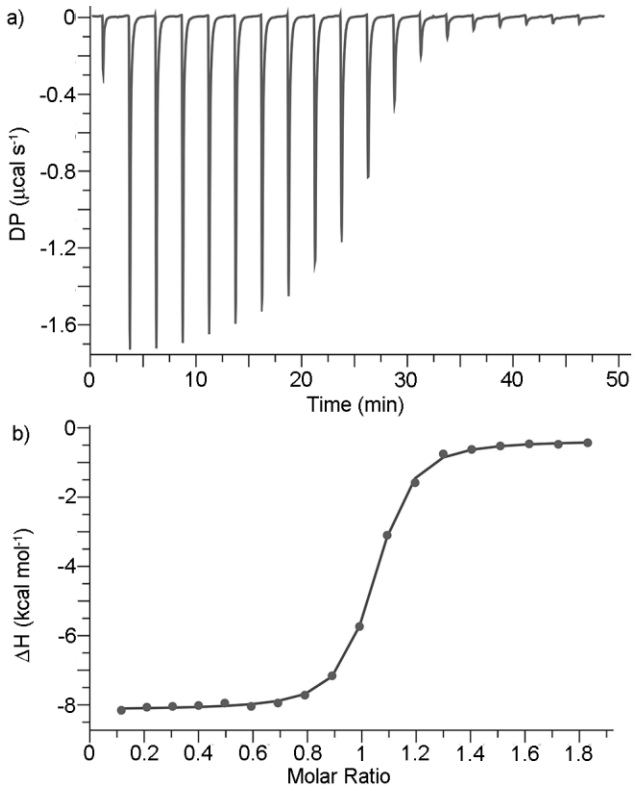

Figure II-11. a) ITC thermogram from the titration of a mixture of **Tet2** (105 mM) and competitor **II-9b** (750 μM) in the cell with guest **II-9** (1.0 mM) in the syringe. b) Plot of ΔH versus molar ratio used to extract K_a and ΔH for **Tet2•II-9**.

Table II-2 also presents the K_a values for complexes of **Tet1** with guests **II-6** – **II-11** measured previously by ITC in 20 mM sodium phosphate buffer (pH 7.4, RT) as a comparator for **P1**.[92] The logical comparator for **P2** is **Tet2**, but unfortunately, the K_a values for **Tet2** complexes with **II-6** – **II-11** were unknown. Accordingly, we measured the K_a values by isothermal titration calorimetry. We attempted direct ITC titrations but quickly found that the K_a values exceeded the dynamic range of the measurements (c-value > 300).[182, 183] Accordingly, we decided to perform competition ITC.[184] In competition ITC, a host and an excess of a weak binding guest of known K_a and ΔH is titrated with an excess of a stronger binding guest; fitting of the data to a competition binding model then

allows extraction of the K_a and ΔH values for the tighter binding complex. Figure II-11a shows the thermogram for the titration of a mixture of host **Tet2** (105 μM) and *trans*-1,4-diamino cyclohexane dihydrochloride (**II-9b**, 750 μM) as competitor in the cell with guest **II-9** (1.0 mM) in the syringe. Figure II-11b shows a plot of the integrated heats versus the **Tet2**:**II-9** molar ratio fitted to a competition binding model in the PEAQ-ITC data analysis software which allowed the determination of the strength of the **Tet2•II-9** complex (K_a = 2.76 x 10^9 M^{-1}; ΔH = -13.3 kcal mol^{-1}). Table II- 2 reports the binding constants for the **Tet2•**guest complexes by competition ITC and the data is given in the Supporting Information.

2.2.8 Modelling of the Conformations of Host•Guest Complexes

The optimized structures of the pentamers **P1'** and **P2'** (Figure II-6) were used to model the complexes with guest **II-8**. In the case of F3, we inserted the guest **II-8** into an artificially created cavity. The structures obtained for **P2'•II-8** fully optimized in implicit water are summarized in Figure II-6 whereas the analogously obtained structures of **P1'•II-8** are shown in Figure II-S105. In the F1 and F2 forms, guest **II-8** binds into the clip-like cavity. In the case of F3, the aromatic walls undergo an out-of-plane twisting and reorganization to maximize contact with the guest, and as a result, they no longer π–π stack with each other anymore. For **P1** and **P2** which bear $O(CH_2)_3SO_3^-$ solubilizing groups, there may be steric interactions or electrostatic interactions between solubilizing groups, and it can be expected that the computationally obtained complexes with the **P1'** and **P2'** hosts in the F3 conformational state may not fully represent the real situation. The computed relative stabilities of the complexes of **II-8** with **P1'** and **P2'** (Table II-1) revealed that the most stable conformer is F3 for **P1'•II-8** and F1 for **P2'•II-8**. This

indicates that the preference for conformational states can change during the binding. Similar to the free hosts, two contributions were not included in our analysis, the thermal motions (entropy) and impact solubilizing groups, which may have a destabilizing effect on the complexes in the F3 conformational state as discussed above.

2.2.9 Discussion of the Trends in the Binding Constants

An examination of the K_a values in Table II-2 reveals a number of significant trends. First, both **P1** and **P2** are relatively poor hosts with the K_a values for the series of (di)ammonium ions (**II-6** – **II-11**) – generally excellent guests for CB[n]-type receptors – ranging from 375 to 1400 M^{-1} for **P1** and from 1950 to 19800 M^{-1} for **P2**. Amongst guests **II-6** – **II-11**, guests **II-7** and **II-8** which contain aromatic rings bind most tightly to **P1** and **P2**, presumably due to π–π interactions in the complexes. Second, **P2** is always a better host than **P1** toward **II-6** – **II-11** with ratios of K_a values as follows: **II-6** (19.9-fold), **II-7** (12.6-fold), **II-8** (18-fold), **II-9** (4.6-fold), **II-10** (4.7-fold), **II-11** (5.2-fold). We believe that **P2** is a slightly better host than **P1** due to either a larger population of the F3 conformer or the larger π-surfaces of **P2** which form stronger non-covalent interactions with guest, or a combination of the two. Similarly, a comparison of the K_a values of **Tet2** and **Tet1** toward **II-6** – **II-11** shows that **Tet2** is uniformly the superior host (**II-6** (5.1-fold), **II-7** (15-fold), **II-8** (4.5-fold), **II-9** (123-fold), **II-10** (4200-fold), **II-11** (42-fold)). Related trends have been seen previously for the complexes of **Tet1** and **Tet2** toward insoluble drugs and neuromuscular blocking agents.[169, 180] We attributed these trends to the potential for augmented π–π interactions with the naphthalene walled hosts **Tet2** and **P2**. For hosts **Tet1** and **Tet2** the selectivity is largest for the bulkier alicyclic guests **II-9** – **II-11** and smallest for the narrow aliphatic guest **II-6** which suggests that smaller host **Tet1** must

undergo energetically costly cavity expansion to accommodate the larger guests. The narrow dynamic range of K_a values for hosts **P1** and **P2** does not allow us to draw any firm conclusions regarding guest size preference. Previously, we have observed that **Tet1** is a more potent host than **Tri1** and that **Tet2** is a more potent host than **Tri2**.[73] The data in Table II-2 allows an analogous comparison of **P1** with **Tet1** and **P2** with **Tet2**. We find that **Tet1** is a substantially better host than **P1** toward guests **II-6** – **II-11** (**II-6**: 2.3×10^5-fold, **II-7**: 1.3×10^5-fold, **II-8**: 4.3×10^5-fold, **II-9**: 2.5×10^4-fold, **II-10**: 2.9×10^3-fold, **II-11**: 4.5×10^4-fold) and that **Tet2** is far superior than **P2** (**II-6**: 6.0×10^4-fold, **II-7**: 1.5×10^5-fold, **II-8**: 1.1×10^5-fold, **II-9**: 6.6×10^5-fold, **II-10**: 2.5×10^6-fold, **II-11**: 3.6×10^5-fold). Overall, the binding data shows that **P1** and **P2** are relatively poor hosts toward hydrophobic (di)cations **II-6** – **II-11** which are generally excellent guests for CB[n]-type hosts. We surmise that the poor performance of **P1** and **P2** is because the uncomplexed hosts must undergo an energetically costly folding process to populate the **P1**-F3 and **P2**-F3 conformation before guest binding (Figure II-6).

2.3 Conclusions

In summary, we have described the synthesis of an important new glycoluril oligomer building block (S-shaped pentamer **II-3**) and its transformation into two new acyclic CB[n]-type receptors **P1** and **P2**. Hosts **P1** and **P2** have moderate solubility in water (≈ 9 and ≈ 11 mM); **P1** does not self-associate whereas **P2** undergoes only weak intermolecular self-association ($K_s = 189 \pm 27\ M^{-1}$). **P1** and **P2** are relatively poor hosts toward (di)cationic guests **II-6** – **II-11** as established by ^{1}H NMR titrations (**P1**: 375 to 1400 M^{-1}; **P2**: 1950 to 19800 M^{-1}). Host **P2** with its larger naphthalene rings is the more potent host in all cases relative to **P1**. In sharp contrast, guests **II-6** – **II-11** form much

tighter complexes (10^3 – 10^6 fold) with acyclic CB[n] based on glycoluril tetramers (**Tet1** and **Tet2**). The relatively poor recognition abilities of **P1** and **P2** are traced to their ability to adopt three conformational isomers around their S-shaped segments (F1 – F3). For **P1** there is a computational derived preference for the F1-fold (**TriMe**-F3: +5.1 kcal mol^{-1}; **P1'**-F3: +4.0 kcal mol^{-1}) whereas for **P2** there is a smaller preference for the F3-fold (**P2'**-F1: +2.3 kcal mol^{-1}). The need to pay the energetic cost to shift the conformational equilibrium toward the F3-folded forms of **P1** and induce cavity formation in the F3-folded forms of **P1** and **P2** required for 1:1 host:guest cavity binding results in the observed low K_a values. Interestingly, calculations performed for **TriH** show no preference for the F1-fold which suggests that the Me-substituents play a major steric role in biasing the F1 – F3 equilibrium. In turn, this observation opens up the use of substituted glycolurils as building blocks to rationally design S-shaped glycoluril oligomers with well-defined conformational ensembles. In conclusion, these results highlight the importance of controlling the ensemble of conformations open to a host (e.g. maximizing host pre-organization) and minimizing host self-complexation when attempting to maximize host•guest binding affinity.

Chapter 3: Self-Assembly of Cucurbit[7]uril Based Triangular [4]Molecular Necklaces and their Fluorescence Properties

Work presented in this chapter was taken from Samanta, S. K.; Brady, K. G.; Isaacs, L. *Chem. Commun.* **2017**, *53*, 2756-2759.

S.K.S. was responsible for the self-assembly of Pd supramolecular coordination complex and characterization of structures. K.G.B was responsible for Pt supramolecular coordination complex, binding constants by ITC, and quantum yield values.

3.1 Introduction

Pioneering work by the groups of Stoddart, Sauvage and Leigh have resulted in an in depth knowledge of the nature of the mechanical bond and utilisation of mechanically interlocked molecules (MIMs) to create functional molecular devices.[185-187] In the intervening years, these groups and others have used MIMs as the basis for advanced applications like molecular motors and machines, nanoscale devices and smart materials for drug delivery and imaging.[128, 188-191] Whereas MIMs comprise at least one molecular ring threaded onto one molecular axle, a subset of MIMs known as [*n*]molecular necklaces ([*n*]MNs) comprise *n-1* molecular rings threaded onto a macrocycle. The first example of a [3]MN, also known as a [3]catenane, was reported by Sauvage based on metal ion templation.[192] In 1998, Stoddart reported the preparation of [4]MNs by templation based on aromatic donor-acceptor interactions.[193] More recently, Kim, Stang and others synthesized [*n*]MNs

(n = 4, 5) by utilising pairs of orthogonal (non)covalent interactions (e.g. metal-ligand coordination and host-guest complexation.[194-197]

Since the discovery of cucurbit[n]uril homologues (CB[n] (n = 5, 6, 7, 8, 10), Chart III-1) in 2000, the supramolecular chemistry of CB[n]-type receptors has developed rapidly.[39, 55, 59, 63, 147] In particular, the high binding affinities and selectivities that CB[n] display toward their guests along with the stimuli responsiveness (e.g. pH, chemical, photochemical, electrochemical) of CB[n] complexes have made them prime components for the preparation of complex functional systems.[39, 63, 147, 198-200] For example, CB[n] have been used to create chemical sensors, supramolecular materials, molecules and materials for drug solubilization, delivery, and reversal, and as promotors of biological dimerization events.[19, 60-62, 148, 201-203] Over the past two decades, the strategic combination of rigid ligands and metal-ions with well defined coordination geometries has led to the creation of a variety of functional self-assemblies.[10, 95, 96, 112, 139, 204, 205] Furthermore, some scientists have sought to extend the abilities of these systems by decorating them with molecular containers (e.g. crown ethers, pillarenes).[196] However, the strategic merger of the structural features of macrocyclic metal-organic assemblies with the outstanding recognition properties of CB[n]-type receptors is relatively unexplored.[206] Very recently, we reported a Fujita-type metal organic cubooctahedron studded with 24 methyl viologen groups which non-covalently recruits CB[8] and doxorubicin prodrugs by heteroternary complexation and its ability to deliver doxorubicin to HeLa cells.[139] To make robust multivalent systems for imaging, delivery, and theranostic applications, namely those whose CB[n] components cannot dissociate, requires that CB[n] units be incorporated within MIMs. Herein, we

report that ligand **III-1** self-assembles with $M(en)(NO_3)_2$ (M = Pd, Pt) and CB[n]-type receptors to form [4]MNs.

3.2 Results and Discussion

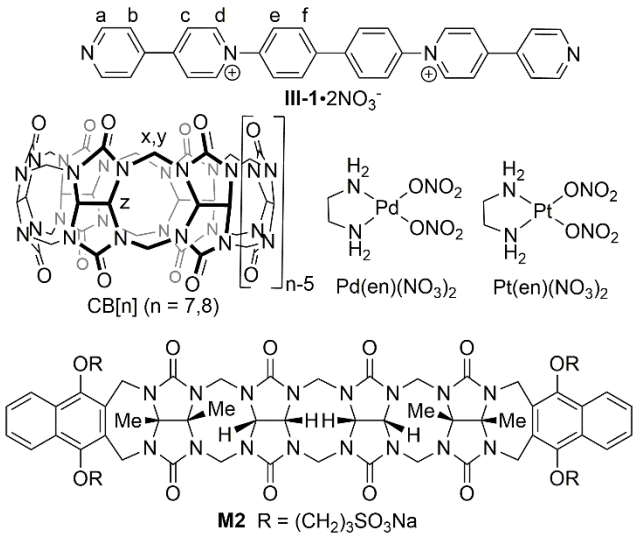

Chart III-1. Molecular structures of compounds used in this study.

Chart III-1 shows the structure of rigid-rod ligand **III-1** which features two terminal monocationic 4,4'-bipyridinium units and a central dicationic benzidinium unit.[207] All three units constitute binding sites for CB[n]-type receptors, but the central dicationic benzidinium unit was expected to be preferred. The synthesis of **III-1** was accomplished in two steps (Supporting Information). First, reaction of 4,4'-bipyridine with 2,4-dinitrochlorobenzene gave N-(2,4-dintrophenyl)-4,4'-bipyridine (**III-2**).[208] Next, the Zincke reaction[209, 210] of **III-2** with benzidine followed by anion exchange gave **III-1**•$(NO_3^-)_2$ in 40% yield.

First, we studied the complexation behavior of **III-1** with CB[7] by ^{1}H NMR and UV/Vis spectroscopy. The ^{1}H NMR spectra recorded at various **III-1**:CB[7] stoichiometries (Figure III-1 and III-2) established that two different complexes

(**III-1**•CB[7] and CB[7]•**III-1**•CB[7]) coexist depending on the stoichiometry. When ≤1 equiv. of CB[7] is used, a single **III-1**•CB[7] complex is formed selectively. The ^{1}H NMR of **III-1**•CB[7] is shown in Figure III-2b and displays substantial upfield shifts for H_e & H_f (7.15 and 7.64 ppm) relative to free **III-1**. Conversely, the resonances for H_a – H_d of **III-1** shift slightly downfield upon complexation. The CB[7] cavity constitutes an NMR shielding region whereas the region just outside the C=O portals is slightly deshielding region,[59] which establishes that CB[7] binds to the benzidinium core of **III-1** whose geometry (**III-1**•CB[7]) is shown in Figure III-1. Addition of more CB[7] (1 equiv.) to [**III-1**•CB[7]] causes H_e and H_f to shift downfield whereas H_a – H_d shift upfield indicating translocation of CB[7] from benzidinium core to the terminal bipyridinium units to form **III-1**•CB[7]$_2$ (Figure III-1). UV/Vis titration of **III-1** (6.6 μM) with CB[7] (0-17.4 μM) results in a decreased absorbance at λ = 320 nm along with a bathochromic shift. A plot of A_{320} versus [CB[7]] showed saturation at 2.0 molar ratio indicating tight 1:2 binding for the **III-1**/CB[7] system in agreement with the NMR results. Figure III-2h-i show the results from isothermal titration calorimetry. The data could be fitted using the one set of sites binding model indicating that the two binding events behave independently (ΔH = −34.9±0.42 kcal mol^{-1} and $K_a = 2.26 \times 10^6$ M^{-1}). Similarly, addition of **M2** to **III-1** initially gives **III-1•M2** followed by translocation to the terminal bipyridinium sites upon formation of **III-1•M2**$_2$ (Supporting Information, Figure III-S13 and III-S14).

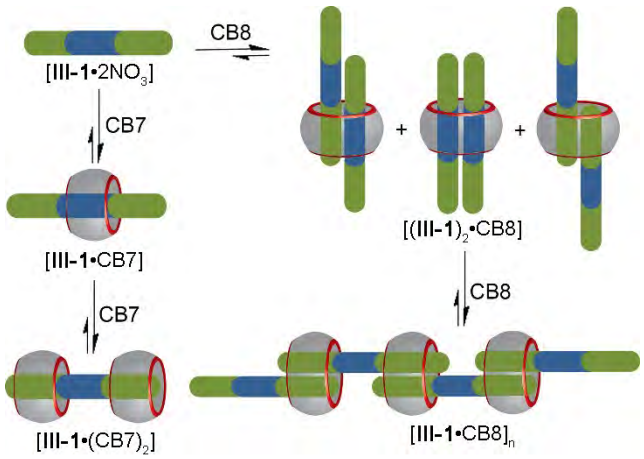

Figure III-1. Complexation of **III-1** with CB[7] and CB[8].

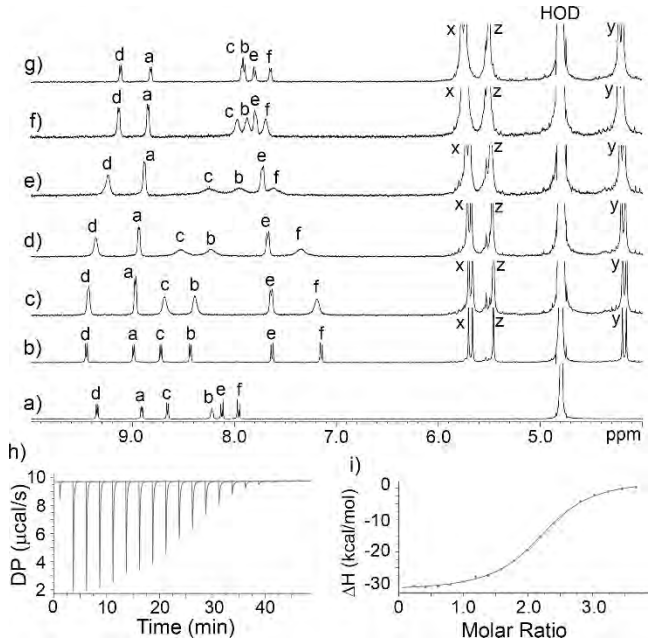

Figure III-2. ^{1}H NMR recorded (400 MHz, D_2O, RT) for a) **III-1** (0.3 mM) and b-g) with various equiv. of CB[7] – b) 1.0, c) 1.25, d) 1.50, e) 1.75, f) 2.0, g) 3.0, h) Isothermal titration calorimetry of **III-1** (65 µM) in the cell upon titrating with CB[7] (1.243 mM). i) ITC data fitting. Next, we studied the interaction between **III-1** and CB[8]. We hoped that CB[8] would bind in a 1:1 fashion to the central benzidinium unit which would leave cavity volume available for ternary complex

formation. Unfortunately, the ^{1}H NMR titration at **III-1**:CB[8] ratios below 1:0.5 show the formation of the **III-1**$_2$•CB[8] (Supporting Information, Figure III-S8). Analysis of the complexation induced chemical shifts for H_a – H_f (all upfield) with **III-1**$_2$•CB[8] suggests that the benzidinium unit is the major binding site although other complex geometries may be populated as shown in Figure III-1. Further addition of CB[8] up to a 1:1 **III-1**:CB[8] ratio results in the disappearance of the resonances for **III-1**•CB[8]$_2$ and the presence of broadened resonances which suggests the formation of a [**III-1**•CB[8]]$_n$ oligomer based on CB[8]-induced homodimerisation of the bipyridinium binding sites.[211, 212] DOSY NMR measurements confirm that [**III-1**•CB[8]]$_n$ ($D = 7.94 \times 10^{-11}$ m^2/s m^2/s) is substantially larger than **III-1**$_2$•CB[8] ($D = 3.16 \times 10^{-10}$ m^2/s m^2/s). Our inability to obtain the 1:1 **III-1**•CB[8] complex, suggested that the planned synthesis of [n]MNs incorporating CB[8] might be challenging.

Next, we prepared the unthreaded SCCs[213, 214] by heating ligand **III-1** (5.5 mM) with an aqueous solution of $Pd(en)(NO_3)_2$ (100 °C, 24 h). ^{1}H NMR displayed resonances for two SCC's (ratio = 86:14) that were of different size (Figure III-3) as determined by diffusion ordered spectroscopy (DOSY) analysis. Diagnostic downfield shifts of H_a were observed for **III-3** ($\Delta\delta = 0.09$ ppm) and for **III-4** ($\Delta\delta = 0.21$ ppm), which establishes that the Pd^{2+} center is bound to the terminal pyridine groups. We hypothesised that two products are triangle **III-3** (most abundant, $D = 3.02 \times 10^{-10}$ m^2/s) and square **III-4** ($D = 2.18 \times 10^{-10}$ m^2/s). When [**III-1**] was reduced from 5.5 to 2.5 mM, the relative abundance of **III-3** with respect to **III-4** increased upon dilution from 86% to >99% ([**III-4**] is below NMR detection limit).

When **III-3** was subjected to ESI-MS, molecular ion peaks at 466.2 ([Pd_3 **III-1**$_3$]$(NO_3)_7^{5+}$), 615.2 ([Pd_3 **III-1**$_3$]$(NO_3)_8 + 4H_2O]^{4+}$) and 815.8 ([Pd_3 **III-1**$_3$]$(NO_3)_9^{3+}$) were observed corresponding to triangle **III-3**. Similar phenomena were observed during the preparation of platinum complexes **III-5** and **III-6**. A concentrated solution of **III-1** (5.6 mM) and Pt(en)$(NO_3)_2$ afforded a mixture **III-5** and **III-6** in a 80:20 ratio, whereas a dilute solution of **III-1** (2.3 mM) afforded only triangle **III-5** as evidenced by ^{1}H NMR and DOSY (Supporting Information).

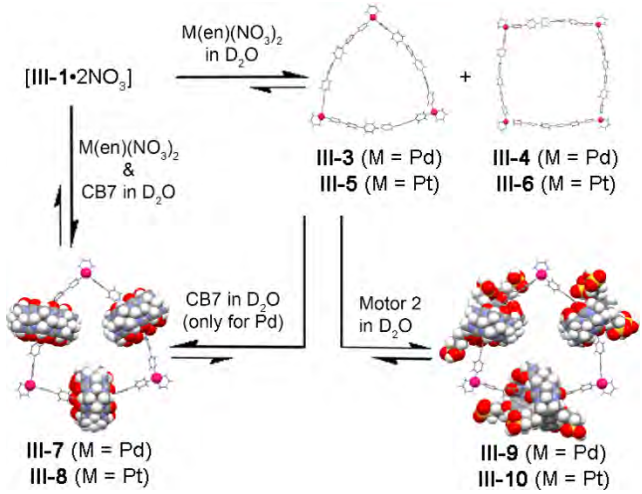

Figure III-3. Synthesis of [4]MNs from **III-1** with Pd(en)$(NO_3)_2$ and Pt(en)$(NO_3)_2$ to afford mixture of triangle and square. Using CB[7] or **M2** give [4]MNs or pseudo [4]MNs in water.

The kinetically labile nature of the Pd•••pyridine interaction suggested that CB[7] could be threaded postsynthetically to give the desired [*n*]MN. Addition of CB[7] (3.0 equiv.) to **III-3** followed by refluxing at 100 °C for 24 h gave only [4]MN **III-7** ([Pd_3(**III-1**•CB[7])$_3$]$(NO_3)_{12}$) as evidenced by ^{1}H, DOSY NMR and ESI-MS. Diagnostically, H_e and H_f undergo significant upfield shift ($\Delta\delta$ = 0.55 and 0.86 ppm

compared to **III-1**) reflecting their inclusion in the anisotropic shielding region of CB[7] (Figure III-4a,b). DOSY NMR shows the formation of a single species (D = 2.24×10^{-10} m^2/s) that diffuses slower than free its components CB[7] (D = 5.0×10^{-10} m^2/s) and triangle **III-3** (D = 3.02×10^{-10} m^2/s). ESI-MS provided final evidence of the formation of [4]MN **7**. A molecular ion peak at m/z = 813.7 was assigned to $[Pd_3(\textbf{III-1}\bullet CB[7])_3](NO_3)_5^{7+}$. One pot self-assembly of **III-1**, CB[7] and $Pd(en)(NO_3)_2$ or CB[7]•**III-1** and $Pd(en)(NO_3)_2$ also successfully delivered [4]MN **III-7**. The postsynthetic threading approach was not successful for [4]MN **III-8** due to the kinetically inert Pt•••pyridine interaction. However, a one pot process involving the self-assembly of equimolar quantities **III-1**, CB[7], and $Pt(en)(NO_3)_2$ in aq. $NaNO_3$ (1.0 M) afforded [4]MN **III-8** (reflux, 5d) as evidenced by ^1H NMR (Figure III-4e). DOSY NMR showed that **III-8** (D = 1.58×10^{-10} m^2/s) diffuses at similar rate as **III-7** (*vide supra*). ESI-MS also exhibited peaks for [4]MN **III-8**. Acyclic CB[n]-type container **M2** was also able to self assemble with equimolar amounts of **III-1** and $M(en)(NO_3)_2$ (M = Pd, Pt) to give the analogous clipped [4]MN **III-9** (for Pd) and **III-10** (for Pt) as shown in Figure III-3.[215]

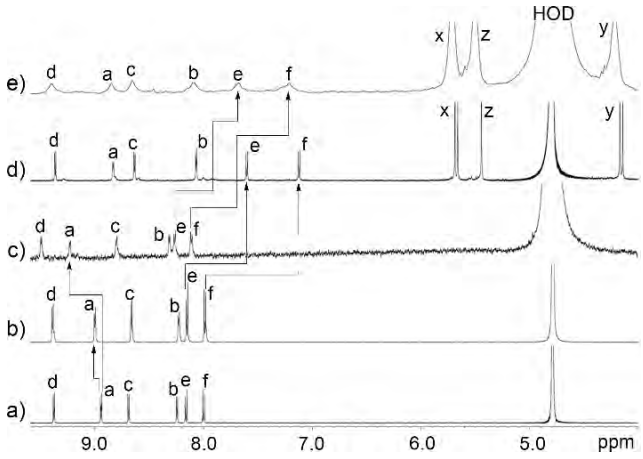

Figure III-4. Partial ^{1}H NMR (D_2O, 600 MHz) recorded for a) **III-1**, b) **III- 3**, c) **III-5**, d) [4]MN **III-7**, and e) [4]MN **III-8**.

Next, we set out to synthesize [4]MNs incorporating CB[8]. Unfortunately, the direct self-assembly of **III-1**, CB[8], and M(en)$(NO_3)_2$ was unsuccessful likely due to the preferred formation of [**III-1**•CB[8]]$_n$ as described above. Attempts to form 1:1:1 heteroternary complexes between CB[8], **III-1**, and second guests (e.g. 2,6-dihydroxynaphthalene, 1,4-dihydroxynaphthalene, indole, 4,4'-diaminoazobenzene) as building blocks for [4]MN formation were not successful as monitored by ^{1}H NMR. Nevertheless, we attempted the direct self-assembly of **III-1**, CB[8], second guest, and M(en)$(NO_3)_2$ but did not observe [n]MN formation. We conclude that **III-1** with its central benzidinium unit must be redesigned to disfavor ternary complexation and promote [n]MN formation.

It is known that conformational restriction (e.g. rotational, geometrical) of chromophores by inclusion within metal-organic frameworks (MOFs) or SCCs or by host-guest binding can slow down non-radiative decay of the excited state and thereby enhance luminescence.[104, 209, 216-218] Accordingly, we next turned our

attention to the photophysical properties of the [4]MNs and their components. Rigid-rod ligand **III-1** exhibits a high fluorescence quantum yield (Φ = 20%) in water. Addition of 1 equiv. of CB[7] results in a 20 nm blue shift of the fluorescence emission band to λ_{max} = 526 nm and the fluorescence emission intensity of **III-1**•CB[7] at this wavelength increases ≈ 2-fold due to the higher molar extinction coefficient of **III-1**•CB[7]. The quantum yield measured for **III-1**•CB[7] (Φ = 31%) is significantly higher than free **III-1** presumably due to restricted rotation upon complexation. Triangular SCC **III-3** and triangular [4]MN **III-7** display broad absorption bands centered at ca. 260 nm and 320 nm. As expected, platinum analogues **III-5** and **III-8** show red shifted absorption bands (303 and 351 nm) relative to **III-3** and **III-7**.[219, 220] The quantum yield measured for triangle **III-3** (Φ = 22%) is similar to that measured for free ligand **III-1**. In contrast, the quantum yield of **III-5** is dramatically decreased (Φ = 1.6%) due to the heavy atom effect of Pt which promotes the intersystem crossing leading to nonradiative decay.[219, 220] Threading of CB[7] onto the ligands comprising **III-3** and **III-5** to give [4]MNs **III-7** and **III-8** conformationally restrict the chromophore and lead to 1.5-fold and 8.8-fold (**III-5** to **III-8**) higher quantum yields (**III-7**: Φ = 32%; **III-8**: Φ =14%). Interestingly, the fluorescence emission was quenched in **III-9** and **III-10** due to charge−transfer interaction between the electron rich dialkoxynaphthalene walls of **M2** and ligand **III-1**.

3.3 Conclusions

In conclusion, we prepared rigid rod ligand **III-1** which forms stable inclusion complexes with CB[7], CB[8], and **M2**. An equimolar mixture of **III-1**

and M(en)(NO_3)$_2$ (M = Pd, Pt) gave triangular and square SCCs. Under more dilute conditions, assembly of **III-1** and M(en)(NO_3)$_2$ afforded only triangles **III-3** and **III-5**. Threading of CB[7] onto the SCCs to give [4]MNs **III-7** and **III-8** occurs by postsynthetic transformation or by a one-pot approach for kinetically labile Pd triangle **3** but only by the one-pot process for kinetically inert Pt triangle **III-5**. Attempts to form MNs incorporating CB[8] were unsuccessful due to ternary complex formation. The fluorescence and quantum yields of **III-1**, SCCs, and [4]MNs were quite different due to complexation induced conformational restriction and charge transfer processes. For this reason, we believe that CB[n] derived MNs will perform well as components of sensing arrays. Furthermore, when MNs incorporating larger CB[n] (e.g. n = 8) become available we believe they will constitute robust plug-and-play scaffolds for imaging, targeted drug delivery, and theranostic application. We will report on these possibilities in due course.

Chapter 4: Self-Assembled Cages with Mechanically Interlocked Cucurbiturils

Work presented in this chapter was taken from Brady, K.G.; Liu, B.; Li, X.; Isaacs, L. Manuscript Accepted *Supramol. Chem.* **2021**.

4.1 Introduction

A wide variety of molecular container compounds have been studied over the past decades including cyclodextrins, cyclophanes, calixarenes, cavitands, and more recently cucurbit[n]uril (CB[n]) and pillararenes (Figure IV-1).[3, 16, 17, 35, 39-43] When molecular containers bind guest compounds within their cavity, they can fundamentally alter their optical properties (e.g. UV/Vis, fluorescence), physical properties (e.g. solubility, vapor pressure), chemical properties (e.g. conformation, reactivity, pK_a), and even their biological properties.[18-25] Accordingly, molecular containers have been used in numerous applications including as supramolecular catalysts, as components of separations processes, as components of sensing ensembles, as components of smart materials and molecular machines, and to construct drug delivery systems.[26, 28-34] Amongst these molecular containers, cyclodextrin derivatives have found a wide variety of practical real world applications including the formulation of insoluble pharmaceuticals for human use, as the active ingredient in the household product Febreeze™, and as an *in vivo* reversal agent for rocuronium and vecuronium in the form of Sugammadex.[36, 221-223]

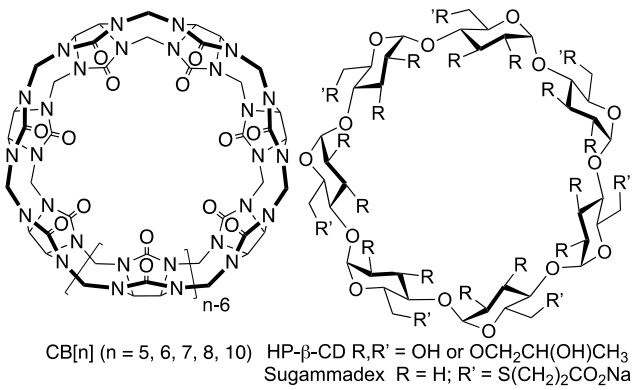

Figure IV-1. Structures of cyclodextrins and cucurbit[n]urils.

Our group has been most interested in the chemistry of the CB[n] family of molecular container compounds (Figure IV-1).[27, 39, 53, 55, 59] CB[n] are composed of *n* glycoluril repeat units connected by 2*n* methylene bridges which define a central hydrophobic cavity and two symmetry equivalent ureidyl carbonyl portals that are regions of highly negative electrostatic potential.[54] Accordingly, CB[n] hosts bind to a wide variety of guest molecules that present hydrophobic and cationic functionality including the N-terminus of peptides and proteins, cationic dyes, alkyl and aryl (di)ammonium ions, neurotransmitters, active pharmaceutical ingredients, drugs of abuse, and electrochemically active guests like ferrocene and viologen derivatives.[50, 60, 62, 63, 91, 198, 224-227] Advantageously, CB[n]-type receptors typically display high *in vitro* and *in vivo* biocompatibility.[228] Compared to other molecular containers, CB[n]-type hosts are special because they display high affinity and highly selective binding events in water (K_a commonly 10^6 M^{-1}; K_a up to 10^{17} M^{-1}).[27, 49] Because CB[n]•guest complexes are so selective they are responsive toward chemical, pH, photochemical, and electrochemical stimuli.[63, 147, 148, 198] For all these reasons, CB[n]-type containers have been used in a variety of applications including chemical sensing, promotors of protein dimerization, drug

formulation, delivery and sequestration, separations materials, and to construct molecular machines and devices.[27, 62, 64, 66, 67, 169] CB[n] are even beginning to appear in household deodorizing products.[229]

Self-assembly processes driven by hydrogen bonding,[7] the hydrophobic effect,[8] or metal-ligand interactions[5, 9-12] represent powerful alternative approaches toward functional molecular container compounds. Metal-ligand coordination-driven self-assembly has been particularly widely employed due to the well defined geometry of the metal coordination sphere and the strength of the metal-ligand interactions which lead to more predictable self-assembly processes. The vibrant fields of metal organic frameworks (MOF) and metal organic cages fall within the category of molecular containers self-assembled via metal-ligand interactions. MOFs are extended solids that have been used for a variety of applications including as materials for hydrogen storage, water and gas capture and separation, carbon capture and sequestration, biological imaging and sensing, and drug delivery processes.[11, 121, 122] The Loeb and Stoddart groups have studied the incorporation of macrocycles into MOFs and studied their dynamic and host-guest recognition properties.[230-233] Related supramolecular organic frameworks (SOFs) incorporating CB[n] have been developed in recent years by the Li group.[61, 234, 235] Very recently, Trabolsi has reported a covalent organic framework containing mechanically interlocked CB[7] units.[236] Conversely, metal organic cages are discrete self-assembled structures that are soluble in organic or aqueous solution whose properties can be tailored by altering the structures of the constituent building blocks. Metal organic cages have been used for basic studies of molecular recognition processes, to tame highly reactive species (e.g. P_4), as catalysts, for sensing and imaging, for drug delivery, and even as therapeutics themselves.[9, 10, 96, 123-125]

Several years ago, we saw the opportunity to integrate the desirable molecular recognition properties and stimuli responsiveness of CB[n] hosts with the desirable structural features of metal organic polyhedra (MOP) to create multivalent architectures that would be particularly well suited toward (targeted) therapeutic and imaging applications. Toward this goal, we reported the synthesis of bis(pyridyl) ligand **L1** and its self-assembly with $Pd(NO_3)_2$ to yield the cubooctahedral Fujita type sphere **A1** which is studded with 24 methyl viologen (MV) units (Scheme 1).[139] The methyl viologen units of **A1** allow the primary recruitment of CB[8] to form CB[8]•MV binary complexes which can undergo subsequent ternary complex formation with a naphthol functionalized doxorubicin prodrug. The results of MTS assays showed that **A1** exhibited 10-fold higher cytotoxicity toward HeLa cancer cells than an equivalent amount of doxorubicin prodrug alone which could be traced to the enhanced cellular uptake of the larger (≈ 6 nm) multivalent MOP-CB architecture. In follow up work we showed that related Fujita-type MOPs could be covalently functionalized with CB[7] and co-functionalized *via* click chemistry with dyes (e.g. fluorescein, cyanine 5.5), targeting ligands (e.g. biotin, RGD), and PEG groups.[140, 237]

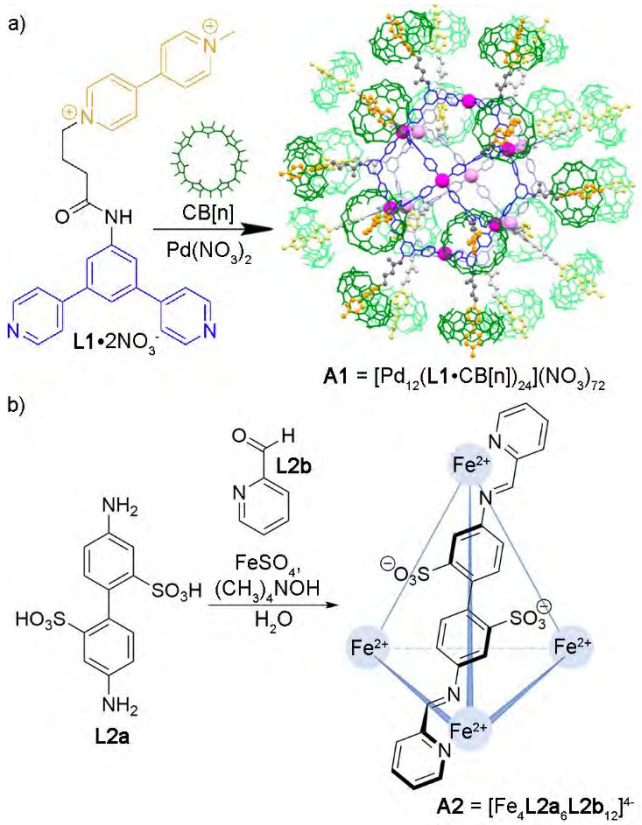

Scheme IV-1. a) Self-assembly of palladium MOP conjugated with CB[n]s. b) Self-assembly of water-soluble iron-based tetrahedra utilizing dynamic covalent coordinative bonds developed by the Nitschke group.

Despite these advances, the Fujita type systems are made using transition metals such as palladium and platinum which can be cytotoxic on their own. Furthermore, the non-covalent attachment of the CB[n] units discussed above was deemed less attractive for future *in vivo* biomedical application due to the potential for premature decomplexation. Accordingly, we envisioned that related MOP architectures based on biocompatible metals that feature either mechanically interlocked or covalently connected CB[n] would be desirable. We were drawn to the pioneering work of Nitschke and co-workers who have developed iron-based metal organic cages that are based on subcomponent self-assembly

of iron salt, aniline derivatives, and aryl aldehydes (e.g. $FeSO_4$ + **L2a** + **L2b**; Scheme 1).[238, 239] Nitschke has created water soluble versions of these metal organic cages, demonstrated their biocompatibility, and their use in materials science (e.g. hydrogels) and for uptake and release applications.[115, 117, 120, 240, 241] Accordingly, we decided to explore a strategic merger of the structural features of iron based MOPs with the recognition properties of CB[n]. In this paper we report our work directed toward the preparation of iron based Nitschke type MOPs with mechanically interlocked CB[n] units which was envisioned to allow uptake and release of drugs within a multivalent architecture.

4.2 Results and Discussion

This results and discussion section is organized as follows. First, we describe the self-assembly of Nitschke-type tetrahedron **IV-6** by the self-assembly of viologen dianiline **IV-4** and aldehyde **IV-5** in the presence of $Fe(OTf)_2$ and the threading of CB[7] to yield tetrahedron **IV-7** with mechanically interlocked CB[7] units. Next, we describe the preparation of analogous viologen bipyridine ligands **IV-11** and **IV-16** and their self-assembly with Fe^{II} salts in CH_3CN to deliver tetrahedra **IV-12** and **IV-13** and cubes **IV-17** and **IV-18**.

4.2.1 Synthesis of Dianiline Ligand IV-4 with Viologen Binding Domain

In order to create a self-assembled MOP that features CB[n] binding domains according to Nitschke's subcomponent self-assembly strategy required the preparation of a linear dianiline containing a CB[n] binding domain. For this purpose, we designed compound **IV-4** (Scheme IV-2) which features a central viologen unit which was introduced to the CB[n] field by Kaifer and Kim as an excellent guest for the CB[7] and

CB[8] hosts.[54, 63, 198] Compound **IV-1** was prepared by reaction of 4,4-bipyridine with 2,4-dinitrofluorobenzene in anhydrous CH_3CN according to a literature procedure.[242] Separately, benzidine was reacted with $(Boc)_2O$ to deliver **IV-2** as described in the literature.[243] Subsequently, **IV-1** was heated with 2.0 equiv. **IV-2** in refluxing EtOH overnight followed by addition of THF which caused **IV-3** to precipitate in 96% yield; this type of reaction is referred to as the Zincke reaction.[244] Finally, the t-butoxycarbonyl groups of **IV-3** were deprotected by treatment with CH_3CO_2H (TFA) in CH_2Cl_2 to deliver **IV-4** as its chloride salt in 98% yield. In accord with its high symmetry, Figure IV-2a shows the ^1H NMR spectrum recorded for **IV-4** in CD_3CN which shows two ^1H NMR resonances for the symmetry equivalent viologen protons at 9.22 and 8.64 ppm (H_e and H_f, respectively) and four additional resonances (H_a – H_d) for the phenylene spacer and terminal aniline rings. The ^{13}C NMR spectrum of **IV-4** shows 11 resonances in the aromatic region as expected based on symmetry considerations.

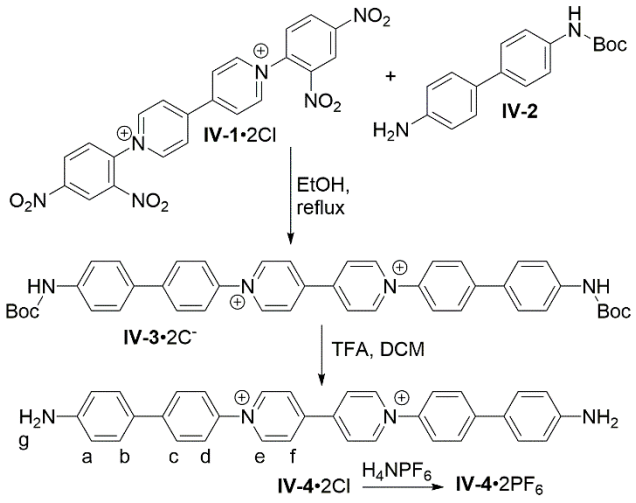

Scheme IV-2. Synthesis of dianiline ligand **IV-4** as its chloride and PF_6 salts.

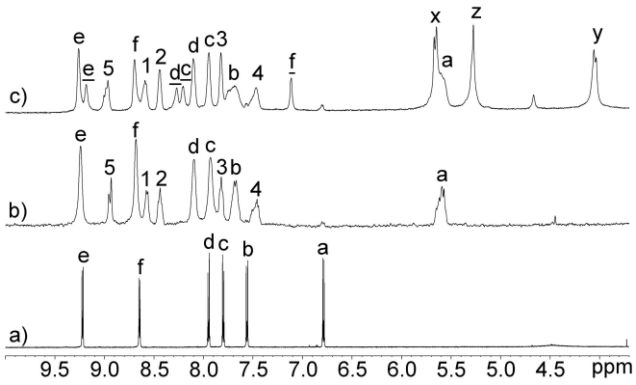

Figure IV-2. ^{1}H NMR spectra recorded (600 MHz, CD_3CN, RT) for: a) **IV-4**•2PF_6, b) **IV-6**•20PF_6 , and c) **IV-7**•20PF_6. The resonances marked with an underscore (_) denote protons on ligand that contain mechanically interlocked CB[7].

4.2.2 Self-Assembly of Nitschke-type Tetrahedron IV-6

With dianiline ligand **IV-4**•2Cl in hand, we sought to react it with pyridine-2-carboxyaldehyde (**IV-5**) and $FeSO_4$ in water to deliver self-assembled tetrahedron **IV-6**. Unfortunately, under aqueous conditions no product was formed which in retrospect is due to the hydrolysis of the labile imine linkages.[118] Accordingly, we performed counterion exchange of **IV-4** from the chloride salt to the PF_6 salt by treatment of an aqueous solution of **IV-4** with NH_4PF_6 to precipitate **IV-4**•2PF_6 (Scheme IV-2). Compound **IV-4**•2PF_6 is soluble in CH_3CN. Next, we performed the self-assembly reaction of a solution of **IV-4**•2PF_6, **IV-5**, and $Fe(OTf)_2$ in dry acetonitrile at 60 °C for 24 hours (Scheme IV-3). Upon addition of $Fe(OTf)_2$, an immediate color change from dark brown to deep purple was observed. UV/Vis spectroscopy shows the presence of a new absorption band from 500 – 615 nm (Supporting Information, Figure IV-S31). This dramatic color change is commonly observed during the formation of Nitschke-type cages due to the metal-to-ligand

charge-transfer interactions associated with low-spin Fe^{II} in a hexaimine ligand environment.[245] The ^1H NMR spectra of tetrahedron **IV-6** is shown in Figure 2b which displays a total of 10 aromatic CH resonances and one imine CH resonance in accord with the depicted structure. The assignments of $H_1 - H_4$ to the pyridine portion of cage **IV-6** and $H_a - H_f$ to the extended viologen region of cage **IV-6** was determined by the cross peaks in the two dimensional COSY spectrum (Supporting Information, Figure IV-S22). The resonance for H_a undergoes a dramatic upfield shift (Figure IV-2a,b) from 6.79 ppm to 5.60 ppm which is diagnostic of self-assembly because H_a is in the anisotropic shielding region of an adjacent ligand at the Fe corner. Importantly, the resonance at 8.84 ppm is characteristic of the newly formed imine bond (HC=N) group. Nitschke has shown that this resonance is particularly sensitive to the presence of diastereomers of the self-assembled tetrahedral cage.[246, 247] Each metal ion corner of **IV-6** can possess either the Δ or Λ stereochemistry which leads to 3 possible combinations (ΔΔΔΔ, ΔΔΔΛ, and ΔΔΛΛ) and their enantiomers. Figure IV-2b shows the presence of two peaks for H_5 at 8.97 and 8.94 ppm which indicates the presence of at least two diastereomeric forms of **IV-6** are formed. Unfortunately, we were unable to obtain either an x-ray crystal structure or observe a parent ion by electrospray ionization mass spectrometry for **IV-6**. Accordingly, we turned to diffusion ordered spectroscopy (DOSY) to obtain information about the size of **IV-6**.[248] The diffusion coefficient of **IV-6** was measured as $D = 3.68 \times 10^{-10}$ m^2 s^{-1} in CD_3CN at 298 K which is 4.7-fold lower than that measured for dianiline **IV-4** ($D = 1.74 \times 10^{-9}$ m^2 s^{-1}) under identical conditions which indicates formation of a significantly larger species. We used the Stokes-Einstein equation[248, 249] to calculate the hydrodynamic

diameter for **IV-6**•20PF_6 as 34.6 Å. We created an MMFF94s minimized molecular model of **IV-6** and measured the distance from the centroid of the four Fe centers to the furthest point of the assembly (22.1 Å) which gives a diameter of 44.2 Å which is slightly larger than that determined by DOSY. This discrepancy may be due to the fact that the assembly is tetrahedral rather than spherical. The diffusion coefficient measured for **IV-6** is slightly smaller than that measured by Nitschke for an assembly constructed from an 2,6-bis(4-aminophenyl)anthracene based ligand (D = 3.82 x 10^{-10} m^2 s^{-1})[247] which provides added support for our formulation of the tetrahedral geometry shown in Scheme IV-3.

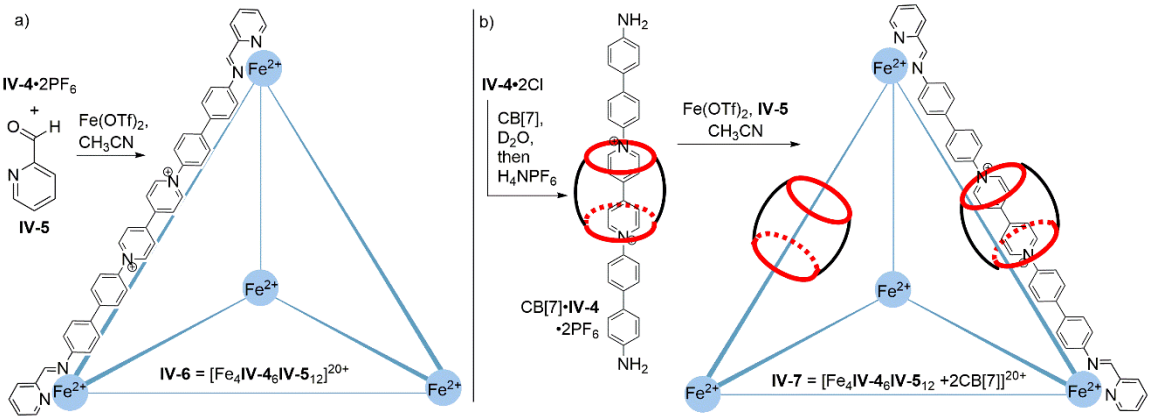

Scheme IV-3. Self-assembly of Nitschke-type tetrahedron **IV-6** and its analogue **IV-7** with mechanically interlocked CB[7].

Table IV-1. Diffusion coefficients (m/s^2) and calculated hydrodynamic diameters (Å) for the different ligands and self-assembled structures. Conditions: CD_3CN, 298 K.

Compound	$D_{MeCN}(m^2/s)$	Hydrodynamic Diameter (Å)
IV-4•$2PF_6$	$(1.74 \pm 0.01) \times 10^{-9}$	7.3
IV-4•CB[7]•$2PF_6$	$(5.53 \pm 0.28) \times 10^{-10}$	23.0
IV-6•$20PF_6$	$(3.68 \pm 0.80) \times 10^{-10}$	34.6
IV-7•$20PF_6$	$(2.71 \pm 0.07) \times 10^{-10}$	46.8
IV-11•$2PF_6$	$(7.30 \pm 0.39) \times 10^{-10}$	17.4
IV-11•CB[7]•$2PF_6$	$(5.08 \pm 0.38) \times 10^{-10}$	25.1
IV-12•$20PF_6$	$(3.08 \pm 0.12) \times 10^{-10}$	41.4
IV-13•$20PF_6$	$(3.06 \pm 0.15) \times 10^{-10}$	41.7
IV-16•$2PF_6$	$(7.71 \pm 0.11) \times 10^{-10}$	16.5
IV-16•CB[7]•$2PF_6$	$(5.66 \pm 0.34) \times 10^{-10}$	22.5
IV-17•$40PF_6$	$(1.40 \pm 0.01) \times 10^{-10}$	91.3
IV-18•$40PF_6$	$(1.25 \pm 0.24) \times 10^{-10}$	102

4.2.3 Investigation of the Complexation of Dianiline IV-4 with CB[n] (n = 7, 8)

The ultimate goal of this project is to create a mechanically interlocked scaffold with CB[8] units on the edges of the MOP that will allow complexation of a multiplicity of drug molecules by the second binding site of CB[8] for drug delivery purposes. As a prelude to such studies, we performed separate titration experiments of dianiline ligand **IV-4**•2Cl with CB[7] and CB[8] in D_2O. At a 1:1 stoichiometric ratio of **IV-4**:CB[7], ^1H NMR spectroscopy (Supporting Information, Figure IV-S11) shows that the resonances for H_e and H_f shift significantly upfield (H_e from 9.48 ppm to 9.20 ppm; H_f from 8.83 ppm to 7.86 ppm) compared to **IV-4** alone. The cavity of CB[n] constitutes a magnetically shielding

environment,[56] which provides strong evidence that CB[7] resides on the central viologen in the CB[7]•**IV-4** complex. As additional quantities of CB[7] is added, the ^{1}H NMR resonances for H_e and H_f shift back toward those observed for free **IV-4** whereas the resonances for the terminal aniline units (H_a - H_d) shift upfield. At a 1:2 **IV-4**:CB[7] stoichiometry a simple spectrum is observed which is indicative of a CB[7]•**IV-4**•CB[7] complex where the CB[7] units reside on each terminal aniline unit. This change in binding site occurs when the free energy of CB[7] binding to two aniline units is larger than one CB[7] binding event at the central viologen unit. Subsequently, we attempted a titration experiment with CB[8] and **IV-4**. Unfortunately, at equimolar ratios, we observed the immediate formation of a precipitate.[250] The small amount of material remaining in solution appears to be the CB[8]$_2$•**IV-4**$_2$ complex based on DOSY measurements (Supporting Information, Figure IV-S17). It is well known that CB[8] can bind two aromatic guests simultaneously.[46, 63, 251] At a 1:1 CB[8]:**IV-4** stoichiometric ratio, this opens up the possibility that CB[8] will bind two aniline termini in a head-to-tail fashion which ultimately leads to oligomerization. A 2:1 mixture of **IV-4** and CB[8] was soluble in D_2O and the ^{1}H NMR showed that the aniline termini were encapsulated inside CB[8] (Supporting Information, Figure IV-S15). Although we were disappointed by our inability to obtain a discrete 1:1 CB[8]•**IV-4** complex we decided to move on toward the mechanical interlocking of CB[7] onto the edges of tetrahedron **IV-6**.

4.2.4 Incorporation of Mechanically Interlocked CB[n] onto the Edges of Assembly IV-6 to Create Assembly IV-7

Given our successful formation of the CB[7]•**IV-4** complex where the central viologen binding domain is complexed, we turned our efforts toward mechanically

interlocking CB[7] on the edges of **IV-6** (Scheme IV-3b). Initially, we tried to perform the one-pot self-assembly of a 6:12:4:6 mixture of **IV-4**•2Cl, **IV-5**, $FeSO_4$, and CB[7] in water but were unsuccessful. Based on the precedent of Nitschke,[118] we also explored the addition of K_2SO_4 to increase ligand solubility and product stability and separately tested $Fe(OTf)_2$ as the iron source, but were uniformly unable to detect any self-assembled tetrahedral assembly. We surmise that the product is hydrolytically unstable under aqueous conditions, or that the iron salt may preferentially interact with the portals of CB[7] which disfavors the desired assembly pathway. Accordingly, we decided to perform the self-assembly process in CH_3CN as was successful for **IV-6**. First, we created the discrete 1:1 CB[7]•**IV-4** complex by mixing equimolar amounts of CB[7] and **IV-4**•2Cl in water, followed by the addition of excess NH_4PF_6 or $LiNTf_2$ which causes the precipitation of the CB[7]•**IV-4**•$2PF_6$ or CB[7]•**IV-4**•$2NTf_2$ salts. The use of counterion exchange to solubilize CB[7] complexes in organic solution was first reported by Kaifer.[252] CB[7]•**IV-4**•$2PF_6$ and CB[7]•**IV-4**•$2NTf_2$ are soluble in CH_3CN and DMSO. Subsequently, self-assembly of a 6:12:4 mixture of CB[7]•**IV-4**•$2PF_6$ salt, **IV-5**, and $Fe(OTf)_2$ was performed in dry acetonitrile at 60 ˚C for 24 hours. The ^{1}H NMR spectrum recorded in CD_3CN (Figure IV-2c) shows two sets of peaks for each of the viologen protons (H_e, H_f) and each of the aniline protons (H_c, H_d) in a 1.95:1 ratio as determined by integration. Of particular note is that $\underline{H_f}$ is upfield shifted by 1.57 ppm to 7.11 ppm whereas $\underline{H_c}$ and $\underline{H_d}$ are slightly downfield shifted (≈ 0.2 – 0.3 ppm) within assembly **IV-7**•$20PF_6$ relative to assembly **IV-6**•$20PF_6$. These changes in chemical shift are comparable to that observed during the formation of the CB[7]•**IV-4** complex which is strong evidence for the mechanical interlocking of an average of 1.95 CB[7] molecules onto the cage **IV-6** to give the depicted

structure of cage **IV-7**. Conversely, the major resonances for H_f, H_c, and H_d in **7** for the uncomplexed edges appear at chemical shifts that are comparable to that observed for **IV-6**. Approximately two edges of **IV-7** are complexed with CB[7] and four edges remain uncomplexed. The DOSY spectrum of **IV-7**•$20PF_6$ shows the presence of a single species with a diffusion coefficient ($D = 2.71 \times 10^{-10}$ m^2 s^{-1}) with a diameter of 46.8 Å calculated according to the Stokes-Einstein equation. The calculated diameter of **IV-7** is 12.2 Å larger than that of **IV-6**•$20PF_6$ which is approximately twice the radius of CB[7] (8.0 Å).[53, 54] Unfortunately, we were unable to obtain ESI-MS data for assembly **IV-7**. We observe the precipitation of CB[7] during the self-assembly of cage **IV-7** which establishes that the CB[7] can decomplex from CB[7]•**IV-4** complex during the reaction. Related experiments conducted with lower amounts of CB[7] (e.g. three free **IV-4** and three CB[7]•**IV-4**), still lead to assembly **IV-7**. Attempts to prepare **IV-7** by a slippage[253] process involving heating **IV-6** and CB[7] in CD_3CN (60 ˚C) were unsuccessful due to the insolubility of CB[7]. Having successfully mechanically interlocked least 2 CB[7] molecules onto the edges to create **IV-7** we tested the stability of **IV-7** in water as a precursor step to the envisioned use of these assemblies in drug delivery. When water was added to either assembly **IV-6** or **IV-7**, we observed the disappearance of the characteristic purple color and the ^1H NMR displayed resonances for the starting materials **IV-4** and **IV-5**. In particular, the loss of the imine H_5 peak and the emergence of the aldehyde O=C-H resonance provide strong evidence that the cage underwent hydrolysis in water due to hydrolytic instability. Given this finding it appeared that the envisioned mechanical interlocking of CB[n] onto the edges of Nitschke-type assemblies was a dead end which prompted us to explore ligands whose assemblies would be stable in water.

4.2.5 Synthesis of Bipyridine Based Viologen Ligand IV-11 and its Self-Assembly to give MOP IV-12

To circumvent the problems with the aqueous hydrolysis of the imine bonds that hold assembly **IV-7** together, we redesigned our system using a more robust ligand that is not prepared in a subcomponent self-assembly process. We settled on ligand **IV-11** which features 2,2'-bipyridine termini as ligands and a central viologen unit as the CB[n] binding domain (Scheme IV-4). First, we performed the Suzuki reaction between commercially available starting materials **IV-8** and **IV-9** using $Pd(Ph_3)_4$ as catalyst to deliver **IV-10** in 92% yield.[254] Next, we allowed aniline **IV-10** to react with **IV-1** by a double Zincke reaction in refluxing EtOH to deliver target ligand **IV-11**•2Cl in 97% yield. Compound **IV-11** was fully characterized spectroscopically (^1H, ^{13}C, ESI-MS). For example, the ^1H NMR spectrum of **IV-11** recorded in D_2O (Supporting Information, Figure IV-S32) show the characteristic viologen protons (H_j and H_k) resonances at 9.50 ppm and 8.83 ppm, a pair of coupled doublets for the phenylene linker (H_i and H_h) at 8.14 ppm and 8.00 ppm, and the expected seven additional aromatic resonances (H_a – H_g) for the 2,2'-bipyridyl end groups (two triplets (H_a and H_b), a singlet (H_g), and three pairs of doublets (H_d – H_f)). In the ^{13}C NMR spectrum, all 17 resonances expected for **IV-11** on the basis of its depicted C_{2v}-symmetric structure were observed experimentally. Compound **IV-11**•2Cl could be transformed into the corresponding PF_6 or NTf_2 salts by treatment of aqueous solutions of **IV-11**•2Cl with an excess of NH_4PF_6 or $LiNTf_2$ which resulted in precipitation of **IV-11**•2PF_6 and **IV-11**•2NTf_2 which are used in some of the self-assembly reactions described below.

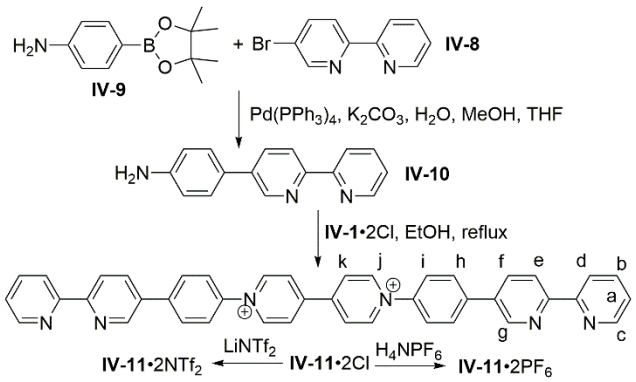

Scheme IV-4. Synthesis of modified bipyridyl ligand **IV-11**.

Before proceeding to the self-assembly of **IV-11•**2Cl we decided to test its complexation with CB[7] and separately with CB[8] in the absence of iron salts. Simple ^{1}H NMR spectroscopic titration shows that **IV-11•**2Cl binds to CB[7] in D_2O (Supporting Information, Figure IV-S42). At a 1:0.9 ratio of **IV-11**:CB[7], we observe upfield changes in chemical shift for viologen protons H_j and H_k as well as phenylene protons H_h and H_i whereas the resonances for H_c and H_g which are on the 2,2-bipyridine end groups do not experience significant changes in chemical shift. This indicates that the CB[7] units in the CB[7]**•IV-11** complex are not at a fixed location but rather shuttle between the phenylene and viologen binding sites. At a 1:2 **IV-11**:CB[7] ratio, the resonances for the phenylene linker H_h and H_i undergo further upfield changes in chemical shift as the CB[7] units become localized on the phenylene binding sites to accommodate the presence of two molecules of CB[7]. Somewhat differently, the ^{1}H NMR spectrum of a 1:1 mixture of **IV-11** and CB[8] (Supporting Information, Figure IV-S46 and IV-S47) shows only small shifting for the viologen protons H_j and H_k (H_j from 9.50 to 9.40 ppm, H_k from 8.83 to 8.96 ppm) whereas the phenylene protons undergo more substantial upfield shifts (H_h from 8.00 to 7.36 ppm; H_i from 8.14 to 7.60 ppm) upon complexation.

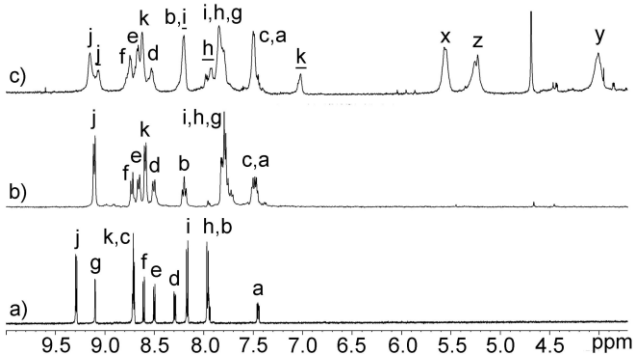

Figure IV-3. ^{1}H NMR spectra recorded (600 MHz, CD_3CN, RT) for: a) **IV-11**•$2PF_6$, b) **IV-12**•$20NTf_2$, and c) **IV-13**•$20PF_6$. The resonances marked with an underscore (_) denote protons on ligand that contain mechanically interlocked CB[7].

Encouraged by the ability to observe 1:1 complexation between **IV-11** and CB[7] or CB[8], we moved on to the self-assembly studies. Initially, we performed the self-assembly of **IV-11**•$2PF_6$ and $Fe(OTf)_2$ (6:4 molar ratio) in CH_3CN at 60 ˚C for 24 hours which delivers self-assembled tetrahedron **IV-12**•$20PF_6$ (Scheme IV-5). Immediately after mixing, we observed a color change from yellow-brown to red which is characteristic of the formation of the iron-bipyridine complex. Figure IV-3a,b shows the ^{1}H NMR spectra recorded for **IV-11**•$2PF_6$ and for the self-assembled MOP **IV-12**•$20NTf_2$. Upon self-assembly, the resonances for H_c and H_g which are adjacent to the bipyridine N-atoms undergo significant upfield shifts (H_c: 8.71 ppm to 7.50 ppm; H_g: 9.10 ppm to 7.79 ppm) which reflects that these protons feel the anisotropic shielding effect of an adjacent bipyridine when complexed to the metal center.[255, 256] Conversely, H_a, H_d, H_e, and H_f undergo slight downfield shifts upon self-assembly (H_a: 7.94 to 8.20 ppm, H_d: 8.29 to 8.50 ppm, H_e: 8.50 to 8.65 ppm, and H_f: 8.61 to 8.72 ppm) likely due to changes in the electronics of the bipyridine ring upon coordination to iron. In this case, the observation

of a single set of sharp ^{1}H and ^{13}C NMR (Supporting Information, Figure IV-S50) resonances of the expected number and multiplicity strongly suggests the formation of a single diastereomer of **IV-12** which we formulate as the racemic mixture of ΔΔΔΔ-**IV-12** and ΛΛΛΛ-**IV-12**. The UV/Vis spectra recorded for **IV-11** and assembly **IV-12** in CH_3CN is given in the Supporting Information (Supporting Information, Figure IV-S70). The spectra for **IV-12** shows a new band with λ_{max} = 539 nm which is due to metal to ligand charge transfer upon complexation,[256, 257] as well as the shifting of a shorter wavelength λ_{max} from 294 (for **IV-11**) to 315 nm (for **IV-12**). We used DOSY NMR to determine the diffusion coefficient for **IV-12**•20PF_6 in acetonitrile at 25 ˚C (D = 3.08 x 10^{-10} m^2 s^{-1}) as given in Table 1 which is 2.4-fold slower than the free ligand **IV-11**•2PF_6 (D = 7.30 x 10^{-10} m/s^2) which provides support for self-assembly. The calculated hydrodynamic diameter of **IV-12**•20PF_6 is 41.4 Å which is somewhat larger than Nitschke-type cage **IV-6**•20PF_6 (34.6 Å).[116] Finally, Figure IV-4a shows the electrospray ionization mass spectrum recorded for assembly **IV-12** as its PF_6 salt. We observe the presence of ions in the mass spectrum that correspond to the 6+ to 9+ ions of **IV-12**•20PF_6 ($[Fe_4$**IV-11**$_6$ +14(PF_6)$]^{6+}$ *m/z* = 994.23; $[Fe_4$**IV-11**$_6$ +13(PF_6)$]^{7+}$ *m/z* = 831.35; $[Fe_4$**IV-11**$_6$ +12(PF_6)$]^{8+}$ *m/z* = 709.30; $[Fe_4$**IV-11**$_6$ +11(PF_6)$]^{9+}$ *m/z* = 614.38) upon successive loses of PF_6 counterions. The **IV-12**•20PF_6 salt could be transformed to the **IV-12**•10SO_4 salt by treatment of a CH_3CN solution with excess K_2SO_4 which gave the sulfate salt as a solid precipitate. MOP **IV-12**•10SO_4 was soluble in water and did not undergo any change by ^{1}H NMR upon standing at 25 ˚C for > 2 weeks. MOP **IV-12**•10SO_4 could also be synthesized directly under aqueous conditions from a 6:60:4 mixture of **IV-11**•2Cl, K_2SO_4, and $FeSO_4$ by sonicating

for 30 minutes at room temperature and then heating at 60 °C for 24 hours (Scheme IV-5, Figure IV-S57).

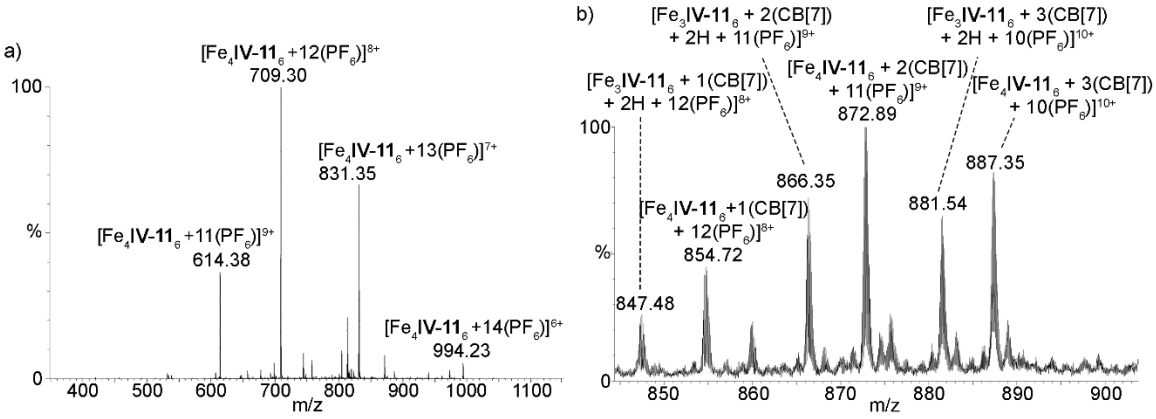

Figure IV-4. Mass spectra recorded for CH_3CN:DMSO solutions of: a) **IV-12**•$20PF_6$, and b) **IV-13**•$20PF_6$.

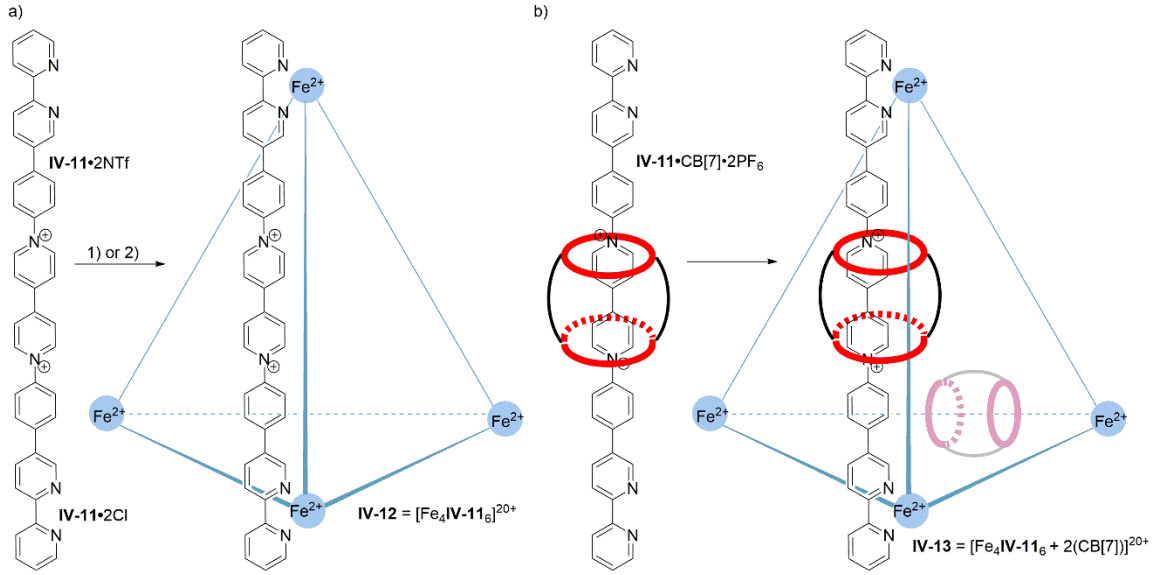

Scheme IV-5. Self-assembly of: a) tetrahedron **IV-12** performed in either CH_3CN or H_2O, and b) tetrahedron **IV-13** which incorporates CB[7] units. Conditions: 1) $Fe(NTf_2)_2$, CH_3CN, 60 °C, 2) K_2SO_4, $FeSO_4$, 60 °C.

4.2.6 Mechanical Interlocking of CB[n] onto the Edges of Cage IV-12 to Give Cage IV-13

Encouraged by the successful self-assembly of **IV-12** under aqueous conditions, we decided to target the incorporation of mechanically interlocked CB[n] components. For this purpose, we performed the self-assembly of **IV-11**•2Cl, CB[7], K_2SO_4, $FeSO_4$ (6:6:60:4) in water (60 ˚C) for 24 hours. The reaction mixture did not change color over this time period as was expected and remained heterogenous throughout. Furthermore, we did not observe upfield shifting for H_c and H_g in the ^{1}H NMR spectrum which would be expected upon formation of the iron(bipyridine)$_3$ corners. Our interpretation is that the conformation heterogeneity of the **IV-11**•CB[7] complex in water (e.g. mainly on the phenylene rather than the viologen binding site hinders formation of the targeted self-assembled cage perhaps by promoting protonation of the bipyridine units. In contrast, the ^{1}H NMR spectrum recorded in acetonitrile for the CB[7]•**IV-11**•2PF_6 complex that had been prepared in water shows a substantial upfield shift for viologen resonance H_k from 8.71 ppm for free **IV-11**•2PF_6 to 7.17 ppm as part of the CB[7]•**IV-11**•2PF_6 complex which provides clear evidence for the CB[7] residing on the viologen unit (Supporting Information, Figure IV-S43). Proton H_j also undergoes a small upfield shift upon complexation whereas the remaining protons on ligand **IV-11** undergo small downfield changes in chemical shift. Accordingly, we next performed the self-assembly of a mixture of CB[7]•**IV-11**•2PF_6 and $Fe(OTf)_2$ in acetonitrile at 60 ˚C for 24 hours (Scheme IV-5b). The self-assembly process is also successful when CB[7]•**IV-11**•2NTf_2 and $Fe(NTf_2)_2$ are employed. The reaction mixture rapidly changes color from yellow to ruby red. MOP **IV-13**•20PF_6 was isolated after precipitation from the reaction mixture by the addition of Et_2O

followed by centrifugation, decanting the supernatant, and drying. The ^{1}H NMR of **IV-13**•20PF_6 recorded in CD_3CN is shown in Figure IV-3c. The assignment of the resonances is based upon the correlations observed in the COSY spectrum (Supporting Information, Figure IV-S65). Most strikingly, the resonance for viologen proton H_k in **IV-13** shifts dramatically upfield to 7.02 ppm compared to that observed for **IV-12** (8.59 ppm, Figure IV-2b) which lacks CB[7] units. Furthermore, we observe two sets of resonances for protons H_h, H_i, H_j, and H_k of unequal (1.80 by integration) ratio by ^{1}H NMR. This ^{1}H NMR data suggests that on average four **IV-11** ligands that are part of assembly **IV-13** do not have mechanically interlocked CB[7] units whereas two ligands of **IV-11** possess a mechanically interlocked CB[7] unit. Integration of the resonances for the CB[7] unit (H_x, H_y, H_z) versus the ligand protons (H_j and $\underline{H_j}$ combined) also shows that 1.80 CB[7] are mechanically interlocked on **IV-13**. The slight upfield shift observed for $\underline{H_j}$ (9.10 to 9.06 ppm) and the slight downfield shifts observed for $\underline{H_h}$ (7.80 to 7.97 ppm) and $\underline{H_i}$ (7.80 to 8.20 ppm) relative to H_j, H_h, and H_i support the notion that the CB[7] units reside on the viologen binding domain in assembly **IV-13**. To gauge the size of assembly **IV-13**•20PF_6 we performed DOSY NMR which allowed us to calculate the diffusion coefficient (D = 3.06 x 10^{-10} m/s^2) and the hydrodynamic diameter of assembly **IV-13** (41.7 Å) in acetonitrile. The resonances for ligand **IV-11** and CB[7] within assembly **IV-13** diffuse at the same rate which provides further evidence for the interlocked nature of **IV-13**. The diffusion coefficient and hydrodynamic radius of **IV-13** are very similar to those measured for the Nitschke-type assembly **IV-7** which also contains interlocked CB[7] units (Table IV-1). Figure IV-4b shows a region of ESI mass spectrum obtained for **IV-13** as its PF_6 salt. We observe dominant ions at *m/z* 887.35 ([Fe_4**IV-11**$_6$ + 3(CB[7]) + 10(PF_6)]$^{10+}$),

872.89 ([Fe_4**IV-11**$_6$ + 2(CB[7]) + 11(PF_6)]$^{9+}$), and 854.72 ([Fe_4**IV-11**$_6$ + 1(CB[7]) + 12(PF_6)]$^{8+}$) which correspond to cage **IV-13** with three, two, and one interlocked CB[7], respectively, as their 10+, 9+, and 8+ ions (Supporting Information, Figures IV-S67 – IV-S69). The combined inference of the ^{1}H NMR, DOSY, and ESI-MS data provides strong support for the formulation of **IV-13** as a tetrahedral cage that possesses an average of 1.80, but a range of 1–3, mechanically interlocked CB[7] units. We also attempted the self-assembly of **IV-11**•2Cl, $FeSO_4$, K_2SO_4, and CB[8] in water at 60 ˚C, but we did not observe any color change which is strong evidence against the formation of iron(bipyridine)$_3$ complexes under these conditions. We suspect that the ureidyl C=O groups of CB[8] scavenge the $FeSO_4$ and prevent assembly. Attempts to prepare the organic soluble CB[8]•**IV-11**•2PF_6 complex were not successful according to ^{1}H NMR analysis.

4.2.7 Molecular Modelling of Self-Assembled Tetrahedra IV-12 and IV-13

We performed molecular modelling of tetrahedra **IV-12** and its analogue fully interlocked with six CB[7] rings **IV-12**•CB[7]$_6$. Figure IV-5a,b shows the structures of **IV-12** and **IV-12**•CB[7]$_6$ minimized by molecular mechanics using the MMFF94s force field implemented within the Spartan ‘16 software package. As can be seen, **IV-12** features a roughly tetrahedral geometry with a large central cavity. The average distance between Fe atoms of MOP **IV-12** is 24.9 Å and the distance from the centroid of the four Fe atoms to the outside edge of the MOP is 19.1 Å. Accordingly, the rough diameter of the MMFF94s mininimzed structure of **IV-12** is 38.2 Å which is slightly smaller than the hydrodynamic diameter (41.4 Å) calculated from the DOSY data. The hydrodynamic diameter of **IV-12** in solution also reflects the contributions of the 20 PF_6 counterions so

this small difference is not surprising. It should be noted that the edges of **IV-12** are slightly bowed outward in the molecular model which is likely due to electrostatic repulsion between dicationic viologen units in the overall 20+ assembly. Figure IV-5b shows the MMFF94s minimized structure of **IV-12**•$CB[7]_6$ which is roughly tetrahedral with average iron-iron distances of 25.0 Å and centroid to iron distance of 15.3 Å. The structure calculated structure easily accommodates six CB[7] units and there is no evidence of close contacts or even van der Waals interactions between CB[7] units in the minimized structure of **IV-12**•$CB[7]_6$. Accordingly, the experimental observation that assembly **IV-13** contains 1.8 CB[7] units on average must be due to other factors including the poor solubility of CB[7] in the reaction mixture and the potential for repulsive electrostatic interactions between the electrostatically negative convex outer surfaces of CB[7] units.[54] The distance between the centroid of the iron atoms of **IV-12**•$CB[7]_6$ and the outer edge of the ligands is 19.3 Å which corresponds to a calculated diameter of 38.6 Å. This calculated value for **IV-12**•$CB[7]_6$ is very similar to the value measured for **IV-13**•$20PF_6$ by DOSY (Table IV-1).

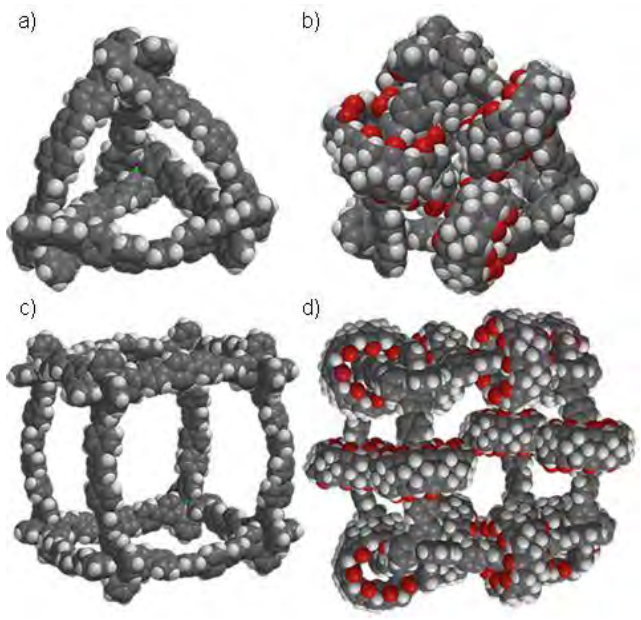

Figure IV-5. a) Molecular modelling of a) **IV-12**, b) **IV-12**•6CB[7], c) **IV-17**, and d) **IV-17**•12CB[7].

4.2.8 Synthesis of Isomeric Bipyridine Ligand IV-16 and Self-Assembly to Give Cubic MOP IV-17

Although we were pleased that cage **IV-12** could be threaded to give cage **IV-13** containing an average of two CB[7] units, we were disappointed that full occupancy of the edges (e.g. six CB[7]) could not be achieved. We decided to create a larger self-assembly that would have a larger central cavity that might be able to better accommodate a larger number of CB[n] rings. We realized that ligand **IV-16** (Scheme IV-6) – which is a constitutional isomer of **IV-11** – possesses a geometry[258] that should deliver a self-assembled cube upon reaction with Fe(II) salts. For the synthesis of **IV-16**, we first performed the Suzuki coupling reaction between commercially available 4-bromo-2,2'-bipyridine **IV-14** and **IV-9** using $Pd(PPh_3)_4$ as catalyst to deliver **IV-15** in 64% yield.

Subsequently, the Zincke reaction[244] between **IV-15** and **IV-1** was performed in refluxing EtOH to deliver **IV-16** in 77% yield. Compound **IV-16** was fully characterized by the standard spectroscopic methods. For example, characteristic ^{1}H NMR resonances for the viologen aromatic protons (H_j and H_k) appear at 9.52 ppm and 8.86 ppm (Supporting Information, Figure IV-S71) whereas a pair of aromatic doublets appear at 8.23 ppm and 8.04 ppm for the phenylene linker (H_i and H_h) along with seven additional aromatic resonances (H_a – H_g) are for the bipyridyl end group (triplets for H_a and H_b, a singlet for H_g, and three doublets for H_d – H_f. The ^{13}C NMR spectrum for **IV-16** recorded in DMSO-d_6 (Supporting Information, Figure IV-S72) displays 17 resonances in the aromatic region of the spectrum which is consistent with the C_{2v}-symmetric structure depicted in Scheme IV-6.

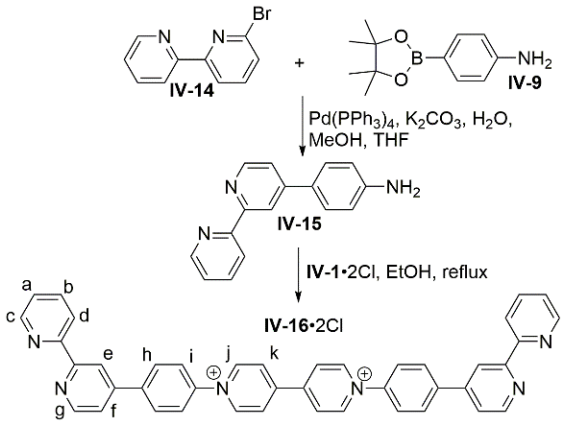

Scheme IV-6. Synthesis of isomeric bipyridine ligand **IV-16**.

Given our previous success in the self-assembly of **IV-12** in acetonitrile, we first converted **IV-16** into the corresponding organic soluble PF_6 and NTf_2 salts. To prepare self-assembled cube **IV-17** we heated a 12:8 mixture of **IV-16**•2PF_6 (or **IV-16**•2NTf_2) with $Fe(OTf)_2$ (or $Fe(NTf_2)_2$) in acetonitrile at 60 ˚C for 24 hours (Scheme IV-7). During the

course of the reaction the color changes from orange-brown to deep purple. The UV/Vis spectra recorded for **IV-16** and **IV-17** is given in the Supporting Information (Figure IV-S94). The spectrum for **17** shows a new λ_{max} at 544 nm which is comparable to that observed for **12** (λ_{max} = 539 nm) which provides strong support for the formation of the iron(bipyridine)$_3$ corners. The ^{1}H NMR spectrum recorded for **IV-17** in CD_3CN is shown in Figure IV-6. The assignments of the resonances to specific protons in Figure IV-6 are based on the correlations observed in the COSY spectrum of **IV-17** (Supporting Information, Figure IV-S88). Most significantly, the protons adjacent to the bipyridine N-atoms undergo substantial upfield changes in chemical shift upon transformation of **IV-16** to **IV-17** (H_c: 8.83 to 7.62 ppm; H_g: 8.73 to 7.53 ppm). These large upfield shifts reflect the fact that these protons are located in the anisotropic shielding region of the adjacent bipyridine within assembly **IV-17** as was also seen for **IV-12**. Bipyridine protons H_b (7.96 to 8.24 ppm), H_d (8.51 to 8.84 ppm), and H_e (8.70 to 8.96 ppm) undergo slight downfield shifts upon formation of **IV-17** which is reflective of the change in electronics of the bipyridine ring upon coordination to Fe^{II}. To gain insight into the size of assembly **IV-17** we performed DOSY NMR in CD_3CN at 298 K that allowed us to calculate the diffusion coefficient for **IV-17** ($D = 1.40 \times 10^{-10}$ m/s^2) and its hydrodynamic diameter (91.3 Å). Cage **IV-17** diffuses 5.51 times slower than ligand **IV-16** ($D = 7.71 \times 10^{-10}$ m/s^2) and 2.20 times slower than tetrahedron **IV-12**. Figure IV-5c shows the structure of an MMFF94S minimized model of **IV-17** which is roughly cubic with an edge length of 27.7 Å. The maximum distance from the centroid of the eight iron atoms to the outer edges of **IV-17** is 28.1 Å which corresponds to a diameter of 56.2 Å. The calculated diameter of **IV-17** and the hydrodynamic diameter of **IV-17** measured in solution differ in part because of the

influence of the 40 PF_6 counterions and perhaps also due to the effects of aggregation.[248] Overall, the confluence of the data provides significant evidence for the formulation of the structure of **IV-17** as a cubic assembly. Unfortunately, despite numerous attempts we were not able to observe ions in the ESI-MS spectrum for either **IV-17**•40PF_6 or **IV-17**•40NTf_2 that could be assigned to the depicted cubic assembly.

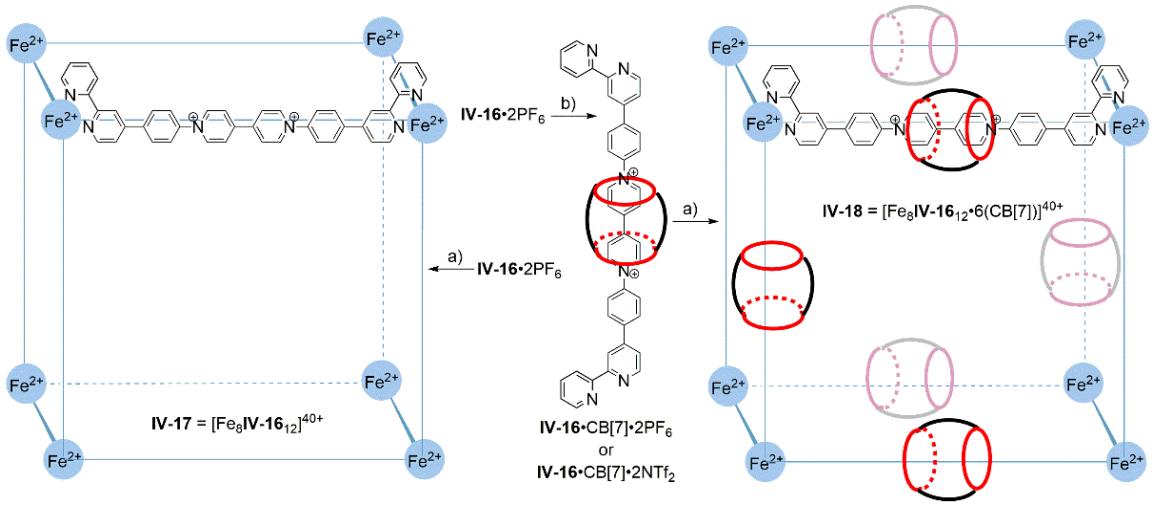

Scheme IV-7. Self-assembly of MOPs **IV-17** and **IV-18**. Conditions: a) $Fe(OTf)_2$, CH_3CN, b) D_2O, CB[7], then NH_4PF_6.

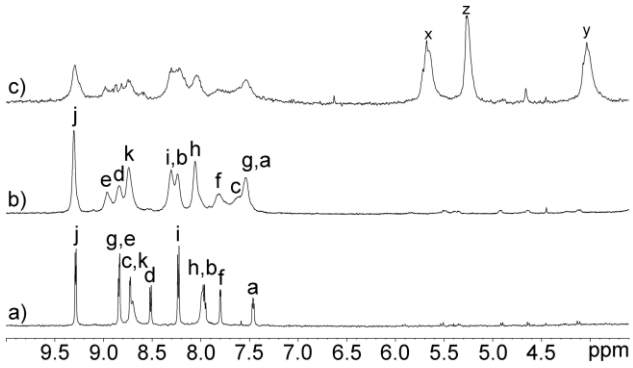

Figure IV-6. ^1H NMR spectra recorded (600 MHz, CD_3CN, RT) for: a) **IV-16**•2PF_6, b) **IV-17**•20PF_6, and c) **IV-18**•40NTf_2.

4.2.9 Mechanical Interlocking of CB[7] onto the Edges of Cage IV-17 to Give Cage IV-18

Next, we set out to mechanically interlock CB[7] units onto the edges of self-assembled cube **IV-17**. Initially, we tested the complexation of an equimolar mixture of CB[7] with **IV-16**•2Cl in D_2O by ^1H NMR (Supporting Information, Figure IV-S79). We observe upfield shifting for phenylene protons H_h (8.05 to 7.14 ppm) and H_i (8.25 to 7.34 ppm) and viologen proton H_j (9.53 to 9.10 ppm) and downfield shifting of viologen proton H_k (8.88 to 8.98 ppm) upon complexation with CB[7]. This data indicates that the primary binding site is the phenylene unit. Accordingly, we decided to follow the strategy employed for the assembly of **IV-13** involving CH_3CN soluble salts. Experimentally, we treated aqueous solutions of CB[7]•**IV-16**•2Cl with excess $LiNTf_2$ and separately with excess NH_4PF_6 which gave CB[7]•**IV-16**•$2NTf_2$ and CB[7]•**IV-16**•$2PF_6$ as precipitates that could be isolated by centrifugation, washing with water, and drying under high vacuum (Scheme IV-7). For the self-assembly reaction, we heated equimolar mixtures of CB[7]•**IV-16**•$2NTf_2$ (or CB[7]•**IV-16**•$2PF_6$) and $Fe(NTf_2)_2$ (or $Fe(OTf)_2$) at 60 ˚C in acetonitrile for 24 hours to give **IV-18**. The reaction mixture rapidly assumes a deep purple color. Assembly **IV-18** can be isolated by precipitation from the reaction mixture by addition of Et_2O followed by centrifugation, decantation, and drying. Figure 6c shows the ^1H NMR spectrum recorded for **IV-18** in CD_3CN which is broadened and unfortunately the multiplicity cannot be observed for individual resonances. The broadness of the ^1H NMR spectrum rendered the COSY spectrum of no value. However, a comparison of the aromatic regions of Figures 6b and 6c make it clear that very similar assemblies are formed

in both cases. Furthermore, integration of the resonances for the CB[7] units (H_x, H_y, H_z) versus those of ligand **IV-16** allow us to determine that assembly **IV-18** contains an average of 6.59 molecules of CB[7]. We acquired the DOSY spectrum for **IV-18** in acetonitrile which established that the CB[7] units of the assembly diffuse at the same rate as aromatic units of the assembly which provides strong evidence for the mechanical interlocking of the CB[7] units onto the edges of the assembly. Figure IV-5d shows an MMFF94s minimized model of **IV-17**•$(CB[7])_{12}$ which does not show any steric interactions between the adjacent CB[7] units. The observation that assembly **IV-18** contains an average of 6.59 CB[7] units must be due to other factors including the poor solubility of CB[7] in the reaction medium or perhaps unfavorable electrostatic interactions between the electrostatically positive convex faces of the CB[7] units. The DOSY spectrum allowed us to calculate the diffusion coefficient for **IV-18** ($D = 1.25 \times 10^{-10}$ m/s^2) along with its hydrodynamic diameter (102 Å). The hydrodynamic diameter of **IV-18** is very similar to that of **IV-17** (91.3 Å) which provides further support for the formulation of both **IV-17** and **IV-18** as cubes. Overall, the data provides clear evidence for the incorporation of multiple CB[7] units onto the edges of assembly **IV-18** but, unfortunately, even with this larger cubic system it was not possible to achieve full occupation of all 12 edges with CB[7] units.

4.3 Conclusions

In summary, we have reported our initial investigations into the preparation of MOPs that contain mechanically interlocked CB[n] units as a precursor to using the

molecular recognition properties of such assemblies for drug delivery purposes. Initially, we prepared dianiline ligand **IV-4**•2Cl – which contains a central viologen unit as a CB[n] binding site – and performed self-assembly with pyridine-2-carboxaldehyde and $Fe(OTf)_2$ in acetonitrile and observed the formation of a single species by ^1H and DOSY NMR that we assign as tetrahedron **IV-6**. When the organic soluble CB[7]•**IV-11**•$2PF_6$ complex was self-assembled with $Fe(OTf)_2$ in acetonitrile, assembly **IV-7** with an average of 1.95 mechanically interlocked CB[7] units was obtained. Unfortunately, MOPs **IV-6** and **IV-7** were hydrolytically unstable in water and therefore are not appropriate for drug delivery studies. Accordingly, analogous organic soluble ligands **IV-11**•$2(NTf_2)$ and **IV-16**•2PF6 that feature terminal 2,2'-bipyridine groups were prepared and their self-assembly with $Fe(NTf_2)_2$ or Fe(OTf) was performed which delivered tetrahedral assembly **IV-12** and cubic assembly **IV-17** as evidenced by analysis of complexation induced changes in ^1H NMR chemical shift, DOSY, and ESI-MS results for **IV-12**. Assemblies **IV-12** and **IV-17** are stable under aqueous conditions. Finally, threading of ligands **IV-11** and **IV-16** with CB[7] gave the acetonitrile soluble complexes CB[7]•**IV-11**•$2PF_6$ and CB[7]•**IV-16**•$2PF_6$ which underwent assembly with $Fe(OTf)_2$ in acetonitrile to give self assembled tetrahedron **IV-13** and cube **IV-18** which on average contain 1.80 and 6.59 CB[7] molecules, respectively. In conclusion, we find that the self-assembly of MOPs with mechanically interlocked CB[7] requires that the CB[7] units reside on the viologen unit which is favored in acetonitrile rather than the phenylene binding epitope. Our inability to achieve full binding of CB[7] to every MOP edge cannot be ascribed to steric effects but probably reflects partial dissociation of the CB[7]•**IV-11** or CB[7]•**IV-16** complexes under

the reaction conditions. Future work targets new ligands with tighter binding and slower dissociating CB[n] binding domains that may assemble to give MOPs fully saturated with mechanically interlocked CB[n].

Appendix 1

Conformationally Mobile Acyclic Cucurbit[n]uril-Type Receptors Derived from an S-shaped Methylene Bridged Glycoluril Pentamer

Kimberly G. Brady,[†] Laura Gilberg,[†‡] David Sigwalt,[†] Joshua Bistany-Riebman,[†] Steven Murkli [†], Jared Klemm,[†] Petr Kulhánek,*[‡] Vladimír Šindelář,*[‡] and Lyle Isaacs*[†]

[†] *Department of Chemistry and Biochemistry, University of Maryland, College Park, Maryland 20742, United States*
[‡] *Department of Chemistry and RECETOX, Faculty of Science, Masaryk University, Kamenice 5, 625 00 Brno, Czech Republic*

Supporting Information

Table of Contents **Pages**

Computational Details.

The relative stabilities of the F1, F2, and F3 conformers were investigated on simplified models employing density functional theory (DFT) approach. These models included **TriMe** and **TriH** containing two S-shaped connections between adjacent glycolurils, models **P1'** and **P2'** with solubilizing groups ($O(CH_2)_3SO_3Na$) absent representing simplified versions of **P1** and **P2**, and complexes of **P1'** and **P2'** with guest **II-8**. Initial structures were built *in silico* in the three conformational states and then their geometries were optimized employing B97-3[259] method in an implicit water described by the SMD[260] model. Finally, the relative stabilities were evaluated at the PBE0-D3BJ/def2-TZVPP level of theory[261-263] in the SMD implicit water on the optimized geometries. The employed computational methodology was thoroughly tested and showed similar accuracy as MP2/CBS. Further computational details, optimized geometries, and their absolute energies are available in the Supporting Information. All quantum chemical calculations presented in the main text were performed in Orca 4.2.1.[264]

A possible structure of the **P2•P2** dimer was investigated by molecular dynamics simulations performed in the Amber 16 package.[265] The **P2** host was considered in the F1 and F2 folds, which resulted in two possible dimeric structures (**P2**-F1•**P2**-F1 and **P2**-F2•**P2**-F2). These dimers were built *in silico* and described by the GAFF force field in MD simulations.[266] Each dimer was immersed into a box filled by an explicit water solvent described the TIP3P model with electroneutrality maintained by 8 sodium cations. In total, each system was simulated for 1 μs at a temperature of 300 K and a pressure of 100 kPa.

Experimental Details. Compounds **II-4** and **II-5** were prepared according to the literature procedures.[82] NMR spectra were measured on 400 MHz, 500 MHz, 600, and 800 MHz spectrometers (400, 500, 600, 800 MHz for ^{1}H NMR; 126 MHz for ^{13}C NMR) at room temperature in the stated deuterated solvents.

Compound II-3. Glycoluril **II-1** (4.78 g, 33.6 mmol) was dissolved in 90% aq. methanesulfonic acid (80 mL). Then the solution was cooled to 8-12 °C using an ice bath within 20 min. and **II-2** (15.97 g, 62.8 mmol) was added in one portion and the reaction was stirred at 8-12 °C for 2 h and then 2 h at room temperature. The reaction mixture was poured into acetone (1.4 L) that had been cooled in ice for 30 min. to give a precipitate which was obtained by filtration. The crude solid was washed with ethanol. The crude solid was then dissolved in acetonitrile/water (1:1 v:v, 200 mL) and stored in the refrigerator for 2-3 days. The resulting precipitate was isolated by filtration and then purified by successive cycles of stirring and centrifuging using the following solvent series: DMSO (6 mL), H_2O (12 mL), CH_3CN/H_2O 1:1 (20 mL), acetone (30 mL), Et_2O (30 mL). The final off-white residue was dried under high vacuum to give **II-3** (847 mg, 5%). M.p. > 300 °C. IR (ATR, cm^{-1}): 2917w, 2849w, 1711s, 1452s, 1371m, 1308m, 1250m, 1224m, 1187m, 1079m, 1012w, 958w, 918w, 862w, 770m. ^{1}H NMR (DMSO-d_6, 800 MHz, 30 °C): 5.54 (d, J = 15.2, 4H), 5.51 (d, J = 8.6, 2H), 5.21 (d, J = 13.7, 4H), 5.16 (d, J = 11.0, 4H), 5.09 (d, J = 8.6, 2H), 4.86 (d, J = 11.0, 4H), 4.71 (d, J = 13.7, 4H), 4.27 (d, J = 15.2, 4H), 1.82 (s, 6H), 1.70 (s, 6H), 1.64 (s, 6H).^{13}C NMR (DMSO- d_6, 126 MHz, 30 °C): 154.7, 154.7, 153.8, 78.00, 77.0, 72.4, 70.6, 69.5, 62.4, 48.2, 47.5, 17.8, 16.6, 15.8. HR-MS (ESI):

m/z 1091.4953 ([M + hexanediamine + H]$^{+}$), $C_{44}H_{63}N_{22}O_{12}$, calculated 1091.4996; 546.2520 ([M + hexanediammonium]$^{2+}$), $C_{44}H_{64}N_{22}O_{12}$, calculated 546.2532.

Host P1. Compound **II-3** (1.57 g, 1.60 mmol) was charged to a round bottomed flask followed by trifluoroacetic acid (5.1 mL), Ac_2O (5.1 mL), and then finally **II-4** (1.47 g, 3.68 mmol) was added. The reaction mixture was stirred and heated at 75 °C for 3 h. The reaction mixture was poured into MeOH (65 mL) and the resulting precipitate was isolated by filtration. The crude solid was triturated with boiling water (30 mL) and then cooled in the refrigerator. The resulting solid was collected by centrifugation, dissolved in water and adjusted to pH 7 with 1 M aqueous NaOH. The solution was filtered to remove dust and then concentrated to dryness by rotary evaporation to afford host **P1** as an off-white solid (597 mg, 22%). M.p. > 300 °C. IR (ATR, cm^{-1}): 3427m, 2944w, 1703s, 1460s, 1374m, 1311m, 1182s, 1081m, 1036s, 844w, 796w, 786w. ^{1}H NMR (DMSO-d_6, 400 MHz, 30 °C): 6.84 (s, 4H), 5.50 (d, *J* = 15.9 Hz, 4H), 5.41 (d, *J* = 8.6 Hz, 2H), 5.28 (d, *J* = 16.2 Hz, 4H), 5.13 (d, *J* = 13.8 Hz, 4H), 5.05 (d, *J* = 8.6 Hz, 2H), 4.59 (d, *J* = 13.8 Hz, 4H), 4.17 (d, *J* = 15.9 Hz, 4H), 4.13 (d, *J* = 16.2 Hz, 4H), 4.00 - 3.93 (m, 8H), 2.69 – 2.56 (m, 8H), 2.03 - 1.97 (m, 8H), 1.73 (s, 6H), 1.67 (s, 6H), 1.60 (s, 6H). ^{13}C NMR (D_2O, 126 MHz, 30°C, dioxane as internal reference): 157.3, 157.1, 156.5, 150.7, 128.6, 115.6, 80.0, 79.7, 78.3, 71.6, 69.4, 64.4, 49.4, 48.7, 48.3, 35.6, 25.2, 16.5, 16.2, 15.4. HR-MS (ESI): *m/z* 547.8031 ([M-H]$^{3-}$), $C_{62}H_{75}N_{20}O_{26}S_4$, calculated 547.8020; 410.5995 ([M-H]$^{4-}$), $C_{62}H_{74}N_{20}O_{26}S_4$, calculated 410.5997.

Host P2. A round bottomed flask was charged with **II-3** (976 mg, 1.00 mmol), trifluoroacetic acid (3.2 mL), Ac_2O (3.2 mL), and then finally **II-5** (1.01 g, 2.3 mmol). The reaction mixture was stirred and heated at 75 °C for 3 h. The reaction mixture was poured into MeOH (50 mL) and the precipitate was isolated by filtration. The crude solid was dissolved in water (25 mL) and precipitated by the addition of KCl (900 mg, 12.0 mmol). The precipitate was isolated by centrifugation and then dissolved in water and adjusted to pH 7 with 1 M aqueous NaOH. The solution was filtered to remove dust and then concentrated to dryness by rotary evaporation to afford **P2** as a pale yellow solid (492 mg, 27%). M.p. > 300 °C. IR (ATR, cm^{-1}): 3421w, 2999w, 2979w, 2944w, 1707s, 1458s, 1373m, 1311m, 1225m, 1183s, 1079m, 1034m, 950w, 785w, 757w. ^1H NMR (DMSO-d_6, 400 MHz, 30 °C): 7.99 (m, 4H), 7.56 (m, 4H), 5.51 (d, J = 15.5 Hz, 4H), 5.38 (d, J = 8.7 Hz, 2 H), 5.34 (d, J = 15.8 Hz, 4H), 5.06 (d, J = 13.9 Hz, 4H), 4.97 (d, J = 8.7 Hz, 2H), 4.51 (d, J = 13.9 Hz, 4H), 4.41 (d, J = 15.8, 4H), 4.22 - 4.18 (m, 4H), 4.16 (d, J = 15.5 Hz, 4H), 3.93- 3.91 (m, 4H), 2.77 – 2.73 (m, 8H), 2.18 – 2.15 (m, 8H), 1.76 (s, 12H), 1.63 (s, 6H). ^{13}C NMR (D_2O, 126 MHz, 30 °C, dioxane as internal reference): 157.0, 156.7, 156.1, 148.9, 128.1, 127.3, 127.0, 122.9, 79.7, 79.3, 78.1, 74.8, 71.4, 64.2, 49.2, 48.6, 48.2, 36.8, 25.8, 16.4, 16.1, 15.9. HR-MS (ESI): *m/z* 872.2222 ($[M-H]^{2-}$), $C_{70}H_{80}N_{20}O_{26}S_4$, calculated 872.2223; 581.1456 ($[M-H]^{3-}$), $C_{70}H_{79}N_{20}O_{26}S_4$, calculated 581.1458; 435.6078 ($[M-H]^{4-}$), $C_{70}H_{78}N_{20}O_{26}S_4$, calculated 435.6075.

^{1}H and ^{13}C NMR spectra of new compounds

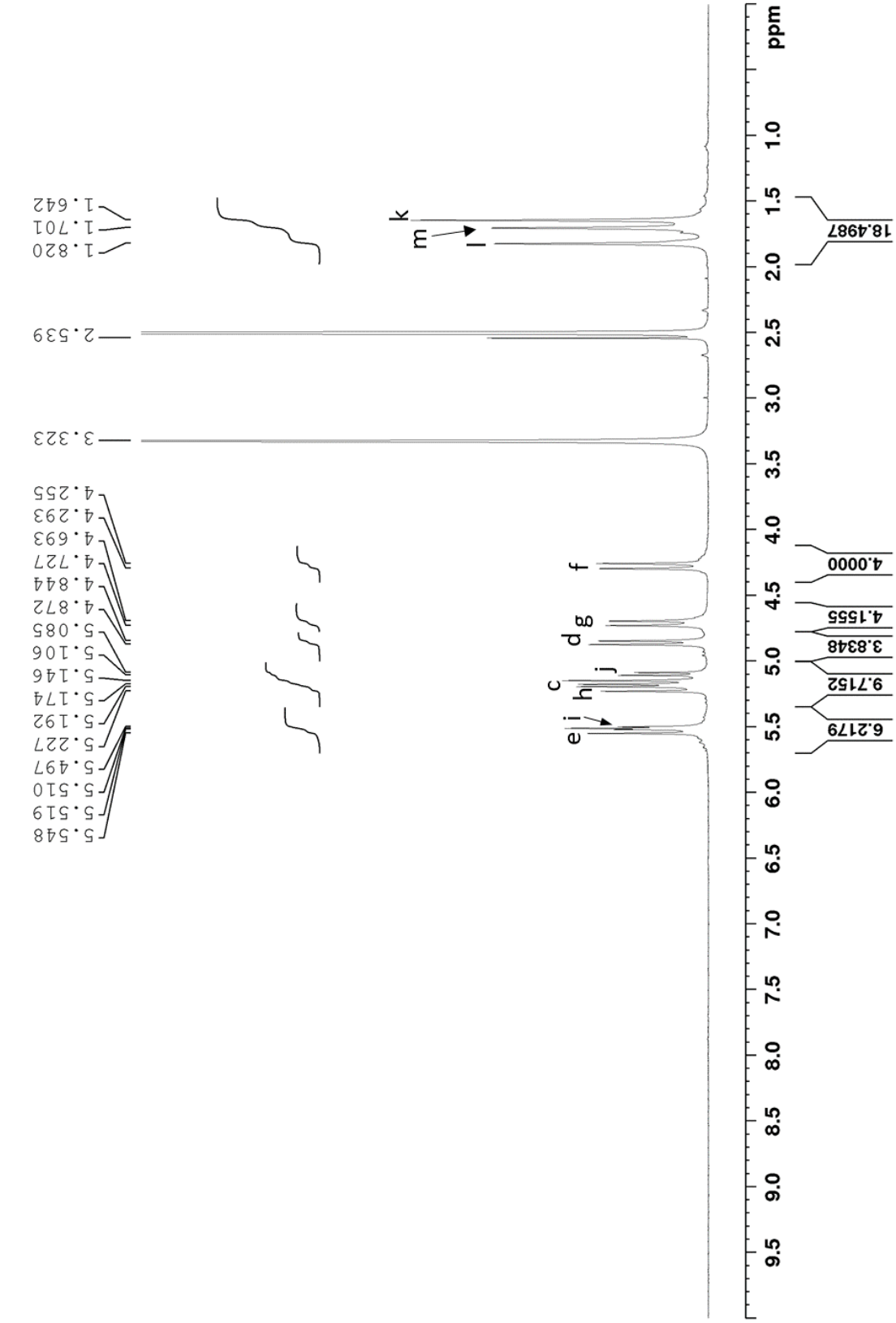

Figure II-S1. ^{1}H NMR (400 MHz, DMSO-d_6, RT) recorded for compound **II-3**.

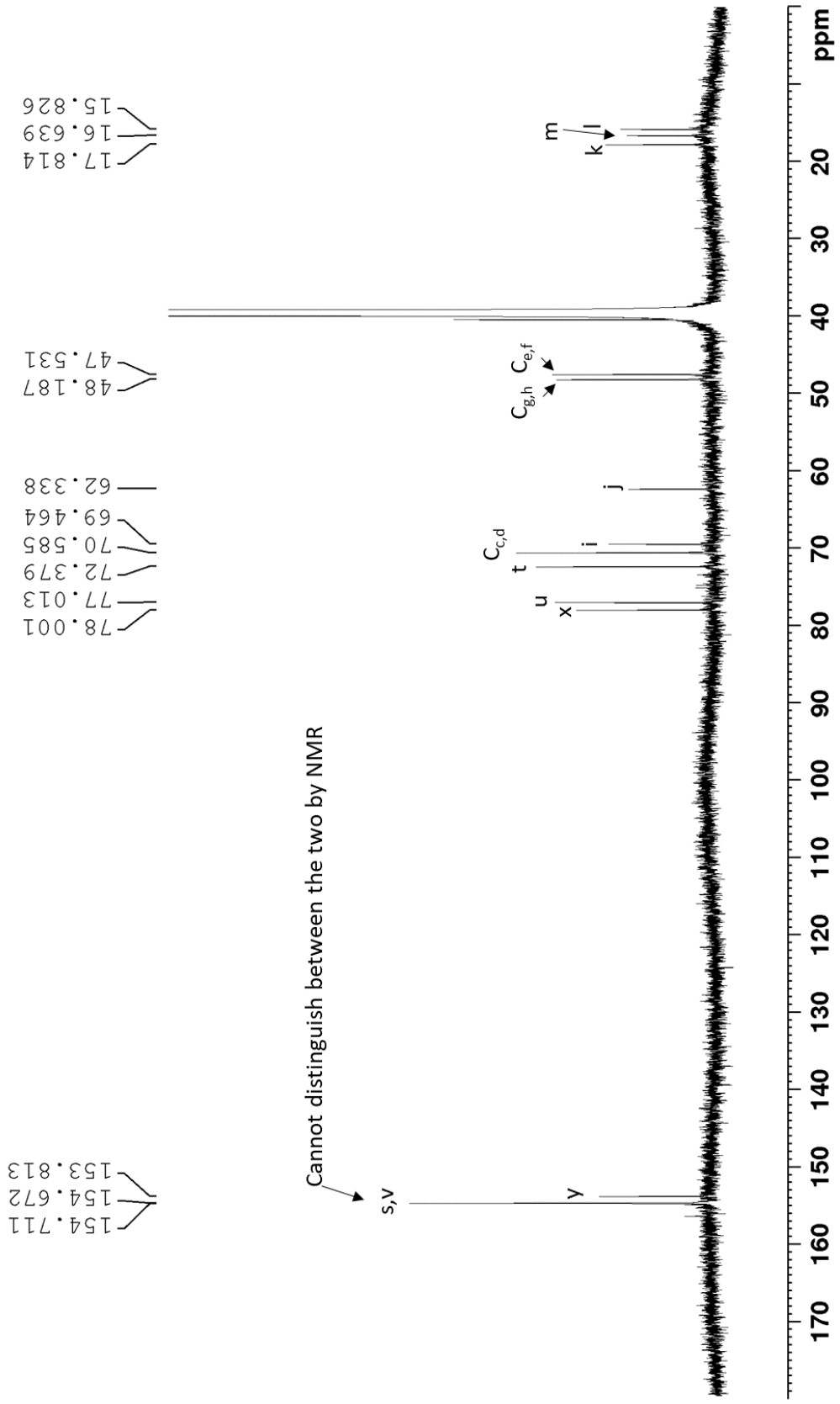

Figure II-S2. ^{13}C NMR spectrum (201 MHz, DMSO-d_6, RT) recorded for **II-3**.

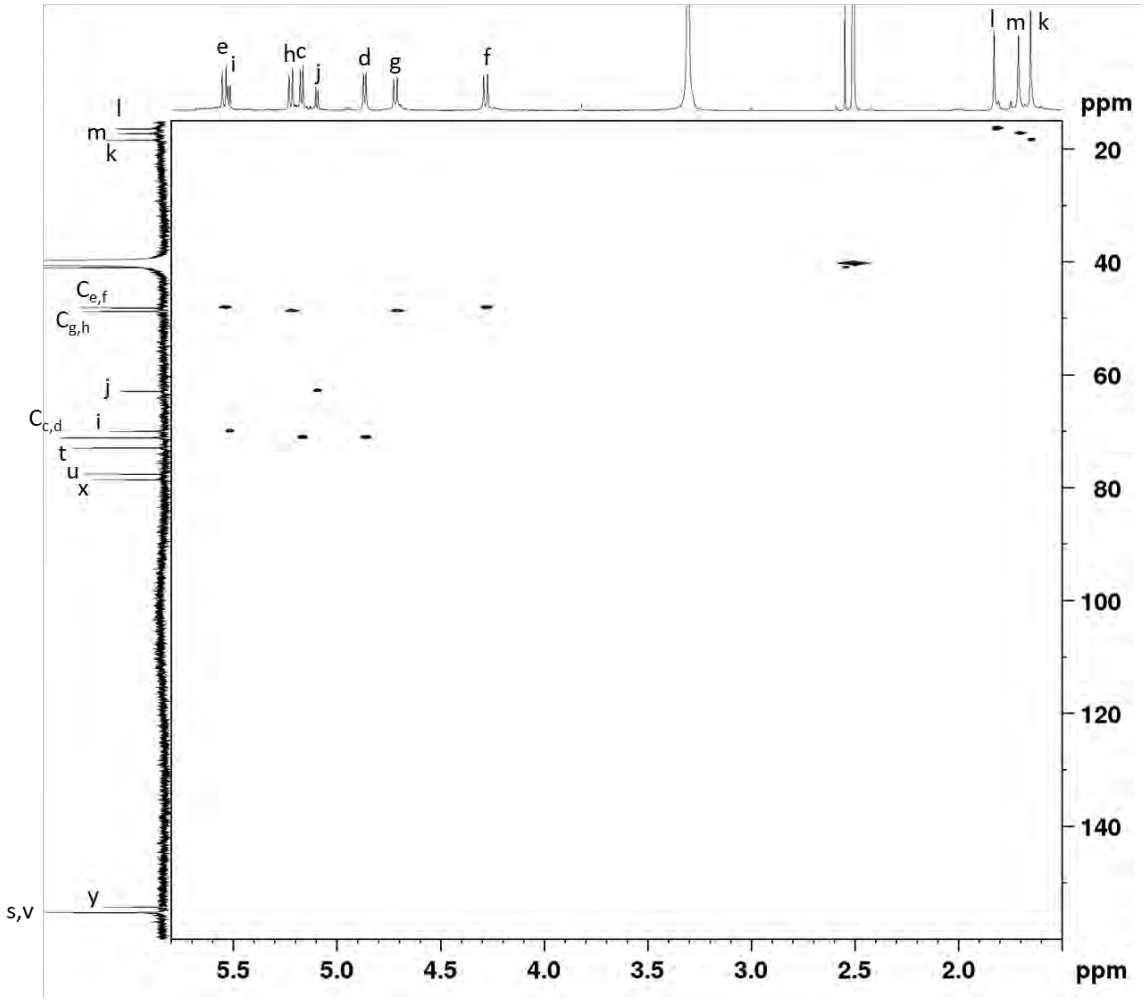

Figure II-S3. HMQC spectrum (DMSO-d_6, RT) recorded for **II-3**.

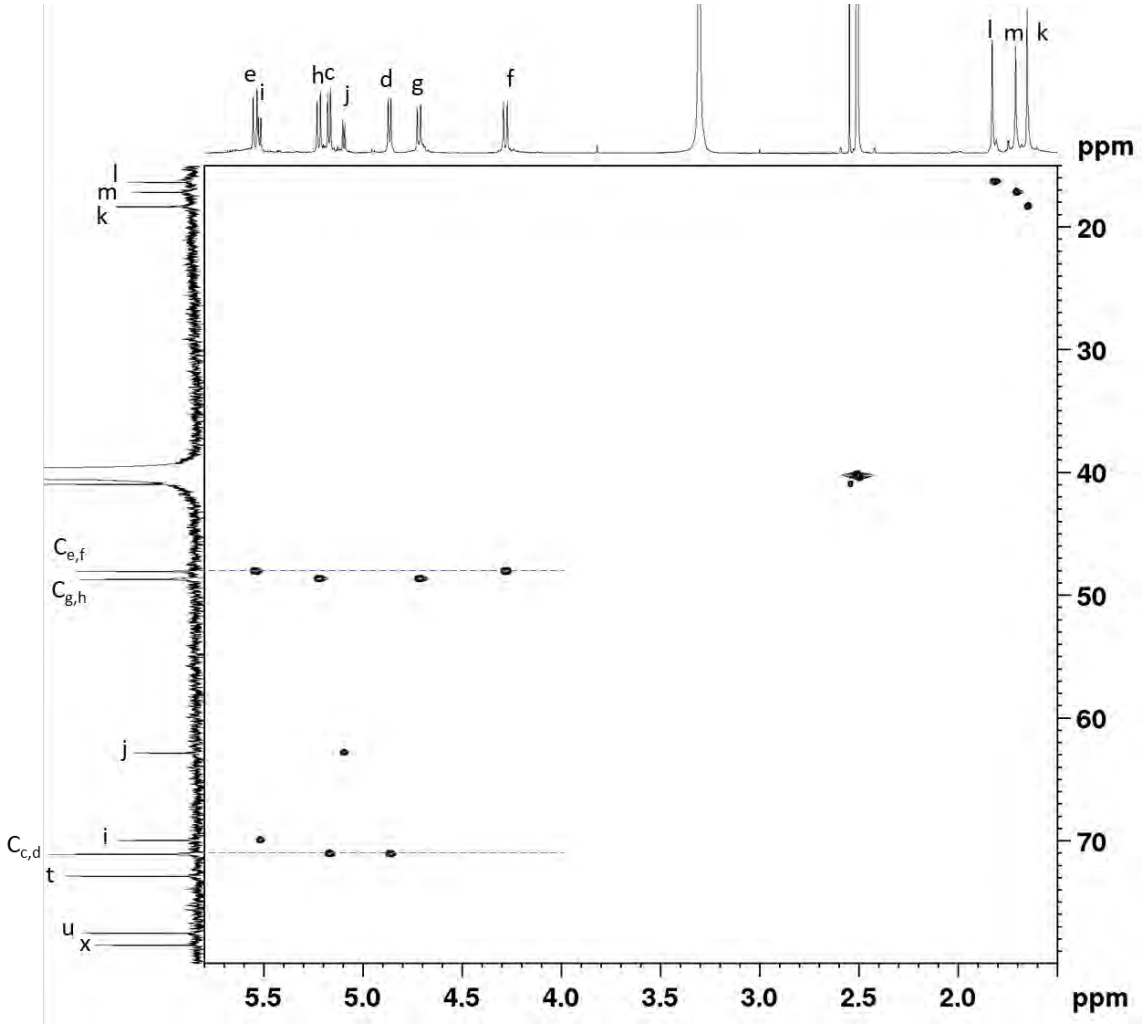

Figure II-S4. Segment of the HMQC spectrum (DMSO-d_6, RT) for **II-3** from 15 – 80 ppm on y-axis.

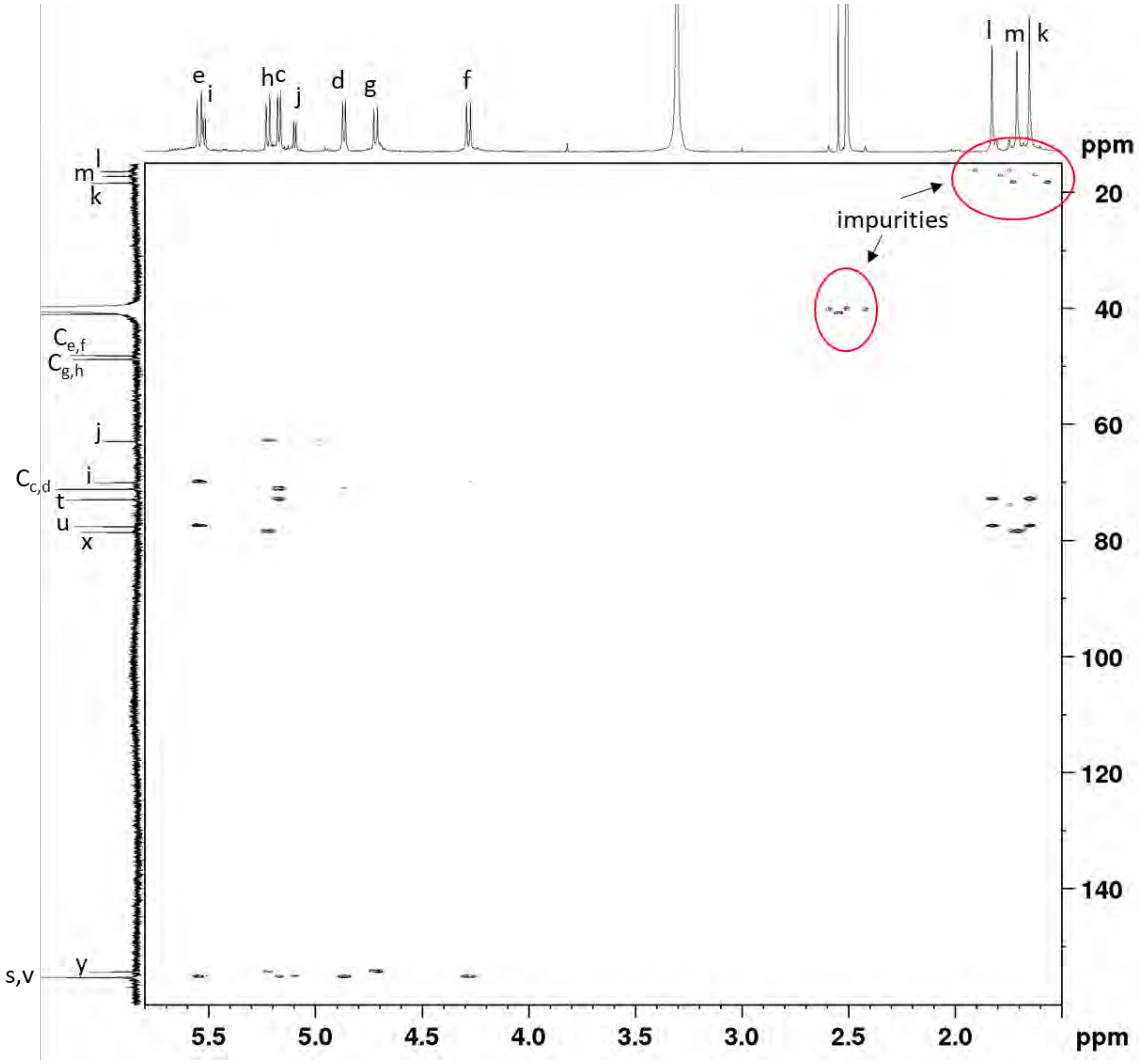

Figure II-S5. HMBC spectrum (DMSO-d_6, RT) recorded for **II-3**.

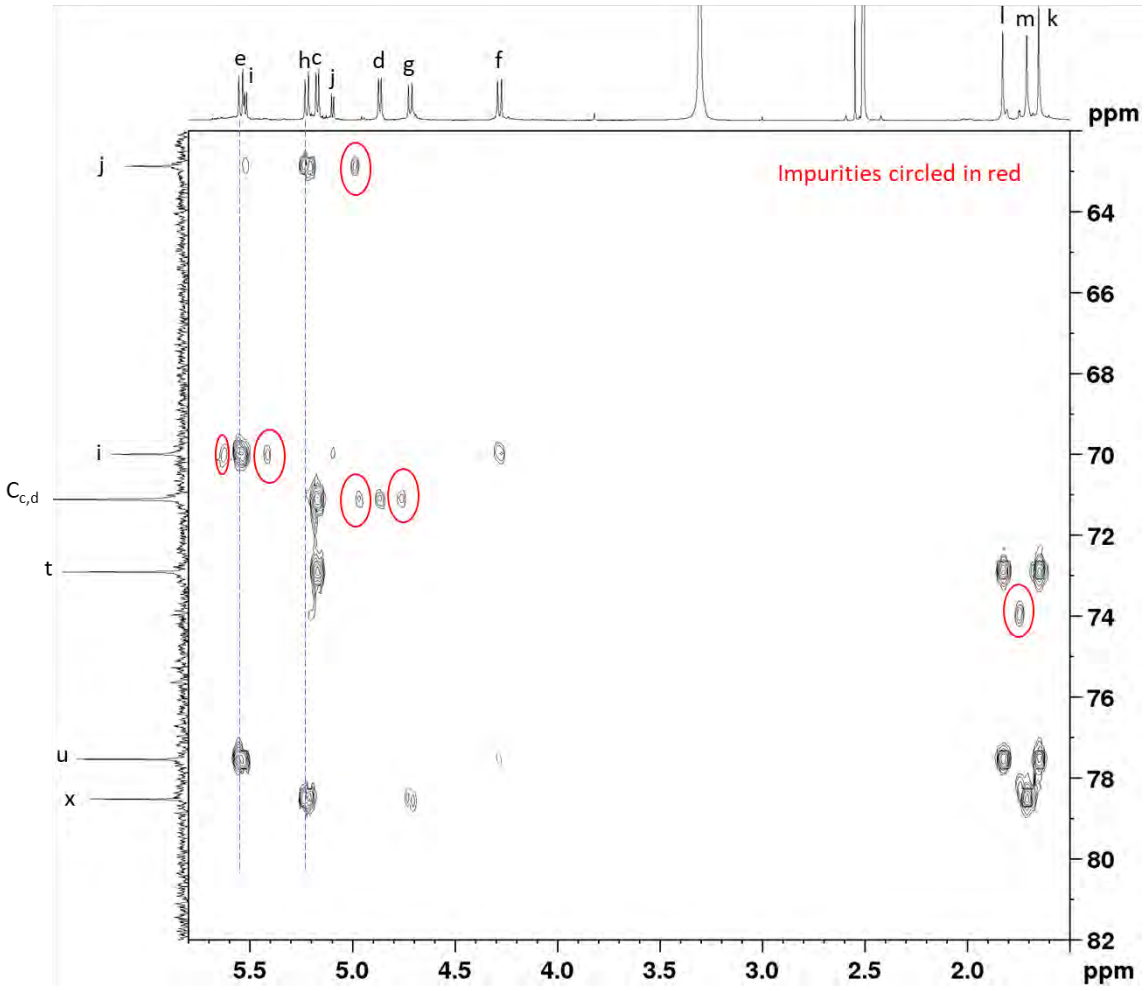

Figure II-S6. Segment of the HMBC spectrum (DMSO-d_6, RT) for **II-3** from 62 – 82 ppm on y-axis.

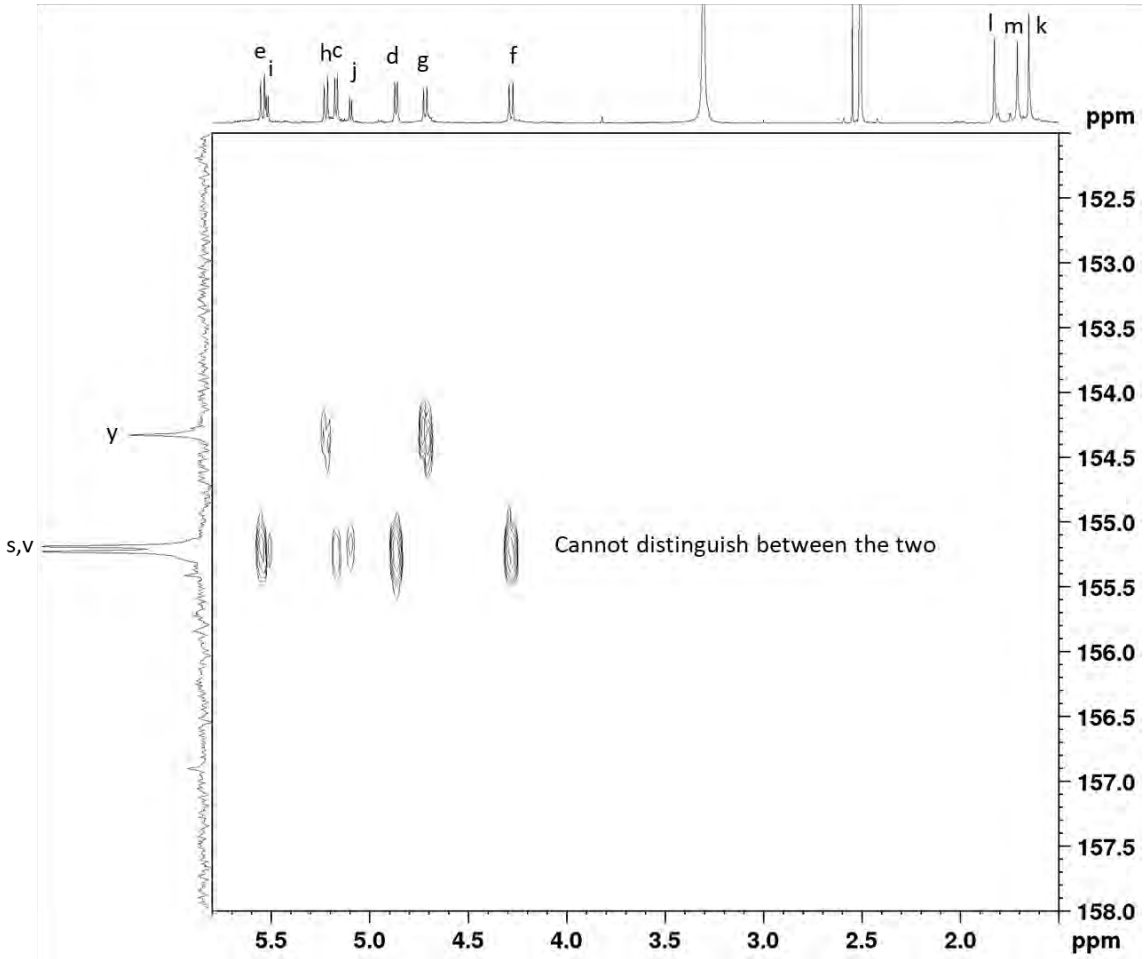

Figure II-S7. Segment of the HMBC spectrum (DMSO-d_6, RT) for **II-3** from 152 – 158 ppm on y-axis.

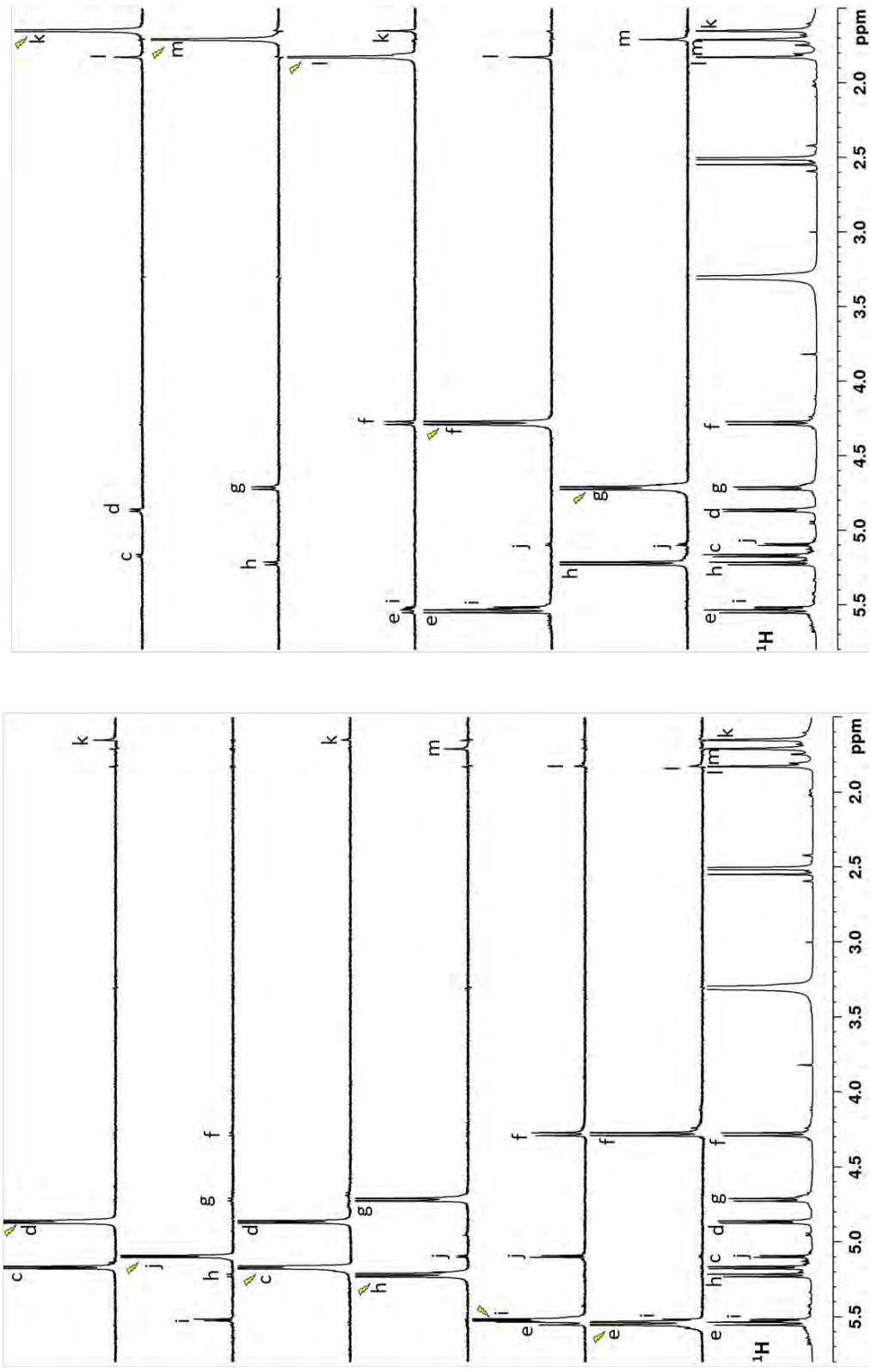

Figure II-S8. Selective 1D NOE spectra (800 MHz, DMSO-d_6, 30 °C) recorded for **II-3**. The thunderbolt indicates which proton was irradiated.

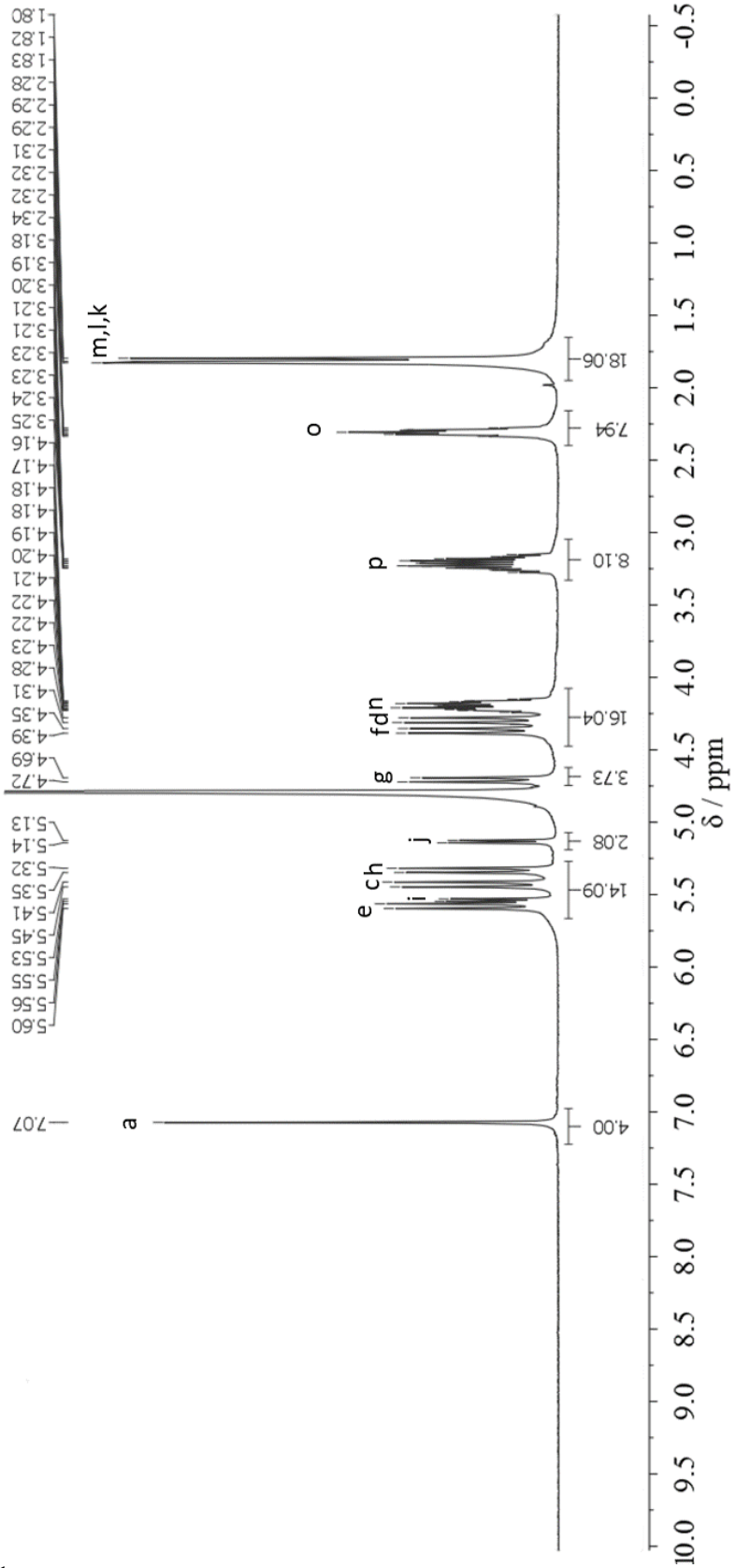

Figure II-S9. ^{1}H NMR spectrum (500 MHz, D_2O, RT) recorded for compound **P1**.

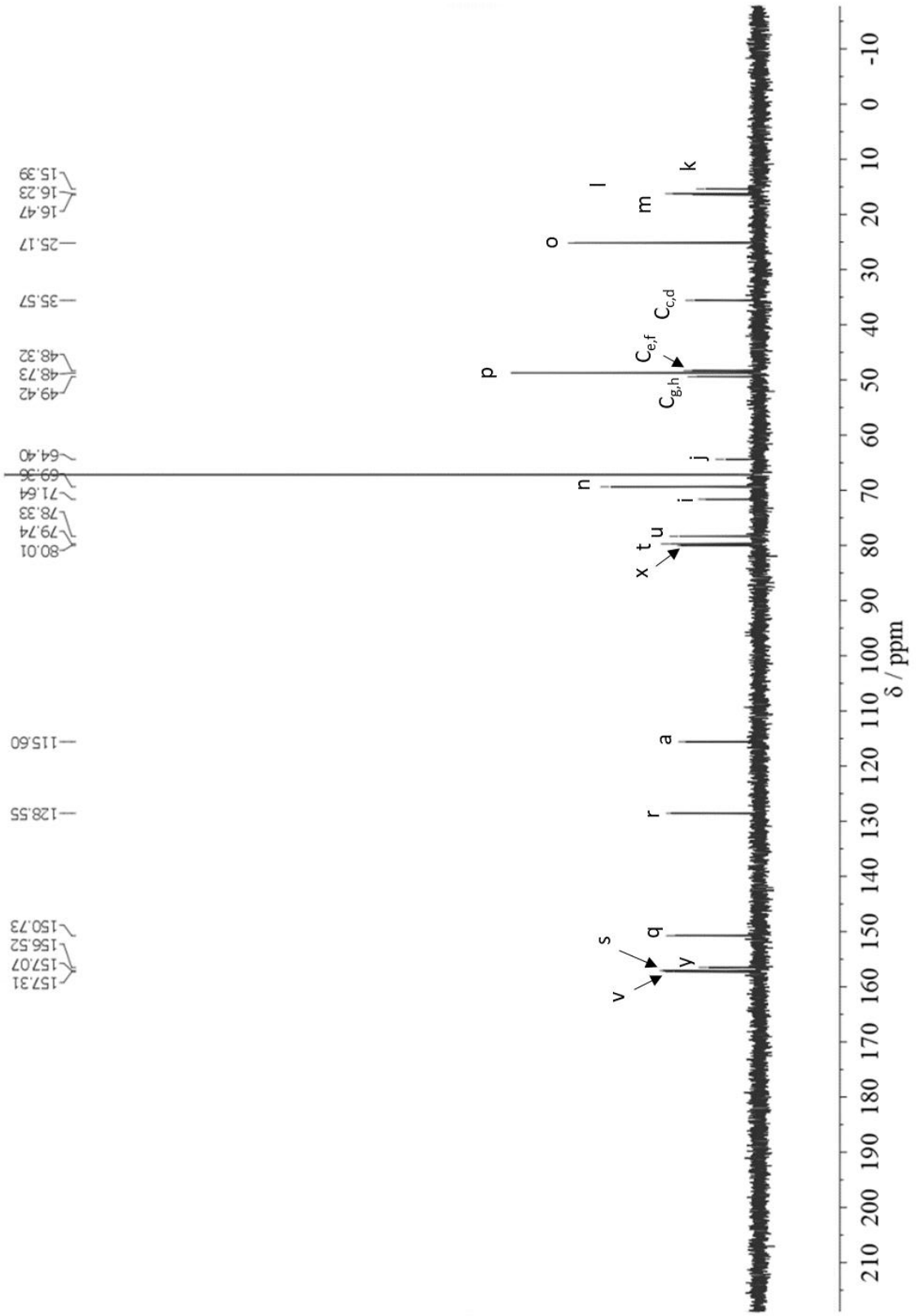

Figure II-S10. ^{13}C NMR spectrum (126 MHz, D_2O, dioxane as internal reference, RT) recorded for compound **P1**.

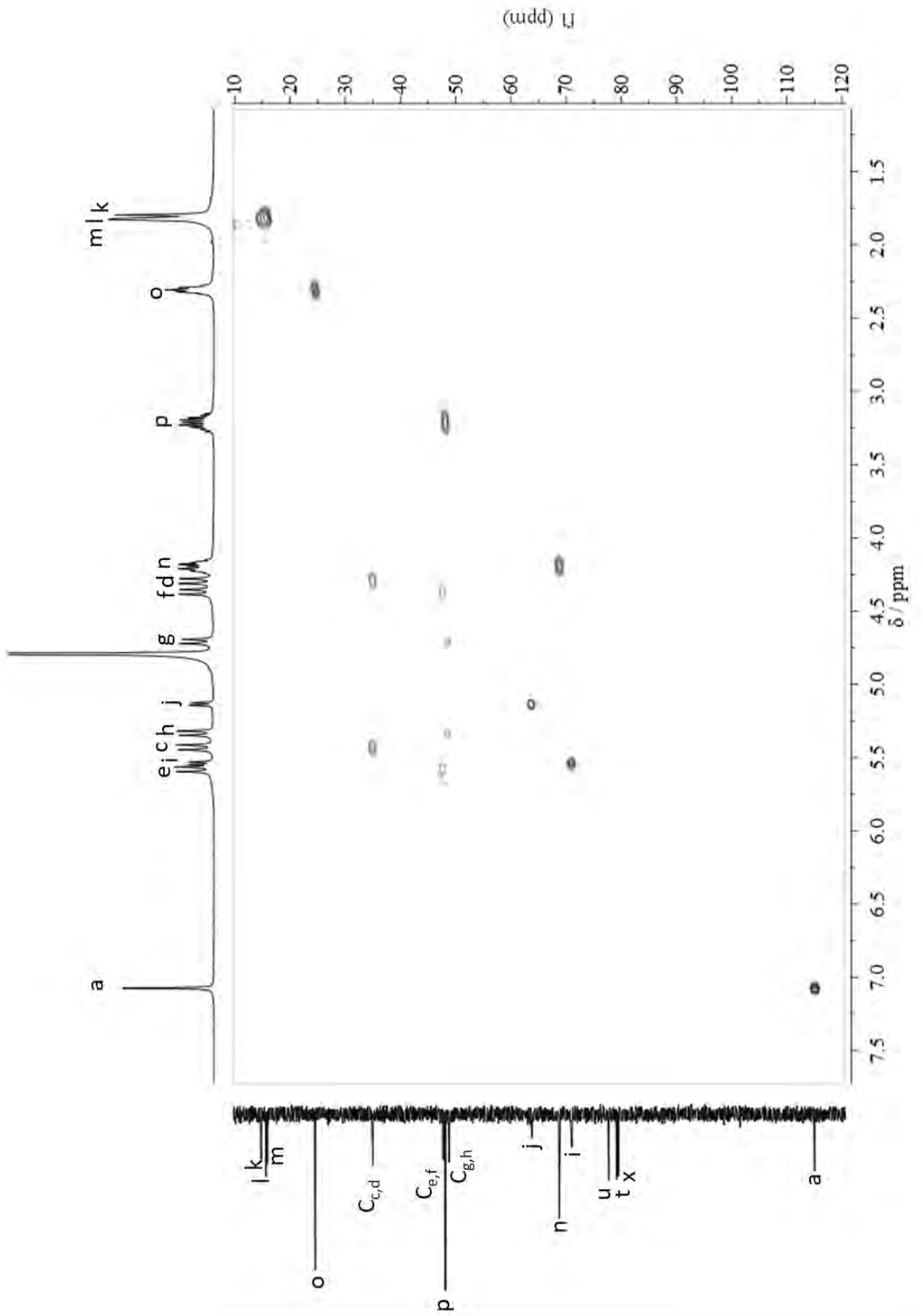

Figure II-S11. HMQC spectrum (D_2O, RT) recorded for **P1**.

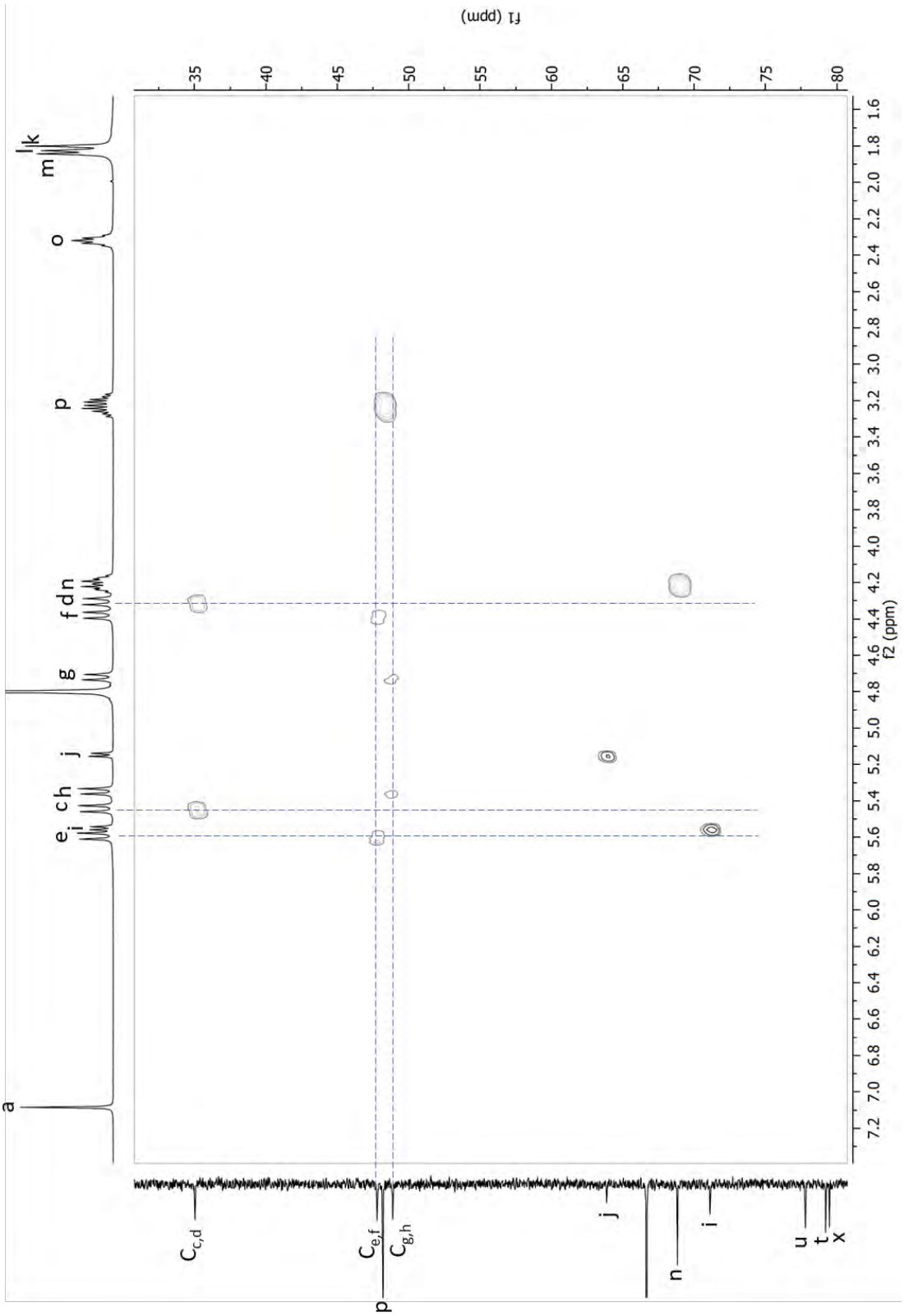

Figure II-S12. Segment of the HMQC spectrum (D_2O, RT) for **P1** from 30 – 80 ppm on y-axis.

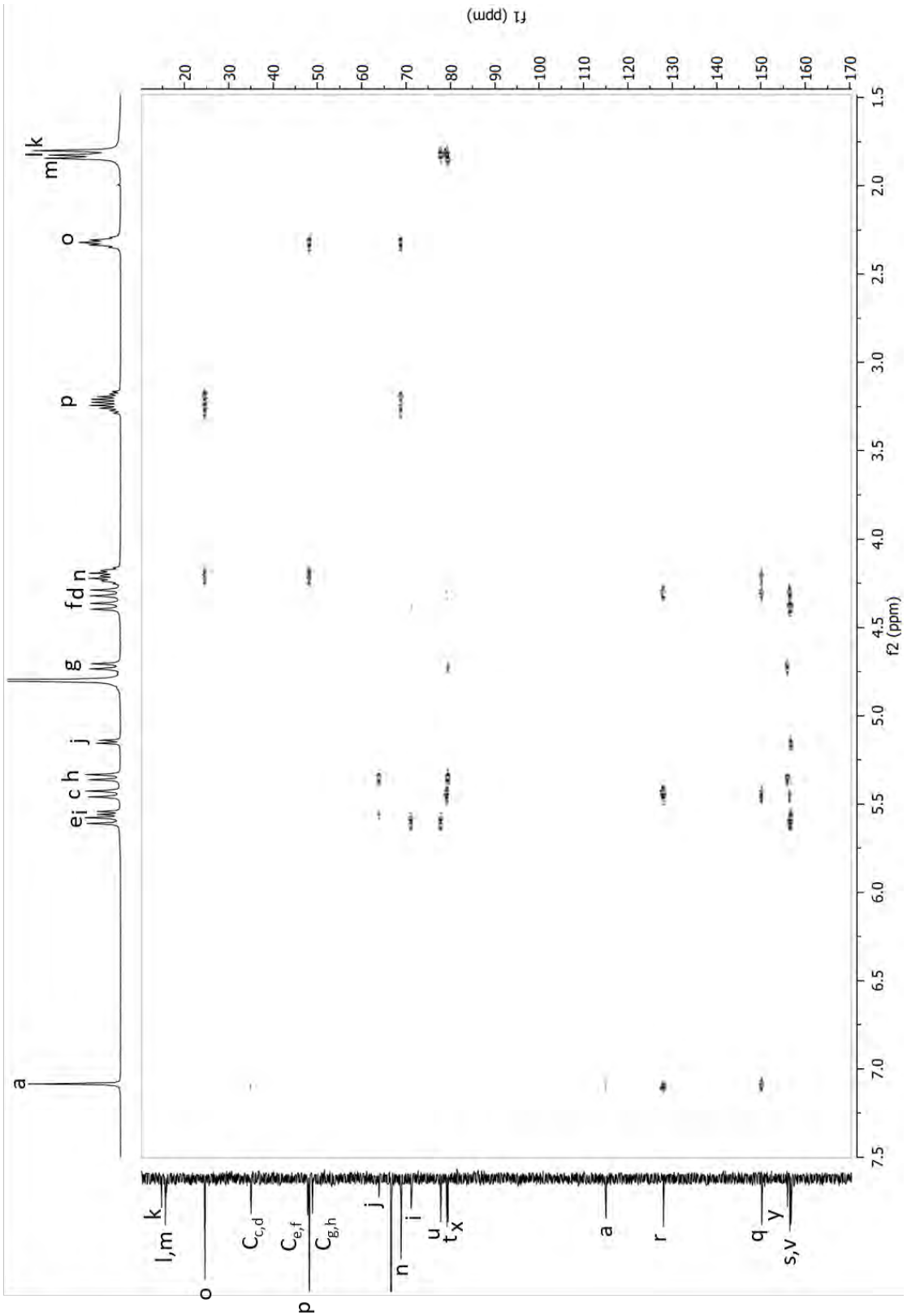

Figure II-S13. HMBC spectrum (D_2O, RT) recorded for **P1.**

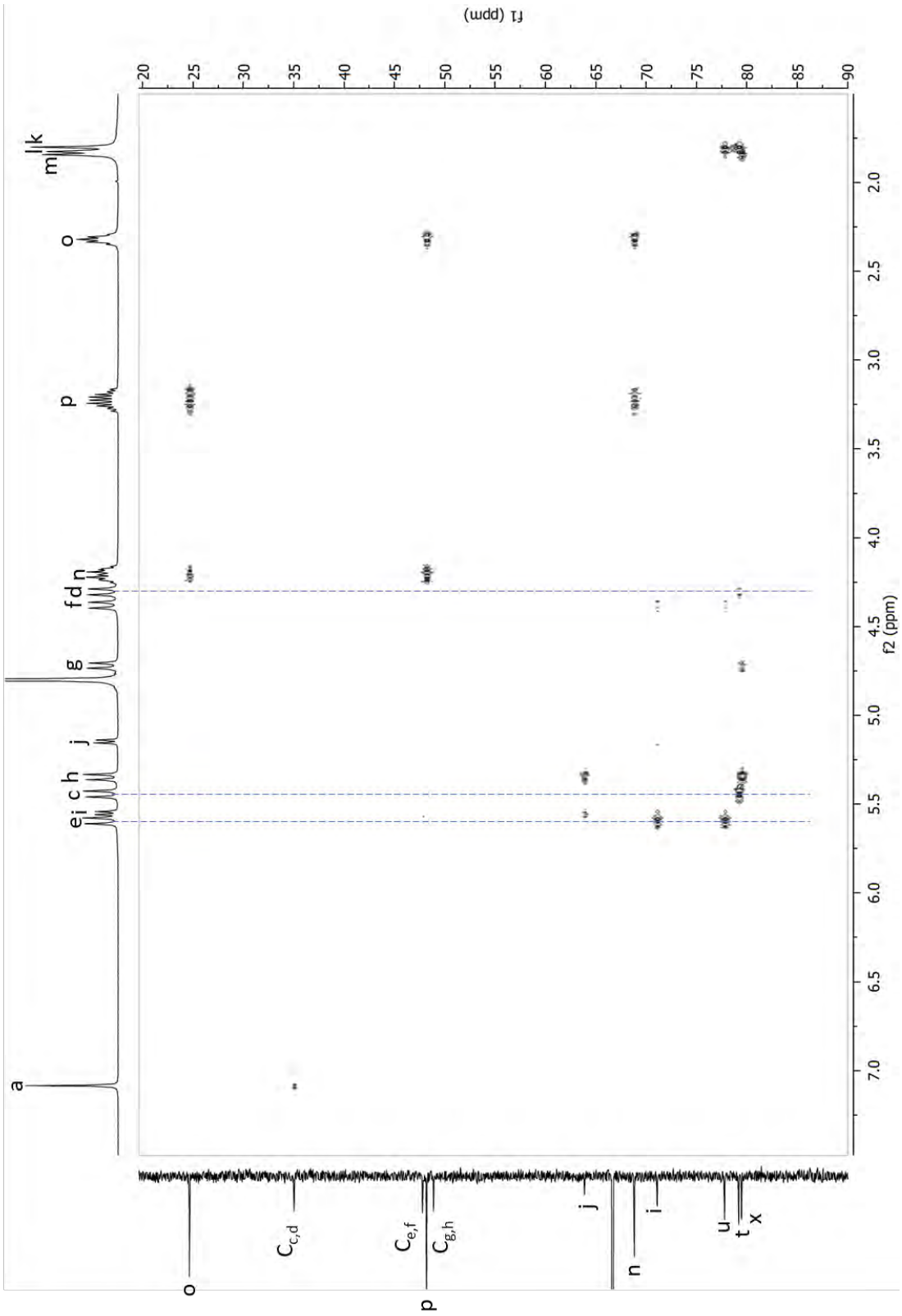

Figure II-S14. Segment of the HMBC spectrum (D_2O, RT) for **P1** from 20 – 90 ppm on y-axis.

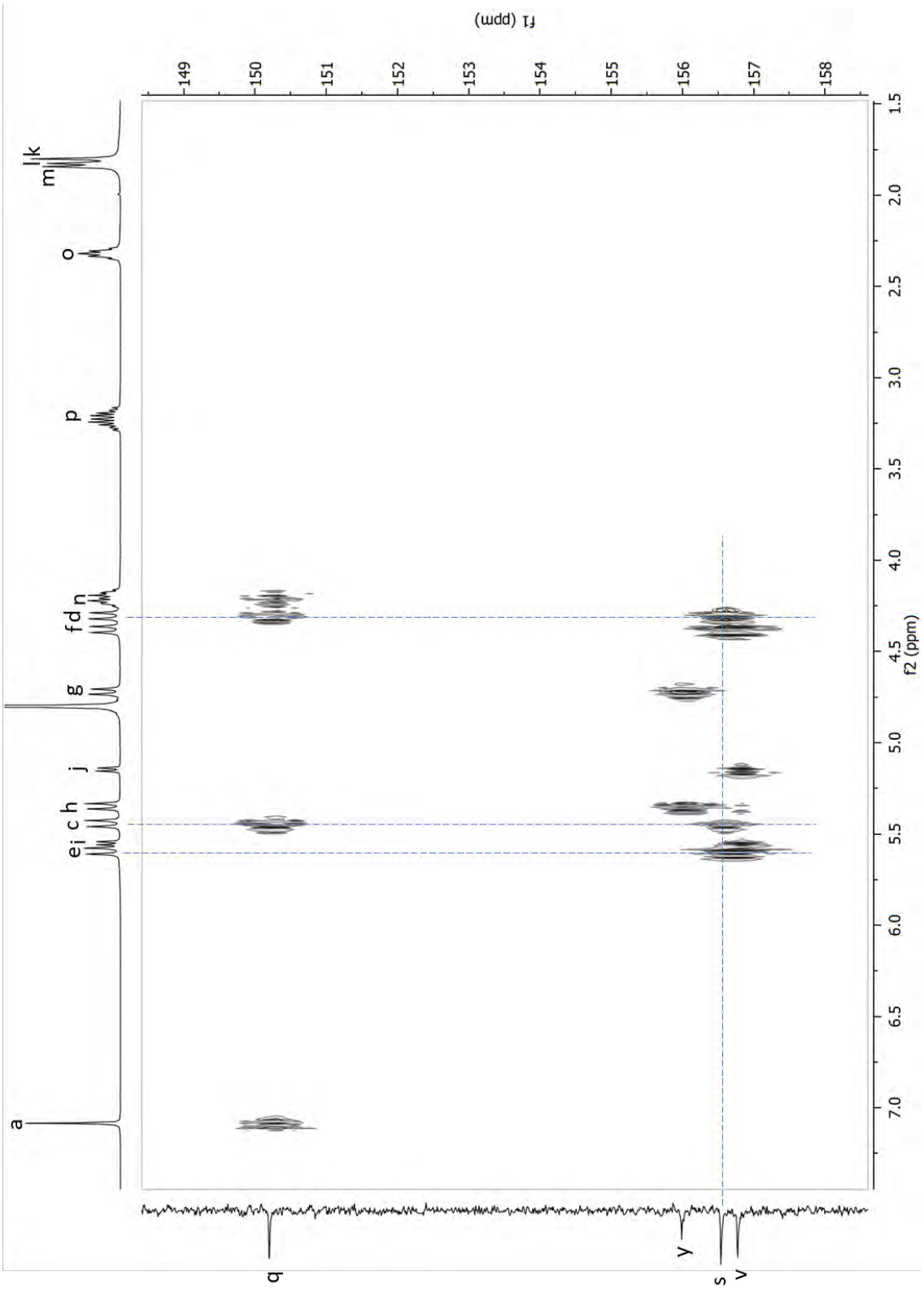

Figure II-S15. Segment of the HMBC spectrum 1(D_2O, RT) for **P1** from 148.5 – 158.5 ppm on y-axis.

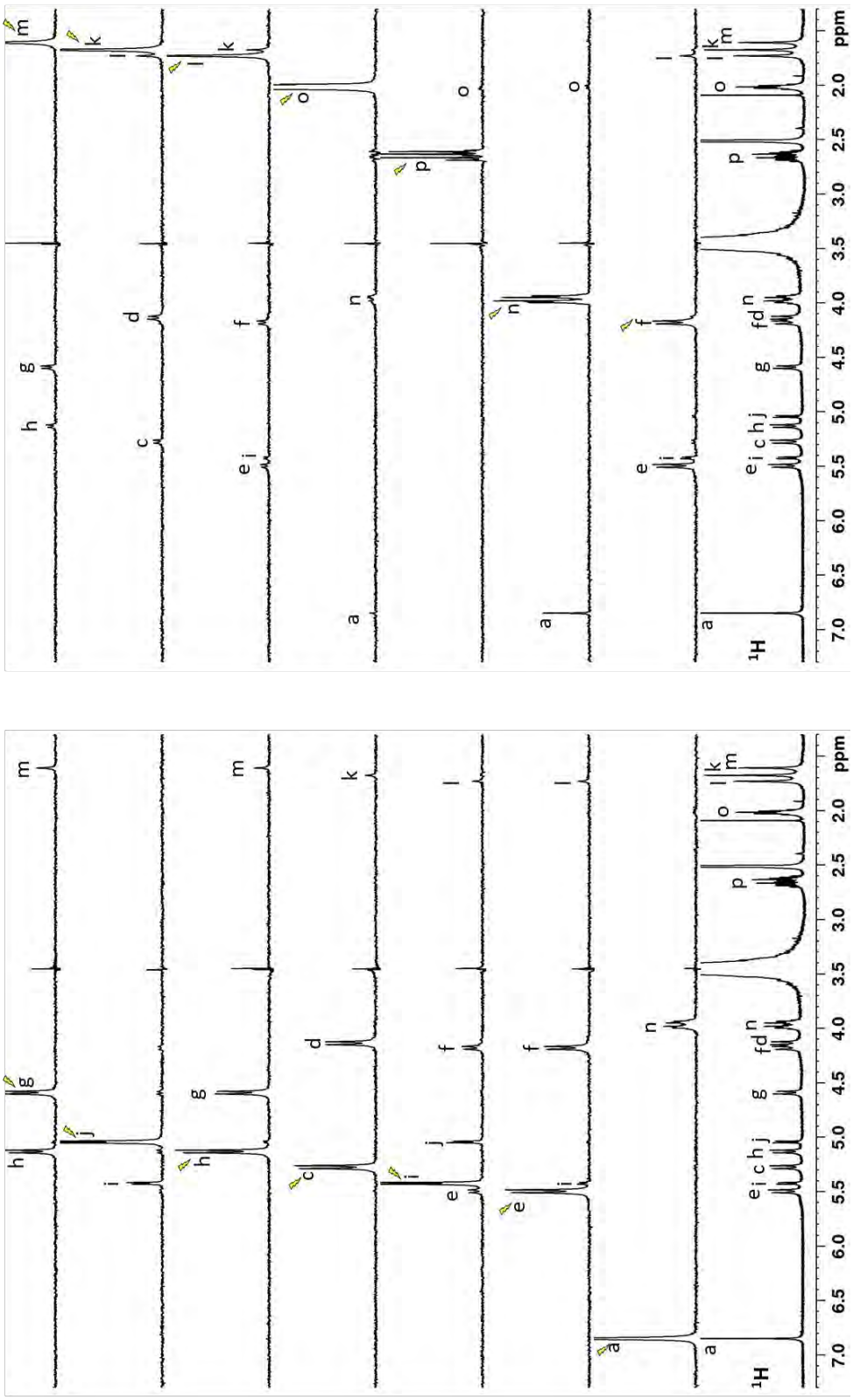

Figure II-S16. Selective 1D NOE spectra recorded (600 MHz, DMSO-d_6, RT) for **P1**. The thunderbolt indicates which proton was irradiated.

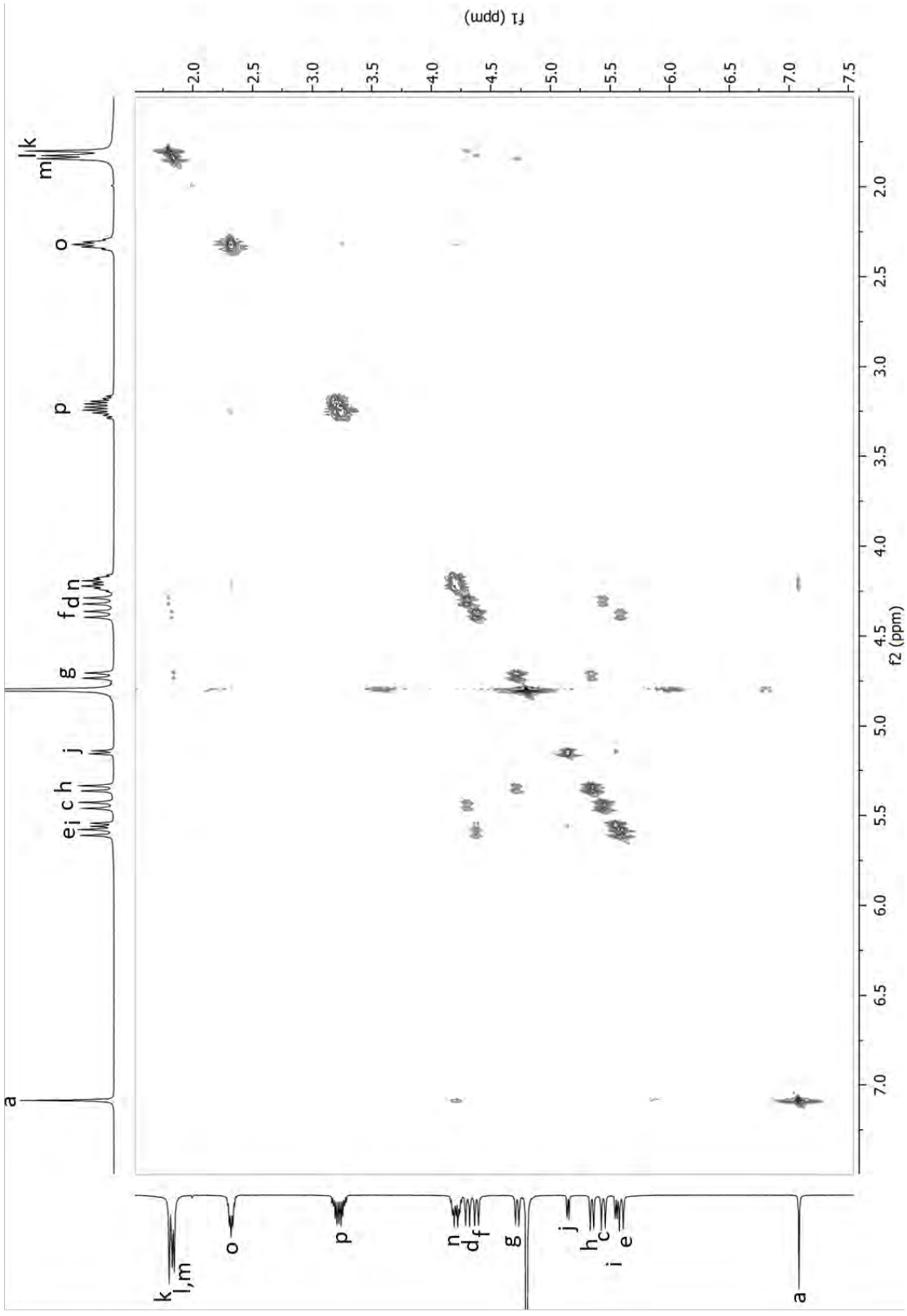

Figure II-S17. NOESY spectrum (600 MHz, D_2O, RT) recorded for **P1.**

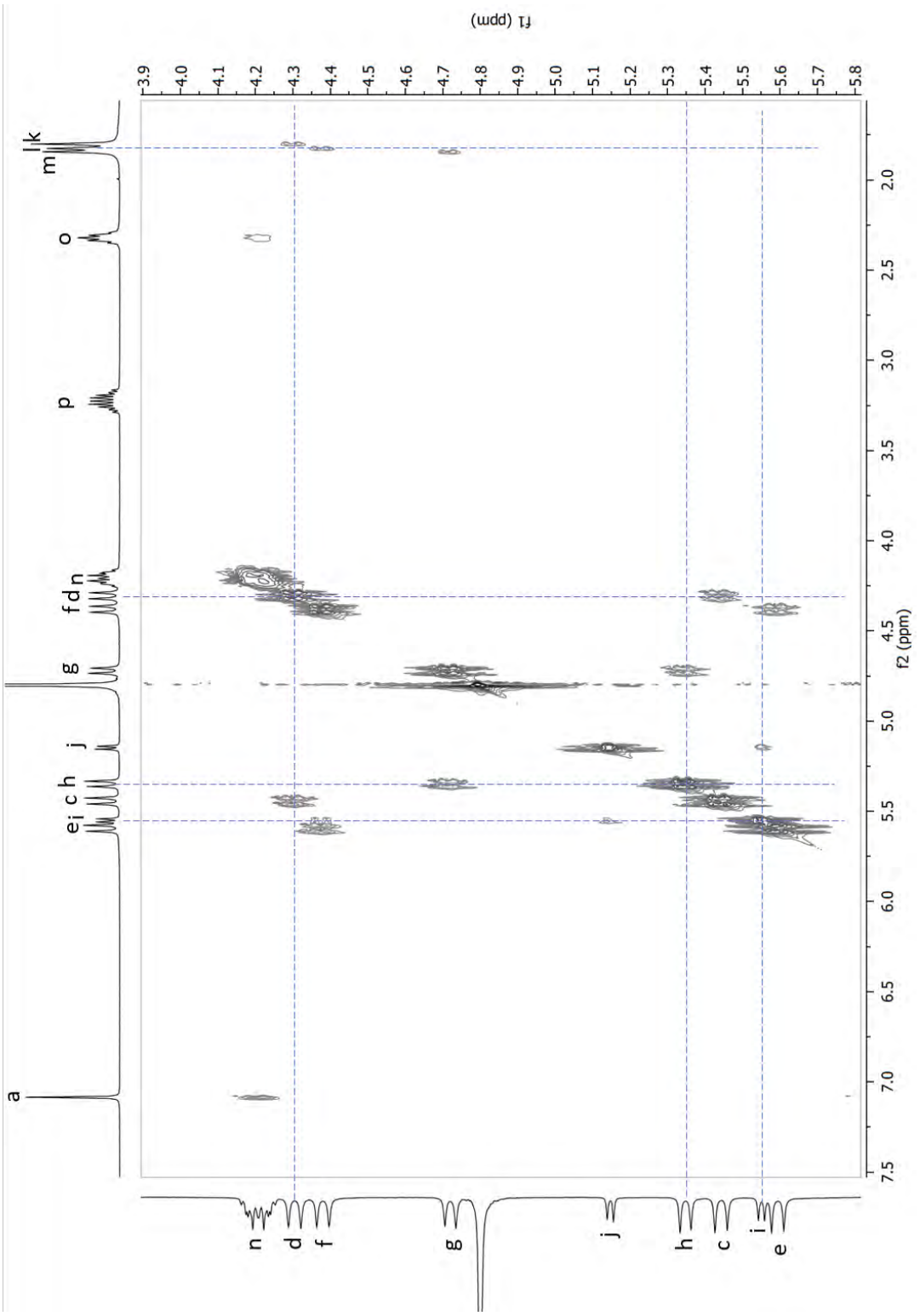

Figure II-S19. Segment of the NOESY spectrum (D_2O, RT) for **P1** from 3.9 – 5.8 ppm on y-axis.

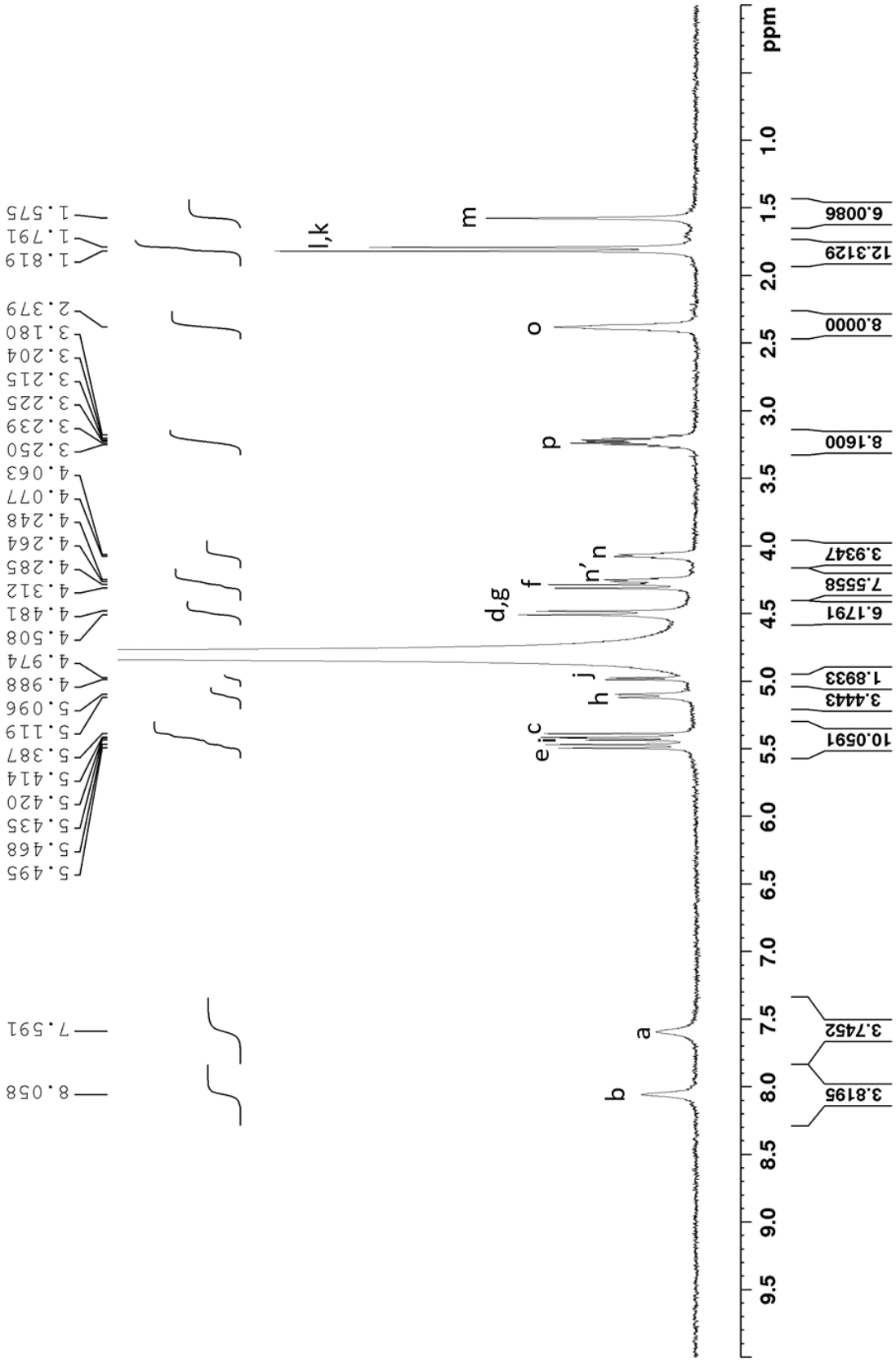

Figure II-S20. ^{1}H NMR spectrum (500 MHz, D_2O, RT) recorded for compound **P2**.

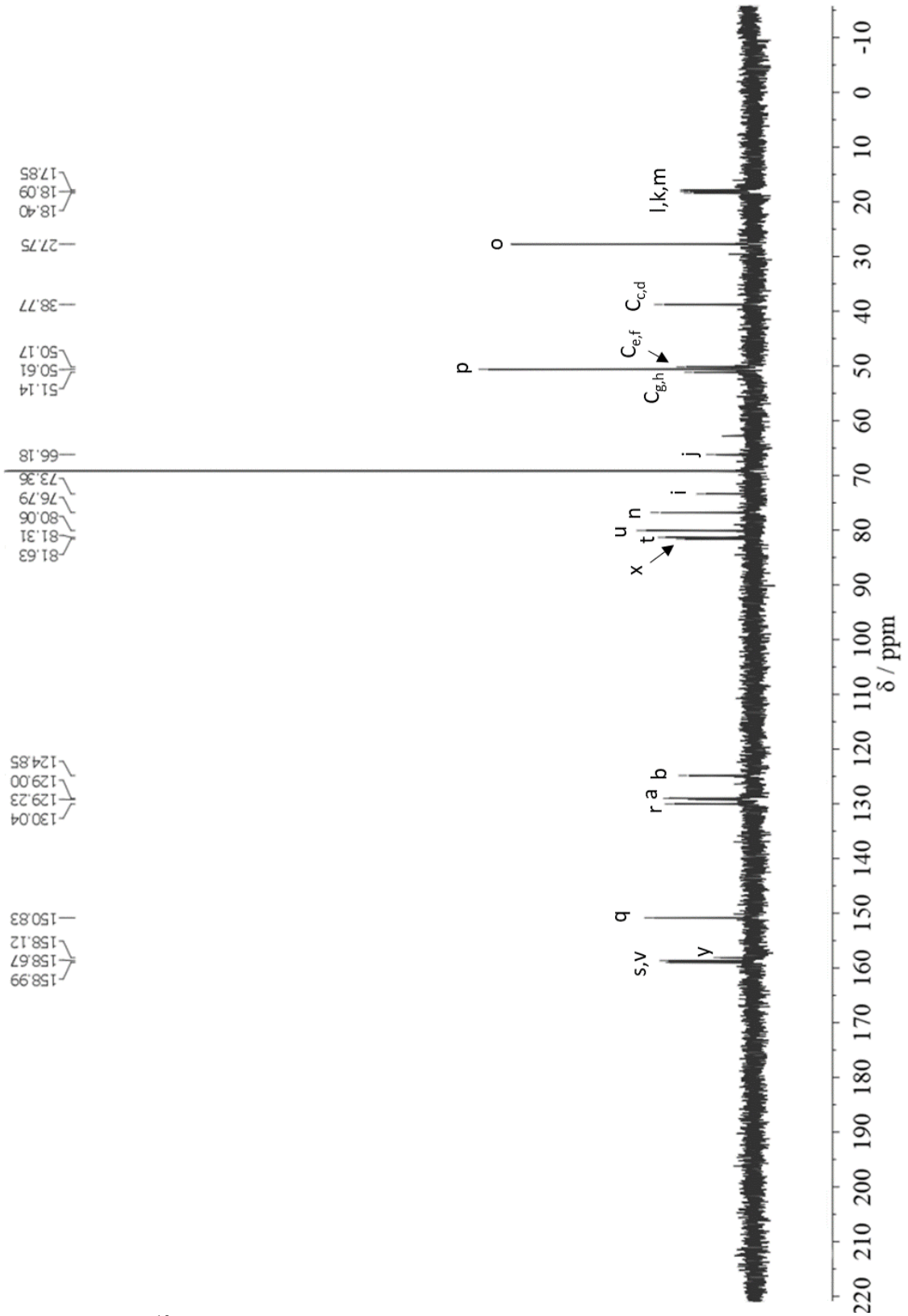

Figure II-S21. ^{13}C NMR spectrum (126 MHz, D_2O, dioxane as internal reference, RT) recorded for compound **P2**.

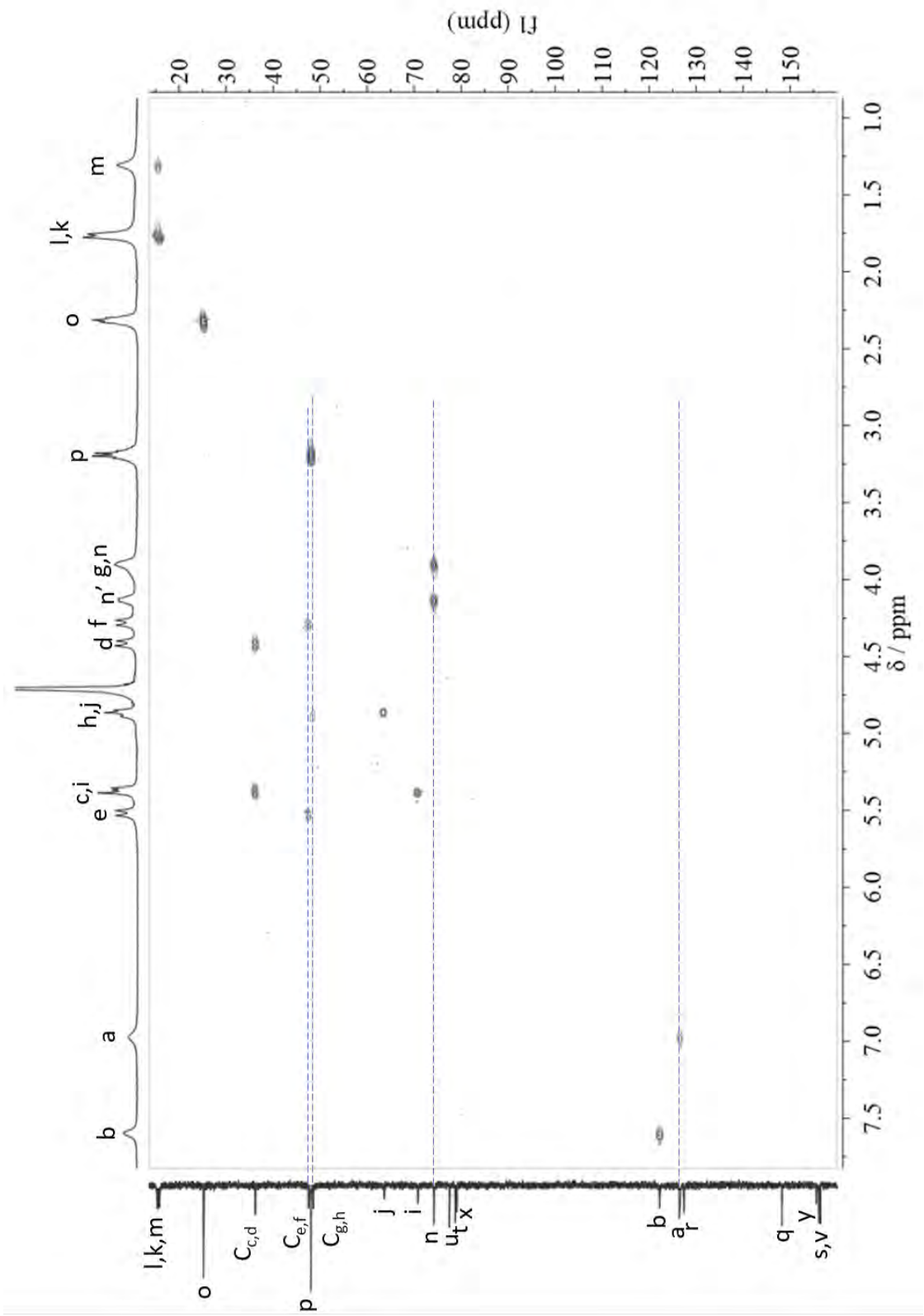

Figure II-S22. HMQC spectrum (D_2O, RT) recorded for **P2**.

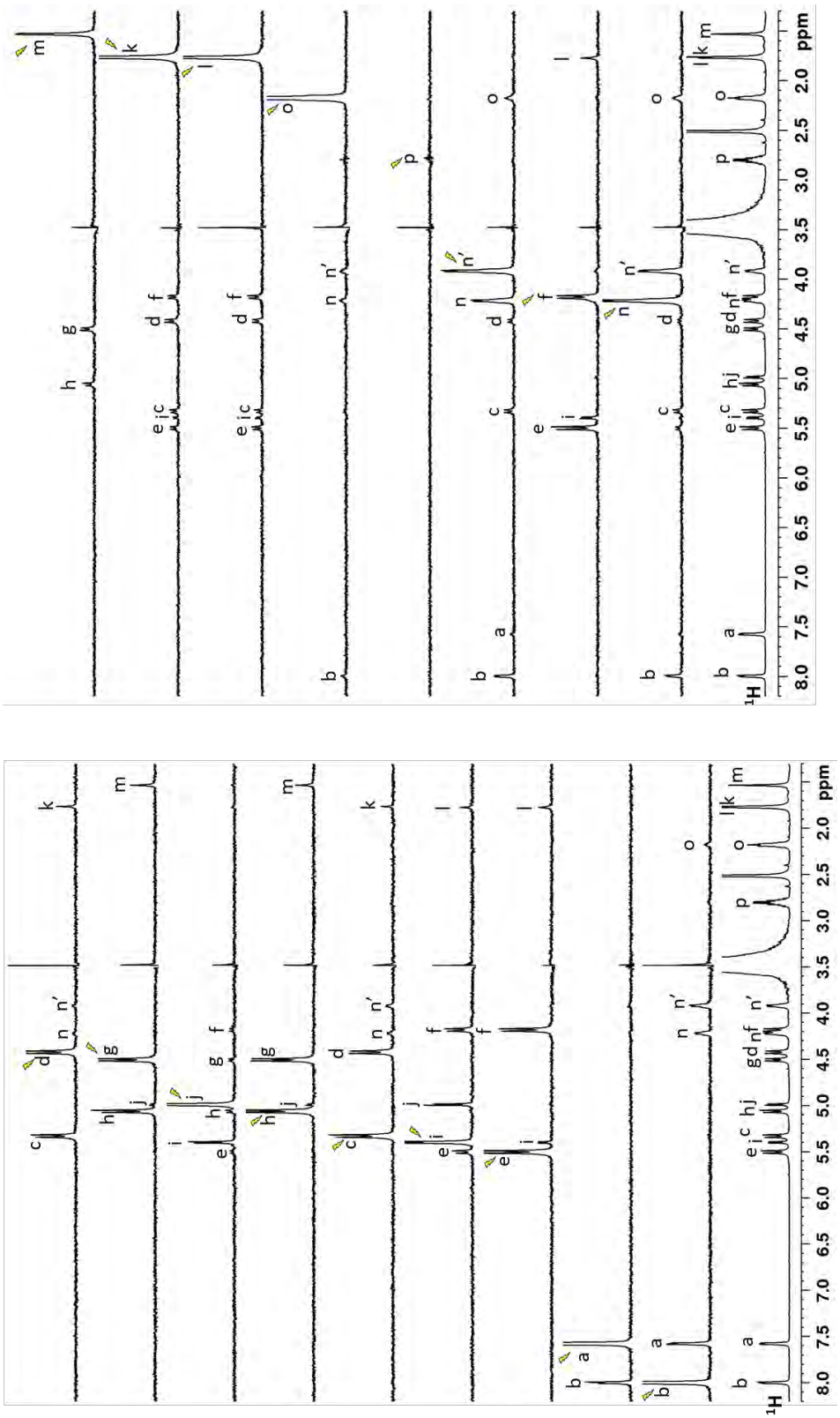

Figure II-S23. Selective 1D NOESY spectra (600 MHz, DMSO-d_6, RT) recorded for **P2**. The thunderbolt indicates which proton was irradiated.

^{1}H NMR Dilution (Self-Association) Experiments

Self-association Binding Model implemented in Scientist™
// Micromath Scientist Model File
// self-association model for NMR
IndVars: concTot
DepVars: Deltaobs
Params: Ka, Deltasat, Deltazero
Ka = concBound/(concFree*concFree)
concTot=concFree + (concBound * 2)
Deltaobs = Deltazero + (Deltasat – Deltazero) * ((2*concBound)/concTot)
//Constraints
0 < Ka
0 < concFree <concTot
0 < concBound < concTot
***

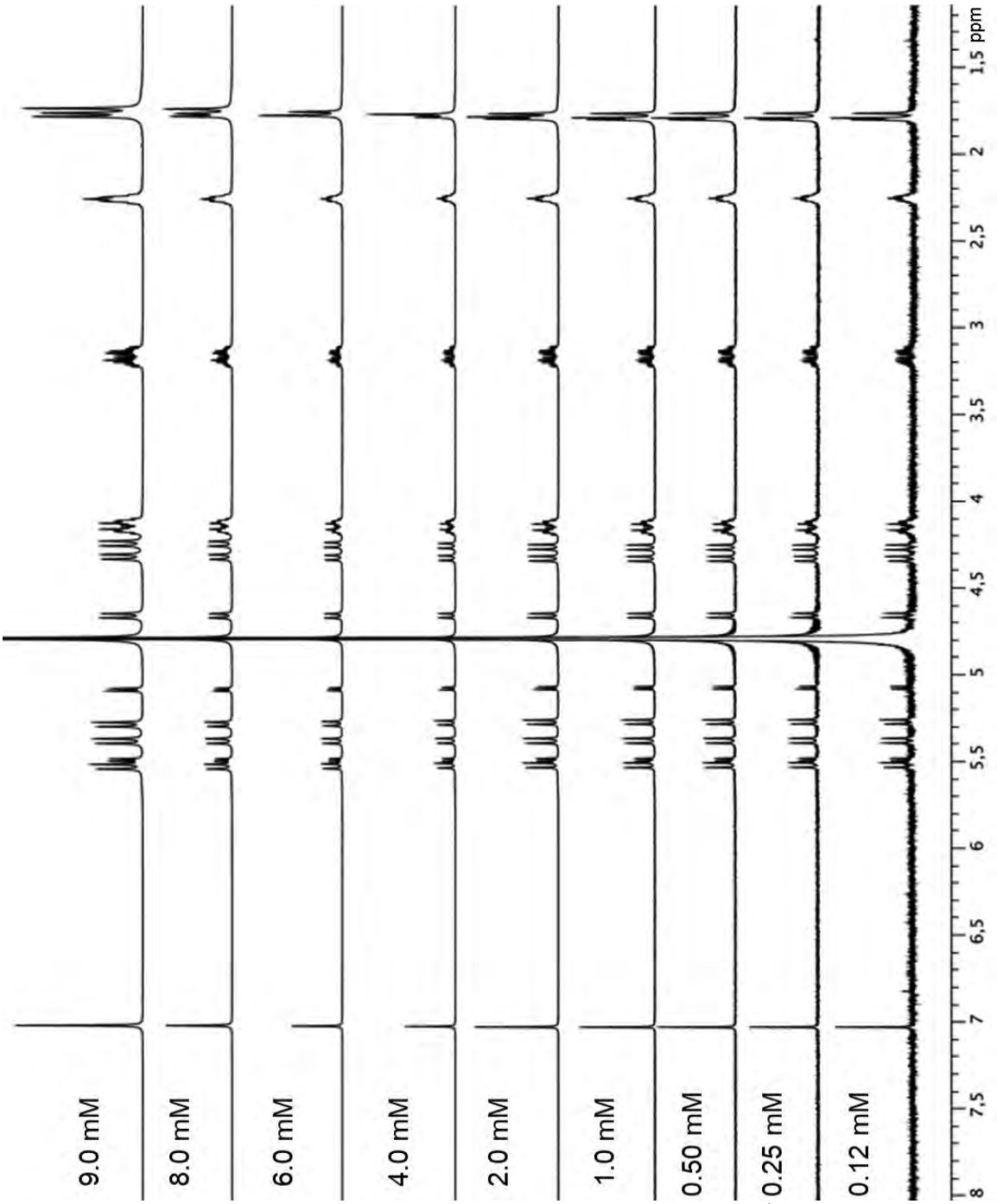

Figure II-S24. Dilution experiment (9 mM – 0.12 mM) for **P1** by ^{1}H NMR (600 MHz, D_2O, RT). A fitting was attempted with the aromatic proton. No self-association was detected.

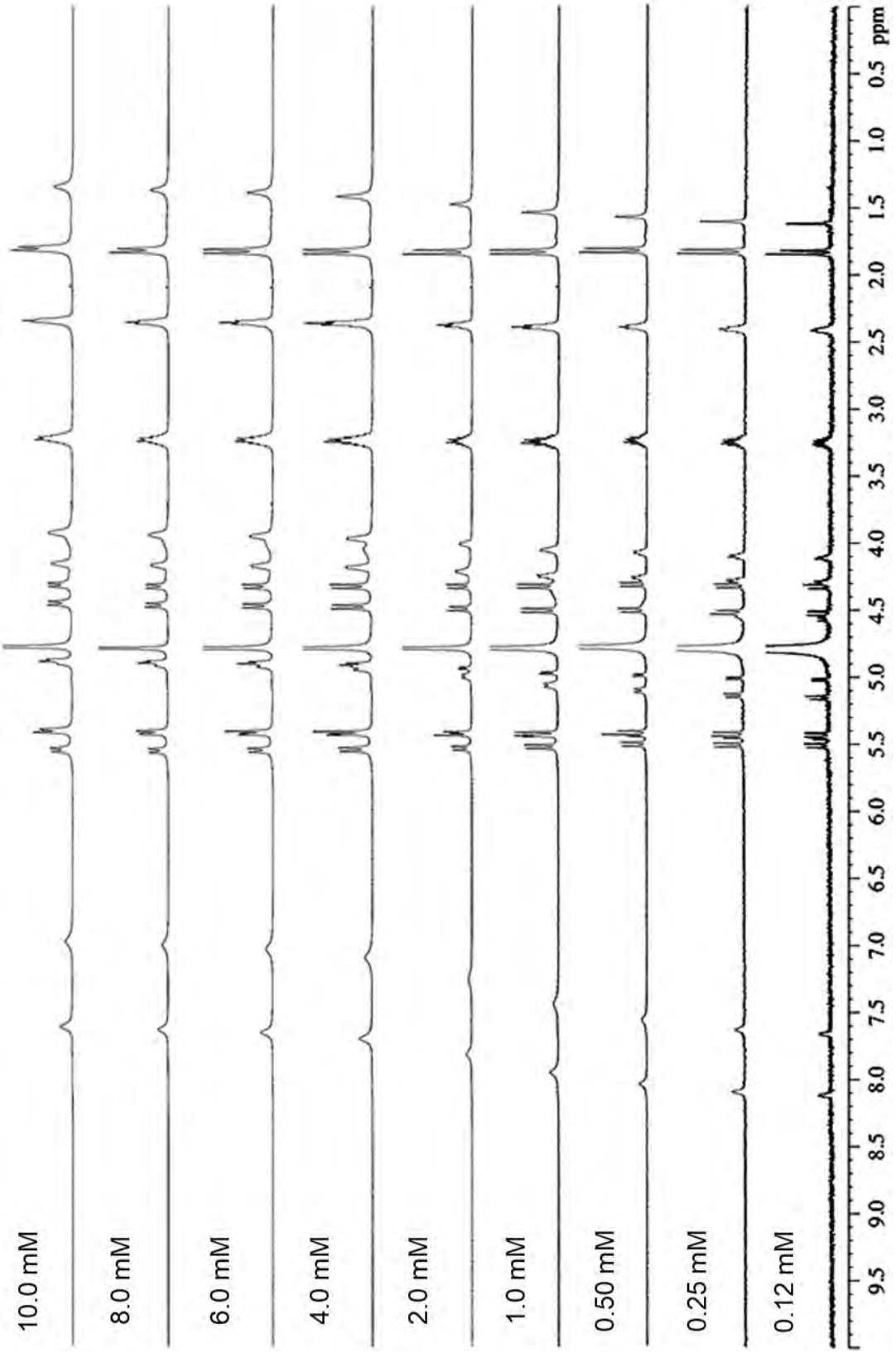

Figure II-S25. Dilution experiment (10 mM – 0.12 mM) for **P2** by ^{1}H NMR (600 MHz, D_2O, RT).

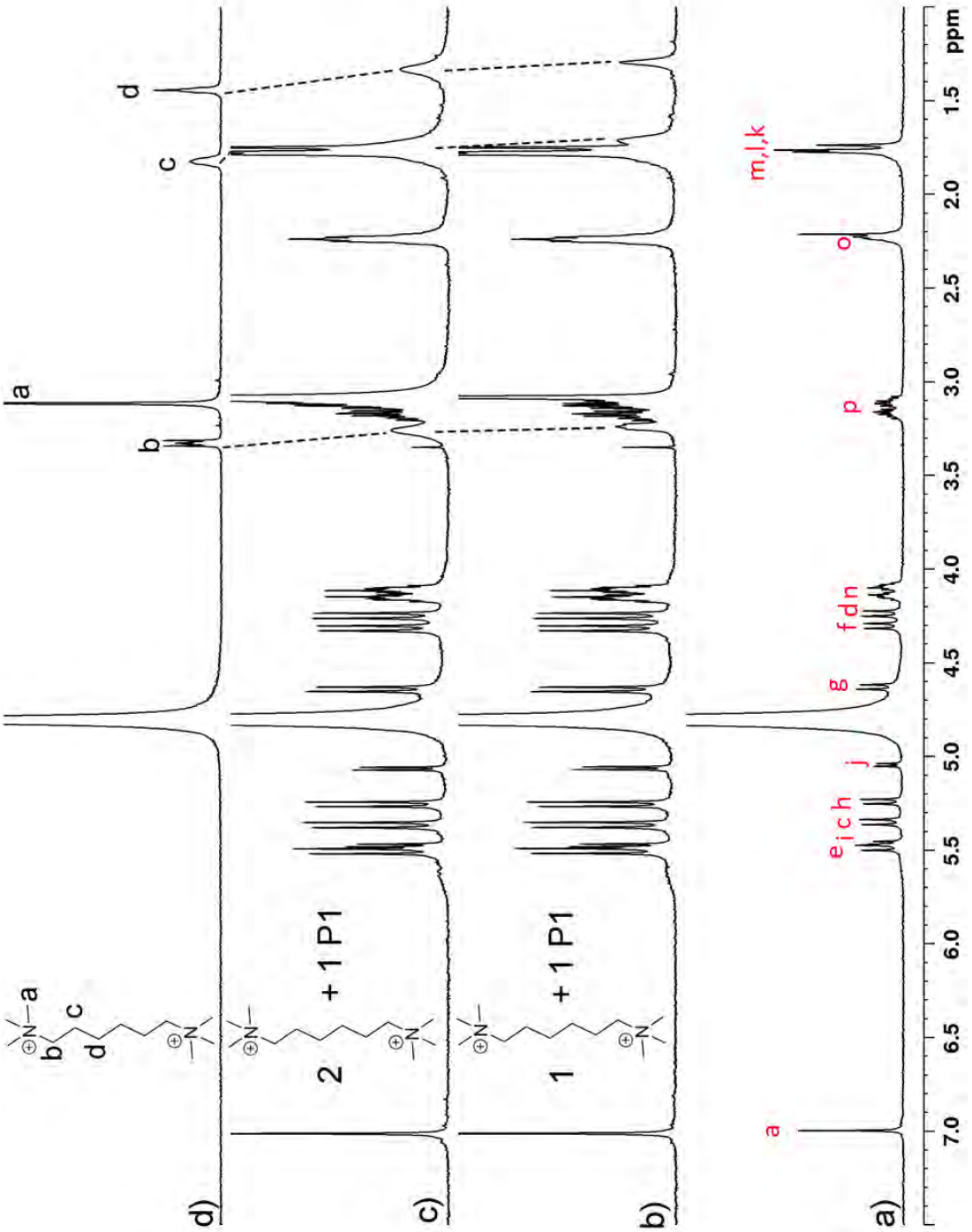

Figure II-S26. ^{1}H NMR spectra recorded (600 MHz, D2O, RT) for: a) **P1** (0.1 mM, labelled in red), b) a 1:1 mixture of **P1** (0.5 mM) and **II-6** (0.5 mM), c) a 1:2 mixture of **P1** (0.5 mM) and **II-6** (1.0 mM), and d) **II-6** (0.5 mM, labelled in black).

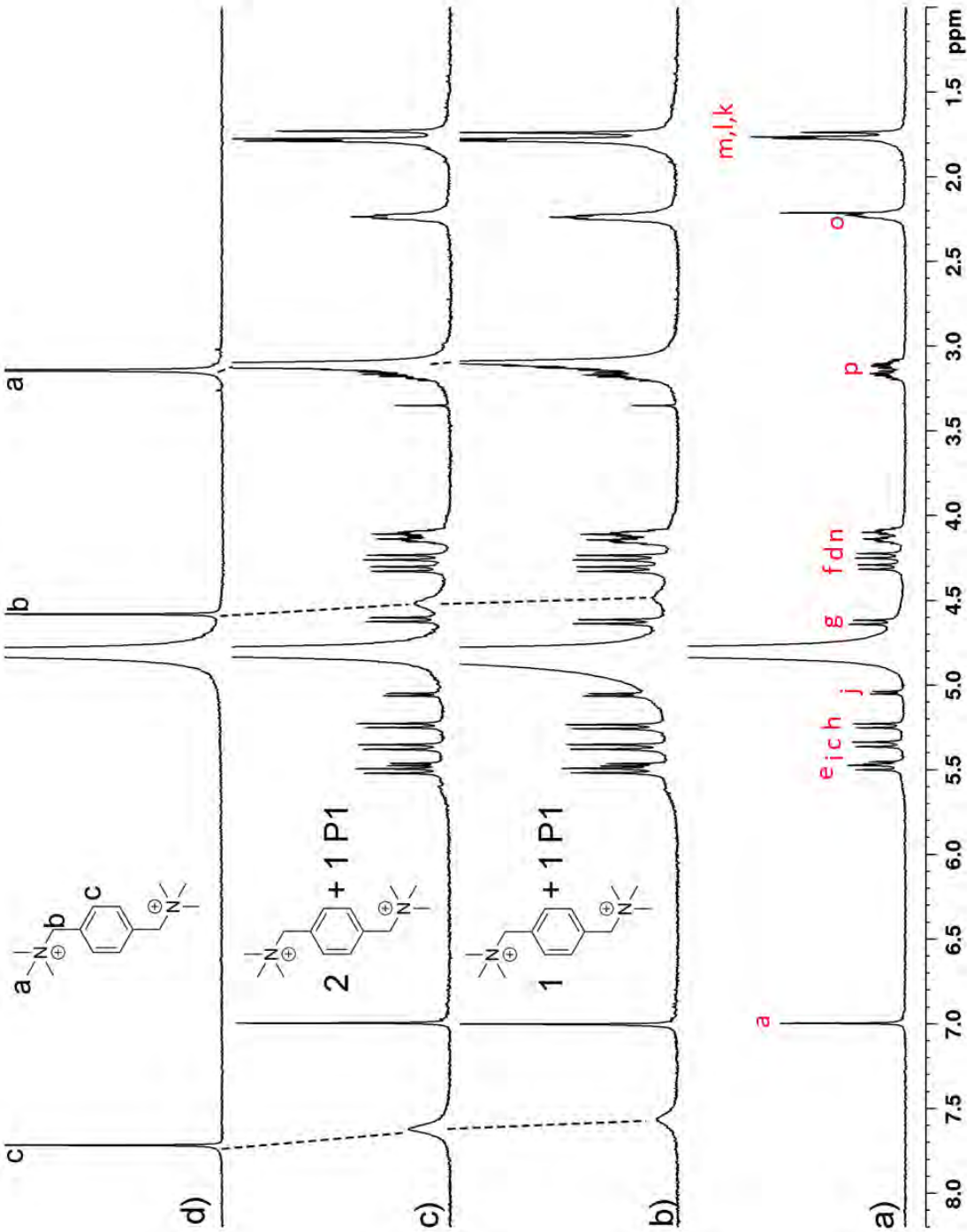

Figure II-S27. ^{1}H NMR spectra recorded (600 MHz, D_2O, RT) for: a) **P1** (0.1 mM, labelled in red), b) a 1:1 mixture of **P1** (0.5 mM) and **II-7** (0.5 mM), c) a 1:2 mixture of **P1** (0.5 mM) and **II-7** (1.0 mM), and d) **II-7** (0.5 mM, labelled in black).

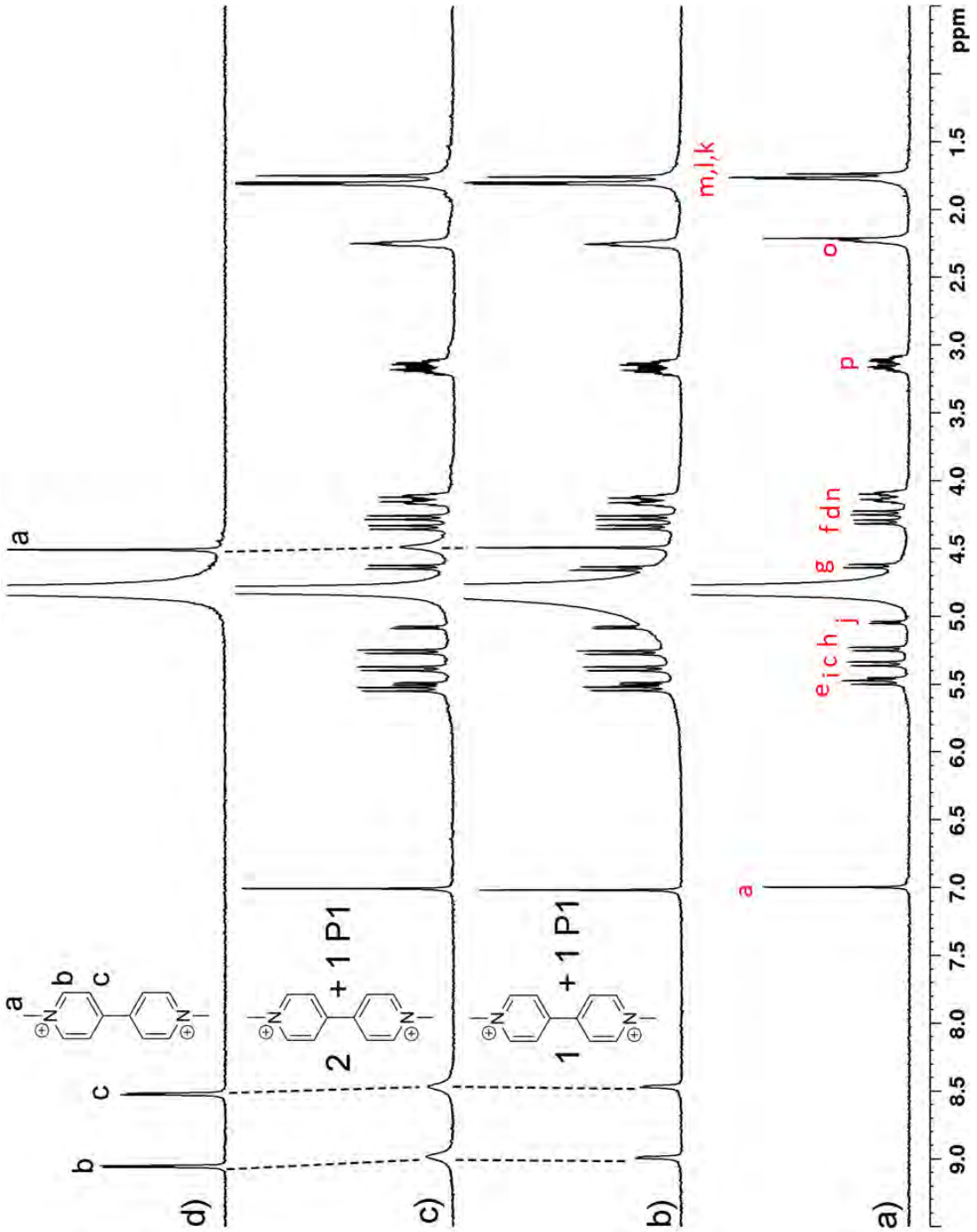

Figure II-S28. ^{1}H NMR spectra recorded (600 MHz, D_2O, RT) for: a) **P1** (0.1 mM, labelled in red), b) a 1:1 mixture of **P1** (0.3 mM) and **II-8** (0.3 mM), c) a 1:2 mixture of **P1** (0.3 mM) and **II-8** (0.6 mM), and d) **II-8** (0.3 mM, labelled in black).

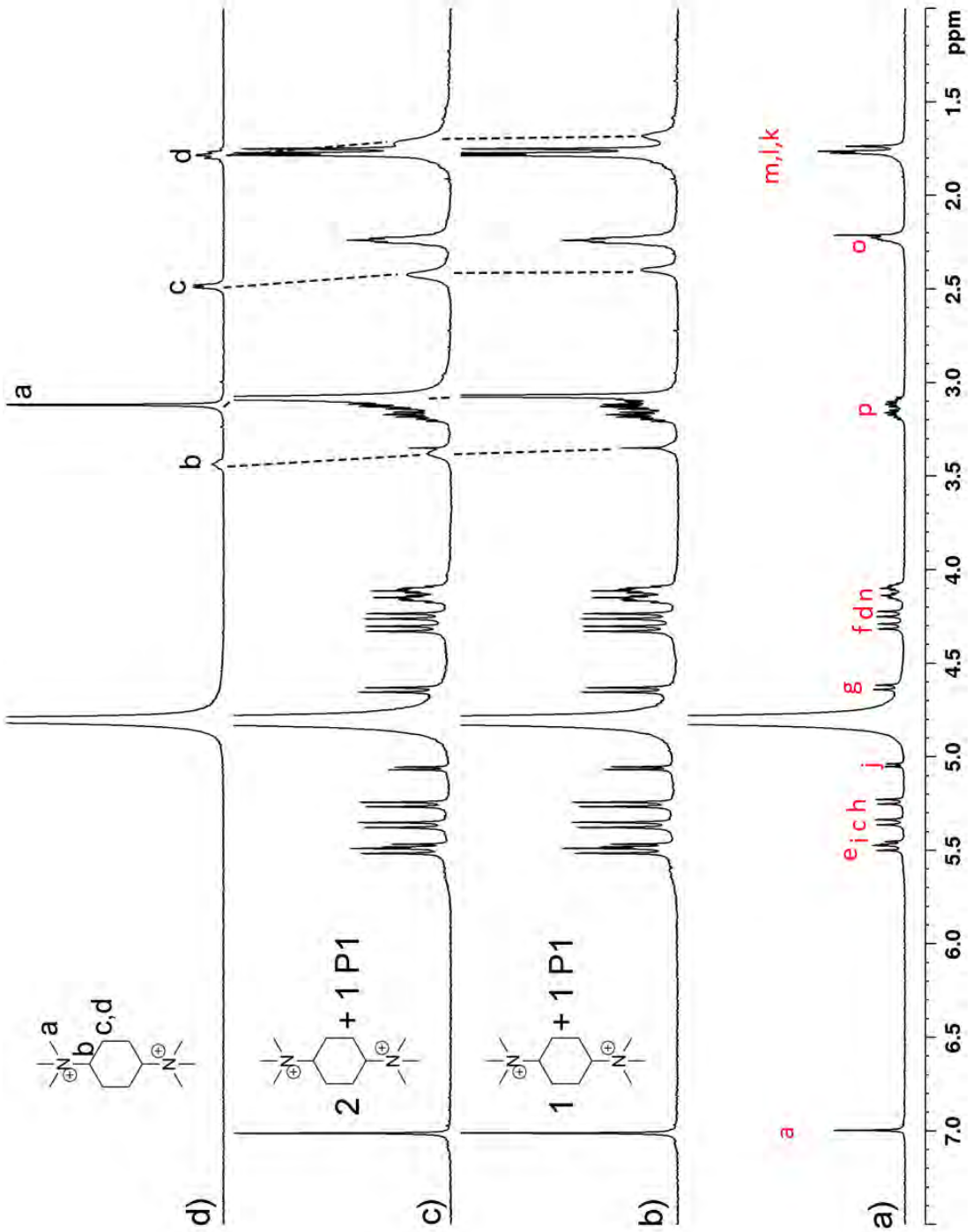

Figure II-S29. ^{1}H NMR spectra recorded (600 MHz, D_2O, RT) for: a) **P1** (0.1 mM, labelled in red), b) a 1:1 mixture of **P1** (0.5 mM) and **II-9** (0.5 mM), c) a 1:2 mixture of **P1** (0.5 mM) and **II-9** (1.0 mM), and d) **II-9** (0.5 mM).

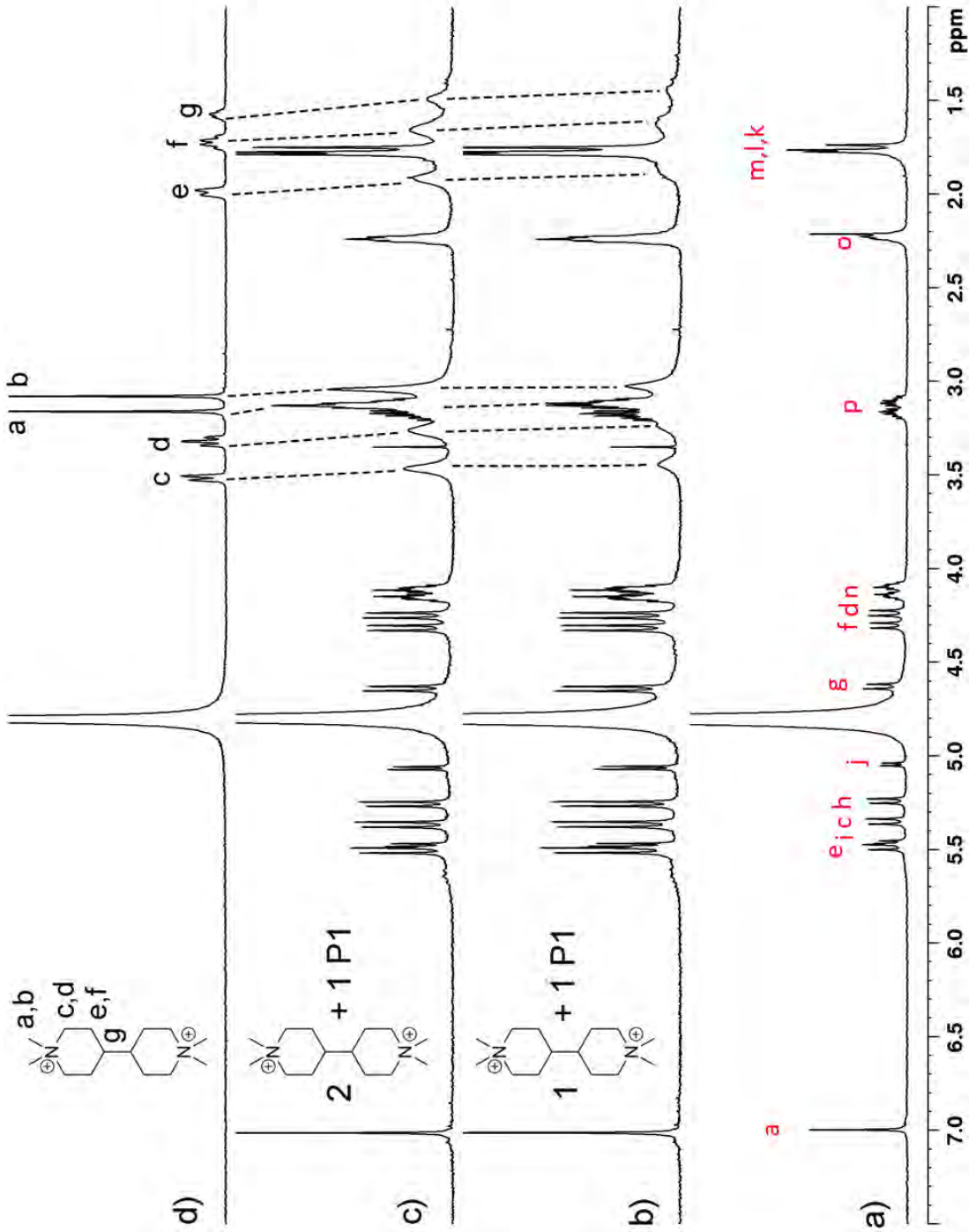

Figure II-S30. ^{1}H NMR spectra recorded (600 MHz, D2O, RT) for: a) **P1** (0.1 mM, labelled in red), b) a 1:1 mixture of **P1** (0.5 mM) and **II-10** (0.5 mM), c) a 1:2 mixture of **P1** (0.5 mM) and **II-10** (1.0 mM), and d) **II-10** (0.5 mM, labelled in black).

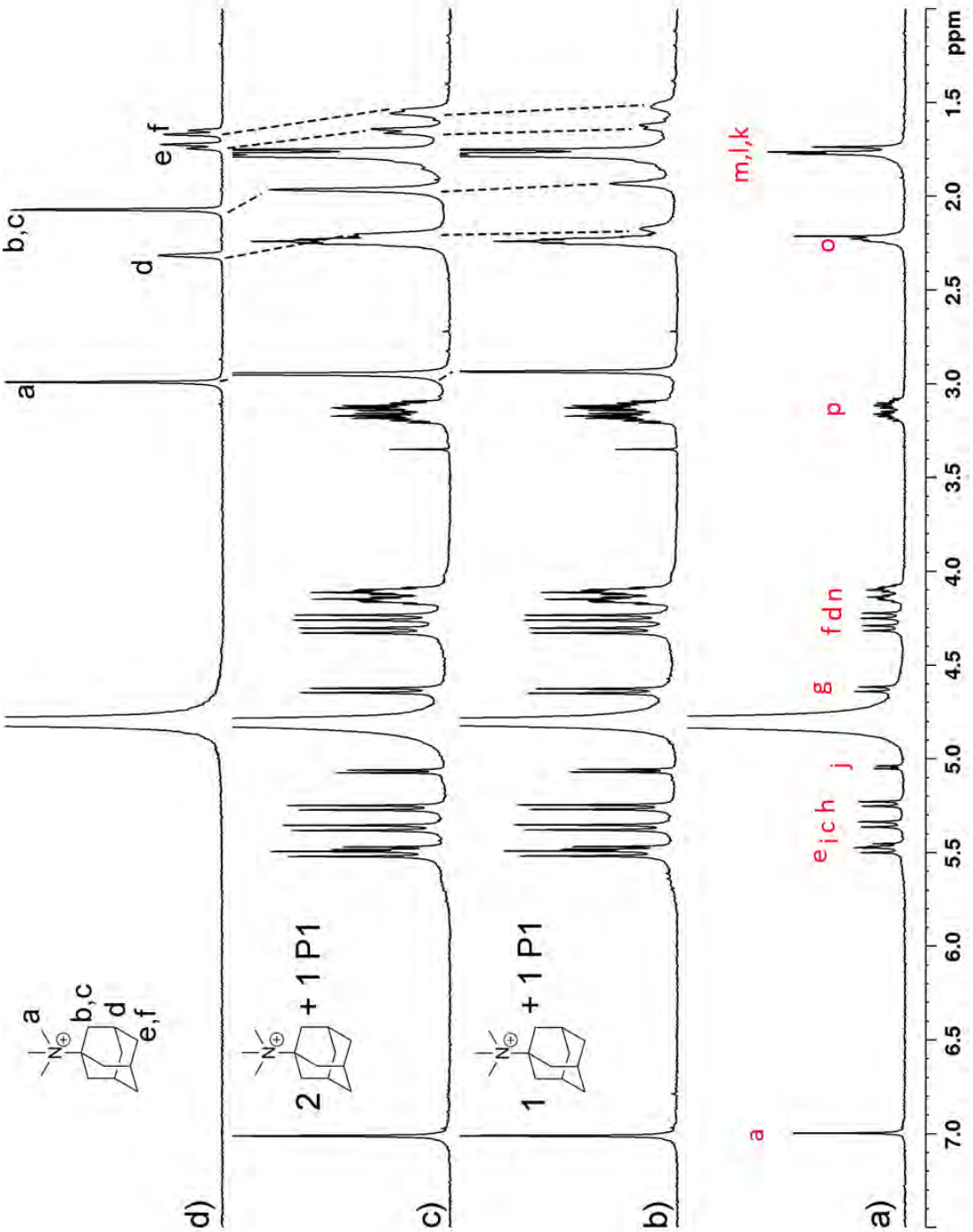

Figure II-S31. ^{1}H NMR spectra recorded (600 MHz, D_2O, RT) for: a) **P1** (0.1 mM, labelled in red), b) a 1:1 mixture of **P1** (1.0 mM) and **II-11** (1.0 mM), c) a 1:2 mixture of **P1** (1.0 mM) and **II-11** (2.0 mM), and d) **II-11** (1.0 mM, labelled in black).

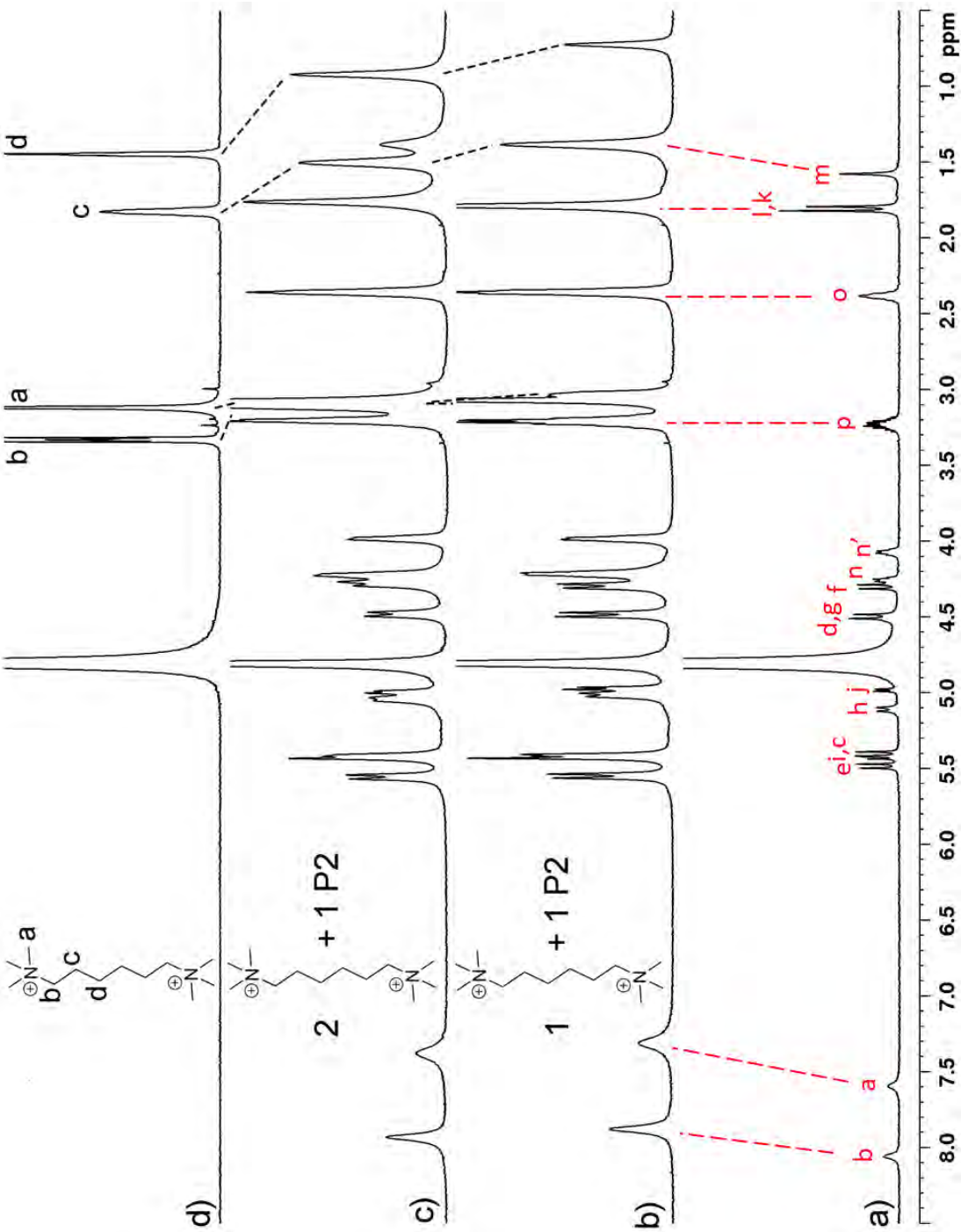

Figure II-S32. ^{1}H NMR spectra recorded (600 MHz, D_2O, RT) for: a) **P2** (0.1 mM, labelled in red), b) a 1:1 mixture of **P2** (2.0 mM) and **II-6** (2.0 mM), c) a 1:2 mixture of **P2** (2.0 mM) and **II-6** (4.0 mM), and d) **II-6** (2.0 mM, labelled in black).

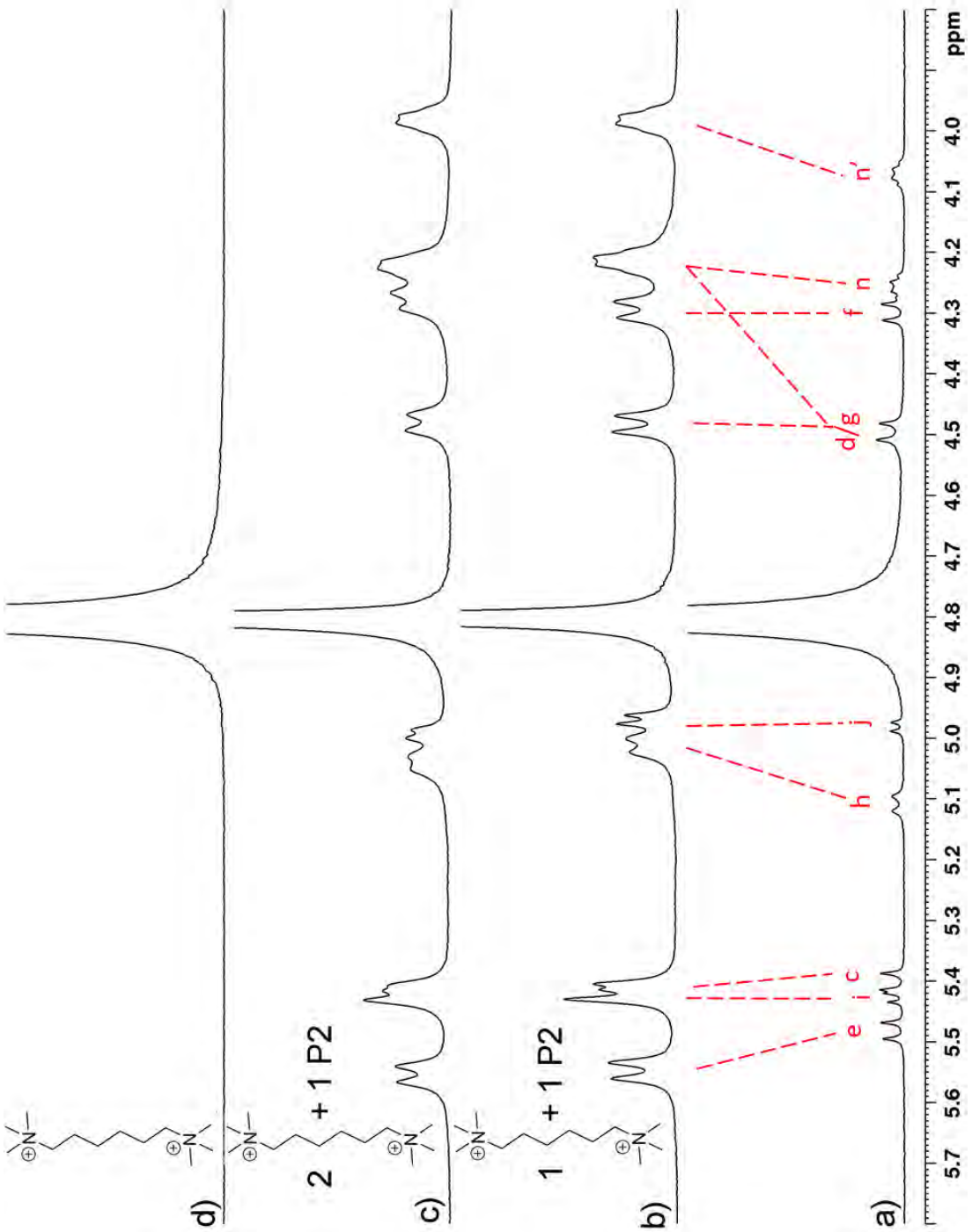

Figure II-S33. Methylene backbone section of ^{1}H NMR spectra recorded (600 MHz, D_2O, RT) for: a) **P2** (0.1 mM, labelled in red), b) a 1:1 mixture of **P2** (2.0 mM) and **II-6** (2.0 mM), c) a 1:2 mixture of **P2** (2.0 mM) and **II-6** (4.0 mM), and d) **II-6** (2.0 mM, labelled in black).

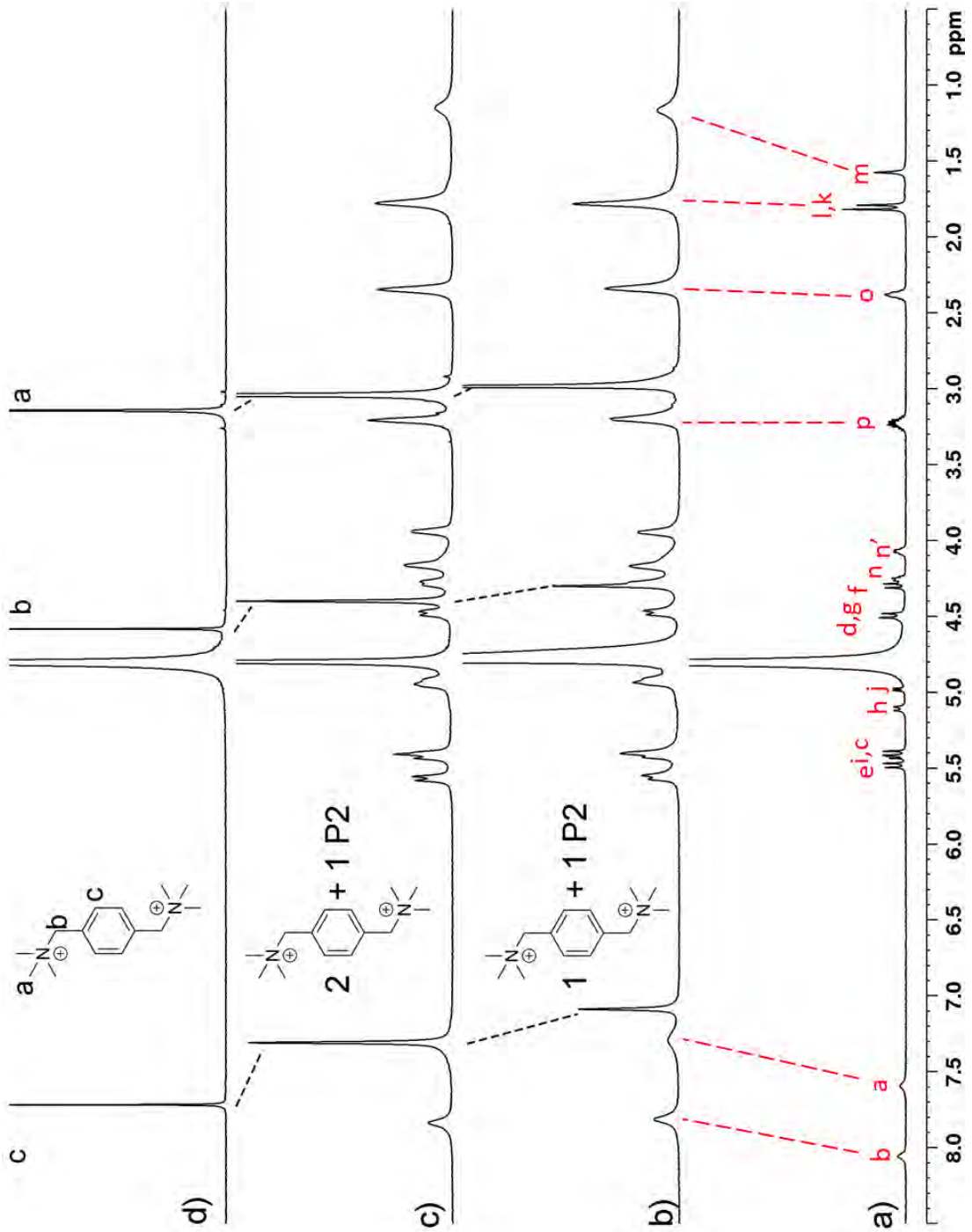

Figure II-S34. ^{1}H NMR spectra recorded (600 MHz, D_2O, RT) for: a) **P2** (0.1 mM, labelled in red) b) a 1:1 mixture of **P2** (1.0 mM) and **II-7** (1.0 mM), c) a 1:2 mixture of **P2** (1.0 mM) and **II-7** (2.0 mM), and d) **II-7** (1.0 mM, labelled in black).

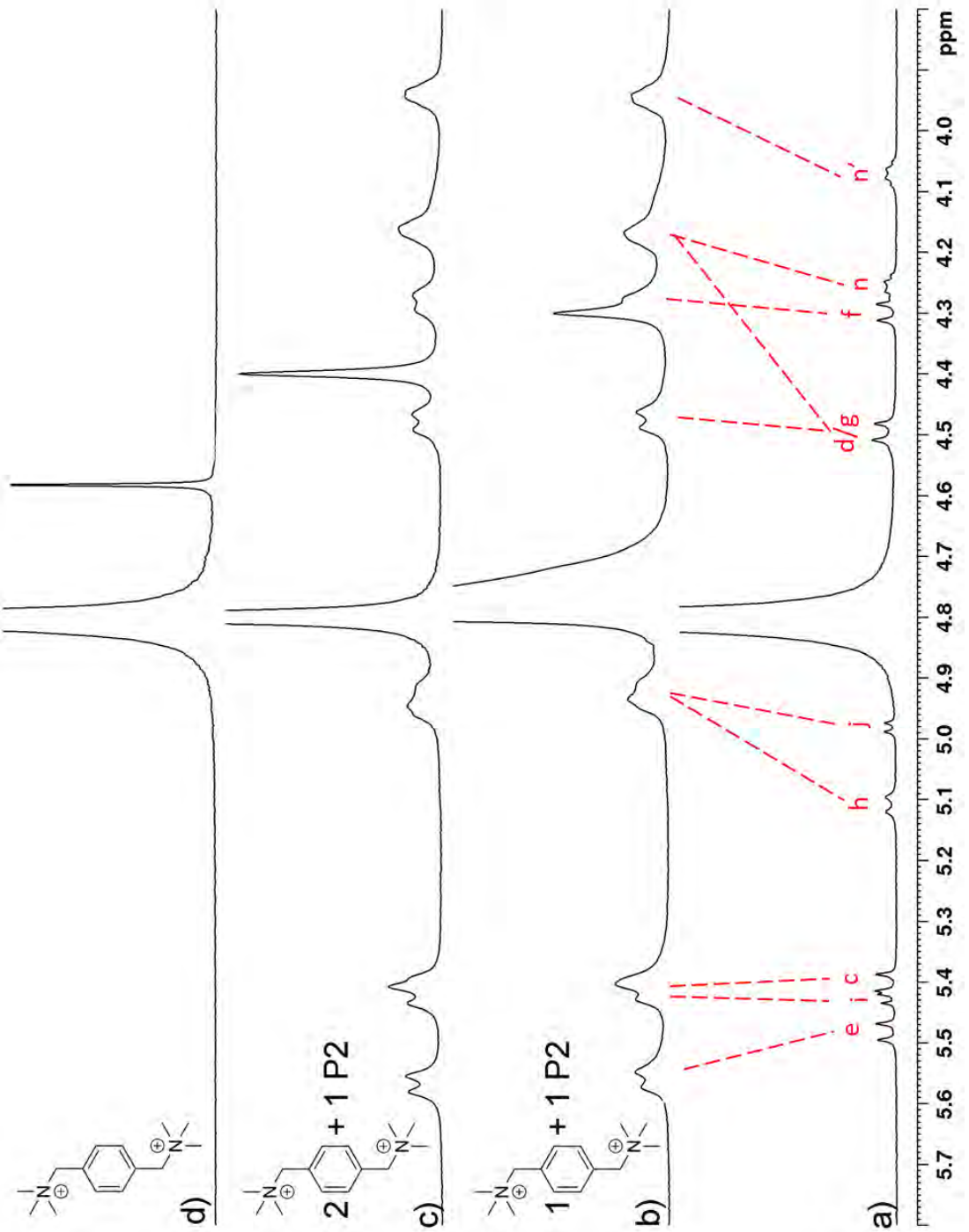

Figure II-S35. Methylene backbone section of ^{1}H NMR spectra recorded (600 MHz, D_2O, RT) for: a) **P2** (0.1 mM, labelled in red) b) a 1:1 mixture of **P2** (1.0 mM) and **II-7** (1.0 mM), c) a 1:2 mixture of **P2** (1.0 mM) and **II-7** (2.0 mM), and d) **II-7** (1.0 mM, labelled in black).

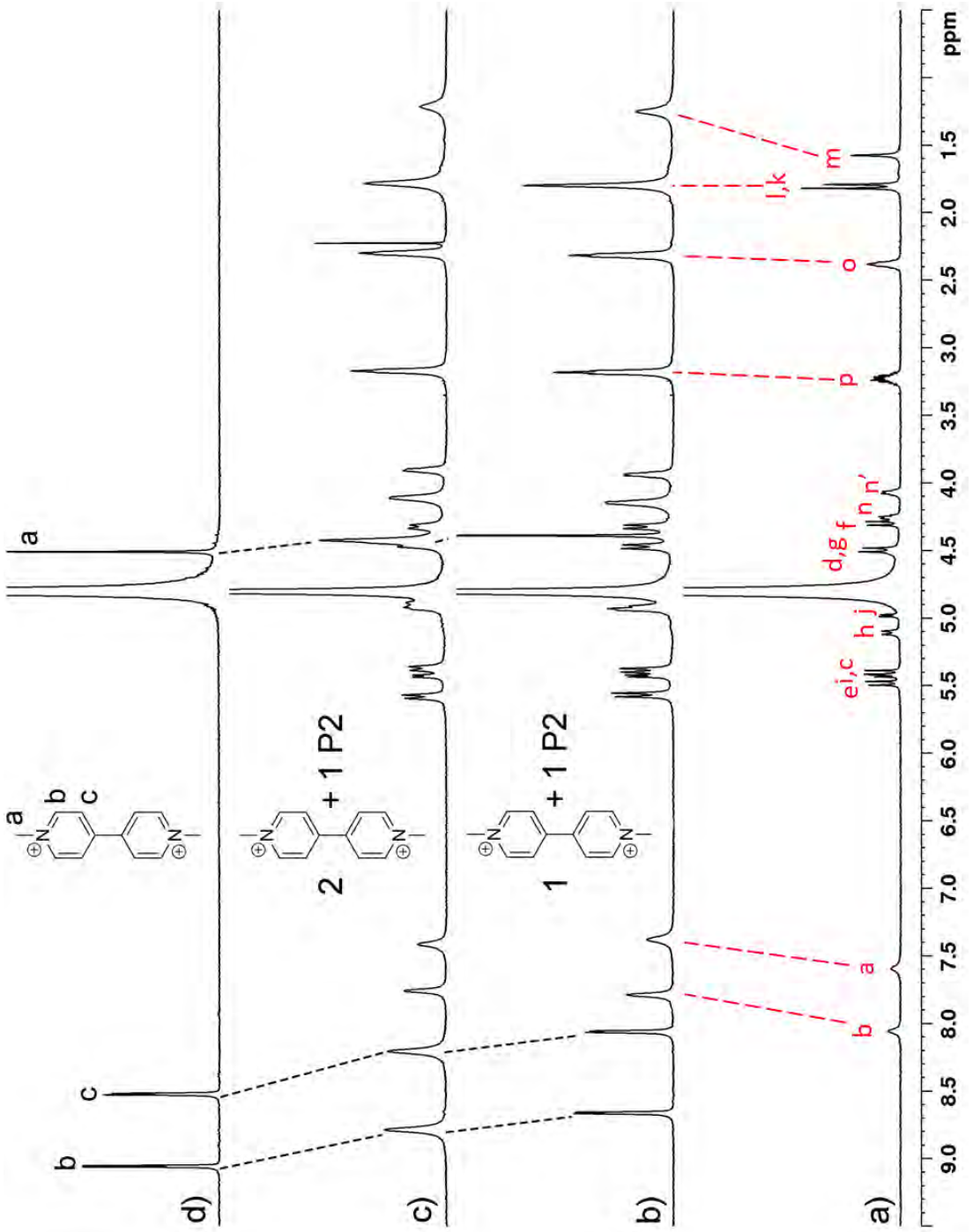

Figure II-S36. ^{1}H NMR spectra recorded (600 MHz, D_2O, RT) for: a) **P2** (0.1 mM, labelled in red) b) a 1:1 mixture of **P2** (1.0 mM) and **II-8** (1.0 mM), c) a 1:2 mixture of **P2** (1.0 mM) and **II-8** (2.0 mM), and d) **II-8** (1.0 mM, labelled in black).

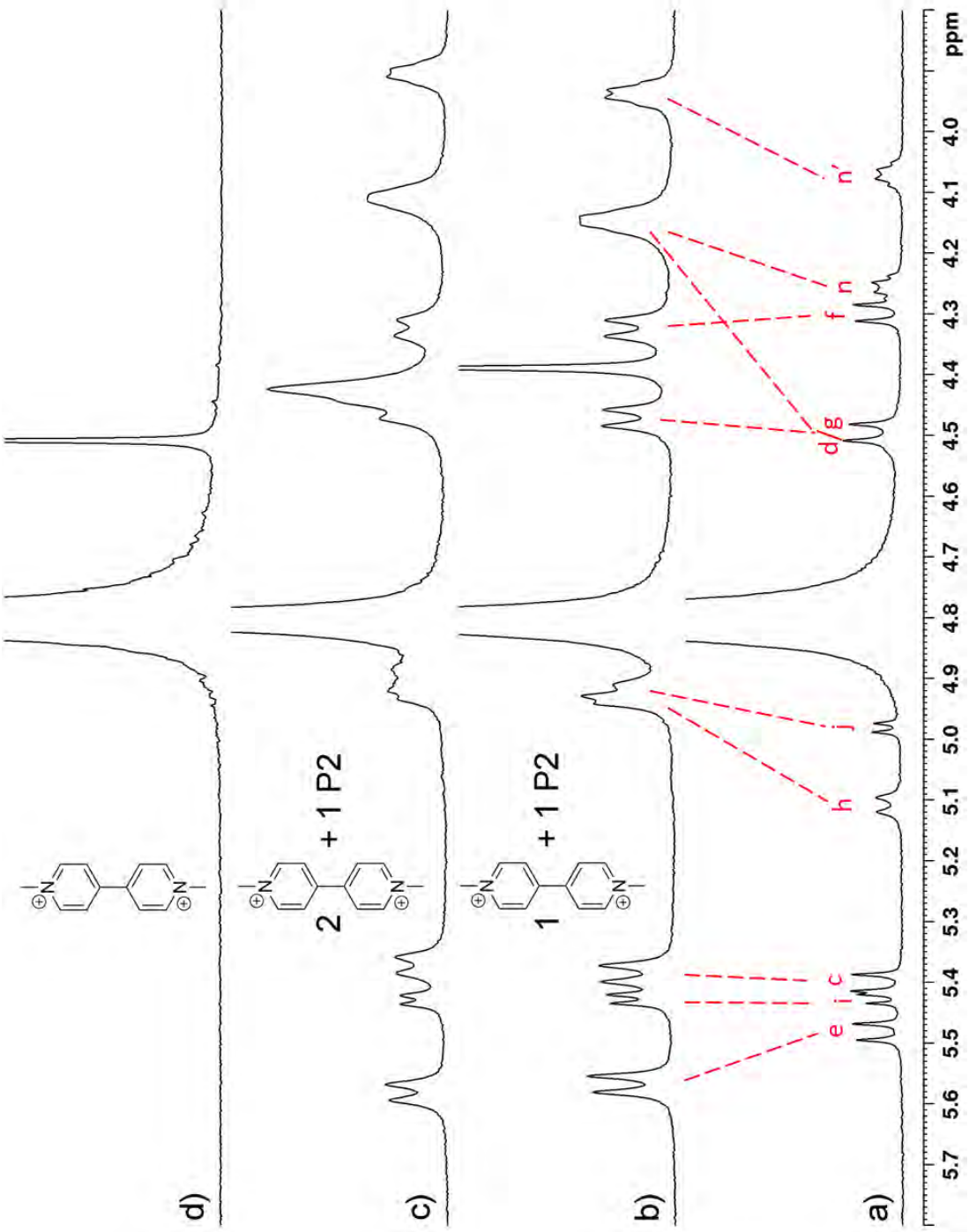

Figure II-S37. Methylene backbone section of ^{1}H NMR spectra recorded (600 MHz, D_2O, RT) for: a) **P2** (0.1 mM, labelled in red) b) a 1:1 mixture of **P2** (1.0 mM) and **II-8** (1.0 mM), c) a 1:2 mixture of **P2** (1.0 mM) and **II-8** (2.0 mM), and d) **II-8** (1.0 mM, labelled in black).

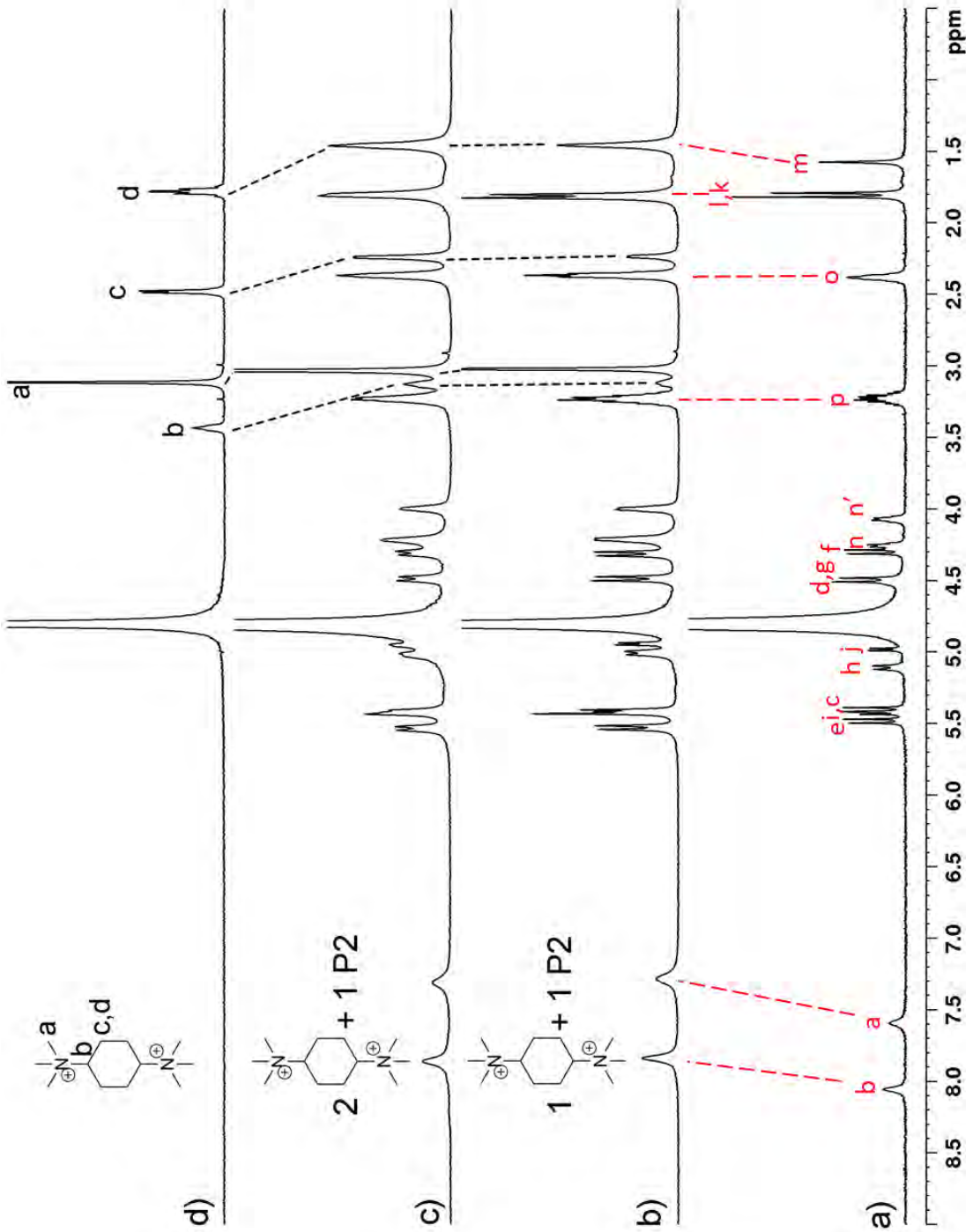

Figure II-S38. ^{1}H NMR spectra recorded (600 MHz, D_2O, RT) for: a) **P2** (0.1 mM, labelled in red), b) a 1:1 mixture of **P2** (2.0 mM) and **II-9** (2.0 mM), c) a 1:2 mixture of **P2** (2.0 mM) and **II-9** (4.0 mM), and d) **II-9** (2.0 mM, labelled in black).

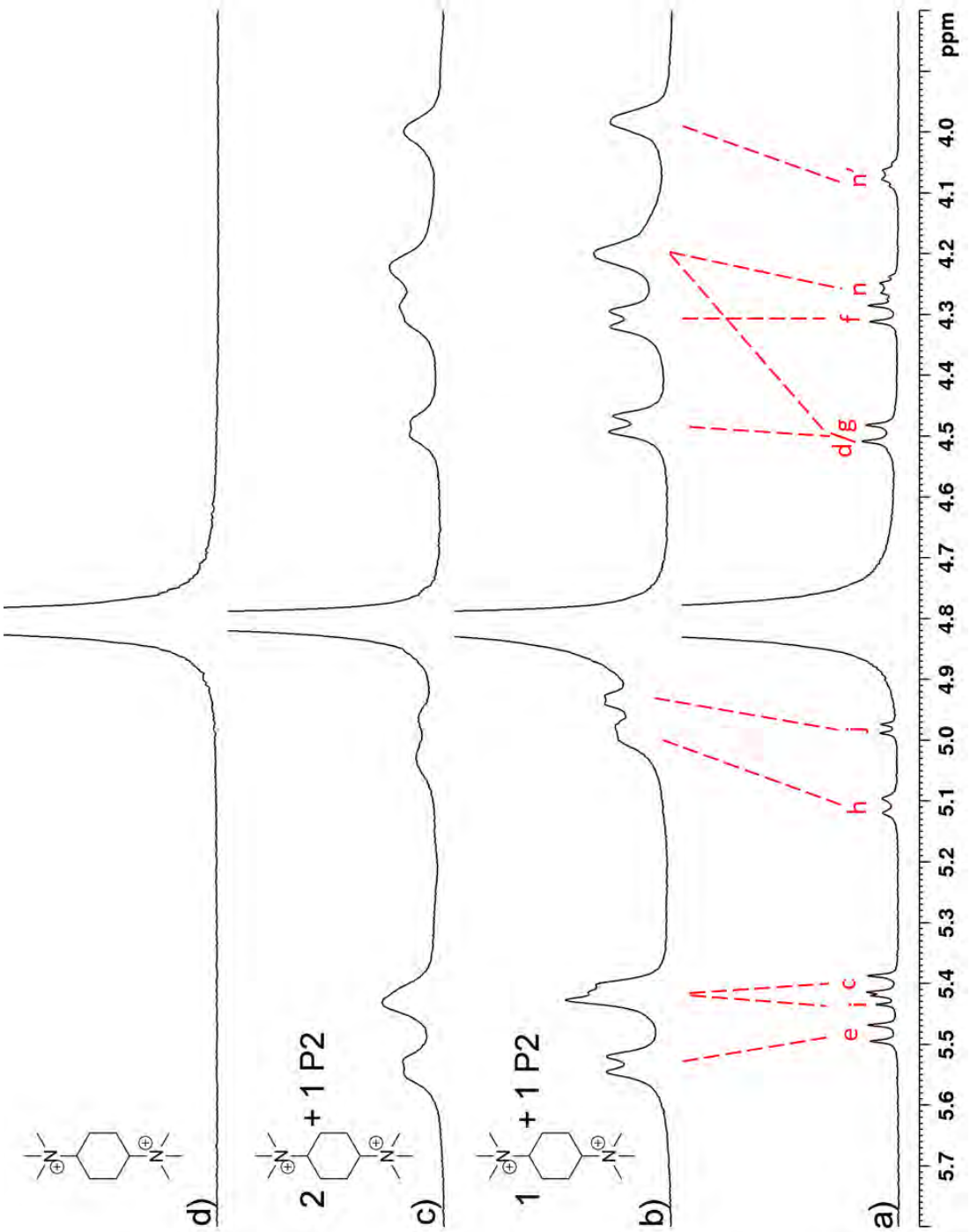

Figure II-S39. Methylene backbone section of ^{1}H NMR spectra recorded (600 MHz, D_2O, RT) for: a) **P2** (0.1 mM, labelled in red), b) a 1:1 mixture of **P2** (2.0 mM) and **II-9** (2.0 mM), c) a 1:2 mixture of **P2** (2.0 mM) and **II-9** (4.0 mM), and d) **II-9** (2.0 mM, labelled in black).

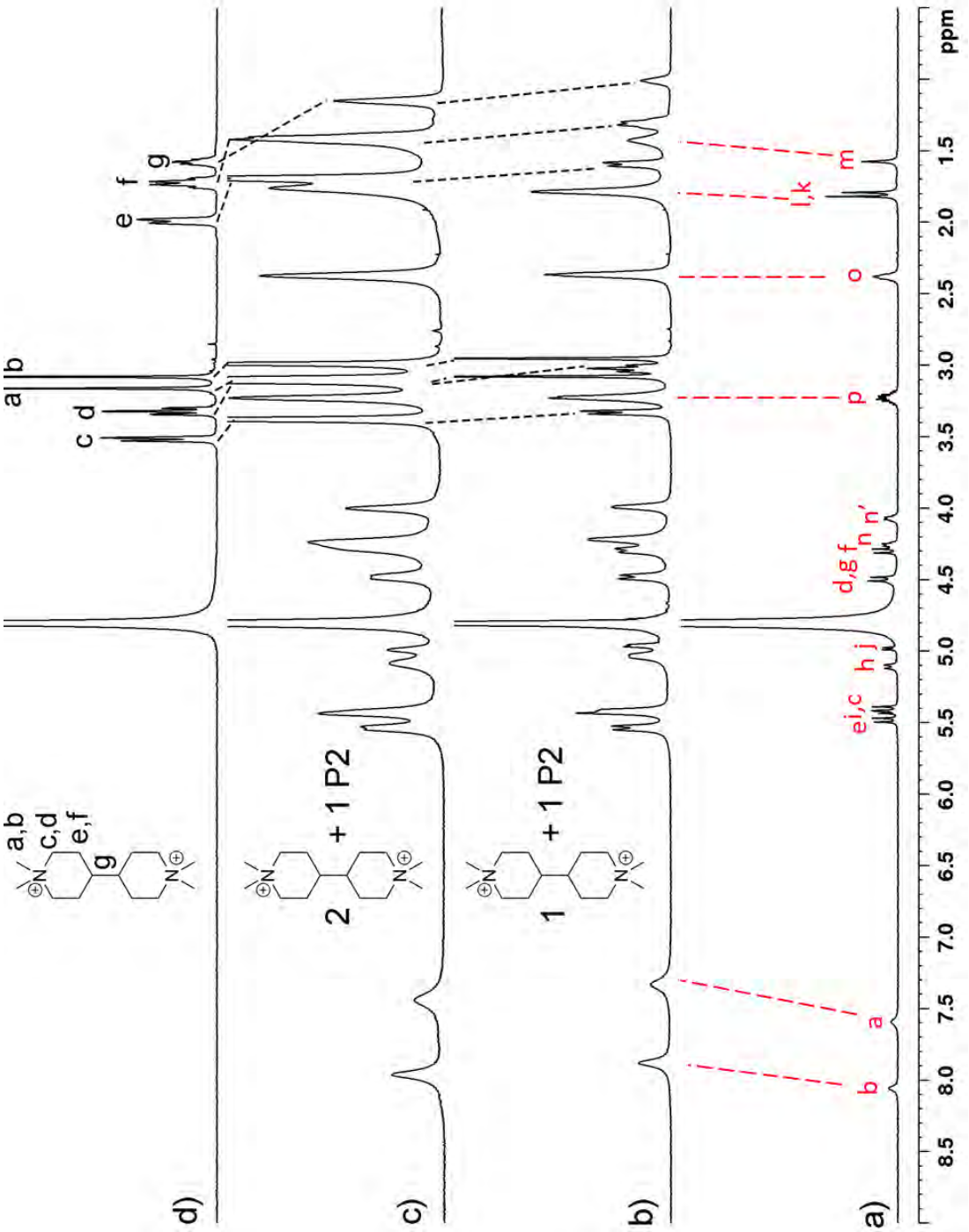

Figure II-S40. ^{1}H NMR spectra recorded (600 MHz, D_2O, RT) for: a) **P2** (0.1 mM, labelled in red), b) a 1:1 mixture of **P2** (2.0 mM) and **II-10** (2.0 mM), c) a 1:2 mixture of **P2** (2.0 mM) and **II-10** (4.0 mM), and d) **II-10** (2.0 mM, labelled in black).

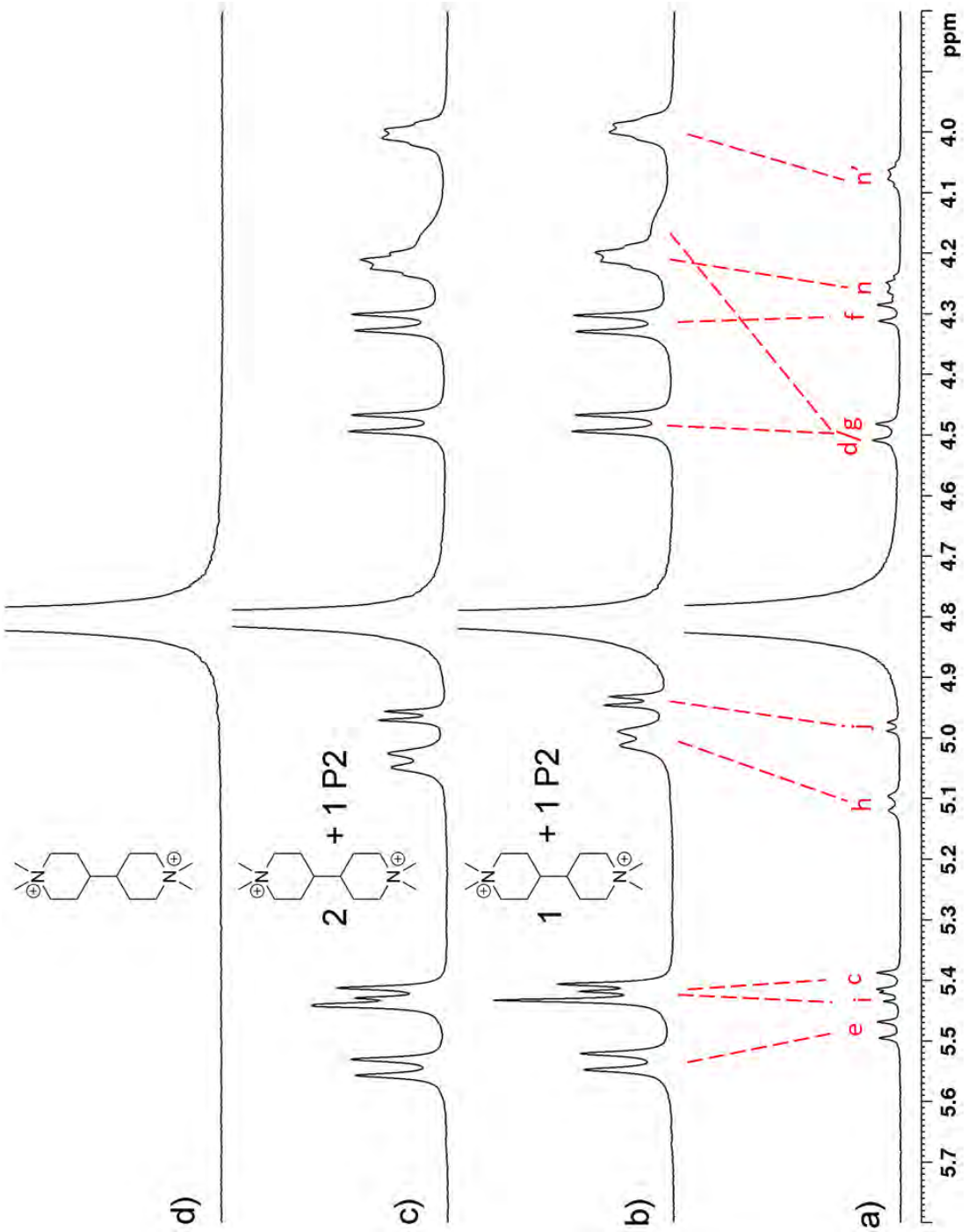

Figure II-S41. Methylene backbone section of ^{1}H NMR spectra recorded (600 MHz, D_2O, RT) for: a) **P2** (0.1 mM, labelled in red), b) a 1:1 mixture of **P2** (2.0 mM) and **II-10** (2.0 mM), c) a 1:2 mixture of **P2** (2.0 mM) and **II-10** (4.0 mM), and d) **II-10** (2.0 mM, labelled in black).

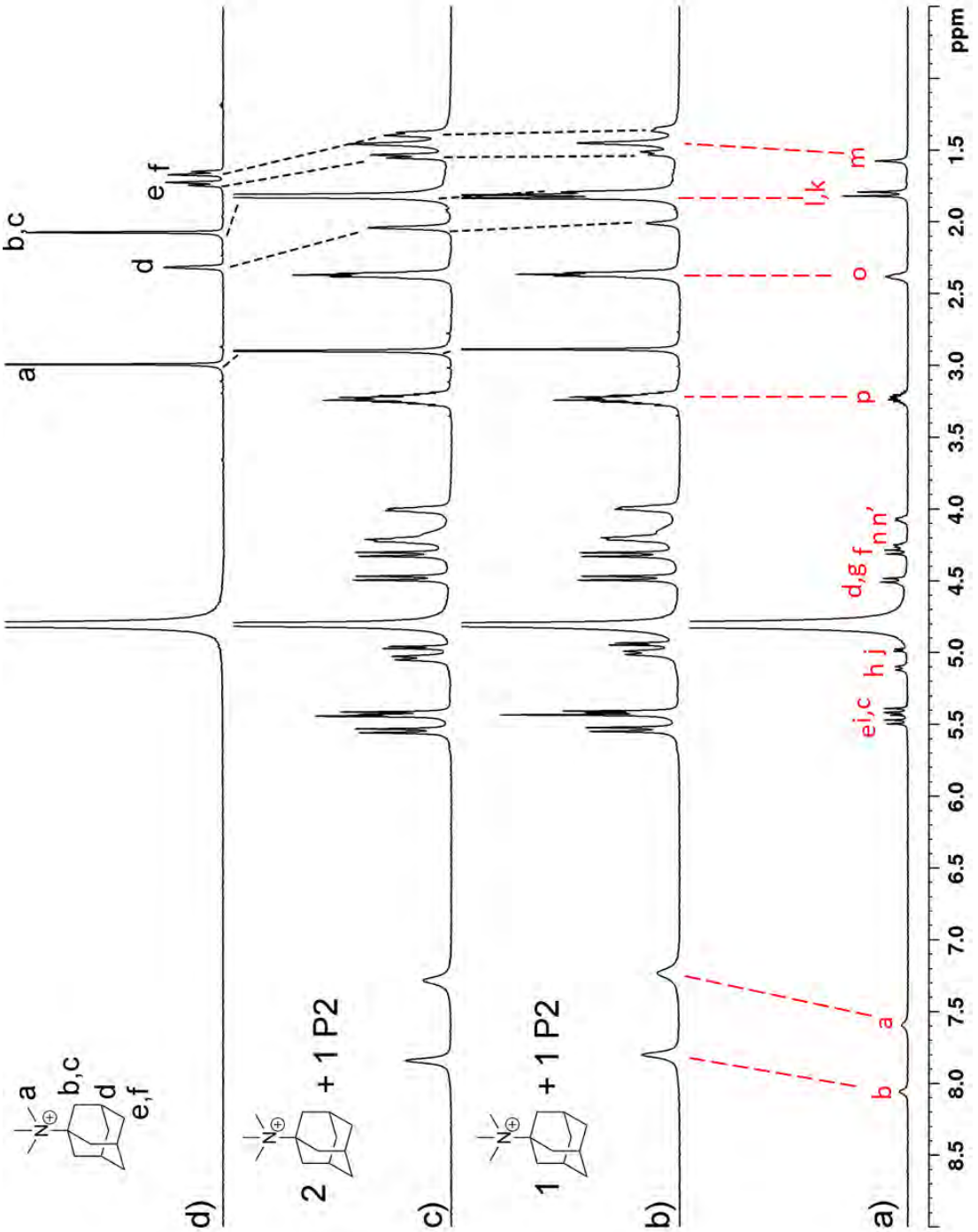

Figure II-S42. ^{1}H NMR spectra recorded (600 MHz, D_2O, RT) for: a) **P2** (0.1 mM, labelled in red), b) a 1:1 mixture of **P2** (2.0 mM) and **II-11** (2.0 mM), c) a 1:2 mixture of **P2** (2.0 mM) and **II-11** (4.0 mM), and d) **II-11** (2.0 mM, labelled in black).

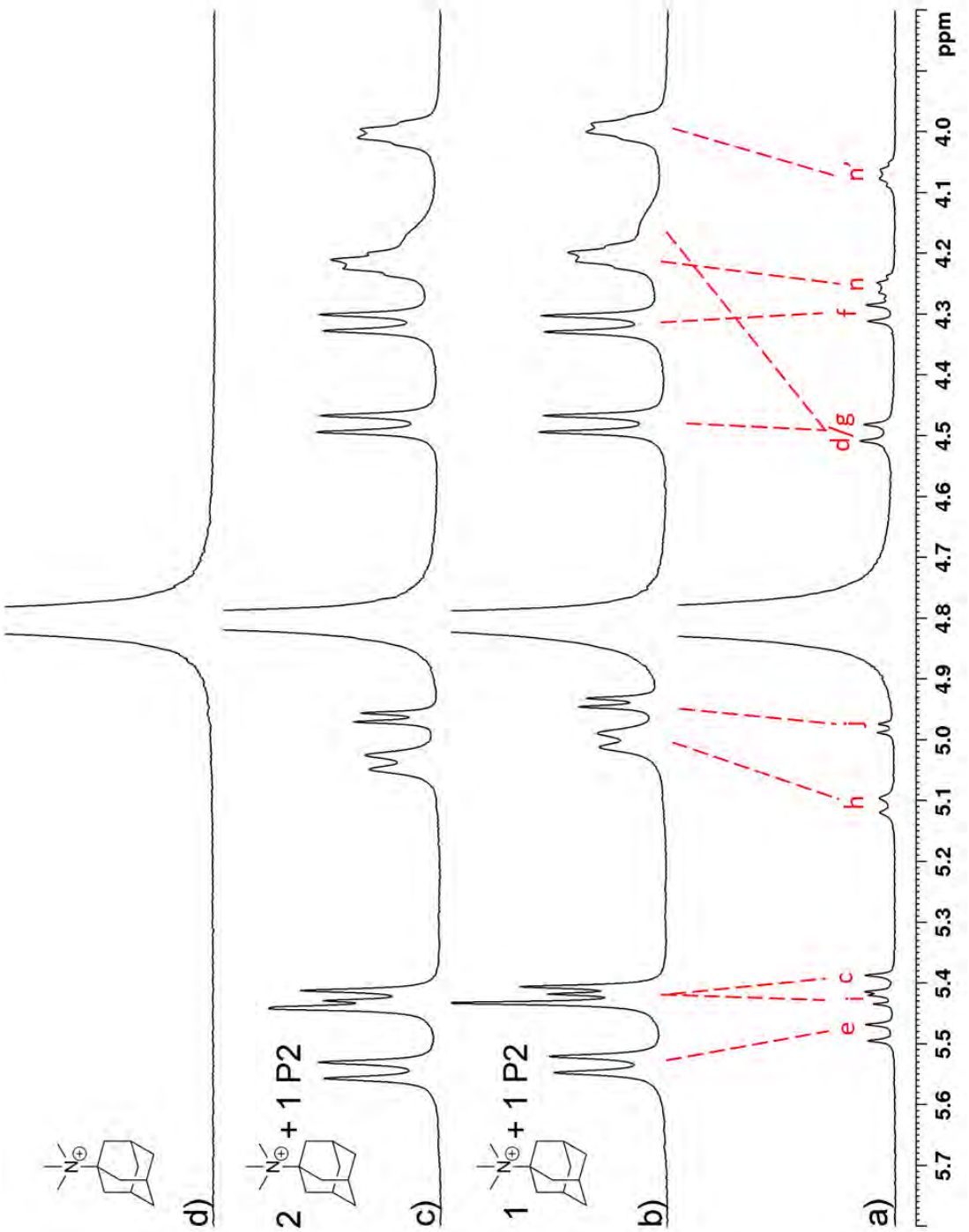

Figure II-S43. Methylene backbone section of ^{1}H NMR spectra recorded (600 MHz, D_2O, RT) for: a) **P2** (0.1 mM, labelled in red), b) a 1:1 mixture of **P2** (2.0 mM) and **II-11** (2.0 mM), c) a 1:2 mixture of **P2** (2.0 mM) and **II-11** (4.0 mM), and d) **II-11** (2.0 mM, labelled in black).

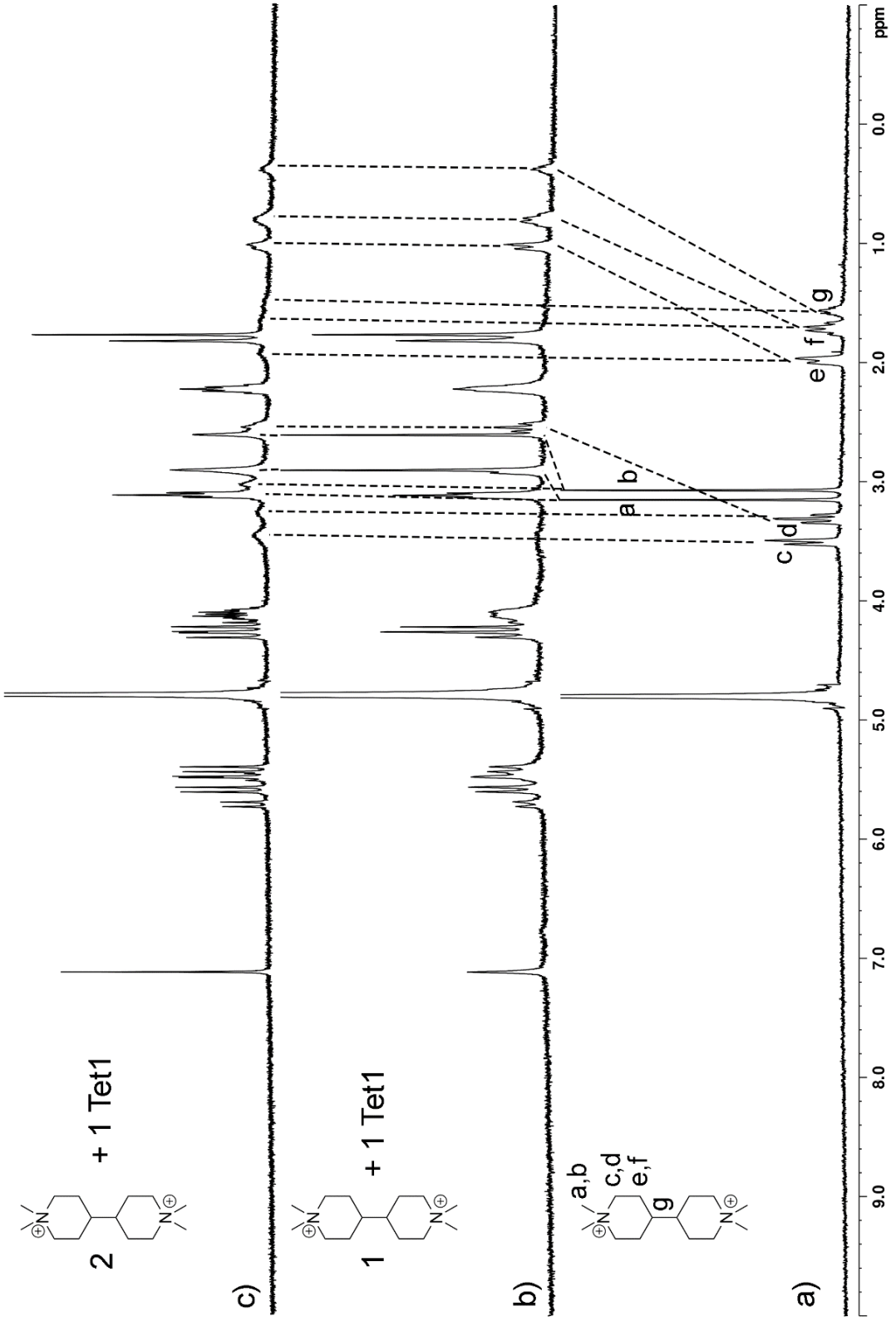

Figure II-S44. ^{1}H NMR spectra recorded (400 MHz, D_2O, RT) for: a) **II-10** (0.5 mM), b) a 1:1 mixture of **Tet1** (0.25 mM) and **II-10** (0.25 mM), and c) a 1:2 mixture of **Tet1** (0.25 mM) and **II-10** (0.5 mM).

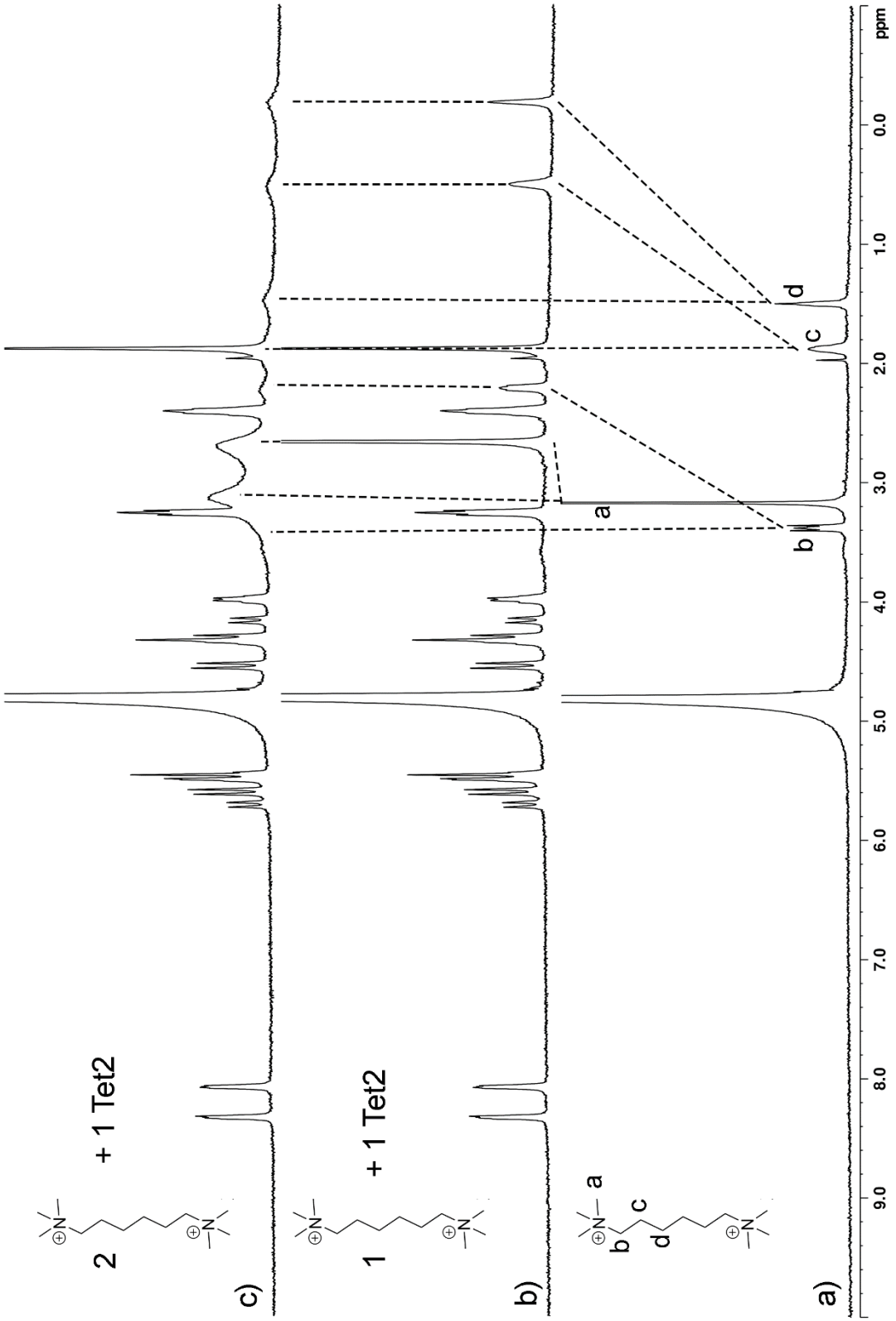

Figure II-S45. ^{1}H NMR spectra recorded (400 MHz, D_2O, RT) for: a) **II-6** (0.5 mM), b) a 1:1 mixture of **Tet2** (0.25 mM) and **II-6** (0.25 mM), and c) a 1:2 mixture of **Tet2** (0.25 mM) and **II-6** (0.5 mM).

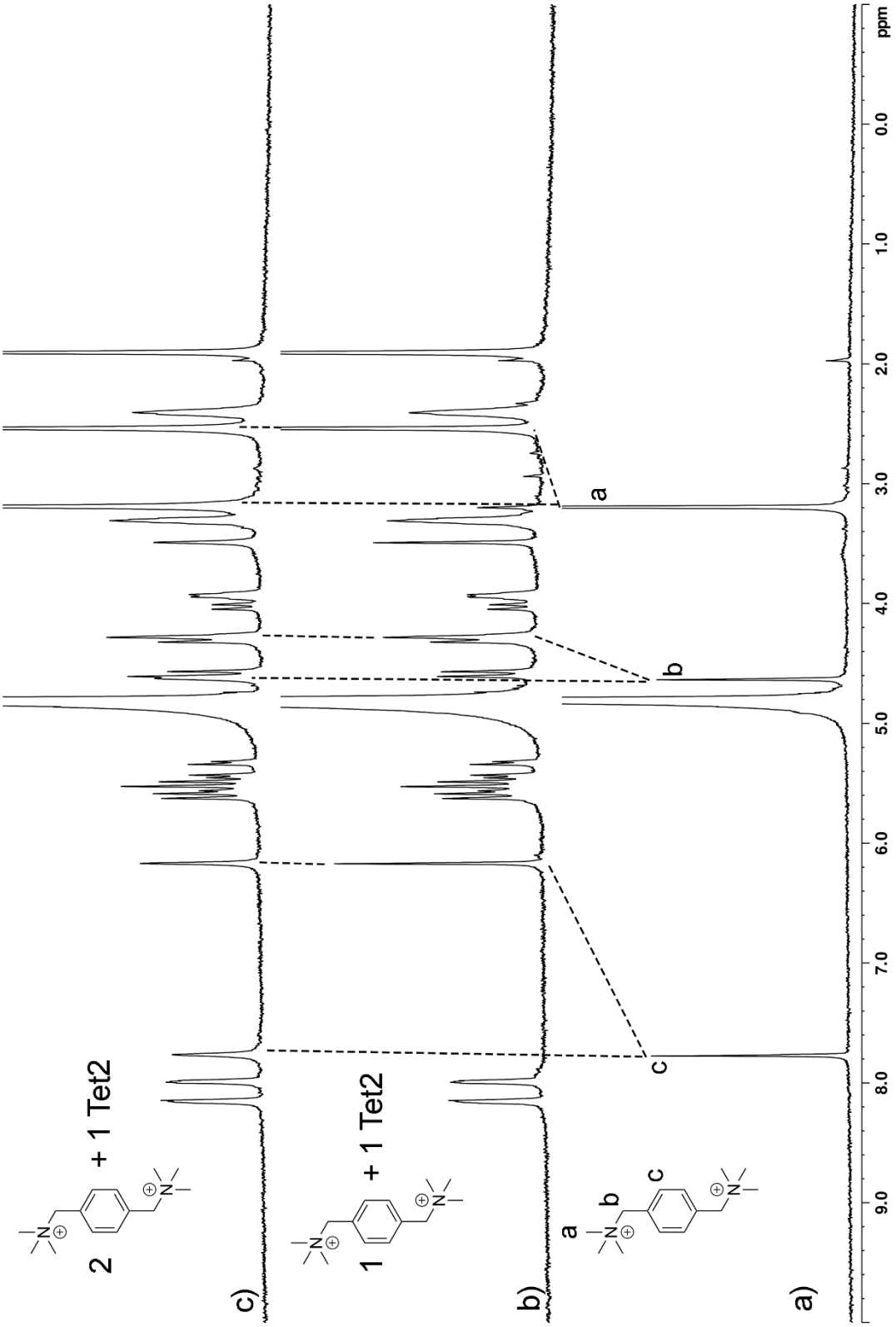

Figure II-S46. ^{1}H NMR spectra recorded (400 MHz, D_2O, RT) for: a) **II-7** (0.5 mM), b) a 1:1 mixture of **Tet2** (0.25 mM) and **II-7** (0.25 mM), and c) a 1:2 mixture of **Tet2** (0.25 mM) and **II-7** (0.5 mM).

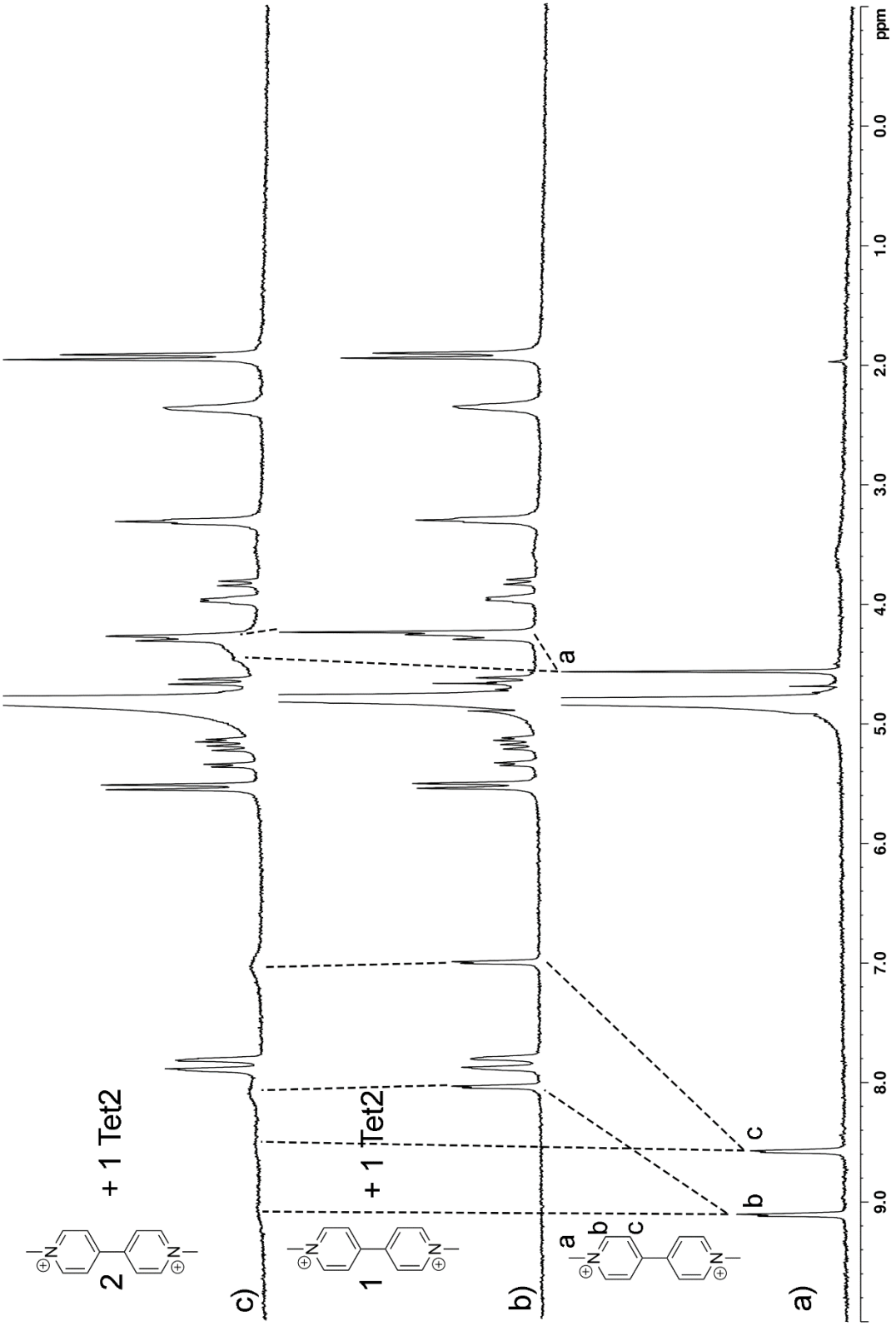

Figure II-S47. ^{1}H NMR spectra recorded (400 MHz, D_2O, RT) for: a) **II-8** (0.5 mM), b) a 1:1 mixture of **Tet2** (0.25 mM) and **II-8** (0.25 mM), and c) a 1:2 mixture of **Tet2** (0.25 mM) and **II-8** (0.5 mM).

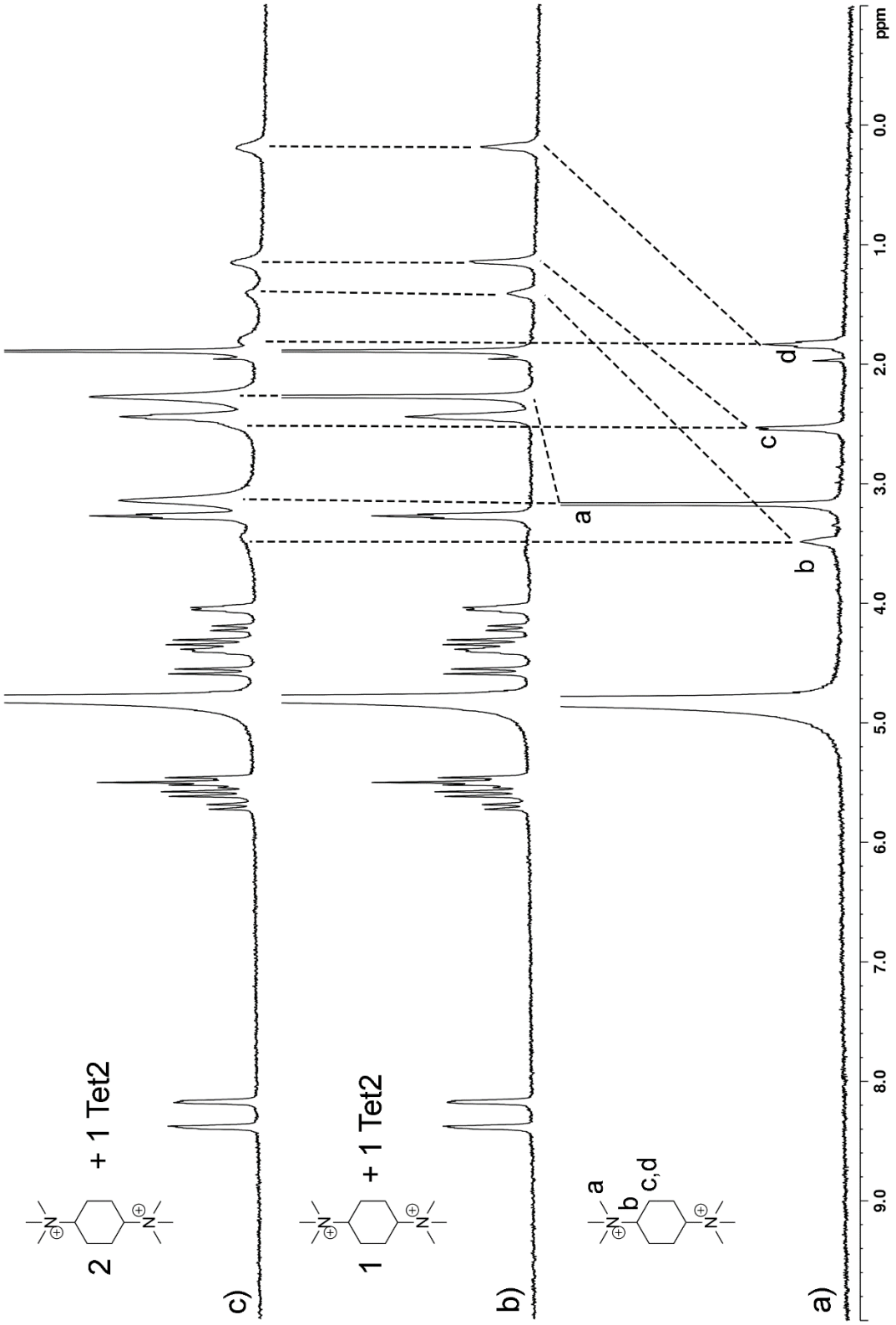

Figure II-S48. ^{1}H NMR spectra recorded (400 MHz, D_2O, RT) for: a) **II-9** (0.5 mM), b) a 1:1 mixture of **Tet2** (0.25 mM) and **II-9** (0.25 mM), and c) a 1:2 mixture of **Tet2** (0.25 mM) and **II-9** (0.5 mM).

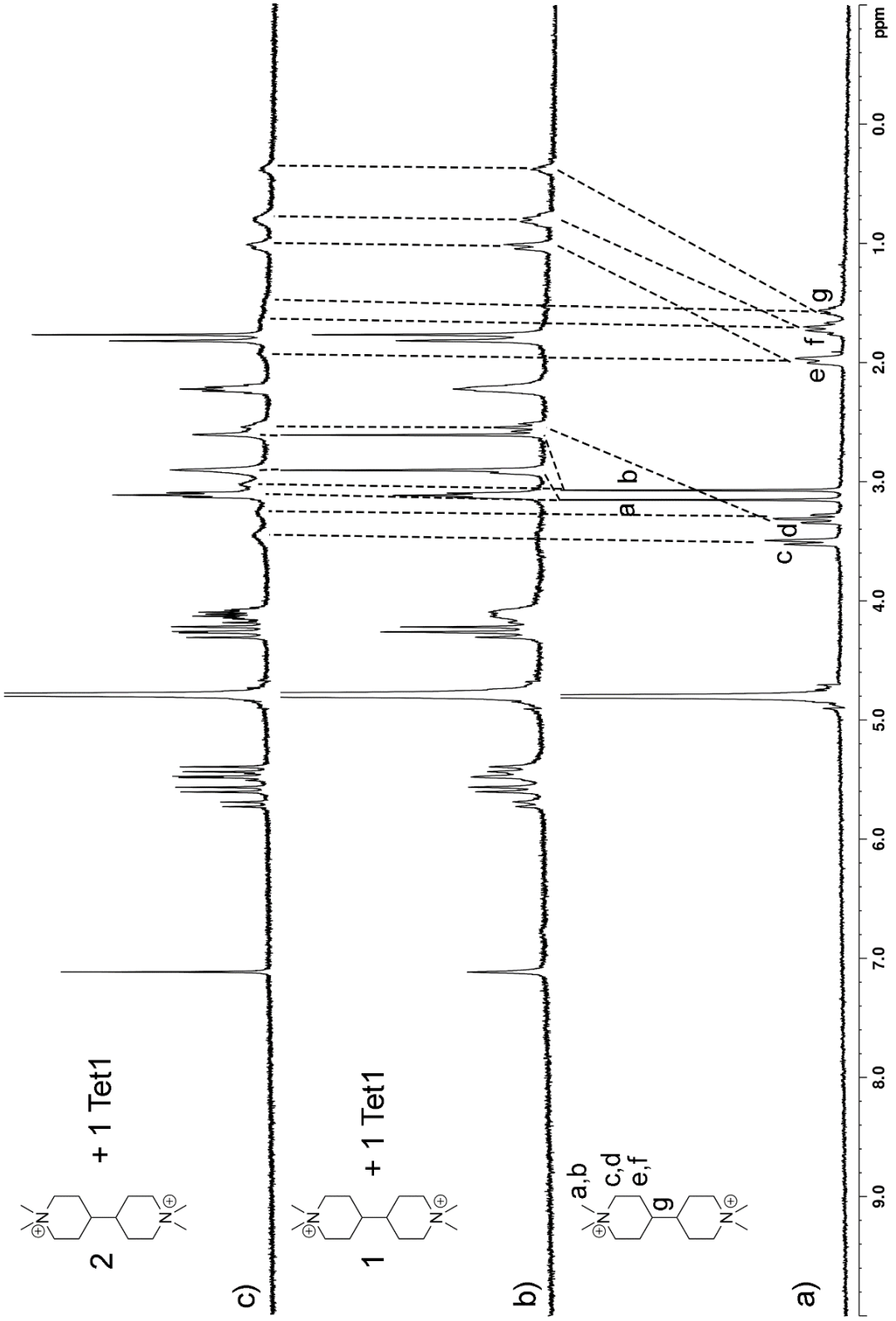

Figure II-S49. ^{1}H NMR spectra recorded (400 MHz, D_2O, RT) for: a) **II-10** (0.5 mM), b) a 1:1 mixture of **Tet2** (0.25 mM) and **II-10** (0.25 mM), and c) a 1:2 mixture of **Tet2** (0.25 mM) and **II-10** (0.5 mM).

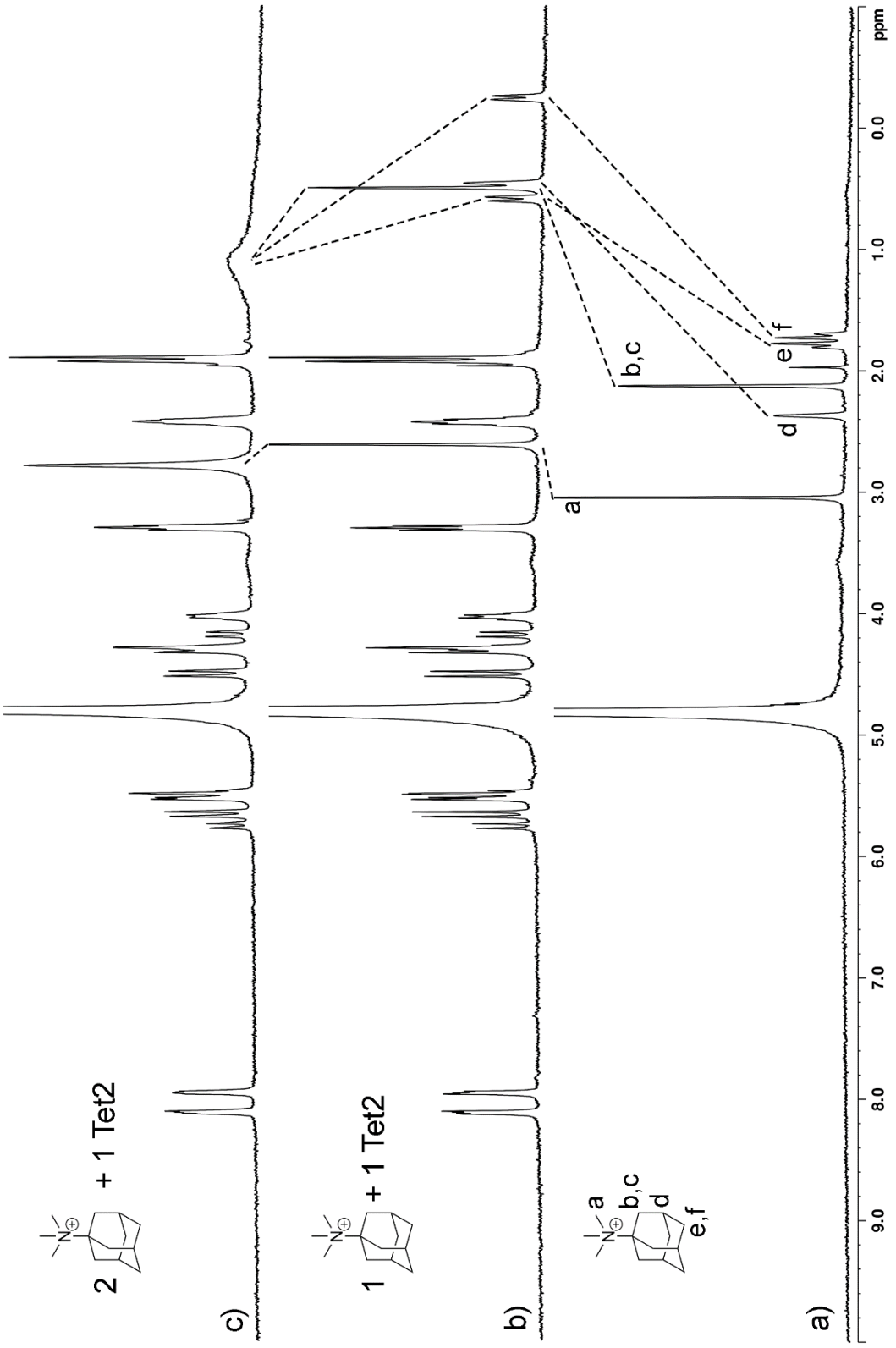

Figure II-S50. ^{1}H NMR spectra recorded (400 MHz, D_2O, RT) for: a) **II-11** (0.5 mM), b) a 1:1 mixture of **Tet2** (0.25 mM) and **II-11** (0.25 mM), and c) a 1:2 mixture of **Tet2** (0.25 mM) and **II-11** (0.5 mM).

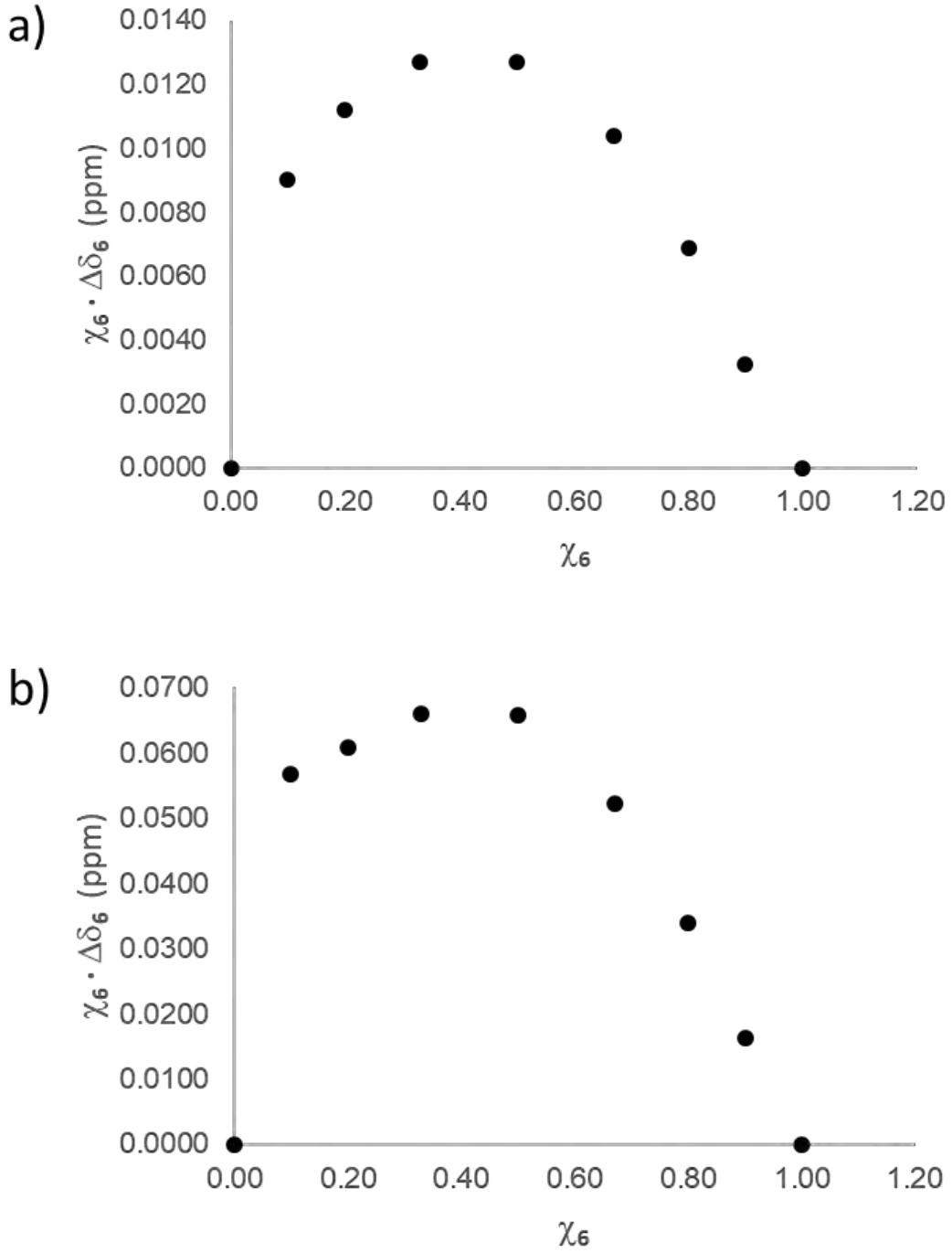

Figure II-S51. Job plots generated for **P1** and **II-6** ([**P1**] + [**II-6**] = 1.0 mM) by monitoring the a) methyl H_a and b) methylene H_d resonances of **II-6**.

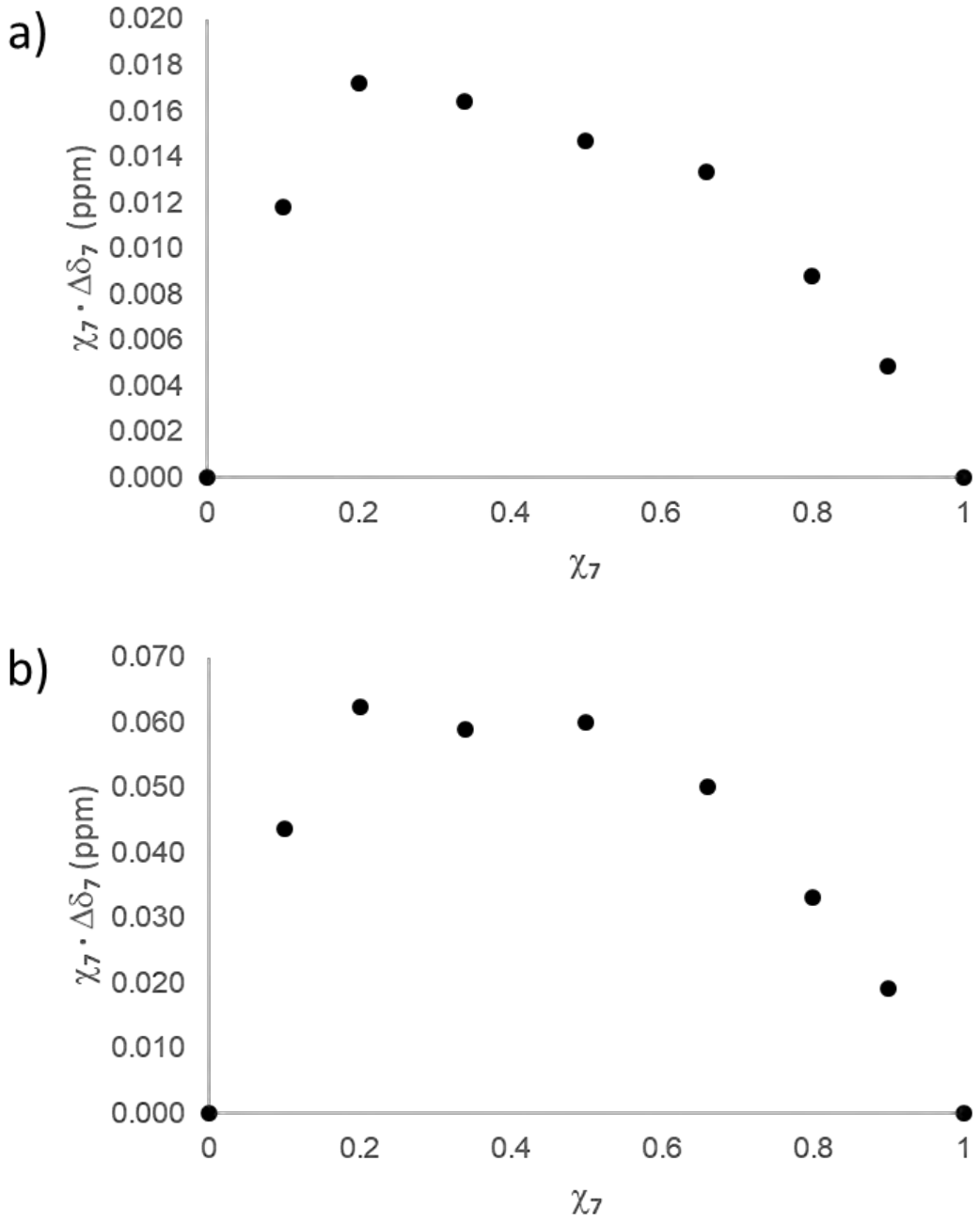

Figure II-S52. Job plots generated for **P1** and **II-7** ([**P1**] + [**II-7**] = 0.5 mM) by monitoring the a) methyl H_a and b) aromatic H_c resonances of **II-7**.

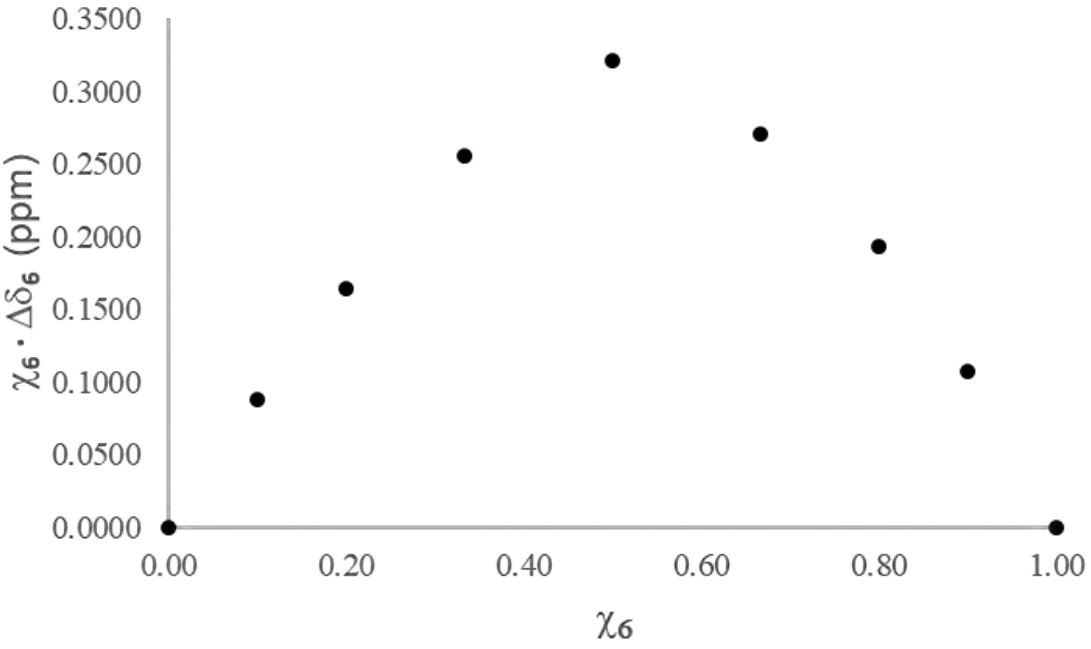

Figure II-S53. Job plot generated for **P2** and **II-6** ([**P2**] + [**II-6**] = 1.5 mM) by monitoring the methylene H_d resonance of **II-6**.

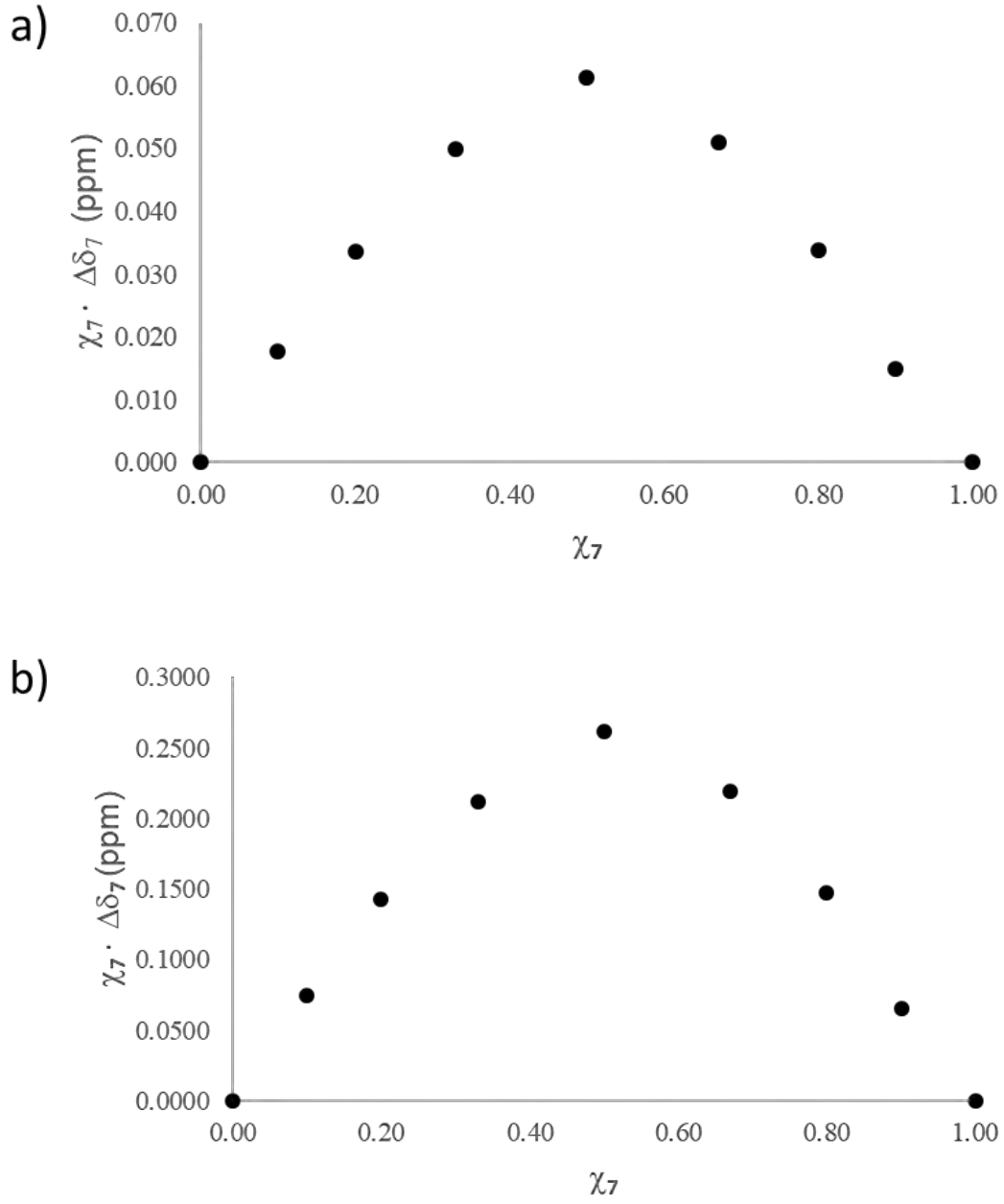

Figure II-S54. Job plots generated for **P2** and **II-7** ([**P2**] + [**II-7**] = 1.0 mM) by monitoring the a) methyl H_a and b) aromatic H_c resonances of **II-7**.

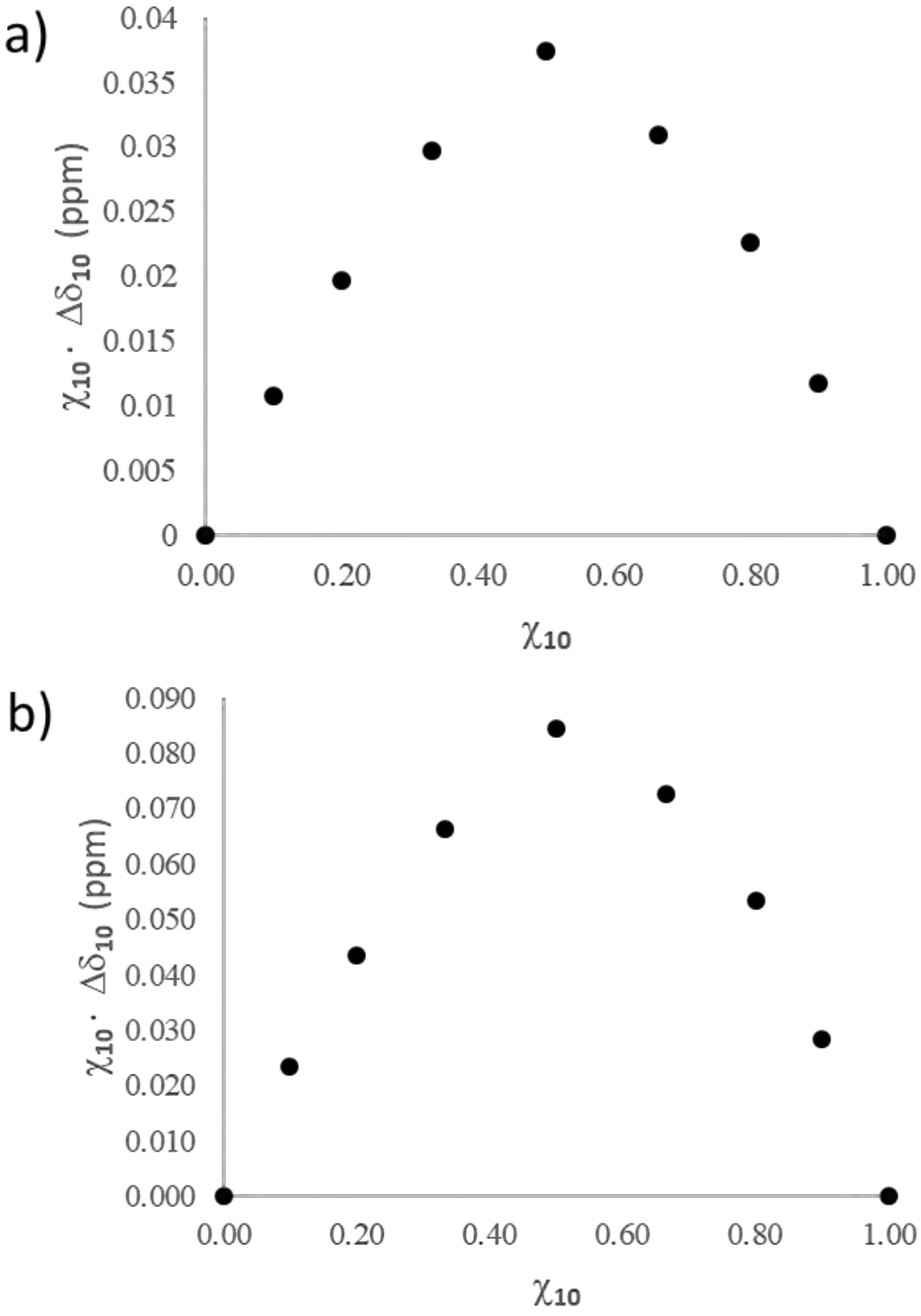

Figure II-S55. Job plot generated for **P2** and **II-10** ([**P2**] + [**II-10**] = 1.0 mM) by monitoring the a) methyl H_a and b) methylene H_c resonances of **II-10**.

^{1}H NMR Global Fit Titration Experiments For P1

Global Fit Binding Model implemented in Scientist™
// Micromath Scientist Model File
IndVars: ConcHost
DepVars: CSA, CSB, CSC
Params: Ka, CSAzero, CSAsat, CSBzero, CSBsat, CSCzero, CSCsat
Ka = ConcHG/(ConcHfree*ConcGfree)
ConcHost=ConcHfree+ConcHG
0.0003=ConcGfree+ConcHG
CSA = CSAzero + ((CSAsat-CSAzero)*(ConcHG/0.0003))
CSB = CSBzero + ((CSBsat-CSBzero)*(ConcHG/0.0003))
CSC = CSCzero + ((CSCsat-CSCzero)*(ConcHG/0.0003))
0<ConcHfree<ConcHost
0<ConcGfree<0.0003
***

Number of dependent variables and concentration used were changed based on the sample and how many guest resonances were monitored.

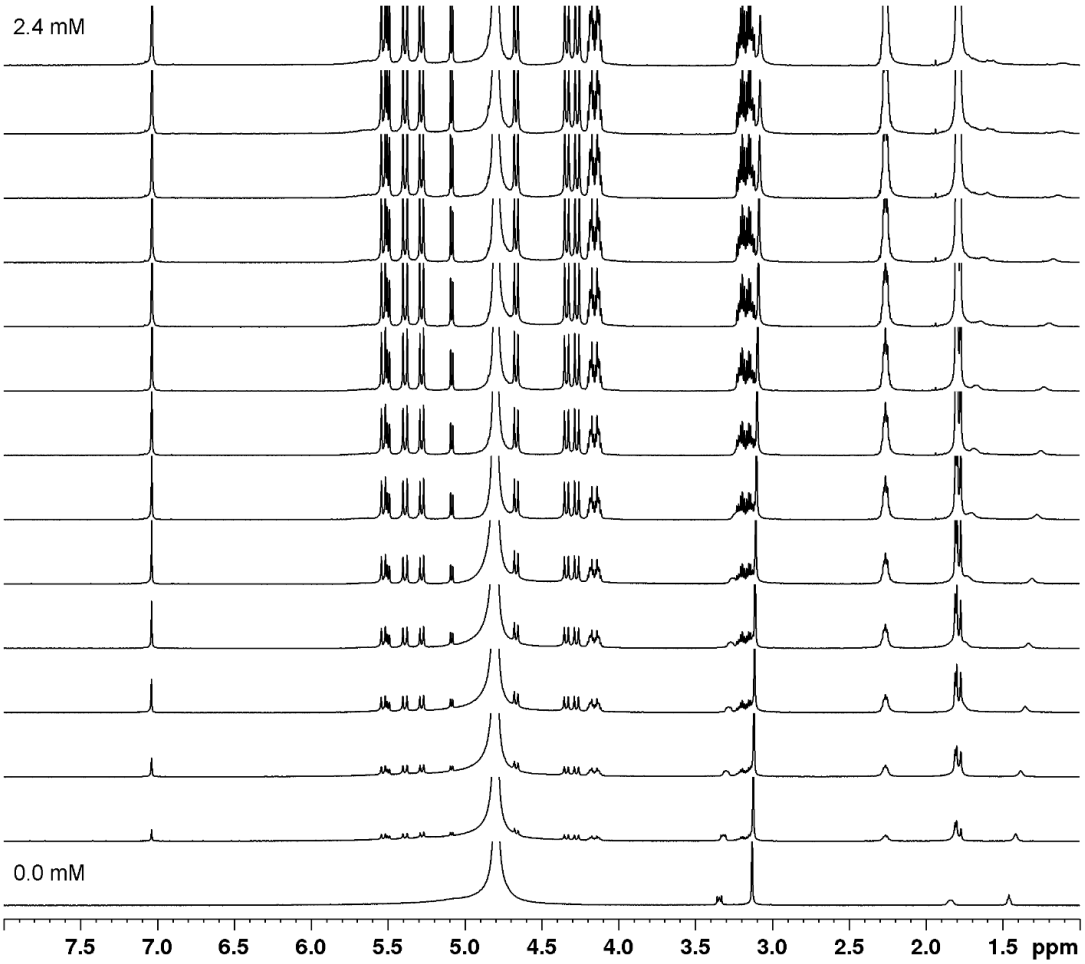

Figure II-S56. ^{1}H NMR (600 MHz, D_2O, RT) titration of **II-6** (0.3 mM) with increasing amounts of **P1** (0 mM – 2.4 mM).

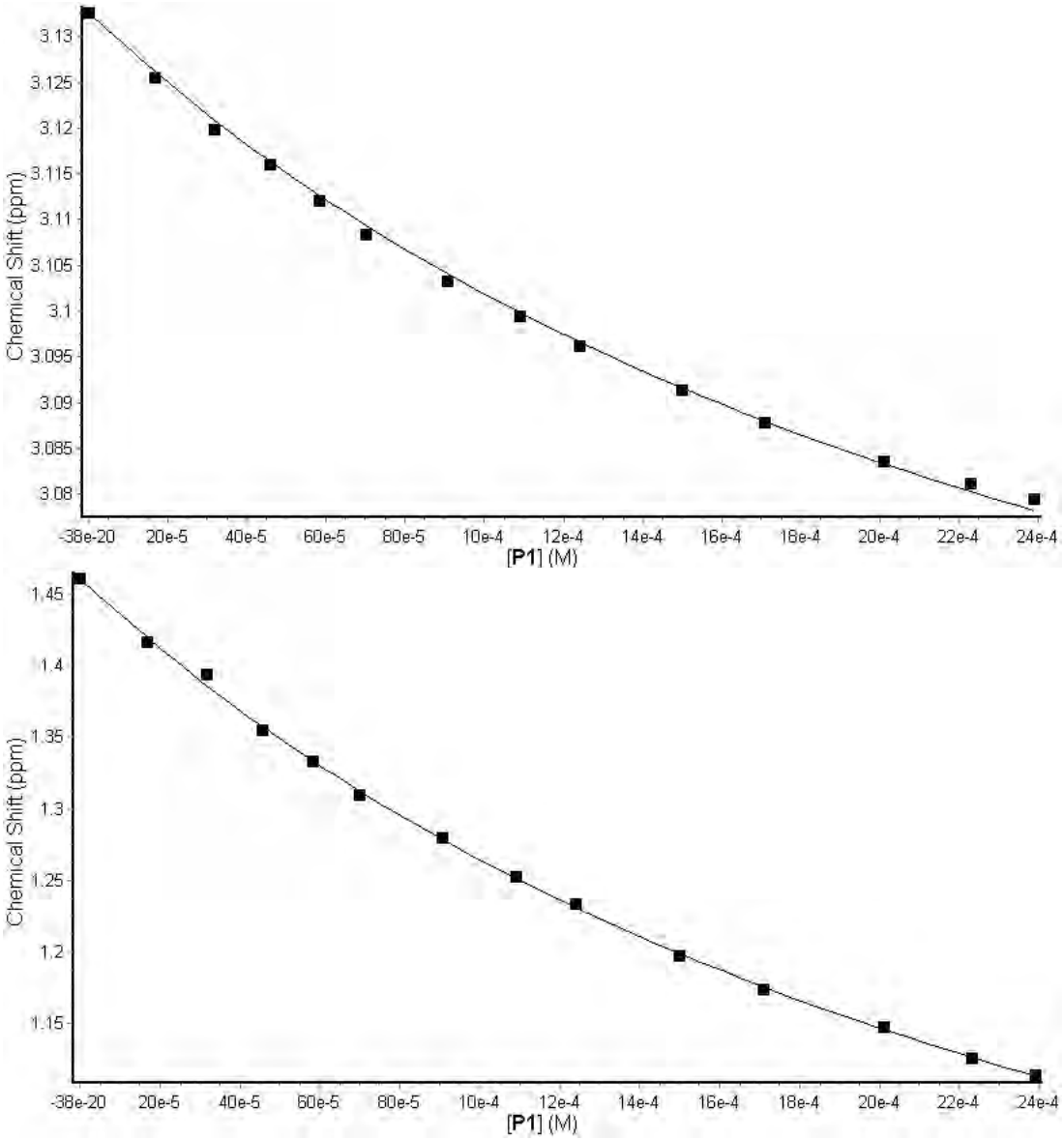

Figure II-S57. Chemical shifts of **II-6** resonances as a function of [**P1**]. The solid lines represent the best non-linear fit of the resonances simultaneously inputted into a global fit model ($K_a = 3.87 \pm 0.12 \times 10^2\ M^{-1}$).

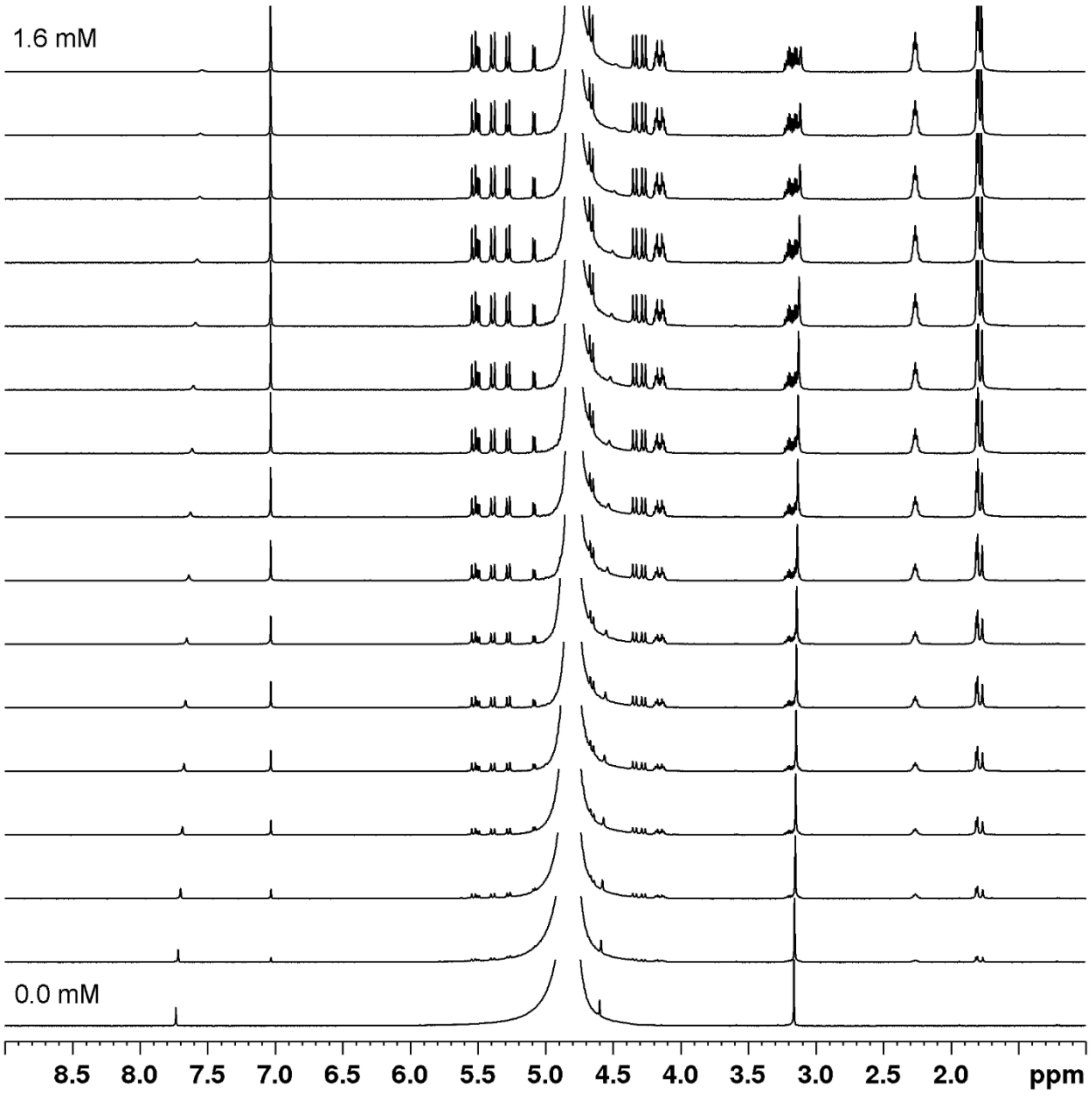

Figure II-S58. ^{1}H NMR (600 MHz, D_2O, RT) titration of **II-7** (0.3 mM) with increasing amounts of **P1** (0 mM – 1.6 mM).

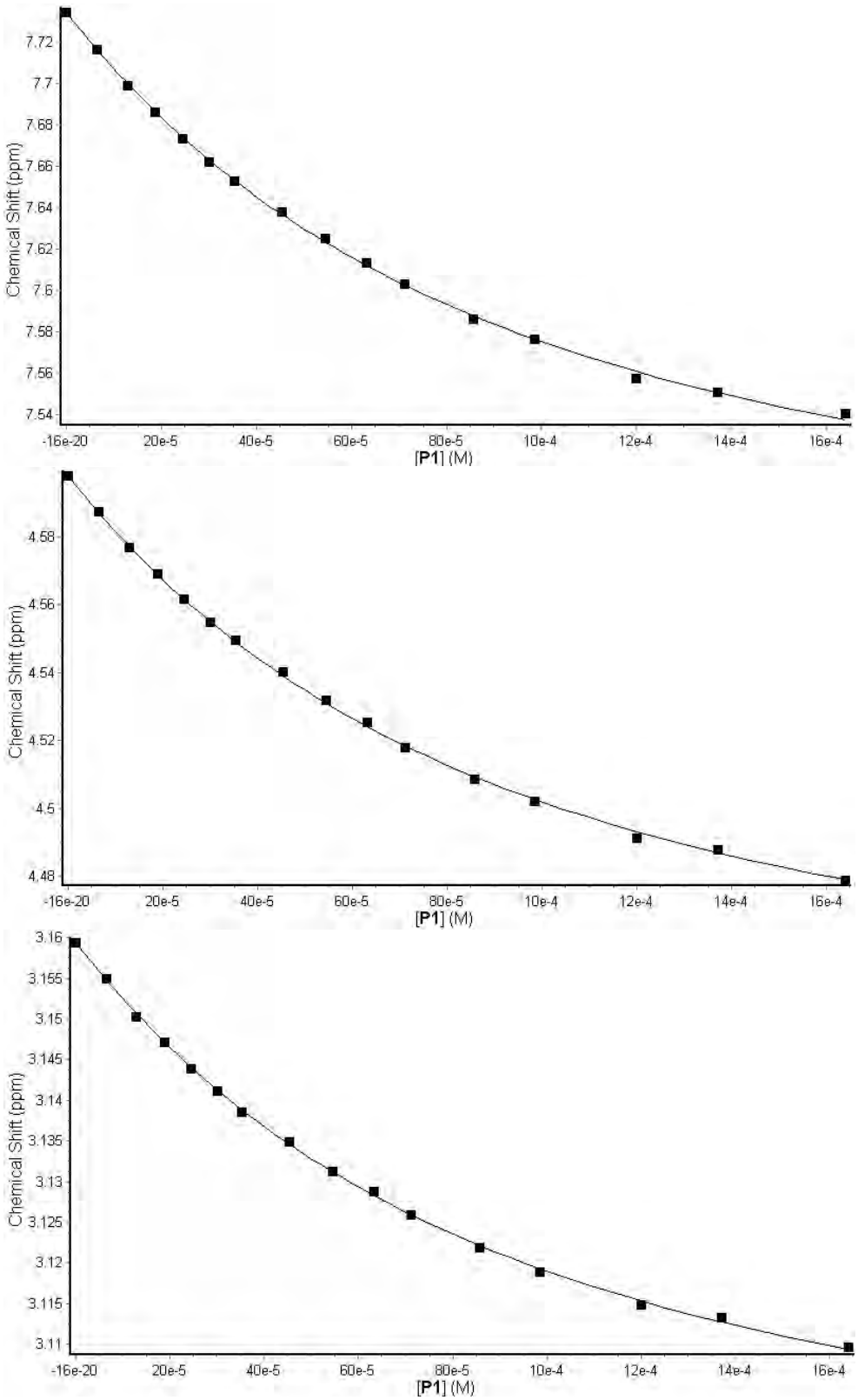

Figure II-S59. Chemical shifts of **II-7** resonances as a function of [**P1**]. The solid lines represent the best non-linear fit of the resonances simultaneously inputted into a global fit model ($K_a = 1.40 \pm 0.03 \times 10^3\ M^{-1}$).

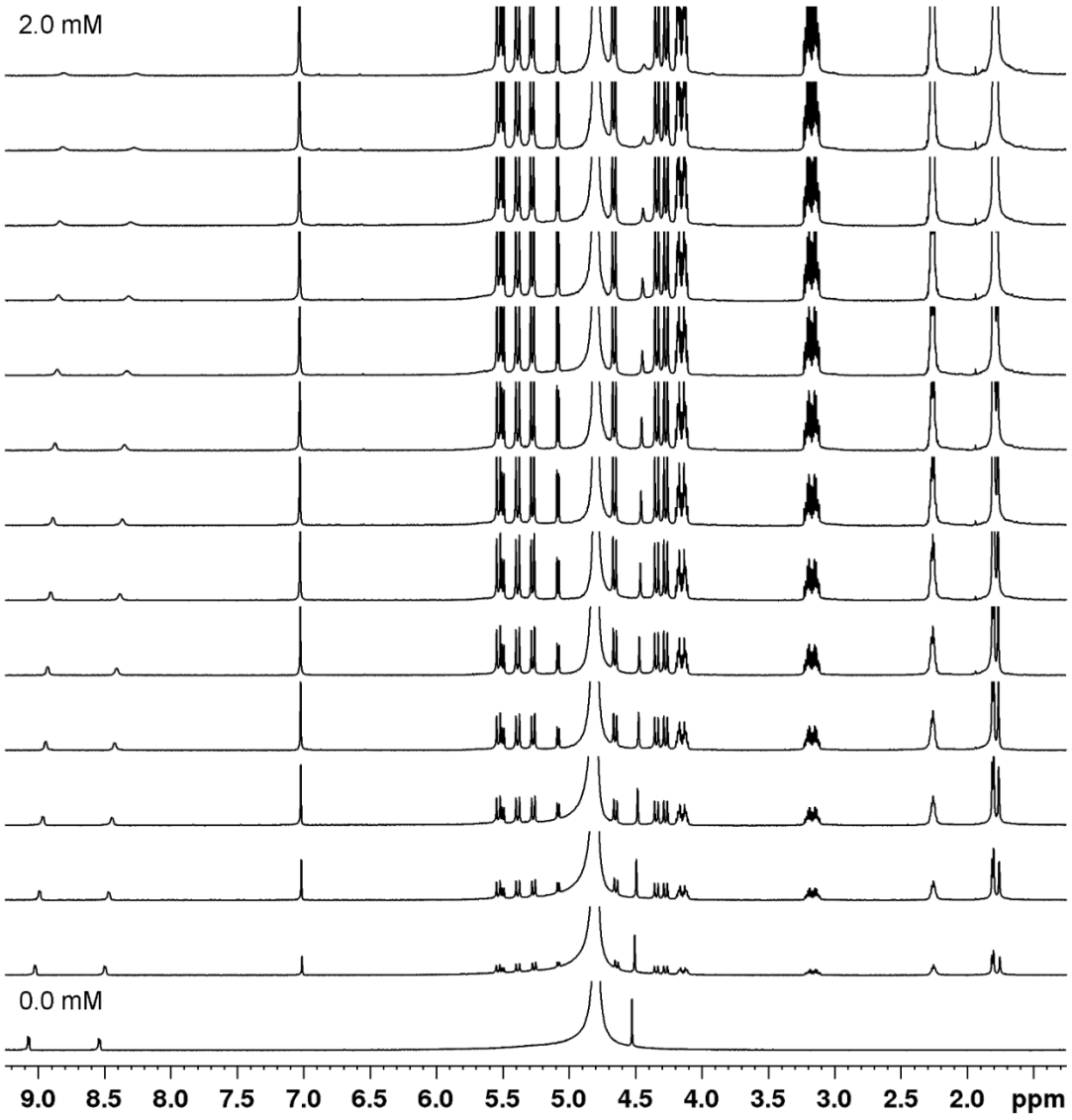

Figure II-S60. ^{1}H NMR (600 MHz, D_2O, RT) titration of **II-8** (0.3 mM) with increasing amounts of **P1** (0 mM – 2.4 mM).

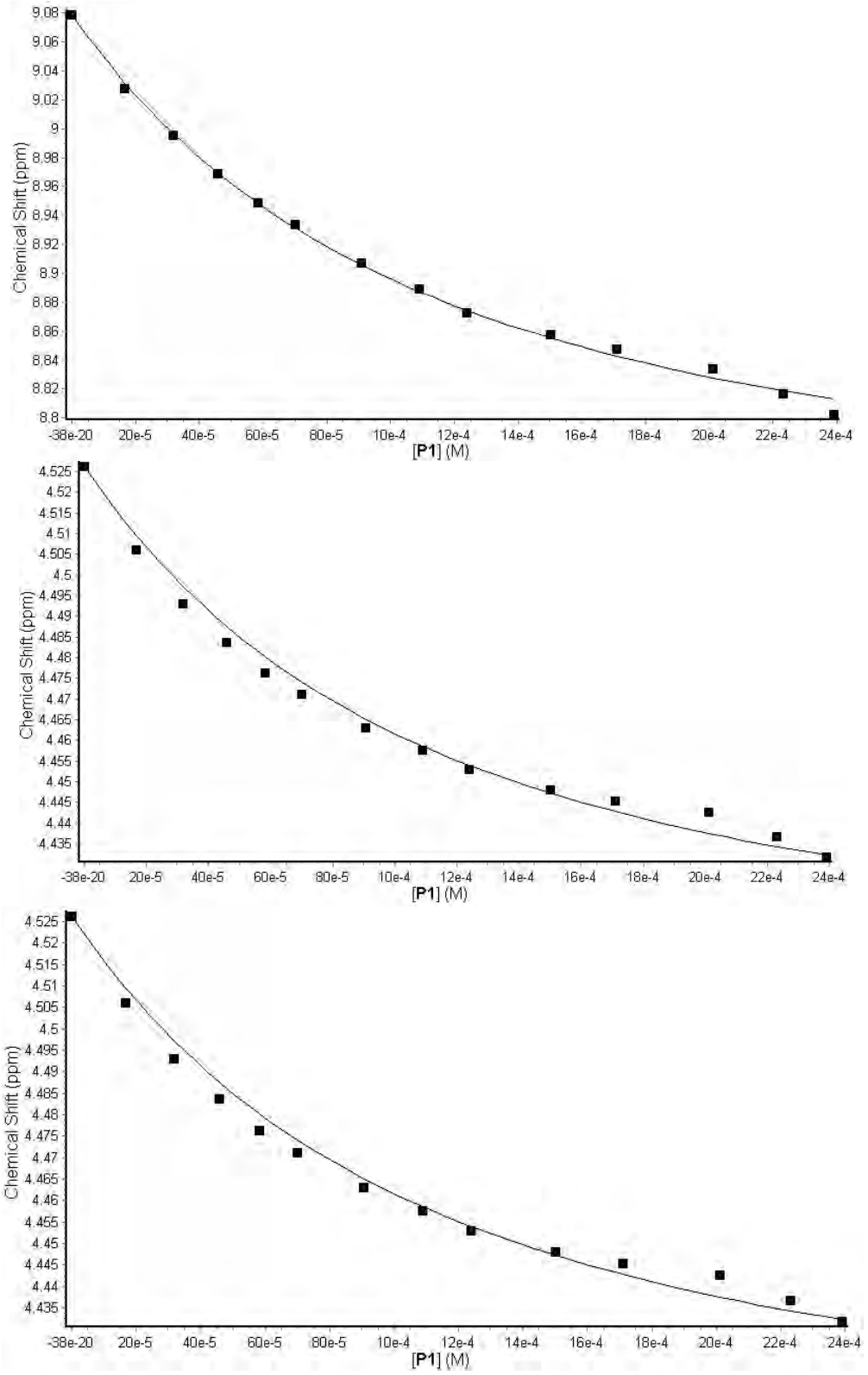

Figure II-S61. Chemical shifts of **II-8** resonances as a function of [**P1**]. The solid lines represent the best non-linear fit of the resonances simultaneously inputted into a global fit model ($K_a = 1.10 \pm 0.05 \times 10^3\ M^{-1}$).

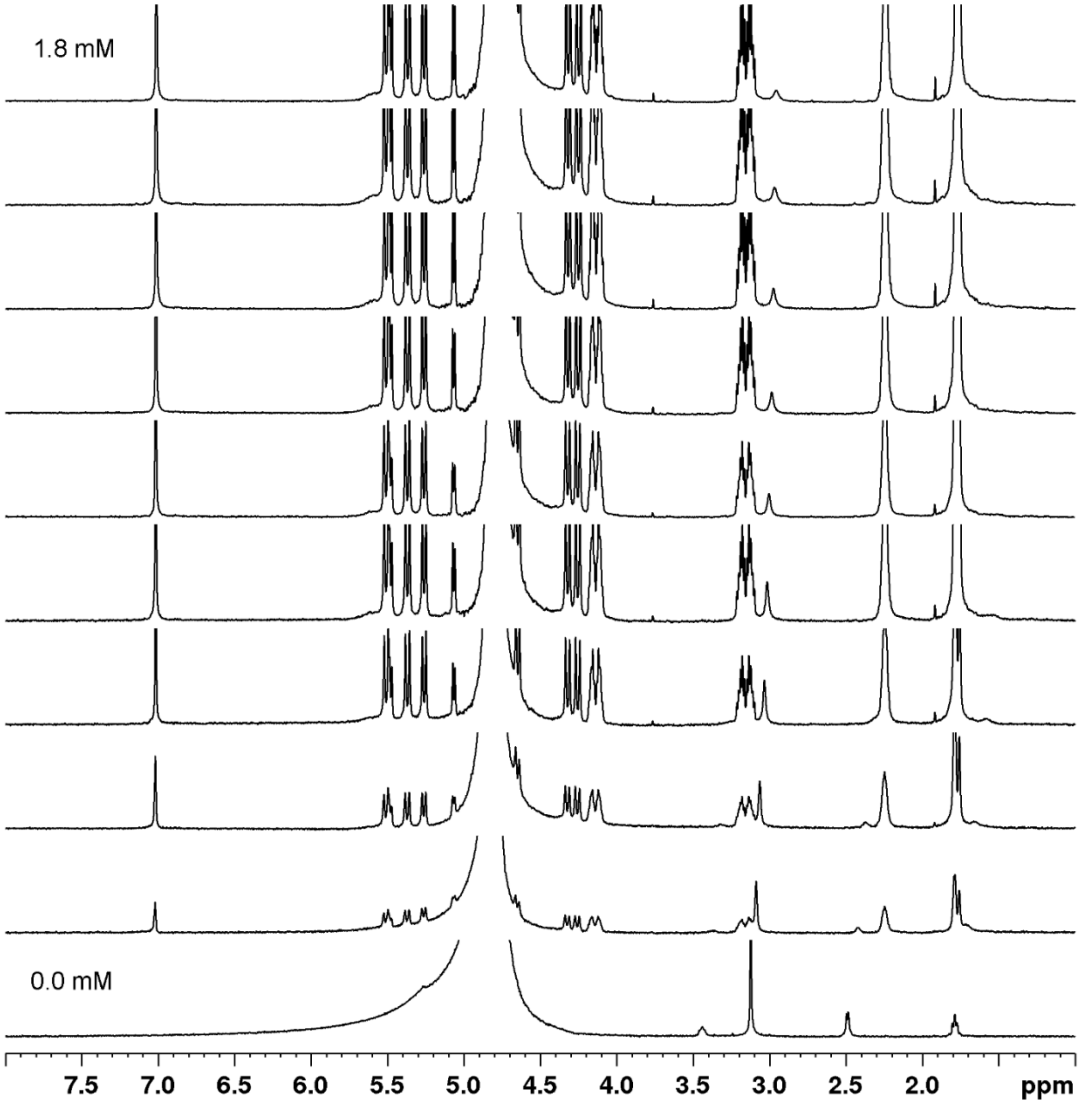

Figure II-S62. ^{1}H NMR (600 MHz, D_2O, RT) titration of **II-9** (0.1 mM) with increasing amounts of **P1** (0 mM – 1.75 mM).

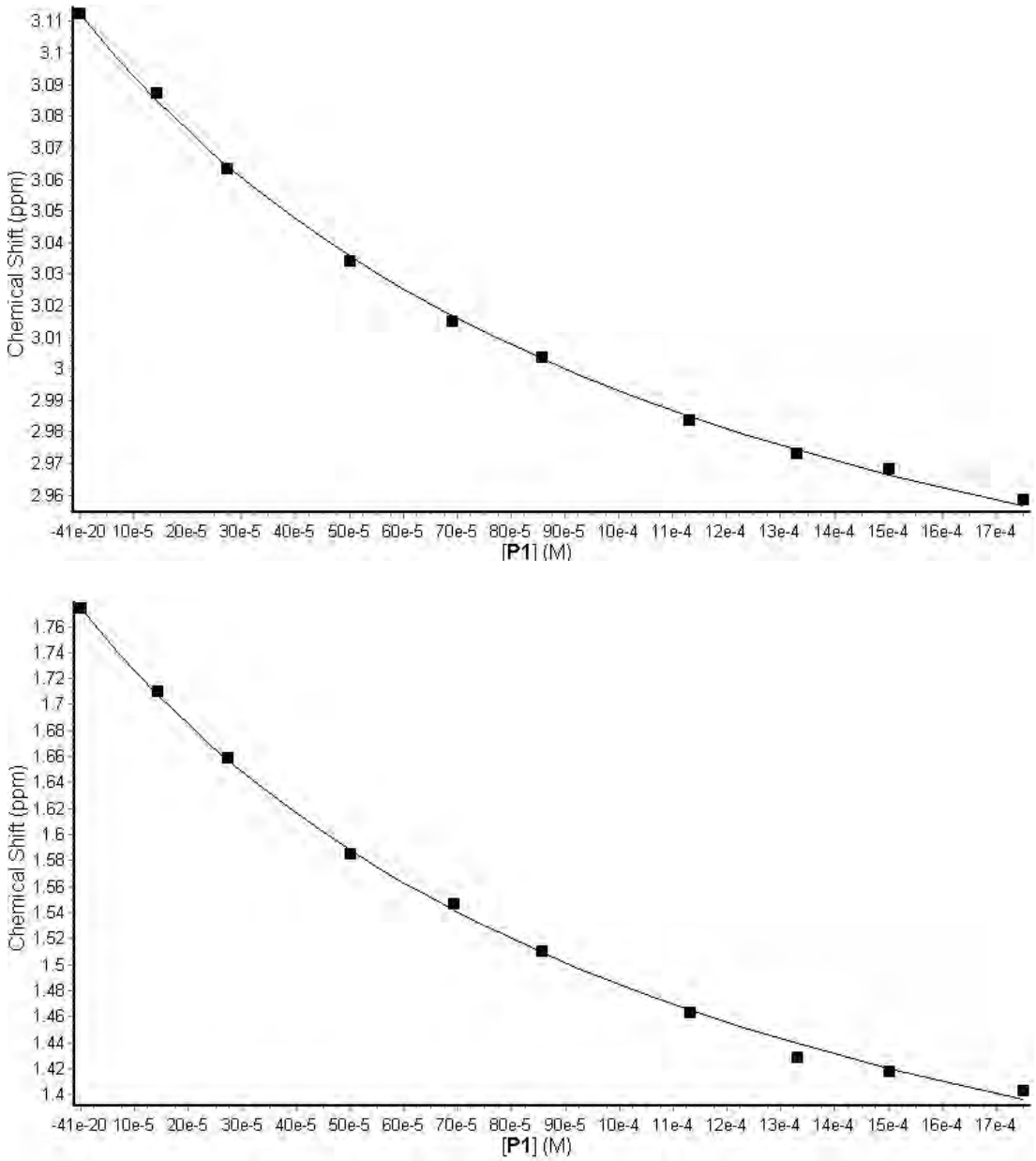

Figure II-S63. Chemical shifts of **II-9** resonances as a function of [**P1**]. The solid lines represent the best non-linear fit of the resonances simultaneously inputted into a global fit model ($K_a = 9.00 \pm 0.40 \times 10^2\ M^{-1}$).

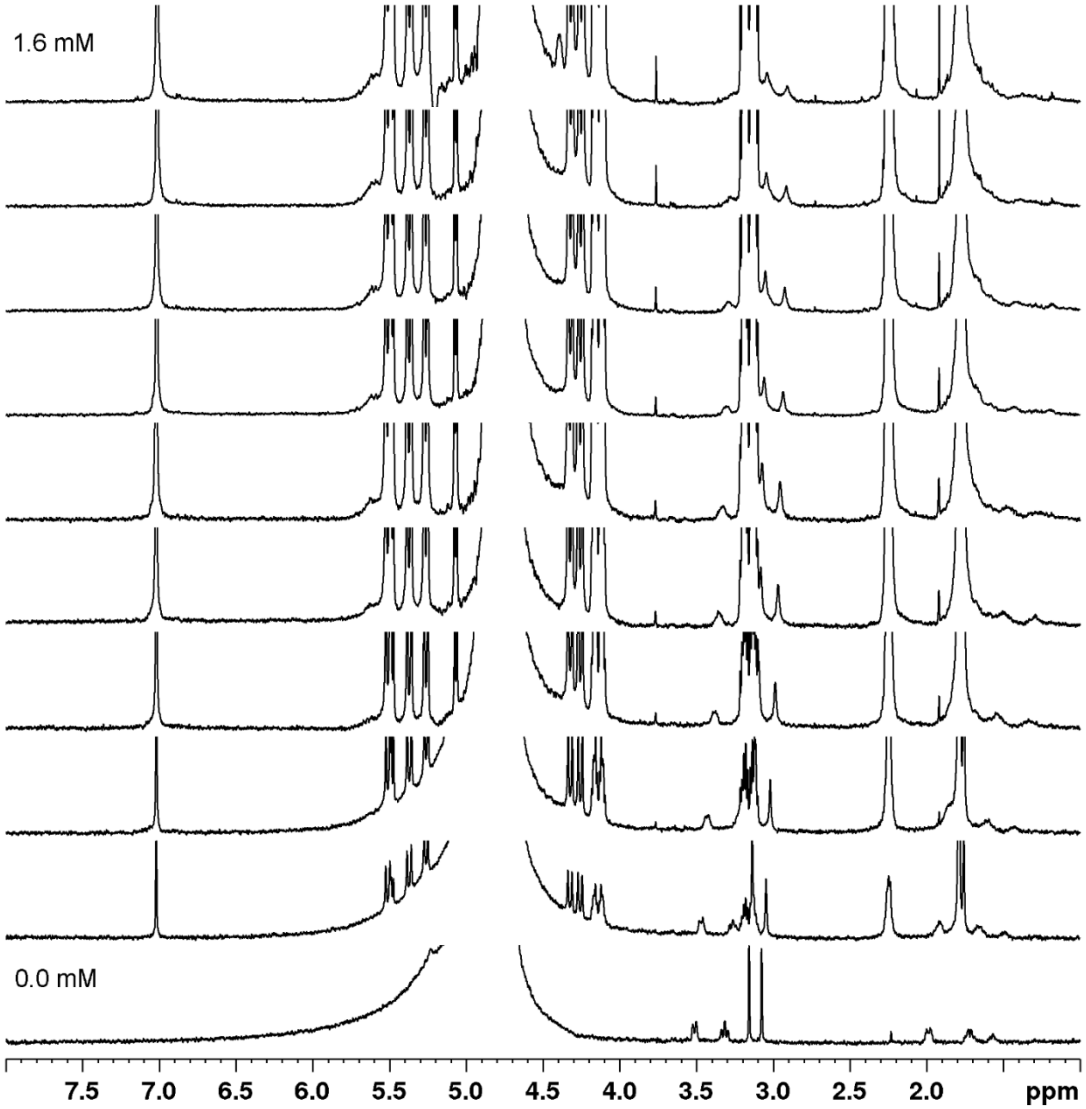

Figure II-S64. ^{1}H NMR (600 MHz, D_2O, RT) **II-10** (0.1 mM) with increasing amounts of **P1** (0 mM – 1.6 mM).

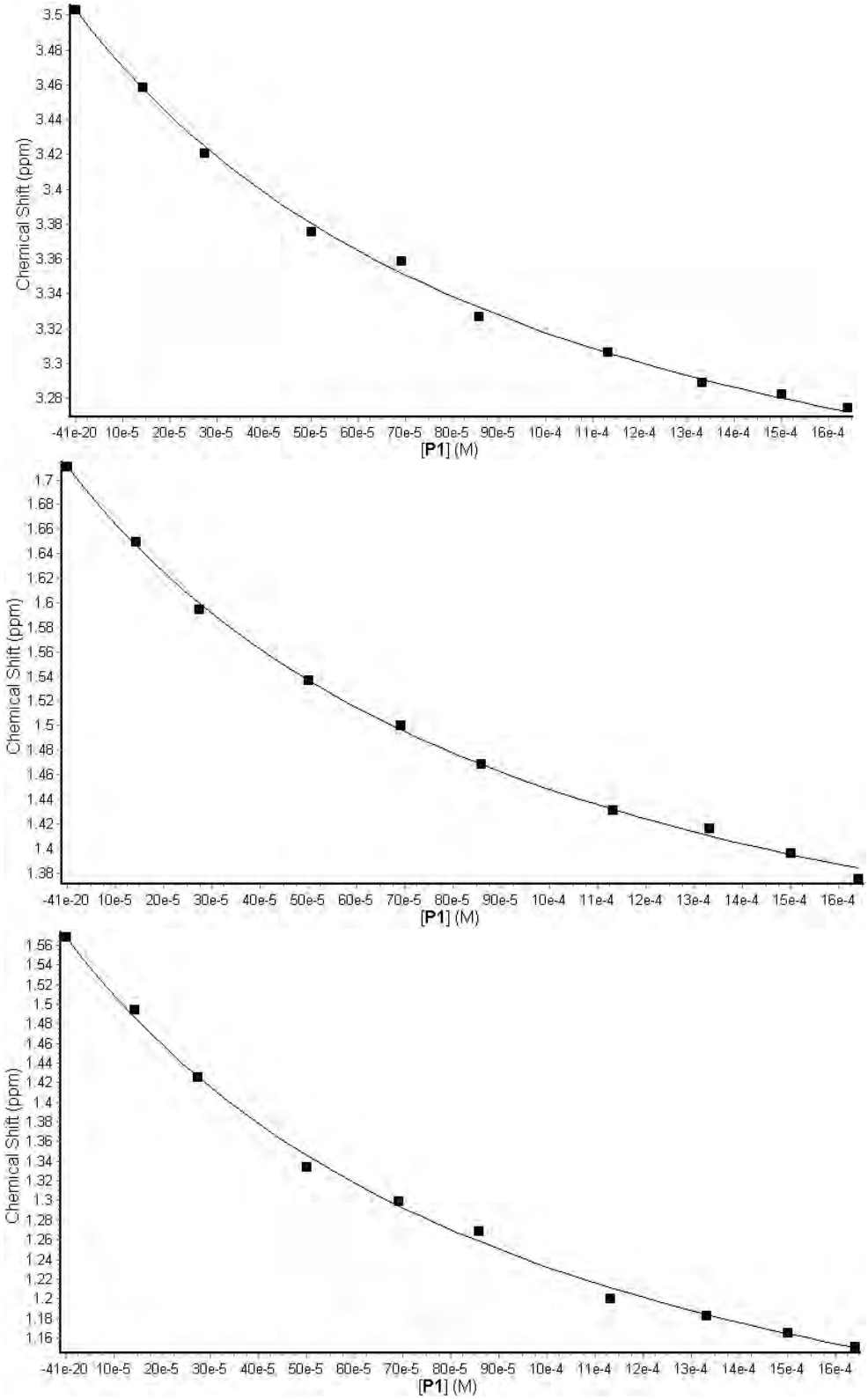

Figure II-S65. Chemical shifts of **II-10** resonances as a function of [**P1**]. The solid lines represent the best non-linear fit of the resonances simultaneously inputted into a global fit model ($K_a = 1.08 \pm 0.05 \times 10^3\ M^{-1}$).

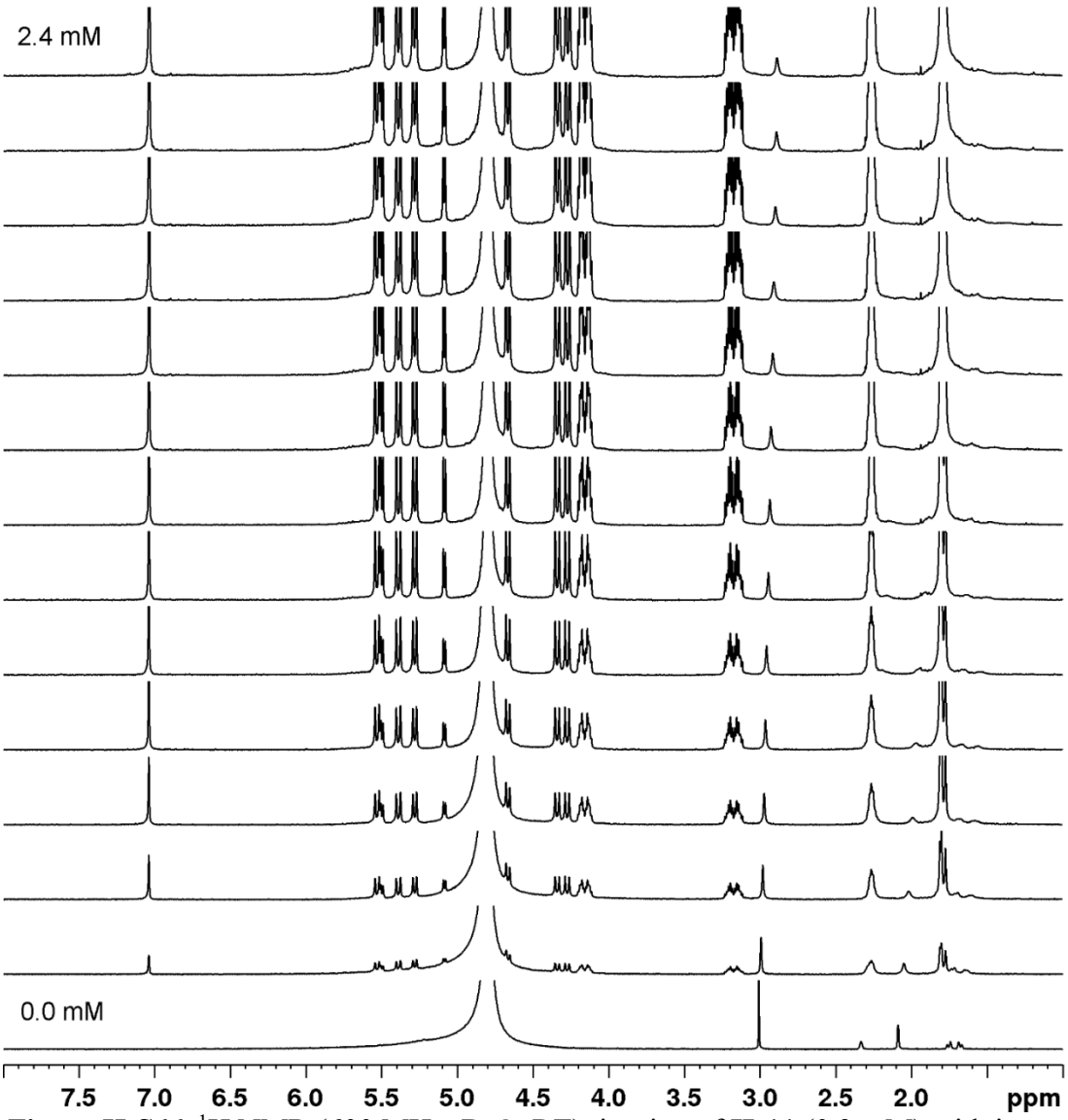

Figure II-S66. ^{1}H NMR (600 MHz, D_2O, RT) titration of **II-11** (0.3 mM) with increasing amounts of **P1** (0 mM – 2.4 mM).

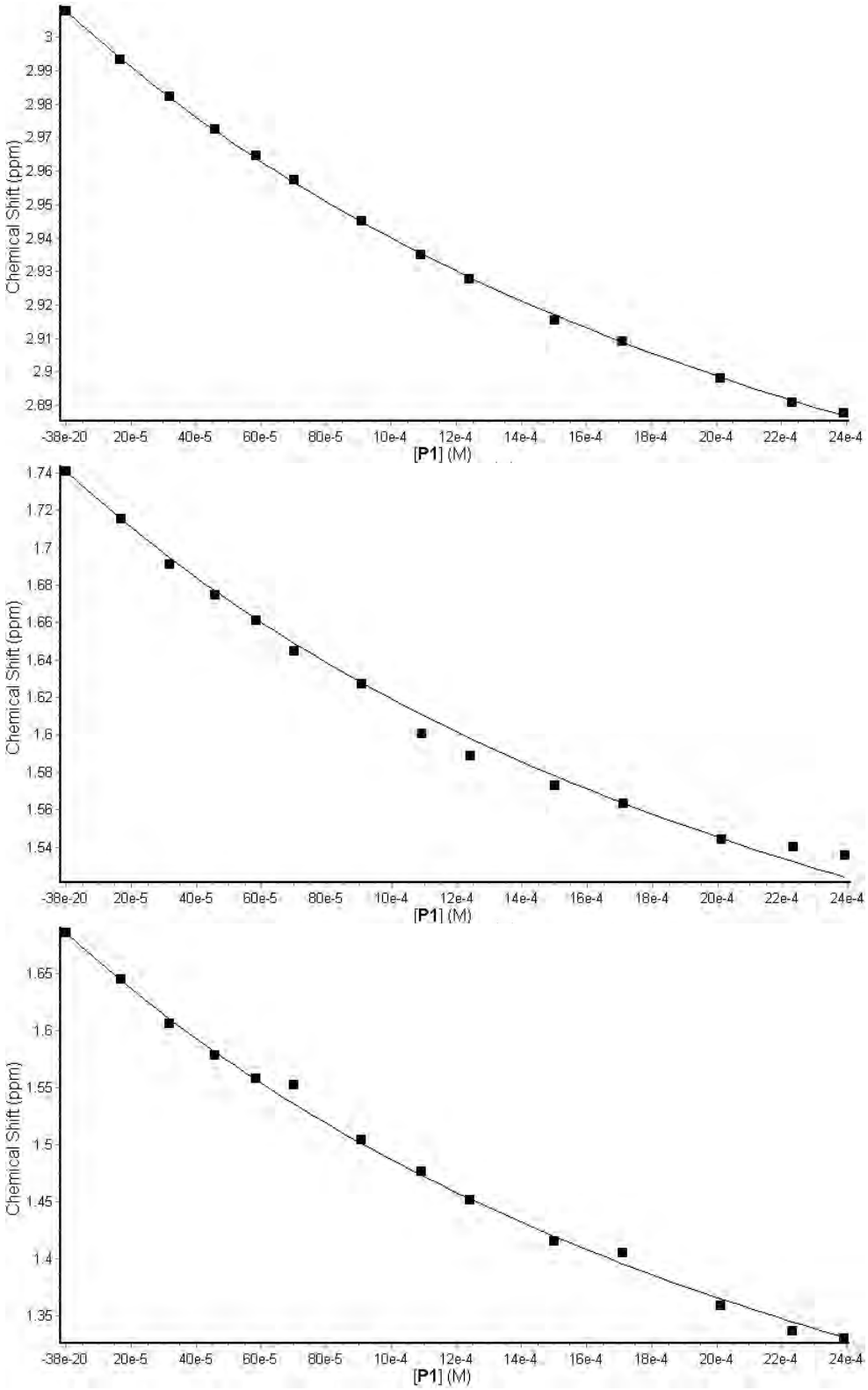

Figure II-S67. Chemical shifts of **II-11** resonances as a function of [**P1**]. The solid lines represent the best non-linear fit of the resonances simultaneously inputted into a global fit model ($K_a = 3.75 \pm 0.24 \times 10^2\ M^{-1}$).

^{1}H NMR Global Fit Titration Experiments for P2 including the influence of self-association

Global Fit Binding Model with Self-Association implemented in Scientist™
// Micromath Scientist Model File
IndVars: Htot
DepVars: Deltaobs
Params: Ka, Ks, Gtot, CSAzero, CSAsat, CSBzero, CSBsat, CSCzero, CSCsat
Ka = HG/(Hfree*Gfree)
Ks= HH/(Hfree*Hfree)
Htot= Hfree + HG + 2HH
Gtot= Gfree + HG
CSA = CSAzero + ((CSAsat-CSAzero)*(HG/Gtot))
CSB = CSBzero + ((CSBsat-CSBzero)*(HG/Gtot))
CSC = CSCzero + ((CSCsat-CSCzero)*(HG/Gtot))
0<Hfree<Htot
0<Ka
0<Gfree<Gtot
0<HH<(Htot*0.5)
***

Number of dependent variables changed based on the sample and how many guest resonances were monitored.

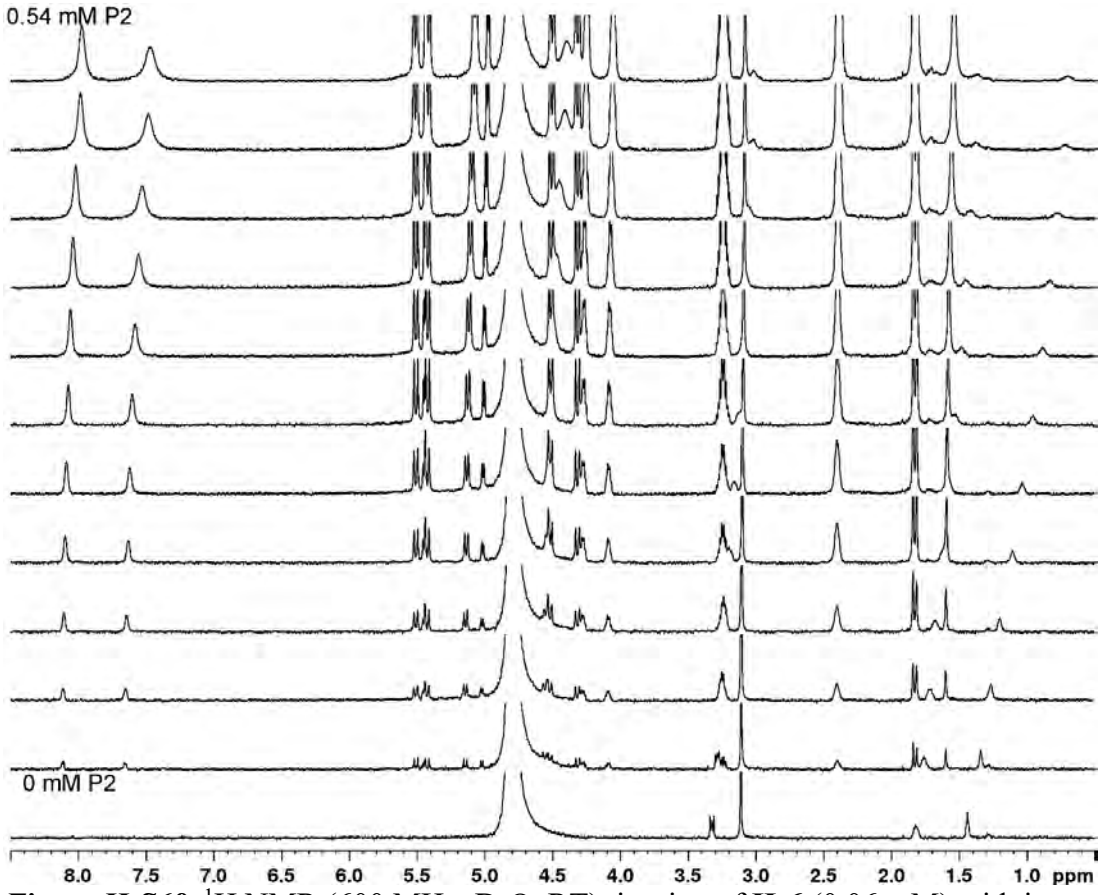

Figure II-S68. ^{1}H NMR (600 MHz, D_2O, RT) titration of **II-6** (0.06 mM) with increasing amounts of **P2** (0 mM - 0.54 mM).

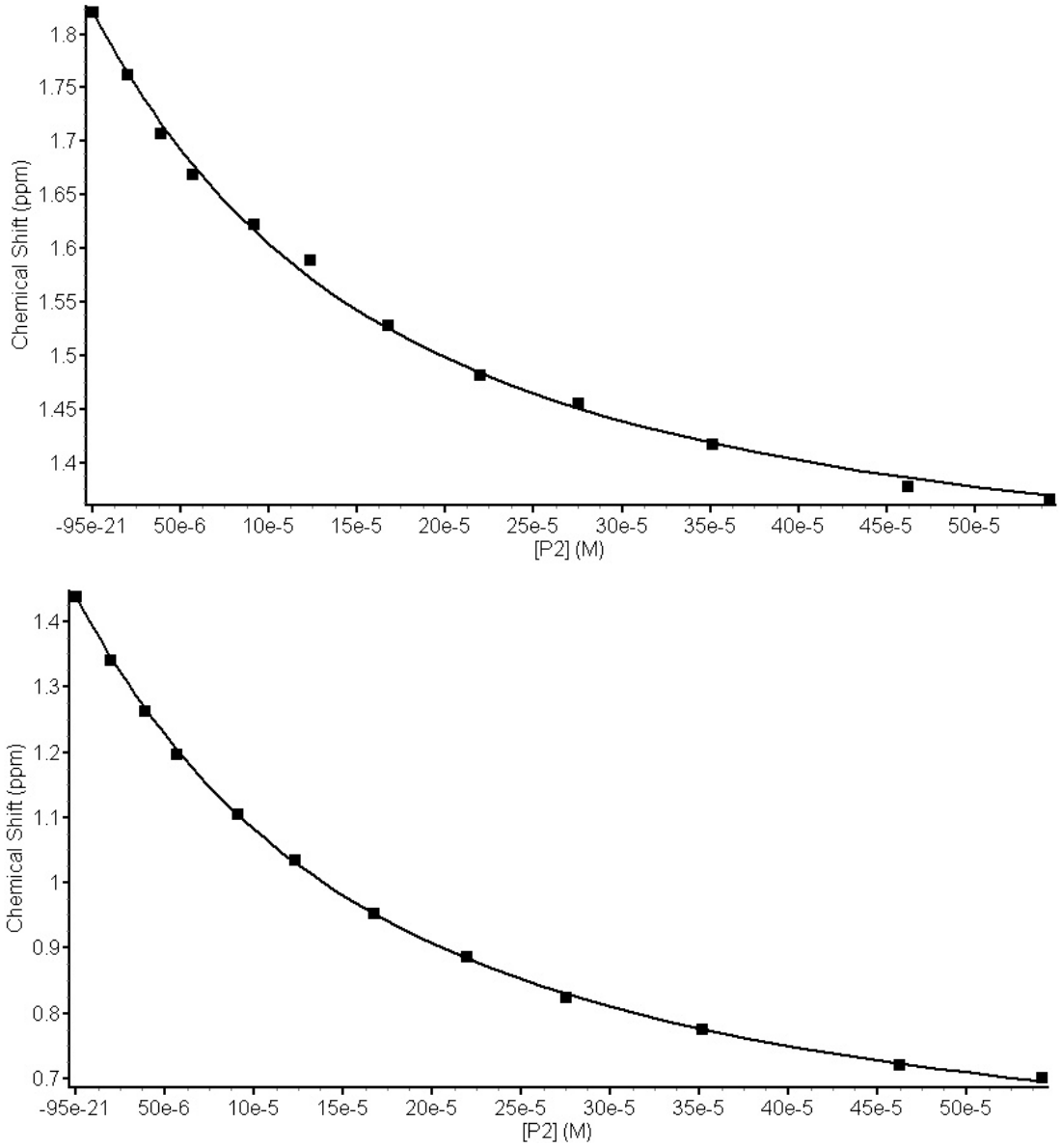

Figure II-S69. Chemical shifts of **II-6** resonances as a function of [**P2**]. The solid lines represent the best non-linear fit of the resonances simultaneously inputted into a global fit with self-association model ($K_a = 7.71 \pm 0.22 \times 10^3\ M^{-1}$).

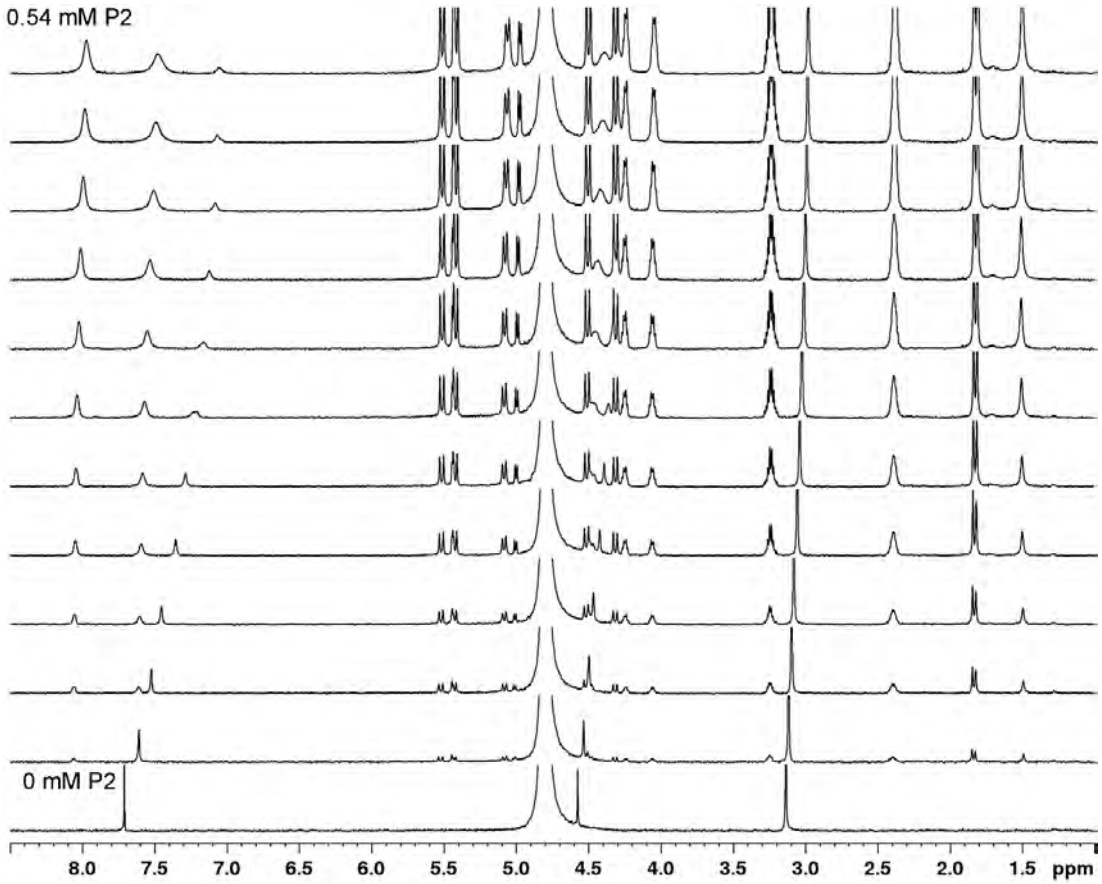

Figure II-S70. ^{1}H NMR (600 MHz, D_2O, RT) titration of **II-7** (0.08 mM) with increasing amounts of **P2** (0 mM - 0.54 mM).

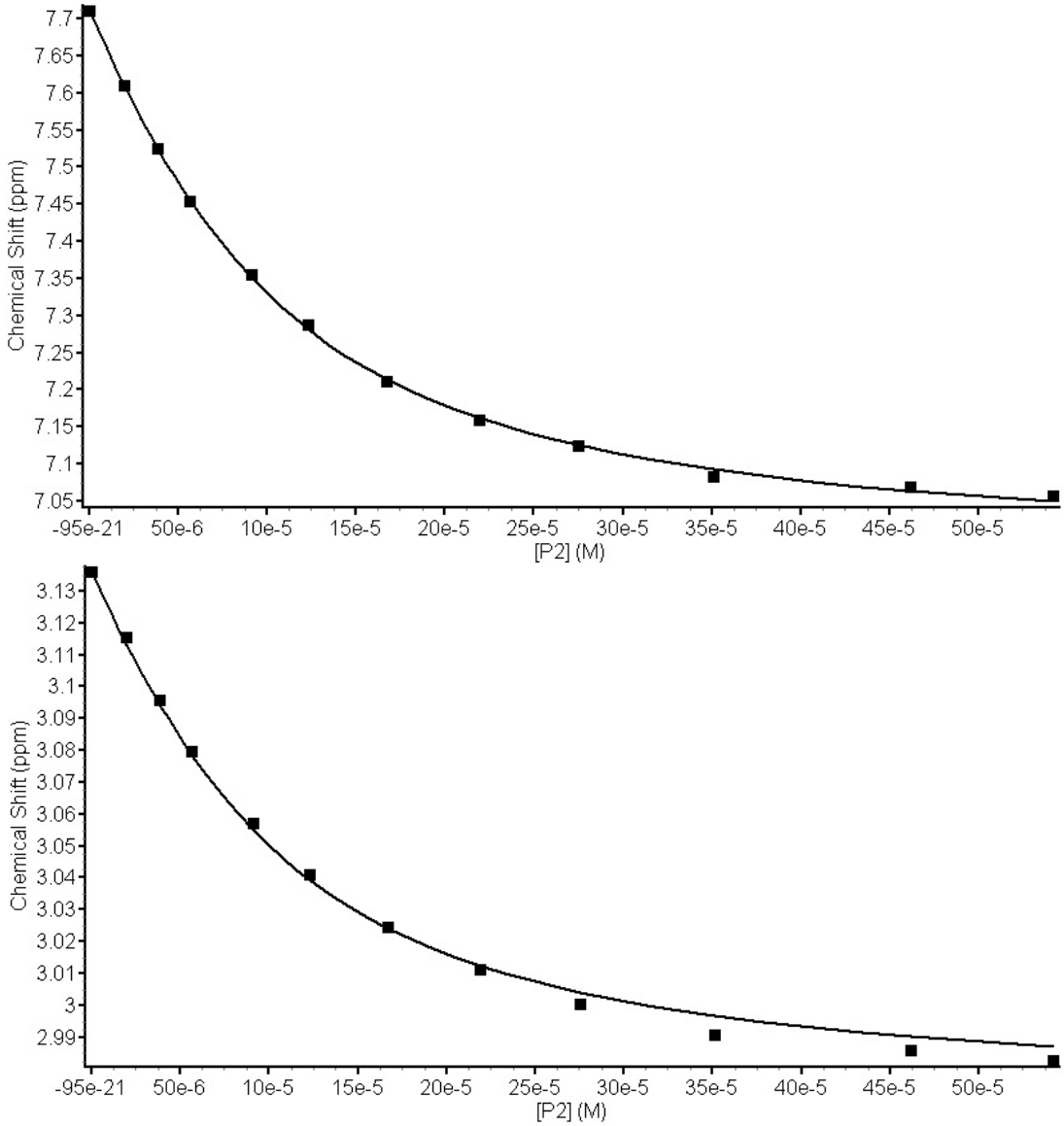

Figure II-S71. Chemical shifts of **II-7** resonances as a function of [**P2**]. The solid lines represent the best non-linear fit of the resonances simultaneously inputted into a global fit with self-association model ($K_a = 1.76 \pm 0.05 \times 10^4\ M^{-1}$).

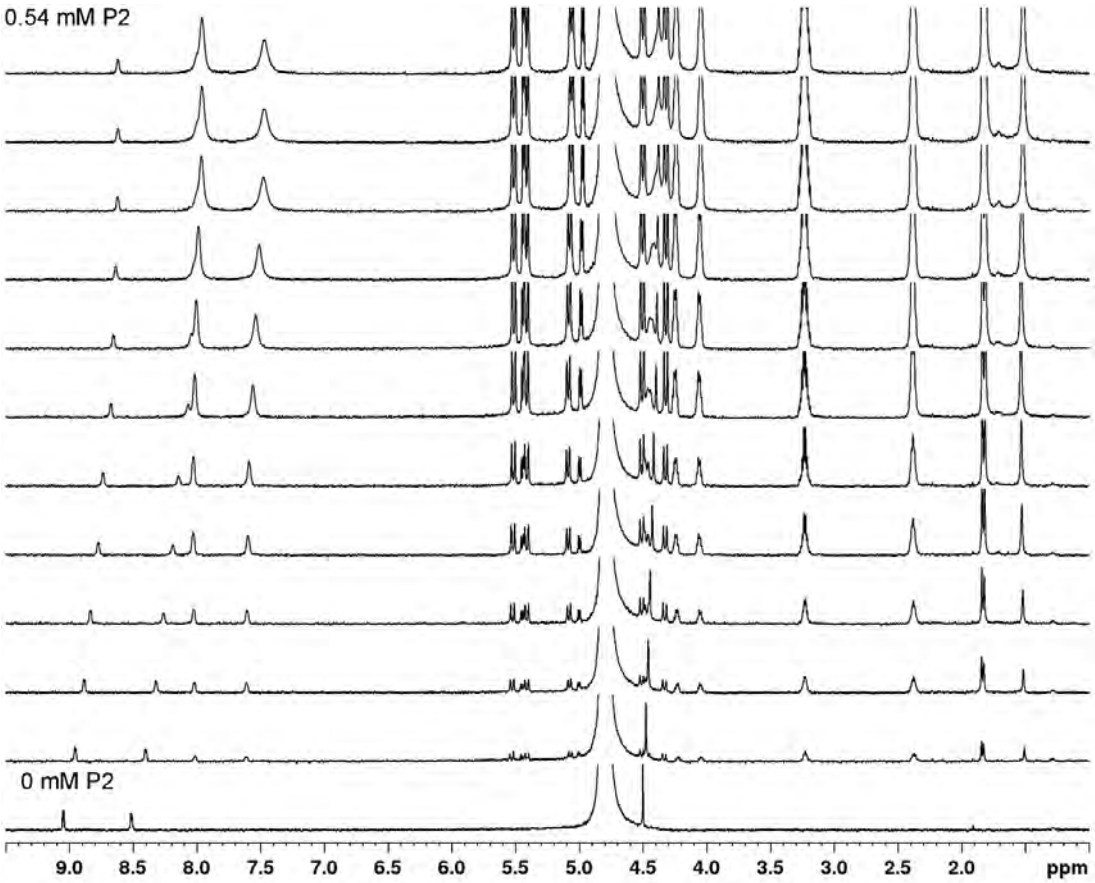

Figure II-S72. ^{1}H NMR (600 MHz, D_2O, RT) titration of **II-8** (0.04 mM) with increasing amounts of **P2** (0 mM - 0.54 mM).

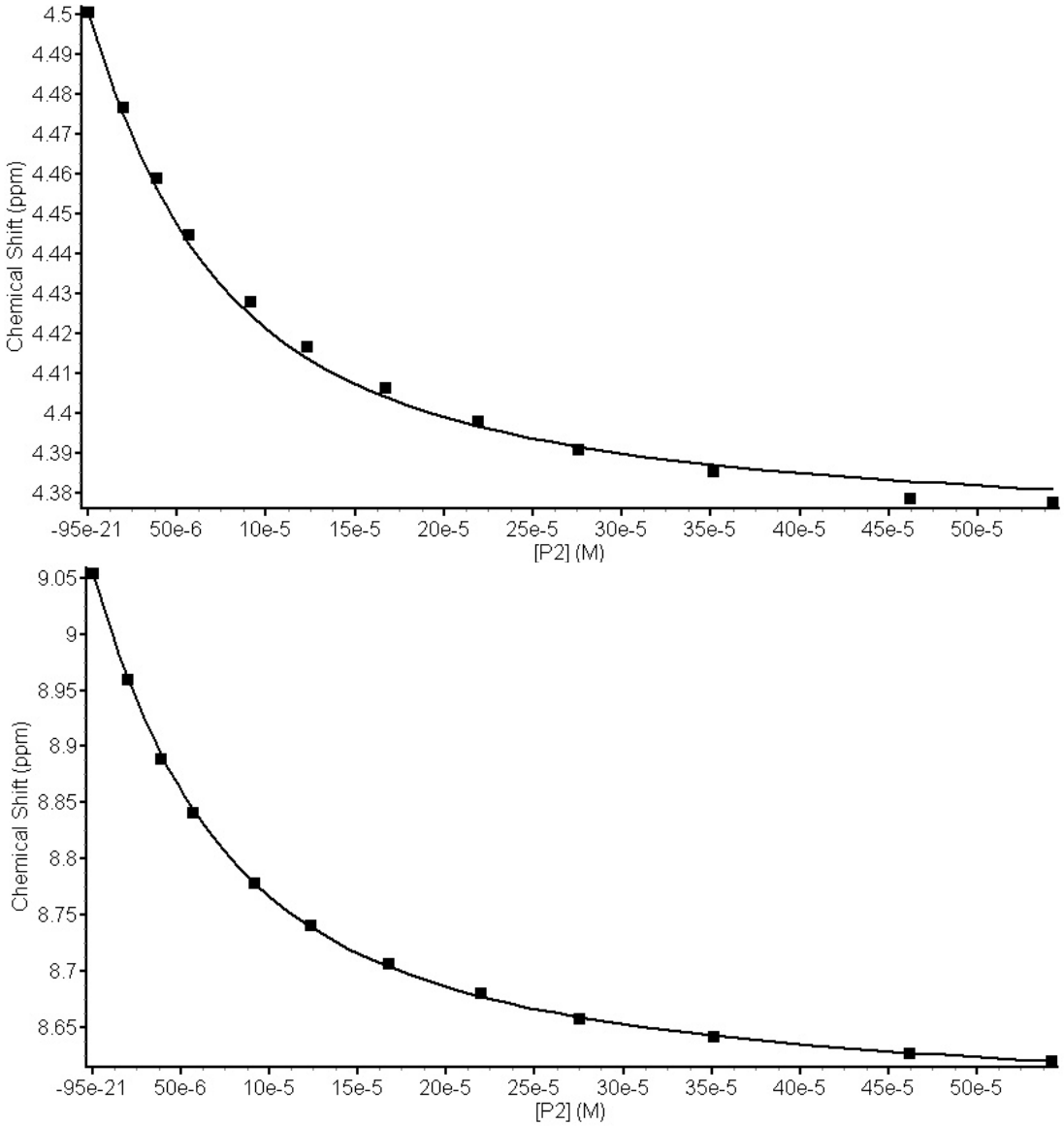

Figure II-S73. Chemical shifts of **II-8** resonances as a function of [**P2**]. The solid lines represent the best non-linear fit of the resonances simultaneously inputted into a global fit with self-association model ($K_a = 1.98 \pm 0.04 \times 10^4\ M^{-1}$).

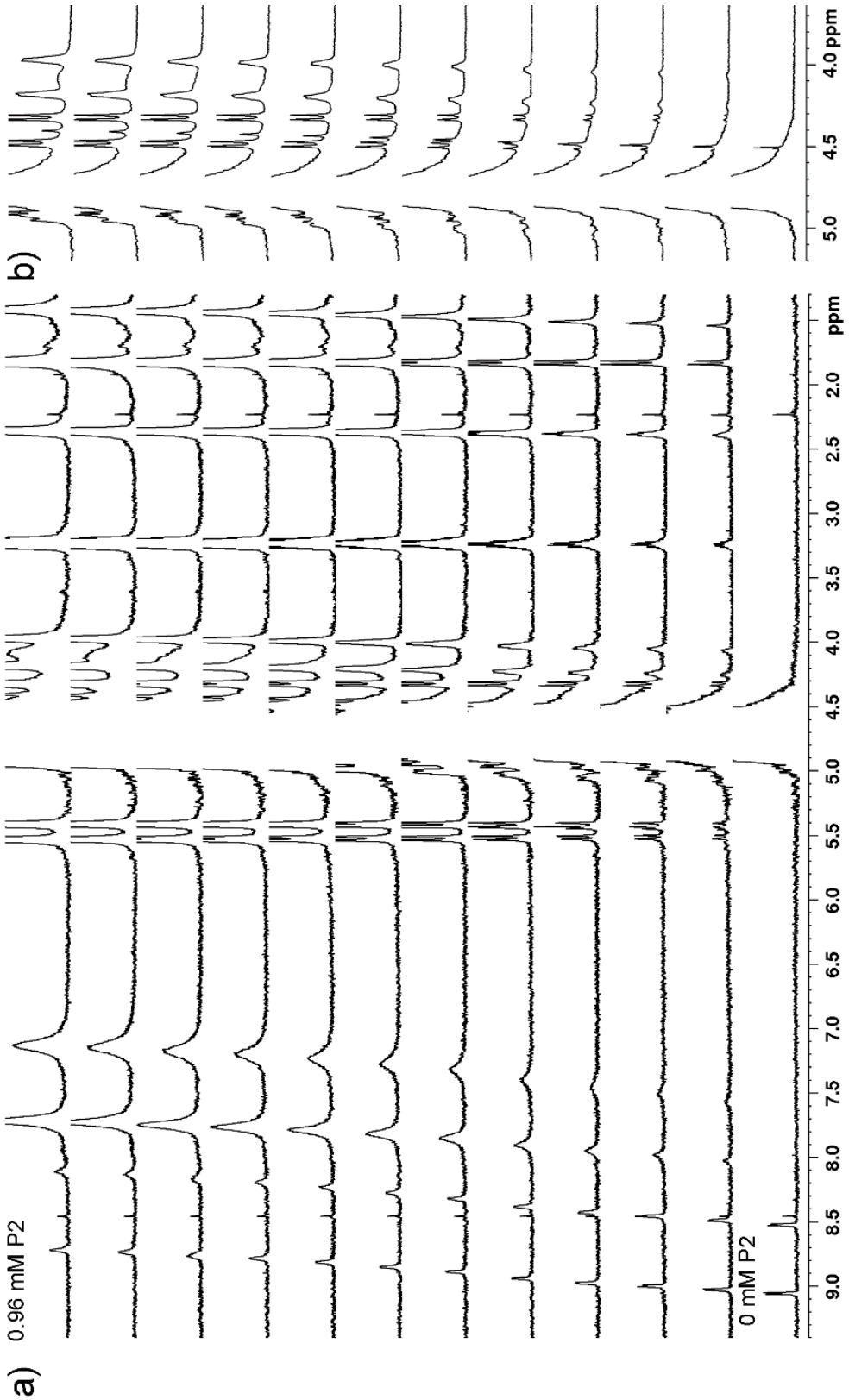

Figure II-S74. ^{1}H NMR (600 MHz, 20mM phosphate buffered D_2O, pD = 7.4, RT) titration of **II-8** (0.06 mM) with increasing amounts of **P2** (0 mM - 0.96 mM): a) full spectra; b) zoomed in region from 3.5 to 5.2 ppm.

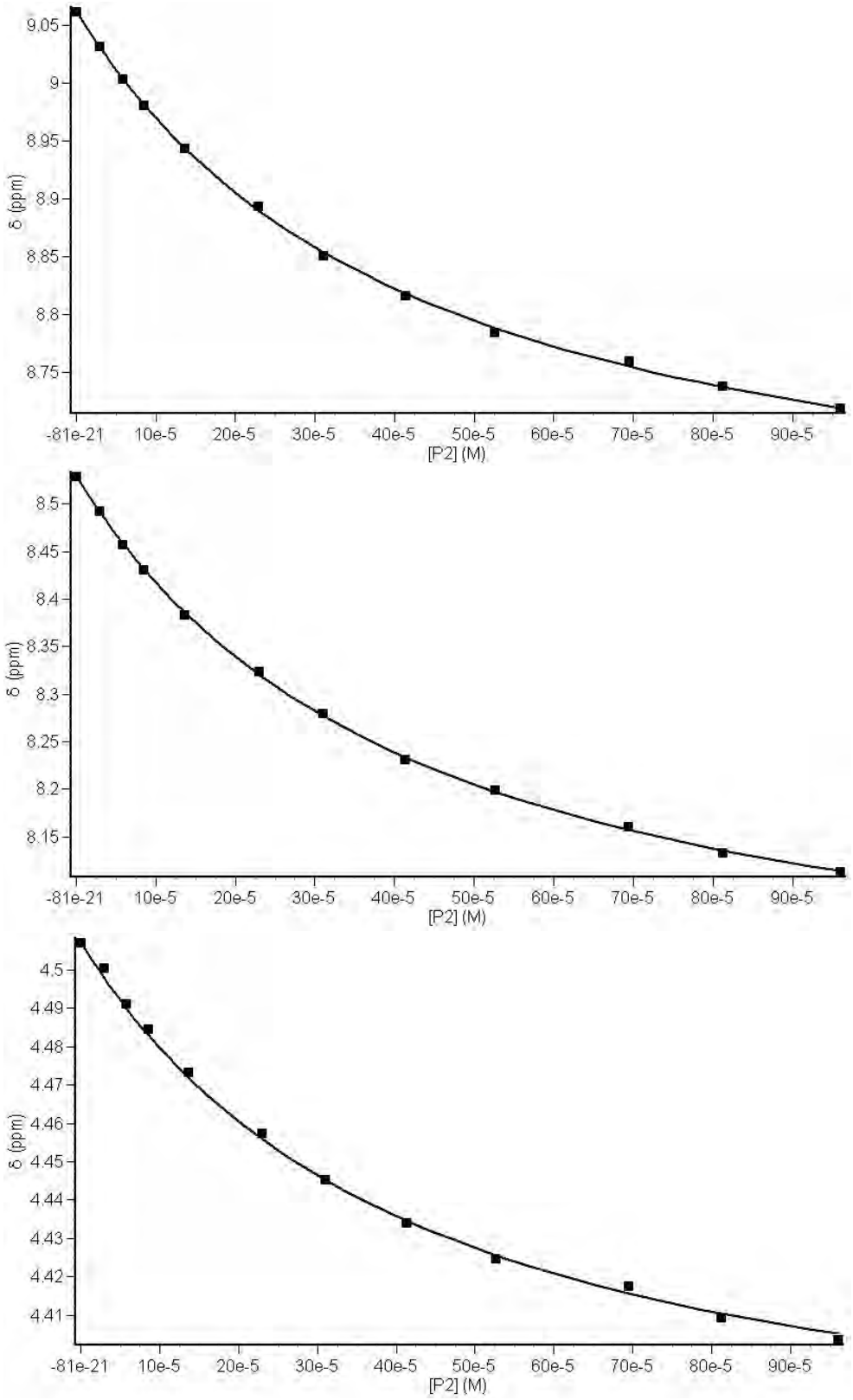

Figure II-S75. Chemical shifts of **II-8** resonances as a function of [**P2**]. The solid lines represent the best non-linear fit of the resonances simultaneously inputted into a global fit model ($K_a = 2.67 \pm 0.04 \times 10^3\ M^{-1}$).

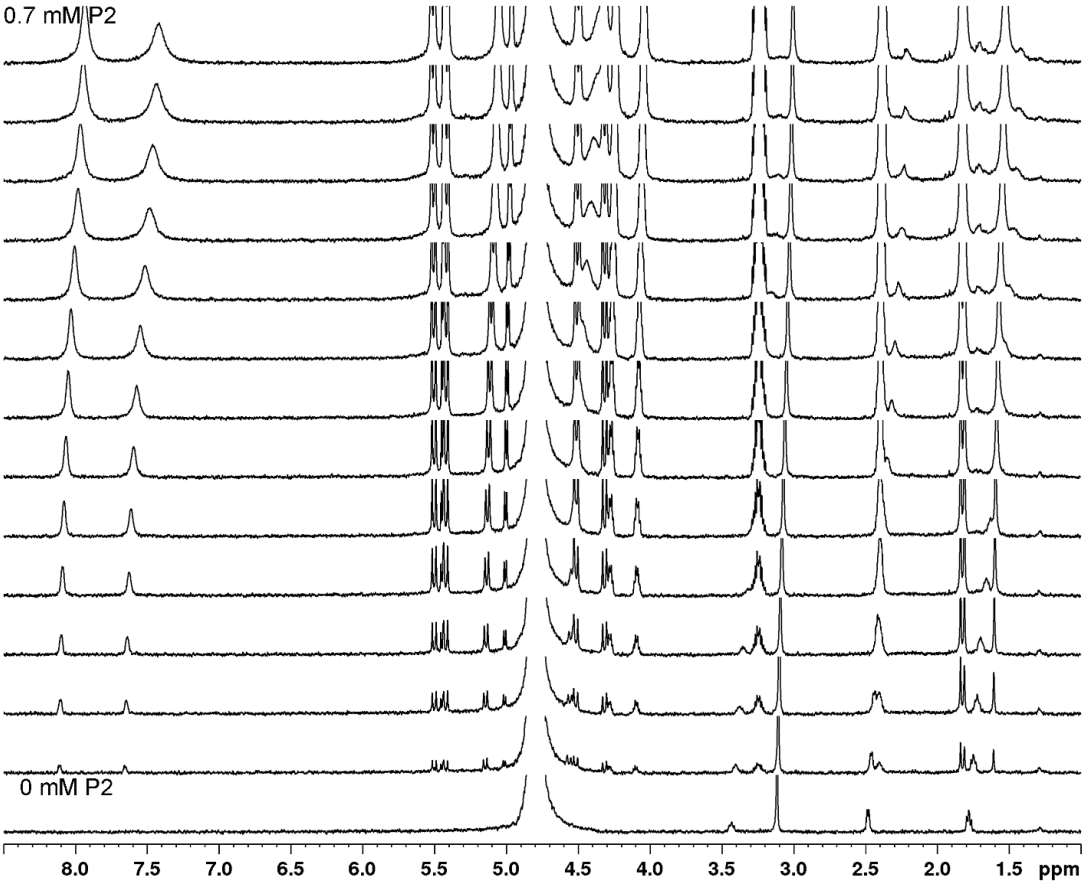

Figure II-S76. ^{1}H NMR (600 MHz, D_2O, RT) titration of **II-9** (0.06 mM) with increasing amounts of **P2** (0 mM - 0.7 mM).

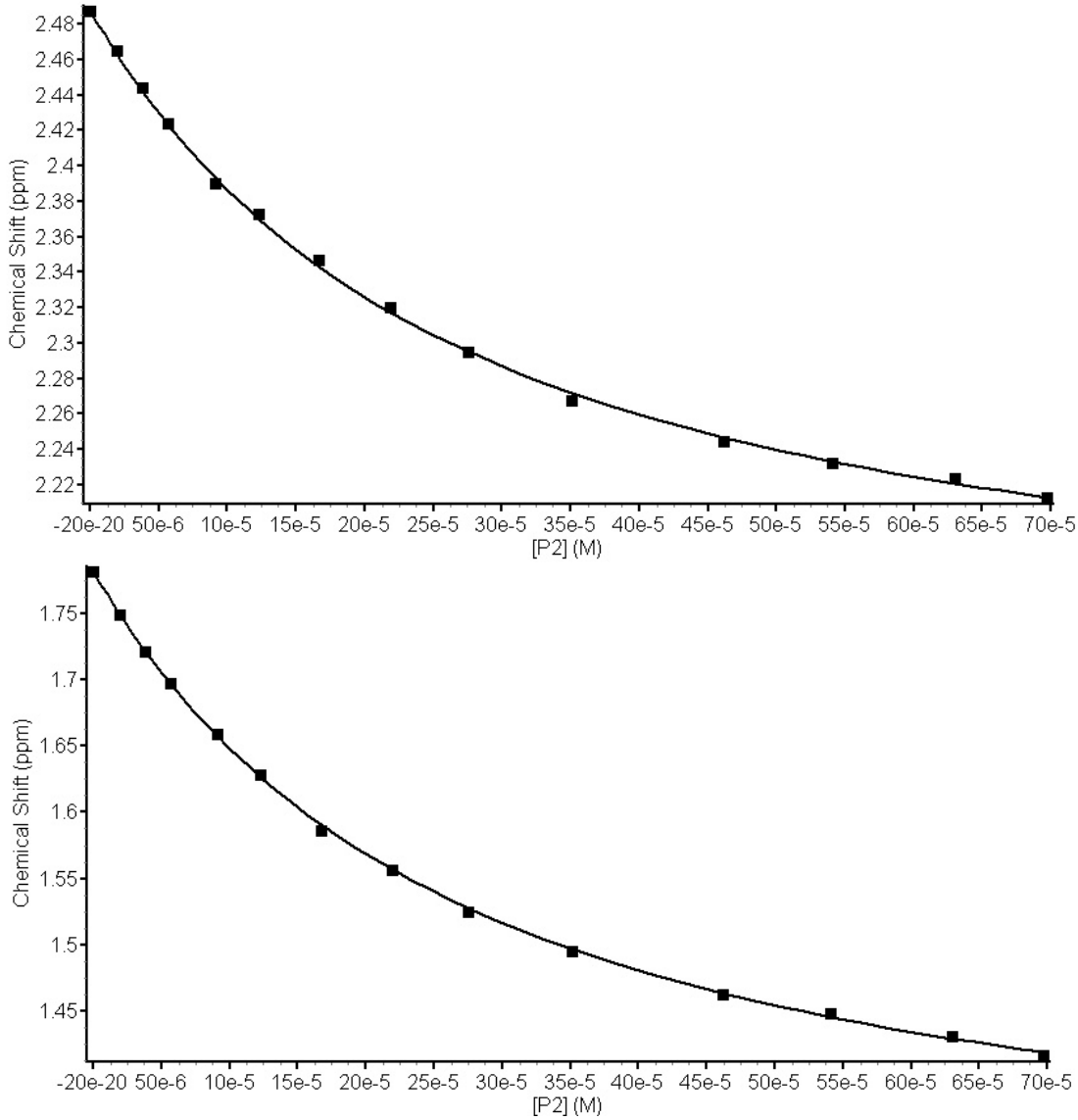

Figure II-S77. Chemical shifts of **II-9** resonances as a function of [**P2**]. The solid lines represent the best non-linear fit of the resonances simultaneously inputted into a global fit with self-association model ($K_a = 4.17 \pm 0.08 \times 10^3\ M^{-1}$).

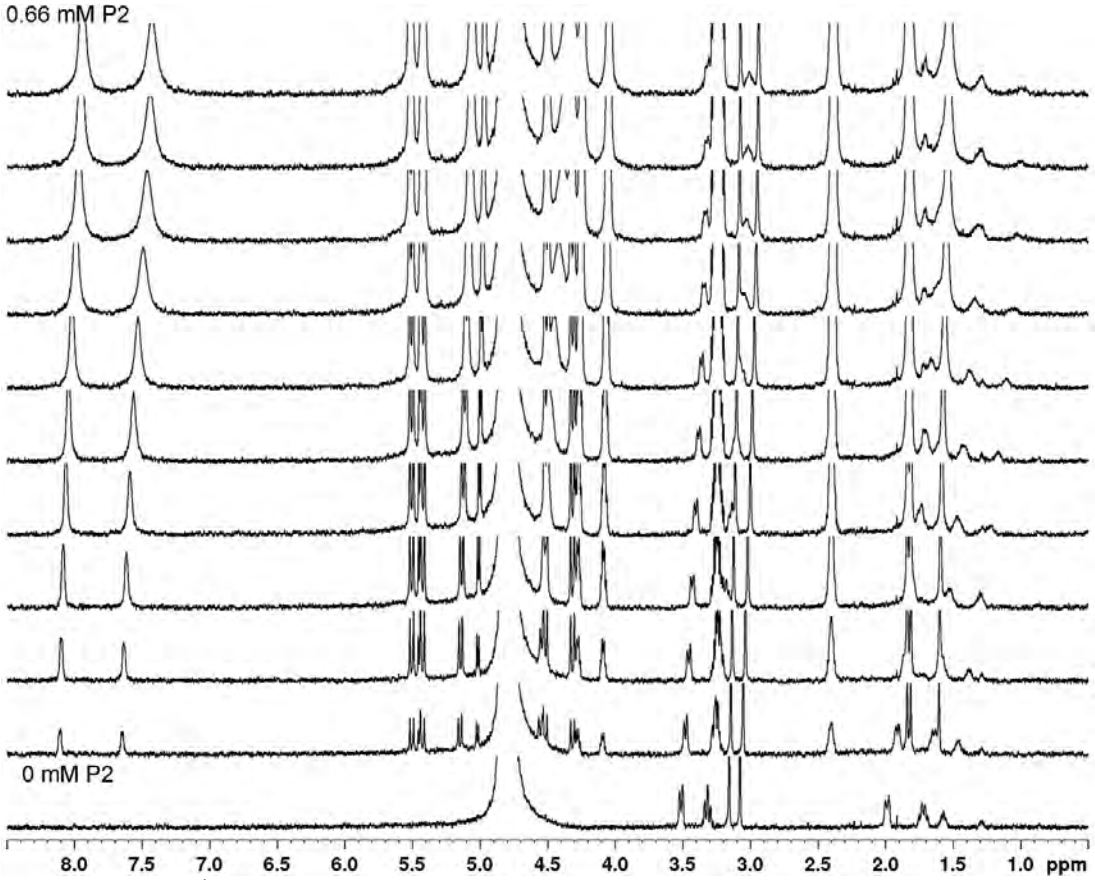

Figure II-S78. ^{1}H NMR (600 MHz, D_2O, RT) titration of **II-10** (0.06 mM) with increasing amounts of **P2** (0 mM - 0.66 mM).

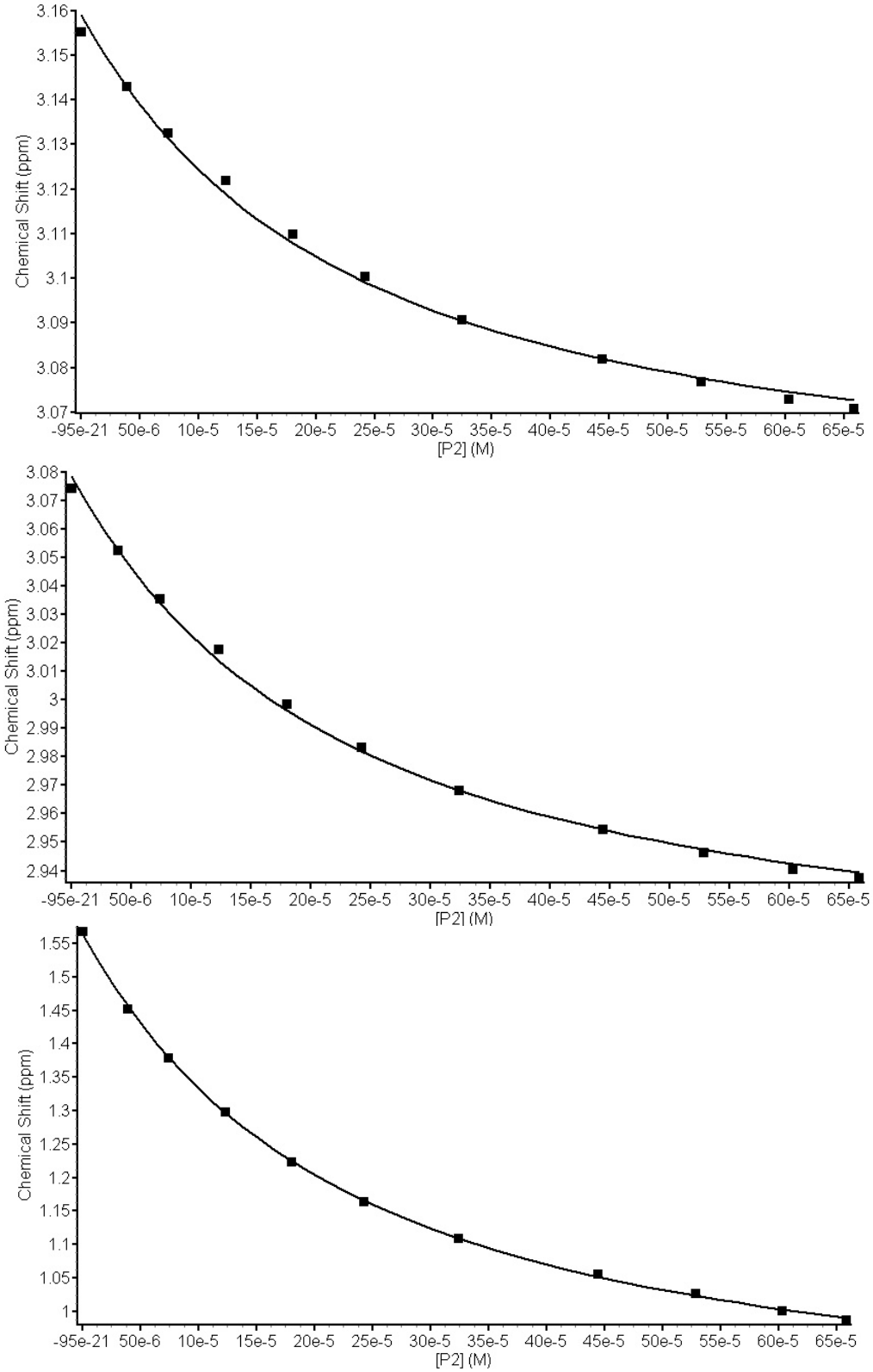

Figure II-S79. Chemical shifts of **II-10** resonances as a function of [**P2**]. The solid lines represent the best non-linear fit of the resonances simultaneously inputted into a global fit with self-association model ($K_a = 5.12 \pm 0.12 \times 10^3\ M^{-1}$).

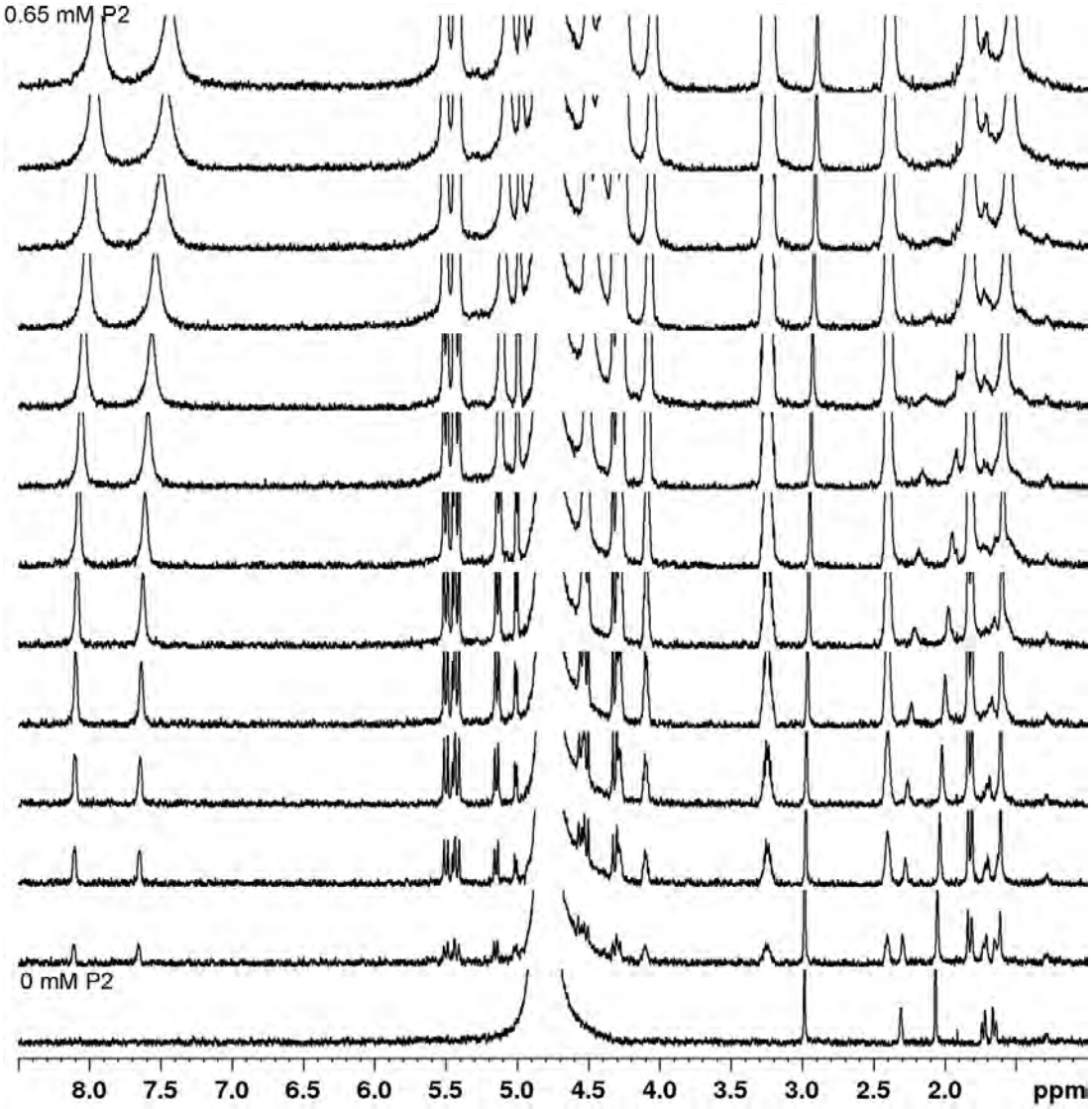

Figure II-S80. ^{1}H NMR (600 MHz, D_2O, RT) titration of **II-11** (0.04 mM) with increasing amounts of **P2** (0 mM - 0.65 mM).

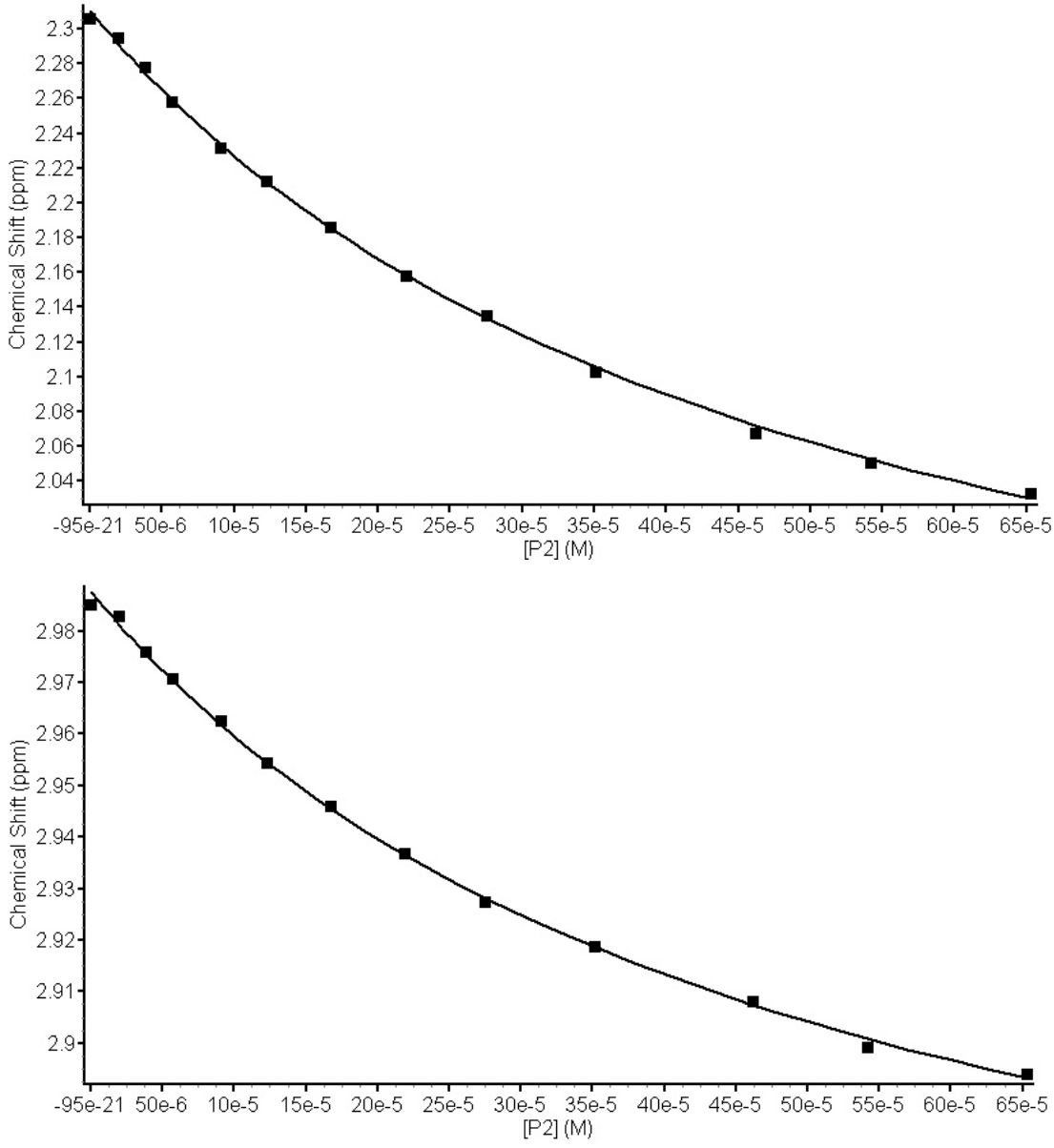

Figure II-S81. Chemical shifts of **II-11** resonances as a function of [**P2**]. The solid lines represent the best non-linear fit of the resonances simultaneously inputted into a global fit model with self-association ($K_a = 1.95 \pm 0.10 \times 10^3\ M^{-1}$).

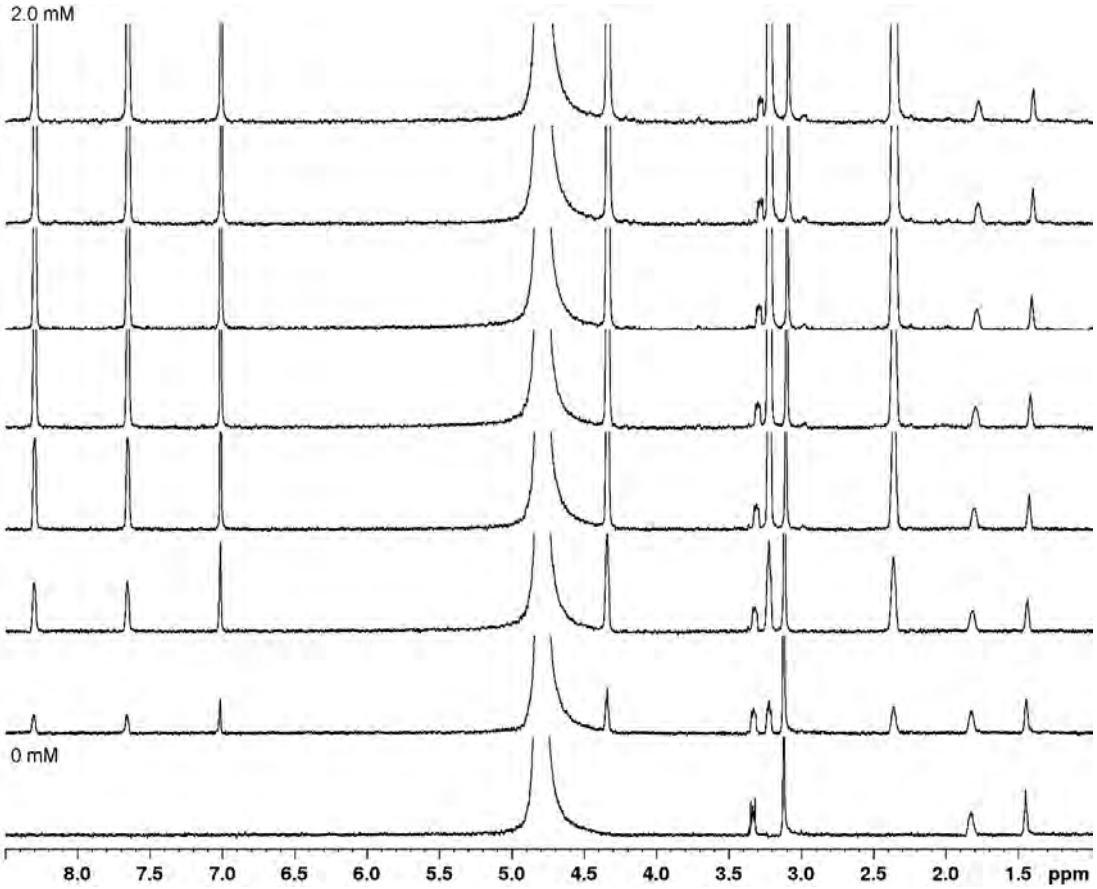

Figure II-S82. ^{1}H NMR (600 MHz, D_2O, RT) titration of **II-6** (0.1 mM) with increasing amounts of **II-5** (0 mM – 2.0 mM).

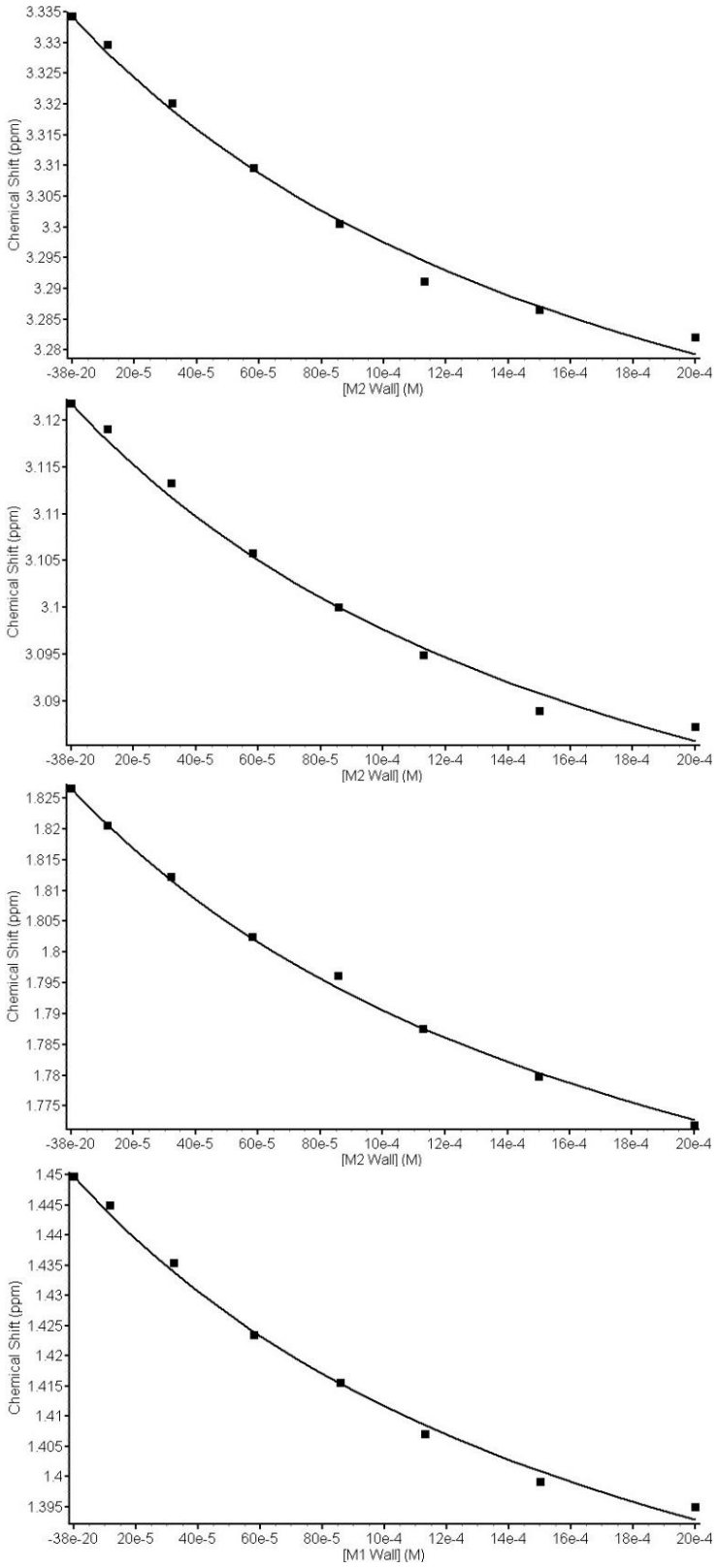

Figure II-S83. Chemical shifts of **II-6** resonances as a function of [**II-5**]. The solid lines represent the best non-linear fit of the resonances simultaneously inputted into a global fit ($K_a = 5.46 \pm 0.46 \times 10^2\ M^{-1}$).

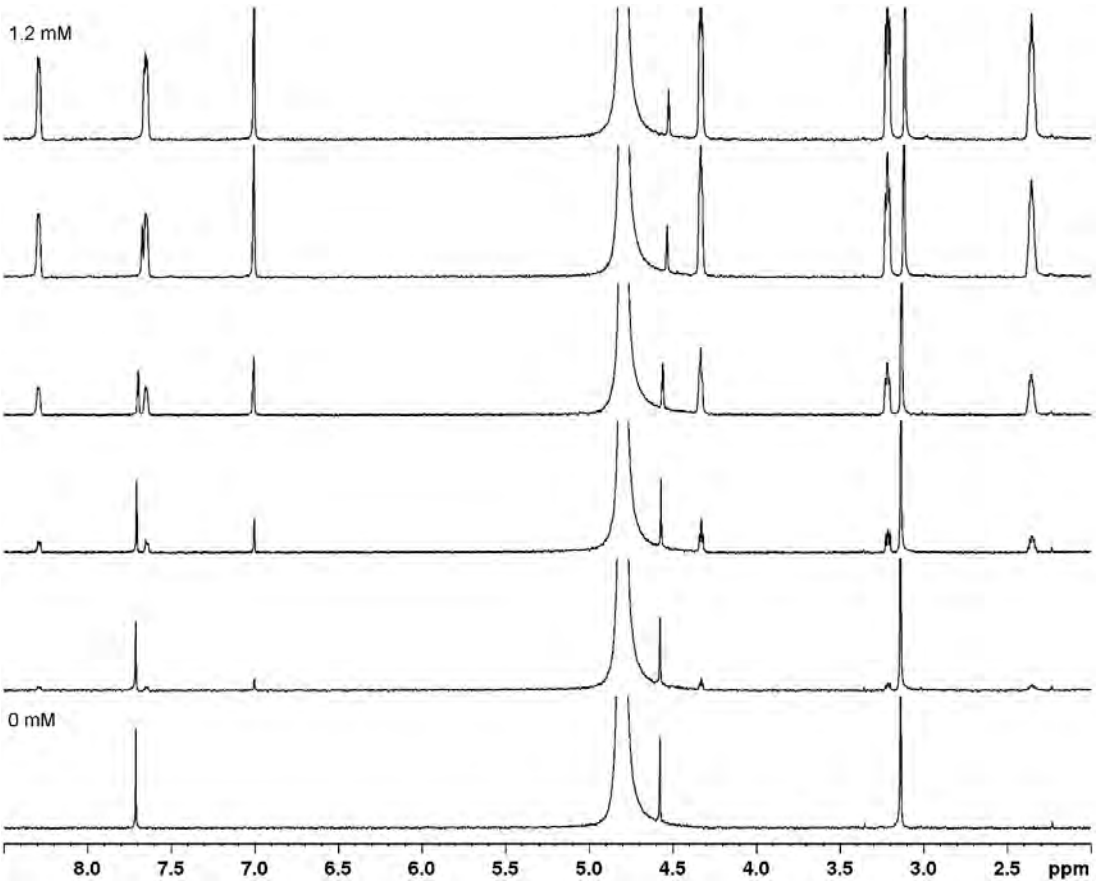

Figure II-S84. ^{1}H NMR (600 MHz, D_2O, RT) titration of **II-7** (0.08 mM) with increasing amounts of **II-5** (0 mM – 1.22 mM).

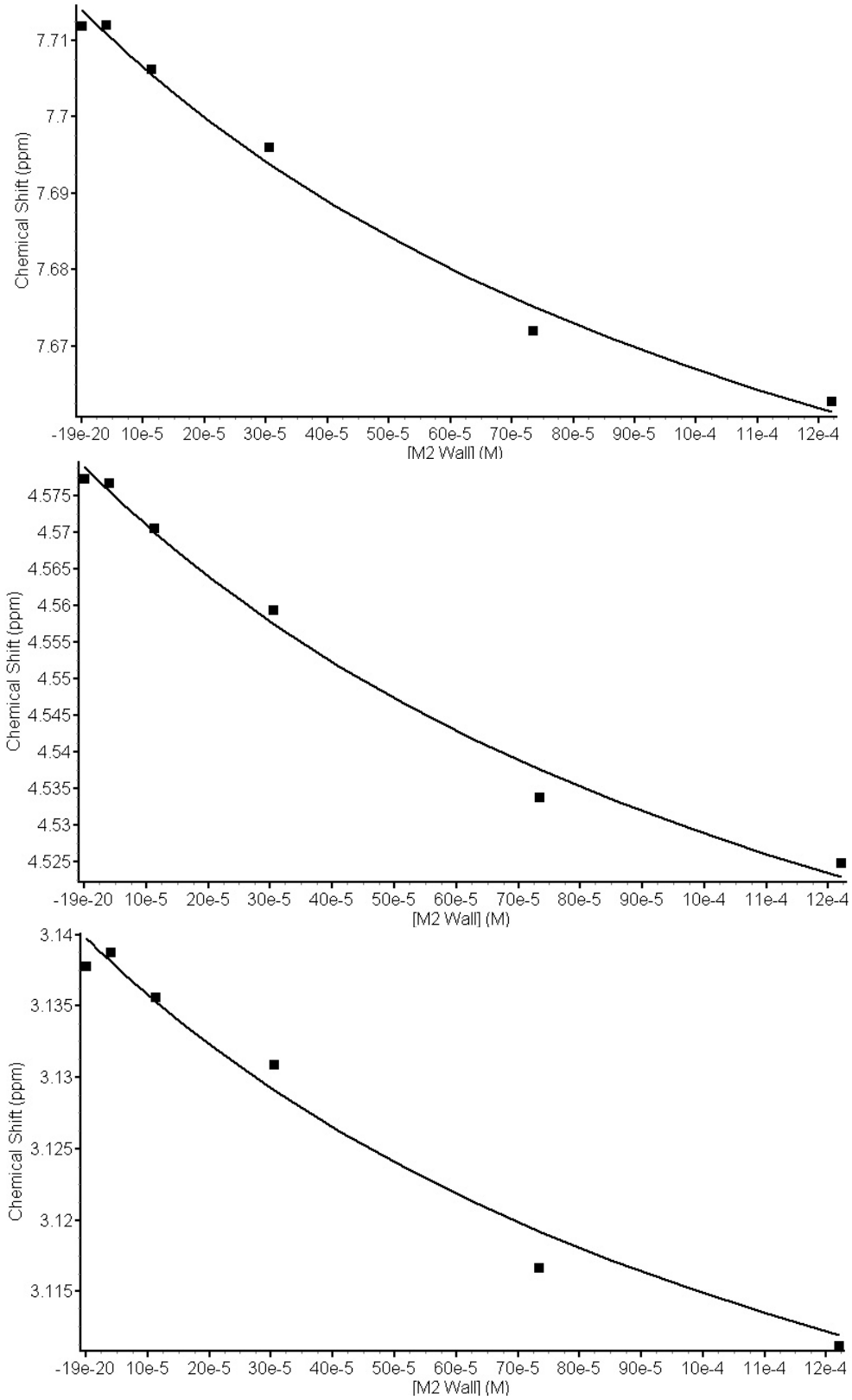

Figure II-S85. Chemical shifts of **II-7** resonances as a function of [**II-5**]. The solid lines represent the best non-linear fit of the resonances simultaneously inputted into a global fit ($K_a = 7.47 \pm 2.14 \times 10^2\ M^{-1}$).

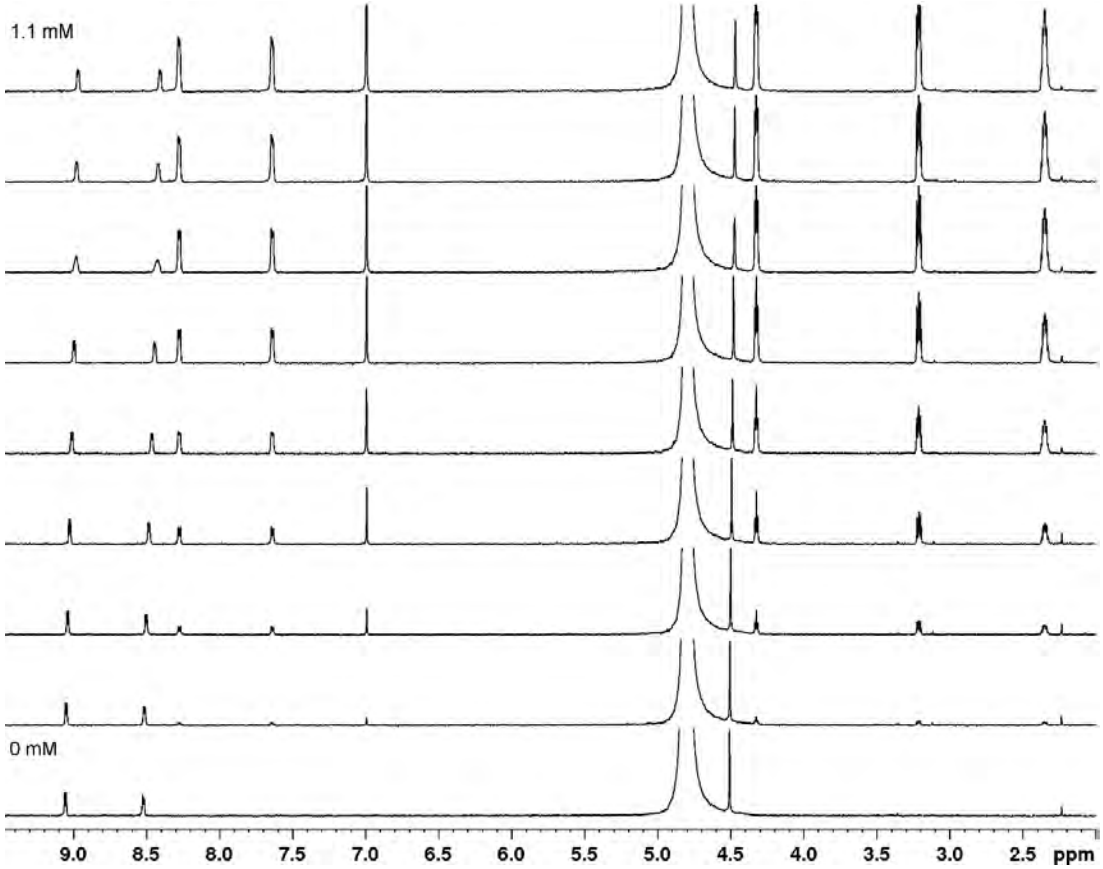

Figure II-S86. ^{1}H NMR (600 MHz, D_2O, RT) titration of **II-8** (0.1 mM) with increasing amounts of **II-5** (0 mM – 1.11 mM).

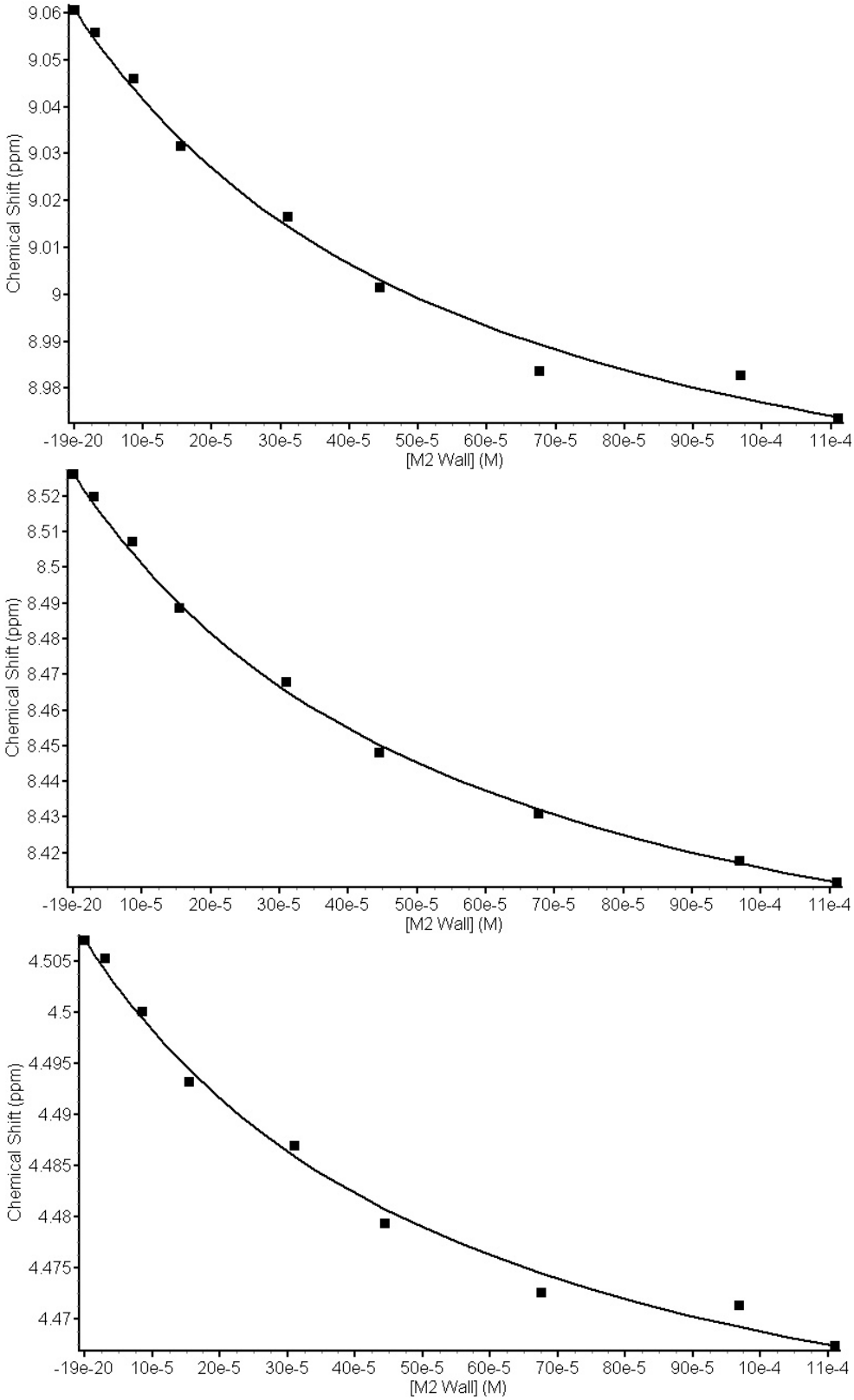

Figure II-S87. Chemical shifts of **II-8** resonances as a function of [**II-5**]. The solid lines represent the best non-linear fit of the resonances simultaneously inputted into a global fit ($K_a = 1.94 \pm 0.13 \times 10^3\ M^{-1}$).

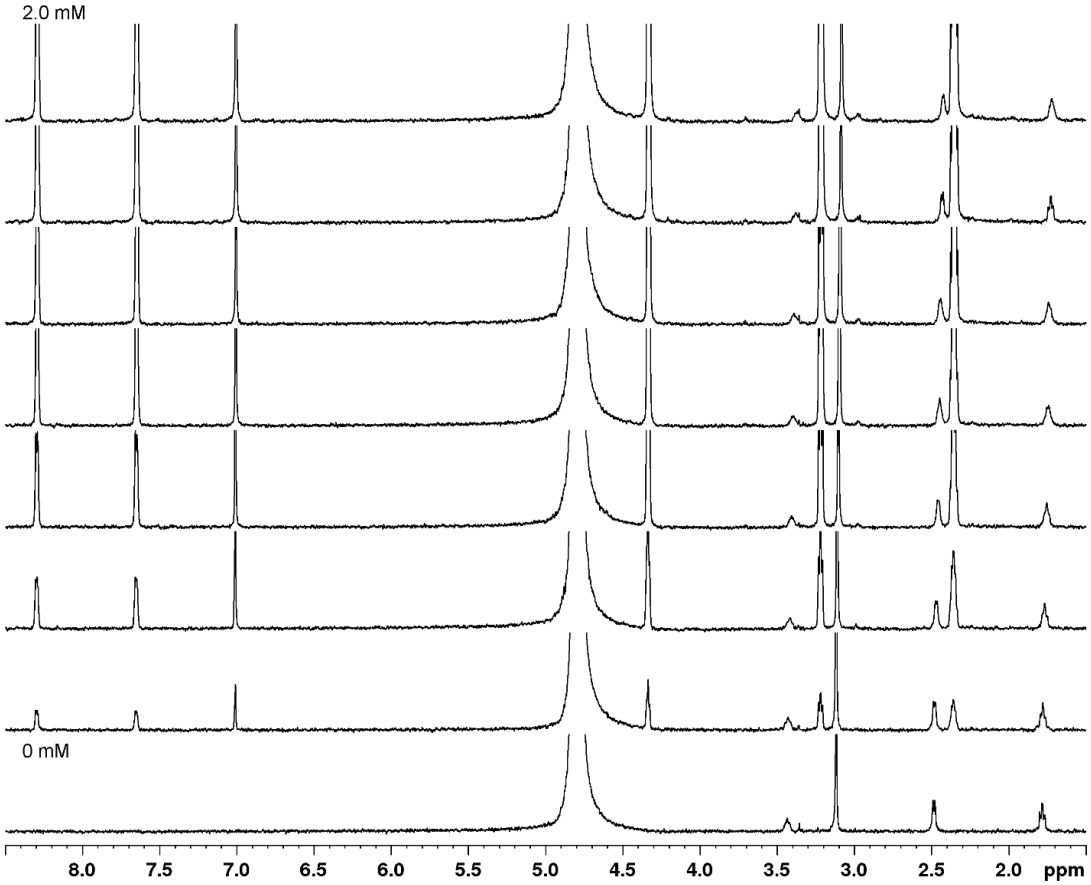

Figure II-S88. ^{1}H NMR (600 MHz, D_2O, RT) titration of **II-9** (0.1 mM) with increasing amounts of **II-5** (0 mM – 2.0 mM).

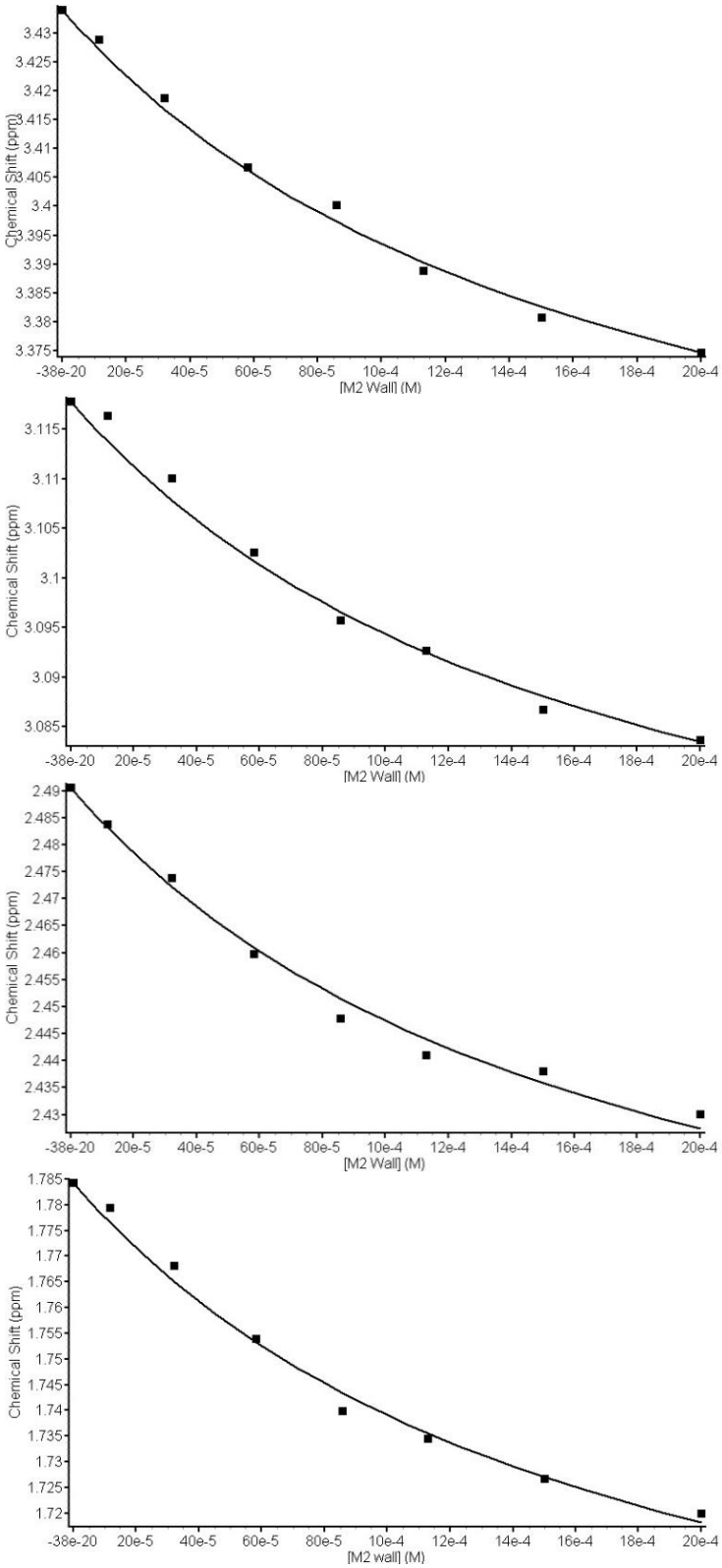

Figure II-S89. Chemical shifts of **II-9** resonances as a function of [**II-5**]. The solid lines represent the best non-linear fit of the resonances simultaneously inputted into a global fit ($K_a = 6.21 \pm 0.65 \times 10^2\ M^{-1}$).

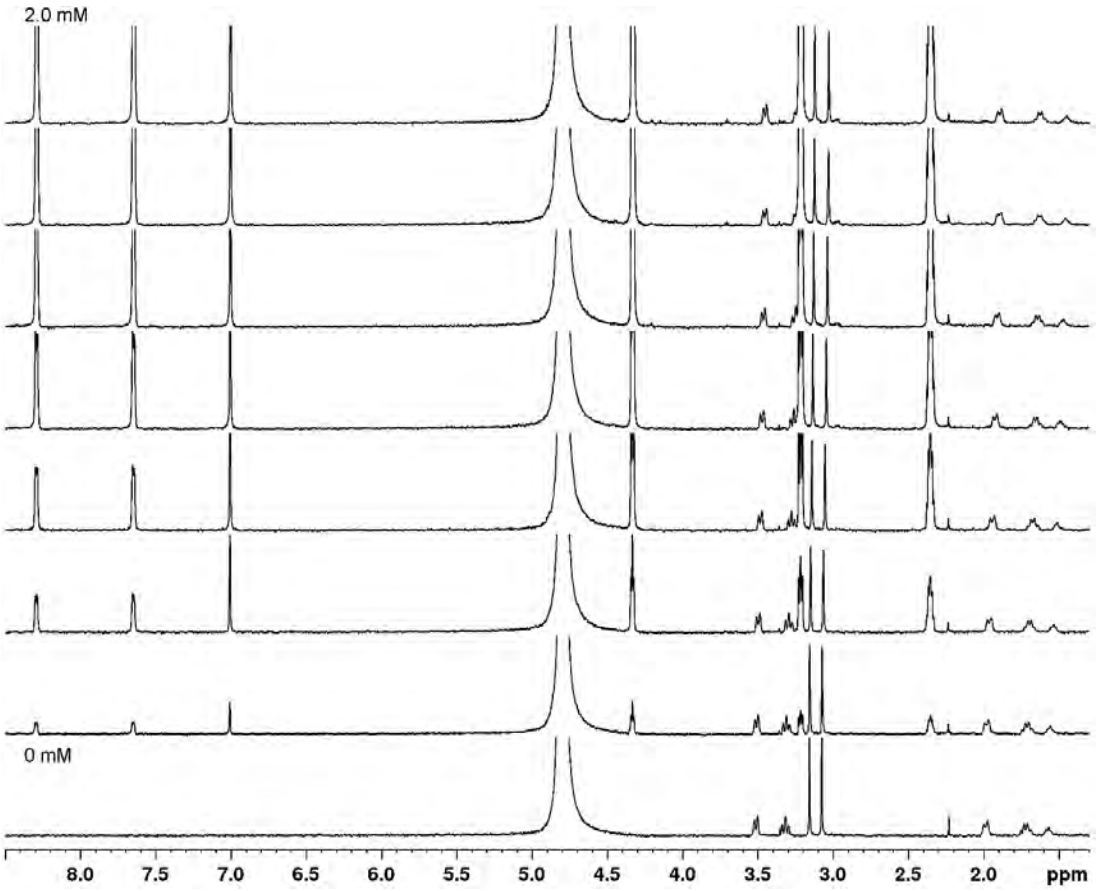

Figure II-S90. ^{1}H NMR (600 MHz, D_2O, RT) titration of **II-10** (0.1 mM) with increasing amounts of **II-5** (0 mM – 2.0 mM).

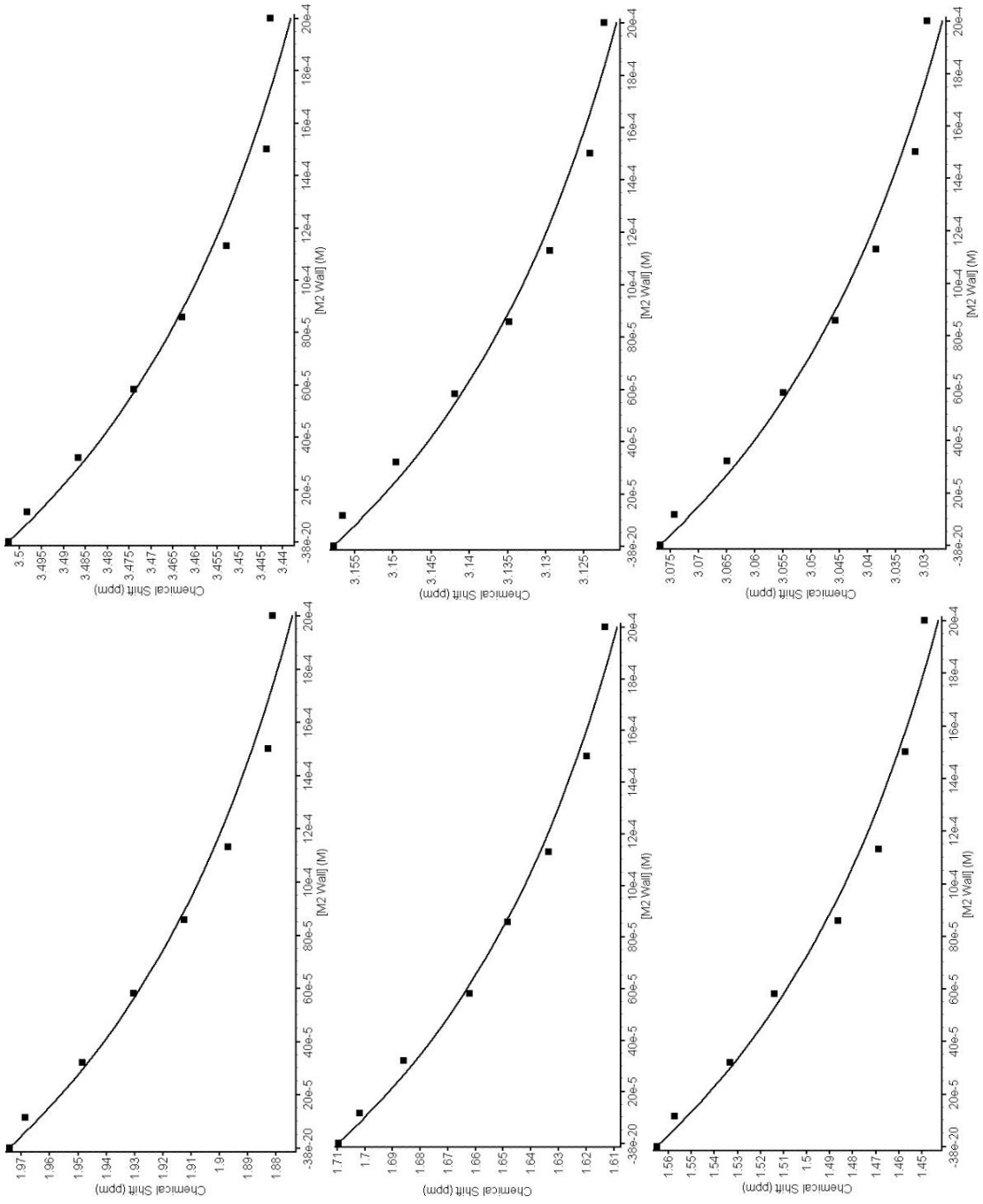

Figure II-S91. Chemical shifts of **II-10** resonances as a function of [**II-5**]. The solid lines represent the best non-linear fit of the resonances simultaneously inputted into a global fit ($K_a = 5.40 \pm 0.58 \times 10^2\ M^{-1}$).

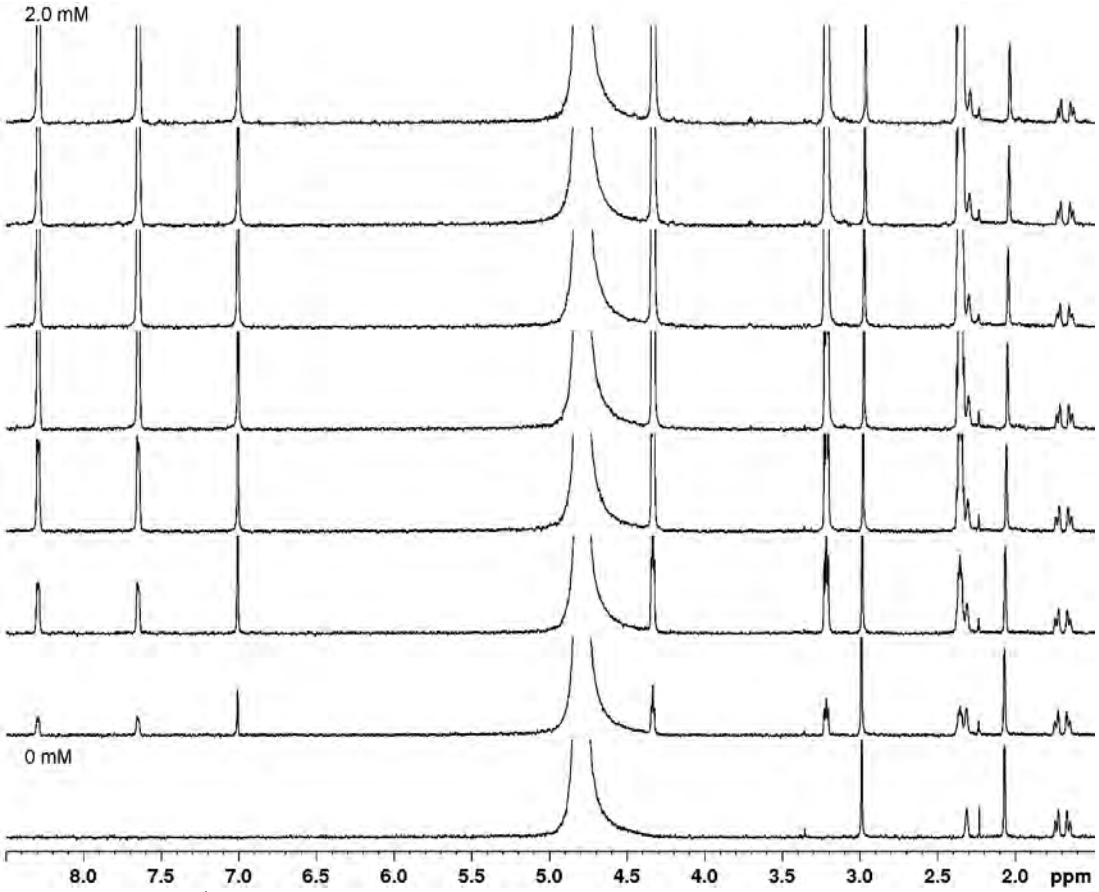

Figure II-S92. ^{1}H NMR (600 MHz, D_2O, RT) titration of **II-11** (0.1 mM) with increasing amounts of **II-5** (0 mM – 2.0 mM).

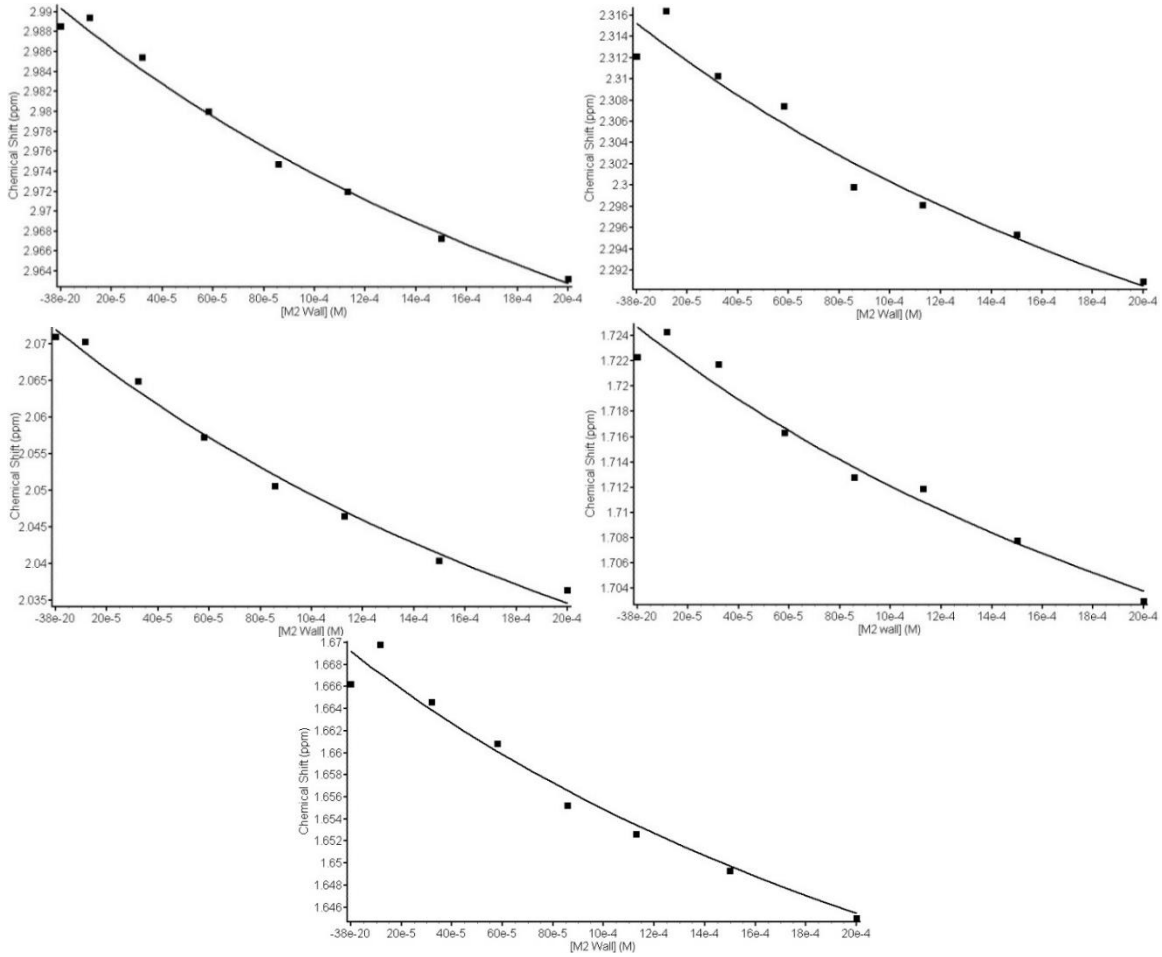

Figure II-S93. Chemical shifts of **II-11** resonances as a function of [**II-5**]. The solid lines represent the best non-linear fit of the resonances simultaneously inputted into a global fit ($K_a = 2.70 \pm 0.83 \times 10^2\ M^{-1}$).

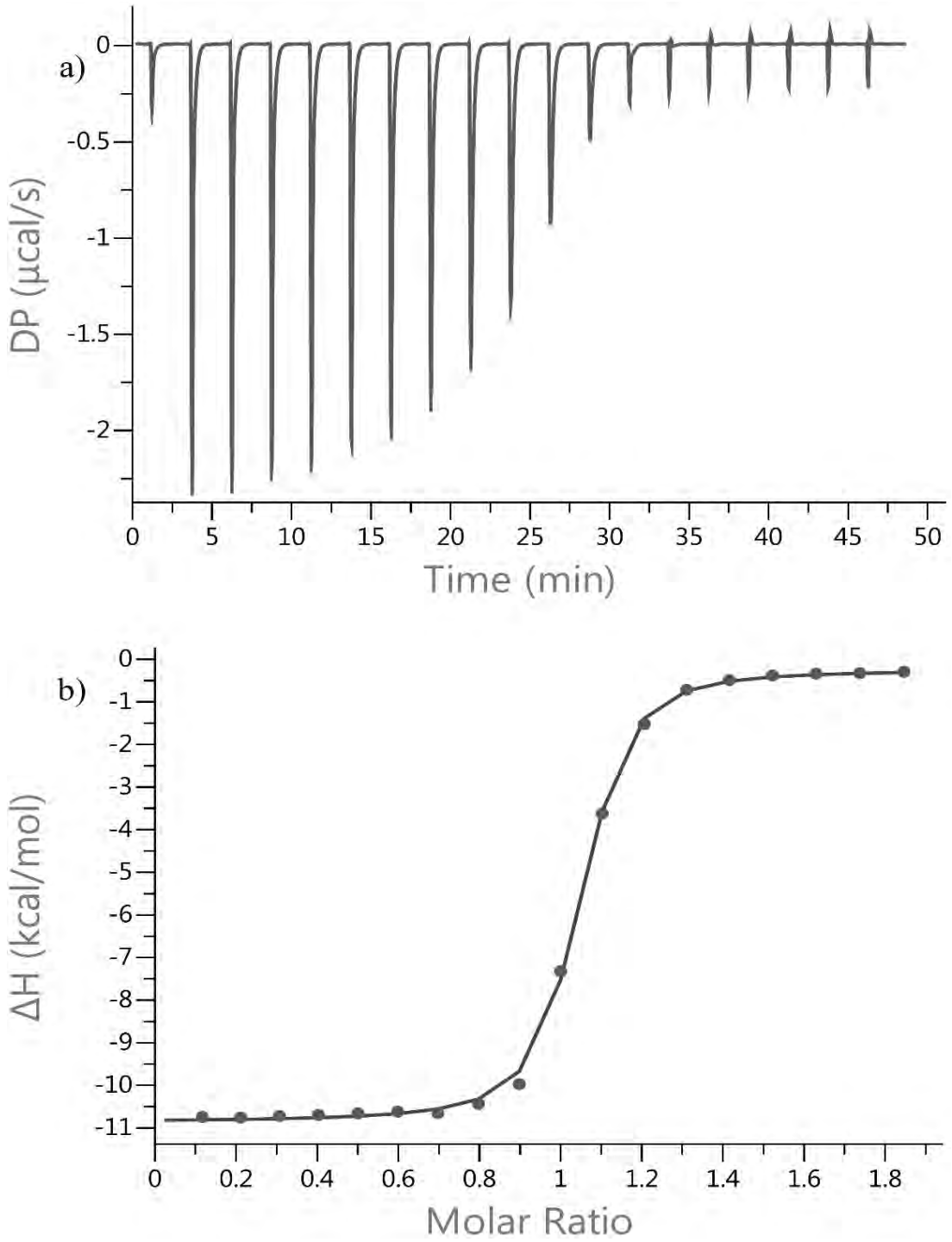

Figure II-S94. a) Plot of change in DP vs time from the titration of **Tet1** (104 µM) in the cell with guest **II-10** (1.0 mM) in the syringe in 20 mM NaH_2PO_4 buffer (pH = 7.4); b) plot of ΔH as a function of molar ratio of **II-10** to **Tet1**. The solid line represents the best non-linear fit of the data to the single set of sites model (K_a = (3.09 ± 0.24) x 10^6 M^{-1} and ΔH = -10.6 ± 0.08 kcal mol^{-1}).

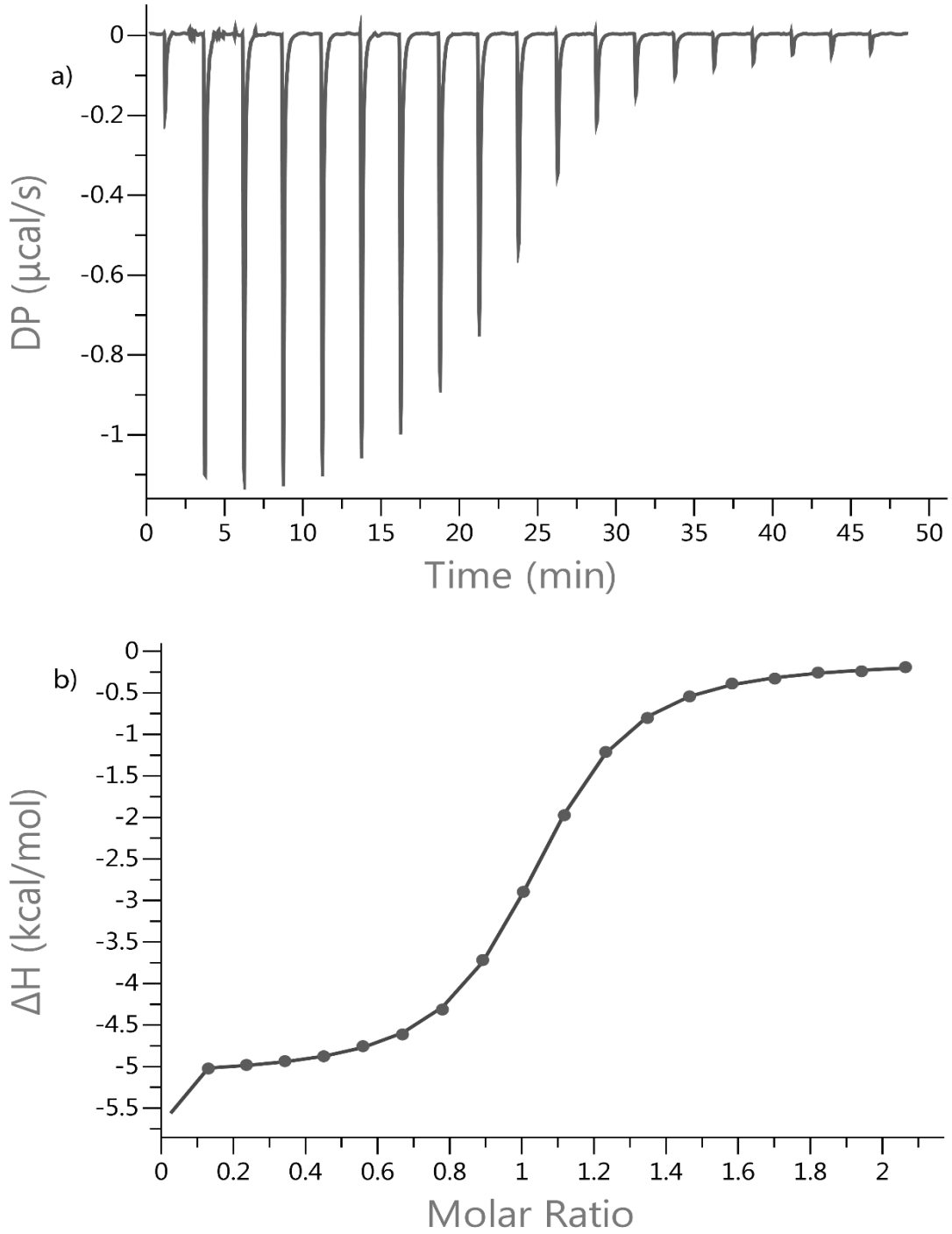

Figure II-S95. a) Plot of change in DP vs time from the titration of **Tet2** (93.3 µM) and **II-9b** (500 µM) in the cell with guest **II-6** (1.00 mM) in the syringe in 20 mM NaH_2PO_4 buffer (pH = 7.4); b) plot of ΔH as a function of molar ratio of **Tet2** to **II-6**. The solid line represents the best non-linear fit of the data to the single set of sites model (K_a = (4.59 ± 0.09) x 10^8 M^{-1} and ΔH = -10.6 ± 0.15 kcal mol^{-1}).

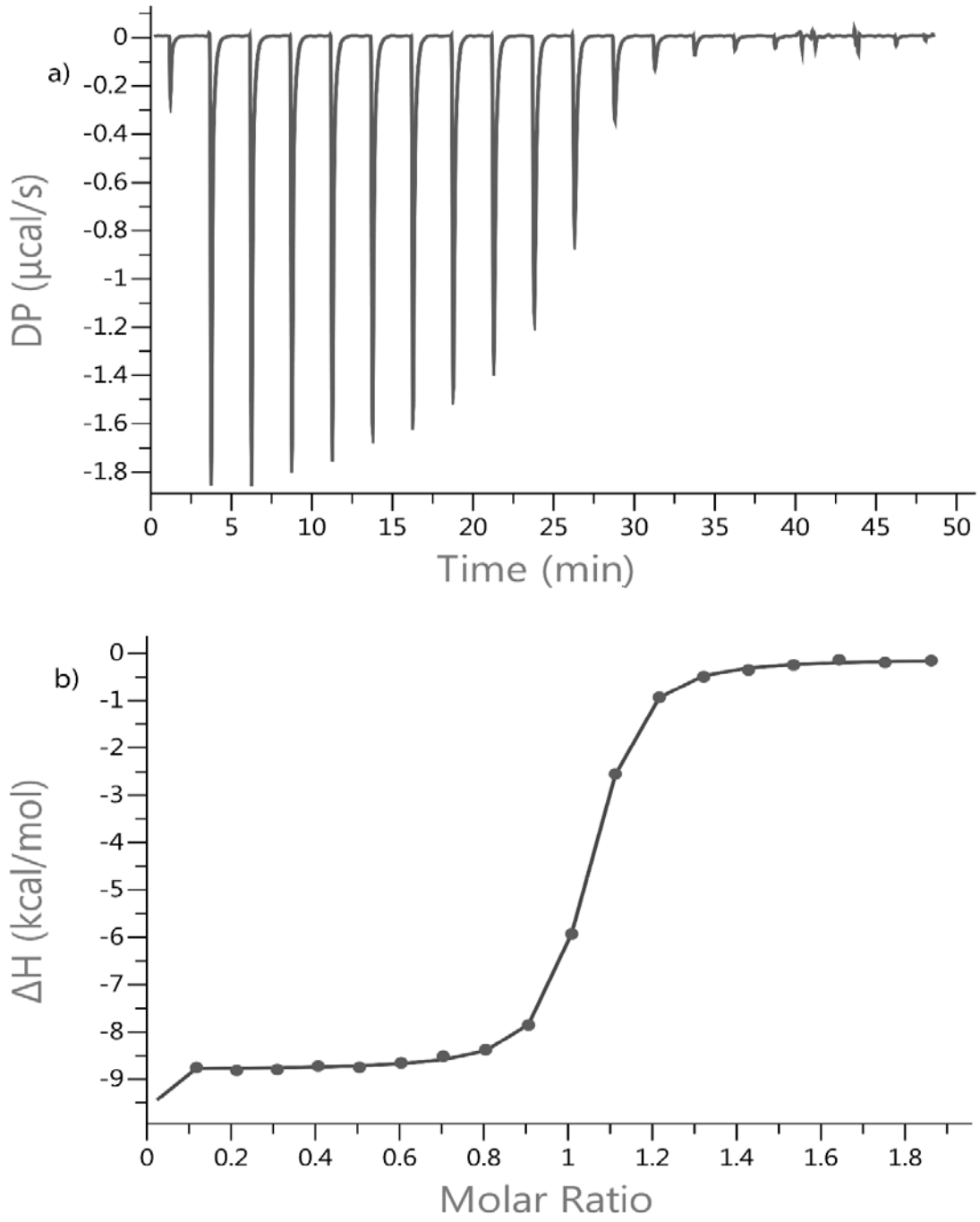

Figure II-S96. a) Plot of change in DP vs time from the titration of **Tet2** (103 µM) and **II-9b** (500 µM) in the cell with guest **II-7** (1.00 mM) in the syringe in 20 mM NaH_2PO_4 buffer (pH = 7.4); b) plot of ΔH as a function of molar ratio of **Tet2** to **II-7**. The solid line represents the best non-linear fit of the data to the single set of sites model (K_a = (2.69 ± 0.09) x 10^9 M^{-1} and ΔH = -14.2 ± 0.02 kcal·mol^{-1}).

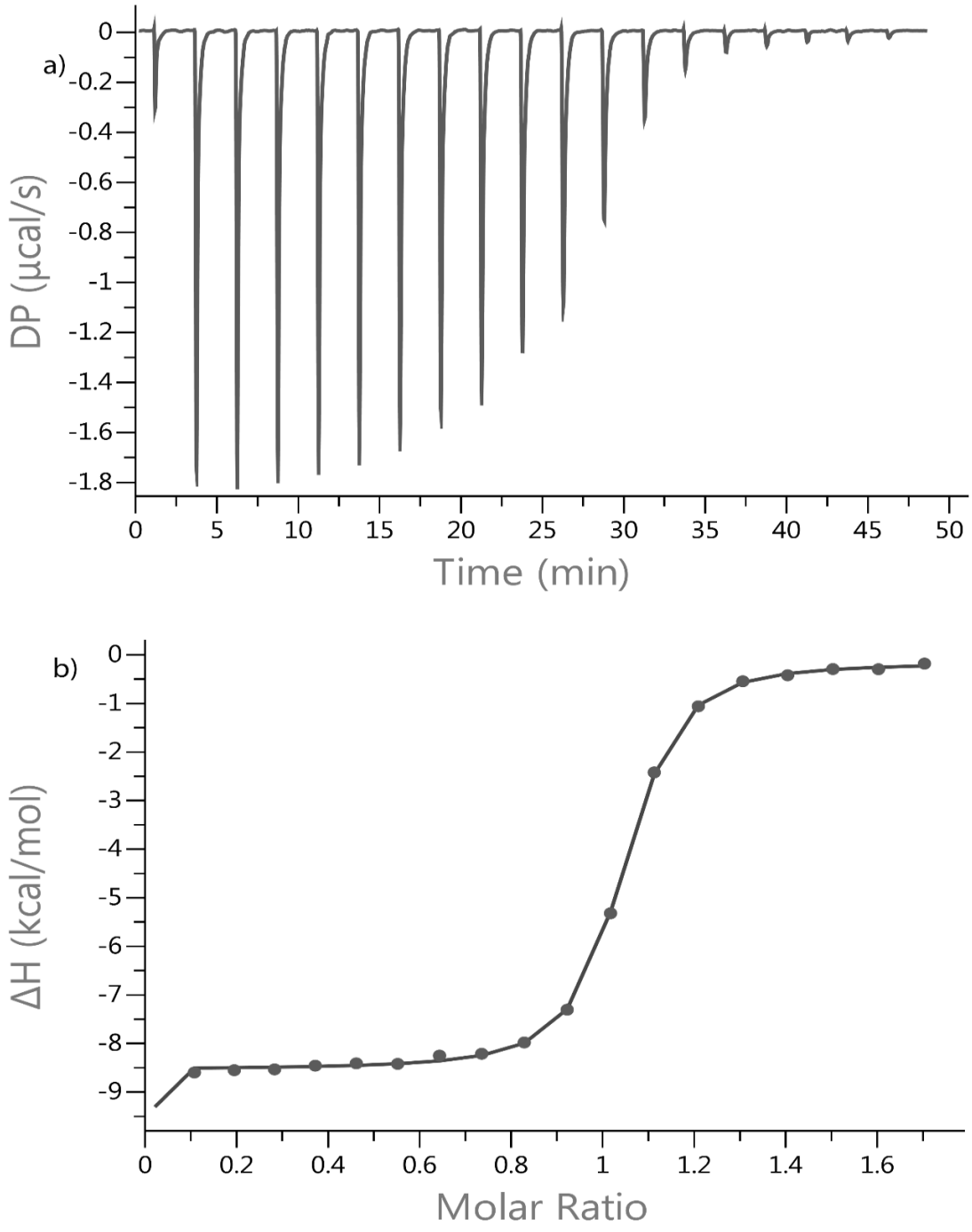

Figure II-S97. a) Plot of change in DP vs time from the titration of **Tet2** (113 µM) and **II-9b** (500 µM) in the cell with guest **II-8** (1.00 mM) in the syringe in 20 mM NaH_2PO_4 buffer (pH = 7.4); b) plot of ΔH as a function of molar ratio of **Tet2** to **II-8**. The solid line represents the best non-linear fit of the data to the single set of sites model (K_a = (2.14 ± 0.09) x 10^9 M^{-1} and ΔH = -13.9 ± 0.04 kcal·mol^{-1}).

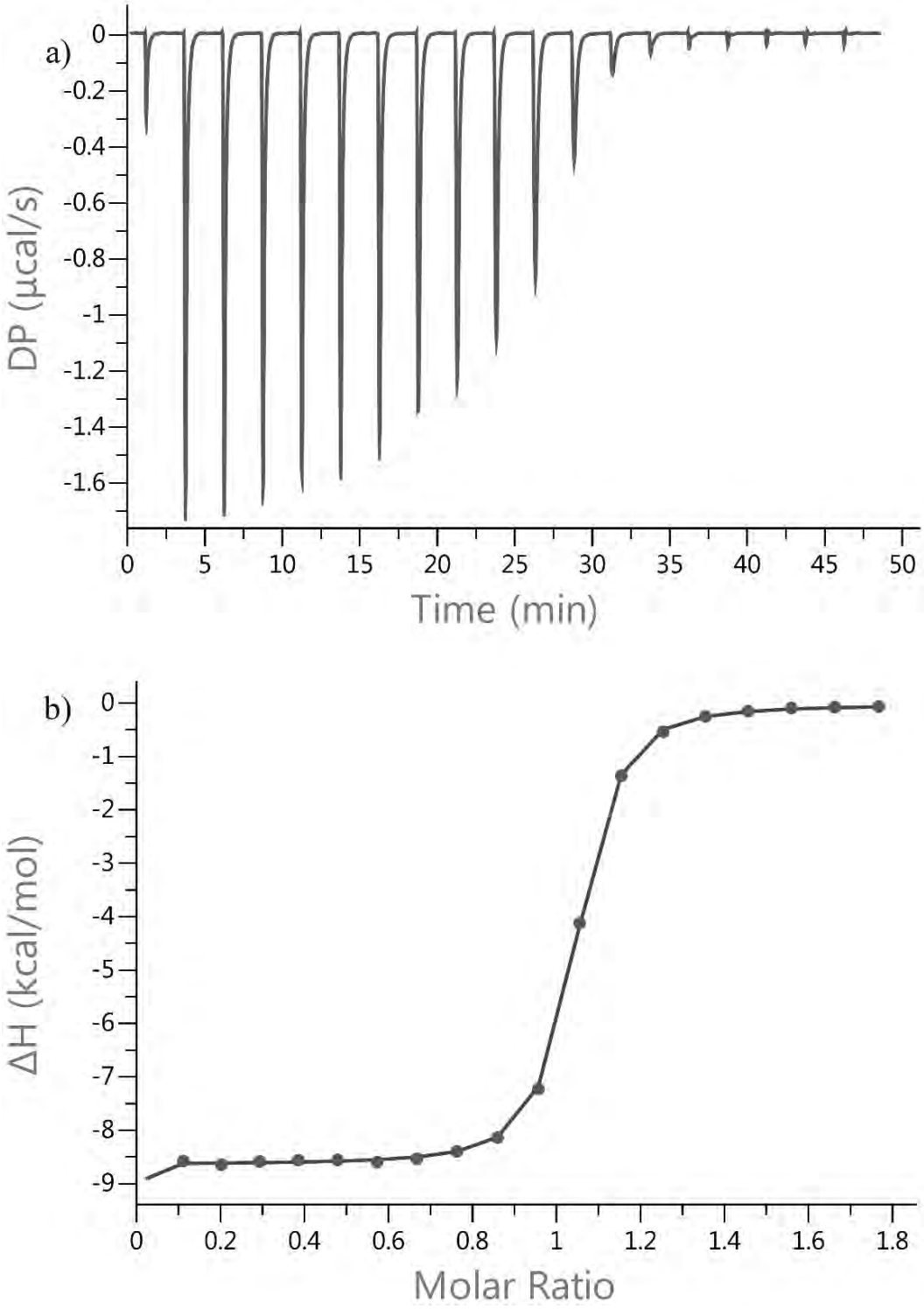

Figure II-S98. a) Plot of change in DP vs time from the titration of **Tet2** (109 µM) and **II-9b** (2.0 mM) in the cell with guest **II-10** (1.0 mM) in the syringe in 20 mM NaH_2PO_4 buffer (pH = 7.4); b) plot of ΔH as a function of molar ratio of **II-10** to **Tet2**. The solid line represents the best non-linear fit of the data to the single set of sites model (K_a = (1.30 ± 0.03) x 10^{10} M^{-1} and ΔH = -14.2 ± 0.02 kcal·mol^{-1}).

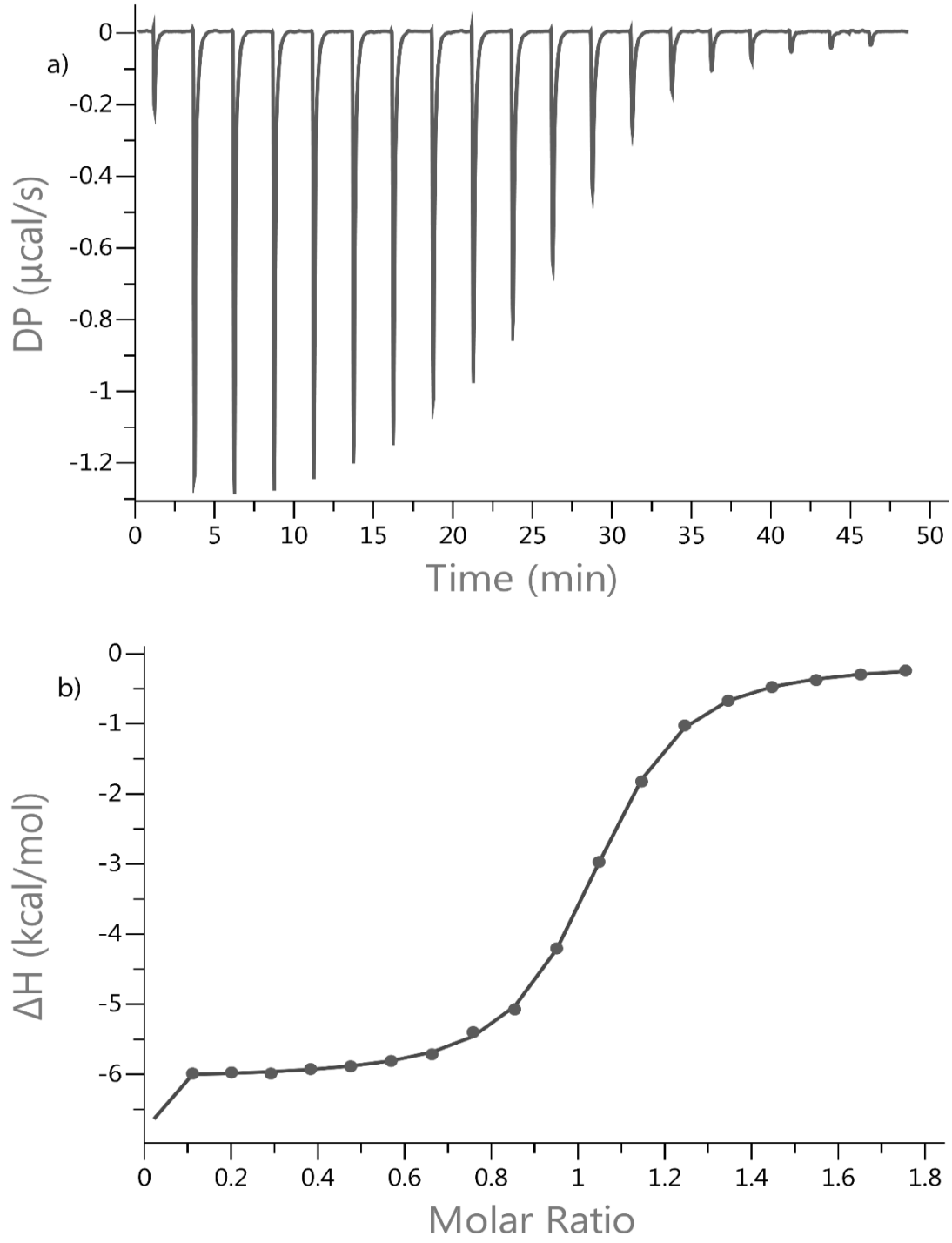

Figure II-S99. a) Plot of change in DP vs time from the titration of **Tet2** (110 µM) and **II-9b** (500 µM) in the cell with guest **II-11** (1.00 mM) in the syringe in 20 mM NaH_2PO_4 buffer (pH = 7.4); b) plot of ΔH as a function of molar ratio of **Tet2** to **II-11**. The solid line represents the best non-linear fit of the data to the single set of sites model (K_a = (7.09 ± 0.21) x 10^8 M^{-1} and ΔH = -11.5 ± 0.02 kcal·mol^{-1}).

Induced Chemical Shifts – Tables S1 – S6 reproduce the information from Table 3 of the main text, but also presents the limiting chemical shift values from the non-linear least squares fitting of titrations of **P1**, **P2**, and **II-5** or directly from the NMR spectra of the guests and the host•guest complexes for the slow exchange complexes based on **Tet1** and **Tet2**.

Table II-S1: Induced chemical shifts (ppm) of **II-6** with different containers.

	b	Δδ	a	Δδ	c	Δδ	d	Δδ
II-4	NO SHIFT		NO SHIFT		NO SHIFT		NO SHIFT	
P1[a]	3.34-2.91	0.43	3.13-3.01	0.12	1.84-1.46	0.38	1.46-0.68	0.78
Tet1[b]	3.33-2.55	0.78	3.11-3.00	0.11	1.82-0.73	1.09	1.44-0.06	1.38
II-5[a]	3.33-3.23	0.10	3.12-3.05	0.07	1.83-1.72	0.11	1.45-1.34	0.11
P2[a]	3.33-2.92	0.41	3.11-3.07	0.04	1.82-1.23	0.59	1.44-0.47	0.97
Tet2[b]	3.38-2.21	1.17	3.17-2.67	0.50	1.88-0.51	1.37	1.50-0.18	1.32

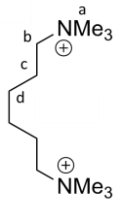

[a] Final Chemical shift determined from non-linear fitting of NMR titration data
[b] Final Chemical shift extracted from 1:1 ^{1}H NMR

Table II-S2: Induced chemical shifts (ppm) of **II-7** with different containers.

	c	Δδ	b	Δδ	a	Δδ
II-4	NO SHIFT		NO SHIFT		NO SHIFT	
P1[a]	7.73-7.44	0.29	4.59-4.42	0.17	3.16-3.08	0.08
Tet1[b]	7.71-6.44	1.27	4.58-3.86	0.72	3.14-2.97	0.17
II-5[a]	7.71-7.56	0.15	4.58-4.42	0.16	3.13-3.06	0.07
P2[a]	7.71-6.95	0.76	4.58-4.24	0.34	3.14-2.96	0.18
Tet2[b]	7.78-6.17	1.61	4.64-4.28	0.36	3.20-2.54	0.66

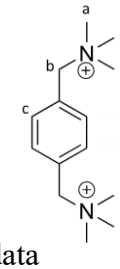

[a] Final Chemical shift determined from non-linear fitting of NMR titration data
[b] Final Chemical shift extracted from 1:1 ^{1}H NMR

Table II-S3: Induced chemical shifts (ppm) of **II-8** with different containers.

	b	Δδ	c	Δδ	a	Δδ
II-4	NO SHIFT		NO SHIFT		NO SHIFT	
P1[a]	9.08-8.71	0.37	8.54-8.19	0.35	4.53-4.39	0.14
Tet1[b]	9.05-7.97	1.08	8.52-7.71	0.81	4.50-4.30	0.20
II-5[a]	9.06-8.93	0.13	8.52-8.36	0.16	4.51-4.45	0.06
P2[a]	9.05-8.57	0.48	8.52-7.95	0.57	4.50-4.37	0.13
Tet2[b]	9.12-8.07	1.05	8.57-7.01	1.56	4.56-4.26	0.30

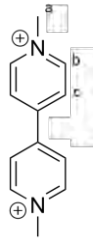

[a] Final Chemical shift determined from non-linear fitting of NMR titration data
[b] Final Chemical shift extracted from 1:1 ^{1}H NMR

Table II-S4: Induced chemical shifts (ppm) of **II-9** with different containers.

	b	Δδ	a	Δδ	c	Δδ	d	Δδ
P1[a]	3.43-2.64	0.79	3.11-2.84	0.27	2.47-1.85	0.62	1.77-1.10	0.67
Tet1[b]	3.43-2.62	0.81	3.12-2.24	0.88	2.49-1.58	0.91	1.78-0.70	1.08
II-5[a]	3.43-3.23	0.20	3.11-3.06	0.05	2.49-2.38	0.11	1.78-1.66	0.12
P2[a]	3.43-2.93	0.50	3.12-2.96	0.16	2.49-2.08	0.41	1.78-1.25	0.53
Tet2[b]	3.48-1.42	2.06	3.17-2.28	0.89	2.53-1.15	1.38	1.83-0.19	1.64

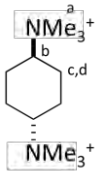

[a] Final Chemical shift determined from non-linear fitting of NMR titration data
[b] Final Chemical shift extracted from 1:1 ^{1}H NMR

Table II-S5: Induced chemical shifts (ppm) of ***II*-10** with different containers.

	c	Δδ	d	Δδ	a	Δδ	b	Δδ	e	Δδ	f	Δδ	g	Δδ
P1[a]	3.50-3.13	0.37	3.32-2.91	0.41	3.16-2.97	0.19	3.07-2.89	0.18	1.98-1.39	0.59	1.71-1.17	0.54	1.57-0.88	0.69
Tet1[b]	3.52-2.92	0.60	3.32-2.55	0.77	3.16-2.91	0.25	3.07-2.62	0.45	1.98-1.02	0.96	1.72-0.83	0.89	1.56-0.39	1.17
II-5[a]	3.50-3.34	0.16	3.31-3.13	0.18	3.16-3.09	0.07	3.08-2.98	0.10	1.97-1.78	0.19	1.71-1.51	0.20	1.57-1.33	0.24
P2[a]	3.53-3.26	0.27	3.32-2.90	0.42	3.16-3.04	0.12	3.08-2.89	0.19	2.00-1.41	0.59	1.73-1.13	0.60	1.56-0.78	0.78
Tet2[b]	3.52-2.50	1.02	3.31-2.03	1.28	3.15-2.81	0.34	3.07-2.30	0.77	1.98-0.54	1.44	1.73-0.26	1.47	1.56-0.46	1.09

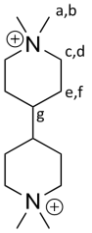

[a] Final Chemical shift determined from non-linear fitting of NMR titration data
[b] Final Chemical shift extracted from 1:1 ^{1}H NMR

Table II-S6: Induced chemical shifts (ppm) of **II-11** with different containers.

	a	Δδ	d	Δδ	b,c	Δδ	e	Δδ	f	Δδ
P1[a]	3.01-2.74	0.27	2.33-1.59	0.74	2.09-1.32	0.77	1.74-1.26	0.48	1.69-0.90	0.79
Tet1[b]	2.98-2.69	0.29	2.31-1.17	1.14	2.07-0.85	1.22	1.72-0.99	0.73	1.67-0.39	1.28
II-5[a]	2.99-2.91	0.08	2.32-2.25	0.07	2.07-1.96	0.11	1.72-1.66	0.06	1.67-1.60	0.07
P2[a]	2.98-2.80	0.18	2.31-1.76	0.55	2.07-1.56	0.51	1.72-1.37	0.35	1.67-1.07	0.60
Tet2[b]	3.04-2.62	0.42	2.37-0.47	1.90	2.12-0.50	1.62	1.77-0.61	1.16	1.72-0.22	1.5

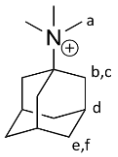

[a] Final Chemical shift determined from non-linear fitting of NMR titration data
[b] Final Chemical shift extracted from 1:1 ^{1}H NMR

SUPPORTING INFORMATION – COMPUTATIONAL PART

BENCHMARKING QUANTUM CHEMICAL METHODS ON TriMe CONFORMERS

Computational Methods. We built three possible conformers of **TriMe** in silico by modifying conformations of methylene bridges (C1a and C3a carbon atoms, Figure II-S100). Conformers were labeled as F1, F2, and F3. For their characterizations, we employed two pseudo-dihedral angles, ϕ_1 and ϕ_2, which were defined by three vectors between centers of masses of atoms specified by the AMBER atom mask format[1] as follows: ϕ1(:1@C6,N7,N5->:1@C2,N1,N3; :1@C1a->:1@C3a; :2@C2,N1,N3->:2@C6,N7,N5) and ϕ2 (:2@C6,N7,N5->:2@C2,N1,N3; :2@C3a->:2@C1a; :3@C2,N1,N3->:3@C6,N7,N5).

The geometry of each conformer was optimized by several methods in a vacuum (Figure II-S100, Table II-S7). Optimizations employing B3LYP-D3BJ/def2-TZVPP,[2,3] PBE0-D3BJ/def2-TZVPP,[4] and PM7[5] were performed in Gaussian 16.[6] Optimization using PBE-D3BJ/def2-TZVPP,[7] PBEh-3c,[8] B97-3c,[9] and HF-3c[10] were performed in Orca 4.2.1.[11] Optimization employing GAFF[12] was done in Amber 16.[1] D3BJ indicates the atom-pairwise dispersion correction with the Becke-Johnson damping scheme.[13,14]

The quality of each geometry was evaluated by a single point energy calculation at the RI-MP2 level of theory in Orca. Reported energies were obtained by extrapolation to Complete Basis Set (CBS) employing two points (cc-pVDZ and cc-pVTZ basis sets) and independent extrapolations of HF and RI-MP2 correlation energies.[15]

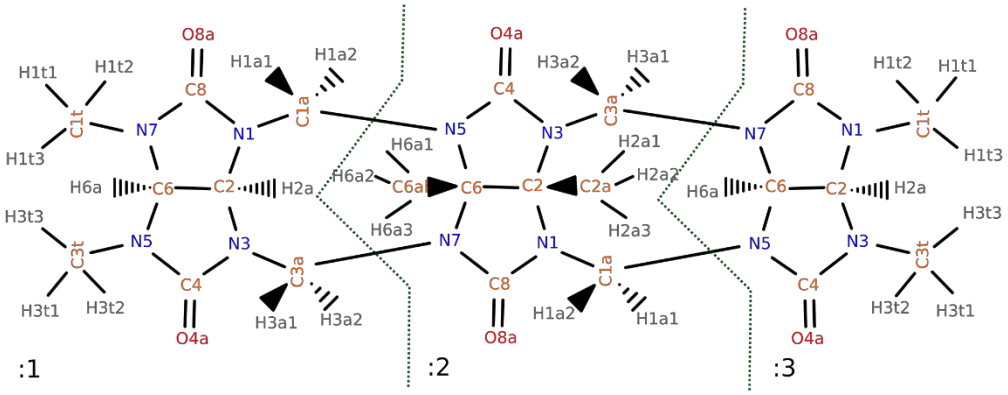

Figure II-S100. Structure of **TriMe** with depicted atom numbering and division into three residues (dashed green lines) employed in the GAFF force field calculations.

We found that the geometry of the glycoluril belt was twisted, and the size of the structure twisting was dependent on the level of theory employed during geometry of optimization. To quantify the level of geometry distortion, we evaluated two dihedral angles τ_1 and τ_2, which describes the local twist on the inverted glycoluril and global twist of glycoluril belt, respectively. Using the AMBER atom mask format, they were defined as follows: τ_1(:2@C6a, :2@C6, :2@C2, and :2@C2a) and τ_2 (:1@H2a, :2@C6, :2@C2,

:3@H6a). Further, we determined distances between terminal methyl groups, d_{MM1} (:1@C1t; :3@C1t), d_{MM2} (:1@C3t; :3@C3t) and their average value $<d_{MM}>$.

Table II-S7. Absolute energies of F1, F2, and F3 conformers of **TriMe** in vacuum obtained by various computational methods. Conformer geometries were obtained at the same level of theory, as reported in each table row. Optimized geometries are available in an XYZ format in the attached zip archive. All energies are in atomic units.

Method	F1	F2	F3
B3LYP-D3BJ/def2-TZVPP	-1965.854172	-1965.852971	-1965.851105
B97-3c	-1964.055228	-1964.054514	-1964.053158
GAFF	0.099133	0.106991	0.116086
HF-3c	-1940.700264	-1940.695821	-1940.694213
PBE0-D3BJ/def2-TZVPP	-1963.612786	-1963.611876	-1963.610052
PBE-D3BJ/def2-TZVPP	-1963.529902	-1963.529348	-1963.527949
PBEh-3c	-1960.813660	-1960.810946	-1960.808349
PM7	-0.313659	-0.308589	-0.305159

Table II-S8. Absolute single point energies at RI-MP2/CBS level of theory for **TriMe** conformer geometries optimized by various computational methods in a vacuum. All energies are in atomic units.

Method	F1	F2	F3
B3LYP-D3BJ/def2-TZVPP	-1962.339501	-1962.338489	-1962.336219
B97-3c	-1962.340096	-1962.339481	-1962.337412
GAFF	-1962.294857	-1962.289873	-1962.287137
HF-3c	-1962.323248	-1962.323963	-1962.324102
PBE0-D3BJ/def2-TZVPP	-1962.340050	-1962.339058	-1962.336658
PBE-D3BJ/def2-TZVPP	-1962.332307	-1962.331314	-1962.328954
PBEh-3c	-1962.337398	-1962.336729	-1962.334874
PM7	-1962.287235	-1962.281756	-1962.275920

Results and Discussion. **TriMe** is an acyclic glycoluril trimer with the inverted central unit. **TriMe** represents the same structural motive, which was experimentally determined in the studied pentamers **P1** and **P2**. We modeled the structure of **TriMe** in three conformational states (Figure II-S101). The conformers differed in the mutual rotation of glycoluril units on methylene bridges. To evaluate the quality of obtained geometries (Table II-S9) and conformer relative stabilities (Table II-S10), we tested a wide range of methods, including DFT (B3LYP, PBE0, PBE, PBEh-3c, B97-3c), corrected HF method (HF-3c), semiempirical quantum chemical method (PM7) and empirical force field method (GAFF). For comparison, we employed Møller–Plesset perturbation theory of the second order (MP2) with a complete basis set (CBS). MP2 was selected as a reference, because it is a pure *ab initio* quantum-chemical method, while all the other methods employed some empirical data such as parameters of DFT functionals, empirical dispersion corrections, etc.

Table II-S9. Energy deviations (ΔE_d) from the most stable geometry at RI-MP2/CBS potential energy surface calculated in vacuum for each **TriMe** conformer. Methods are sorted by $<\Delta E_d>$, which is an average deviation calculated from three conformers. Lower values mean better agreement with RI-MP2/CBS. All energies are in kcal mol^{-1}.

	ΔE_d			$<\Delta E_d>$
Method	**F1**	**F2**	**F3**	
B97-3c	0.0	0.0	0.0	0.0
PBE0-D3BJ/def2-TZVPP	0.0	0.3	0.5	0.3
B3LYP-D3BJ/def2-TZVPP	0.4	0.6	0.7	0.6
PBEh-3c	1.7	1.7	1.6	1.7
PBE-D3BJ/def2-TZVPP	4.9	5.1	5.3	5.1
HF-3c	10.6	9.7	8.4	9.6
GAFF	28.4	31.1	31.5	30.4
PM7	33.2	36.2	38.6	36.0

Table II-S10. Relative conformer stabilities (ΔE_r) of **TriMe** and their deviations (ΔE_d) from MP2/CBS//B97-3c energies calculated in a vacuum. Methods are sorted by $<|\Delta E_d|>$, which is an average deviation calculated from three conformers. Lower values mean better agreement with RI-MP2/CBS. All energies are in kcal mol^{-1}.

	ΔE_r			ΔE_d			$<\|\Delta E_d\|>$
Method	**F1**	**F2**	**F3**	**F1**	**F2**	**F3**	
MP2/CBS//B97-3c	0.00	0.39	1.68	0.00	0.00	0.00	0.00
PBE0-D3BJ/def2-TZVPP	0.00	0.57	1.72	0.00	0.18	0.03	0.07
B97-3c	0.00	0.45	1.30	0.00	0.06	-0.39	0.11
PBE-D3BJ/def2-TZVPP	0.00	0.35	1.23	0.00	-0.04	-0.46	0.17
B3LYP-D3BJ/def2-TZVPP	0.00	0.75	1.92	0.00	0.37	0.24	0.20
PBEh-3c	0.00	1.70	3.33	0.00	1.32	1.65	0.99
HF-3c	0.00	2.79	3.80	0.00	2.40	2.11	1.50
PM7	0.00	3.18	5.33	0.00	2.80	3.65	2.15
GAFF	0.00	4.93	10.64	0.00	4.54	8.95	4.50

We found that hybrid functionals PB0 and B3LYP performed well. But due to their computational complexity, which is a limiting factor for study on larger systems such as glycoluril pentamers and their complexes, we considered a different approach. For geometry optimization, we selected the B97-3c method. This method was specially designed for the study of noncovalent interactions of large supramolecular assemblies. Our results (Table II-S9) and recent benchmarks showed its good performance for geometry optimization.[9,16] For energy calculations on optimized geometries, we selected PB0-D3BJ/def2-TZVPP. This method showed the best agreement with the reference MP2/CBS method (Table II-S10).

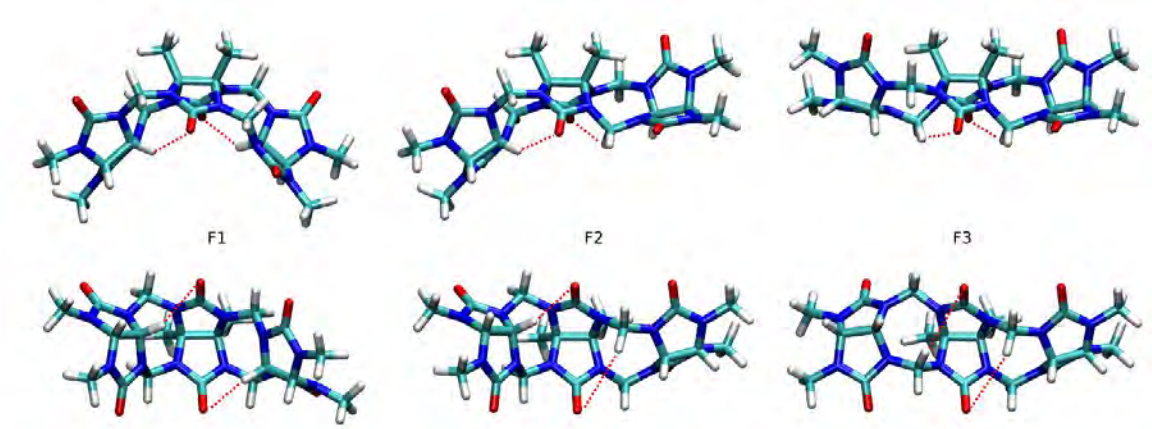

Figure II-S101. Top and side views of F1, F2, and F3 conformer geometries of **TriMe** optimized at B97-3c level of theory in a vacuum. Stabilizing contacts are highlighted by red dashed lines.

Optimized geometries of **TriMe** (Figure II-S101) showed a clearly visible twist, which was quantified by two dihedral angles τ_1 and τ_2 (Table II-S11). The dihedral angle τ_2 indicates the distortion of the glycoluril belt, while τ_1 quantifies the local distortion on the central glycoluril. The twist was found consistently in all conformers optimized by all high-quality methods. Too empirical methods, such as HF-3c, GAFF, and PM7, however, provided more regular structures with a decreased twist as indicated by lower values of τ_1 and τ_2 in comparison to B97-3c.

We expect that the distortion is a result of increased flexibility due to the presence of flexible methylene bridges, which are not limited in their motions by additional structural constraints, such as macrocycle enclosure in cucurbit[n]urils. Moreover, geometry optimizations were performed in a vacuum, which can result in strengthening some interactions. In all conformers, we found short contacts between carbonyl oxygen atoms on the central unit with either methine hydrogen atoms or hydrogen atoms from methylene bridges (Figure II-S101).

Table II-S11. Distortion of **TriMe** in vacuum quantified by distances between terminal methyl groups, d_{MM1} and d_{MM2}, dihedral angles, ϕ_1 and ϕ_2, determining the conformer type, and dihedral angles, τ_1 and τ_2, quantifying the local and global twist, respectively. All distances and angles are in angstroms and degrees, respectively

													τ_1			τ_2		
													F1	F2	F3	F1	F2	F3
													26.2	29.8	32.1	45.3	52.6	56.1
													26.6	29.1	31.3	45.9	51.6	55.3
B3LYP-D3BJ/def2-TZVPP	11.346	13.619	13.813	11.346	13.282	13.813	-44.8	-39.8	19.9	-44.8	20.4	19.9	26.1	28.9	31.4	44.3	50.9	55.2
PBEh-3c	11.219	13.578	13.725	11.219	13.300	13.725	-45.5	-39.7	20.8	-45.5	22.5	20.8	24.4	30.2	33.4	39.7	50.2	57.3
PBE-D3BJ/def2-TZVPP	11.657	13.662	13.916	11.657	13.383	13.916	-41.7	-37.4	18.4	-41.7	18.5	18.4	27.1	29.2	31.4	47.1	51.9	55.0
HF-3c	9.259	13.528	13.300	9.259	12.529	13.300	-62.8	-60.0	30.9	-62.8	34.6	30.9	6.3	23.3	31.2	7.3	34.5	52.6
GAFF	9.758	13.373	12.666	9.759	13.361	12.666	-60.7	-61.3	39.9	-60.8	43.0	40.1	0.0	0.2	18.1	0.0	0.3	23.6
PM7	8.738	13.421	12.048	8.737	12.440	12.048	-65.8	-61.0	43.7	-65.7	49.2	43.7	10.7	9.0	13.7	28.0	28.3	38.0

STABILITIES OF TriMe AND TriH CONFORMERS

Computational Methods. All the calculations were performed in Orca 4.2.1. Starting geometries of **TriMe** conformers F1, F2, and F3 were taken from the previous benchmark study. **TriH** was built from **TriMe** by substituting the methyl groups on C2 and C6 carbon atoms by hydrogen atoms. Geometries of all conformers were optimized on the B97-3c level of theory in the SMD[17] implicit water solvent (Figure II-S102).

Due to numerical problems with the solvent cavity definition observed, especially on large systems (pentamers and their complexes), we had to increase the solvent probe radius to 1.5 Å (standard value is 1.3 Å) and increase the ndiv parameter to 6 (default value is 5). To keep consistent methodology, we employed such modified parameters also for **TriMe** and **TriH** systems even though it was not necessary. A comparison of results obtained with the standard and modified SMD parameters showed only a minor impact on relative stabilities of **TriMe** and **TriH** conformers in order of tenths of kcal mol^{-1}.

PBE0-D3BJ/def2-TZVPP and PBE0-D3BJ-SMD/def2-TZVPP energies were calculated using RIJCOSX approximation[18] with GridX6. Obtained total energies are summarized in Table II-S12**.**

Table II-S12. Absolute energies of **TriMe** and **TriH** conformers calculated on geometries optimized at B97-3c level of theory and in the SMD implicit solvent of water. E_{CDS} is the non-polar only contribution to the SMD solvation energy. Optimized geometries are available in an XYZ format in the attached zip archive. All energies are in atomic units.

System	conf	B97-3c-SMD	PBE0-D3BJ	PBE0-D3BJ-SMD	E_{CDS}
TriMe	F1	-1964.122020	-1963.603114	-1963.680203	0.008730
	F2	-1964.116353	-1963.602149	-1963.674700	0.010392
	F3	-1964.113863	-1963.602341	-1963.672060	0.011977
TriH	F1	-1885.526902	-1885.029552	-1885.110096	0.005944
	F2	-1885.527512	-1885.030692	-1885.110661	0.006723
	F3	-1885.527933	-1885.028805	-1885.111007	0.006745

Results and Discussion. The benchmark study on **TriMe** in vacuum showed that the most stable conformer was F1, while the other conformers were less stable: F2 (+0.6 kcal mol^{-1}) and F3 (+1.7 kcal mol^{-1}). Since the solvent can have a significant impact on conformer stabilities, we re-optimized geometries in an implicit model of water (Figure S102). Also, we included **TriH** to better understand the effect of methyl groups on conformer preferences. As an implicit solvent, we selected the SMD model. This model provides a more realistic solvent description because it gives both electrostatic and non-polar contributions to the solvation energy, while the others widely employed in QM calculations (C-PCM, COSMO) only offer an electrostatic component.[17] Obtained relative conformer stabilities are summarized in Table II-S13.

Interestingly, obtained data showed that the solvent had further destabilizing effect on the F2 (+3.5 kcal mol^{-1}) and F3 (+5.1 kcal mol^{-1}) conformers of **TriMe**. The solvent had also impact on the structure distortion. In a water environment, the F1 structure showed lesser twisting than F2 and F3. The twist of F2 and F3 remained nearly the same as it was observed in a vacuum. This indicates that the destabilization of F2 and F3 is probably caused by steric clashes between methyl groups and concave side(s) of adjacent

glycoluril(s) and weak interactions with the solvent. In the absence of the methyl groups (**TriH**), the difference between conformer stabilities, F1 (0.0 kcal mol-1), F2 (-0.4 kcal mol-1), and F3 (-0.6 kcal mol-1), was small and showed an opposite trend with F3 being the most stable conformer.

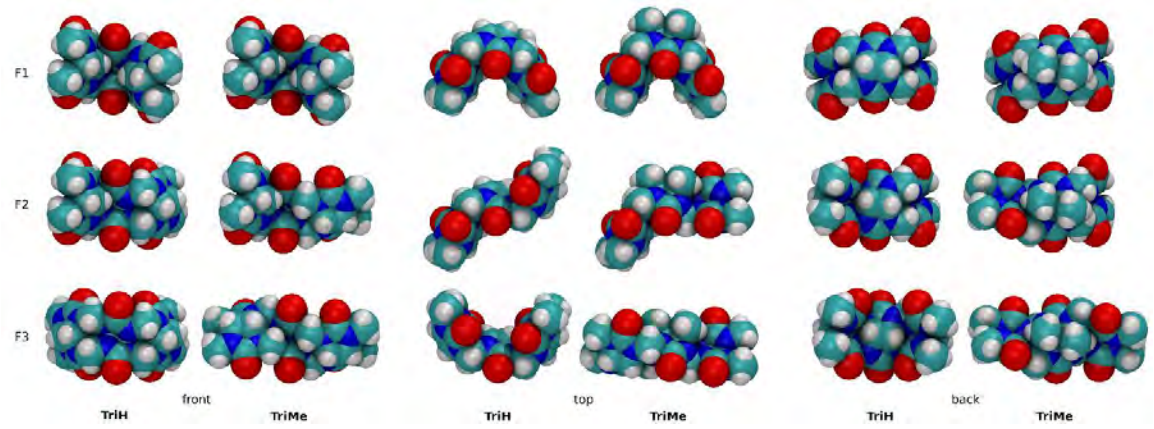

Figure II-S102. F1, F2, and F3 conformer geometries of **TriMe** and **TriH** optimized at the B97-3c level of theory in the SMD implicit water solvent.

Table II-S13. Trimer distortions quantified by distances between terminal methyl groups, d_{MM1} and d_{MM2}, dihedral angles, ϕ_1 and ϕ_2, determining the conformer type, and dihedral angles, τ_1 and τ_2, quantifying the local and global twist, respectively. Relative conformer stability (ΔE_r) and its decomposition into the internal energy (ΔE_{int}), and electrostatic ($\Delta E_{s,el}$) and non-polar ($\Delta E_{s,np}$) components of the solvation energy obtained at PBE0-D3BJ-SMD/def2-TZVPP//B97-3c-SMD level of theory. All energies are in kcal mol^{-1}, distances are in angstroms, and dihedral angles are in degrees.

System	conf	d_{MM1}	d_{MM2}	$<d_{MM}>$	ϕ_1	ϕ_2	τ_1	τ_2	ΔE_{int}	$\Delta E_{s,el}$	$\Delta E_{s,np}$	ΔE_r
TriMe	F1	8.9786	8.9782	8.9784	-64.5	-64.6	21.3	22.3	0.00	0.00	0.00	0.00
	F2	13.216	11.669	12.443	-62.5	17.6	25.2	40.3	0.61	1.81	1.04	3.45
	F3	13.843	13.839	13.841	15.3	15.6	30.5	57.7	0.49	2.59	2.04	5.11
TriH	F1	9.2319	9.2301	9.231	-62.9	-63.1	14.5	18.6	0.00	0.00	0.00	0.00
	F2	13.302	12.189	12.745	-62.5	63.0	19.4	9.4	-0.72	-0.13	0.49	-0.35
	F3	9.7213	9.7263	9.7238	62.9	62.9	24.6	0.2	0.47	-1.54	0.50	-0.57

CONFORMATIONAL PREFERENCES IN PENTAMERS AND THEIR COMPLEXES

Computational Methods. All the calculations were performed in Orca 4.2.1. Due to the size of studied systems, the **P1** and **P2** pentamers had to be simplified by removing the solubilizing groups attached to the aromatic walls. This simplification is indicated by an apostrophe in the pentamer labels. The **P1'** and **P2'** hosts were built in three conformational states on the inverted glycoluril unit, similar to **TriMe**. Host geometries were optimized on the B97-3c level of theory in the SMD implicit water solvent. For each conformational state, we performed four optimization attempts starting from different geometries. In majority cases, they finished in the same lowest-energy geometry, which is reported here. In other cases, we obtained more collapsed structures, probably due to the use of too disturbed initial structures. These collapsed structures showed better stabilization due to an increased number of internal contacts, but total stabilization was worst because of destabilizing solvent contribution.

Complexes were prepared by putting the guest **II-8** into the cleft or cavity of the pentamers. The position of the guest was preoptimized with the frozen host geometry, followed by the full geometry optimization of the entire complex. The final optimization was performed on the B97-3c level of theory in the SMD implicit water solvent. Obtained geometries are shown in Figures II-S103, II-S104, II-S105, and II-S106**.**

Due to numerical problems with the solvent cavity definition, we increased the solvent probe radius to 1.5 Å (standard value is 1.3 Å) and the ndiv parameter to 6 (default value is 5). In the case of the host/guest complexes with the host in the F1 and F2 conformations, another problem appeared. We detected spurious surface points at the interface between the guest and host in the structure interior. Apparently, this was an artifact because there was not enough room for any water molecule. We removed these points by increasing the radii of atoms of the guest 8, which lay at the host/guest interface. The outcome was the removal of spurious points with a minimal impact on the shape of the molecular surface.

PBE0-D3BJ/def2-TZVPP and PBE0-D3BJ-SMD/def2-TZVPP energies were calculated using RIJCOSX approximation with GridX6. Obtained total energies are summarized in Table II-S14.

Table II-S14. Absolute energies of **P1'**, **P1'·II-8**, **P2'**, and **P2'·II-8** calculated on geometries optimized at the B97-3c level of theory and in the SMD implicit water solvent. E_{CDS} is the non-polar only contribution to the SMD solvation energy. Optimized geometries are available in an XYZ format in the attached zip archive. All energies are in atomic units.

System	conf	B97-3c-SMD	PBE0-D3BJ	PBE0-D3BJ-SMD	E_{CDS}
P1'	F1	-3783.828906	-3782.828791	-3782.968361	0.018584
	F2	-3783.823372	-3782.828349	-3782.963495	0.018428
	F3	-3783.820093	-3782.829148	-3782.961969	0.016883
P1'·8	F1	-4358.480223	-4357.133212	-4357.447812	0.021872
	F2	-4358.476086	-4357.148151	-4357.445621	0.021793
	F3	-4358.480404	-4357.182587	-4357.450192	0.021129
P2'	F1	-4090.969915	-4089.880899	-4090.022129	0.020582
	F2	-4090.966275	-4089.882202	-4090.019312	0.020442
	F3	-4090.970932	-4089.893372	-4090.025860	0.019217
P2'·8	F1	-4665.628232	-4664.194506	-4664.507495	0.024166
	F2	-4665.621155	-4664.211356	-4664.502744	0.022523
	F3	-4665.622649	-4664.247303	-4664.505332	0.022518

Results and Discussion. We employed simplified models of pentamers **P1** and **P2**, in which we removed the solubilizing groups from the aromatic walls. This simplification eliminated problematic conformational flexibility of aliphatic chains in the solubilizing groups and avoided the presence of negative charge (-4), which could be problematic for reliable DFT quantum chemical calculations. Each simplified pentamer, **P1'** and **P2'**, was modeled in three conformational states (F1, F2, and F3), whose structural features were kept the same as in **TriMe** (see ϕ_1 and ϕ_2 in Table II-S15).

Geometries optimized in implicit water (Figures II-S103 and II-S104) showed different shapes, which can implicate different binding abilities. The conformer F1 showed two possible binding sites, each formed by an aromatic wall, concave faces of the first(five) and second(fourth) glycoluril unit, and the convex side of the central unit containing inverted glycoluril. In F2, one such binding site was closed due to conformation change, providing only one binding site. No binding site or cavity was found in F3.

Table II-S15. Central part distortions quantified by dihedral angles ϕ_1, ϕ_2, τ_1, and τ_2. Relative conformer stability (ΔE_r) and its decomposition into the internal energy (ΔE_{int}), and electrostatic ($\Delta E_{s,el}$) and non-polar ($\Delta E_{s,np}$) components of the solvation energy obtained at PBE0-D3BJ-SMD/def2-TZVPP//B97-3c-SMD level of theory. All energies are in kcal mol^{-1}, dihedral angles are in degrees.

System	conf	ϕ_1	ϕ_2	τ_1	τ_2	ΔE_{int}	$\Delta E_{s,el}$	$\Delta E_{s,np}$	ΔE_r
P1'	F1	-65.4	-65.4	-20.4	-20.9	0.00	0.00	0.00	0.00
	F2	-63.9*	50.4*	-24.7	-22.0	0.28	2.87	-0.10	3.05
	F3	50.8	55.1	-24.8	-13.6	-0.22	5.30	-1.07	4.01
P2'	F1	-64.8	-65.0	-20.9	-21.5	0.00	0.00	0.00	0.00
	F2	50.1	-63.6	-24.9	-22.0	-0.82	2.67	-0.09	1.77
	F3	50.2	43.6	-26.1	-17.4	-7.83	6.34	-0.86	-2.34
P1'·8	F1	-65.0	-64.8	-21.4	-21.3	0.00	0.00	0.00	0.00
	F2	-57.8*	51.1*	-27.0	-26.7	-9.37	10.80	-0.05	1.37
	F3	49.7	49.7	-25.7	-16.9	-30.98	29.96	-0.47	-1.49
P2'·8	F1	-64.5	-62.8	-21.7	-23.5	0.00	0.00	0.00	0.00
	F2	54.9	-59.7	-25.2	-21.4	-10.57	14.59	-1.03	2.98
	F3	55.5	52.8	-32.1	-26.8	-33.13	35.52	-1.03	1.36

*) these structures are shown as mirrored structures in Figures II-S103 and II-S105 to keep the same perception with **P2'** and **P2'·II-8**

The relative conformer stabilities (Table II-S15) revealed that the most stable conformer is F1 for **P1'** and F3 for **P2'**. The opposite behavior is most likely caused by increased π–π stacking and CH-π interactions in the F3 conformation of **P2'** (two aromatic rings per wall) in comparison to **P1'** (one aromatic ring per wall). To critically assessed obtained results, we must mention two contributions, which are unavailable in our analysis. The first is the entropy. It can be expected that F3 will have lower entropy than F1 because its compact structure will limit motions of aromatic walls (see dynamical behavior of aromatic walls in **P2·P2** dimer, Figure II-S107). This effect will make the F3 conformer more unstable than F1. Secondly, some destabilizations can be expected when negatively charged solubilizing groups will approach each other, which can happen in F3 of the non-simplified pentamers.

Further, we took optimized structures of the pentamers and use them for modeling of complexes with the host **II-8** (dimethyl viologen). In the case of F3, we inserted the guest **II-8** into an artificially created cavity. Obtained structures fully optimized in implicit water are summarized in Figures II-S105 and II-S106. In F1 and F2, the guest was located in the pocket. In the case of F3, aromatic walls were reorganized to maximize contact with the guest. As a result, they do not stack to each other anymore. Since this situation cannot happen in the pentamers containing solubilizing groups, it can be expected that obtained complexes in the F3 conformational state will not fully represent the real situation.

Relative stabilities of pentamer conformers in the complexes (Table II-S15) revealed that the most stable conformer is F3 for of **P1'·II-8** and F1 for **P2'·II-8**. This indicates that the preference for conformational states can change during the binding. Similar to the free hosts, two contributions were not included in our analysis, the entropy and solubilizing groups, which will have most likely a destabilizing effect on the complexes in the F3 conformational state for the same reasons as discussed previously.

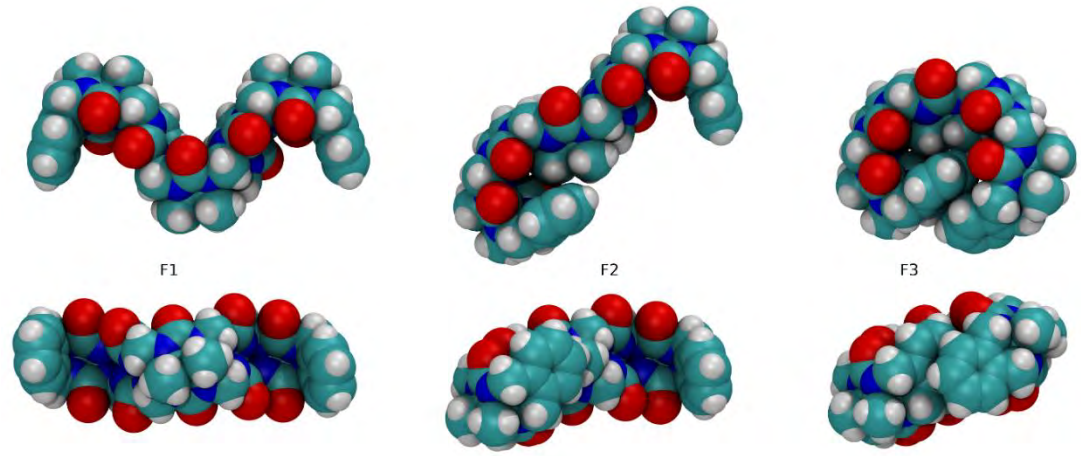

Figure II-S103. Top and front views of F1, F2, and F3 conformer geometries of **P1'** optimized at the B97-3c level of theory in the SMD implicit water solvent.

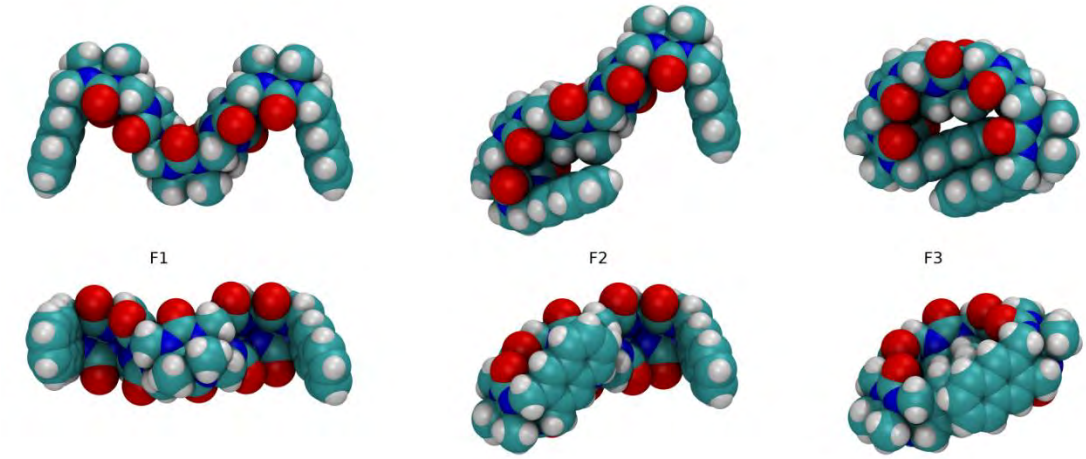

Figure II-S104. Top and front views of F1, F2, and F3 conformer geometries of **P2'** optimized at the B97-3c level of theory in the SMD implicit water solvent.

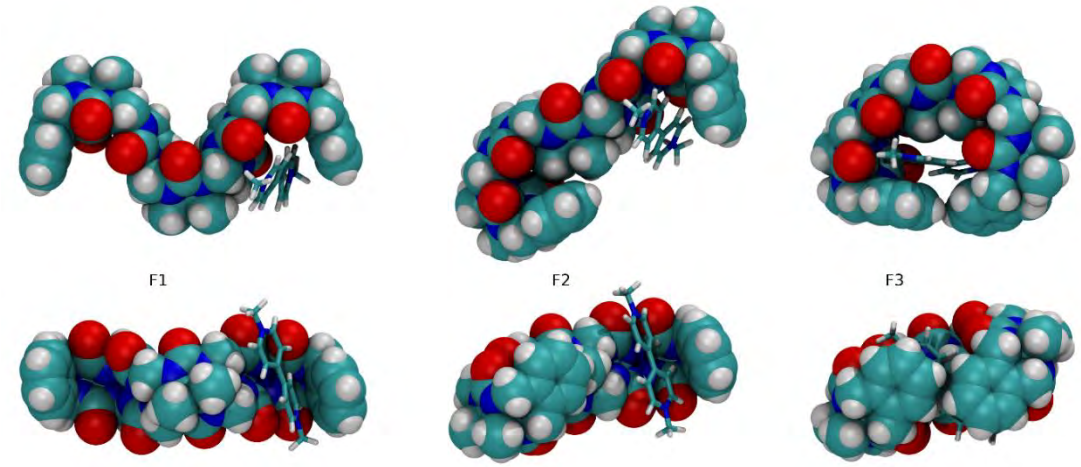

Figure II-S105. Top and front views of **P1'·II-8** complexes optimized at the B97-3c level of theory in the SMD implicit water solvent. Three variants correspond to the host in F1, F2, and F3 conformer geometries (shown as a vdW model). The guest is shown in a stick model.

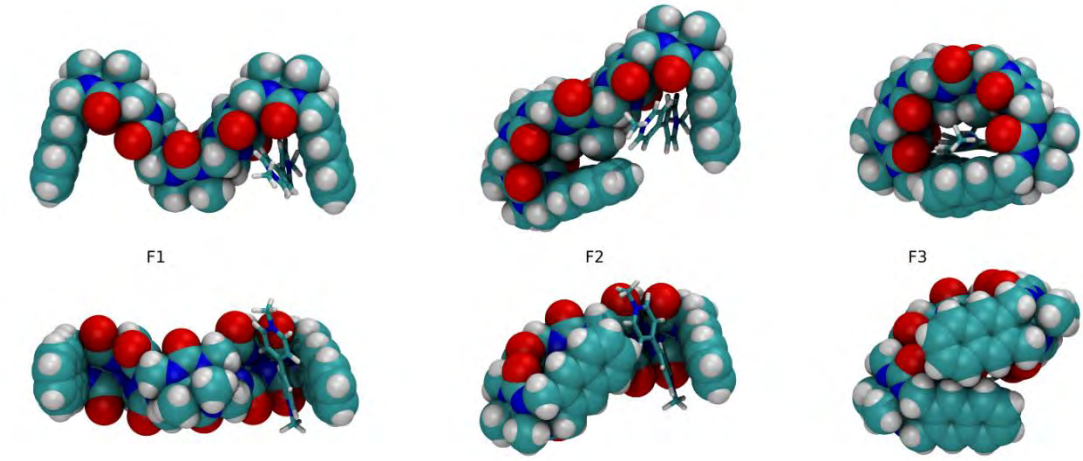

Figure II-S106. Top and front views of **P2'·II-8** complexes optimized at the B97-3c level of theory in the SMD implicit water solvent. Three variants correspond to the host in F1, F2, and F3 conformer geometries (shown as a vdW model). The guest is shown in a stick model.

DIMER OF PENTAMER P2

Computational Methods. The model of the **P2·P2** dimer was built *in silico* from two structures of **P2** in either F1 or F2 conformational state. The **P2** pentamer was described by the GAFF[12] force field. Its partial atomic charges were calculated by RESP procedure[19] employing electrostatic potential. The electrostatic potential was calculated at HF/6-31G* quantum chemical level of theory in Gaussian 16[6] on the geometry of **P2** optimized at the RI-TPSS-D3BJ/def2-TZVPP level of theory[3,14,20] in Turbomole 7.3.[21]

Explicit solvent molecular dynamics simulations were run under the periodic boundary conditions employing the truncated octahedral box filled by the TIP3P water.[22] To maintain electroneutrality, 8 sodium[23] cations were added. Long-range interactions were treated with the particle-mesh Ewald method,[24] with a direct summation cutoff set to 8.0 Å. The same cutoff was used for Lennard-Jones interactions. All molecular dynamics simulations were done in the Amber 16 package.[1]

Each system was equilibrated by geometry optimization followed by heating (100 ps) to 300 K at a constant volume employing the Langevin thermostat with a collision frequency (γ) of 1.0 ps^{-1}. Finally, the proper density was adjusted by short simulation (500 ps) at the constant temperature (the same thermostat as in the previous step) and pressure maintained by the barostat set to 100 kPa with a feedback time constant (t_p) of 1.2 ps.
After equilibration, unbiased MD simulations were performed at a constant temperature of 300 K (Berendsen thermostat, t_T=5 ps) and a pressure of 100 kPa (weak coupling barostat, t_p=6 ps). Unbiased simulations were run on GPU accelerators[25] and were 1 μs long each. Equations of motions were integrated with a time step of 2 fs, and bonds containing hydrogen atoms were constrained by SHAKE.[26]

Results and Discussion. First, we built a dimer from two **P2** pentamers in the F1 conformational states. Dimer was formed by inserting two aromatic walls mutually into two binding pockets of the other monomer (Figure II-S107AB). We found that such an arrangement is stable during 1 μs long molecular dynamics simulation performed in the explicit water. Overlap of snapshots from the trajectory revealed that the unbound aromatic walls are flanking more than those which are at the interface between monomers (Figure II-S107CDE).
We also built a dimer from the pentamer in the F2 conformational state (Figure II-S108AB). However, both monomers underwent a conformational change into F1, each at a different time (Figure II-S108C). While this agrees with the calculated conformer preferences of F1 (0.0 kcal mol-1) and F2 (+1.8 kcal mol-1) (Table S15), in this particular case, the change can also be forced by a deficiency of the employed GAFF force field, which significantly overestimates F1 over F2 and F3 (see Benchmark study).

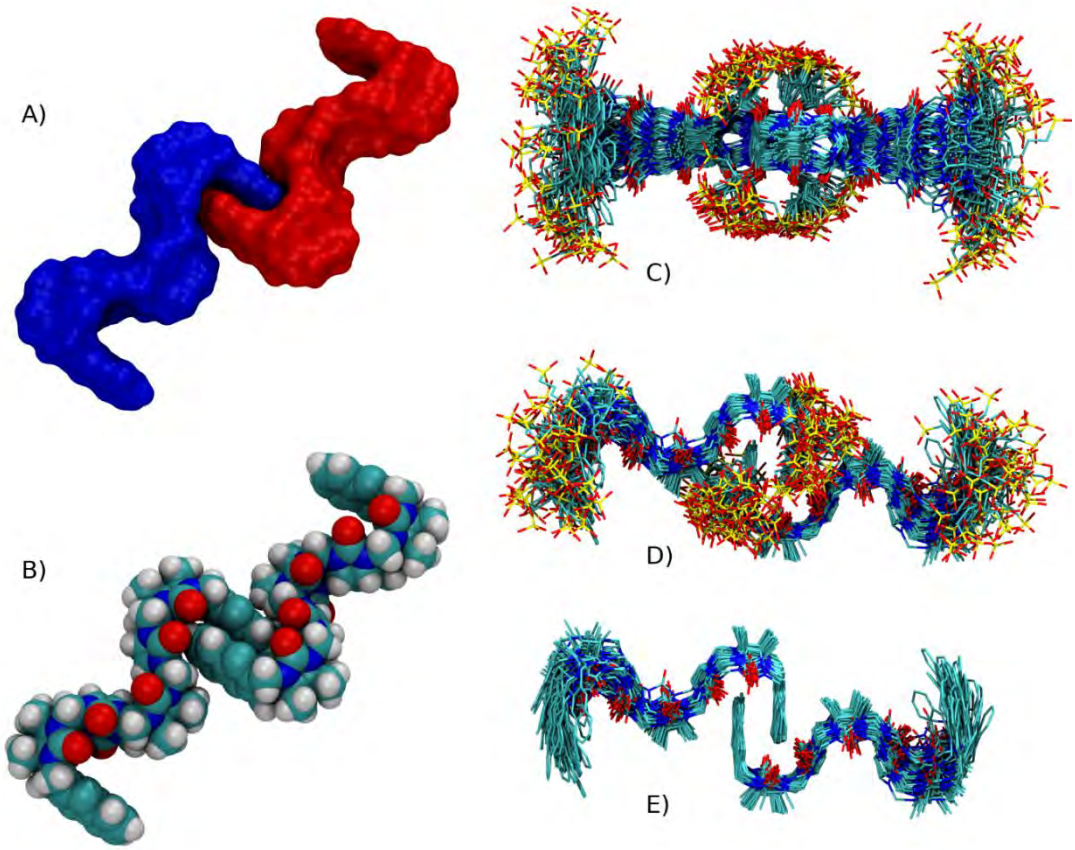

Figure II-S107. Structure of the **P2**·**P2** dimer with monomers in the F1 conformational state. A) and B) two different representations of a selected structure, solubilizing groups were omitted for clarity. C) side and D) top views of overlapped snapshots from 1 μs long molecular dynamics simulations. E) the same as D), but hydrogen atoms and solubilizing groups were omitted for clarity.

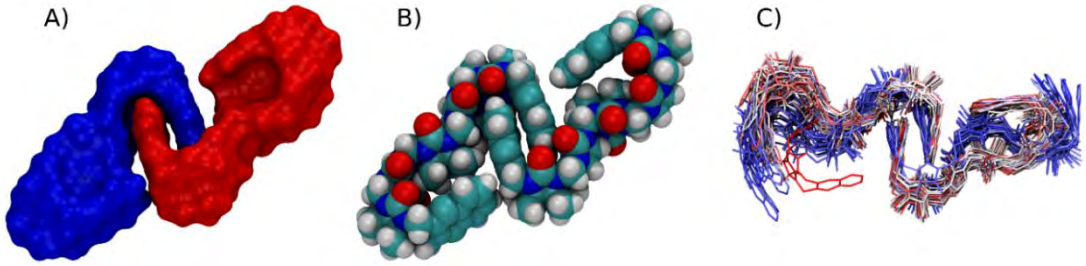

Figure II-S108. Structure of the **P2**·**P2** dimer with monomers in the F2 conformational state. A) and B) two different representations of the initial structure, solubilizing groups were omitted for clarity. C) top view of overlapped snapshots from 1 μs long molecular dynamics simulations. Time is encoded by color from red (beginning) to blue (end). Hydrogen atoms and solubilizing groups were omitted for clarity.

REFERENCES

(1) Case, D. A.; Babin, V.; Berryman, J. T.; Betz, R. M.; Cai, Q.; Cerutti, D. S.; Cheatham III, T. E.; Darden, T. A.; Duke, R. E.; Gohlke, H.; Goetz, A. W.; Gusarov, S.; Homeyer, N.; Janowski, P.; Kaus, J.; Kolossváry, I.; Kovalenko, A.; Lee, T. S.; LeGrand, S.; Luchko, T.; Luo, R.; Madej, B.; Merz, K. M.; Paesani, F.; Roe, D. R.; Roitberg, A.; Sagui, C.; Salomon-Ferrer, R.; Seabra, G.; Simmerling, C. L.; Smith, W.; Swails, J.; Walker, R. C.; Wang, J.; Wolf, R. M.; Wu, X.; Kollman, P. A. *AMBER 16*; University of California: San Francisco, 2016.

(2) Becke, A. Density-Functional Thermochemistry. 3. The Role of Exact Exchange. *J. Chem. Phys.* **1993**, *98* , 5648–5652.

(3) Weigend, F.; Ahlrichs, R. Balanced Basis Sets of Split Valence, Triple Zeta Valence and Quadruple Zeta Valence Quality for H to Rn: Design and Assessment of Accuracy. *Phys. Chem. Chem. Phys.* **2005**, *7*, 3297–3305. https://doi.org/10.1039/b508541a.

(4) Adamo, C.; Barone, V. Toward Reliable Density Functional Methods without Adjustable Parameters: The PBE0 Model. *J. Chem. Phys.* **1999**, *110*, 6158–6170. https://doi.org/10.1063/1.478522.

(5) Stewart, J. J. P. Optimization of Parameters for Semiempirical Methods VI: More Modifications to the NDDO Approximations and Re-Optimization of Parameters. *J. Mol. Model.* **2013**, *19*, 1–32. https://doi.org/10.1007/s00894-012-1667-x.

(6) Frisch, M. J.; Trucks, G. W.; Schlegel, H. B.; Scuseria, G. E.; Robb, M. A.; Cheeseman, J. R.; Scalmani, G.; Barone, V.; Petersson, G. A.; Nakatsuji, H.; Li, X.; Caricato, M.; Marenich, A. V.; Bloino, J.; Janesko, B. G.; Gomperts, R.; Mennucci, B.; Hratchian, H. P.; Ortiz, J. V.; Izmaylov, A. F.; Sonnenberg, J. L.; Williams-Young, D.; Ding, F.; Lipparini, F.; Egidi, F.; Goings, J.; Peng, B.; Petrone, A.; Henderson, T.; Ranasinghe, D.; Zakrzewski, V. G.; Gao, J.; Rega, N.; Zheng, G.; Liang, W.; Hada, M.; Ehara, M.; Toyota, K.; Fukuda, R.; Hasegawa, J.; Ishida, M.; Nakajima, T.; Honda, Y.; Kitao, O.; Nakai, H.; Vreven, T.; Throssell, K.; Montgomery, J. A., Jr.; Peralta, J. E.; Ogliaro, F.; Bearpark, M. J.; Heyd, J. J.; Brothers, E. N.; Kudin, K. N.; Staroverov, V. N.; Keith, T. A.; Kobayashi, R.; Normand, J.; Raghavachari, K.; Rendell, A. P.; Burant, J. C.; Iyengar, S. S.; Tomasi, J.; Cossi, M.; Millam, J. M.; Klene, M.; Adamo, C.; Cammi, R.; Ochterski, J. W.; Martin, R. L.; Morokuma, K.; Farkas, O.; Foresman, J. B.; Fox, D. J. *Gaussian 16, Revision B.01*; Gaussian Inc.: Wallingford CT, 2016.

(7) Perdew, J. P.; Burke, K.; Ernzerhof, M. Generalized Gradient Approximation Made Simple. *Phys. Rev. Lett.* **1996**, *77*, 3865–3868. https://doi.org/10.1103/PhysRevLett.77.3865.

(8) Grimme, S.; Brandenburg, J. G.; Bannwarth, C.; Hansen, A. Consistent Structures and Interactions by Density Functional Theory with Small Atomic Orbital Basis Sets. *J. Chem. Phys.* **2015**, *143*, 054107. https://doi.org/10.1063/1.4927476.

(9) Brandenburg, J. G.; Bannwarth, C.; Hansen, A.; Grimme, S. B97-3c: A Revised Low-Cost Variant of the B97-D Density Functional Method. *J. Chem. Phys.* **2018**, *148*, 064104. https://doi.org/10.1063/1.5012601.

(10) Sure, R.; Grimme, S. Corrected Small Basis Set Hartree-Fock Method for Large Systems. *J. Comput. Chem.* **2013**, *34*, 1672–1685. https://doi.org/10.1002/jcc.23317.

(11) Neese, F. The ORCA Program System. *Wiley Interdiscip. Rev.-Comput. Mol. Sci.* **2012**, *2*, 73–78. https://doi.org/10.1002/wcms.81.

(12) Wang, J. M.; Wolf, R. M.; Caldwell, J. W.; Kollman, P. A.; Case, D. A. Development and Testing of a General Amber Force Field. *J. Comput. Chem.* **2004**, *25*, 1157–1174. https://doi.org/10.1002/jcc.20035.

(13) Grimme, S.; Antony, J.; Ehrlich, S.; Krieg, H. A Consistent and Accurate Ab Initio Parametrization of Density Functional Dispersion Correction (DFT-D) for the 94 Elements H-Pu. *J. Chem. Phys.* **2010**, *132*, 154104. https://doi.org/10.1063/1.3382344.

(14) Grimme, S.; Ehrlich, S.; Goerigk, L. Effect of the Damping Function in Dispersion Corrected Density Functional Theory. *J. Comput. Chem.* **2011**, *32*, 1456–1465.

https://doi.org/10.1002/jcc.21759.
(15) Neese, F.; Valeev, E. F. Revisiting the Atomic Natural Orbital Approach for Basis Sets: Robust Systematic Basis Sets for Explicitly Correlated and Conventional Correlated Ab Initio Methods? *J. Chem. Theory Comput.* **2011**, *7*, 33–43. https://doi.org/10.1021/ct100396y.
(16) Goerigk, L.; Hansen, A.; Bauer, C.; Ehrlich, S.; Najibi, A.; Grimme, S. A Look at the Density Functional Theory Zoo with the Advanced GMTKN55 Database for General Main Group Thermochemistry, Kinetics and Noncovalent Interactions. *Phys. Chem. Chem. Phys.* **2017**, *19*, 32184–32215. https://doi.org/10.1039/C7CP04913G.
(17) Marenich, A. V.; Cramer, C. J.; Truhlar, D. G. Universal Solvation Model Based on Solute Electron Density and on a Continuum Model of the Solvent Defined by the Bulk Dielectric Constant and Atomic Surface Tensions. *J. Phys. Chem. B* **2009**, *113*, 6378–6396. https://doi.org/10.1021/jp810292n.
(18) Neese, F.; Wennmohs, F.; Hansen, A.; Becker, U. Efficient, Approximate and Parallel Hartree–Fock and Hybrid DFT Calculations. A 'Chain-of-Spheres' Algorithm for the Hartree–Fock Exchange. *Chem. Phys.* **2009**, *356*, 98–109. https://doi.org/10.1016/j.chemphys.2008.10.036.
(19) Bayly, C. I.; Cieplak, P.; Cornell, W. D.; Kollman, P. A. A Well-Behaved Electrostatic Potential Based Method Using Charge Restraints for Deriving Atomic Charges - the RESP Model. *J. Phys. Chem.* **1993**, *97*, 10269–10280. https://doi.org/10.1021/j100142a004.
(20) Tao, J. M.; Perdew, J. P.; Staroverov, V. N.; Scuseria, G. E. Climbing the Density Functional Ladder: Nonempirical Meta-Generalized Gradient Approximation Designed for Molecules and Solids. *Phys. Rev. Lett.* **2003**, *91*, 146401. https://doi.org/10.1103/PhysRevLett.91.146401.
(21) *TURBOMOLE V7.3*; a development of University of Karlsruhe and Forschungszentrum Karlsruhe GmbH, 1989-2007, TURBOMOLE GmbH, since 2007; available from http://www.turbomole.com., 2018.
(22) Jorgensen, W.; Chandrasekhar, J.; Madura, J.; Impey, R.; Klein, M. Comparison of Simple Potential Functions for Simulating Liquid Water. *J. Chem. Phys.* **1983**, *79*, 935, 926.
(23) Joung, I. S.; Cheatham, T. E. Determination of Alkali and Halide Monovalent Ion Parameters for Use in Explicitly Solvated Biomolecular Simulations. *J. Phys. Chem. B* **2008**, *112*, 9020–9041. https://doi.org/10.1021/jp8001614.
(24) Darden, T.; York, D.; Pedersen, L. Particle Mesh Ewald - an N.Log(N) Method for Ewald Sums in Large Systems. *J. Chem. Phys.* **1993**, *98*, 10089–10092. https://doi.org/10.1063/1.464397.
(25) Salomon-Ferrer, R.; Götz, A. W.; Poole, D.; Le Grand, S.; Walker, R. C. Routine Microsecond Molecular Dynamics Simulations with AMBER on GPUs. 2. Explicit Solvent Particle Mesh Ewald. *J. Chem. Theory Comput.* **2013**, *9*, 3878–3888. https://doi.org/10.1021/ct400314y.
(26) Ryckaert, J.; Ciccotti, G.; Berendsen, H. Numerical Integration of the Cartesian Equations of Motion of a System with Constraints: Molecular Dynamics of n-Alkanes. *J. Comput. Phys.* **1977**, *23*, 341, 327. https://doi.org/10.1016/0021-9991(77)90098-5.

Appendix 2

Self-Assembly of Cucurbit[7]uril Based Triangular [4]Molecular Necklaces and Their Fluoresecence Properties

Soumen K. Samanta, Kimberly G. Brady, Lyle Isaacs*

Department of Chemistry and Biochemistry, University of Maryland,

College Park, MD 20742, USA

Table of Contents **Pages**

* Email Address for Correspondence: LIsaacs@umd.edu

General Procedure

Starting materials were purchased from commercial suppliers and were used without further purification. Melting points were measured on a Meltemp apparatus in open capillary tubes and uncorrected. IR spectra were measured on a Thermo Nicolet NEXUS 670 FT/IR spectrometer by attenuated total reflectance (ATR) and are reported in cm^{-1}. NMR spectra were measured at 400, 500 or 600 MHz for ^{1}H and 100 and 125 MHz for ^{13}C. The solvent for NMR experiments was deuterated water (D_2O), deuterated chloroform ($CDCl_3$), or deuterated dimethyl sulfoxide (DMSO-d_6). Chemical shifts (δ) are referenced relative to the residual resonances for HOD (4.79 ppm), $CHCl_3$ (7.26 ppm for ^{1}H, 77.16 ppm for ^{13}C), DMSO-d_6 (2.50 ppm for ^{1}H, 39.51 ppm for ^{13}C). Mass spectrometry was performed using a JEOL AccuTOF electrospray instrument. Filtration was done with 25 mm syringe filter with 0.2 μm polyethersulfone membrane. CSI-MS was performed using Bruker 12T Apex IV FT-ICR-MS at the University of Maryland Baltimore County.

Synthetic Procedures and Characterisation Data

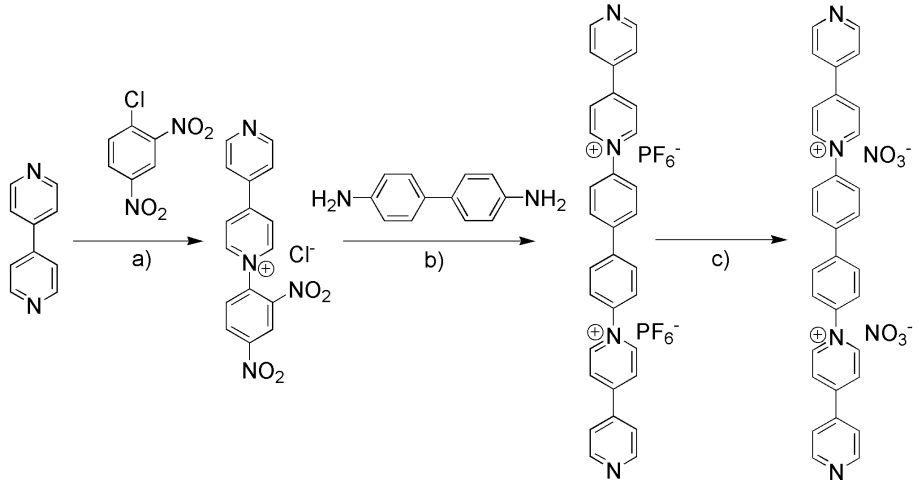

Scheme III-S1. Synthesis of compound **III-1**. Conditions: (a) Acetone, 70°C, 24 h, 80%. (b) DMSO, 100°C, 3 days, NH_4PF_6, 16%. (c) $(n\text{-}Bu)_4N^+Br^-$, CH_3CN, $AgNO_3$ in water, 40%.

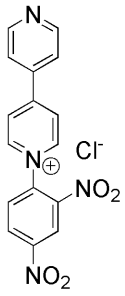

Compound III-2. 4,4′-bipyridine (1.00 g, 6.40 mmol) and 1-chloro-2,4-dinitrobenzene (5.20 g, 25.6 mmol) were dissolved in acetone (20 mL). The solution was heated to reflux for 24 h. During the course of the reaction pale grey precipitate was formed. After the reaction, the precipitate was collected by filtration and air dried. The precipitate was then triturated with *n*-pentane (50 mL). The precipitate was collected by filtration. Finally the precipitate was washed with chloroform (30 mL) by sonication. The product was collected by filtration and dried under vaccum to give compound **III-2** as grey solid. ^{1}H NMR of the compound matches with previously reported data.[1]

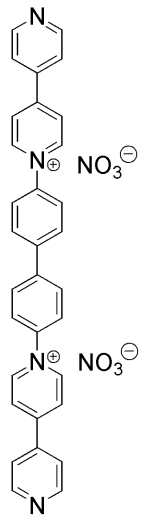

Compound III-1. 4,4′-benzidine (50.0 mg, 0.27 mmol) and compound **III-2** (243 mg, 0.81 mmol) were dissolved in DMSO (3.0 mL) and heated at 100 °C for 3d under N_2. The solvent was removed under reduced pressure to dryness. Residue was redissolved in water (5.0 mL) and to the solution, aqueous NH_4PF_6 (1.0 g in 1.0 mL H_2O) was added leading to yellow precipitation. The precipitate was collected by centrifugation and dried under vaccum. The solid was dissolved in acetone (5.0 mL) and loaded onto a SiO_2 column. Compound **III-1** was eluted using NH_4PF_6 (500 mg) in acetone (100 mL). After removing acetone, the solid was washed with water to remove excess NH_4PF_6. Then the solid was dissolved in acetonitrile (5.0 mL) and was treated with excess $(n\text{-Bu})_4N^+Br^-$ (1.0 g in 1.0 mL acetonitrile). Brown precipitate was collected by centrifugation and dried to afford compound [**III-1**•2Br]. Then [**III-1**•2Br] (76.0 mg) was dissolved in water and treated with aqueous $AgNO_3$ (42.0 mg). The solution was collected by filtration and water was evaporated to dryness to collect compound [**III-1**•2NO_3] (64 mg, 40%). MP > 300 °C. ^{1}H NMR (400 MHz, D_2O): 9.35 (d, J = 7.2 Hz, 4H), 8.91 (d, J = 5.2 Hz, 4H), 8.65 (d, J = 7.2 Hz, 4H), 8.22 (d, J = 5.2 Hz, 4H), 8.12 (d, J = 8.8 Hz, 4H), 7.96 (d, J = 8.8 Hz, 4H) ppm. ^{13}C NMR (150 MHz, D_2O, dioxane as internal refernce): 150.2, 145.3, 142.7, 130.0, 126.8, 126.7, 125.4, 124.8, 123.5, 122.9 ppm. HR-MS: m/z 232.1011 $(M\text{-}2Br)^{2+}$, calcd. for $[C_{32}H_{24}N_4]^{2+}$, 232.1005).

Mixture of triangle III-3 and square III-4: Compound **III-1** (3.9 mg, 6.63 μmol) was added to $Pd(en)(NO_3)_2$ (1.92 mg, 6.63 μmol) solution in D_2O (1.2 mL) and the resulting solution was heated at 100 °C for 24 h. Clear solution was subjected for ^{1}H NMR measurement which reveals the formation of both triangle **III-3** and square **III-4**. ^{1}H NMR (600 MHz, D_2O) trimer **III-3** = 9.39 (d, J = 6.9 Hz, 12 H), 9.00 (d, J = 6.7 Hz, 12 H), 8.66 (d, J = 6.9 Hz, 12 H), 8.23 (d, J = 6.7 Hz, 12 H), 8.15 (d, J = 8.7 Hz, 12 H), 7.98 (d, J = 8.7 Hz, 12 H) ppm. Square **III-4** = 9.37 (d, J = 7.2 Hz, 16 H), 9.11 (d, J = 6.8 Hz, 16 H), 8.63 (d, J = 7.2 Hz, 16 H), 8.21 (d, J = 6.8 Hz, 16 H), 8.13 (d, J = 8.5 Hz, 16 H), 7.96 (d, J = 8.5 Hz, 16 H) ppm.

Mixture of triangle III-5 and square III-6: Compound **III-1** (3.3 mg, 5.60 μmol) was added to 1M $NaNO_3$ solution of $Pt(en)(NO_3)_2$ (2.12 mg, 5.60 μmol) solution in D_2O (1.0 mL) and the resulting solution was heated at 100 °C for 7 days. The resulting solution was filtered. The solution was collected and characterised by ^1H NMR exhibiting the formation of both triangle **III-5** and square **III-6**.

Triangle III-3. Compound **III-1** (1.50 mg, 2.55 μmol) was added to $Pd(en)(NO_3)_2$ (0.74 mg, 2.55 μmol) solution in D_2O (1 mL) and the resulting solution was heated at 100 °C for 24 h. Clear solution was subjected to ^1H NMR measurement exhibiting the formation of triangle **III-3**. MP > 300 °C, ^1H NMR (400 MHz, D_2O) 9.39 (d, J = 6.9 Hz, 12H), 9.00 (d, J = 6.7 Hz, 12H), 8.66 (d, J = 6.9 Hz, 12H), 8.23 (d, J = 6.7 Hz, 12H), 8.15 (d, J = 8.8 Hz, 12H), 7.99 (d, J = 8.8 Hz, 12H), 2.78 (s, 12H). ^{13}C NMR (150 MHz, D_2O, dioxane as internal refernce): 152.7, 143.1, 140.7, 131.2, 130.1, 129.3, 128.2, 127.1, 125.5, 124.3, 37.2 ppm. MS: (CSI, positive). (*m*/*z*): 466.2 ($[Pd_3$**III-1**$_3](NO_3)_7^{5+}$), 615.2 ($[Pd_3$ **III-1**$_3](NO_3)_8$ + $4H_2O]^{4+}$) and 815.8 ($[Pd_3$ **III-1**$_3](NO_3)_9^{3+}$).

Triangle III-5. Compound **III-1** (1.35 mg, 2.30 μmol) was added to 1M $NaNO_3$ solution of $Pt(en)(NO_3)_2$ (0.872 mg, 2.30 μmol) solution in D_2O (1.0 mL) and the resulting solution was heated at 100 °C for 7 days. The resulting solution was filtered. The solution was collected and characterised by ^1H NMR exhibiting the formation of triangle **III-5**. MP > 300 °C, ^1H NMR (600 MHz, D_2O) 9.49 (d, ^3J = 6.2 Hz, 12H), 9.22 (d, ^3J = 5.6 Hz, 12H), 8.79 (d, ^3J = 6.2 Hz, 12H), 8.31 (d, ^3J = 5.6 Hz, 12H), 8.26 (d, ^3J = 8.2 Hz, 12H), 8.11 (d, ^3J = 8.2 Hz, 12H) ppm. ^{13}C NMR (150 MHz, D_2O, dioxane as internal refernce): 150.1, 147.3, 143.0, 134.0, 128.2, 126.6, 124.8, 123.1, 122.3, 119.9, 45.0. We did not get ESI-Ms of triangle **III-5** even after removal of $NaNO_3$ by GPC (Sephadex G-25). ESI-Ms signal was suppressed by $NaNO_3$.

[4]MN III-7: Equimolar mixture of compound **III-1** (0.35 mg, 0.60 µmol) and CB7 (0.70 mg, 0.60 µmol) was mixed with $Pd(en)(NO_3)_2$ (0.174 mg, 0.60 µmol) solution in D_2O (400 µL) and the resulting solution was heated at 100 °C for 24h to give **III-7**. MP > 300 °C, ^{1}H NMR (400 MHz, D_2O), 9.37 (d, *J* = 7.0 Hz, 12H), 8.84 (brs, 12H), 8.64 (d, *J* = 6.9 Hz, 12H), 8.09 (d, *J* = 6.2 Hz, 12H), 7.60 (d, *J* = 8.6 Hz, 12H), 7.13 (d, *J* = 8.6 Hz, 12H), 5.68 (d, *J* = 15.4 Hz, 42H), 5.45 (s, 42H), 4.16 (d, *J* = 15.4 Hz, 42H), 2.73 (s, 12H) ppm. ^{13}C NMR (150 MHz, D_2O, dioxane as internal refernce): MS: (CSI, positive). *m*/*z* = 813.7 $[Pd_3(\textbf{III-1}\bullet CB7)_3](NO_3)_5^{7+}$.

[4]MN III-8: Equimolar mixture of compound **III-1** (2.20 mg, 3.50 µmol) and CB7 (4.07 mg, 3.50 µmol) was added to 1M $NaNO_3$ solution of $Pt(en)(NO_3)_2$ (1.33 mg, 3.50 µmol) solution in D_2O (1.75 mL) and the resulting solution was heated at 100 °C for 7 days. The resulting solution was filtered. The solution was collected and characterised by ^{1}H NMR exhibiting the formation of [4]MN **III-8**. MP > 300 °C, ^{1}H NMR (600 MHz, D_2O) 9.40 (brs, 12H), 8.86 (brs, 12H), 8.66 (brs, 12H), 8.09 (brs, 12H), 7.68 (brs, 12H), 7.22 (brs, 12H), 5.71 (d, 42H), 5.51 (s, 42H), 4.21 (s, 42H), 3.00 (s, 12H) ppm. MS (Conc. of $NaNO_3$ was reduced by GPC (Sephadex G-25) before measuring): (CSI, positive). *m*/*z* = 781.4 $([Pt_3(\textbf{III-1}\bullet CB7)_3](NO_3)_8 + 4Na)^{8+}$, 958.3 $([Pt_3(\textbf{III-1}\bullet CB7)_3](NO_3)_{11} + 6Na + 13H_2O)^{7+}$, 1016.2 $([Pt_3(\textbf{III-1}\bullet CB7)_3](NO_3)_7 + 1Na)^{6+}$, 1132.2 $([Pt_3(\textbf{III-1}\bullet CB7)_3](NO_3)_{11} + 5Na + 19H_2O)^{6+}$, 1308.0 $([Pt_3(\textbf{III-1}\bullet CB7)_3](NO_3)_{11} + 4Na + 7H_2O)^{5+}$, 1657.8 $([Pt_3(\textbf{III-1}\bullet CB7)_3](NO_3)_{11} + 3Na + 13H_2O)^{4+}$, 2185.4 $([Pt_3(\textbf{III-1}\bullet CB7)_3](NO_3)_{11} + 2Na + 10H_2O)^{5+}$.

Pseudo [4]MN III-9: Equimolar mixture of compound **III-1** (2.1 mg, 3.57 µmol) and **M2** (5.86 mg, 3.57 µmol) was mixed with $Pd(en)(NO_3)_2$ (1.04 mg, 3.57 µmol) solution in D_2O (2.0 mL) and the resulting solution was heated at 100 °C for 24h to give **III-9**. MP> 300 °C, ^{1}H NMR (400 MHz, D_2O) 8.93 (d, *J* = 5.5 Hz, 12H), 8.71 (brs, 12H), 8.46 (brs, 12H), 8.20 (d, *J* = 5.7 Hz, 12H), 7. 75 (d, m, 12H), 7.72 (d, m, 12H), 7.02 (d, *J* = 8.0 Hz, 12H), 6.89 (d, *J* = 8.0 Hz, 12H), 5.57 (d, *J* = 15.6 Hz, 12H), 5.50 (d, *J* = 16.3 Hz, 12H), 5.30 (d, *J* = 9.2 Hz, 3H),5.21 (d, *J* = 14.8 Hz, 3H), 5.09 (d, *J* =9.4 Hz, 3H), 4.56 (d, *J* = 16.6 Hz, 12H), 4.24 (d, *J* = 15.6 Hz, 12H), 4.08 (brs, 6H), 3.75 (d, *J* = 15.6 Hz, 3H), 3.65 (brs, 6H),

3.14 (m, 24H), 2.78 (s, 12H), 2.21 (brs, 24H), 2.05 (brs, 24H), 1.88 (d, *J* = 17.7 Hz, 36H) ppm.

Pseudo [4]MN III-10: Equimolar mixture of compound **1** (2.5 mg, 4.25 μmol) and **M2** (6.98 mg, 4.25 μmol) was mixed with 1M $NaNO_3$ solution of $Pt(en)(NO_3)_2$ (1.61 mg, 4.25 μmol) solution in D_2O (2.0 mL) and the resulting solution was heated at 100 °C for 24h to give **III-10** as brown solid. MP > 300 °C, ^{1}H NMR (400 MHz, D_2O): 9.20 (brs, 12H), 9.12 (brs, 12H), 8.73 (brs, 12H), 8.32 (brs, 12H), 7.79 (brs, 24H), 7.25 (brs, 12H), 6.99 (brs, 12H), 5.64 (d, *J* = 14.4 Hz, 12H), 5.54 (d, *J* = 14.4 Hz, 12H), 5.39 (d, *J* = 10.8 Hz, 3H), 5.27 (d, *J* = 16.1 Hz, 3H), 5.18 (d, *J* = 7.2 Hz, 3H), 4.32 (d, *J* = 17.9 Hz, 12H), 4.12 (brs, 12H), 3.85 (d, *J* = 16.1 Hz, 6H), 3.69 (m, 3H), 3.19 (m, 6H), 2.93 (brs, 12H), 2.77 (brs, 24H), 2.16 (d, *J* = 5.08 Hz, 48H), 1.95 (d, *J* = 10.2 Hz, 36H) ppm.

References

1) Yamaguchi, I.; Higashi, H.; Shigesue, S.; Shingai, S.; Sato, M. *Tetrahedron Lett.* **2007**, *48*, 7778-7781.

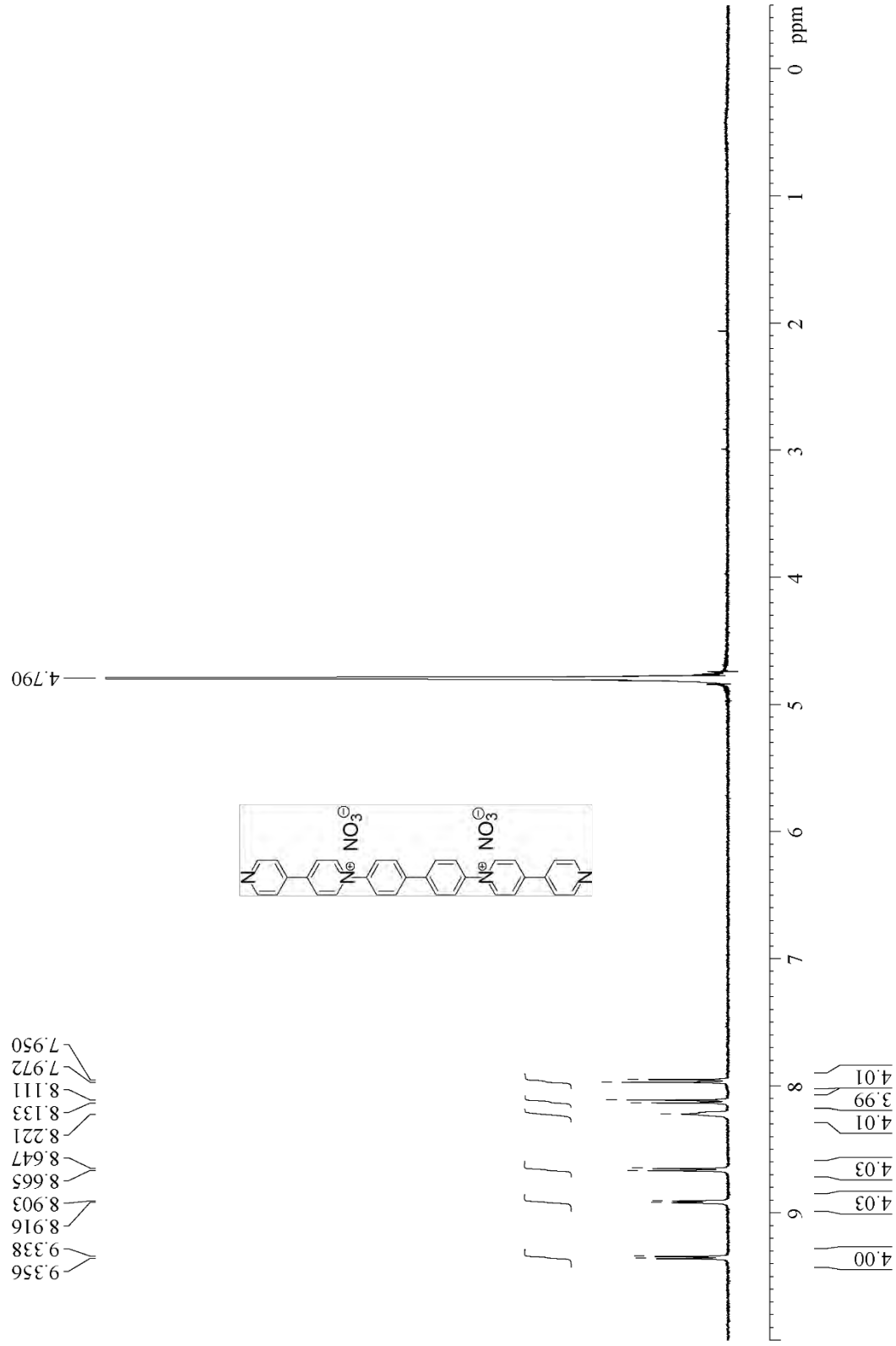

Figure III-S1. ^{1}H NMR recorded (D_2O, 600 MHz, RT) for **III-1**.

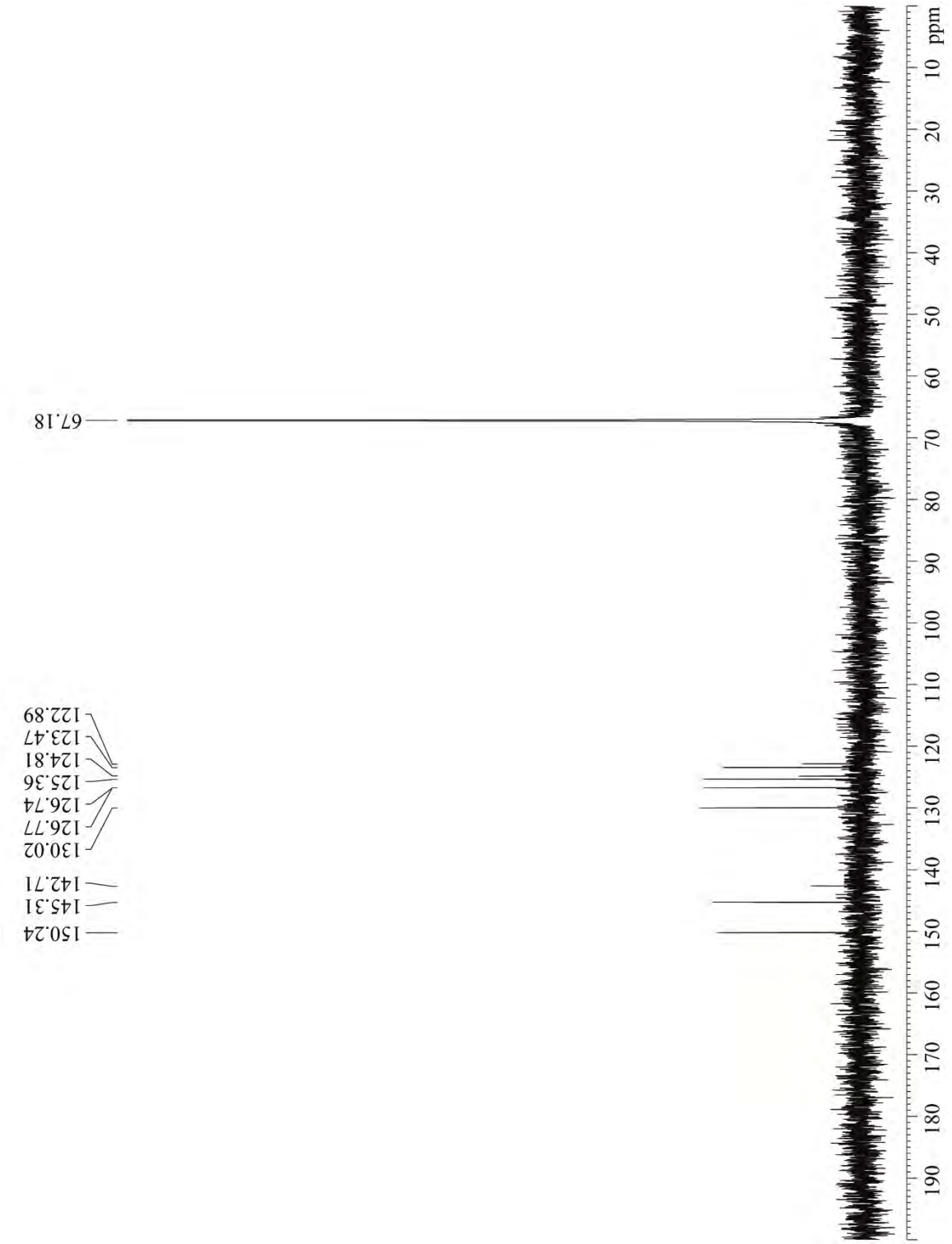

Figure III-S2. ^{13}C NMR recorded (D_2O, 125 MHz, RT) for **III-1**. Internal reference = dioxane (*).

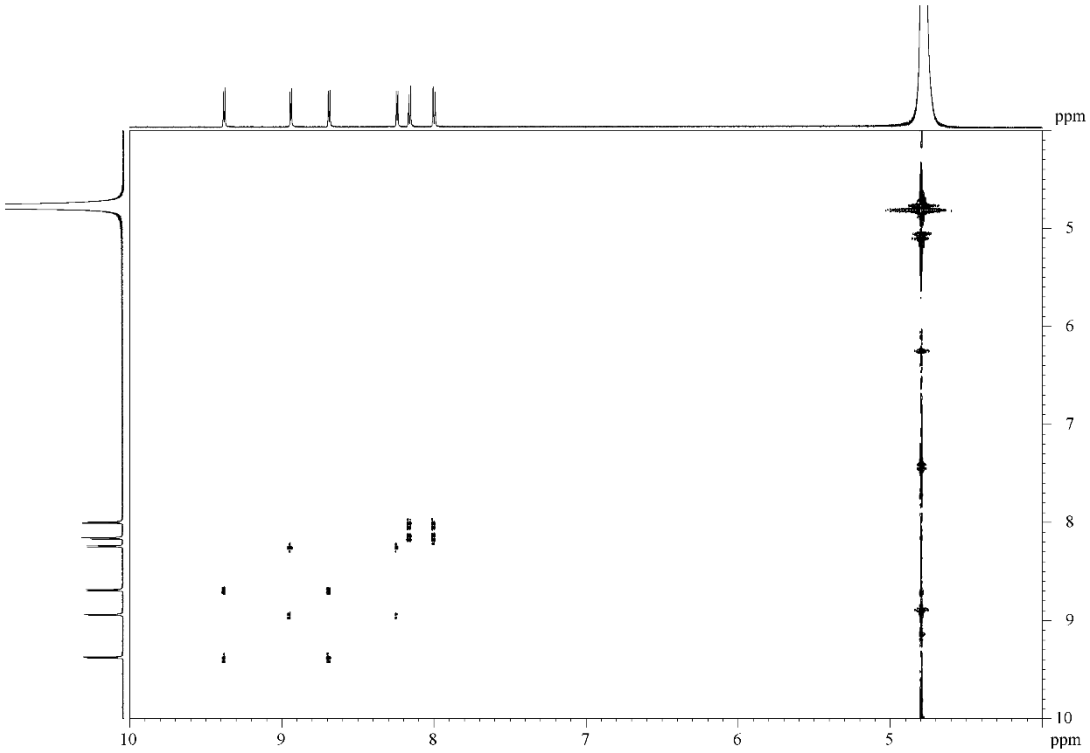

Figure III-S3. DQ-COSY NMR recorded (D_2O, 600 MHz, RT) for **III-1**.

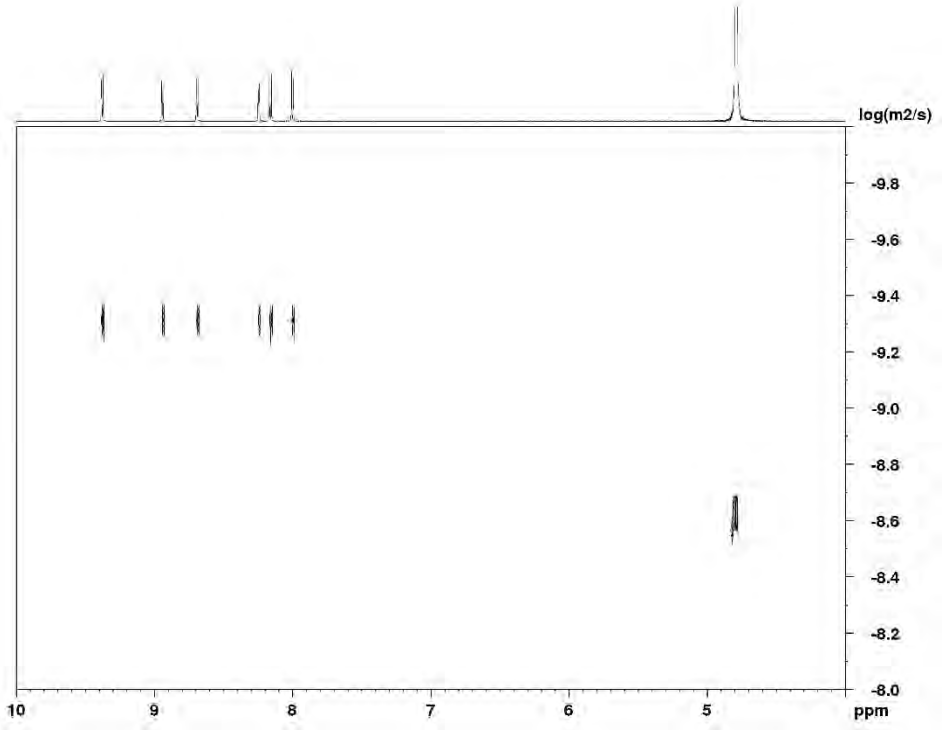

Figure III-S4. DOSY NMR recorded (D_2O, 600 MHz, RT) for **III-1**.

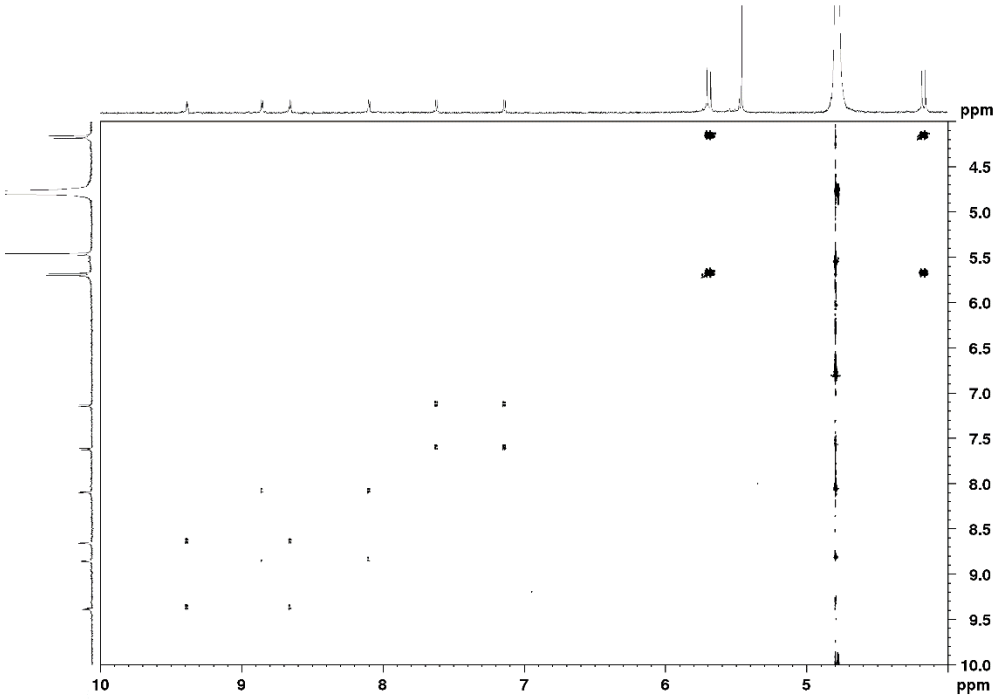

Figure III-S5. DQCOSY NMR recorded (600 MHz, D_2O, RT) for 1:1 mixture of **III-1** and CB7.

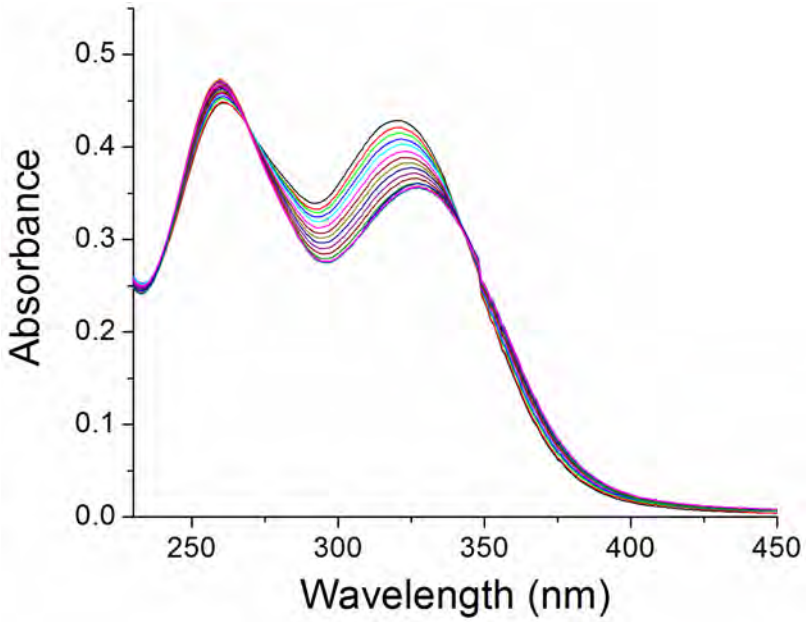

Figure III-S6. UV/Vis titration of **III-1** (6.6 μM) with increasing concentrations (0 – 17.4 μM) of CB7 in aqueous solution at 298 K.

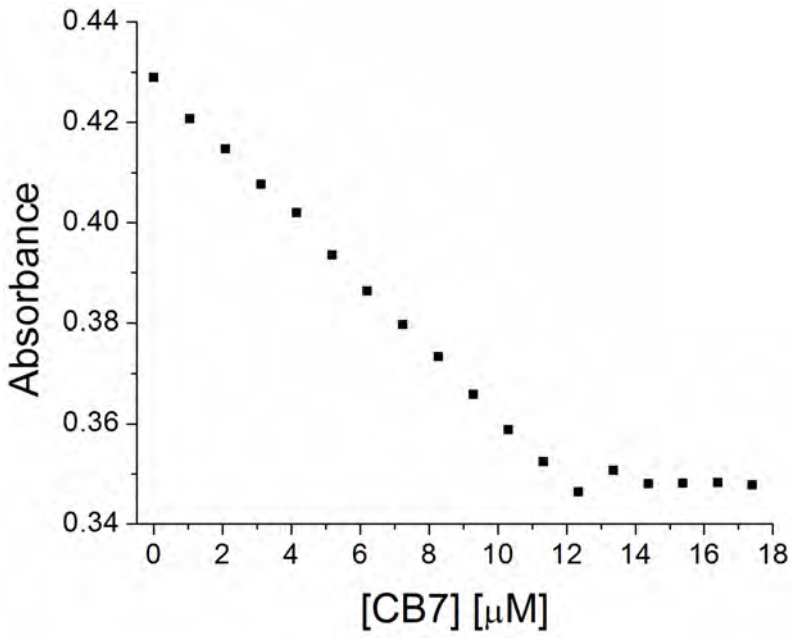

Figure III-S7. Plot of absorbance (λ_{max} = 320 nm) of **III-1** (6.6 μM) with CB[7] (0-17.5 μM) concentration.

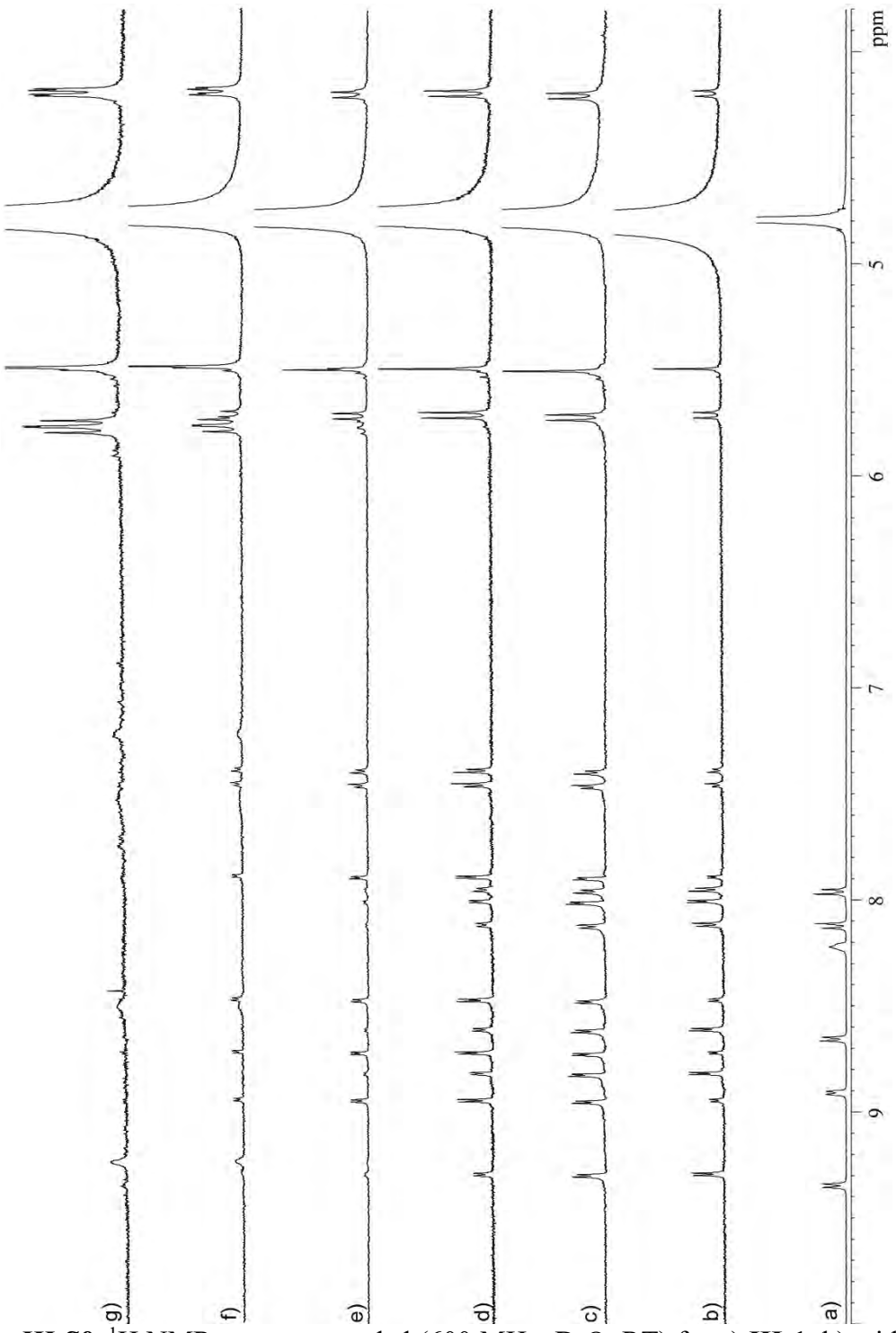

Figure III-S8. ^{1}H NMR spectra recorded (600 MHz, D_2O, RT) for a) **III-1**, b) with 0.12 equiv. of **CB8**, c) 0.25 equiv. of **CB8**, d) 0.37 equiv. of **CB8**, e) 0.5 equiv. of **CB8**, f) 0.75 equiv. of **CB8** and g) 1.0 equiv. of **CB8**.

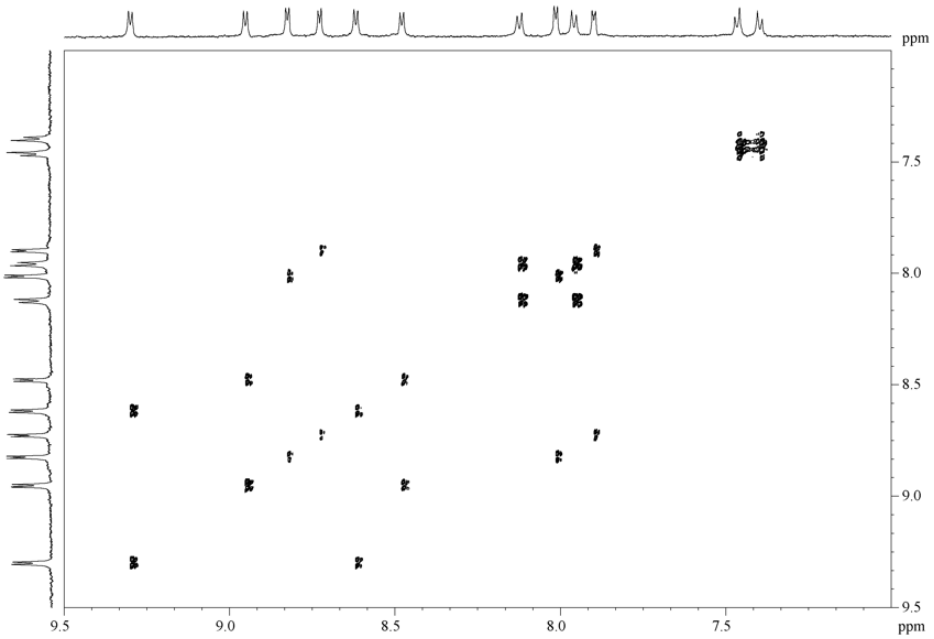

Figure III-S9. DQCOSY NMR recorded (600 MHz, D_2O, RT) for 1:0.25 mixture of **III-1** and **CB8**.

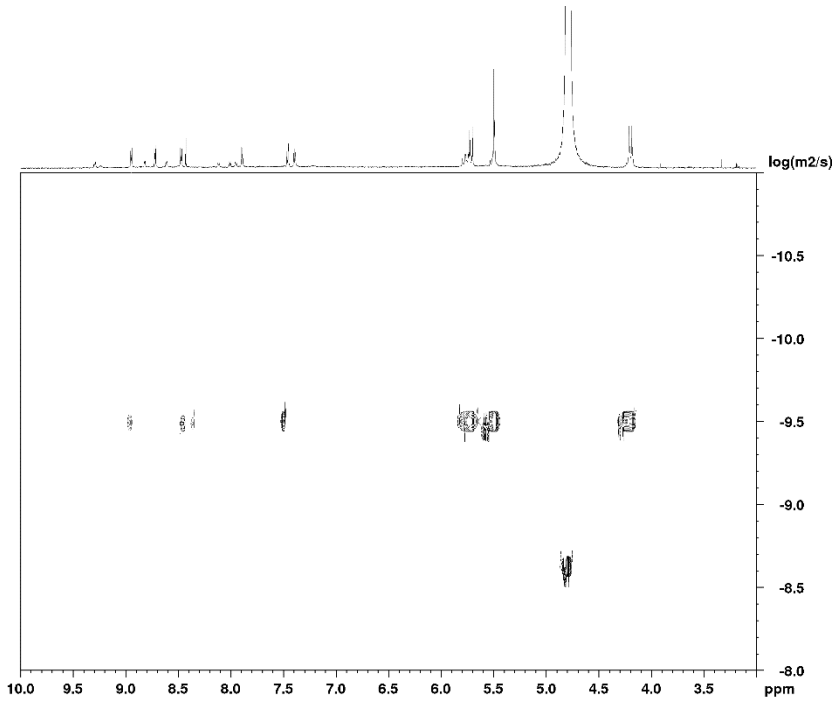

Figure III-S10. DOSY NMR recorded (600 MHz, D_2O, RT) for 1:0.5 mixture of **III-1** and **CB8**.

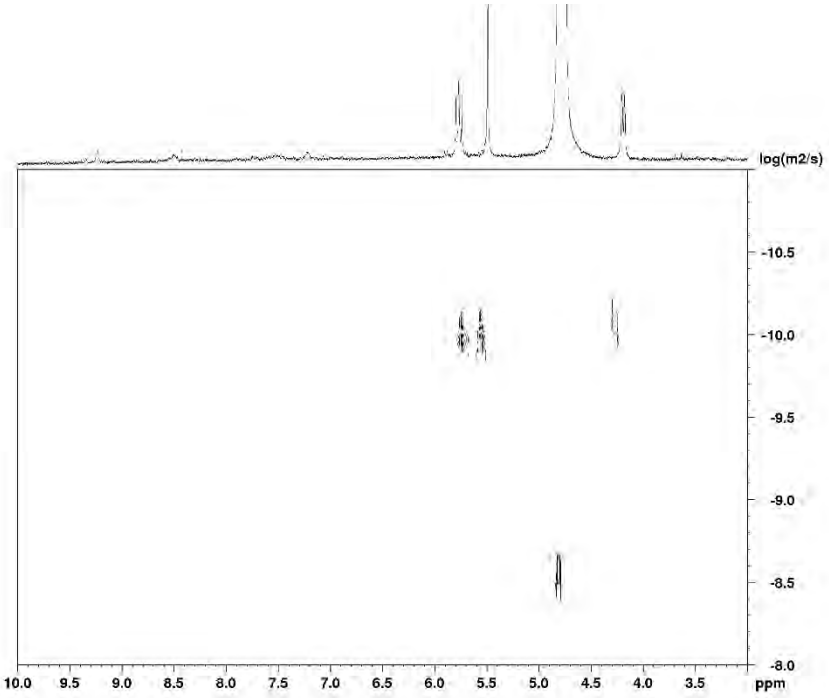

Figure III-S11. DOSY NMR recorded (600 MHz, D_2O, RT) for 1:1 mixture of **III-1** and **CB8**.

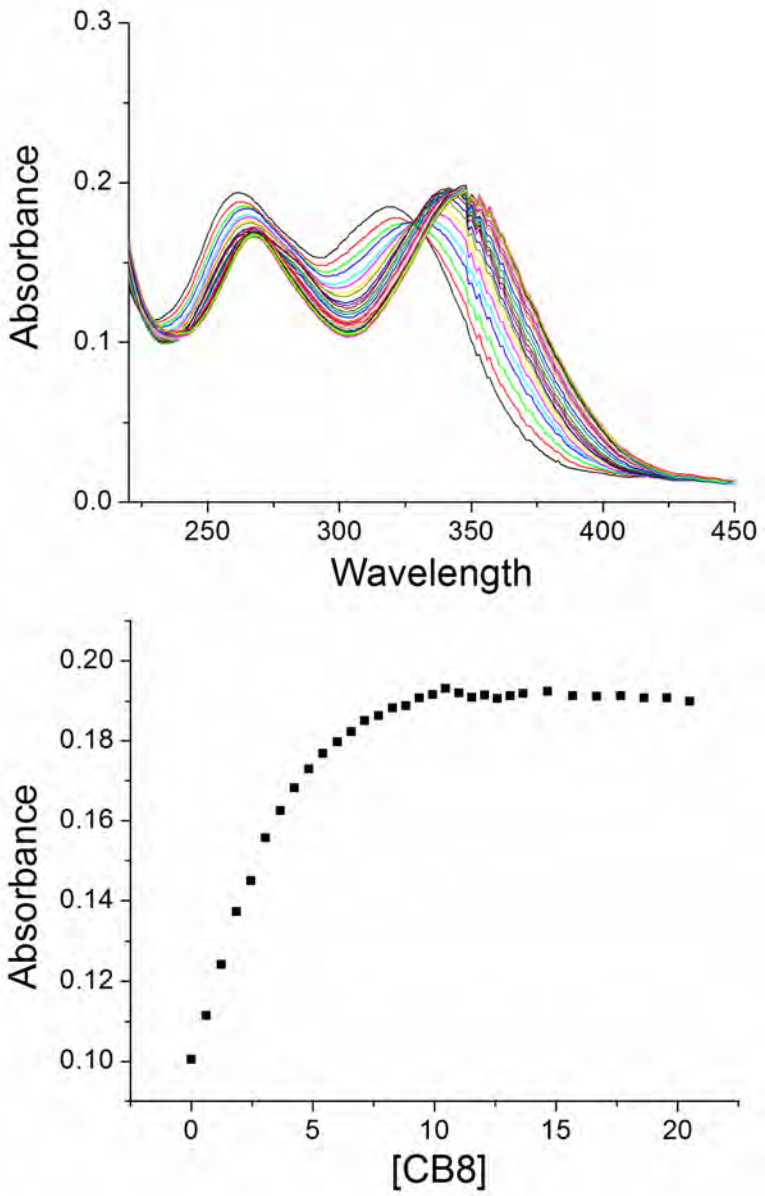

Figure III-S12. *(Left)* UV/Vis titration of **III-1** (6.0 μM) with increasing concentrations (0 – 20.5 μM) of **CB[8]** in aqueous solution at 298 K. *(Right)* Plot of absorbance (λ_{max} = 350 nm) of **III-1** (6.6 μM) with **CB[8]** (0 − 20.5 μM) concentration.

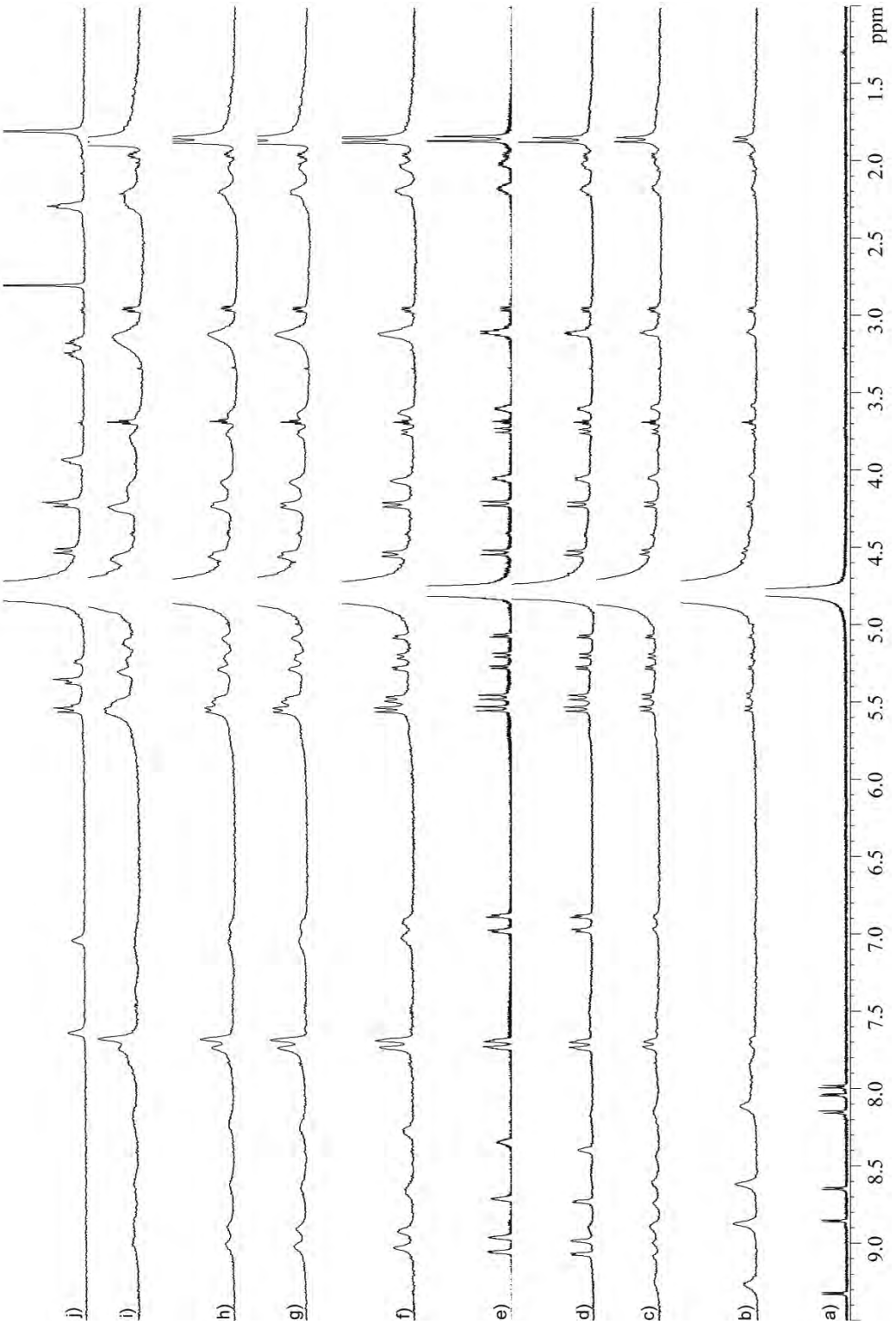

Figure III-S13. ^{1}H NMR (600 MHz, D_2O) recorded for (a) **III-1** with (b) 0.25 equiv. of **M2**, (c) 0.5 equiv. of **M2**, (d) 0.75 equiv. of **M2**, (e) 1.0 equiv. of **M2**, (f) 1.5 equiv. of **M2**, (g) 2.0 equiv. of **M2**, (h) 2.5 equiv. of **M2**, (i) 3.0 equiv. of **M2**, (j) only **M2**.

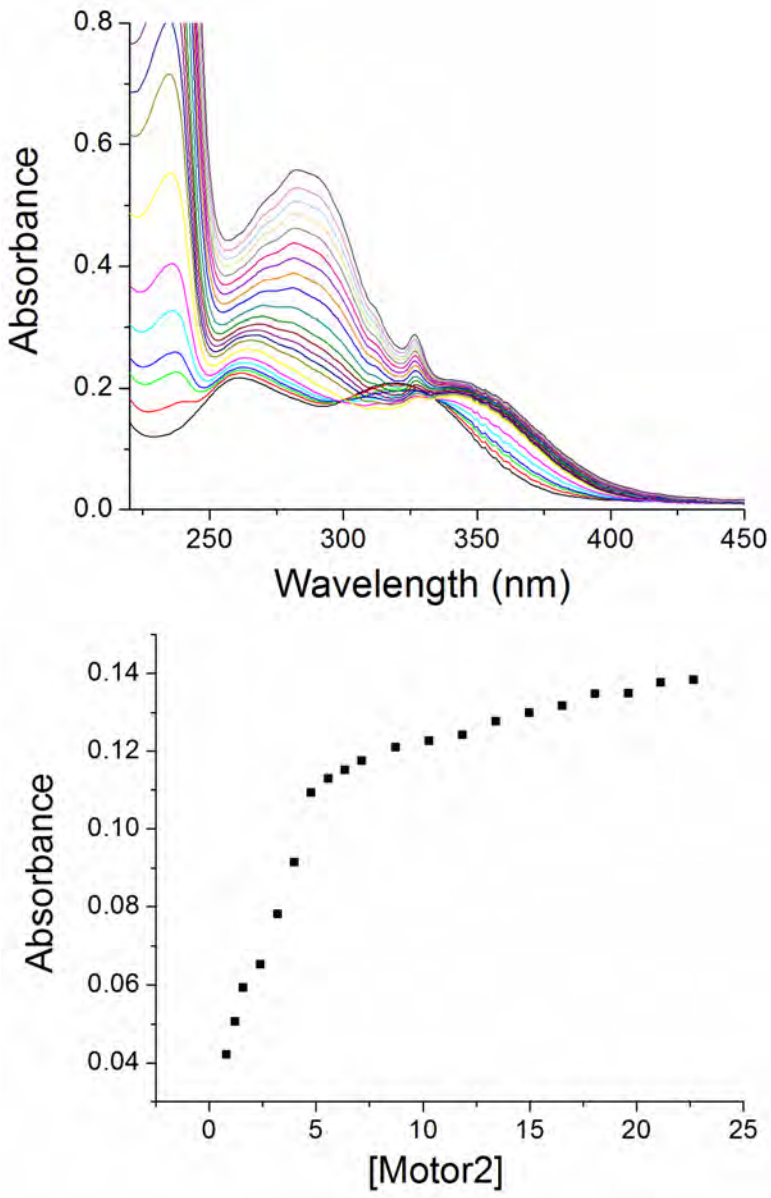

Figure III-S14. *(Left)* UV/Vis titration of **III-1** (6.0 μM) with increasing concentrations (0 – 22.7 μM) of **M2** in aqueous solution at 298 K. *(Right)* Plot of absorbance (λ_{max} = 370 nm) of **III-1** (6.6 μM) with **M2** (0 − 22.7 μM) concentration.

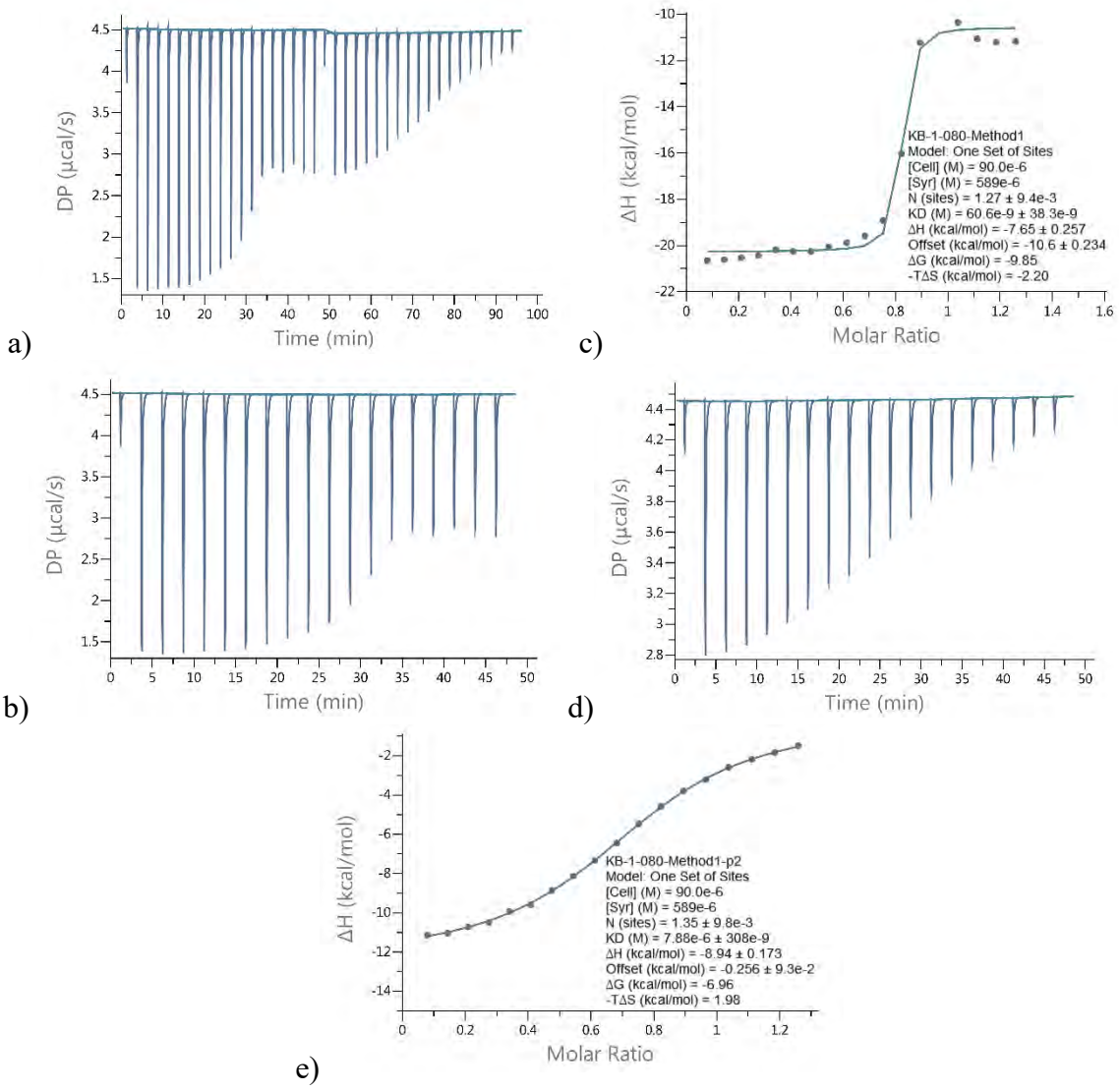

Figure III-S15. ITC data for the titration of compound **III-1** with **M2** in water at 25 ˚C. a) Concatenation of two sequential titrations showing two distinct isotherms, b and c) Zoom in on the first 19 steps of the titration and fitting of the first binding event to a 1:1 binding model corresponding to binding at the central benzidinium site, and d and e) Zoom in on the second set of 19 steps of the titration corresponding to the second binding event that involves translocation of the **M2** molecules to the bipyridinium termini of the rigid rod to give **M2•III-1•M2** and its fitting to a 1:1 binding model.

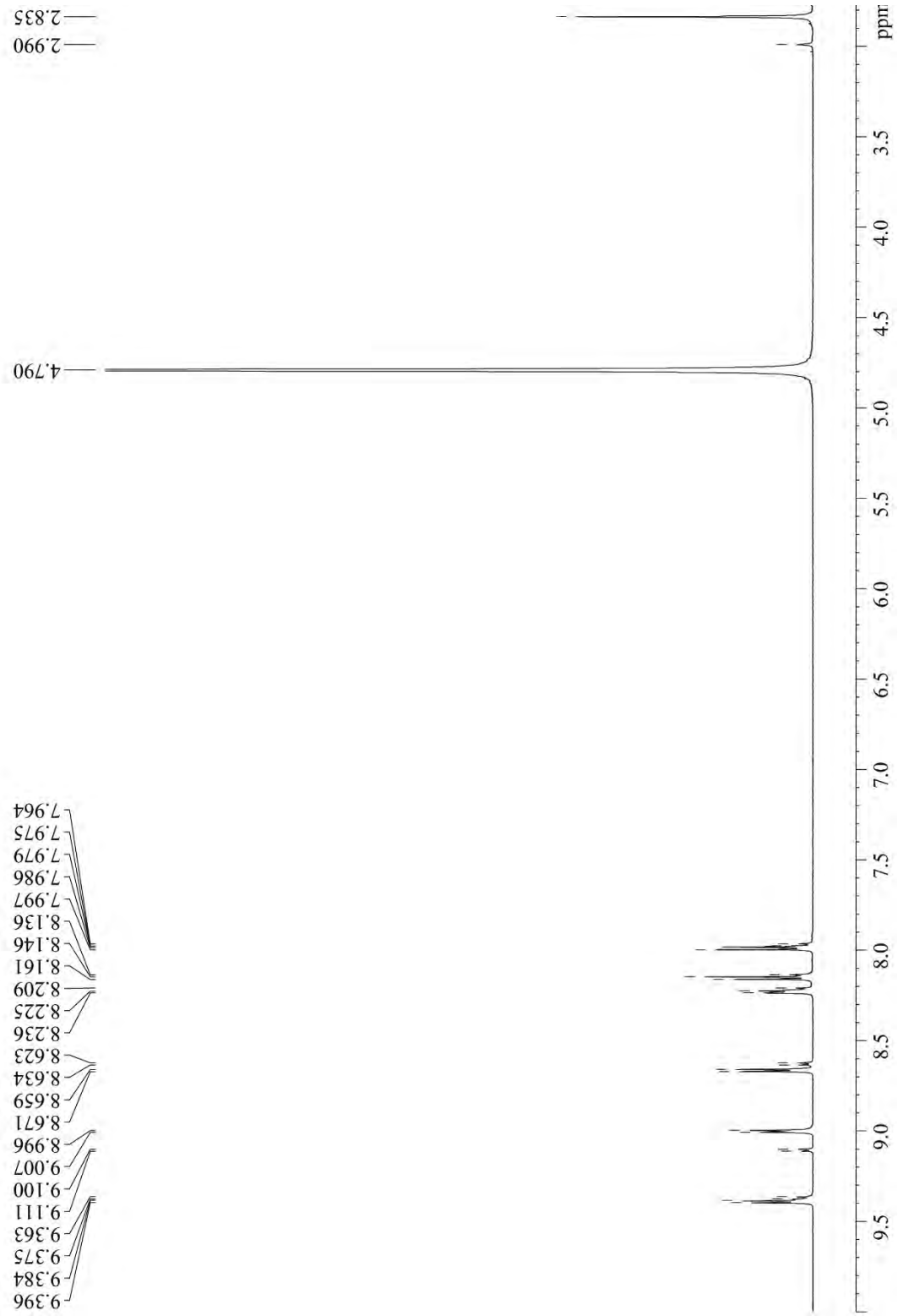

Figure III-S16. ^{1}H NMR recorded (600 MHz, D_2O, RT) for mixture of triangle **III-3** = $[Pd_3$**III-1**$_3](NO_3)_{12}$ and square **III-4** = $[Pd_4$ **III-1**$_4](NO_3)_{16}$.

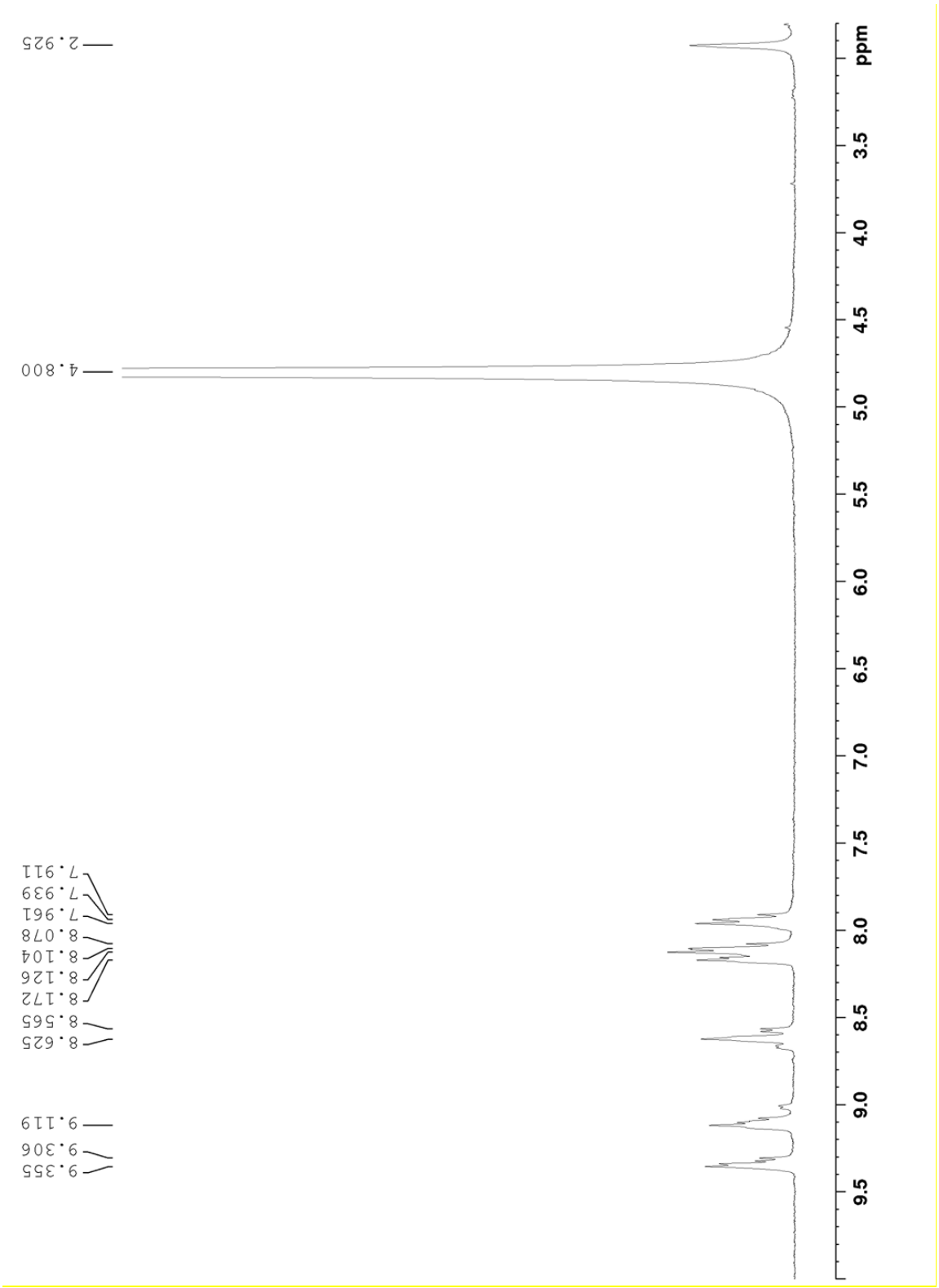

Figure III-S17. ^{1}H NMR recorded (600 MHz, D_2O, RT) for mixture of **III-5** & **III- 6**.

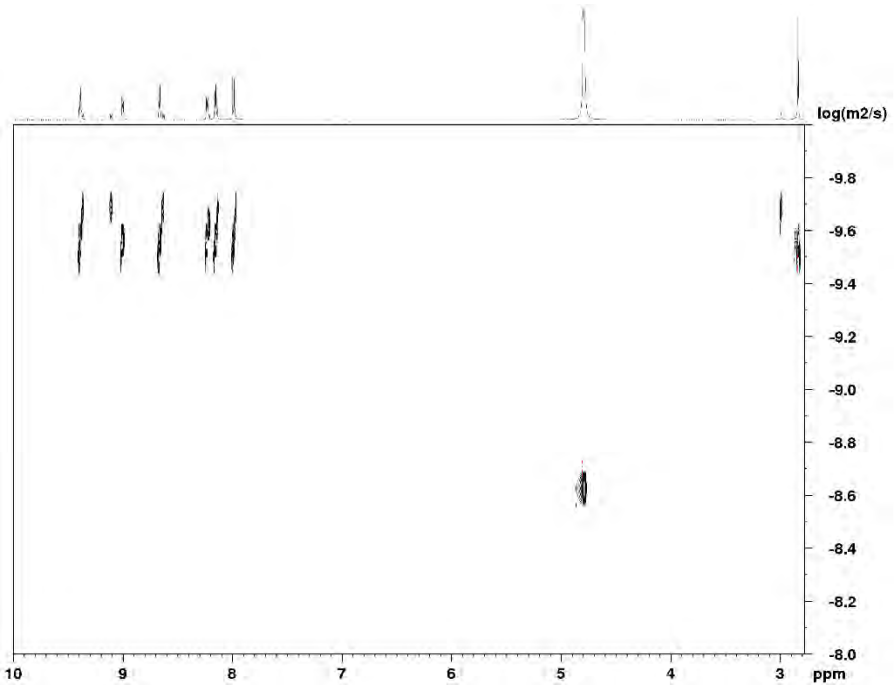

Figure III-S18. DOSY NMR recorded (600 MHz, D_2O, RT) for mixture of triangle **III-3** = [Pd_3 **III-1**$_3$]$(NO_3)_{12}$ & square **III-4** = [Pd_4 **III-1**$_4$]$(NO_3)_{16}$.

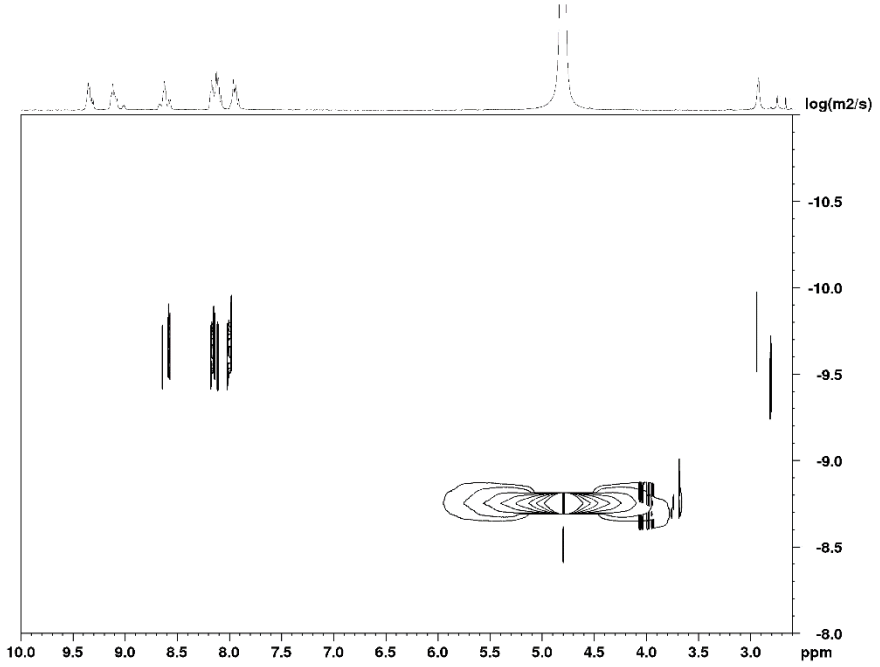

Figure III-S19. DOSY NMR recorded (600 MHz, D_2O, RT) for mixture of **III-5** & **III-6**.

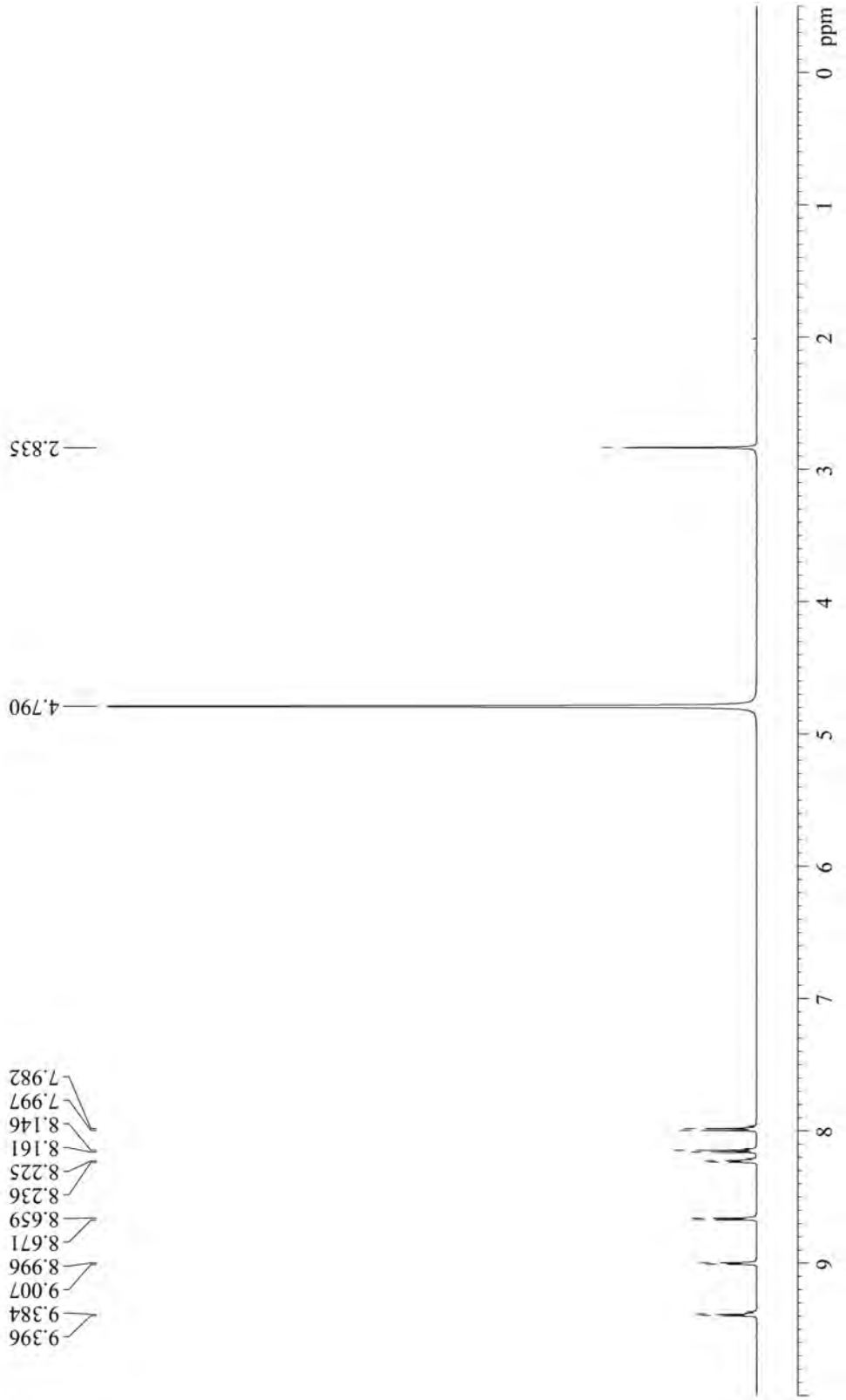

Figure III-S20. ^{1}H NMR recorded (D_2O, 600 MHz, RT) for **III-3** = [Pd_3 **III-1**$_3$]$(NO_3)_{12}$.

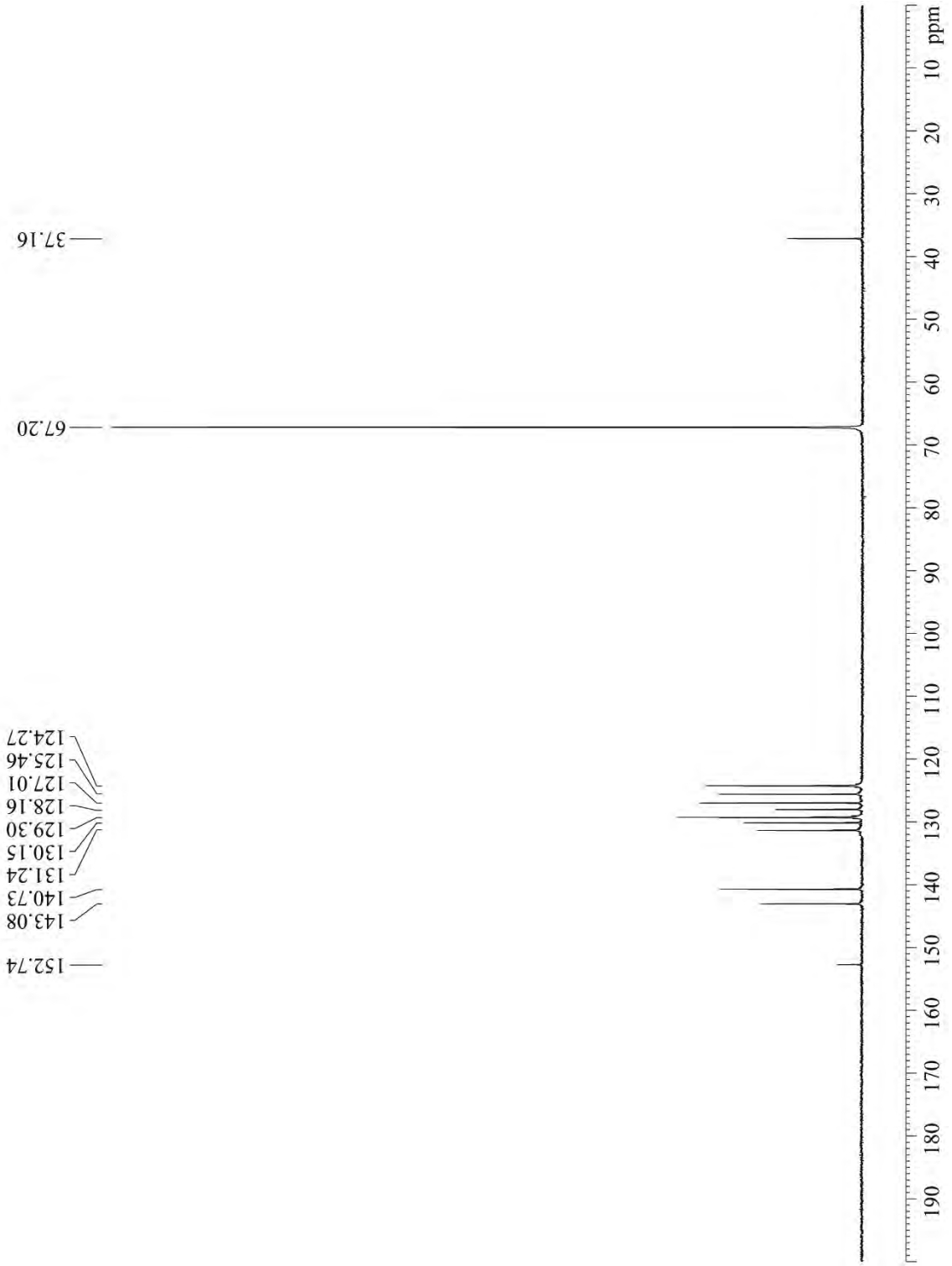

Figure III-S21. ^{13}C NMR recorded (D_2O, 125 MHz, RT) for **III-3** = [Pd_3 **III-1**$_3$]$(NO_3)_{12}$.

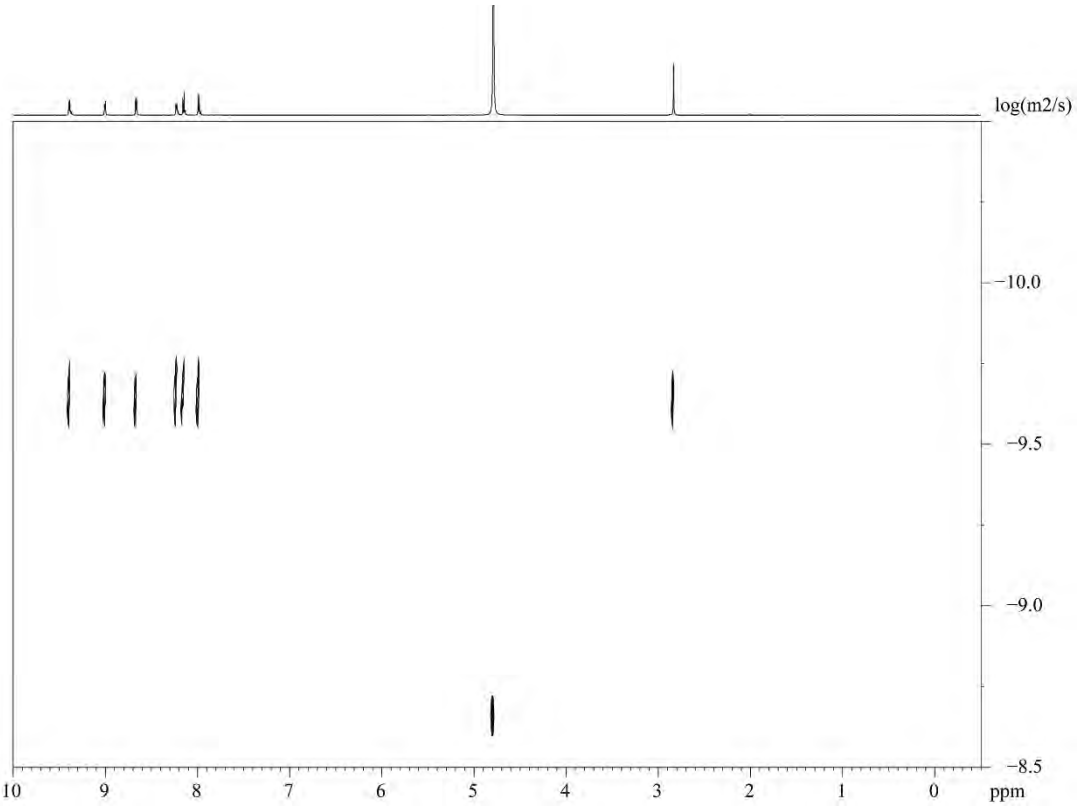

Figure III-S22. DOSY NMR recorded (D_2O, 600 MHz, RT) for **III-3** = [Pd_3 **III-1**$_3$]$(NO_3)_{12}$.

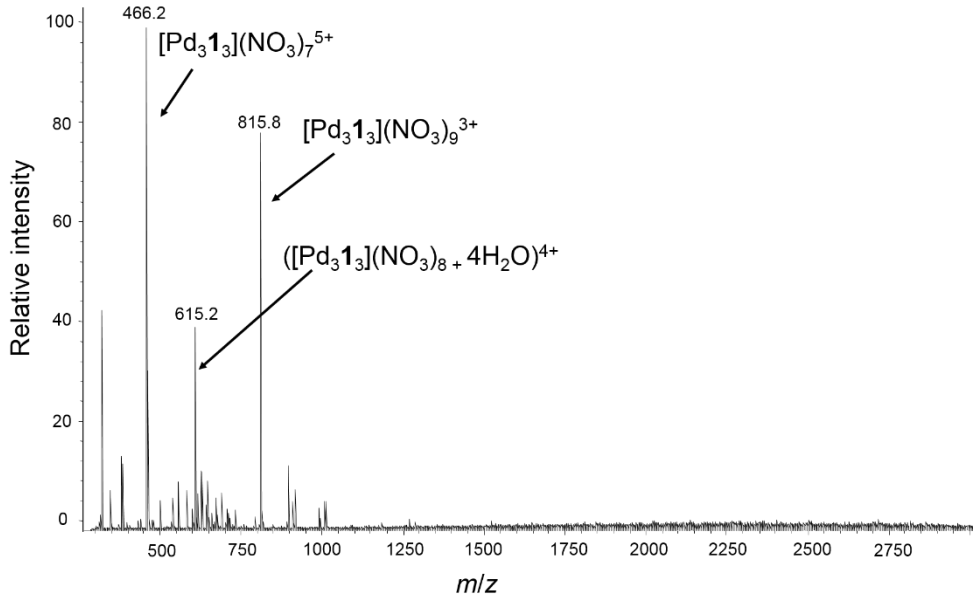

Figure III-S23. ESI-MS recorded for **III-3** = [Pd_3**III-1**$_3$]$(NO_3)_{12}$.

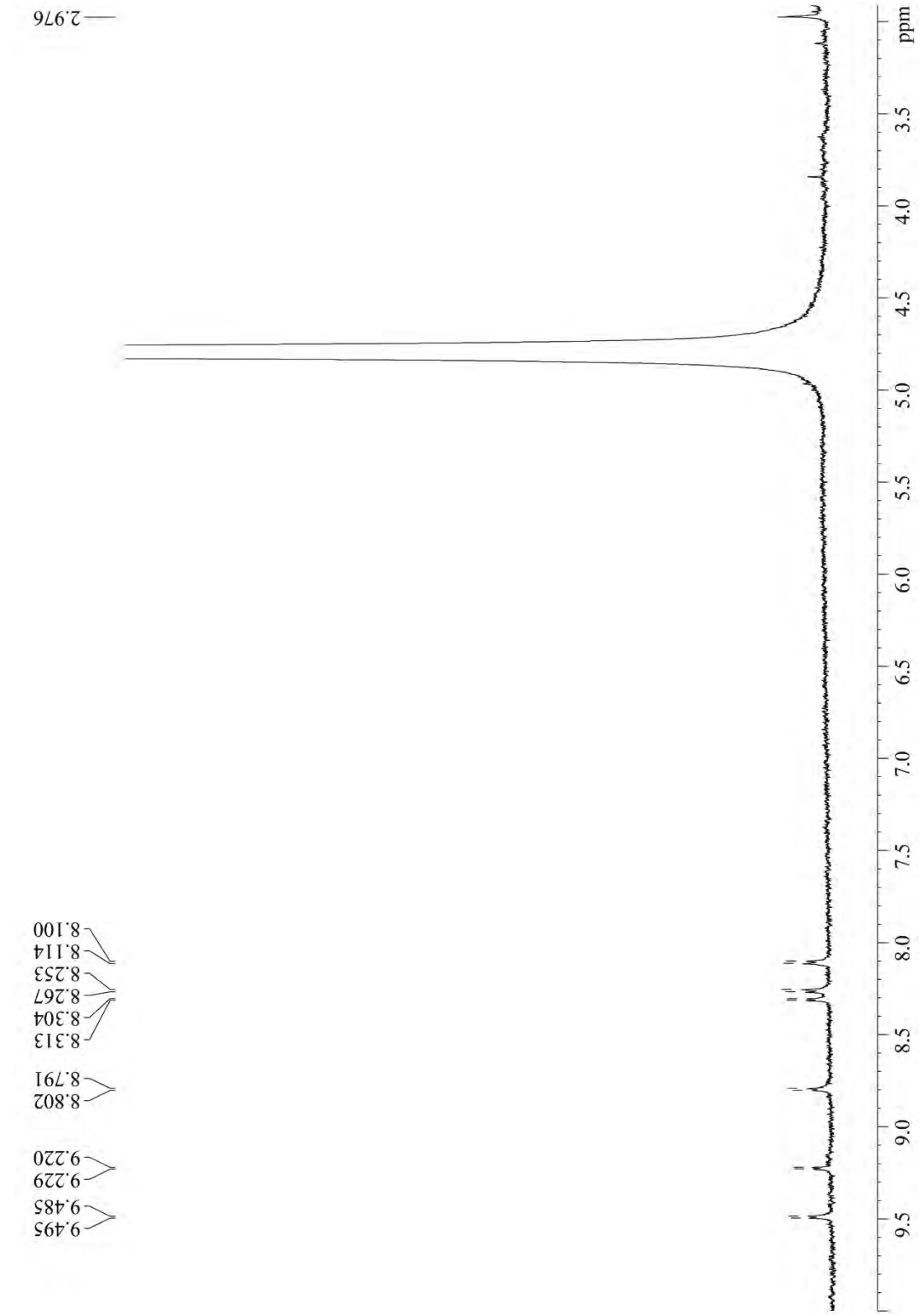

Figure III-S24. ^{1}H NMR recorded (D_2O, 400 MHz, RT) for triangle **III-5** = [Pt_3**III-1**$_3$]$(NO_3)_{12}$.

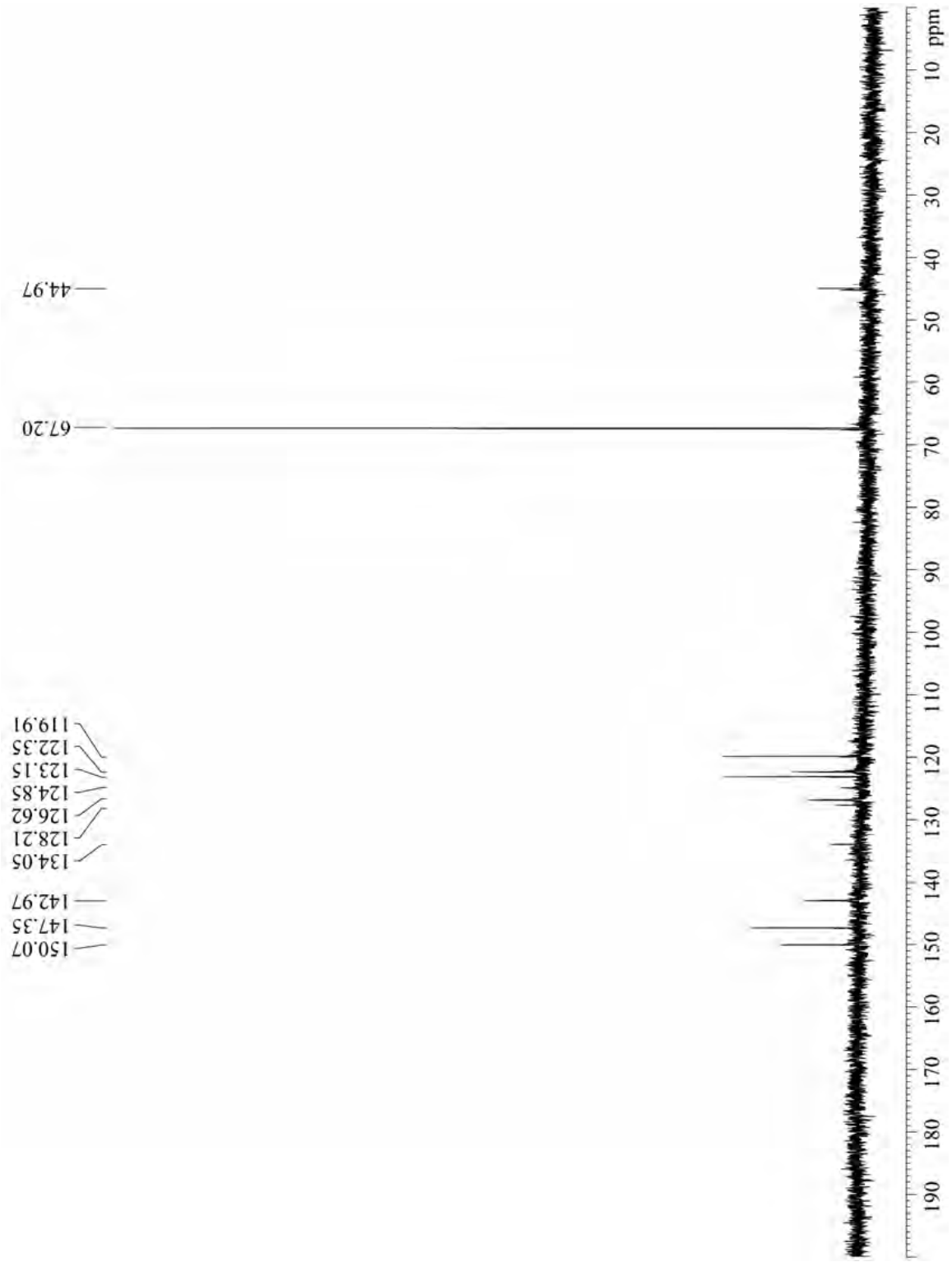

Figure III-S25. ^{13}C NMR recorded (D_2O, 125 MHz, RT) for triangle **III-5** = [Pt_3**III-1**$_3$]$(NO_3)_{12}$.

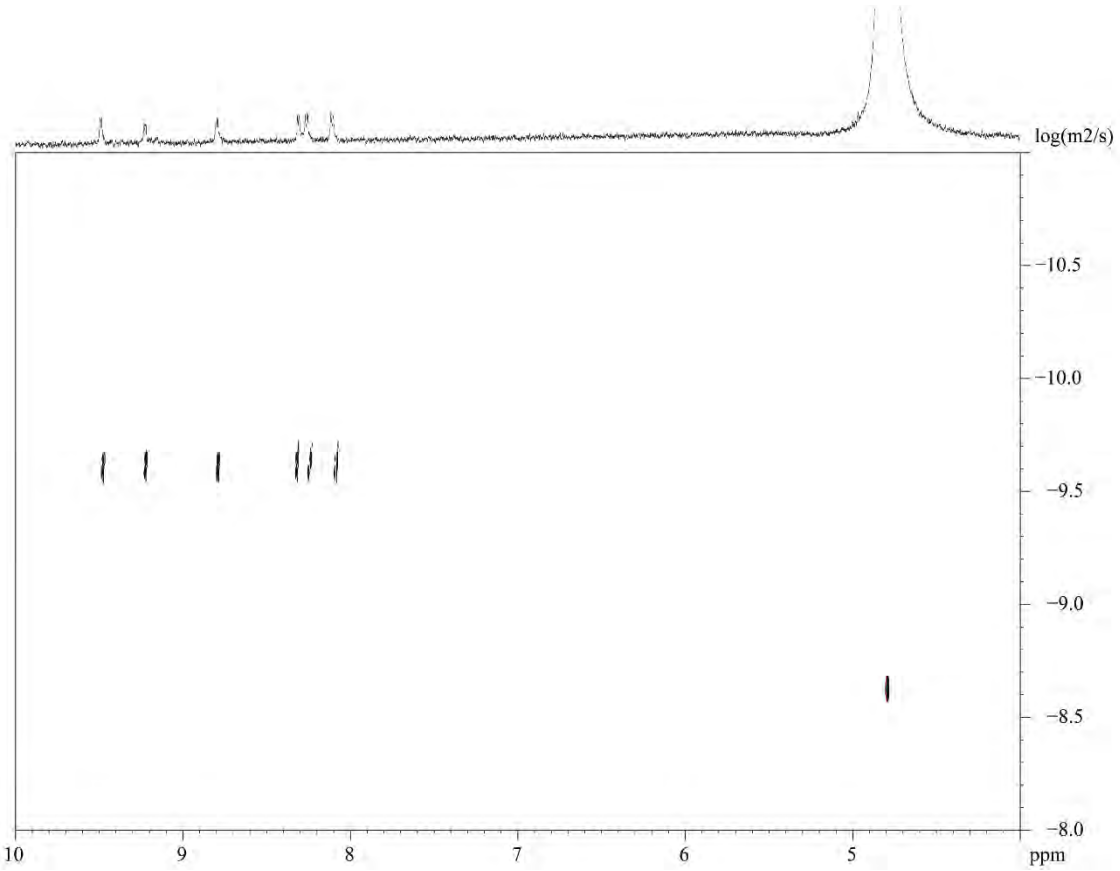

Figure III-S26. DOSY NMR recorded (D_2O, 600 MHz, RT) for **III-5** = [Pt_3 **III-1**$_3$]$(NO_3)_{12}$.

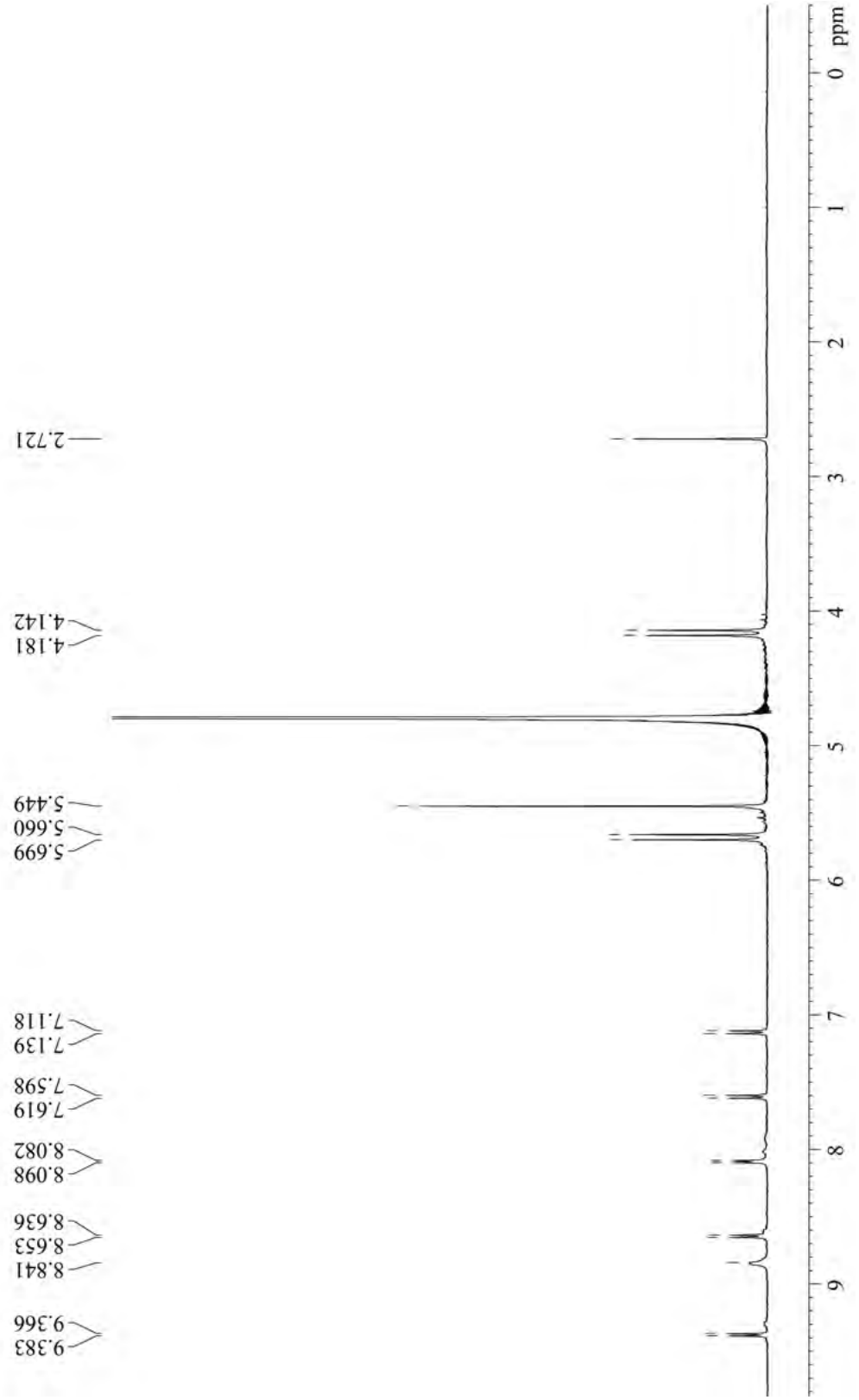

Figure III-S27. ^{1}H NMR recorded (D_2O, 400 MHz, RT) for **III-7** = [Pd_3(**III-1•CB7**)$_3$](NO_3)$_{12}$.

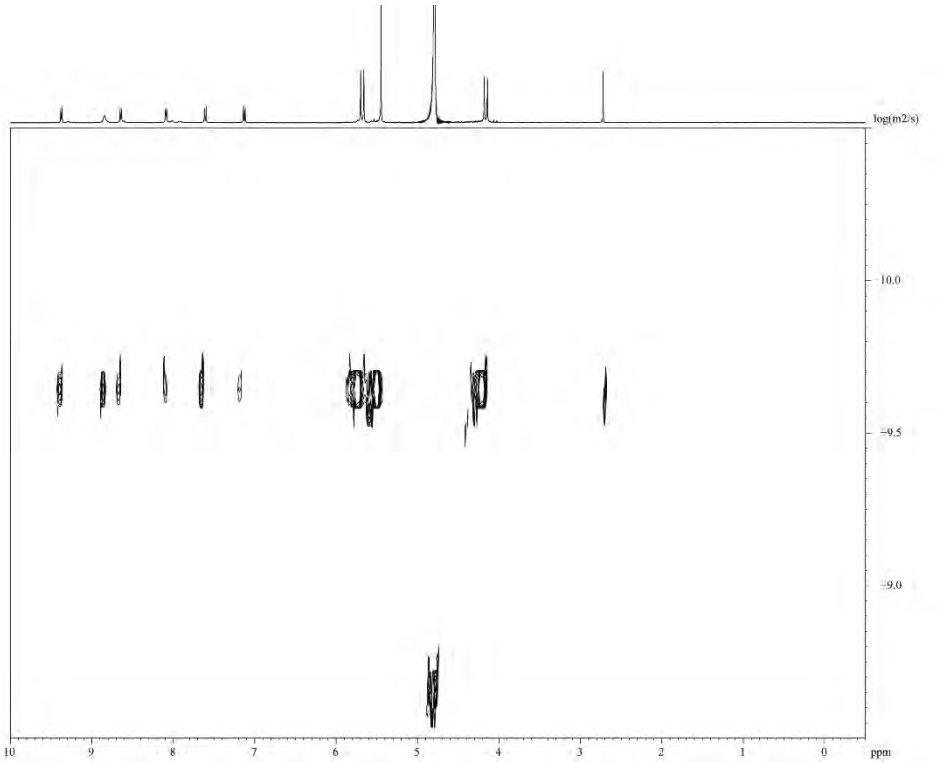

Figure III-S28. DOSY NMR (D_2O, 600 MHz, RT) recorded **III-7** = $[Pd_3(\textbf{III-1•CB7})_3](NO_3)_{12}$.

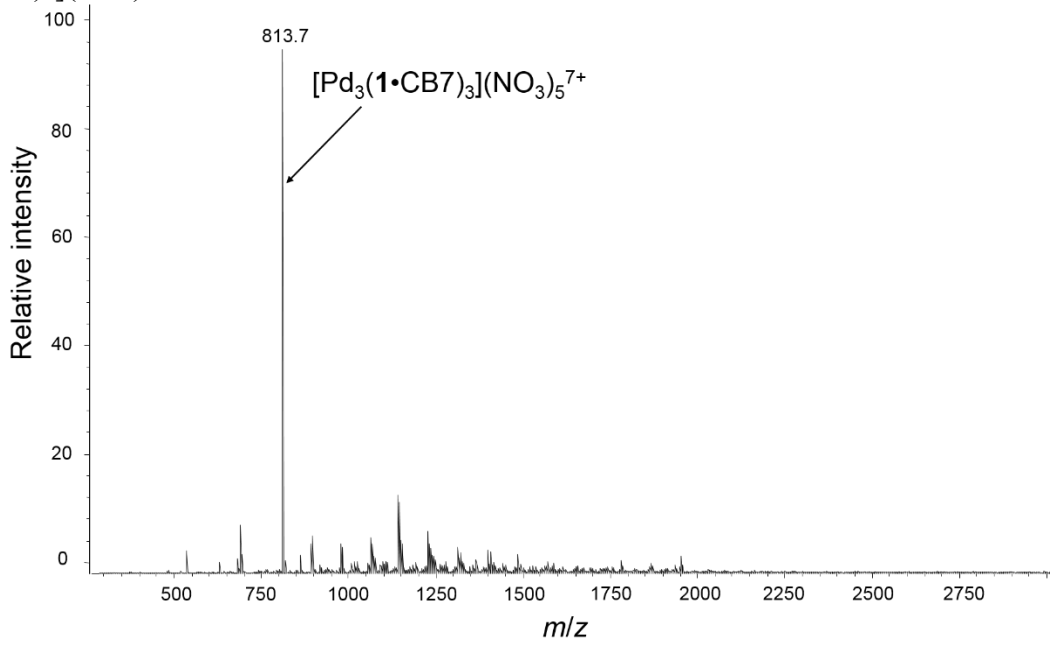

Figure III-S29. ESI recorded for **III-7** = $[Pd_3(\textbf{III-1•CB7})_3](NO_3)_{12}$.

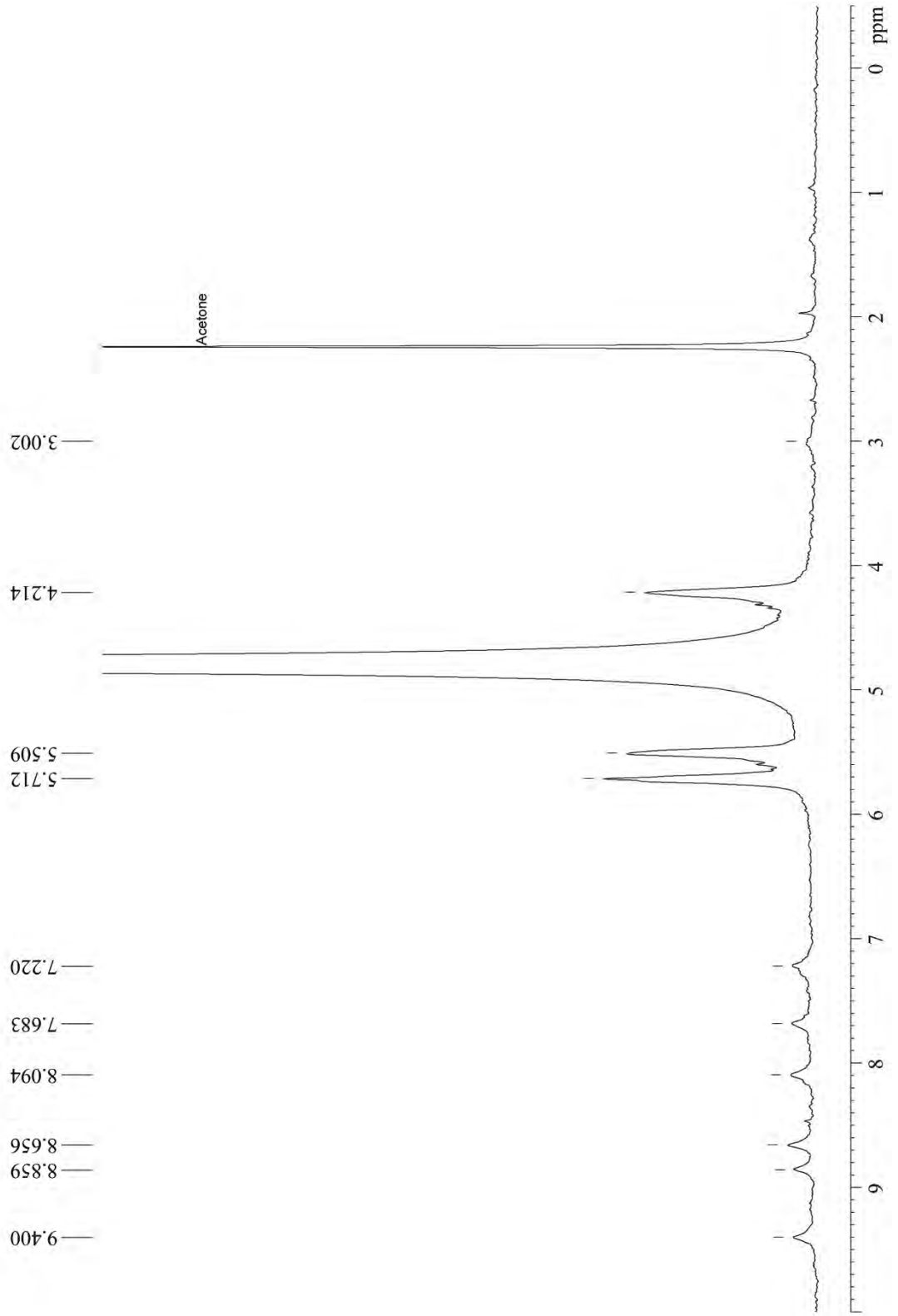

Figure III-S30. ^{1}H NMR recorded (D_2O, 400 MHz, RT) for **III-8** = [Pt_3(**III-1•CB7**)$_3$](NO_3)$_{12}$.

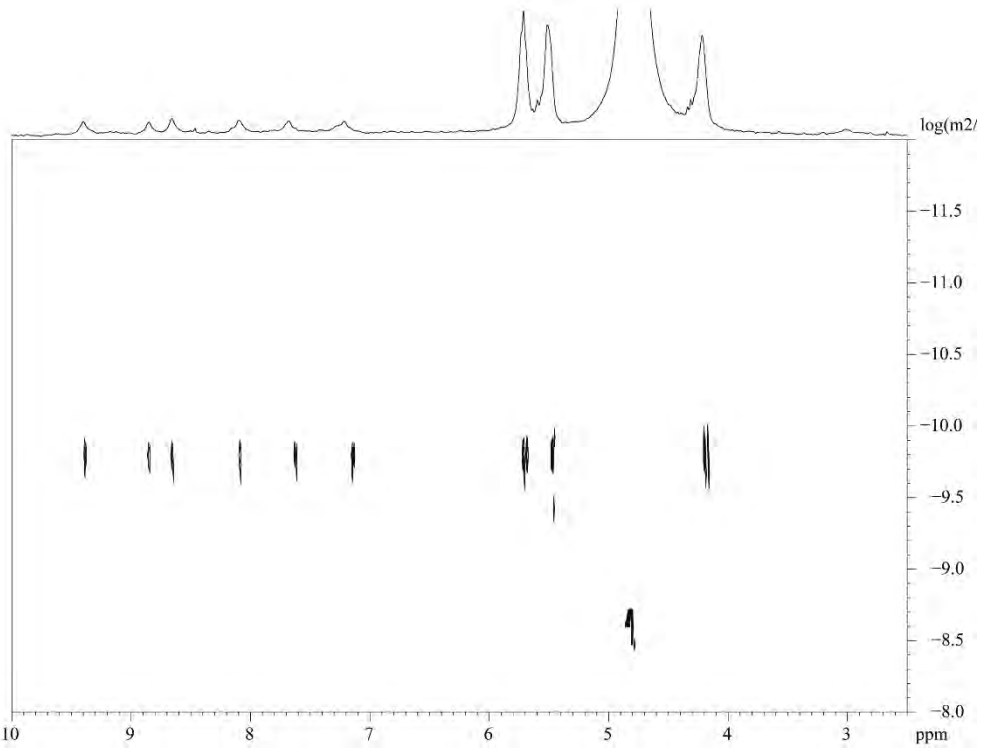

Figure III-S31. DOSY NMR recorded (D_2O, 600 MHz, RT) for **III-8** = [Pt_3(**III-1•CB7**)$_3$](NO_3)$_{12}$.

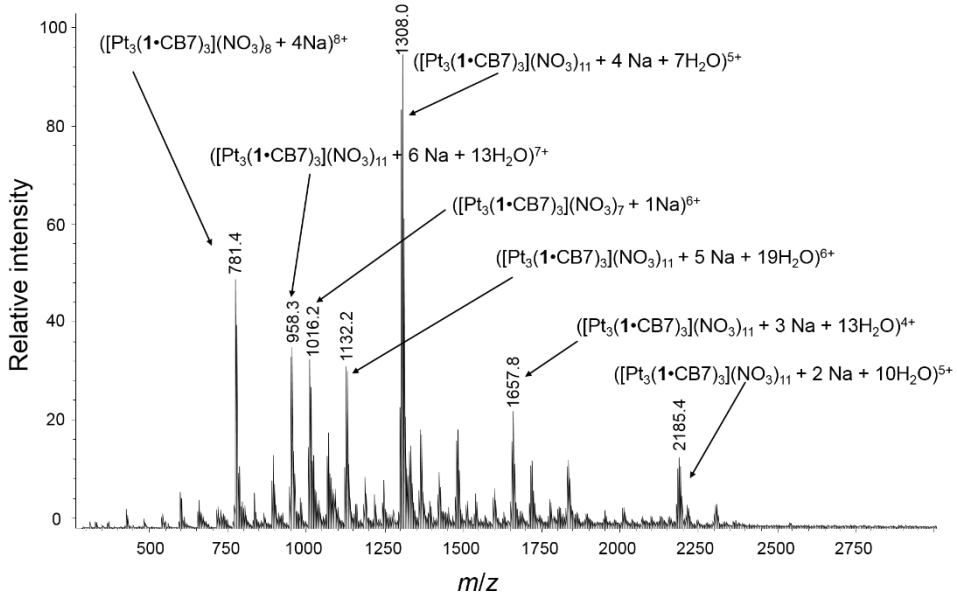

Figure III-S32. ESI recorded for **III-8** = [Pt_3(**III-1•CB7**)$_3$](NO_3)$_{12}$.

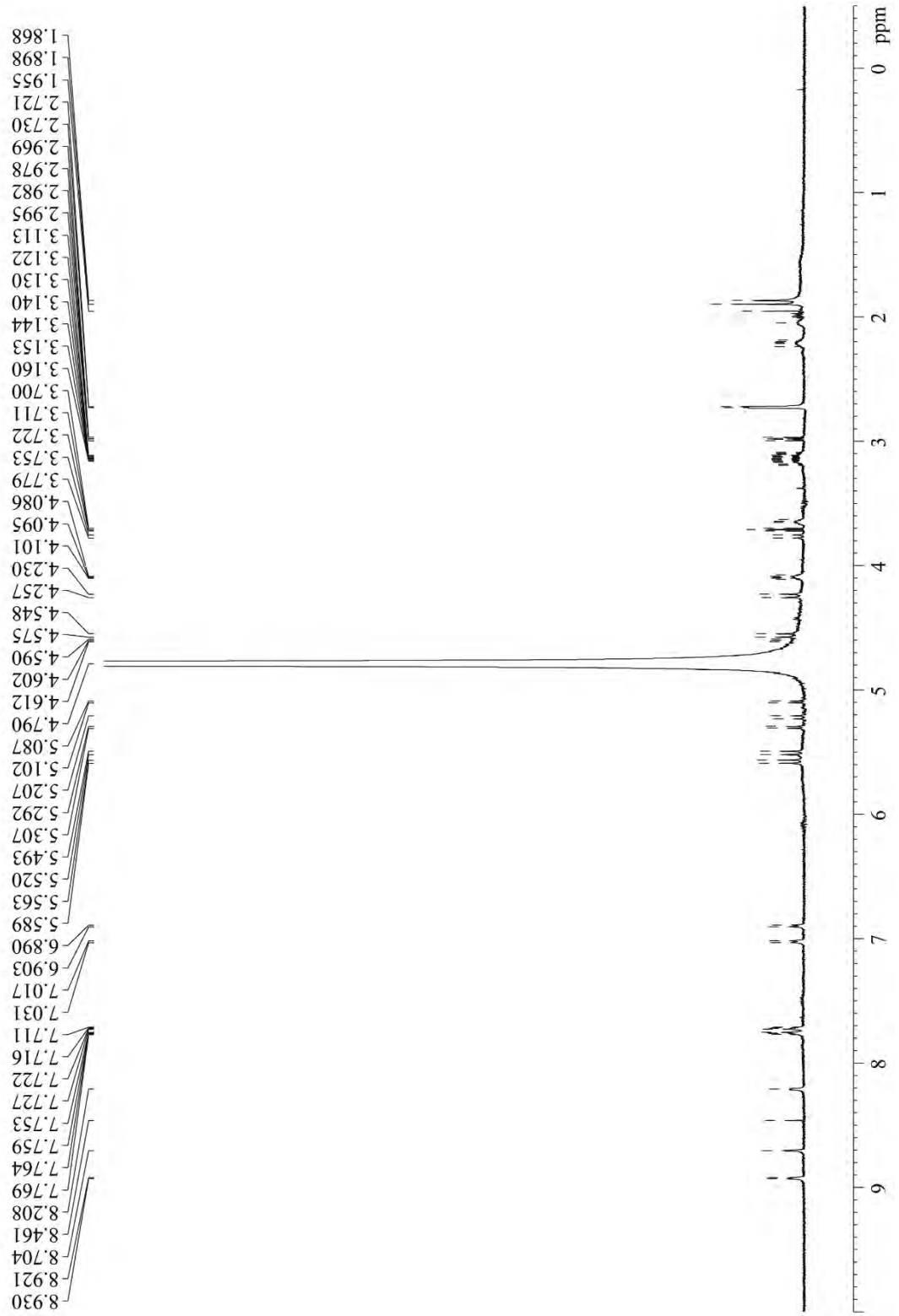

Figure III-S33. ^{1}H NMR recorded (D_2O, 400 MHz, RT) for **III-9** = [Pd_3(**III-1•M2**)$_3$](NO_3)$_{12}$.

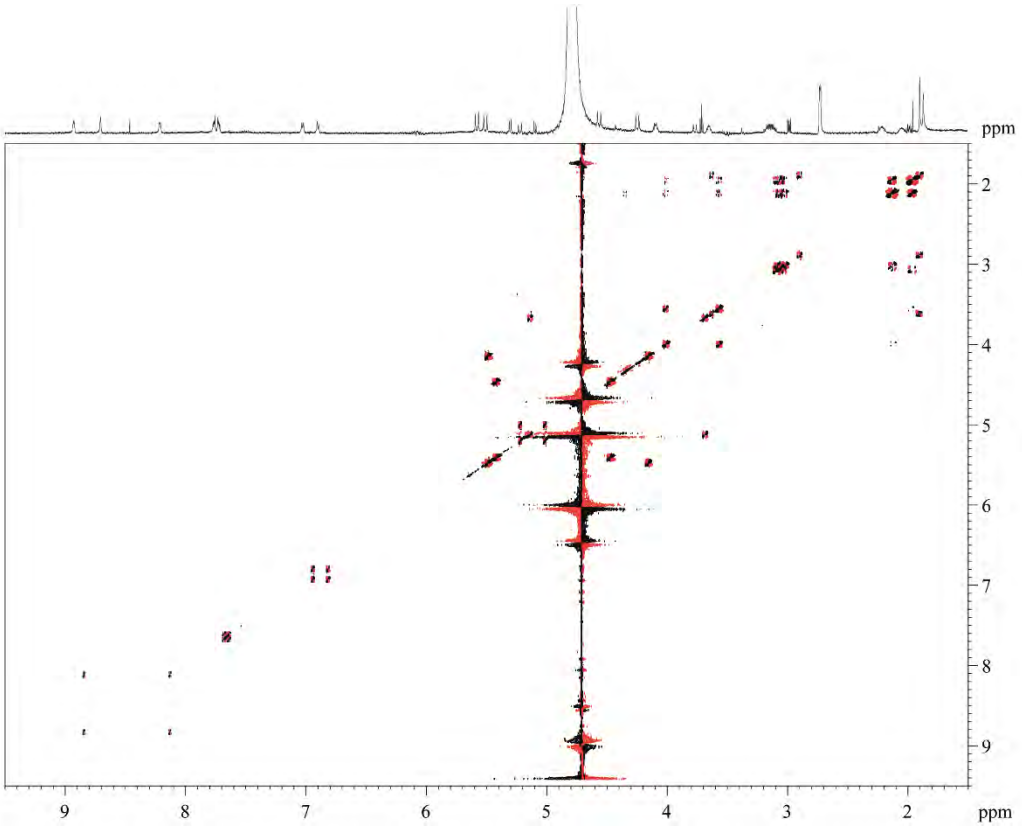

Figure III-S34. COSY NMR recorded (D_2O, 600 MHz, RT) for **III-9** = $[Pd_3(\mathbf{III\text{-}1{\bullet}M2})_3](NO_3)_{12}$.

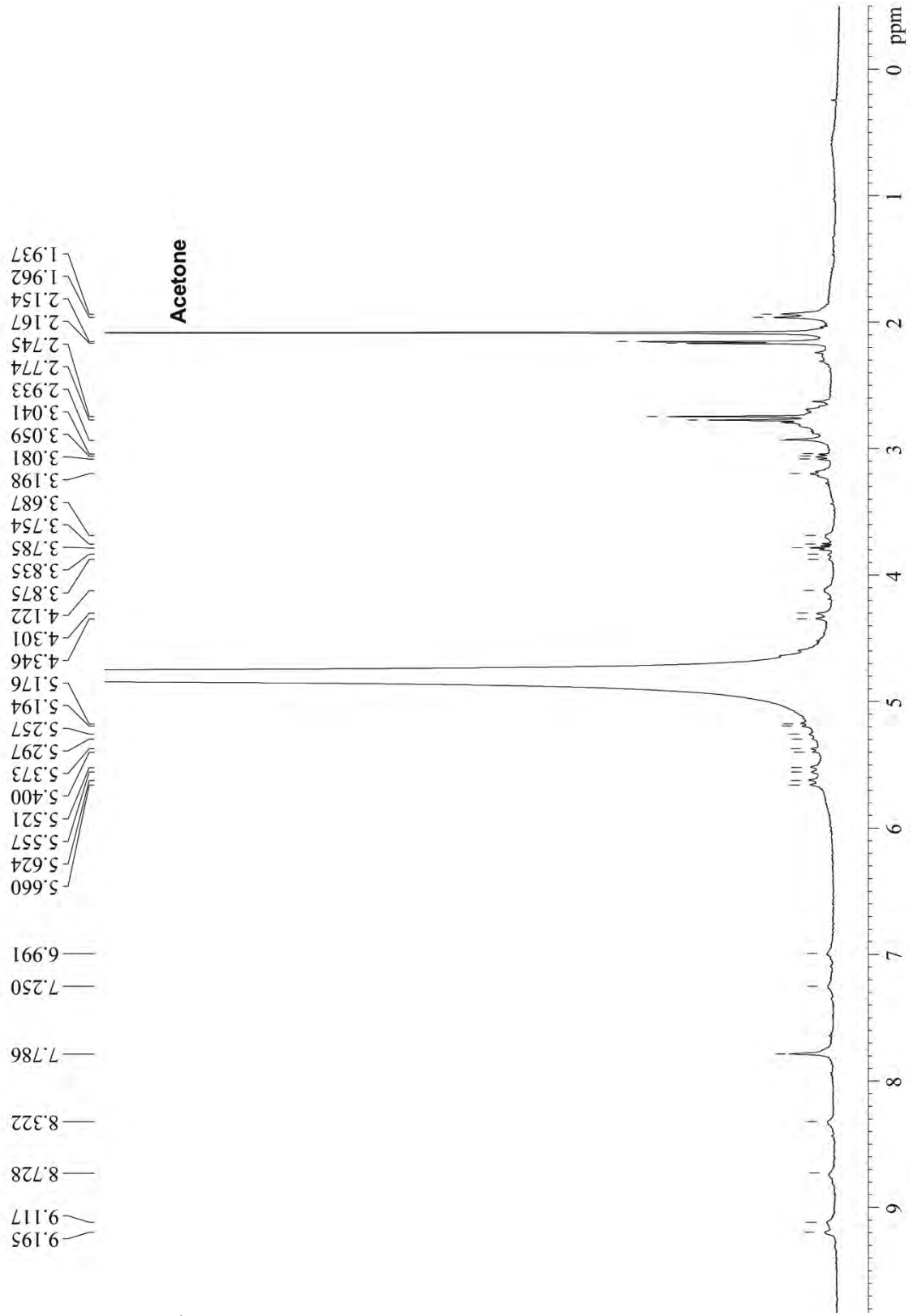

Figure III-S35. ^{1}H NMR recorded (D_2O, 400 MHz, RT) for **III-10** = [Pt_3(**III-1•M2**)$_3$]$(NO_3)_{12}$.

Photophysical Properties of Metallacycles

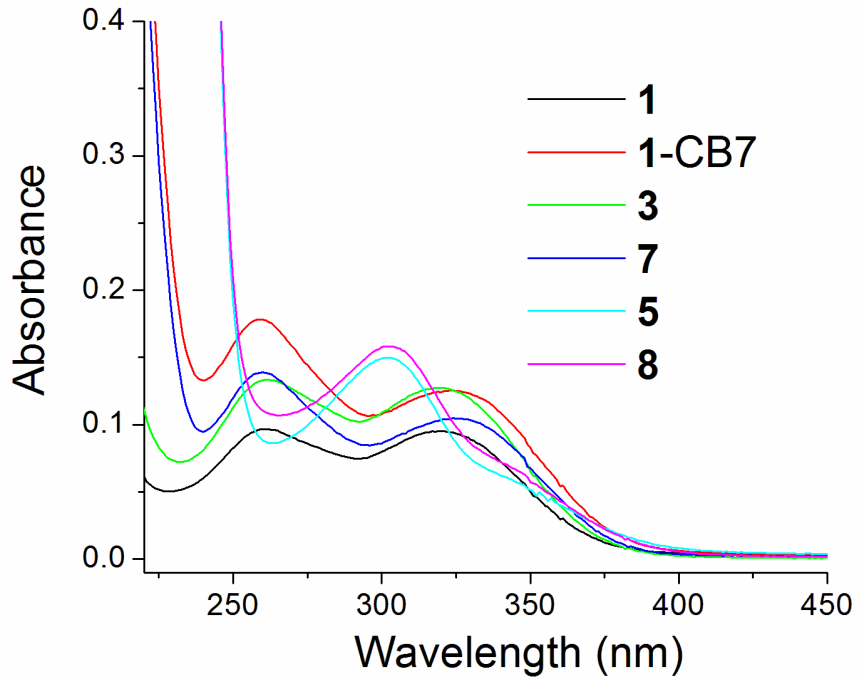

Figure III-S36. UV/vis spectra recorded for **III-1**, **III-1•CB7**, **III-3**, **III-5**, [4]MN **III-7** & [4]MN **III-8** in water where the concentration of ligand is 5μM for all samples.

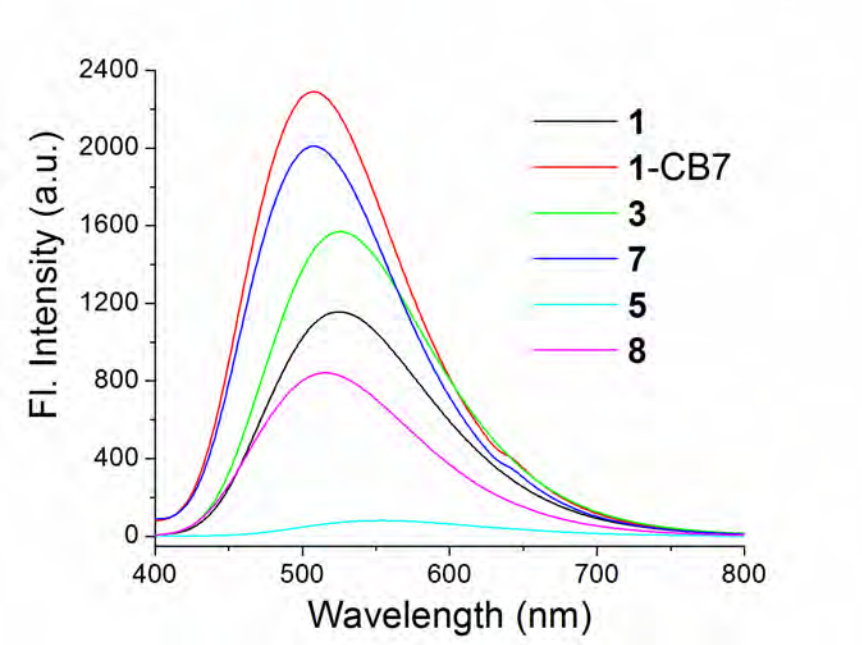

Figure III-S37. Fluorescence emission spectra (λ_{ex} = 320 nm) recorded for **III-1**, **III-1•CB7**, **III-3**, **III-5**, [4]MN **III-7**, and [4]MN **III-8** in water where the concentration of ligand **III-1** is 20 μM for all samples.

Quantum Yield Determination:

Fluorescence quantum yields (Φ) were calculated using
$\Phi_{sample} = \Phi_{ref}(Grad_{sample}/Grad_{ref})(\eta^2_{sample}/\eta^2_{ref})$
Where $Grad_{sample}$ and $Grad_{ref}$ are slope of plot of integrated fluorescence intensity (λ_{ex} = 320 nm) *vs* absorbance for sample and reference dye, respectively. η_{sample} and η_{ref} are the refractive indexes of the solvent used for the sample and reference solutions, respectively. Stilbene 420 (Φ_{ref} = 0.52 in water) was used as the reference. All measurements were done in water.

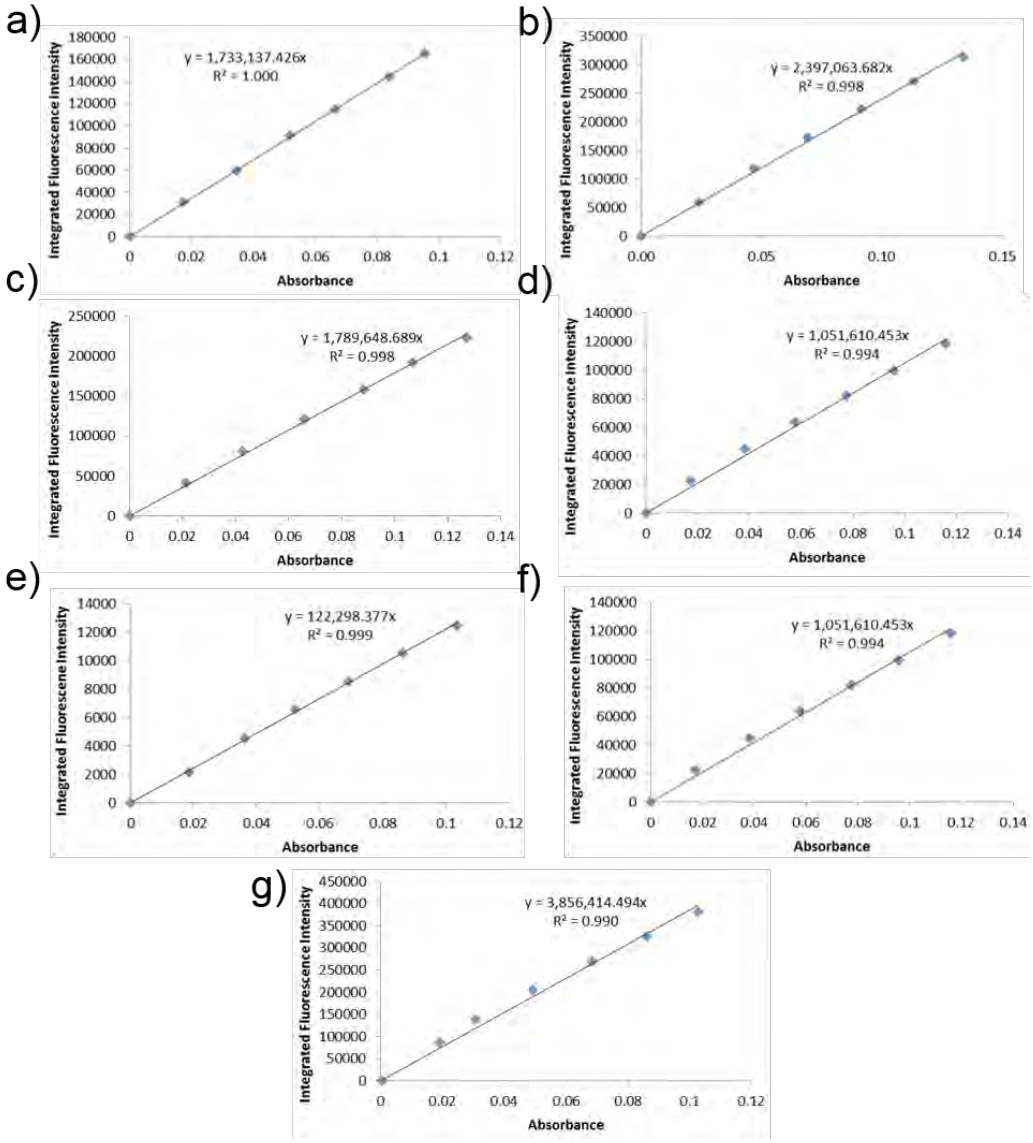

Figure III-S38. Plot of integrated fluorescence intensity *vs* absorbance for a) **III-1**, b) **III-1•CB7**, c) **III-3**, d) **III-5**, e) [4]MN **III-7**, f) [4]MN **III- 8** and g) stilbene 420.

Appendix 3

Self Assembled Cages with Mechanically Interlocked Cucurbiturils

By Kimberly G. Brady,[†] Bingqing Liu,[‡] Xiaopeng Li,[‡] and Lyle Isaacs[*†]

[†]*Department of Chemistry and Biochemistry, University of Maryland, College Park, Maryland 20742, United States*
[‡]*Department of Chemistry, University of South Florida, Tampa, Florida 33620, United States*

Table of Contents **Pages**

Experimental Details. Compounds **IV-1**,[242] **IV-2**,[243] and **IV-10**[254] were prepared according to literature procedures. NMR spectra were measured on 400 MHz, 500 MHz, and 600 MHz spectrometers (400, 500, 600 MHz for ^{1}H NMR; 100, 126 MHz for ^{13}C NMR) at room temperature in the stated deuterated solvents unless otherwise stated. Low resolution mass spectrometry was performed using a JEOL AccuTOF electrospray instrument. Electrospray ionization-mass spectrometry (ESI-MS) for cage samples was performed on a Waters Synapt G2 mass spectrometer, using sample solutions (1 mg mL^{-1}) in DMSO/CH_3CN (1/1, v/v). The ESI-MS experiments were carried out under the following conditions: ESI capillary voltage, 3 kV; sample cone voltage, 30 V; extraction cone voltage, 0.1 V; source temperature 100 ºC; desolvation temperature, 100 ºC; cone gas flow, 10 L/h; desolvation gas flow, 700 L/h (N_2).

Compound IV-3 (Chloride salt). Compound **IV-1** (0.437 g, 0.778 mmol) was dissolved in EtOH (75.0 mL) and then **IV-2** (0.446 g, 1.57 mmol) was added to the reaction flask causing the yellow solution to turn dark brown. The reaction mixture was stirred and heated at reflux overnight. The reaction mixture was allowed to cool to room temperature and then the majority of the solvent (20 mL remaining) was removed by rotary evaporation. The heterogenous mixture was then poured into THF (800 mL) and stirred at room temperature for 2 h which resulted in a brown precipitate. The solid was collected by filtration to afford **IV-3** as a dark red powder (569 mg, 96% yield). M.p. > 300 °C. IR (ATR, cm^{-1}) 3359m, 3030m, 1702m, 1630m, 1584m, 1529m, 1489m, 1367m, 1319m, 1234m, 1152s, 1053m, 818s. ^{1}H NMR (600 MHz, DMSO-d_6): 9.73 (d, J = 6.0 Hz, 4H), 9.57 (s, 2H), 9.09 (d, J = 6.0 Hz, 4H), 8.05 (d, J = 8.4 Hz, 4H), 8.03 (d, J = 8.4 Hz, 4H), 7.77 (d, J = 8.3Hz, 4H), 7.64 (d, J = 8.3Hz, 4H), 1.50 (s, 18H). ^{13}C NMR (126 MHz, DMSO-d_6): 152.8, 148.8,

145.7, 142.9, 140.7, 140.2, 131.4, 127.5, 127.4, 126.7, 125.3, 118.6, 79.4, 20.1. ESI-MS (ESI): *m/z* 346.3 ($[M]^{2+}$), calcd. for $C_{44}H_{44}N_4O_4$, 346.4.

Compound IV-4 (Chloride salt). Compound **IV-3** (0.301 g, 0.395 mmol) was suspended in CH_2Cl_2 (30 mL) and the slurry was cooled in an ice-water bath. TFA (6.0 mL) was added dropwise over 30 minutes which resulted in a red solution. The solution was removed from the ice bath and stirred at room temperature for 2 hours. The solvent was removed by rotary evaporation yielding a dark yellow oil. The oil was treated with EtOH (10 mL) and then the solvent was removed by rotary evaporation which resulted in a purple gummy solid. Repetition of the treatment with EtOH two more times ultimately gave **IV-4** as the dichloride salt as a dark yellow solid (0.367 g, 98%) after drying on high vacuum overnight. M.p. > 300 °C. IR (ATR, cm^{-1}) 3400w, 2920w, 2851w, 1631m, 1608m, 1592m, 1492m, 1285w, 1199w, 824s. ^1H NMR (600 MHz, D_2O): 9.43 (d, J = 6.9 Hz 4H), 8.78 (d, J = 6.9 Hz, 4H), 7.97 (d, J = 8.6 Hz, 4H), 7.87 (d, J = 8.6 Hz, 4H), 7.66 (d, J = 8.4 Hz, 4H), 6.98 (d, J = 8.4 Hz, 4H). ^{13}C NMR (100 MHz, D_2O, Dioxane as reference): 150.6, 145.4, 143.1, 141.8, 129.2, 129.0, 127.2, 124.7, 123.5. ESI-MS (ESI, sample dissolved in H_2O): *m/z* 246.1 ($[M]^{2+}$), $C_{34}H_{28}N_4$, calculated 246.3.

Compound IV-4 (Hexafluorophosphate salt). First, counter anion exchange from chloride to hexafluorophosphate was performed by dissolving **IV-4** (9.1 mg, 11.5 μmol) in water (5.0 mL) and then adding NH_4PF_6 (22.3 mg, 115 μmol) which caused a purple precipitate to form. The heterogenous mixture was sonicated for 30 minutes. The solid was obtained by centrifugation and the pellet was suspended in water (2.0 mL) with the help of vortexing and sonication and then the mixture was centrifuged. The supernatant was decanted. The process was repeated 3 times to ensure excess NH_4PF_6 was removed followed by drying

under high vacuum to give **IV-4** (hexafluorophosphate salt, 7.1 mg, 9.1 μmol, 79%). M.p. > 300 °C. IR (ATR, cm^{-1}) 3076m, 2833m, 2600m, 1740s, 1679s, 1634m, 1545w, 1520w, 1492m, 1433w, 1406w, 1224w, 1196s, 1131s, 1005w, 862w, 832w, 817m, 805m, 790m, 720m, 666m. ^{1}H NMR (600 MHz, CD_3CN): 9.22 (d, J = 7.08 Hz, 4H), 8.65 (d, J = 7.08 Hz, 4H), 7.95 (d, J = 8.81 Hz, 4H), 7.80 (d, J = 8.81 Hz, 4H), 7.56 (d, J = 8.61 Hz, 4H), 6.79 (d, J = 8.61 Hz, 4H). ^{13}C NMR (126 MHz, DMSO-d_6): 149.7, 148.5, 145.4, 143.8, 139.6, 127.7, 126.5, 126.4, 125.0, 124.6, 114.2. ESI-MS (ESI, sample dissolved in CH_3CN): *m/z* 246.2 ($[M]^{2+}$), $C_{34}H_{28}N_4$, calculated 246.3.

Compound IV-4 (Triflimide salt). First, counter anion exchange from chloride to triflimide was performed by dissolving **IV-4** (11.6 mg, 12.3 μmol) in water (2.0 mL) and then adding $LiNTf_2$ (291 mg, 1.01 mmol) which caused a purple precipitate to form. Heterogenous mixture was sonicated for 30 minutes. The solid was obtained by centrifugation and the pellet was suspended in water (2.0 mL) with the help of vortexing and sonication and then the mixture was centrifuged. The supernatant was decanted. The process was repeated 3 times to ensure excess $LiNTf_2$ was removed followed by drying under high vacuum to give **IV-4** (triflimide salt, 10.7 mg, 10.2 μmol, 83%). M.p. > 300 °C. IR (ATR, cm^{-1}) 3648w, 3401w, 3126w, 2919m, 2851w, 2362w, 1632m, 1609m, 1593m, 1530w, 1492m, 1435w, 1410w, 1285w, 1199w, 1003w, 815s, 740w. ^{1}H NMR (400 MHz, CD_3CN): 9.22 (d, J = 7.1 Hz, 4H), 8.65 (d, J = 7.1, Hz, 4H), 7.95 (d, J = 8.9, Hz, 4H), 7.80 (d, J = 8.9, Hz, 4H), 7.56 (d, J = 8.6 Hz, 4H), 6.79 (d, J = 8.6 Hz, 4H), 4.48 (br. s, 4H). ^{13}C NMR (126 MHz, CD_3CN): 150.8, 150.2, 146.3, 146.0, 141.0, 129.2, 128.5, 128.3, 127.5, 125.8, 115.8. ESI-MS (ESI, sample dissolved in CH_3CN): *m/z* 246.1 ($[M]^{2+}$), $C_{34}H_{28}N_4$, calculated 246.3.

Cage IV-6 (Hexafluorophosphate salt). Hexafluorophosphate salt **IV-4** (10.4 mg, 13.3 μmol) and iron (II) triflate (3.1 mg, 8.8 μmol) were placed in a scintillation vial with a stir bar and capped with a rubber septum. The vial was purged of oxygen by several cycles of high vacuum and then refilling with N_2 gas. Subsequently, **IV-5** (2.5 μL, 26 μmol) and dry acetonitrile (0.9 mL) were added by syringe. The reaction vial was sonicated for 30 minutes which resulted in a dark purple solution. The reaction mixture was then stirred at 60 °C for 24 h. After cooling to room temperature, Et_2O (6.0 mL) was added to the reaction mixture which caused **IV-6** to precipitate. After centrifugation and decantation of the supernatant, **IV-6** was obtained as a purple solid. Purple solid was redissolved in CH_3CN (0.5 mL) and excess NH_4PF_6 (4.4 mg, 27 μmol) was added. Et_2O (6.0 mL) was added to the solution causing **IV-6** to precipitate. After centrifugation and decantation of the supernatant, **IV-6**•$20PF_6$ was air dried and obtained as a purple solid (9.3 mg, 90%). IR (ATR, cm^{-1}): 3125w, 3070w, 1633m, 1595w, 1488m, 1443w, 1400w, 1254m, 1223m, 1160m, 1028m, 1005w, 816s, 774m, 750w, 740w. ^{1}H NMR (400 MHz, CD_3CN): 9.24 (br. s, 24H), 8.95 – 8.90 (m, 12H), 8.68 (br. s, 24H), 8.58 (br. d, 12H), 8.44 (br. t, 12H), 8.09 (br. s, 24H), 7.93 (br. s, 24H), 7.82 (br. t, 12H), 7.70 – 7.65 (m, 24H), 7.50 – 7.45 (m, 12H), 5.60 - 5.55 (m, 24H). ^{13}C NMR (126 MHz, CD_3CN): 175.9, 159.2, 157.1, 151.6, 151.5, 146.8, 144.0, 143.1, 140.9, 140.0, 132.6, 131.3, 130.3, 129.7, 128.7, 128.6, 126.3, 123.3.

Cage IV-6 (Triflimide salt). Triflimide salt **IV-4** (5.7 mg, 5.4 μmol) was placed in a scintillation vial with a stir bar and iron (II) triflimide (2.6 mg, 4.2 μmol) and capped with a rubber septum. The vial was purged of oxygen by several cycles of high vacuum and then refilling with N_2 gas. Subsequently, dry acetonitrile (1.0 mL) and **IV-5** (0.5 μL, 5 μmol) was added by syringe. The reaction vial was sonicated for 30 minutes which resulted

in a dark purple solution. The reaction mixture was then stirred at 60 °C for 24 h. After cooling to room temperature, Et_2O (6.0 mL) was added to the reaction mixture which caused **IV-6** to precipitate. After centrifugation and decantation of the supernatant, **IV-6** was obtained as a purple solid which was air dried. ^{1}H NMR (600 MHz, CD_3CN): 9.24 (br. s, 24H), 9.00 – 8.95 (m, 12H), 8.69 (br. m, 24H), 8.65 - 8.55 (br. m, 12H), 8.50 - 8.40 (br. m, 12H), 8.06 (d, J = 8.6 Hz, 24H), 7.93 (br. m, 24H), 7.83 (br. m, 12H), 7.75 – 7.60 (m, 24H), 7.55 – 7.45 (m, 12H), 5.70 - 5.60 (m, 24H). ^{13}C NMR (126 MHz, CD_3CN): 175.9, 157.1, 151.7, 151.5, 151.4, 146.6, 144.0, 143.0, 140.9, 140.0, 132.5, 131.3, 130.1, 129.5, 128.49, 128.43, 126.2, 126.0, 125.4, 124.1, 123.3, 122.0, 119.9.

Cage IV-7 (Hexafluorophosphate salt). Solid CB[7] (3.0 mg, 2.6 μmol) and **IV-4**•2Cl (2.4 mg, 2.5 μmol) was dissolved in D_2O (1.0 mL). The 1:1 stoichiometric ratio was confirmed by ^{1}H NMR integration of the resonances of CB[7] versus **IV-4**. An excess of NH_4PF_6 (7.7 mg, 47 μmol) was added to the solution causing a dark brown solid to precipitate. The heterogenous mixture was sonicated for 30 minutes before being centrifuged and the supernatant was decanted. The moist solid was suspended in water with the help of sonication followed by centrifugation. The brown solid was dried on high vacuum overnight to give **IV-4**•CB[7] (4.6 mg, 90%). Solid **IV-4**•CB[7] (2.3 mg, 1.2 μmol) was placed in a scintillation vial with a stir bar and capped with a rubber septum. The vial was purged of oxygen by several cycles of high vacuum and then refilling with N_2 gas. Subsequently, **IV-5** (0.2 μL, 2 μmol), a solution of iron (II) triflate (16 mM, 50 μL, 0.8 μmol) in dry acetonitrile, and dry acetonitrile (50 μL) was added by syringe. The reaction vial was sonicated for 30 minutes which gave a dark purple solution. The reaction was then stirred at 60 °C for 24 h. The reaction mixture was cooled to room temperature and then

Et_2O (6.0 mL) was added which resulted in a precipitate. The heterogenous mixture was centrifuged, the supernatant removed, and the pellet was dried in air to give **IV-7** as a purple solid. Purple solid was redissolved in CH_3CN (0.5 mL) and excess NH_4PF_6 (2.0 mg, 12 μmol) was added. Et_2O (6.0 mL) was added to the solution causing **IV-7** to precipitate. After centrifugation and decantation of the supernatant, **IV-7**•$20PF_6$ was air dried and obtained as a purple solid (1.9 mg, 56%). IR (ATR, cm^{-1}): 3366w, 3124w, 1738s, 11632m, 1595w, 1488m, 1464s, 1423m, 1375m, 1320m, 1278m, 1227s, 1189s, 1029m, 1005w, 968m, 830s, 800s, 756m, 672w. ^1H NMR (600 MHz, CD_3CN, RT): 9.26 – 9.18 (m, 24H), 8.97 (br. m, 12H), 8.70 – 8.60 (m, 28H), 8.45 (br., 12H), 8.25 – 8.20 (m, 16H), 8.10 (br. , 18H), 7.94 (br., 18H), 7.82 (br., 16H), 7.69 (br., 24H), 7.47 (br., 12H), 7.11 (br., 8H), 5.67 – 5.58 (m, 52H), 5.27 (s, 28H), 4.06 (d, J = 13.0 Hz, 28H). ^{13}C NMR (126 MHz, CD_3CN): 190.3, 175.8, 159.2, 157.1, 156.3, 151.5, 148.9, 146.7, 144.0, 143.0, 142.8, 140.9, 140.0, 138.8, 132.5, 131.3, 130.3, 130.1, 129.6, 138.5, 128.1, 126.2, 126.0, 124.1, 123.2, 71.7, 53.4.

Cage IV-7 (Triflimide Salt). Solid CB[7] (6.2 mg, 5.3 μmol) and **IV-4** (5.6 mg, 5.9 mmol) was dissolved in D_2O (2.0 mL). The 1:1 stoichiometric ratio was confirmed by ^1H NMR integration of the resonances of CB[7] versus **IV-4**. An excess of $LiNTf_2$ (169 mg, 0.655 mmol) was added to the solution causing a dark brown solid to precipitate. The heterogenous mixture was sonicated for 30 minutes before being centrifuged and the supernatant was decanted. The moist solid was suspended in water with the help of sonication followed by centrifugation. The brown solid was dried on high vacuum overnight to give **IV-4**•CB[7] (12.3 mg, 94%). Solid **IV-4**•CB[7] (6.1 mg, 2.8 μmol) was placed in a vial with a stir bar and iron (II) triflimide (1.3 mg, 2.1 μmol). The vial was

capped with a rubber septum and deoxygenated by repeated cycles of high vacuum and then refilling with N_2 gas. Dry acetonitrile (0.6 mL) and **IV-5** (0.3 μL, 3 μmol) were added by syringe. The reaction vial was sonicated for 30 minutes which gave a dark purple solution. The reaction was then stirred at 60 °C for 24 h. The reaction mixture was cooled to room temperature and then Et_2O (6.0 mL) was added which resulted in a precipitate. The heterogenous mixture was centrifuged, the supernatant removed, and the pellet was dried in air to give **IV-7** as a purple solid. ^{1}H NMR (600 MHz, CD_3CN, RT): 9.25 – 9.15 (m), 8.90 (br. m), 8.70 (br. s), 8.25 – 7.80 (m), 7.70 – 7.65 (m), 7.46 (br. s), 7.40 – 7.25 (m), 7.14 (br. s), 5.70 (d), 5.27 (br. s), 4.06 (d). ^{13}C (126 MHz, CD_3CN, RT): 156.3, 151.9, 148.9, 146.7, 131.4, 130.9, 130.4, 130.1, 128.3, 128.1, 128.0, 127.5, 127.3, 126.3, 126.1, 124.5, 124.2, 124.0, 122.0, 120.3, 119.9, 71.6, 53.4.

Compound IV-11 (Chloride salt). Compound **IV-1** (0.205 g, 0.827 mmol) and **IV-10** (0.211 mg, 0.376 mmol) were dissolved in EtOH (55.0 mL). The solution was heated at reflux for 24 h during which the solution turned brown in color. The reaction was then concentrated by rotary evaporation (to ≈ 20 mL) and then poured into THF (500 mL). After stirring for 2 hours at room temperature, a yellow precipitate was observed which was isolated by filtration. The crude solid was washed on the frit with THF (10 mL) three times to afford **IV-11** as the chloride salt (259 mg, 97%). M.p. > 300 °C. IR (ATR, cm^{-1}): 3368m, 3107w, 1628s, 1587m, 1460s, 1433s, 1417m, 1368m, 1342w, 1244m, 1093w, 1072w, 1034w, 1000s, 832s, 817s. ^{1}H NMR (600 MHz, DMSO-d_6, RT): 9.80 (d, J = 6.4 Hz, 4H), 9.21 (s, 2H), 9.14 (d, J = 6.4 Hz, 4H), 8.76 (d, J = 6.5 Hz, 2H), 8.58 (d, J = 8.2 Hz, 2H), 8.48 (d, J = 6.5 Hz, 2H), 8.45 (d, J = 8.2 Hz, 2H), 8.30 (d, J = 8.3 Hz, 4H), 8.17 (d, J = 8.3 Hz, 4H), 8.02 (t, J = 6.5 Hz, 2H), 7.52 (t, J = 6.5 Hz, 2H). ^{13}C NMR (126 MHz, DMSO-

d$_6$): 155.1, 154.2, 149.4, 149.0, 147.7, 145.9, 139.9, 139.6 137.6, 135.7, 134.4, 128.5, 126.6, 125.7, 125.1 120.6. ESI-MS (ESI, sample dissolved in H_2O): *m/z* 309.1 ($[M]^{2+}$), $C_{42}H_{30}N_6$, calculated 309.4.

Compound IV-11 (Hexafluorophosphate salt). Compound **IV-11** (chloride) was transformed into the hexafluorophosphate salt by dissolving **IV-11**·2Cl (36.8 mg, 53.4 μmol) in water (12 mL) and heating to 80 °C followed by the addition of NH_4PF_6 (90.7 mg, 556 mmol) was resulted in the formation of a precipitate. Heterogenous mixture was stirred at 80 °C for 30 minutes. The heterogenous mixture was cooled to room temperature, centrifuged, and the supernatant was decanted to give a moist solid. The moist solid was suspended in water (2.0 mL) with the help of sonication, followed by centrifugation, and removal of the supernatant. This process was repeated three times to remove excess NH_4PF_6 and then the solid **IV-11**•2PF_6 was dried under high vacuum (39.1 mg, 81%). M.p. > 300 °C. IR (ATR, cm^{-1}): 3135w, 3053w, 2924s, 2362w, 1636m, 1588m, 1552w, 1485w, 1458m, 1435m, 1417w, 1369w, 1264w, 1216w, 1149w, 1094w, 1067w, 1043w, 1002w, 877s, 794m, 752w, 741w, 716w, 695w. ^{1}H NMR (600 MHz, CD_3CN, RT): 9.29 (d, *J* = 7.0, 4H), 9.10 (d, *J* = 4.1 Hz, 2H), 8.75 - 8.70 (m, 6H), 8.61 (d, *J* = 9.5 Hz, 2H), 8.50 (d, *J* = 7.9, 2H), 8.29 (dd, *J* = 4.1, 9.5 Hz, 2H), 8.17 (d, *J* = 8.7 Hz, 4H), 8.00 - 1.90 (m, 6H), 7.45 (t, *J* = 4.8 Hz, 2H). ^{13}C NMR (126 MHz, CD_3CN): 150.4, 148.9, 146.7, 143.0, 138.7, 137.3, 136.9, 130.2, 128.4, 126.3, 125.3, 121.9. ESI-MS (ESI, sample dissolved in CH_3CN): *m/z* 309.0 ($[M]^{2+}$), $C_{42}H_{30}N_6$, calculated 309.4.

Compound IV-11 (Triflimide salt). Compound **IV-11** (chloride) was transformed into the triflimide salt by dissolving **IV-11**·2Cl (23.9 mg, 34.7 μmol) in water (10 mL) and heating to 80 °C followed by the addition of $LiNTf_2$ (107.2 mg, 373 μmol) was resulted in the

formation of a precipitate. Heterogenous mixture was stirred at 80 °C for 30 minutes. The heterogenous mixture was cooled to room temperature, centrifuged, and the supernatant was decanted to give a moist solid. The moist solid was suspended in water (4.0 mL) with the help of sonication, followed by centrifugation, and removal of the supernatant. This process was repeated three times to remove excess LiNTf2 and then the solid **IV-11** (29.2 mg, 71%) was dried under high vacuum. M.p. > 300 °C. IR (ATR, cm^{-1}): 3124w, 3068w, 1632m, 1587w, 1573w, 1550w, 1485w, 1458m, 1436w, 1419w, 1351s, 1331s, 1179s, 1129s, 1093w, 1050s, 1000m, 877w, 828m, 799m, 756m, 739m. ^{1}H NMR (400 MHz, CD_3CN, RT): 9.29 (d, *J* = 6.7, 4H), 9.10 (d, *J* = 2.1 Hz, 2H), 8.75 - 8.70 (m, 6H), 8.61 (d, *J* = 8.3 Hz, 2H), 8.50 (d, *J* = 7.9, 2H), 8.29 (dd, *J* = 2.1, 8.3 Hz, 2H), 8.17 (d, *J* = 8.6 Hz, 4H), 8.00 - 1.90 (m, 6H), 7.45 (t, *J* = 5.1 Hz, 2H). ^{13}C NMR (126 MHz, DMSO-d_6): 155.1, 154.6, 149.5, 149.0, 147.7, 145.9, 141.9, 139.9, 137.5, 135.7, 133.7, 128.5, 126.6, 125.7, 124.5, 120.6, 118.4. ESI-MS (ESI, sample dissolved in CH_3CN): *m/z* 309.0 ($[M]^{2+}$), $C_{42}H_{30}N_6$, calculated 309.4.

Cage IV-12 (Hexafluorophosphate salt). A solution of iron (II) triflate (10.7 mM, 0.5 mL, 5.37 μmol) in CH_3CN was added to a vial with solid hexafluorophosphate salt **IV-12** (5.7 mg, 6.27 μmol) suspended in CH_3CN (1.0 mL). Once iron was added, the yellow suspension turned ruby red. The mixture was sonicated for 30 minutes and then stirred at 60 °C for 24 h resulting in a ruby red homogenous solution. The red solution was cooled to room temperature and then Et_2O (6.5 mL) was added which resulted in a red solid. The heterogenous mixture was centrifuged followed by removal of the supernatant. The solid was resuspended in Et_2O (6.0 mL) with the help of sonication followed by centrifugation and decantation of the supernatant to obtain the red solid. The process was repeated two

more times. Red solid was then redissolved in a solution of NH_4PF_6 (77 mM, 0.25 mL, 3.1 mmol) in CH_3CN. Et_2O (5.0 mL) was added causing **IV-12** to precipitate. Red solid was collected by centrifugation and decantation. The solid was resuspended in Et_2O (6.0 mL) with the help of sonication followed by centrifugation and decantation of the supernatant to obtain the red solid. The process was repeated two more times. Cage **IV-12**•$20PF_6$ was air dried and obtained as a red solid (4.3 mg, 60%). IR (ATR, cm^{-1}): 3657w, 3587w, 3129w, 2360w, 1634m, 1605w, 1490w, 1467m, 1440m, 1377w, 1344w, 1243w, 1168w, 1010w, 1008w, 815s, 752m, 738m. ^1H NMR (600 MHz, CD_3CN, RT): 9.15 (d, J = 5.9 Hz, 24H), 8.74 (d, J = 8.3 Hz, 12H), 8.67 (d, J = 8.3 Hz, 12H), 8.62 (d, J = 5.9 Hz, 24H), 8.52 (d, J = 8.7 Hz, 12H), 8.20 (t, J = 8.4 Hz, 12H), 7.84 (d, J = 5.68 Hz, 24H), 7.80-7.75 (m, 36H), 7.49 (m, 24H). ^{13}C NMR (126 MHz, CD_3CN, RT): 160.0, 159.9, 155.5, 154.0, 151.6, 146.6, 143.8, 140.1, 139.7, 138.7, 138.4, 130.5, 128.9, 128.5, 126.4, 125.9, 125.1. ESI-MS: *m/z* 994.23 ($[Fe_4$**IV-11**$_6 + 14PF_6]^{6+}$), $C_{252}H_{180}F_{84}Fe_4N_{36}P_{14}$, calculated 994.13; 831.35 ($[Fe_4$**IV-11**$_6 + 13PF_6]^{7+}$), $C_{252}H_{180}F_{78}Fe_4N_{36}P_{13}$, calculated 831.40; 709.30 ($[Fe_4$**IV-11**$_6 + 12PF_6]^{8+}$), $C_{252}H_{180}F_{72}Fe_4N_{36}P_{12}$, calculated 709.35; 614.38 ($[Fe_4$**IV-11**$_6 + 11PF_6]^{9+}$) $C_{252}H_{180}F_{66}Fe_4N_{36}P_{11}$, calculated 614.43.

Cage IV-12 (Triflimide salt). Triflimide salt **IV-12** (16.0 mg, 13.6 μmol) was dissolved in CH_3CN (3.4 mL) and then iron (II) triflimide (5.7 mg, 9.3 μmol) was added causing the solution to turn ruby red. The homogenous solution was sonicated for 30 minutes and then stirred at 70 °C for 24 h. The reaction mixture was cooled to room temperature and then Et_2O (6.0 mL) was added which resulted in a red solid. The heterogenous mixture was centrifuged followed by removal of the supernatant. The solid was resuspended in Et_2O (6.0 mL) with the help of sonication followed by centrifugation and decantation of the

supernatant to obtain the red solid. The process was repeated two more times followed by air drying to obtain **IV-12** as a red solid. ^{1}H NMR (400 MHz, CD_3CN, RT): 9.11 (d, *J* = 6.7 Hz, 24H), 8.73 (d, *J* = 8.3 Hz, 12H), 8.66 (d, *J* = 8.3 Hz, 12H), 8.59 (d, *J* = 6.7 Hz, 24H), 8.50 (d, *J* = 8.4 Hz, 12H), 8.20 (t, *J* = 7.4 Hz, 12H), 7.85 - 7.70 (m, 60H), 7.49 (m, 24H). ^{13}C NMR (126 MHz, CD_3CN, RT): 160.0, 159.7, 155.4, 151.5, 146.5, 143.7, 140.0, 139.6, 138.6, 138.2, 130.3, 128.9, 128.4, 126.3, 125.1, 121.9, 119.8.

Cage IV-12 (Sulfate salt). A solution of K_2SO_4 (6.8 mg, 39 μmol) in D_2O (500 μL) was treated with **IV-12**·2Cl (2.6 mg, 3.8 μmol) and $FeSO_4$•$7H_2O$ (13mM, 200 μL, 2.5 μmol) dissolved in D_2O. The reaction mixture was sonicated for 1 hour and then stirred at 50 °C for 24 hours during which the solution changed color from cloudy yellow to clear ruby red. Acetone (5.0 mL) was added to the reaction mixture which results in a red precipitate. The heterogeneous mixture was centrifuged, the supernatant decanted, and the pellet was air dried to give **IV-12** as red solid. ^{1}H NMR (600 MHz, D_2O, RT): 9.39 (d, *J* = 5.8 Hz, 24H), 8.88 (d, *J* = 7.6 Hz, 12H), 8.82 (br. s, 24H), 8.77 (d, *J* = 7.6 Hz, 12H), 8.61 (d, *J* = 7.9 Hz, 12H), 8.25 (br., 12H), 7.90 – 7.85 (m, 36H), 7.75 (d, *J* = 6.8 Hz, 12H), 7.70 (d, *J* = 7.44 Hz, 12H), 7.53 (br., 12H). ^{13}C NMR (126 MHz, D_2O, Acetone as a standard, RT): 158.8, 158.2, 154.0, 151.2, 150.3, 145.0, 142.4, 138.7, 137.9, 137.5, 137.3, 128.7, 127.2, 126.9, 124.9, 124.1, 123.7.

Cage IV-13 (Hexafluorophosphate salt). A mixture of CB[7] (28.7 mg, 24.7 μmol) and **IV-11**·2Cl (17.0 mg, 24.7 μmol) was dissolved in D_2O (6.0 mL) using a heat gun and sonication and the 1:1 stoichiometric ratio was confirmed by measuring the ^{1}H NMR integrals for each component. The solution was heated to 80 °C and treated with NH_4PF_6 (44.8 mg, 275 μmol) which caused the formation of an yellow precipitate. The

heterogenous mixture was stirred at 80 °C for 30 minutes before cooling to room temperature, centrifuged, and the supernatant decanted. The moist solid was resuspended in water (2.0 mL) with the help of sonication followed by centrifugation and decantation. The process was repeated two more times and then the solid (44.1 mg, 86%) was dried on high vacuum overnight. A sample of **IV-11•**CB[7] hexafluorophosphate salt (2.3 mg, 1.1 μmol) was dissolved in CH_3CN (0.15 mL) and then a solution of $FeOTf_2$ (50 μL, 16 mM in CH_3CN) was added which caused the solution to turn ruby red. The reaction mixture was sonicated for 30 min. and then stirred at 60 °C for 24 h. The reaction mixture was cooled to room temperature and then Et_2O (7.0 mL) was added which resulted in a red precipitate. The red precipitate was obtained by centrifugation followed by decanting of the supernatant. The moist solid was resuspended in Et_2O (2.0 mL) with the help of sonication followed by centrifugation and decantation of the supernatant. The process was repeated two more times and then air dried to give **IV-13** as a red solid. Compound **IV-13** was redissolved in CH_3CN (0.5 mL) and excess NH_4PF_6 (1.8 mg, 11 μmol) was added. Et_2O (6.0 mL) was added to the solution causing **IV-13** to precipitate. After centrifugation and decantation of the supernatant, **IV-13•**$20PF_6$ was collected as red solid. The red solid was resuspended in Et_2O (2.0 mL) with the help of vortexing and collected by centrifugation and decantation. This process was repeated two additional time to ensure the removal of excess NH_4PF_6. The red solid was then air dried to yield **IV-13•**$20PF_6$. IR (ATR, cm^{-1}): 3493m, 3115w, 2920w, 2361w, 1733s, 1634m, 1465s, 1422m, 1375m, 1375m, 1320m, 1281m, 1227s, 1188s, 1029m, 967m, 823m, 801s, 757m, 671m. ^1H NMR (600 MHz, CD_3CN, RT): 9.20 - 9.00 (m, 24H), 8.80 – 8.45 (m, 57H), 8.20 (br., 20H), 8.00 – 7.75 (m, 53H), 7.47 (br., 28H), 7.02 (br. s, 7H), 5.56 (br., 26H), 5.35 – 5.15 (m, 26H),

4.01 (br., 26H). ^{13}C NMR (126 MHz, CD_3CN, RT): 165.6, 160.2, 159.8, 156.2, 155.2, 151.4, 148.8, 146.6, 139.9, 139.2, 128.9, 128.4, 126.3, 123.9, 71.6, 53.4. ESI-MS: 1163.73 ([Fe_4**IV-11**$_6$ + 2CB[7] + 13PF_6]$^{7+}$), $C_{336}H_{264}F_{78}Fe_4N_{92}O_{28}P_{13}$, calculated 1163.64; 1145.43 ([Fe_4**IV-11**$_6$ + 3CB[7] + 12PF_6]$^{8+}$), $C_{378}H_{306}F_{72}Fe_4N_{120}O_{42}P_{12}$, calculated 1145.48; 1002.16 ([Fe_4**IV-11**$_6$ + 3CB[7] + 11PF_6]$^{9+}$), $C_{378}H_{306}F_{66}Fe_4N_{120}O_{42}P_{11}$, calculated 1002.10; 1000.27 ([Fe_4**IV-11**$_6$ + 2CB[7] + 12PF_6]$^{8+}$), $C_{336}H_{264}F_{72}Fe_4N_{92}O_{28}P_{12}$, calculated 1000.07; 887.3467 ([Fe_4**IV-11**$_6$ + 3CB[7] + 10PF_6]$^{10+}$), $C_{378}H_{306}F_{60}Fe_4N_{120}O_{42}P_{10}$, calculated 887.39; 872.89 ([Fe_4**IV-11**$_6$ + 2CB[7] + 11PF_6]$^{9+}$), $C_{336}H_{264}F_{66}Fe_4N_{92}O_{28}P_{11}$, calculated 872.84; 854.72 ([Fe_4**IV-11**$_6$ + 1CB[7] + 12PF_6]$^{8+}$), $C_{294}H_{222}F_{72}Fe_4N_{64}O_{14}P_{12}$, calculated 854.77; 793.49 ([Fe_4**IV-11**$_6$ + 3CB[7] + 9PF_6]$^{11+}$), $C_{378}H_{306}F_{54}Fe_4N_{120}O_{42}P_9$, calculated 793.54; 771.11 ([Fe_4**IV-11**$_6$ + 2CB[7] + 10PF_6]$^{10+}$), $C_{336}H_{264}F_{60}Fe_4N_{92}O_{28}P_{10}$, calculated 771.06; 743.64 ([Fe_4**IV-11**$_6$ + 1CB[7] + 11PF_6]$^{9+}$), $C_{294}H_{222}F_{66}Fe_4N_{64}O_{14}P_{11}$, calculated 743.69.

Cage IV-13 (Triflimide salt). A mixture of CB[7] (10.4 mg, 8.9 μmol) and **IV-11**·2Cl (6.2 mg, 9.0 μmol) was dissolved in D_2O (7.0 mL) and the 1:1 stoichiometric ratio was confirmed by measuring the ^{1}H NMR integrals for each component. The solution was heated to 80 °C and treated with $LiNTf_2$ (0.5 mL, 0.2 mM in CH_3CN) which caused the formation of an orange-brown precipitate. The heterogenous mixture was stirred at 80 °C for 30 minutes. The heterogenous mixture was cooled to room temperature, centrifuged, and the supernatant decanted. The moist solid was resuspended in water (1.0 mL) with the help of sonication followed by centrifugation and decantation. The process was repeated two more times and then the solid (16.5 mg, 81%) was dried on high vacuum overnight. A sample of **IV-11**•CB[7] triflimide salt (7.9 mg, 4.3 μmol) was dissolved in CH_3CN (0.5 mL) and then a solution of $Fe(NTf_2)_2$ (0.5 mL, 6.2 mM in CH_3CN) was added which caused

the solution to turn ruby red. The reaction mixture was sonicated for 30 min. and then stirred at 70 °C for 24 h. The reaction mixture was cooled to room temperature and then Et_2O (10.0 mL) was added which resulted in a red precipitate. The red precipitate was obtained by centrifugation followed by decanting of the supernatant. The moist solid was resuspended in Et_2O (5.0 mL) with the help of sonication followed by centrifugation and decantation of the supernatant. The process was repeated two more times and then air dried to give **IV-13** as a red solid. ^{1}H NMR (600 MHz, CD_3CN, RT): 9.25-9.00 (br. m), 8.85 – 8.45 (m), 8.19 (br.s), 8.0 – 7.70 (br. m), 7.49 (br. m), 6.99 (br. s), 5.55 (br.), 5.17 (br.), 3.94 (br.). ^{13}C NMR (200 MHz, CD_3CN, RT): 160.0, 156.2, 155.3, 153.7, 151.5, 149.0, 143.7, 140.0, 139.5, 138.6, 130.3, 128.9, 128.4, 126.3, 125.1, 123.7, 123.3, 121.7, 120.1, 71.5, 53.3.

Compound IV-15. A solution of H_2O (16.7 mL), MeOH (5.1 mL), and THF (5.1 mL) was purged with N_2 for 15 min. and then compound **IV-14** (0.154 g, 0.66 mmol), **IV-9** (0.158 g, 0.72 mmol), and potassium carbonate (2.62 g, 29.2 mmol) were added to solution. The reaction mixture was heated and stirred at 70 °C under N_2 for 24 hours. The reaction mixture was then cooled to room temperature and solvents were removed under vacuum. The crude solid was dissolved in CH_2Cl_2 (100 mL) and partitioned against aq. KOH (1 mM, 100 mL) in a separatory funnel. The organic layer was collected and dried over Na_2SO_4 prior to removing the solvent by rotary evaporation. Compound **IV-15** was purified by column chromatography (SiO_2, DCM/EtOAc/NEt_3 50:50:3). ^{1}H NMR analysis revealed residual triphenyl phosphine so the solid was triturated three times with hexanes (10 mL) to give **IV-15** (0.103 g, 64%) as a brown solid. The ^{1}H NMR of **IV-15** recorded in $CDCl_3$ matches with data reported previously.[267]

Compound IV-16 (Chloride salt). A suspension of **IV-15** (95.0 mg, 0.38 mmol) and **IV-1** (102 mg, 0.18 mmol) in EtOH (25 mL) was heated at reflux for 3 days during which the solution turned brown. The reaction mixture was concentrated by rotary evaporation (to ≈10 mL) and then poured into THF (200 mL) and then stirred for 2 hours which gave an orange-brown precipitate. The precipitate was obtained by filtration and then washed on the frit with THF (100 mL) to give **IV-16** (96.0 mg, 77%) as an orange-brown solid. M.p. > 300 °C. IR (ATR, cm^{-1}): 3368m, 3007w, 1629m, 1601m, 1601m, 1583m, 1546w, 1531w, 1512w, 1492w, 1459m, 1436m, 1386m, 1342w, 1257w, 991w, 825s, 810s. ^{1}H NMR (400 MHz, DMSO-d_6, RT) 9.80 (d, J = 5.6 Hz, 4H), 9.07 (d, J = 5.6 Hz, 4H), 8.89 (d, J = 6.1 Hz, 2H), 8.81 (s, 2H), 8.77 (d, J = 6.1 Hz, 2H), 8.49 (d, J = 6.1 Hz, 2H), 8.35 (d, J = 8.6 Hz, 2H), 8.19 (d, J = 8.6 Hz, 4H), 8.03 (dt, J = 6.1 and 1.8 Hz, 4H), 7.97 (dd, J = 6.1 and 1.8 Hz, 2H), 7.54 (dt, J = 6.1 and 1.8 Hz, 2H). ^{13}C NMR (126 MHz, DMSO-d_6): 156.0, 154.7, 150.3, 149.2, 149.0, 146.5, 146.1, 142.8, 140.4, 137.7, 128.8, 126.4, 125.8, 124.7, 122.0, 120.9, 118.1**.** ESI-MS (ESI, sample dissolved in H_2O): *m/z* 309.1 ($[M]^{2+}$), $C_{42}H_{30}N_6$, calculated 309.4.

Compound IV-16 (Hexafluorophosphate salt). Compound **IV-16** (chloride) was transformed into the hexafluorophosphate salt by dissolving **IV-16**·2Cl (15.4 mg, 22.3 μmol) in water (5.0 mL) and heating to 80 °C followed by the addition of NH_4PF_6 (39.7 mg, 244 μmol) was resulted in the formation of a precipitate. Heterogenous mixture was stirred at 80 °C for 30 minutes. The heterogenous mixture was cooled to room temperature, centrifuged, and the supernatant was decanted to give a moist solid. The moist solid was suspended in water (2.0 mL) with the help of sonication, followed by centrifugation, and removal of the supernatant. This process was repeated three times to remove excess

NH_4PF_6 and then the solid **IV-16**•$2PF_6$ (13.8 mg, 68%) was dried under high vacuum. M.p. > 300 °C. IR (ATR, cm^{-1}): 3133w, 3070w, 2925w, 2361w, 2339w, 1733w, 1638m, 1602w, 1585m, 1568w, 1541w, 1515w, 1491w, 1460m, 1440m, 1387m, 1352w, 1216w, 1188w, 1132w, 1096w, 1039w, 1007w, 827s, 796s, 752w, 739w, 716w, 707w, 662w. ^{1}H NMR (600 MHz, CD_3CN, RT): 9.29 (d, *J* = 6.5, 4H), 8.84 (m, 4H), 8.75 - 8.65 (m, 6H), 8.52 (d, *J* = 7.9 Hz, 2H), 8.23 (d, *J* = 8.4, 4H), 7.96 (m, 6H), 7.80 (d, *J* = 3.5 Hz, 2H), 7.46 (t, *J* = 5.0 Hz, 2H). ^{13}C NMR (126 MHz, CD_3CN): 157.9, 156.4, 151.3, 150.4, 147.8, 146.8, 143.1, 138.4, 130.4, 128.4, 126.4, 125.5, 123.0, 122.0, 119.6. ESI-MS (ESI, sample dissolved in CH_3CN): *m/z* 309.1 ($[M]^{2+}$), $C_{42}H_{30}N_6$, calculated 309.4.

Compound IV-16 (Triflimide salt). Counter anion exchange from chloride to triflimide was performed by dissolving **IV-16**·2Cl (16.3 mg, 23.6 μmol) in water (5 mL) and heated to 80 °C, followed by addition of excess $LiNTf_2$ (70.4 mg, 245 μmol) which resulted in the formation of an brown precipitate. The heterogenous mixture was centrifuged, the supernatant was decanted, and the moist solid was resuspended in water (4.0 mL) with the help of sonication followed by centrifugation and the decantation of the precipitate. The process was repeated 2 more times to give **IV-16**•$2NTf_2$ after drying under high vacuum (19.2 mg, 69%). M.p. > 300 °C. IR (ATR, cm^{-1}): 3119w, 3064w, 1634m, 1601m, 1584m, 1547w, 1495w, 1472w, 1459w, 1432w, 1390w, 1347s, 1226m, 1174s, 1130s, 1051s, 1006w, 993w, 826m, 790m, 762w,790m, 762w, 739m, 706w. ^{1}H NMR (600 MHz, CD_3CN, RT): 9.28 (d, *J* = 6.8, 4H), 8.84 (m, 4H), 8.75 - 8.65 (m, 6H), 8.52 (d, *J* = 8.0 Hz, 2H), 8.23 (d, *J* = 8.6, 4H), 7.97 (m, 6H), 7.80 (dd, *J* = 1.6, 5.0 Hz, 2H), 7.46 (t, *J* = 5.0 Hz, 2H). ^{13}C NMR (126 MHz, CD_3CN): 151.4, 151.2, 150.2, 147.9, 146.7, 143.7, 143.0, 138.7,

130.4, 128.5, 126.4, 125.5, 123.1, 122.1, 122.0, 119.9, 119.7. ESI-MS (ESI, sample dissolved in CH_3CN): *m/z* 309.1 ($[M]^{2+}$), $C_{42}H_{30}N_6$, calculated 309.4.

Cubic Cage IV-17 (Hexafluorophosphate salt). The obtained hexafluorophosphate salt of **IV-17** (5.7 mg, 26.3 μmol) was dissolved in CH_3CN (1.0 mL) followed by the addition of iron (II) triflate (10.7 mM, 0.5 mL, 5.4 μmol) in CH_3CN which resulted in a color change to dark purple. The reaction mixture was sonicated for 30 minutes followed by stirring at 60 °C for 24 h. The reaction mixture is cooled to room temperature and then Et_2O (6.0 mL) is added which results in a purple precipitate. The heterogenous mixture is centrifuged, the supernatant decanted, and the moist solid is resuspended in Et_2O (6.0 mL) with the help of sonication followed by centrifugation and decantation. The process is repeated two more times. Compound **IV-17** was redissolved in CH_3CN (0.5 mL) and excess NH_4PF_6 (12.9 mg, 79.1 μmol) was added. Et_2O (6.0 mL) was added to the solution causing **IV-17** to precipitate. After centrifugation and decantation of the supernatant, **IV-17**•$40PF_6$ was collected as purple solid. The purple solid was resuspended in Et_2O (2.0 mL) with the help of vortexing and collected by centrifugation and decantation. This process was repeated two additional time to ensure the removal of excess NH_4PF_6. The purple solid was then air dried to yield **IV-17**•$40PF_6$ (7.2 mg, 78%). IR (ATR, cm^{-1}): 3124w, 2087w, 1633w, 1615w, 1476w, 1440w, 1400w, 1218w, 1029w, 817s, 739m. ^1H NMR (600 MHz, CD_3CN, RT): 9.30 (br. s, 48H), 8.96 (br. s, 24H), 8.84 (br. s, 24H), 8.74 (br. s, 48H), 8.30 – 8.24 (m, 72H), 8.06 (br. s, 48H), 7.81 (br. s, 24H), 7.62 – 7.53 (m, 72H). ^{13}C NMR (126 MHz, CD_3CN, RT): 165.7, 161.1, 157.5, 155.6, 151.8, 149.4, 146.8, 144.6, 140.2, 130.8, 128.6, 126.7.

Cubic Cage IV-17 (Triflimide salt). The obtained triflimide salt of **IV-17** (15.3 mg, 13.0 μmol) was dissolved in CH_3CN (3.3 mL) followed by the addition of iron (II) triflimide (5.3 mg, 8.6 μmol) which resulted in a color change to dark purple. The reaction mixture was sonicated for 30 minutes followed by stirring at 70 °C for 24 h. The reaction mixture is cooled to room temperature and then Et_2O (7.0 mL) is added which results in a red precipitate. The heterogenous mixture is centrifuged, the supernatant decanted, and the moist solid is resuspended in Et_2O (6.0 mL) with the help of sonication followed by centrifugation and decantation. The process is repeated two more times and then solid **IV-17** is air dried. ^{1}H NMR (400 MHz, CD_3CN, RT): 9.29 (br. s, 48H), 8.94 (br. m, 24H), 8.83 (br. m, 24H), 8.72 (br., 48H), 8.35 – 8.20 (m, 72H), 8.04 (br., 48H), 7.79 (br. s, 24H), 7.70 – 7.45 (m, 72H). ^{13}C NMR (126 MHz, CD_3CN, RT): 160.9, 159.9, 158.9, 155.4, 151.5, 149.7, 146.7, 144.4, 140.3, 139.9, 130.7, 128.4, 126.6, 123.3, 121.8, 119.7, 177.6.

Cubic Cage with CB[7] (IV-18·40PF$_6$). A mixture of CB[7] (22.7 mg, 19.5 μmol) and **IV-16**·2Cl (13.4 mg, 19.4 μmol) was dissolved in D_2O (5.0 mL) by sonication and using a heat gun. The 1:1 stoichiometric ratio was confirmed by the integrals for each component in the ^{1}H NMR spectrum. The solution was heated to 80 °C and treated with NH_4PF_6 (32.4 mg, 199 μmol) which caused the formation of a tan precipitate. The heterogenous mixture continued to stir at 80 °C for 30 minutes. The heterogenous mixture was centrifuged, the supernatant decanted, and the moist solid was resuspended in water (2.0 mL) followed by centrifugation and decantation two additional times. The solid was then dried at high vacuum overnight to yield the triflimide salt (34.0 mg, 85%). Complex **IV-16**·CB[7] hexafluorophosphate salt (3.3 mg, 0.16 μmol) was dissolved in CH_3CN (1.0 mL). The solution was treated with $Fe(OTf)_2$ (22 mM, 50 μL, 0.11 μmol) dissolved in acetonitrile

which gave a dark purple solution when added. The reaction mixture was sonicated for 30 min. and then stirred at 70 °C for 24 h. The reaction mixture is cooled to room temperature and then Et_2O (6.0 mL) is added which results in a purple precipitate. The heterogenous mixture is centrifuged, the supernatant decanted, and the moist solid is then resuspended in Et_2O followed by centrifugation and decantation of the precipitate. Compound **IV-18** was redissolved in CH_3CN (0.5 mL) and excess NH_4PF_6 (1.0 mg, 6.1 μmol) was added. Et_2O (6.0 mL) was added to the solution causing **IV-18** to precipitate. After centrifugation and decantation of the supernatant, **IV-18**•$40PF_6$ was collected as purple solid. The purple solid was resuspended in Et_2O (2.0 mL) with the help of vortexing and collected by centrifugation and decantation. This process was repeated two additional time to ensure the removal of excess NH_4PF_6. The purple solid was then air dried to yield **IV-18**•$40PF_6$. IR (ATR, cm^{-1}): 3486m, 3123w, 2916m, 2849w, 2362w, 2338w,1735s, 1631m, 1463s, 1423m, 1375m, 1319m,1280m, 1227s, 1188s, 1029m, 967m, 841m, 822m, 800s, 757m, 671w. ^1H NMR (600 MHz, CD_3CN, RT): 9.30 (d, J = 5.6 Hz), 9.00 - 8.65 (m), 8.50 – 8.00 (m), 8.00 – 7.40 (m), 5.75 - 5.55 (br. m), 5.35 - 5.15 (br. m), 4.10 - 3.90 (br. m). ^{13}C NMR (126 MHz, CD_3CN, RT): 161.3, 159.8, 156.2, 148.8, 146.6, 144.5, 140.6, 139.7, 130.6, 128.4, 126.5, 124.0, 121.8, 119.7, 71.5, 53.2.

Cubic Cage with CB[7] (IV-18·40NTf$_2^-$). A mixture of CB[7] (13.8 mg, 11.9 μmol) and **IV-16**·2Cl (9.6 mg, 13.9 μmol) was dissolved in D_2O (4.0 mL) and the 1:1 stoichiometric ratio was confirmed by the integrals for each component in the ^1H NMR spectrum. Solid $LiNTf_2$ (43.6 mg, 152 μmol) was added to the solution which resulted in the formation of a precipitate. The heterogenous mixture was centrifuged, the supernatant decanted, and the moist solid was resuspended in water (2.0 mL) followed by centrifugation and decantation.

The solid was then dried at high vacuum overnight to yield the triflimide salt (25.0 mg, 97%). Complex **IV-16**·CB[7] triflimide salt (7.3 mg, 3.9 μmol) and $Fe(NTf_2)_2$ (1.8 mg, 2.9 μmol) were dissolved in CH_3CN (1.0 mL) which gave a dark purple solution. The reaction mixture was sonicated for 30 min. and then stirred at 70 °C for 24 h. The reaction mixture is cooled to room temperature and then Et_2O (6.0 mL) is added which results in a purple precipitate. The heterogenous mixture is centrifuged, the supernatant decanted, and the moist solid is then resuspended in Et_2O followed by centrifugation and decantation of the precipitate. The process is repeated two more times followed by air drying to give **IV-18**·40$(NTf_2)^-$ as a purple solid. ^{1}H NMR (400 MHz, CD_3CN, RT): 9.29 (br. s), 9.00 - 8.60 (m), 8.45 – 7.95 (m), 7.95 – 7.40 (m), 5.75 - 5.55 (br. m), 5.35 - 5.15 (br. m), 4.10 - 3.90 (br. m). ^{13}C NMR (126 MHz, CD_3CN, RT): 161.3, 159.8, 156.2, 148.8, 146.6, 144.5, 140.6, 139.7, 130.6, 128.4, 126.5, 124.0, 121.8, 119.7, 71.5, 5

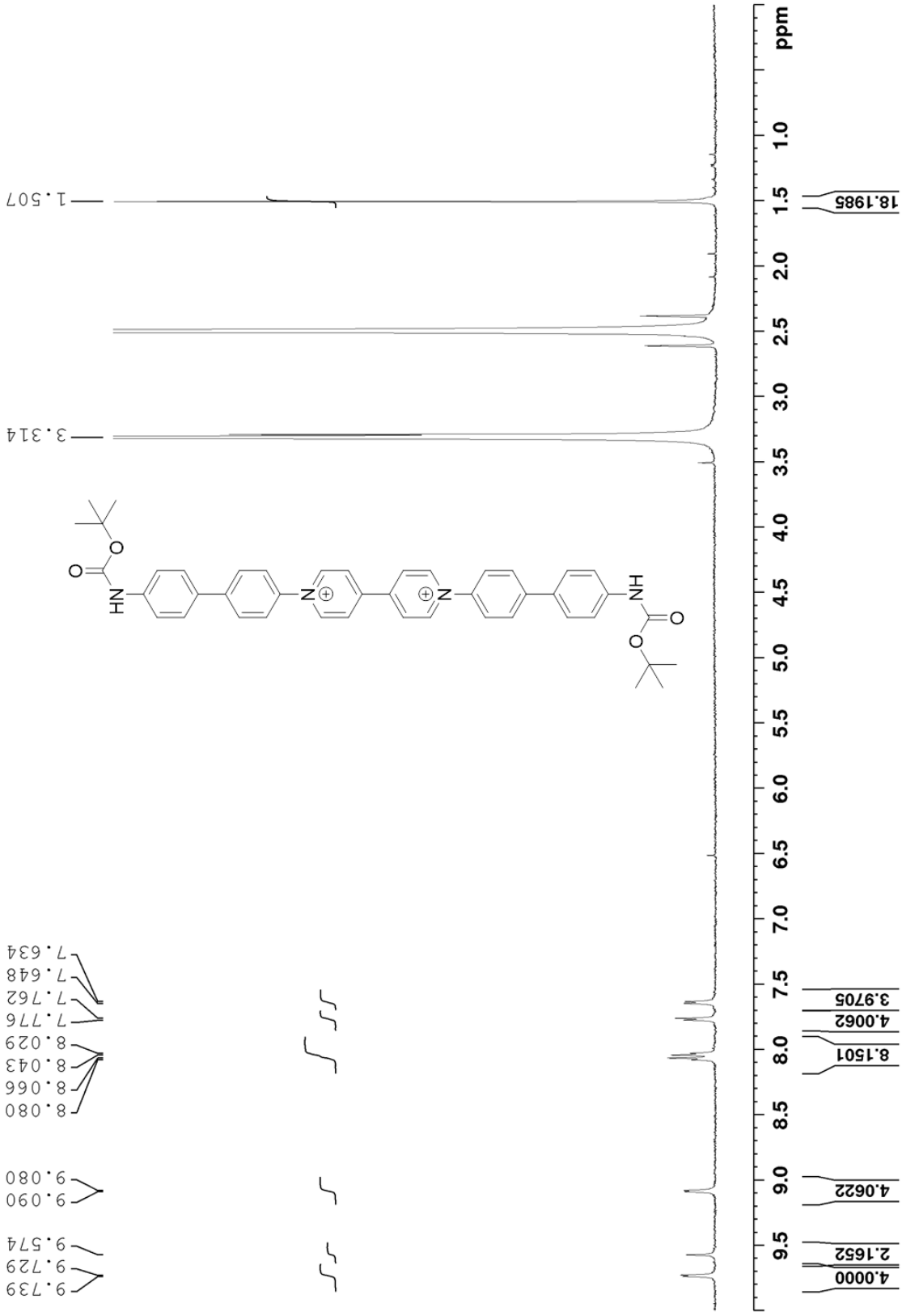

***Figure* IV-S1.** ^{1}H NMR (600 MHz, DMSO-d_6, RT) recorded for compound **IV-3**.

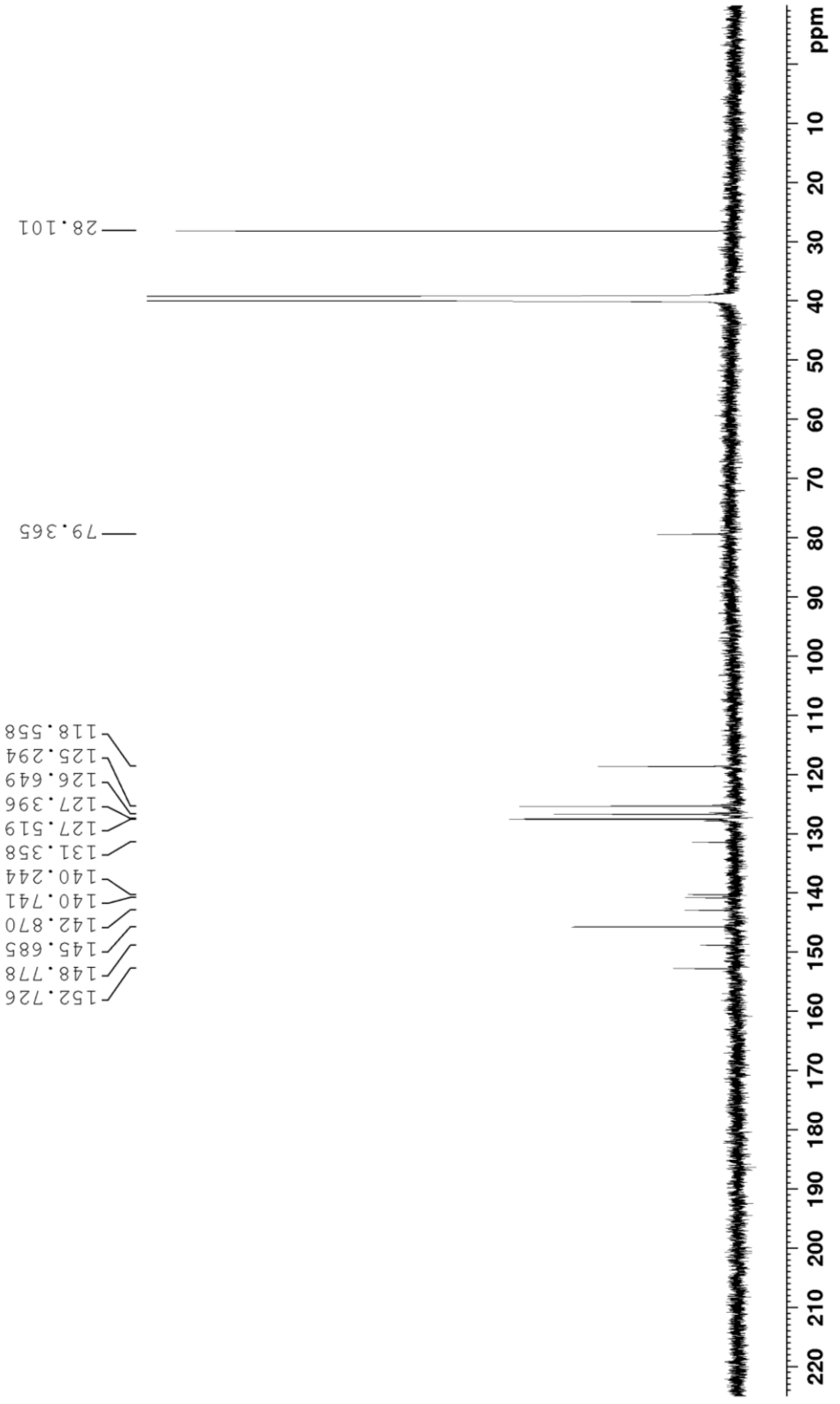

Figure IV-S2. ^{13}C NMR (126 MHz, DMSO-d_6, RT) recorded for compound **IV-3**·2Cl.

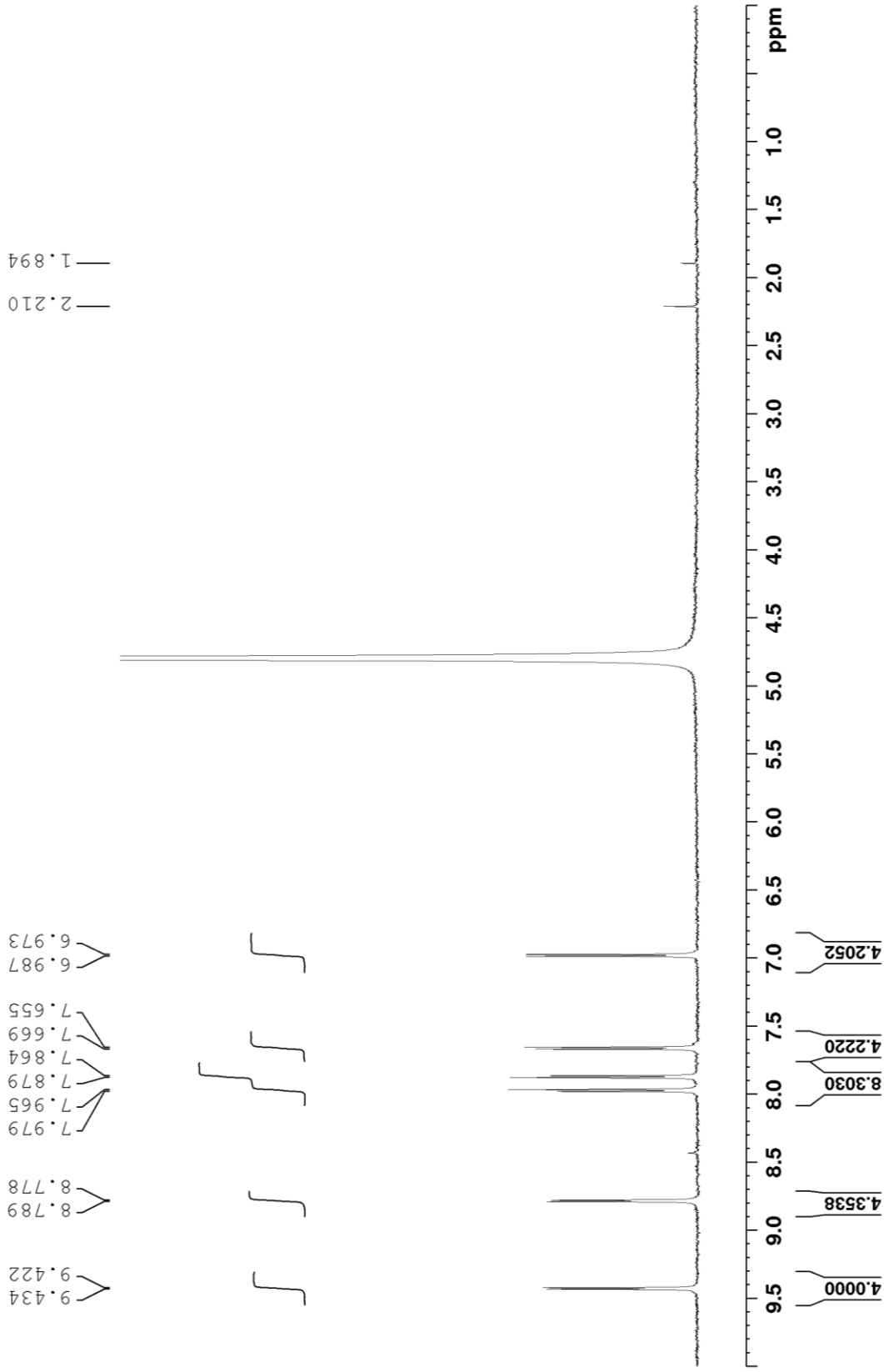

Figure IV-S3. ^{1}H NMR (600 MHz, D_2O, RT) recorded for compound **IV-4**·2Cl.

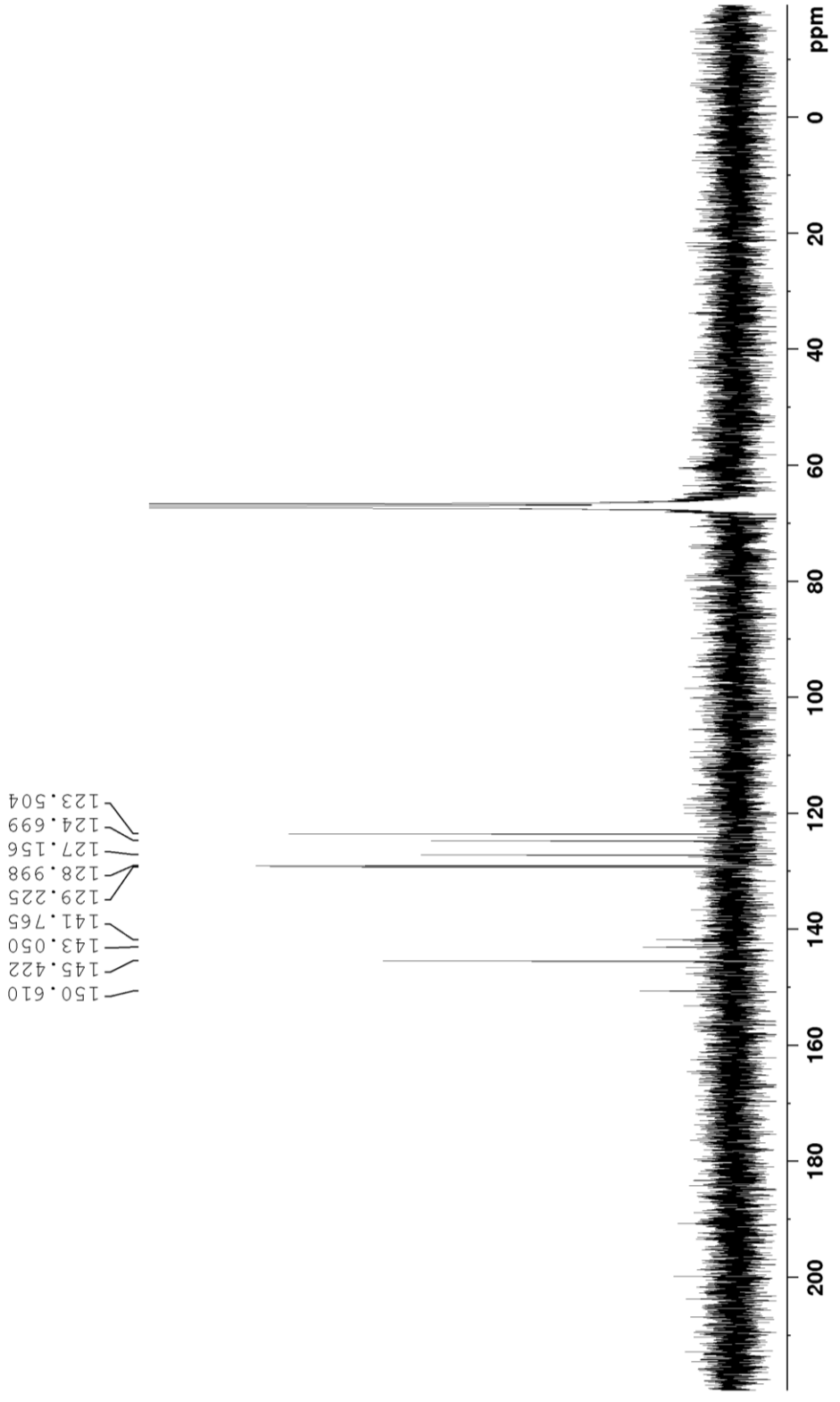

Figure IV-S4. ^{13}C NMR (100 MHz, D_2O, Dioxane as reference, RT) recorded for compound **IV-4**·2Cl.

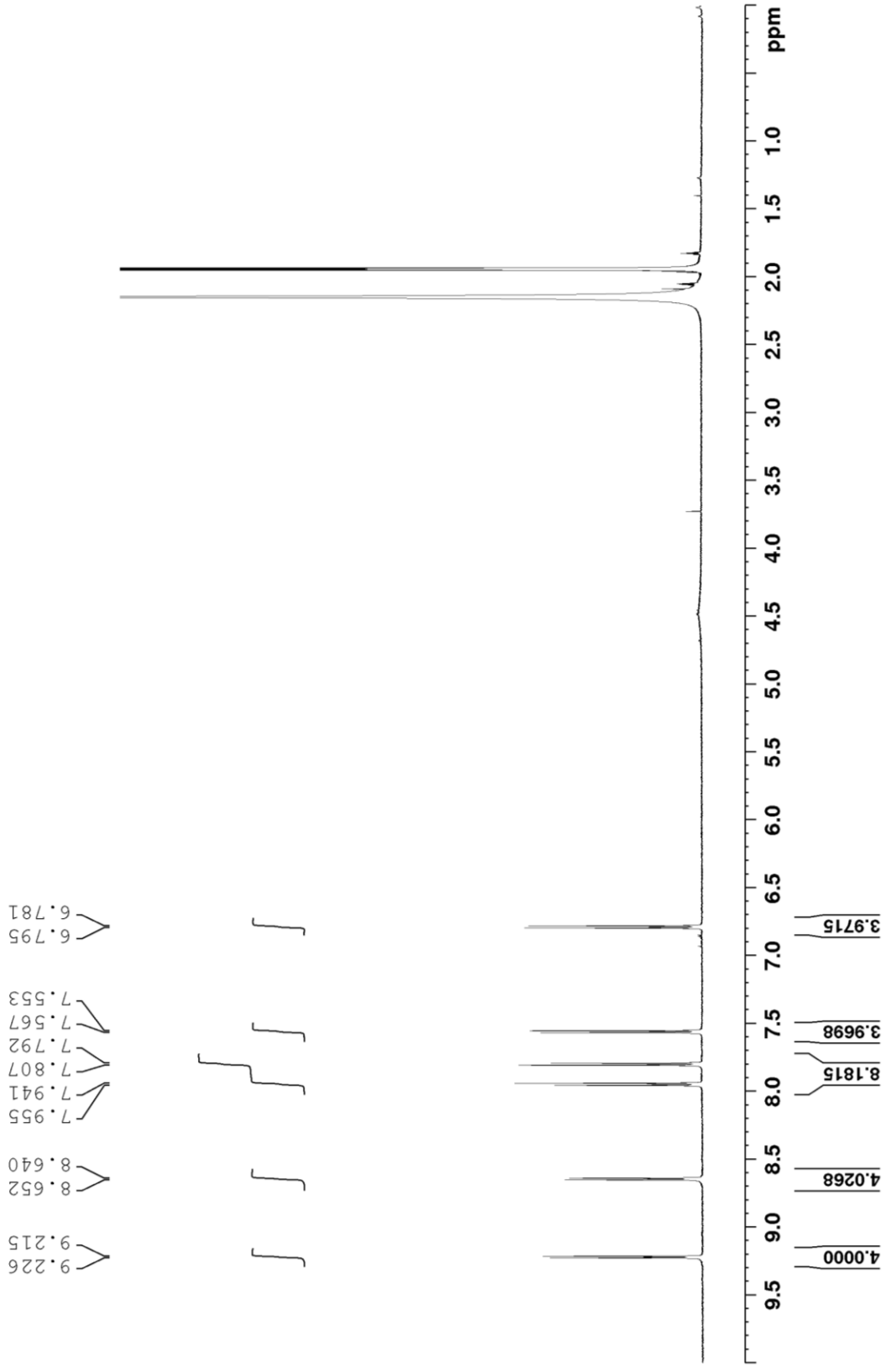

Figure IV-S5. ^{1}H NMR (600 MHz, CD_3CN, RT) recorded for **IV-4**·$2PF_6$.

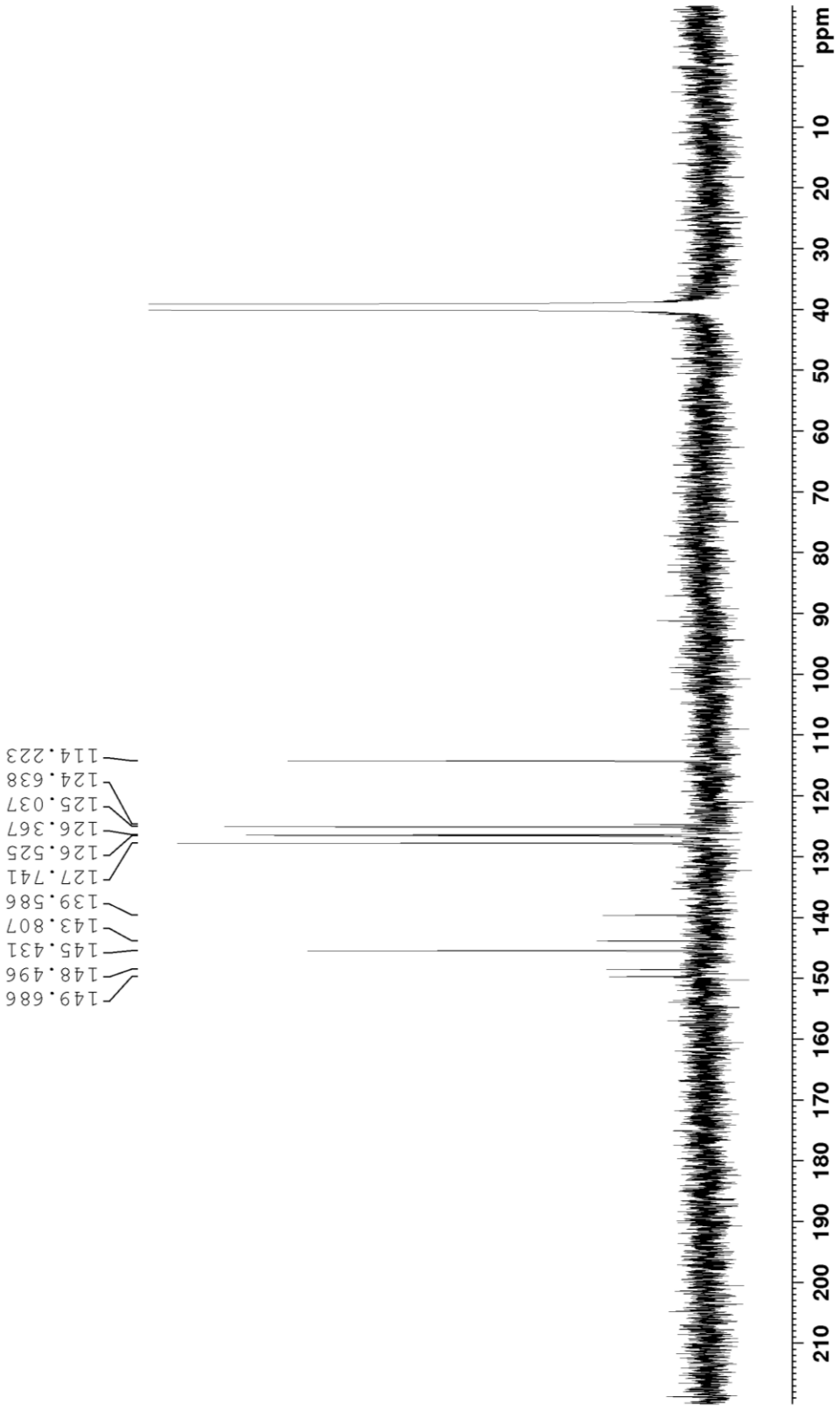

Figure IV-S6. ^{13}C NMR (126 MHz, DMSO-d_6, RT) recorded for **IV-4**·2PF_6.

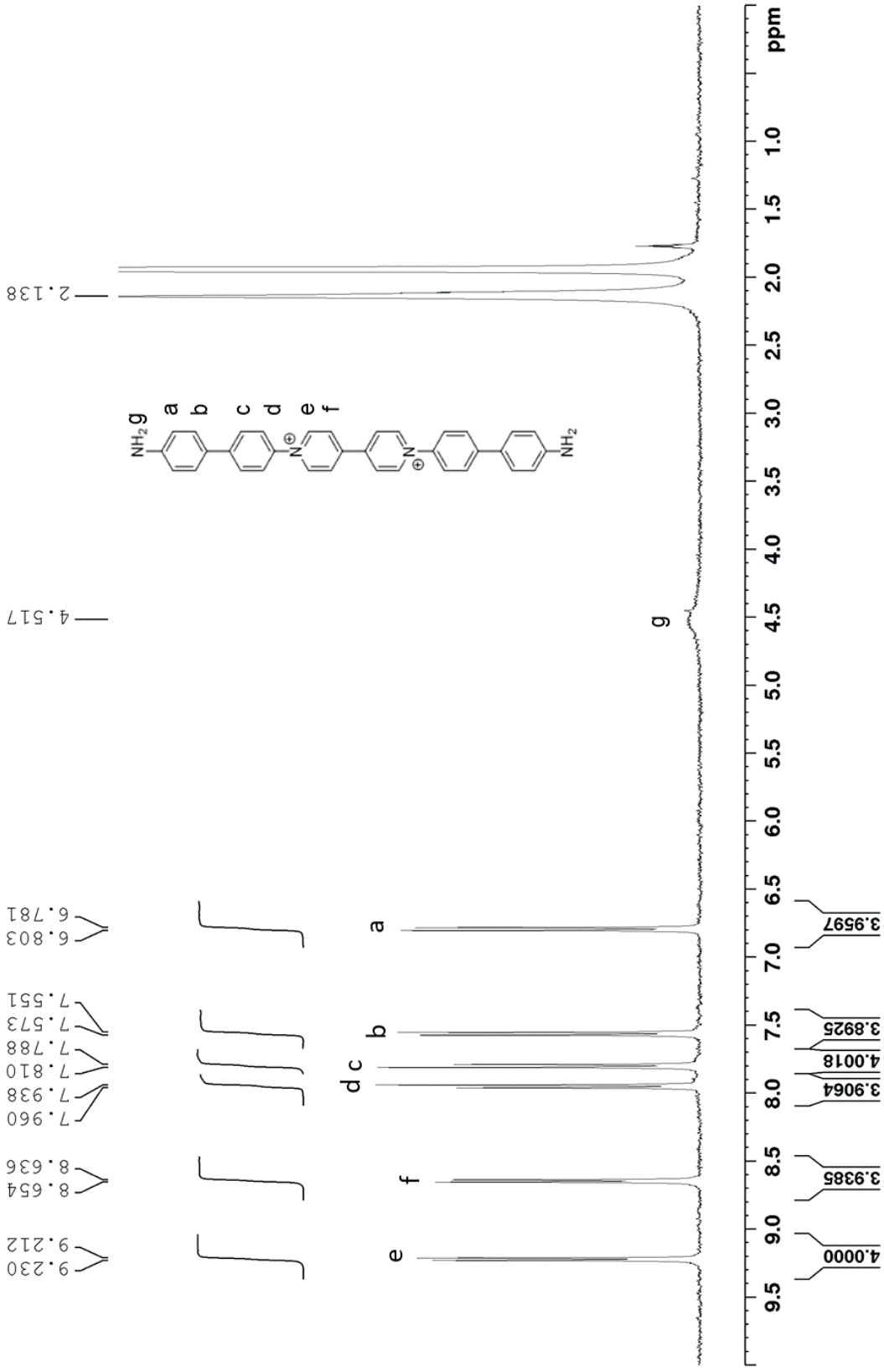

Figure IV-S7. ^{1}H NMR (400 MHz, CD_3CN, RT) recorded for **IV-4**·2NTf_2.

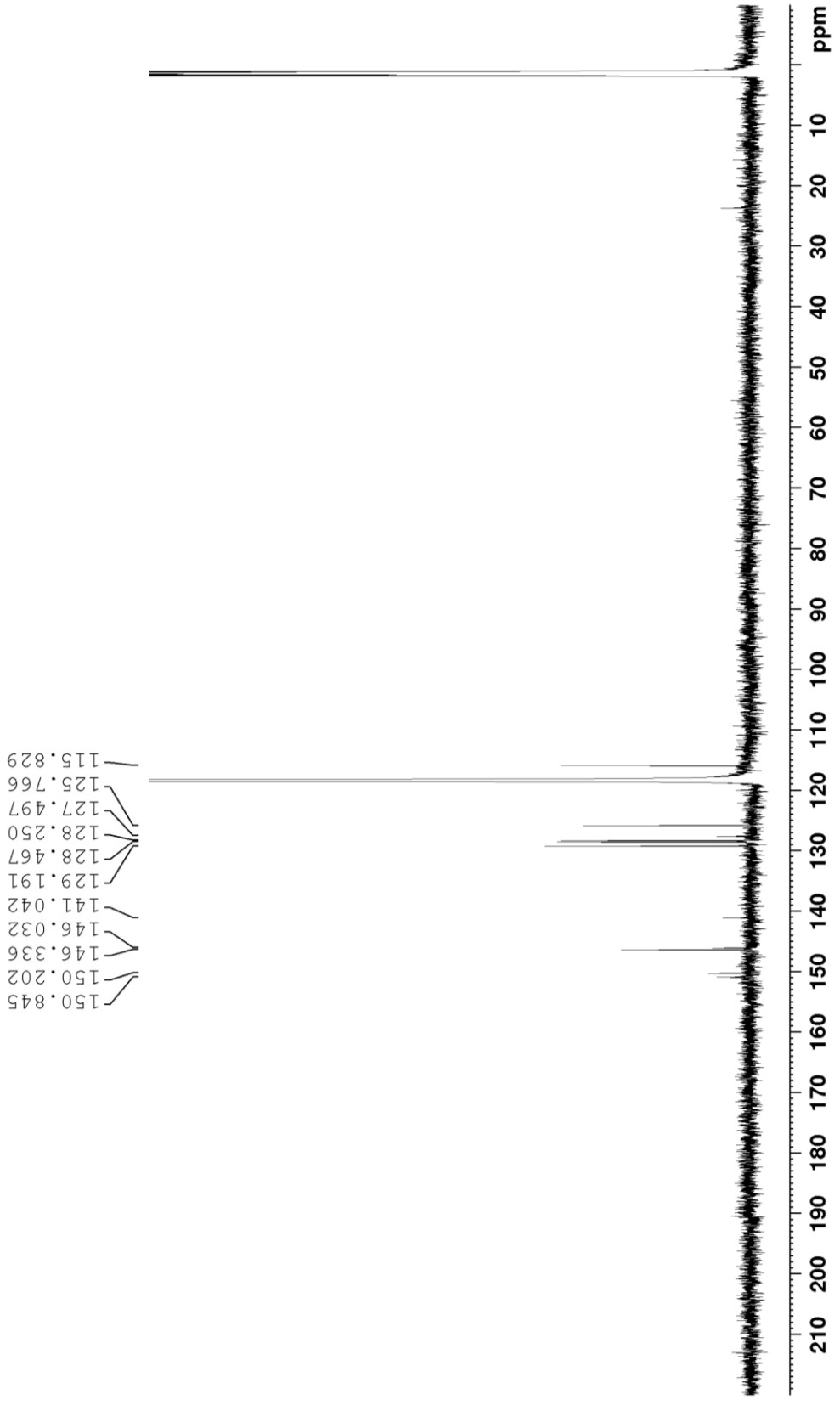

Figure IV-S8. ^{13}C NMR (126 MHz, CD_3CN, RT) recorded for **IV-4**·2NTf_2.

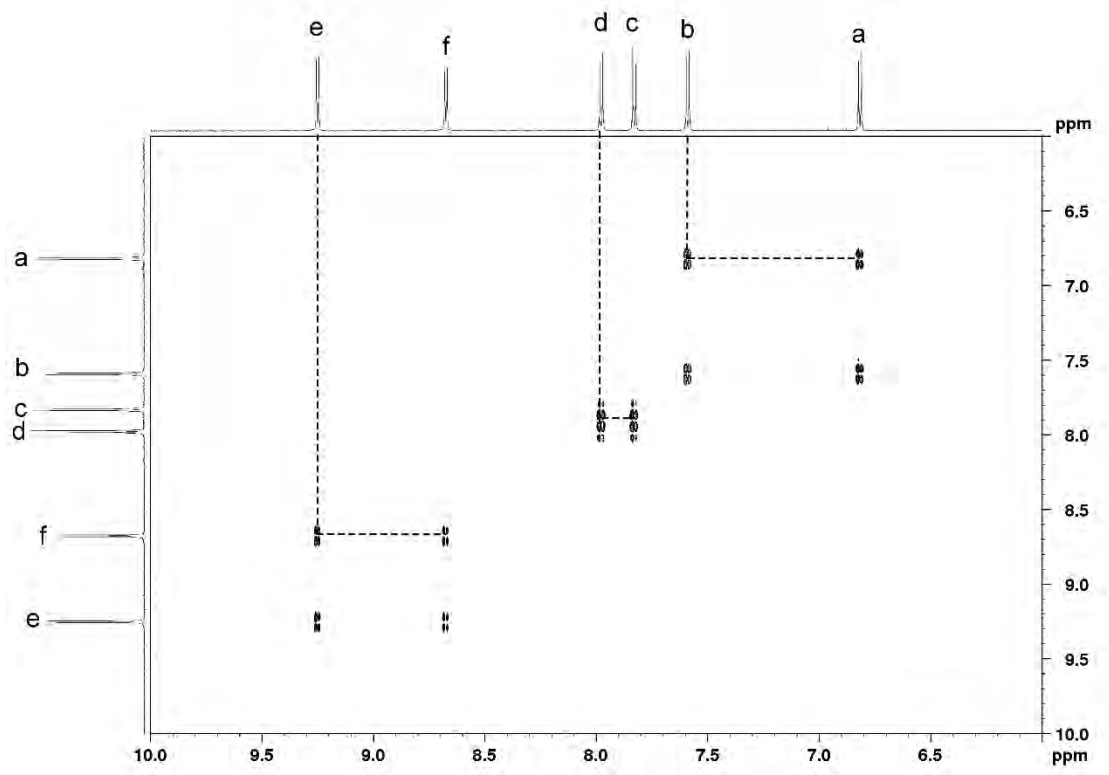

Figure IV-S9. COSY NMR (600 MHz, CD_3CN, 298 K) recorded **IV-4**·$2PF_6$.

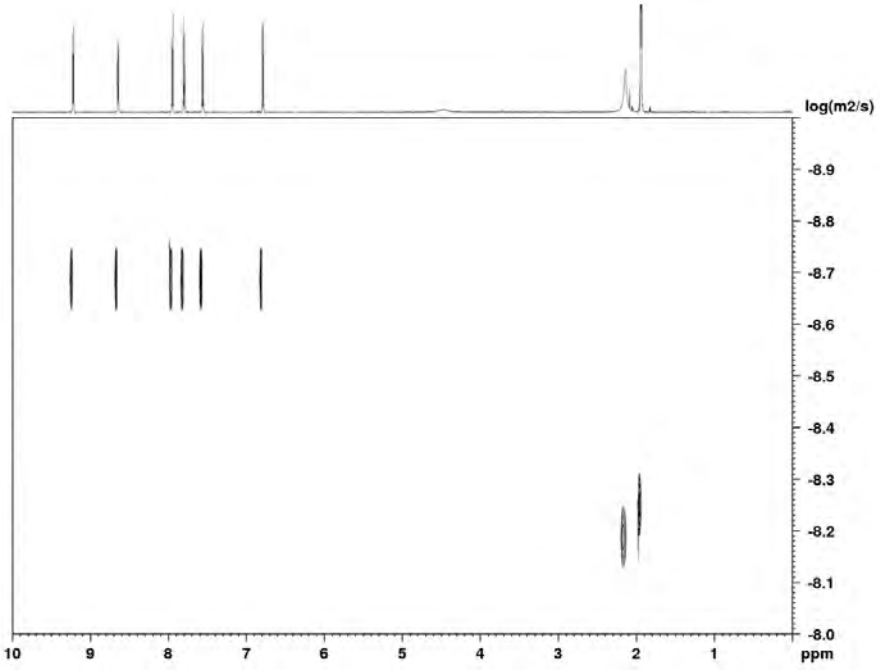

Figure IV-S10. DOSY NMR (600 MHz, CD_3CN, 298 K) recorded for **IV-4**·$2PF_6$ (D = 1.74 x 10^{-9} m^2/s).

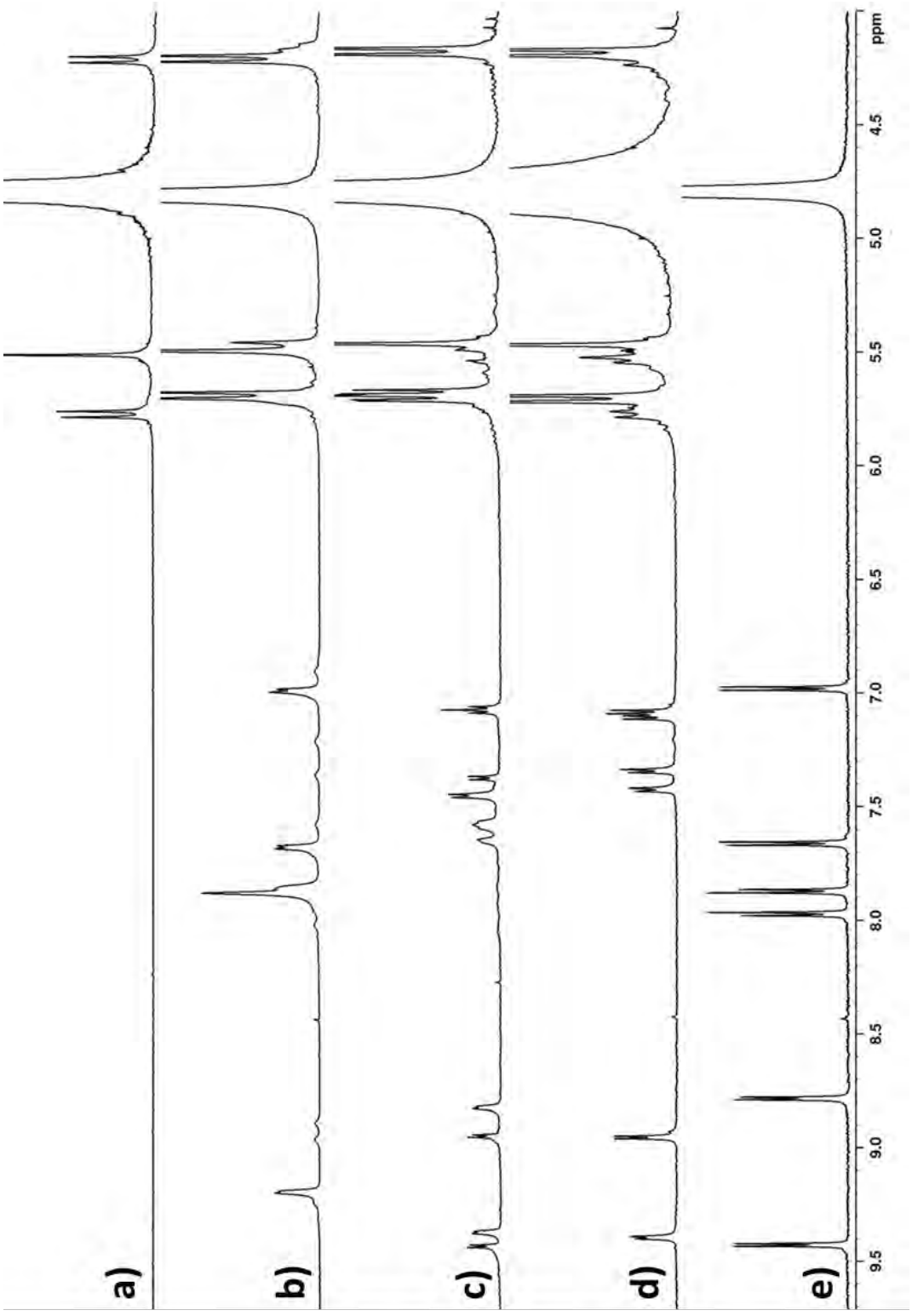

Figure IV-S11. ^{1}H NMR (600 MHz, D_2O, RT) recorded for the titration of CB[7] with various equivalents of **IV-4**·2Cl. (a) CB[7] alone, (b) 1.0 equiv. **IV-4**, (c) 1.5 equiv. **IV-4**, (d) 2.0 equiv. **IV-4**, (e) **IV-4** alone.

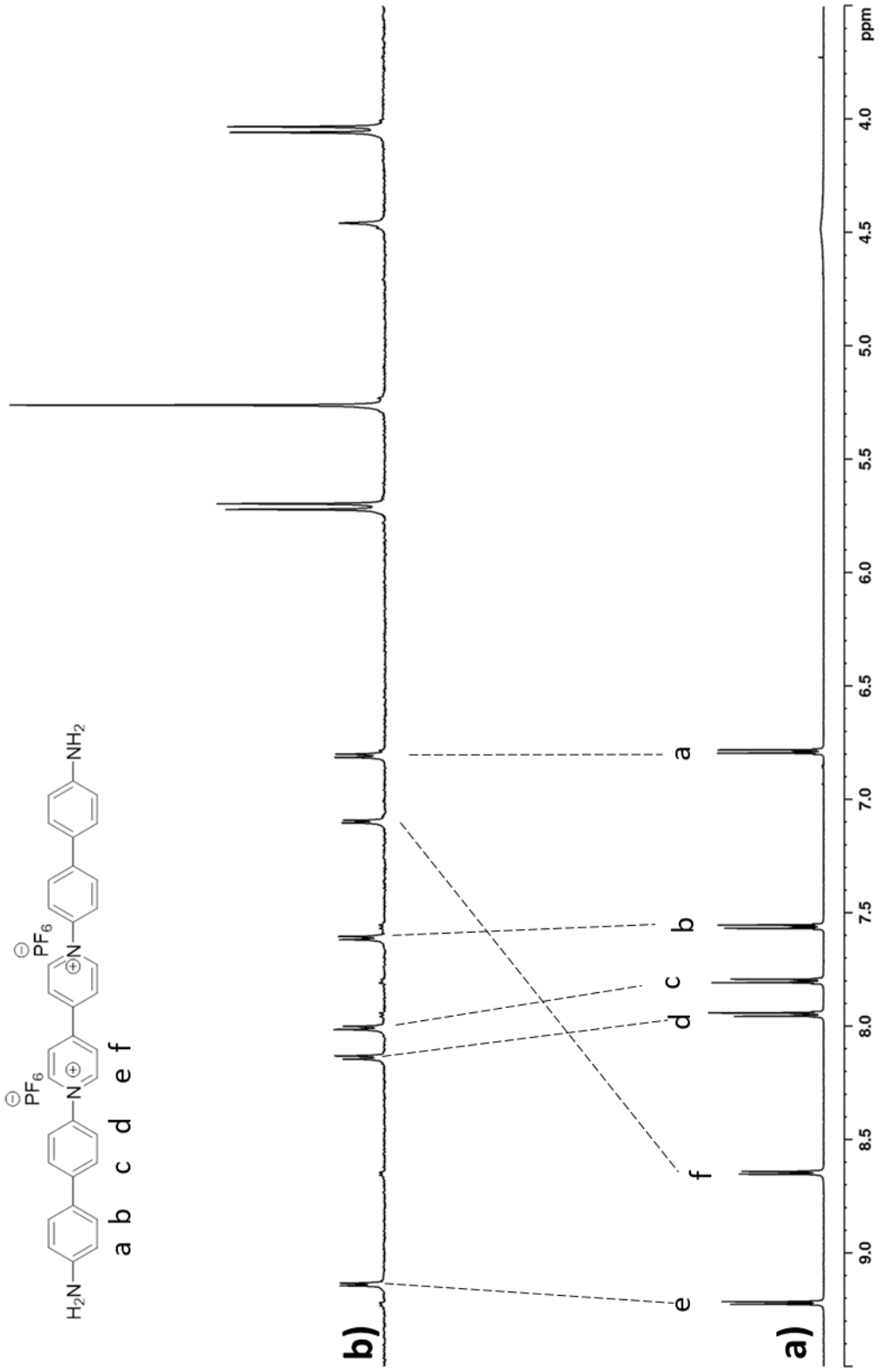

Figure IV-S12. ^{1}H NMR (600 MHz, CD_3CN, RT) recorded for **IV-4**·$2PF_6$ (a) alone, (b) with 1 equivalent of CB[7].

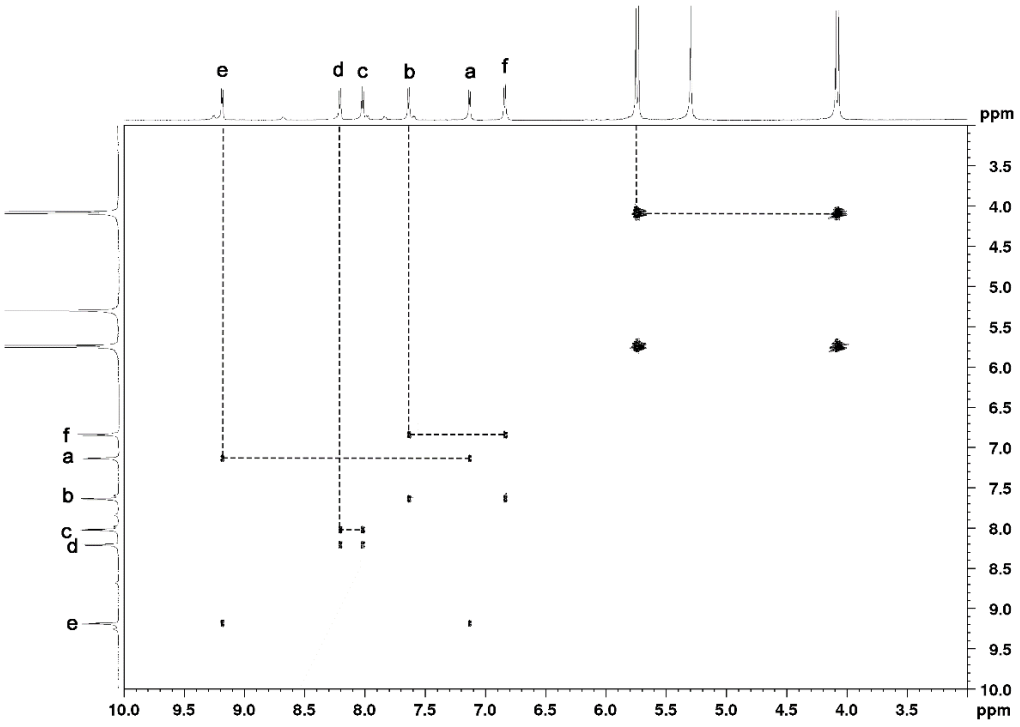

Figure IV-S13. COSY NMR (600 MHz, CD_3CN, 298 K) recorded for **IV-4**·CB[7]·$2PF_6$.

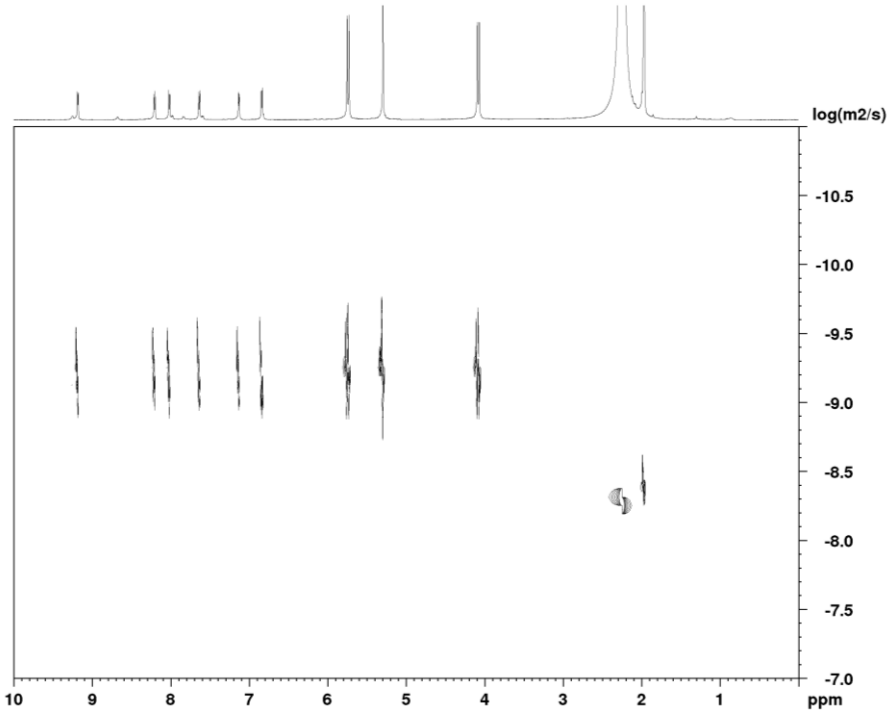

Figure IV-S14. DOSY NMR (600 MHz, CD_3CN, 298 K) recorded for **IV-4**·CB[7]·$2PF_6$ ($D = 5.53 \times 10^{-10}$ m^2/s).

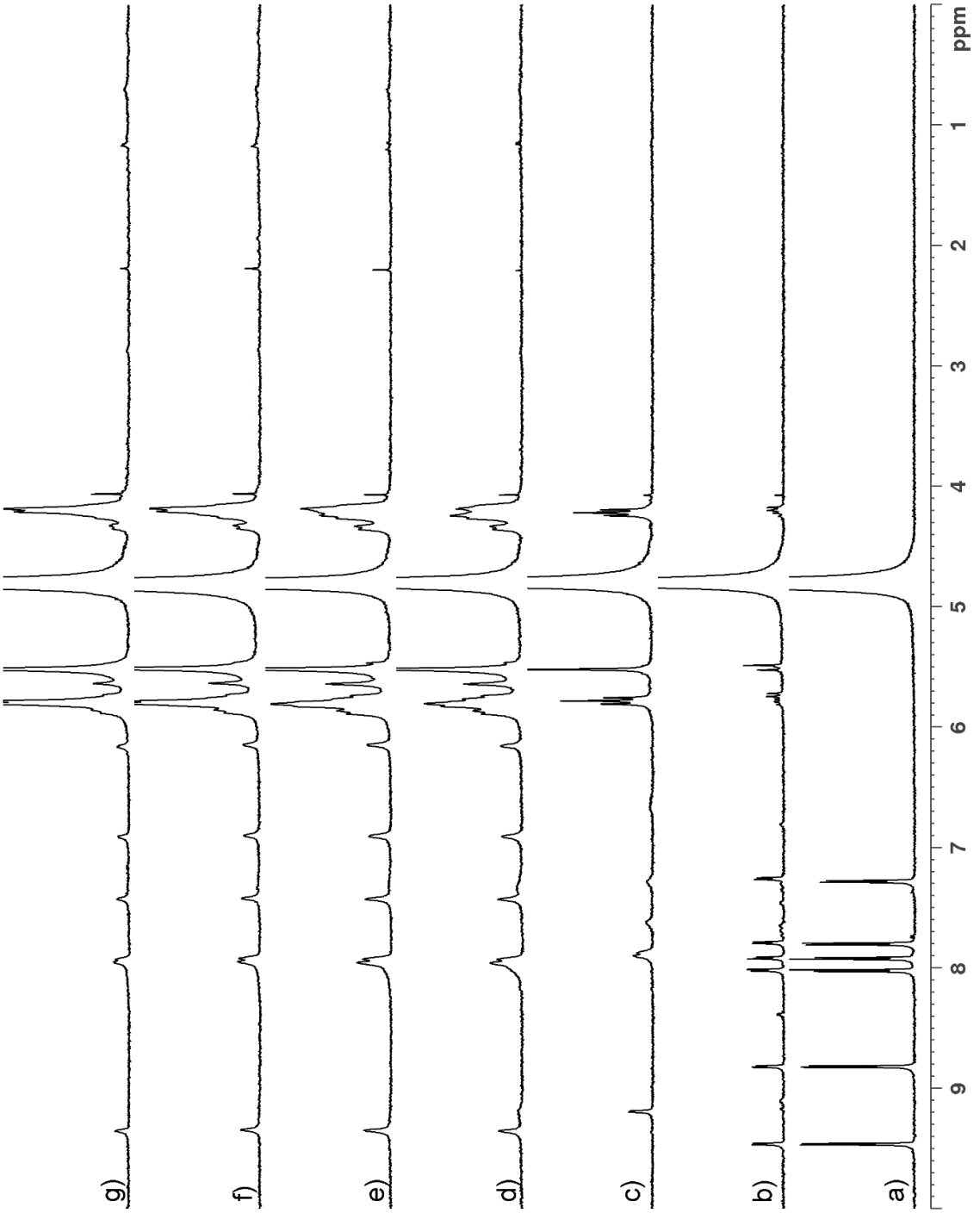

Figure IV-S15. ^{1}H NMR (600 MHz, D_2O, RT) recorded for the titration of **IV-4**·2Cl with various equivalents of CB[8]: a) **IV-4** alone; b) 0.25 eq CB[8]; c) 0.5 eq CB[8]; d) 0.75 eq. CB[8]; e) 1.0 eq. CB[8]; f) 1.5 eq CB[8]; g) 2.0 eq. CB[8].

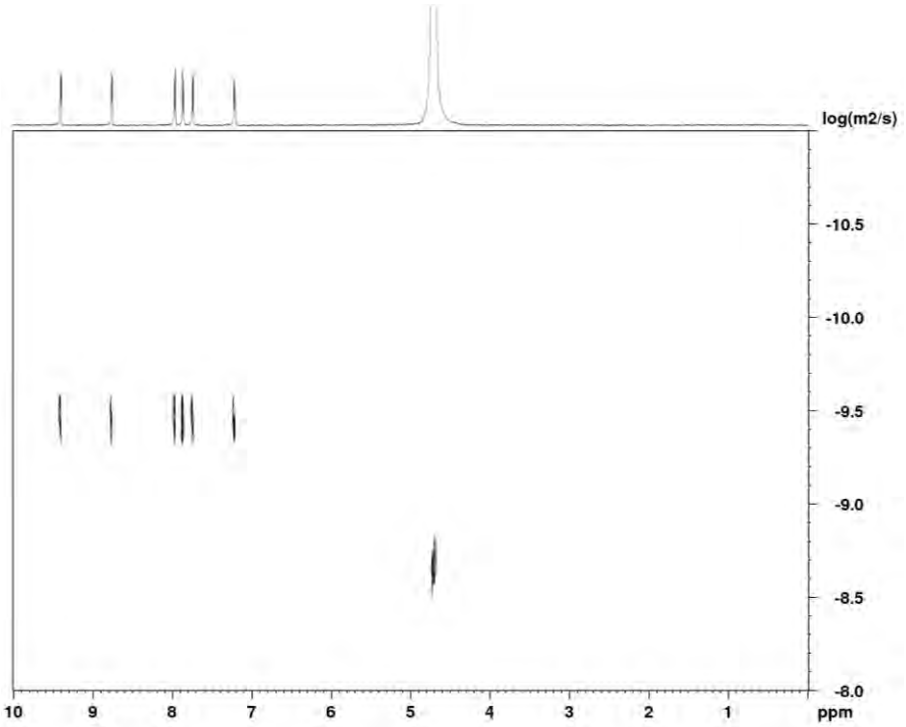

Figure IV-S16. DOSY NMR (600 MHz, D_2O, 298 K) recorded for **IV-4**·2Cl·(D = 2.82 x 10^{-10} m^2/s).

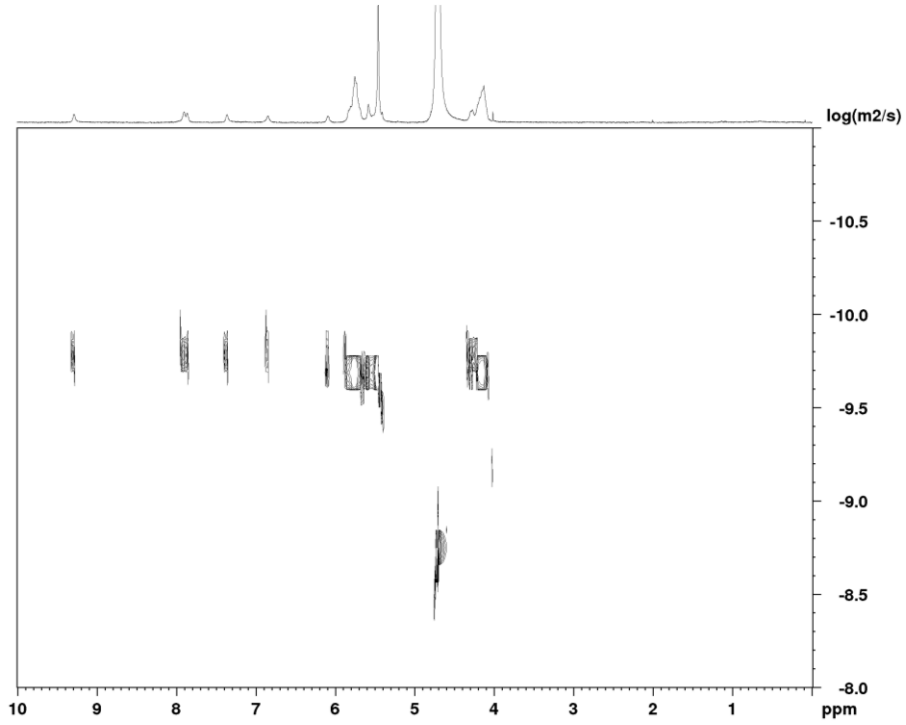

Figure IV-S17. DOSY NMR (600 MHz, D_2O, 298 K) recorded for 1:1 ratio of **IV-4**:CB[8]·(D = 1.48 x 10^{-10} m^2/s).

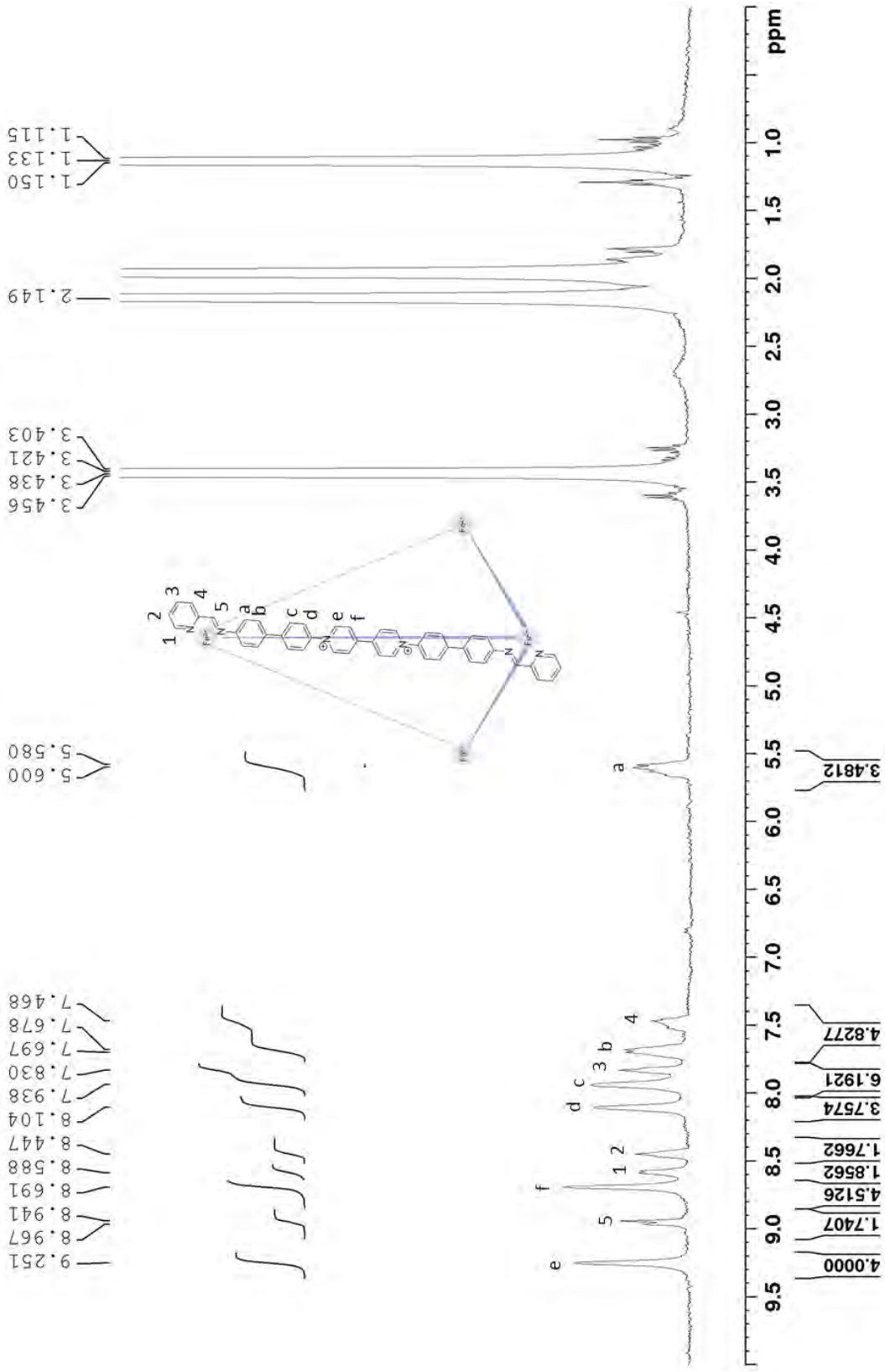

Figure IV-S18. ^{1}H NMR (400 MHz, CD_3CN, RT) recorded for cage **IV-6**·20PF_6.

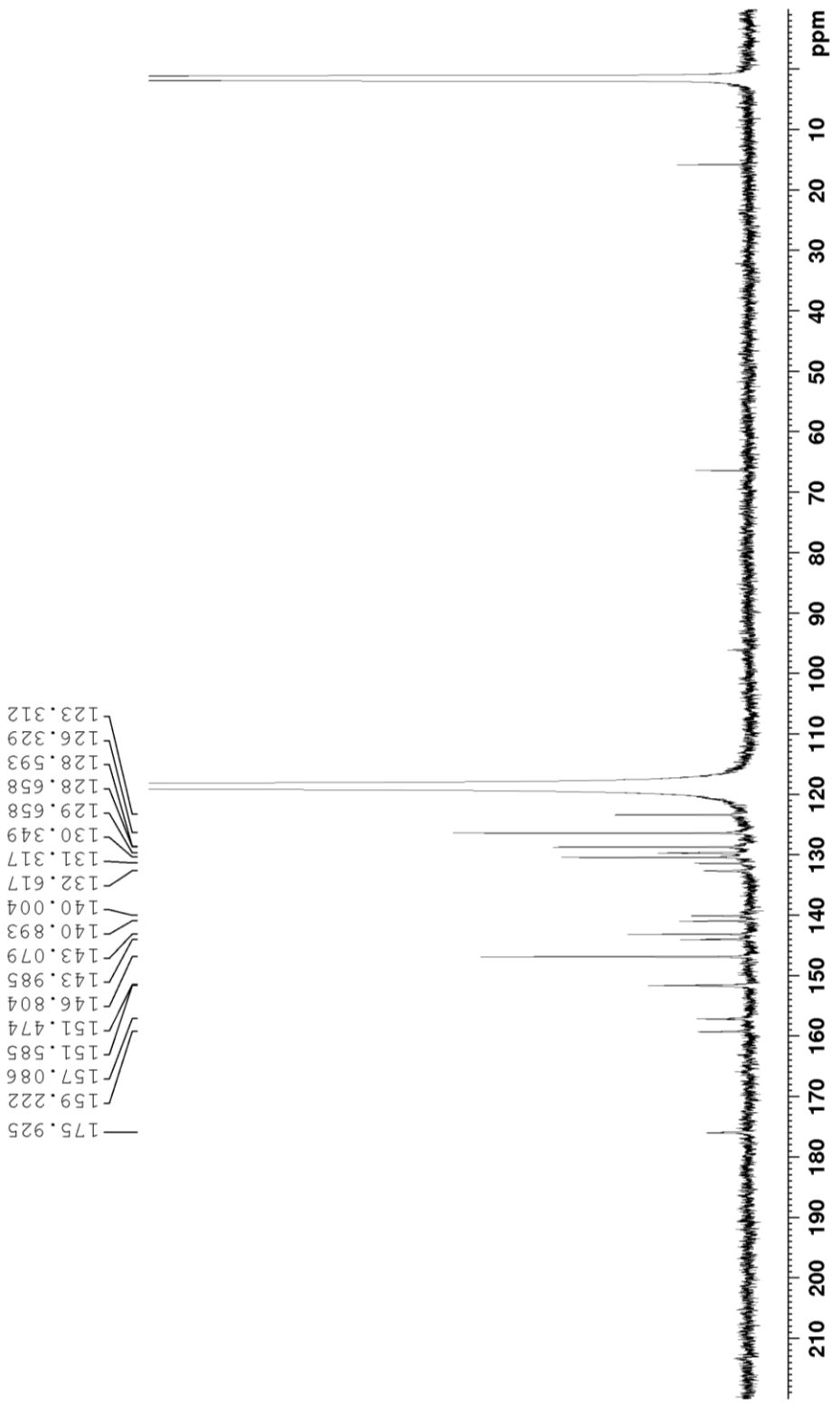

Figure IV-S19. ^{13}C NMR (126 MHz, CD_3CN, RT) recorded for cage **IV-6**·$20PF_6$.

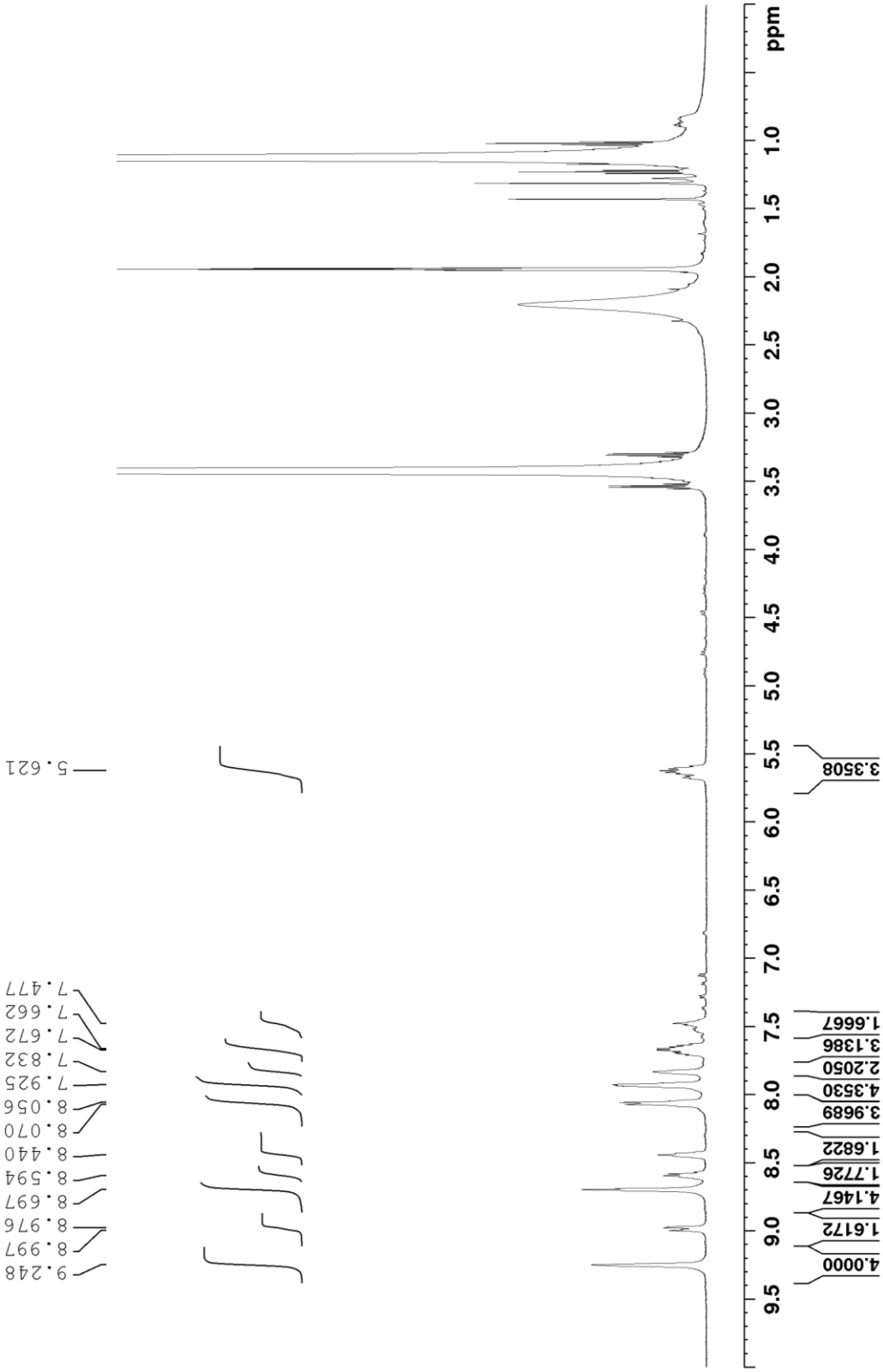

Figure IV-S20. ^{1}H NMR (400 MHz, CD_3CN, RT) recorded for cage **IV-6**·20NTf_2.

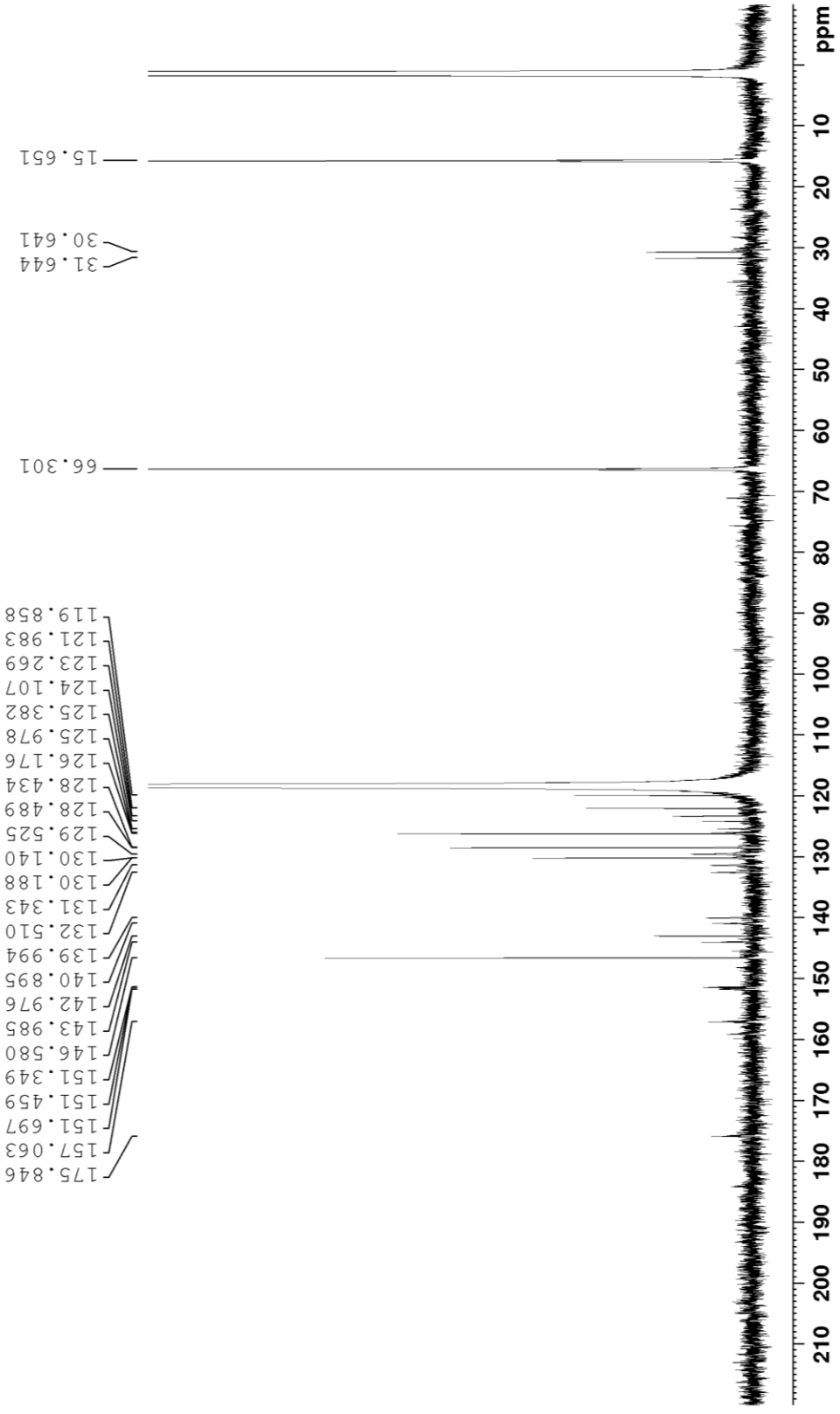

Figure IV-S21. ^{1}H NMR (126 MHz, CD_3CN, RT) recorded for cage **IV-6**·20NTf_2.

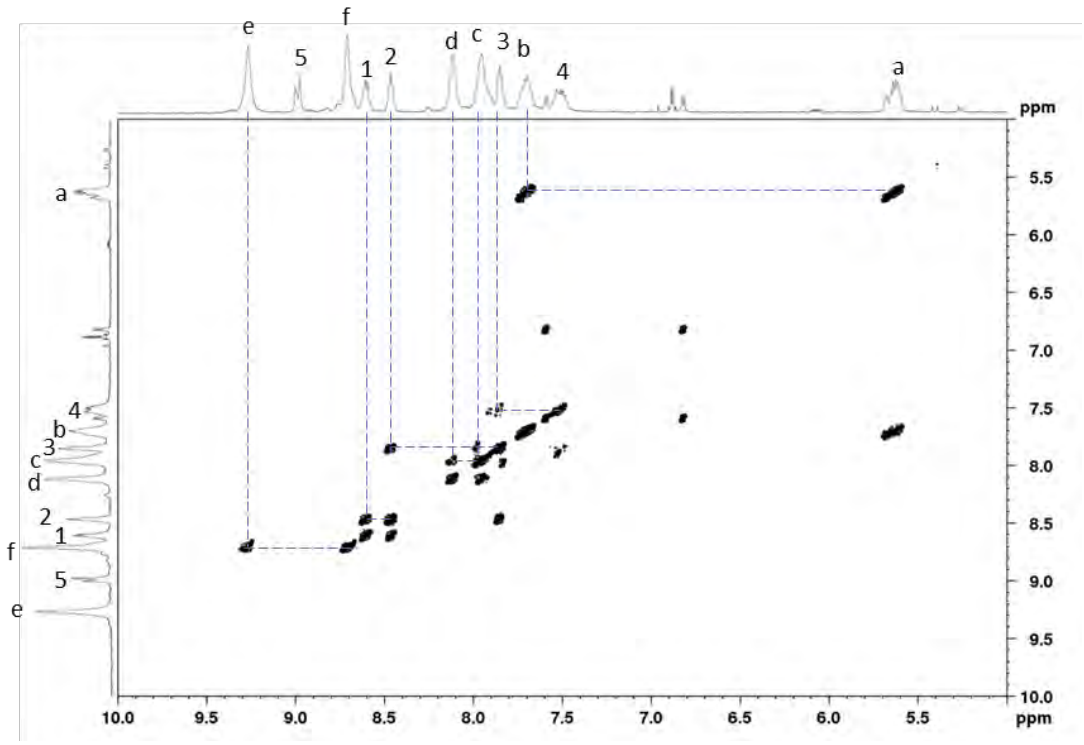

Figure IV-S22. COSY NMR (600 MHz, CD_3CN, 298 K) recorded of **IV-6**·$20PF_6$**.**

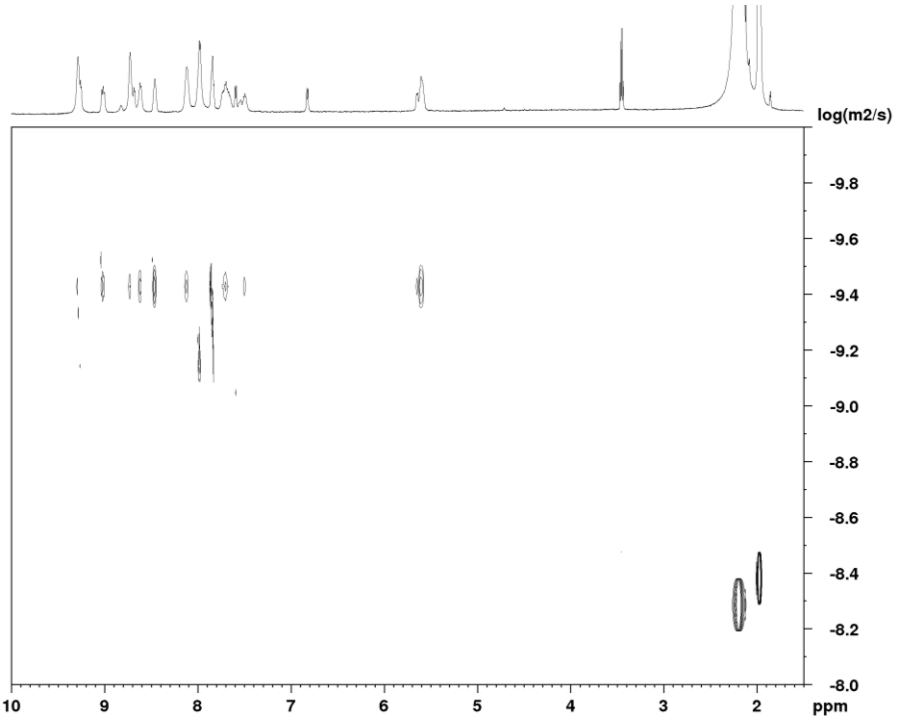

Figure IV-S23. DOSY NMR (600 MHz, CD_3CN, 298 K) recorded of **IV-6**·$20PF_6$ (D = 3.68 x 10^{-10} m^2/s, red square).

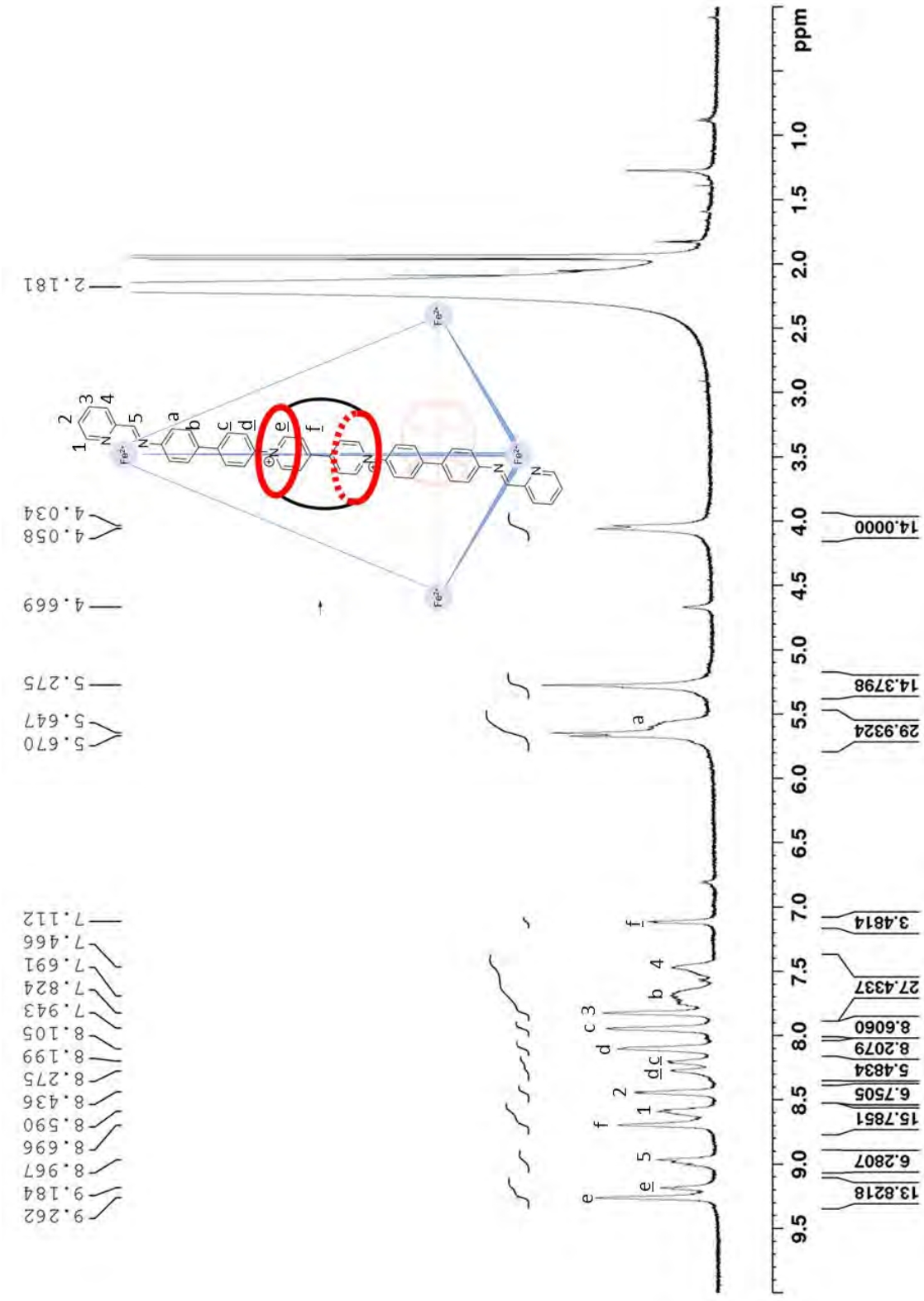

Figure IV-S24. ^{1}H NMR (600 MHz, CD_3CN, RT) recorded for **IV-7**·20PF_6. Underline represents resonances complexed with CB[7].

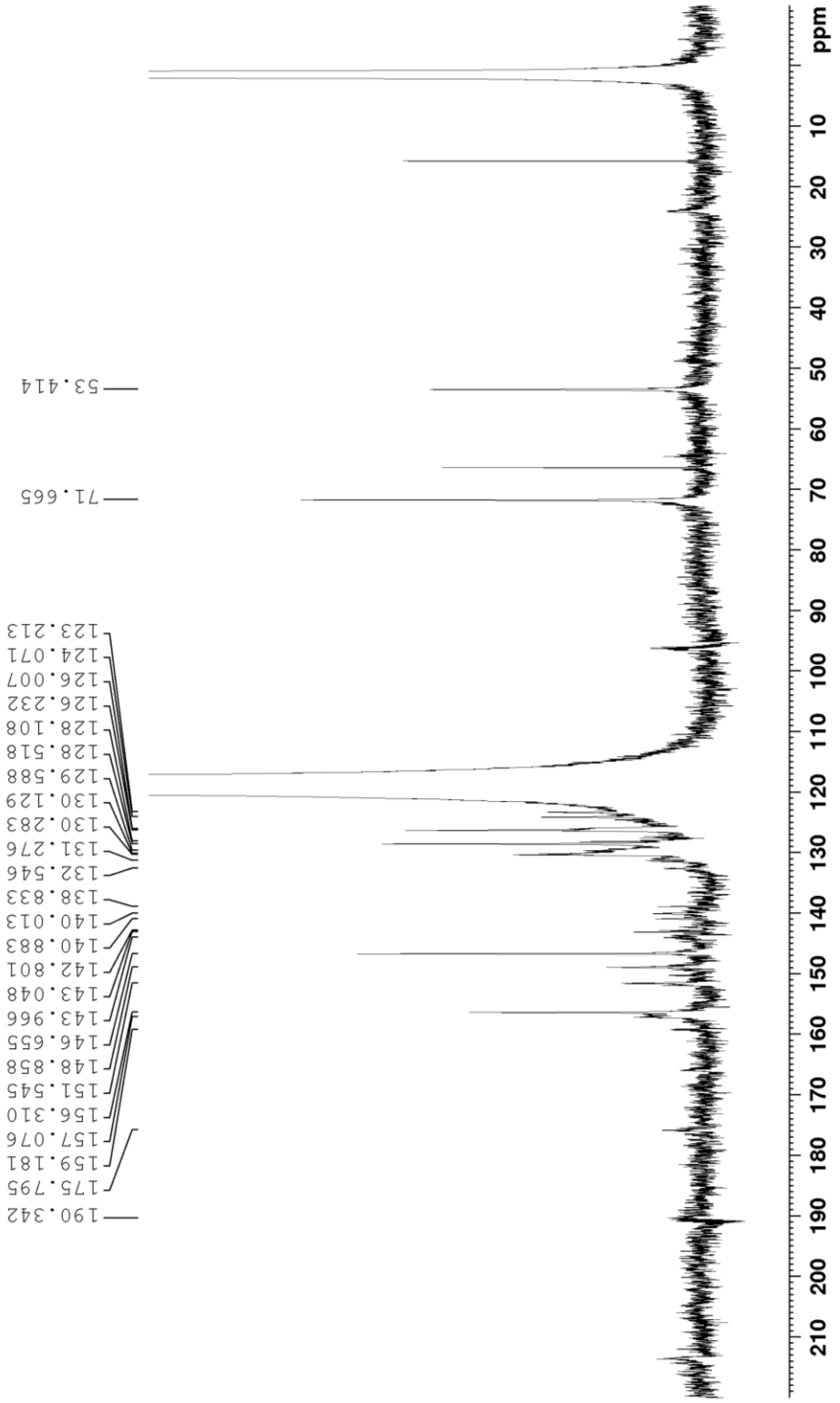

Figure IV-S25. ^{13}C NMR (126 MHz, CD_3CN, RT) recorded for **IV-7**·20PF_6.

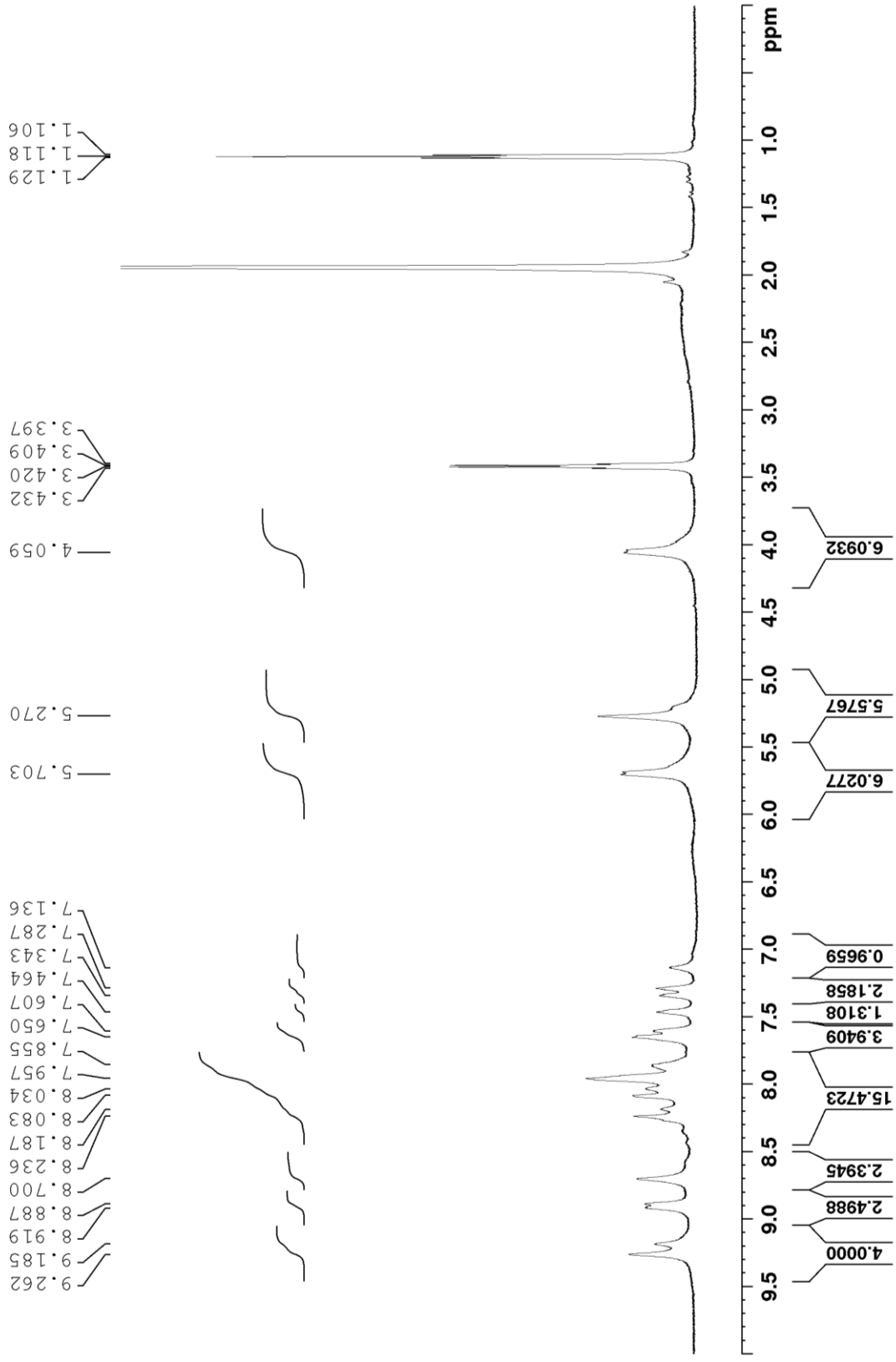

Figure IV-S26. ^{1}H NMR (600 MHz, CD_3CN, RT) recorded for **IV-7**·20NTf_2.

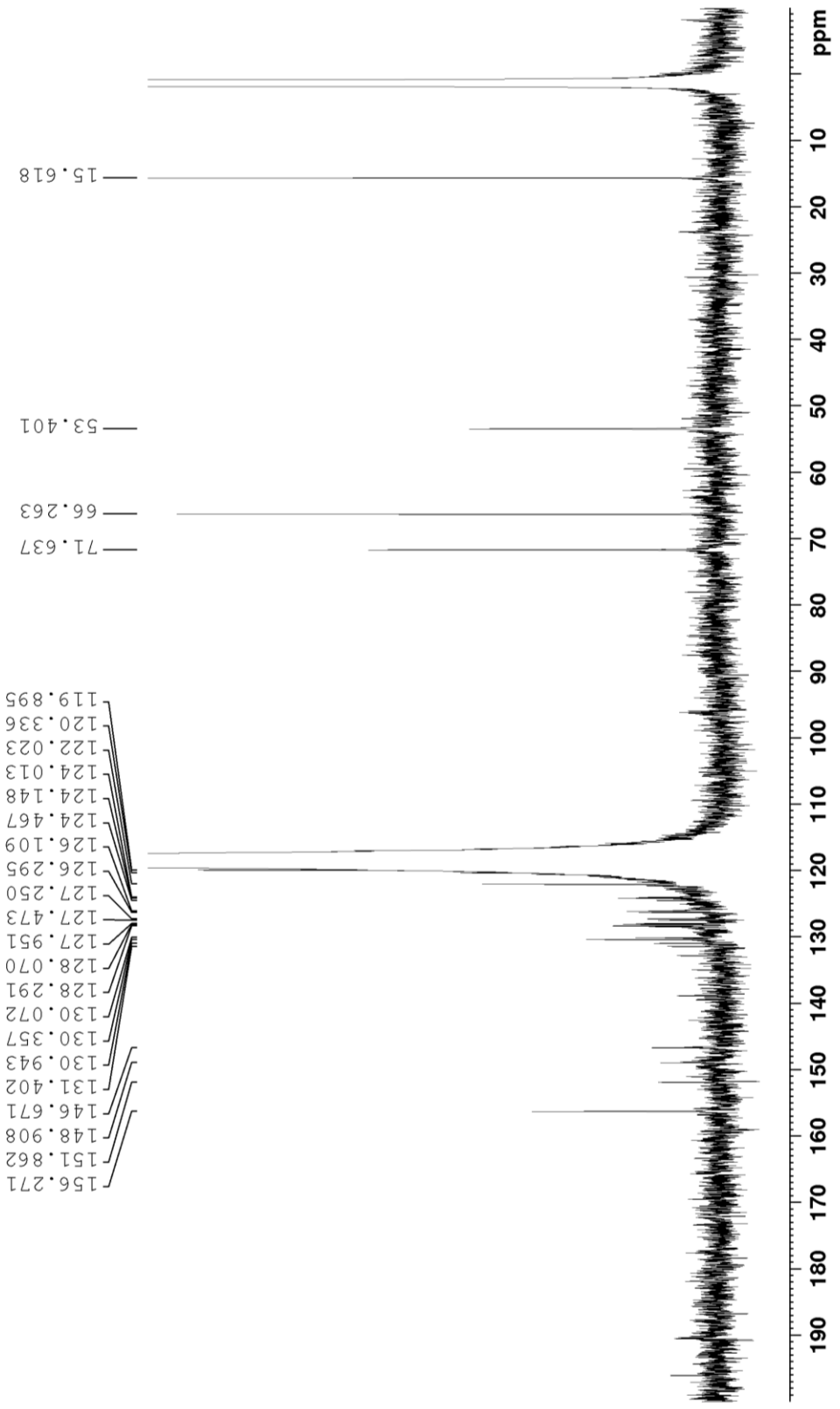

Figure IV-S27. ^{13}C NMR (126 MHz, CD_3CN, RT) recorded for **IV-7**·20NTf_2.

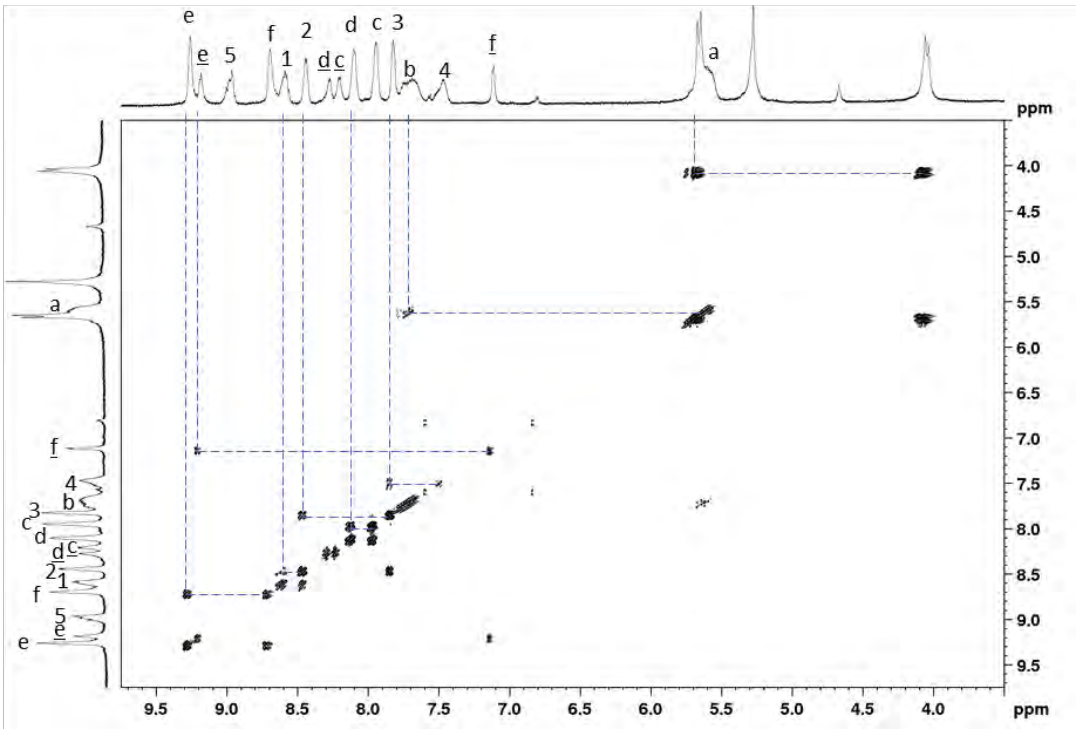

Figure IV-S28. COSY NMR (600 MHz, CD_3CN, 298 K) recorded for **IV-7**·20PF_6. Underline represents resonances complexed with CB[7].

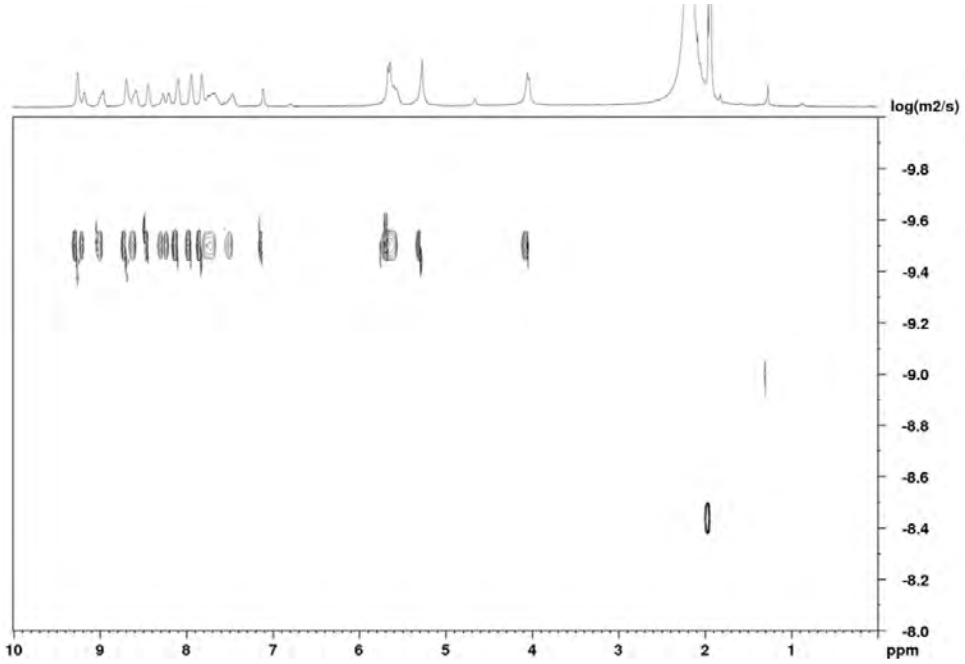

Figure IV-S29. DOSY NMR (600 MHz, CD_3CN, 298 K) recorded for **IV-7**·20PF_6 (D = 2.71 x 10^{-10} m^2/s).

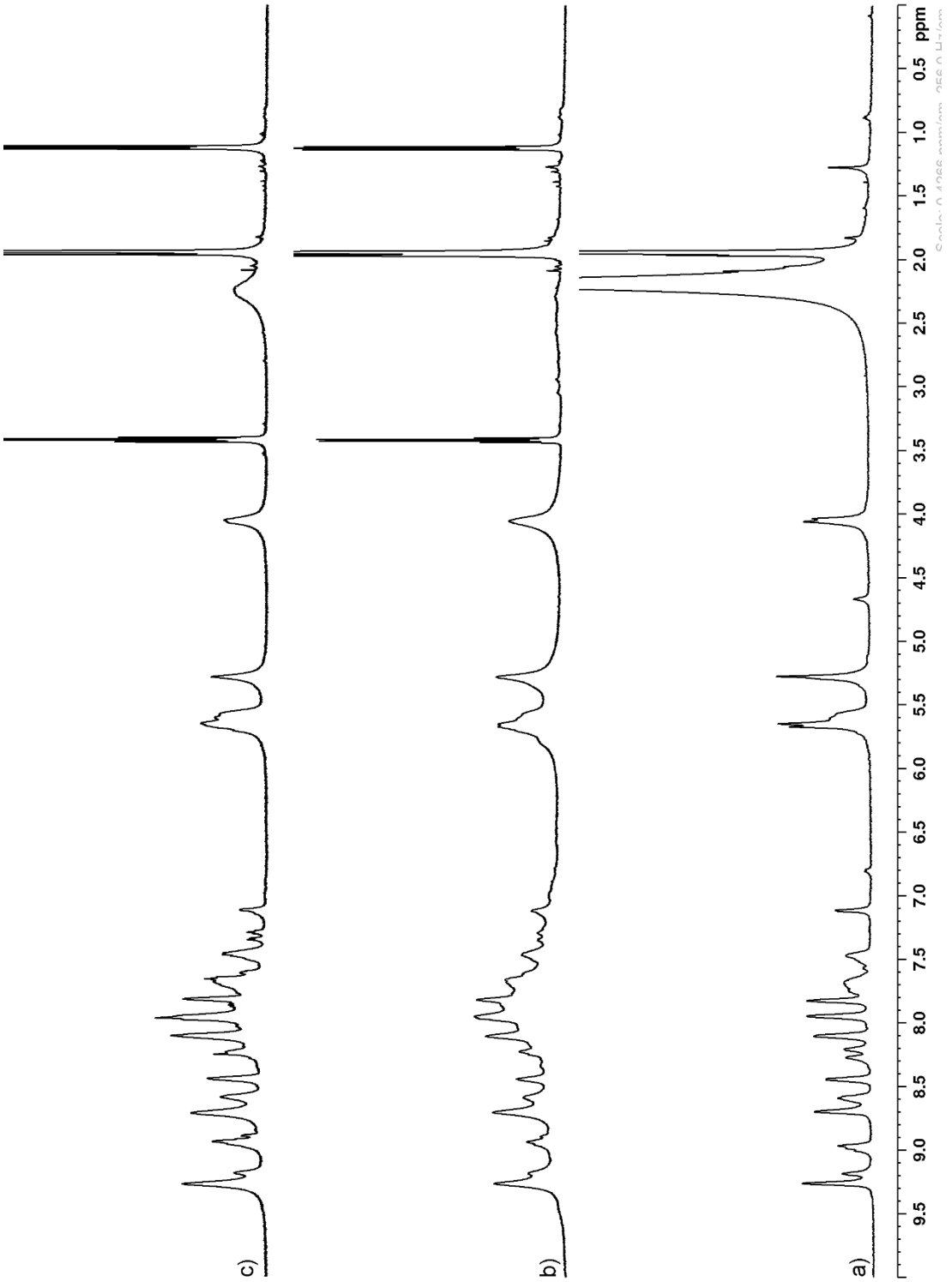

Figure IV-S30. ^{1}H NMR (600 MHz, CD_3CN, RT) recorded for the self-assembly of **IV-7**·20PF_6 with varying equivalence of CB[7]: a) **IV-4**·CB[7]·2PF_6 alone; b) 1.0 eq of **IV-4**·2PF_6 with 1.0 eq **IV-4**·CB[7] 2PF_6; c) 5.0 eq of **IV-4**·2PF_6 with 1.0 eq **IV-4**·CB[7] 2PF_6.

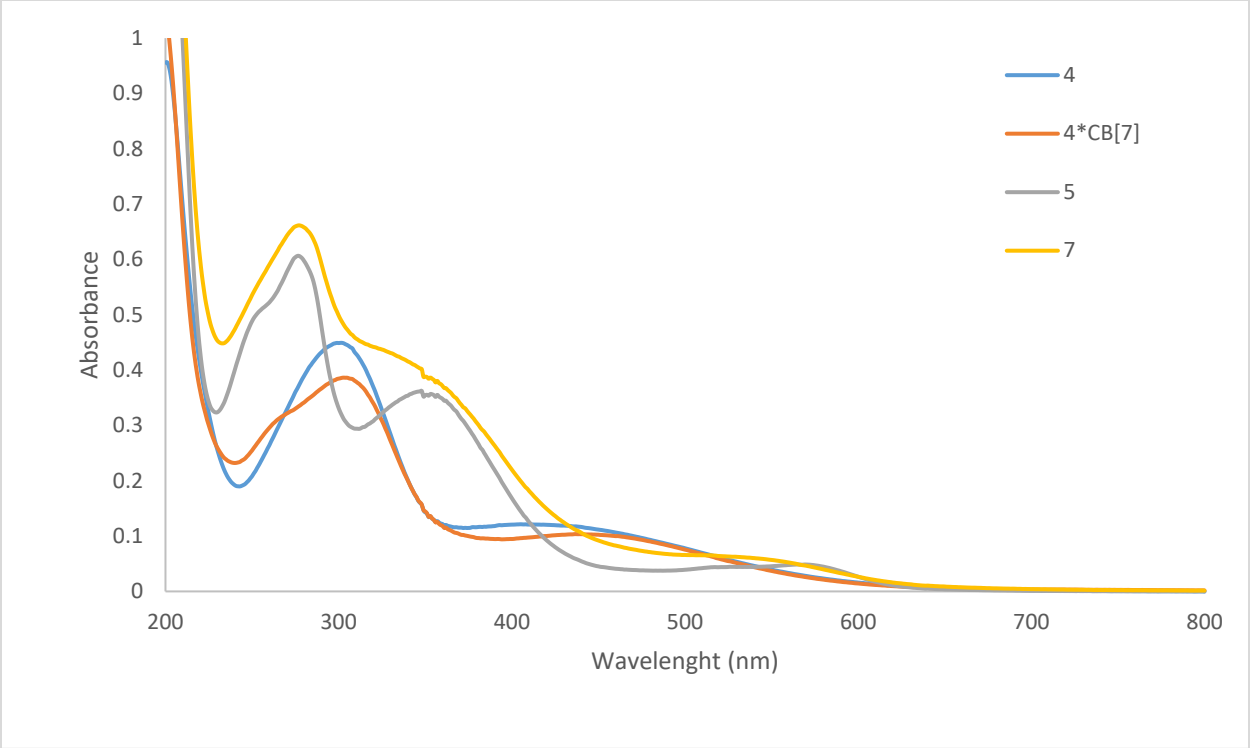

Figure IV-S31. UV VIS recorded for **IV-4**, **IV-4**·CB[7], Self-assembly **IV-6**, and Self-assembly **IV-7** in CH_3CN at room temperature.

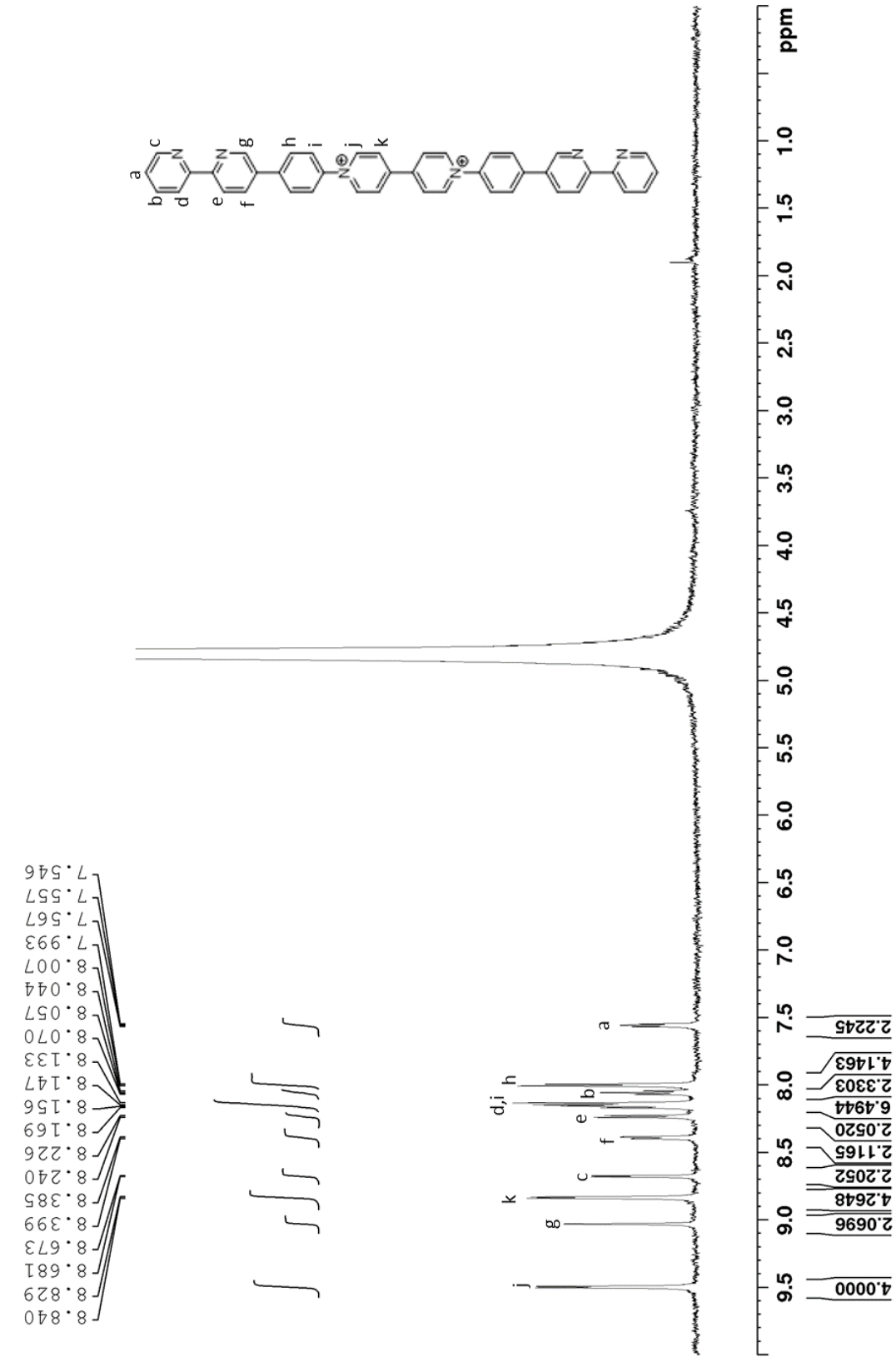

Figure IV-S32. ^{1}H NMR (600 MHz, D_2O, RT) recorded for **IV-11**·2Cl.

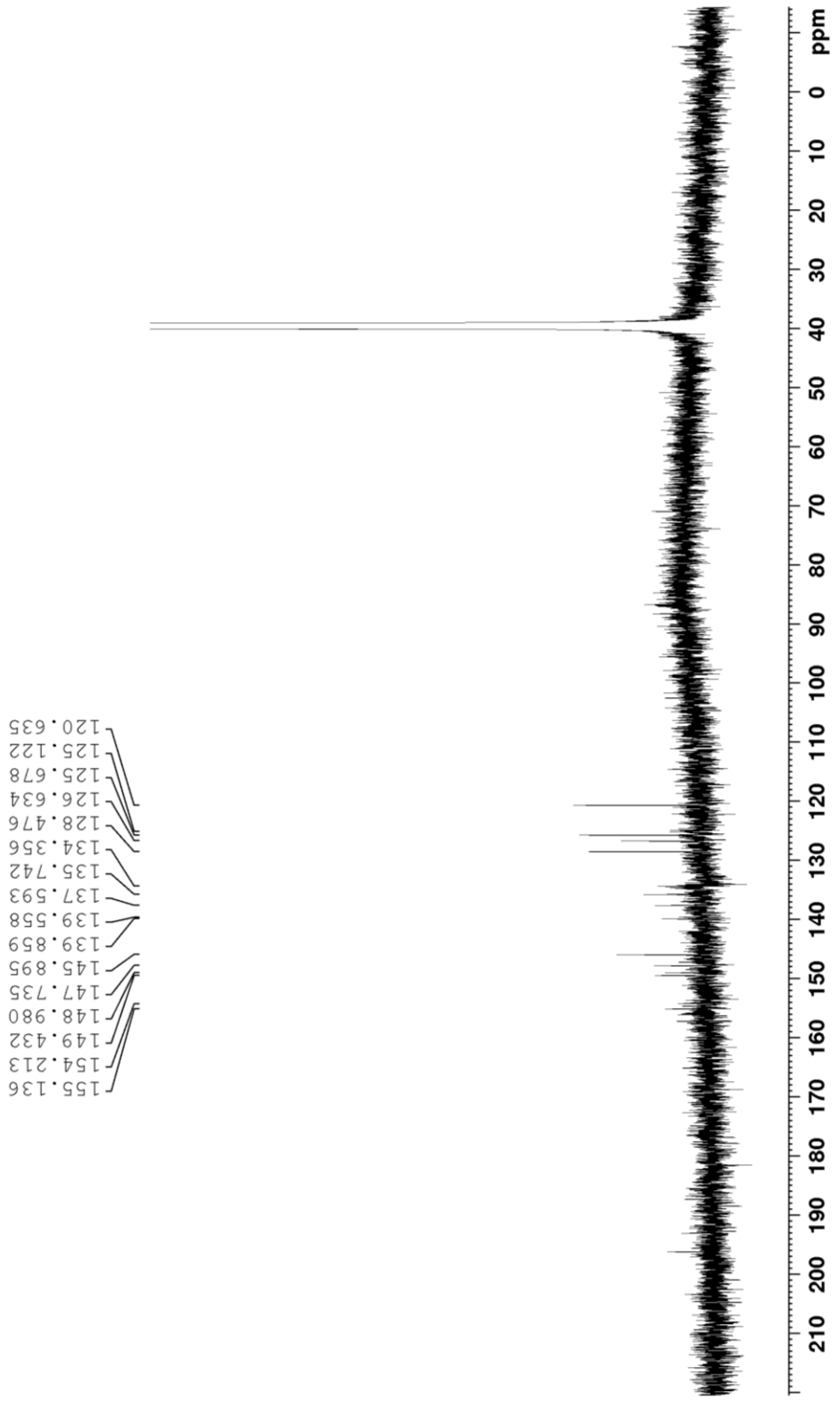

Figure IV-S33. ^{13}C NMR (126 MHz, D_2O, Dioxane as reference, RT) recorded for **IV-11**·2Cl.

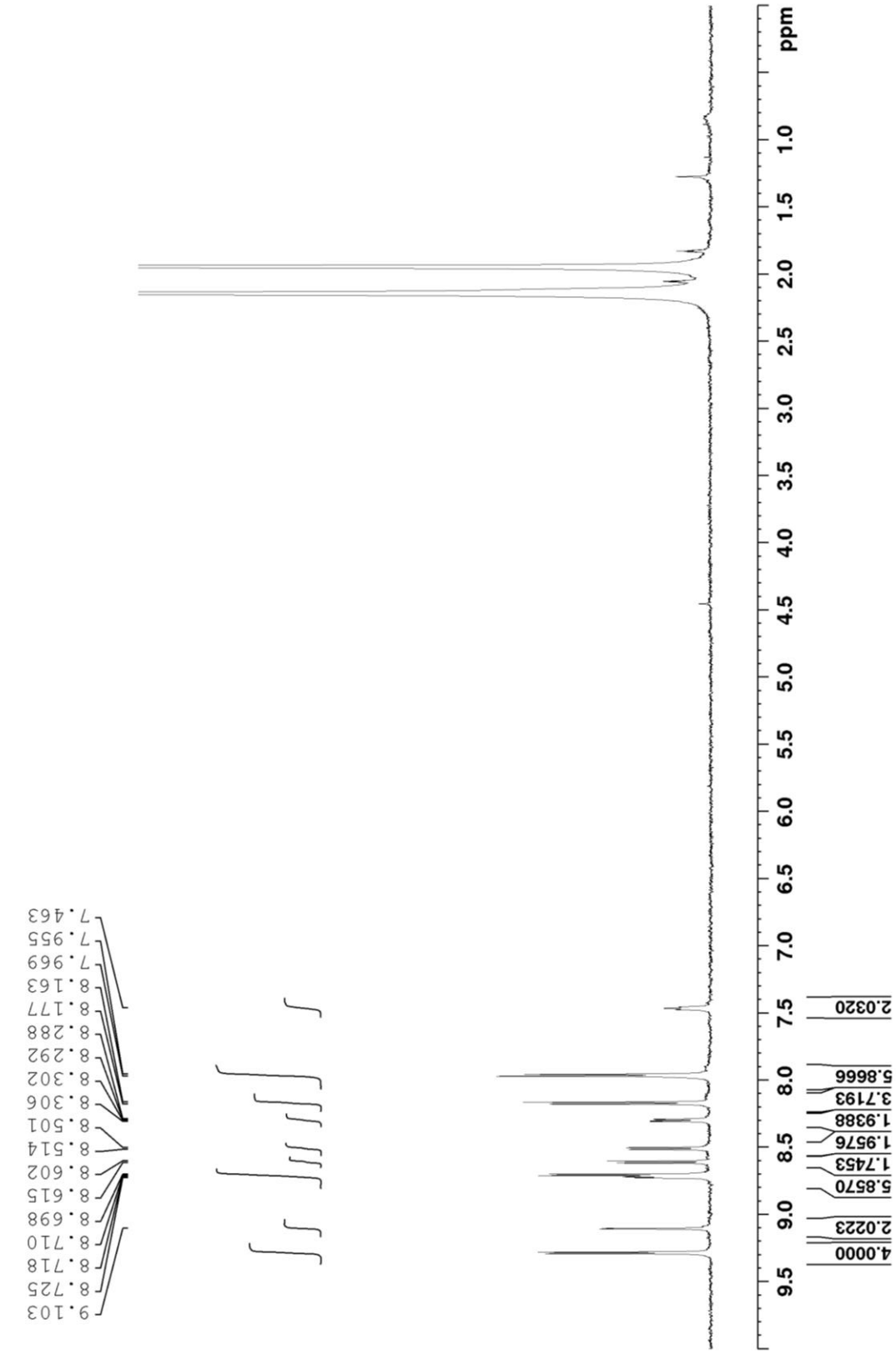

Figure IV-S34. ^{1}H NMR (600 MHz, CD_3CN, RT) recorded for **IV-11**·$2PF_6$.

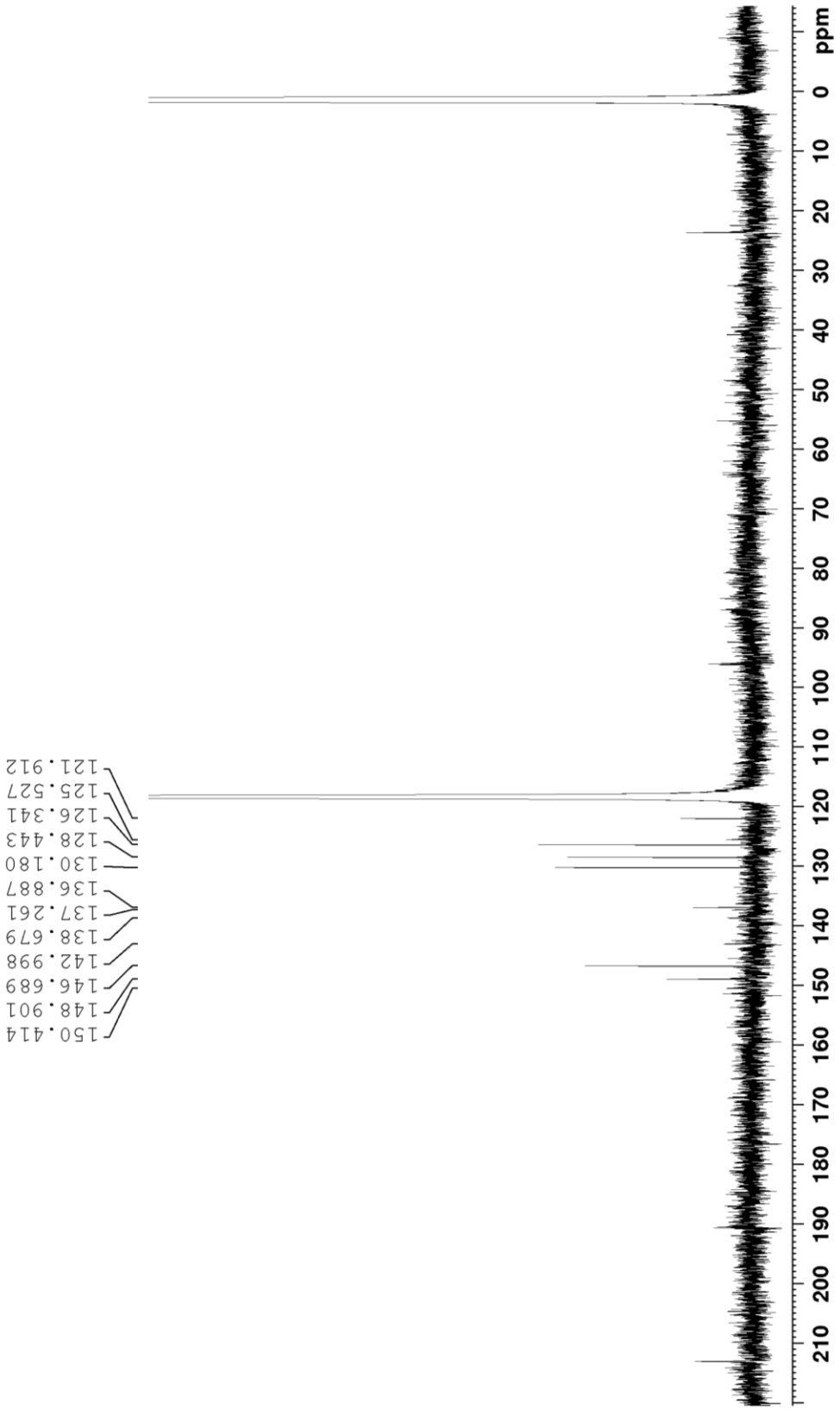

Figure IV-S35. ^{13}C NMR (126 MHz, CD_3CN, RT) recorded for **IV-11**·$2PF_6$.

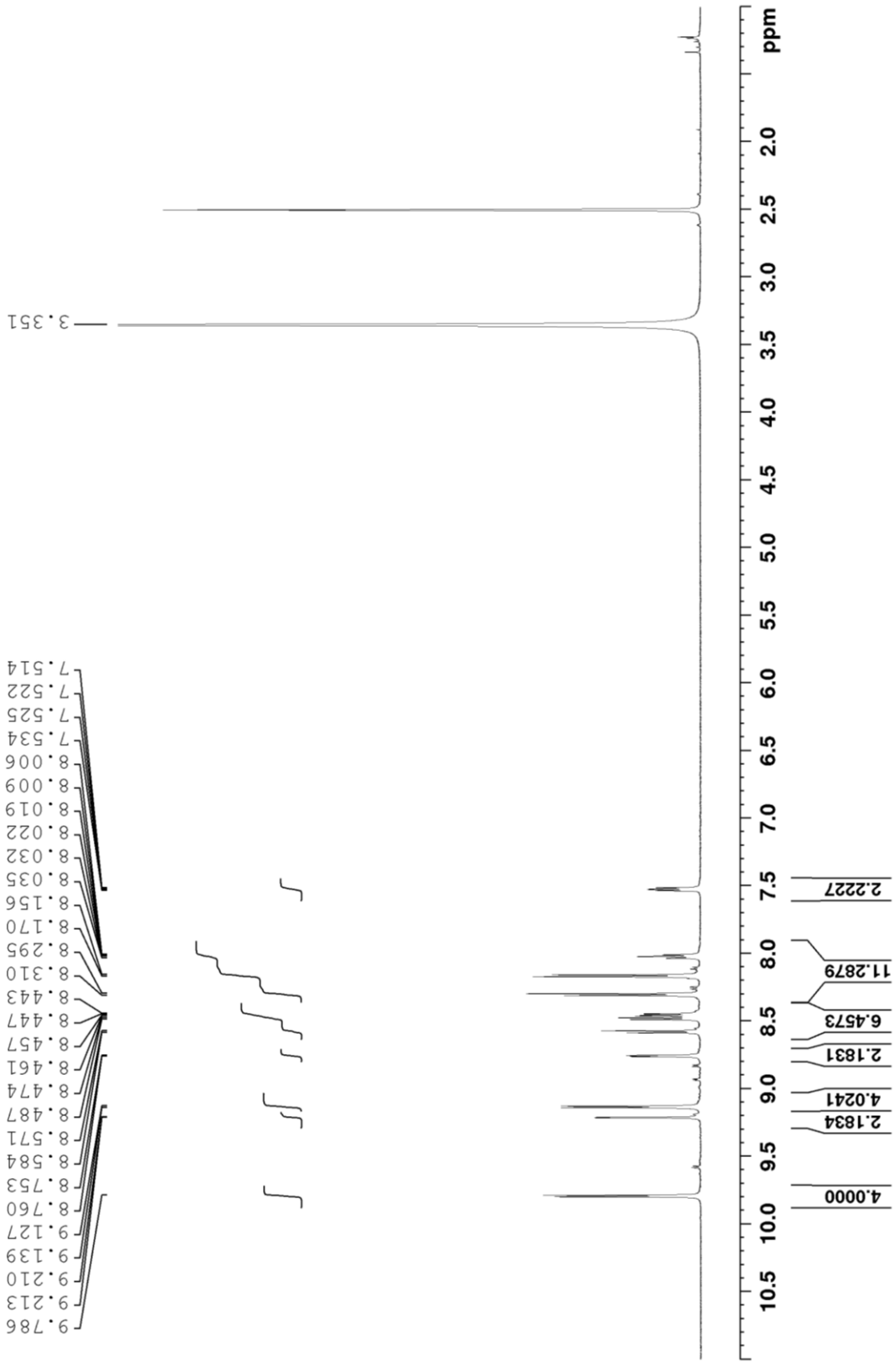

Figure IV-S36. ^{1}H NMR (600 MHz, DMSO-d_6, RT) recorded for **IV-11**·2NTf$_2$.

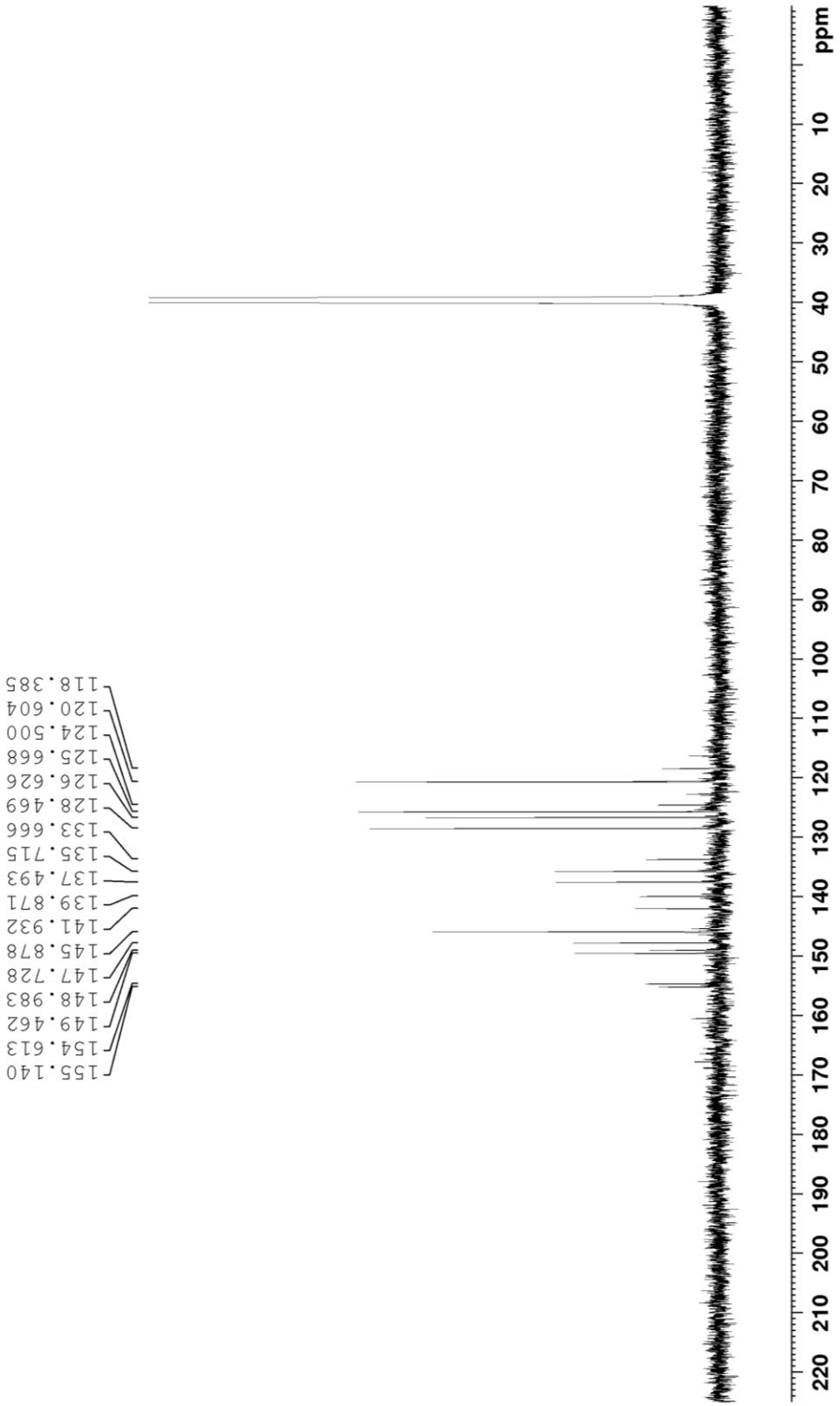

Figure IV-S37. ^{1}H NMR (126 MHz, DMSO-d_6, RT) recorded for **IV-11**·2NTf$_2$.

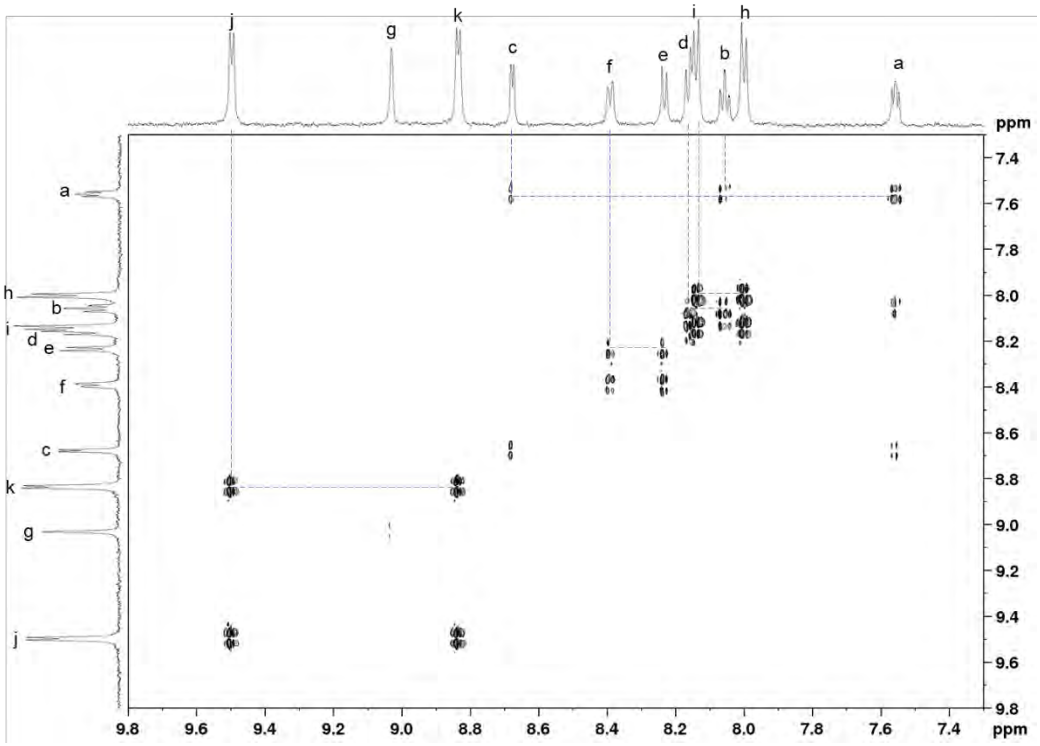

Figure IV-S38. COSY NMR (600 MHz, D_2O, 287 K) recorded for **IV-11**·2Cl.

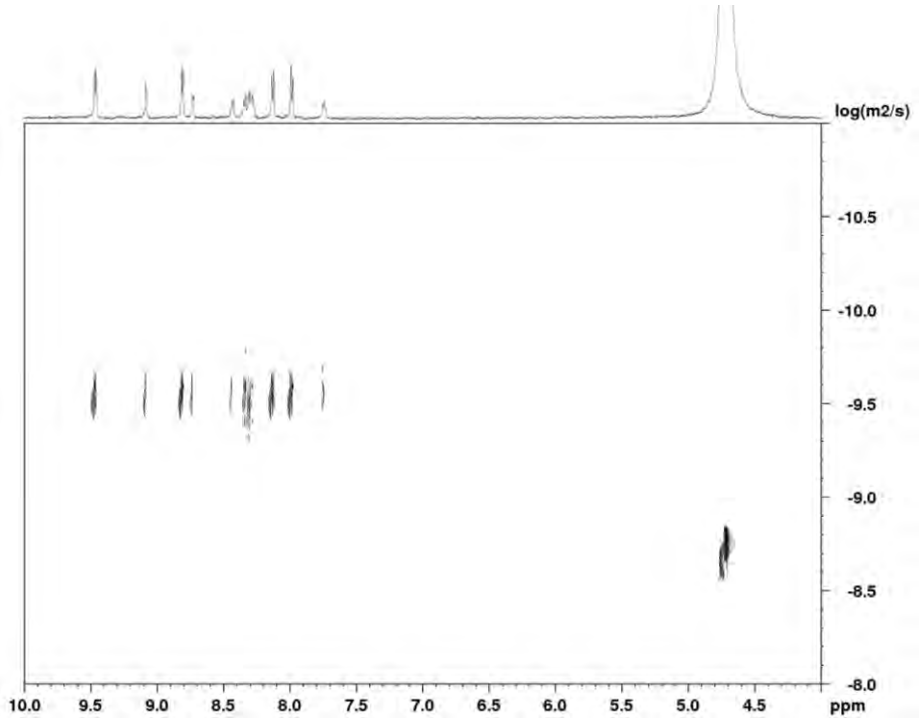

Figure IV-S39. DOSY NMR (600 MHz, D_2O, 287 K) recorded for **IV-11**·2Cl (D = 2.31 x 10^{-10} m^2/s).

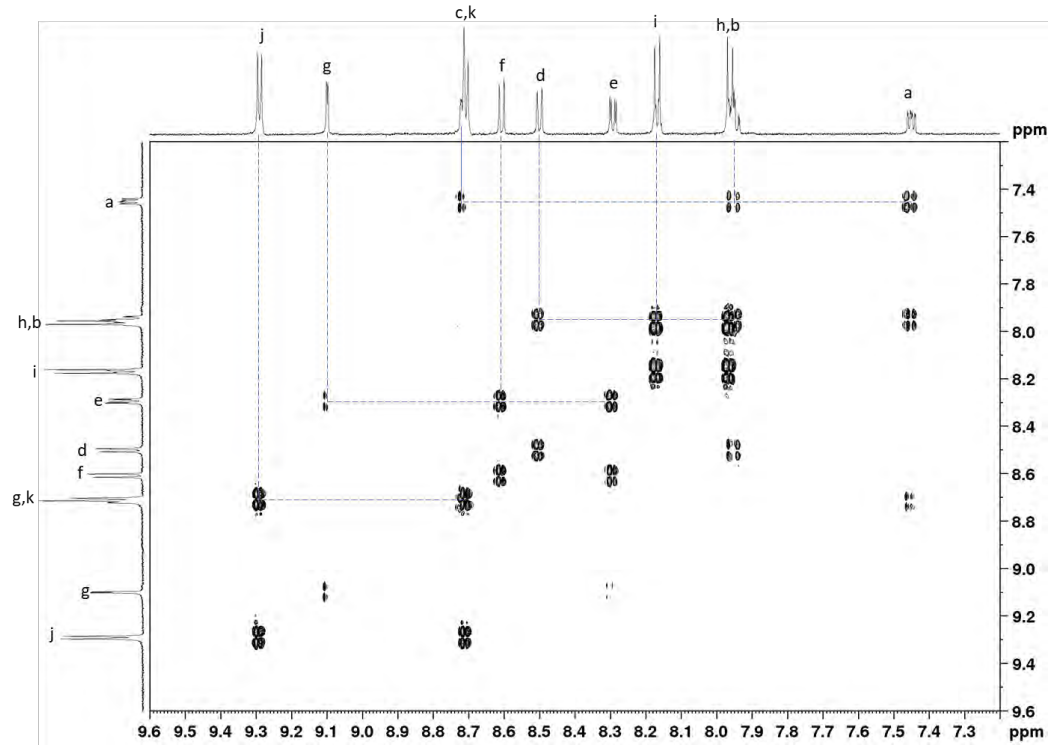

Figure IV-S40. COSY NMR (600 MHz, CD_3CN, 287 K) recorded for **IV-11**·$2PF_6$.

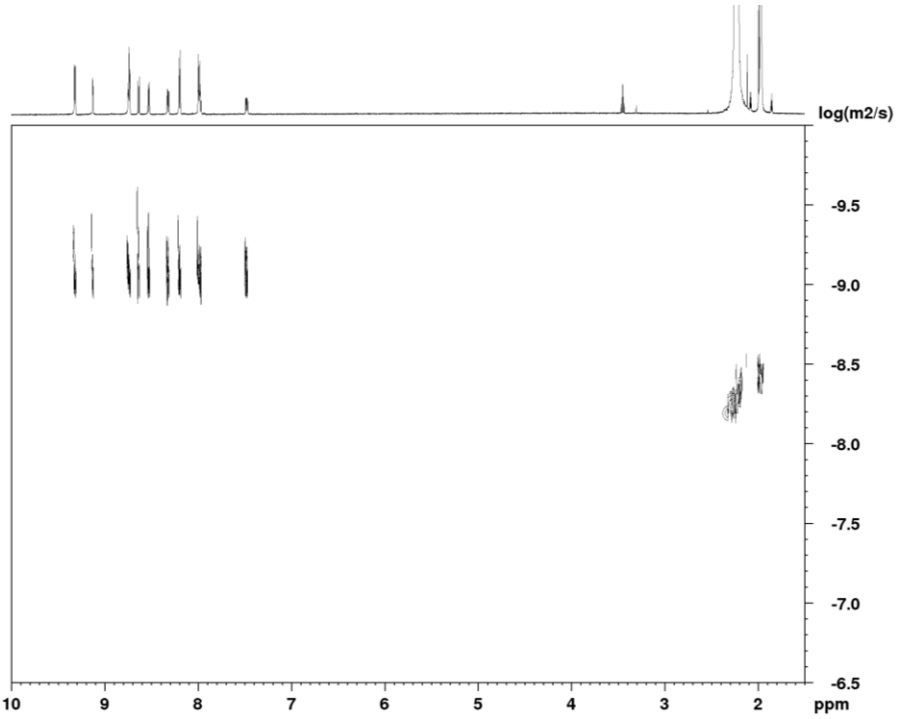

Figure IV-S41. DOSY NMR (600 MHz, CD_3CN, 287 K) recorded for **IV-11**·$2PF_6$ (D = 7.30 x 10^{-10} m^2/s).

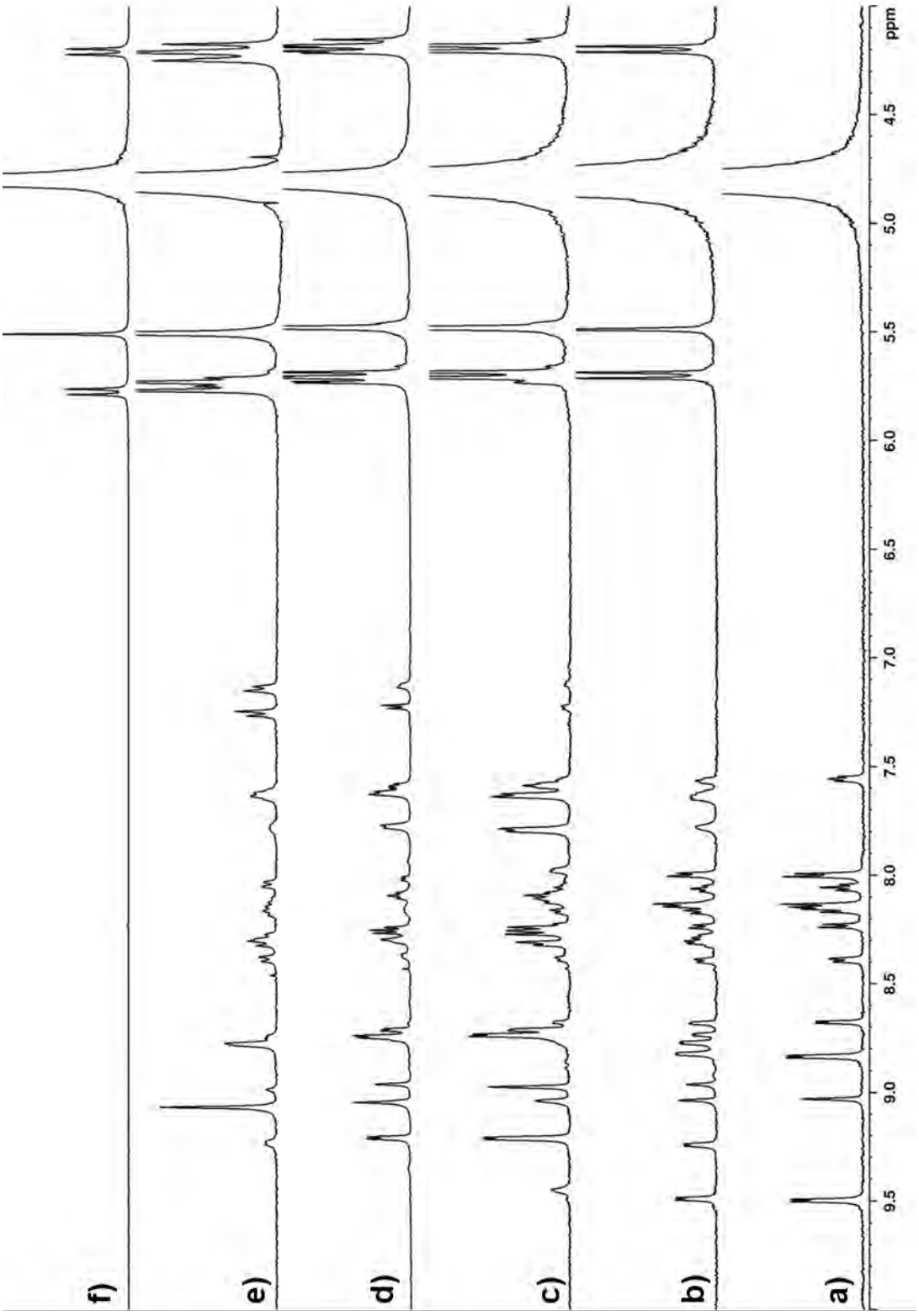

Figure IV-S42. ^{1}H NMR (600 MHz, D_2O, RT) titration of **IV-11**·2Cl with CB[7] (a) 0 equiv., (b) 0.5 equiv., (c) 0.9 equiv., (d) 1.3 equiv., (e) 1.7 equiv., (f) CB[7] alone.

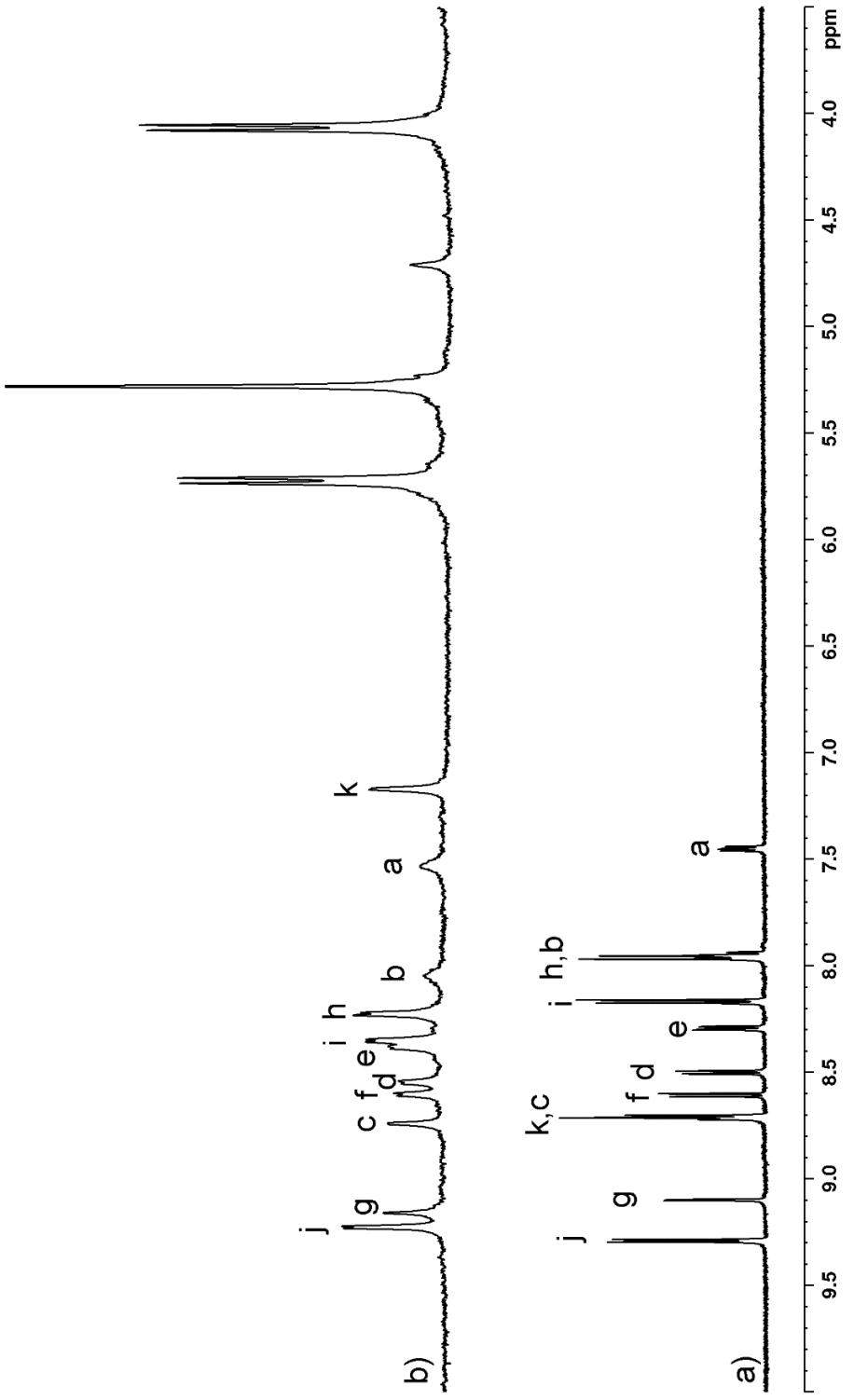

Figure IV-S43. ^{1}H NMR (600 MHz, CD_3CN, RT) recorded for **IV-11**·$2PF_6$ (a) alone, (b) with 1 equivalent of CB[7].

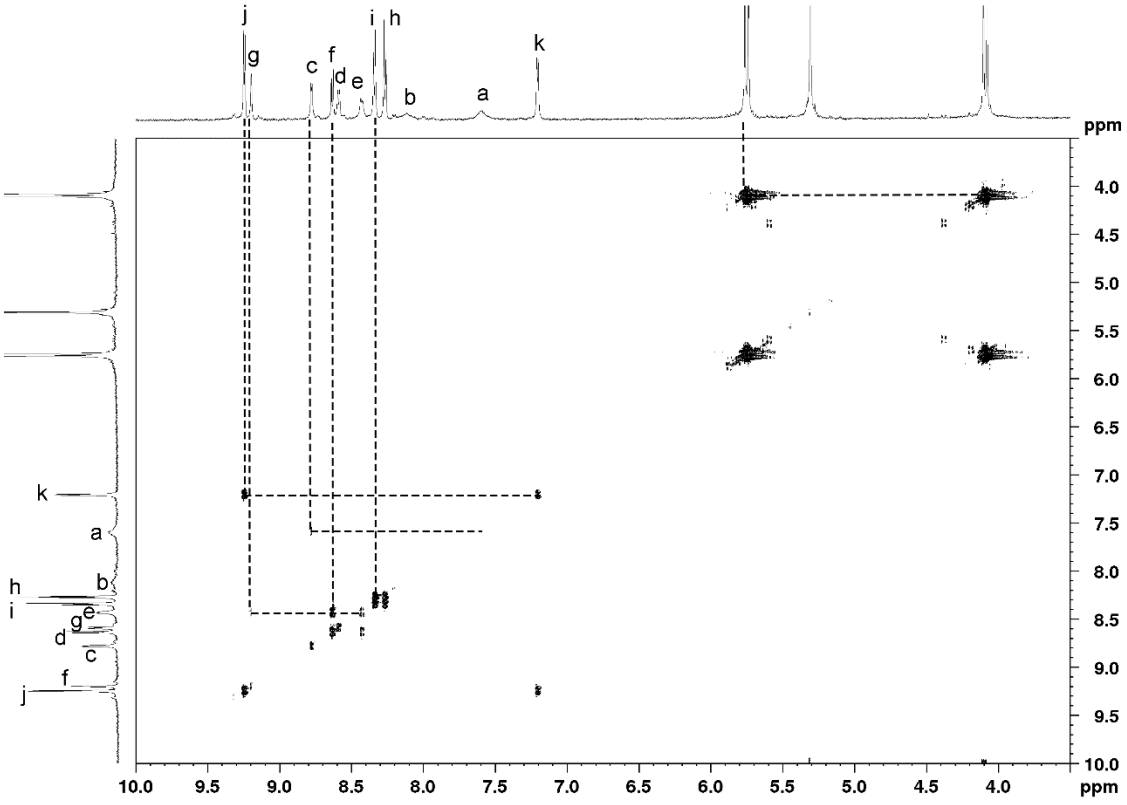

Figure IV-S44. COSY NMR (600 MHz, CD_3CN, 287 K) recorded for **IV-11**·CB[7].

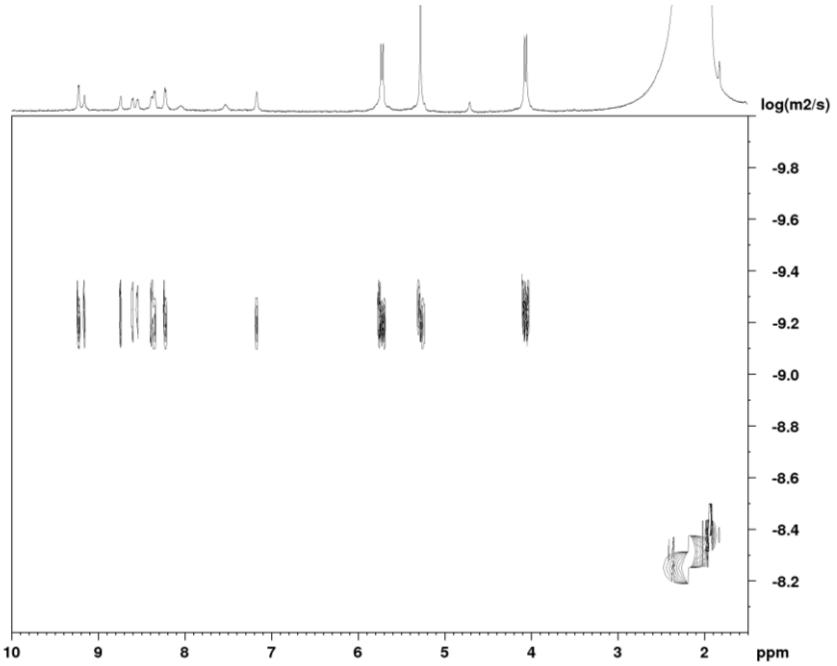

Figure IV-S45. DOSY NMR (600 MHz, CD_3CN, 287 K) recorded for **IV-11**·CB[7]·$2PF_6$ ($D = 5.08 \times 10^{-10}$ m^2/s).

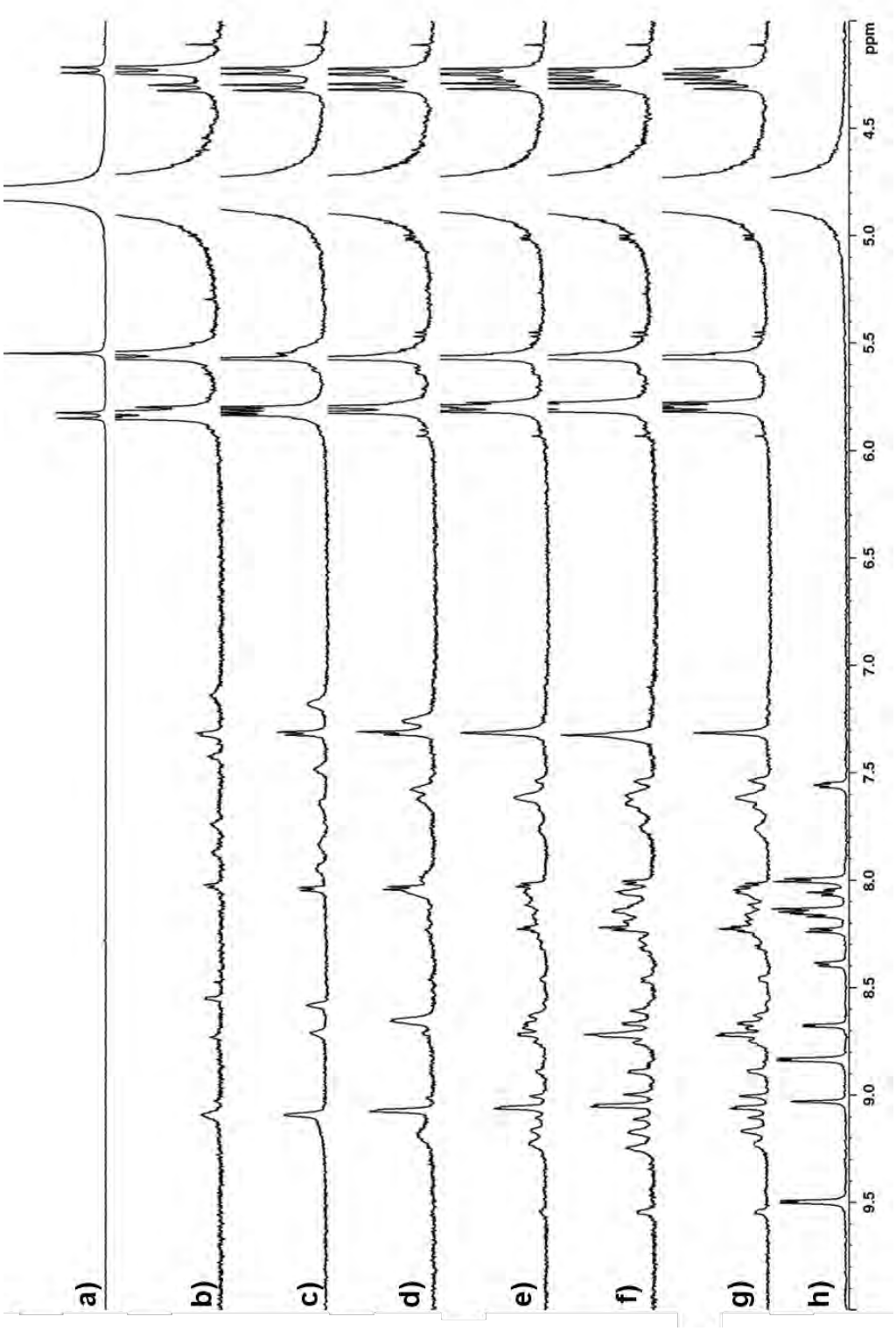

Figure IV-S46. ^{1}H NMR (600 MHz, D_2O, RT) titration of CB[8] (100μM) with **IV-11**·2Cl (a) 0 equiv., (b) 0.5 equiv., (c) 1.0 equiv., (d) 1.5 equiv., (e) 2.0 equiv., (f) 2.5 equiv., (g) 3.0 equiv., (h) ligand alone.

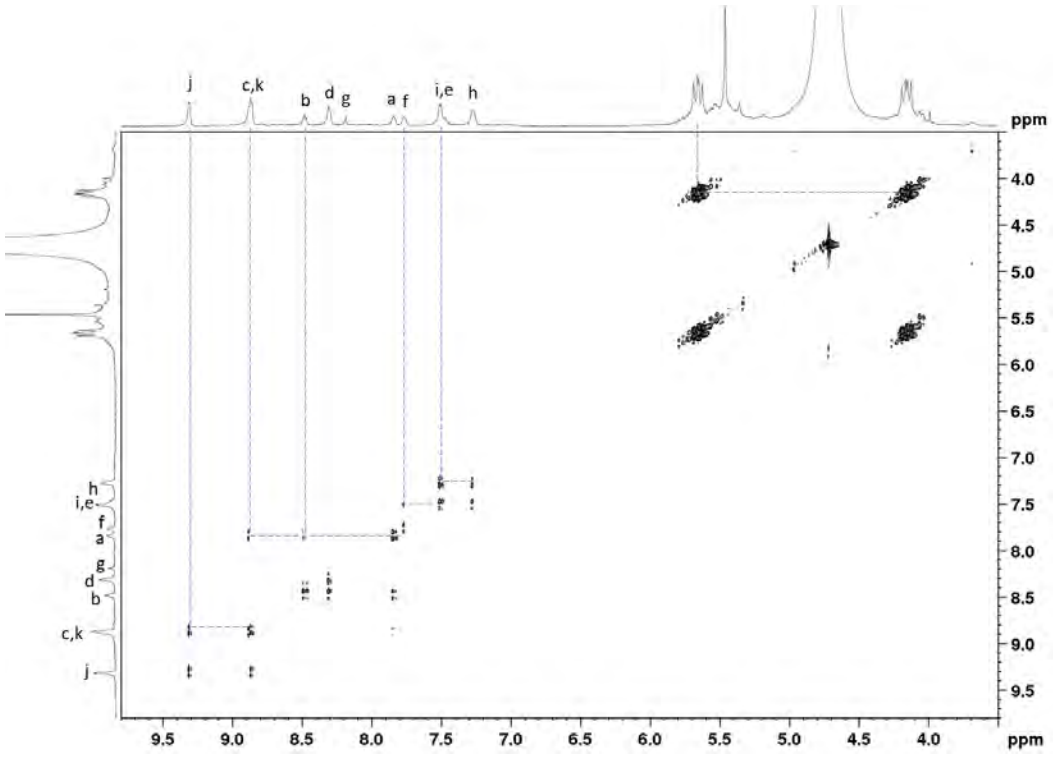

Figure IV-S47. COSY NMR (600 MHz, D_2O, 287 K) recorded for **IV-11**·CB[8]·2Cl.

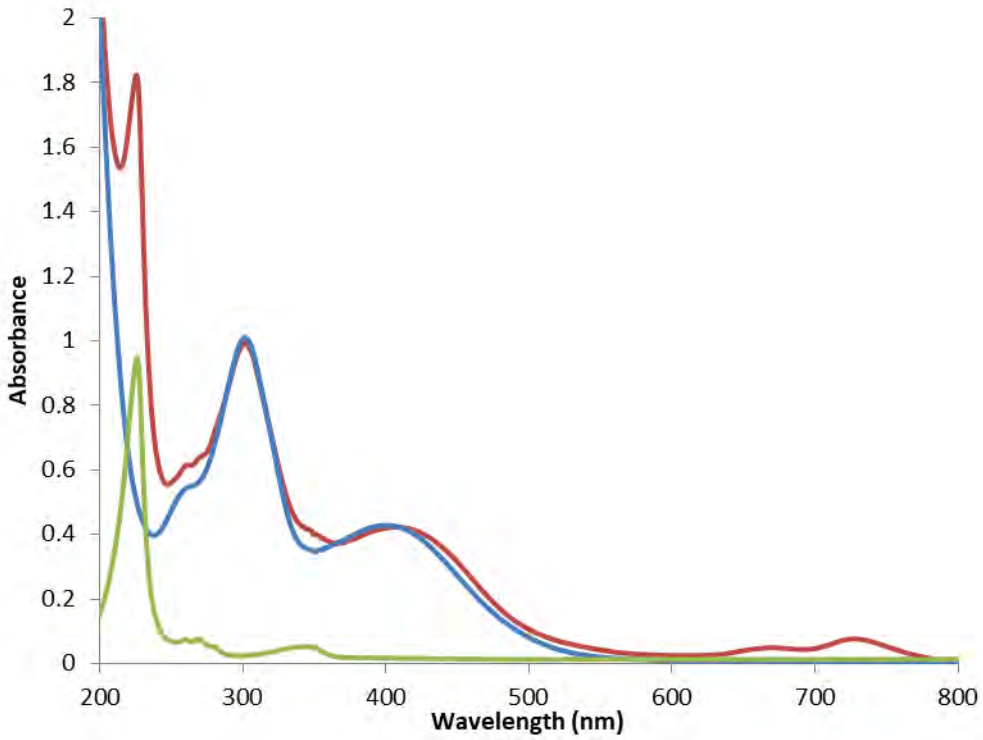

Figure IV-S48. UV/vis spectra recorded for charge transfer complex of CB[8] with **IV-11**·2Cl and 2,6-dihydroxynapthalene: 1:1 solution of CB[8]:**IV-11**·2Cl (18 μM, blue); 1:1:1 solution of CB[8]:**IV-11**:2,6-dihydroxynapthalene (18 μM, red); 2,6-dihydroxynapthalene alone (15 μM, green).

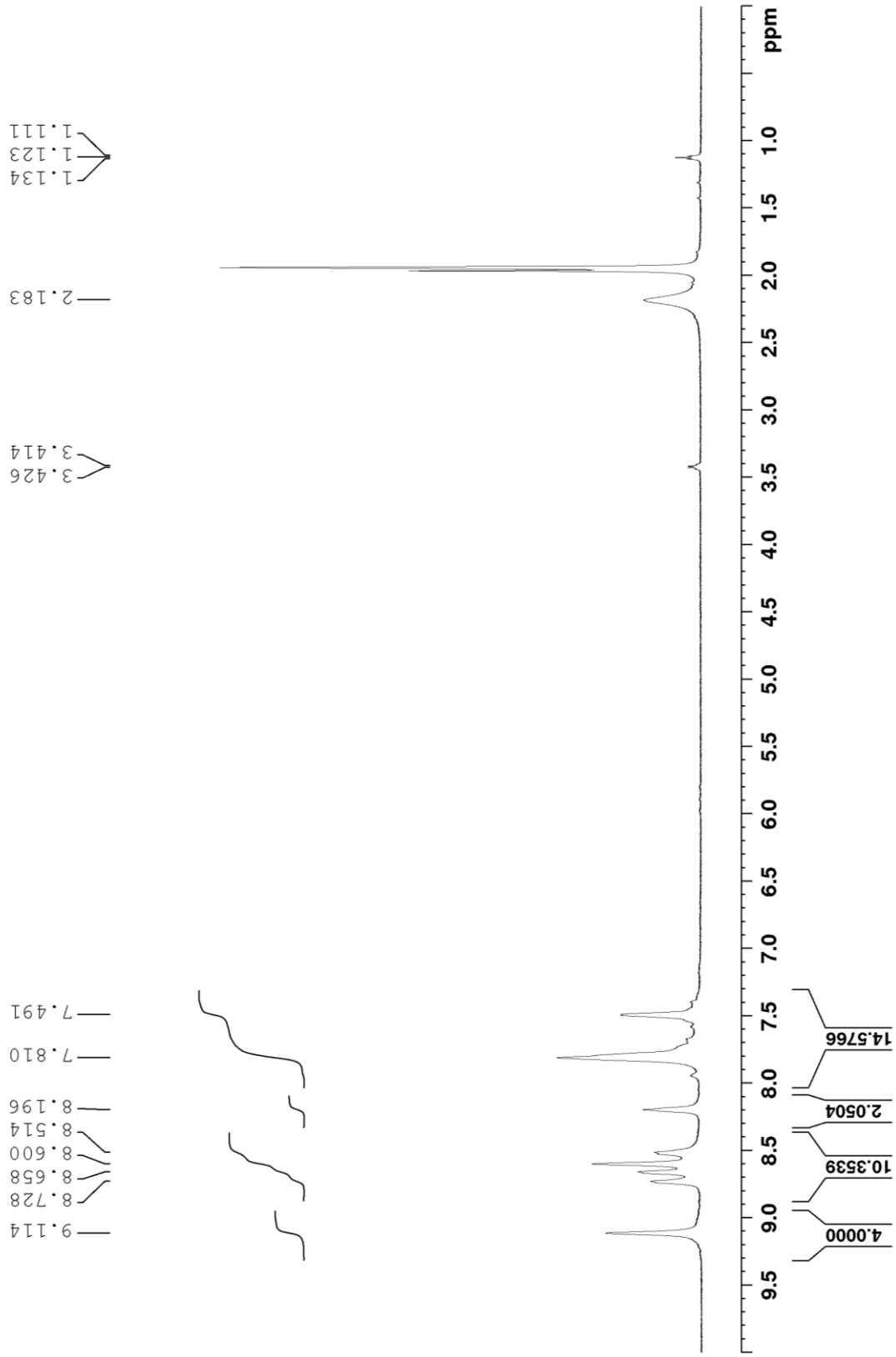

Figure IV-S49. ^{1}H NMR (600 MHz, CD_3CN, RT) recorded for **IV-12**·$20PF_6$.

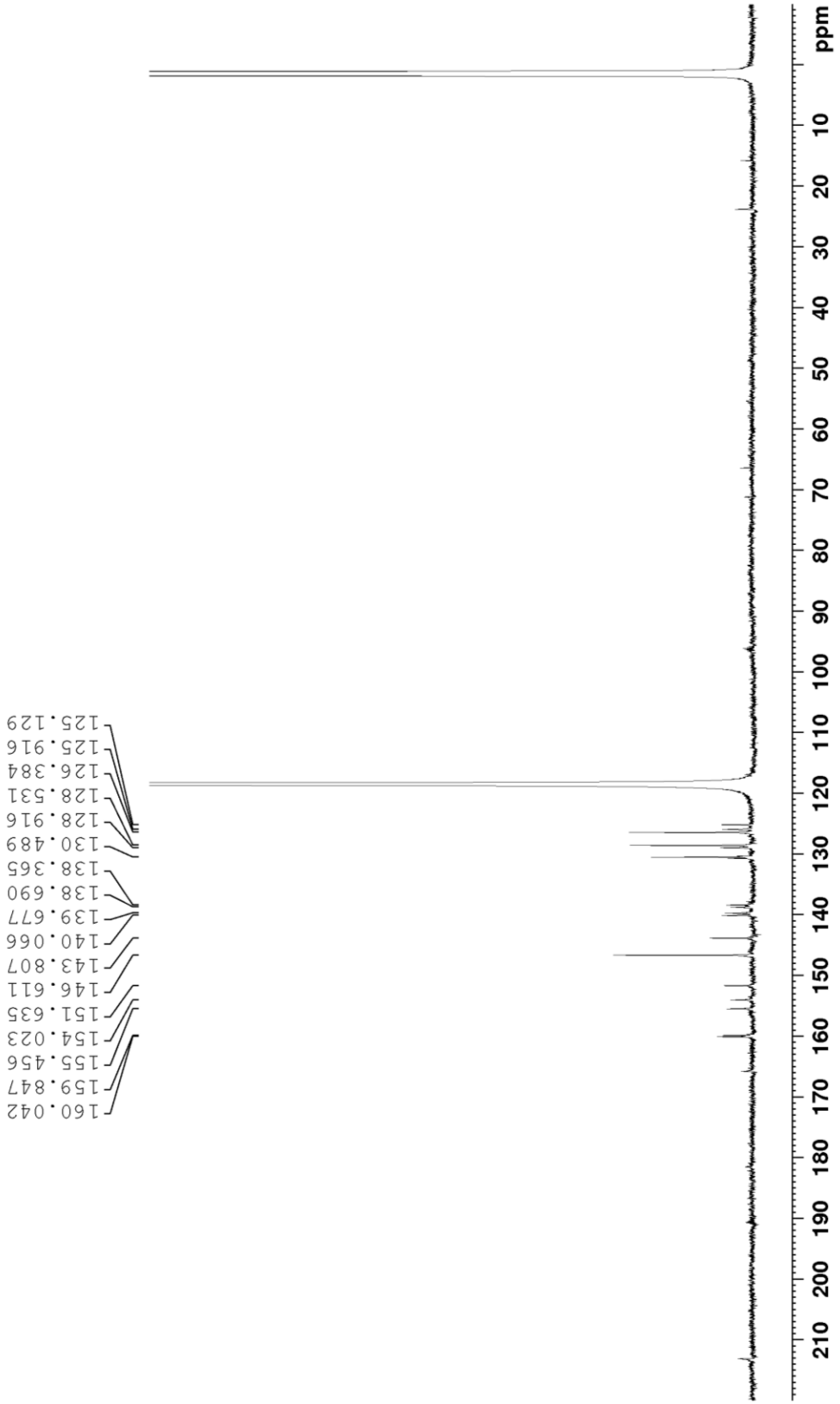

Figure IV-S50. ^{13}C NMR (126 MHz, CD_3CN, RT) recorded for cage **IV-12**·20PF_6.

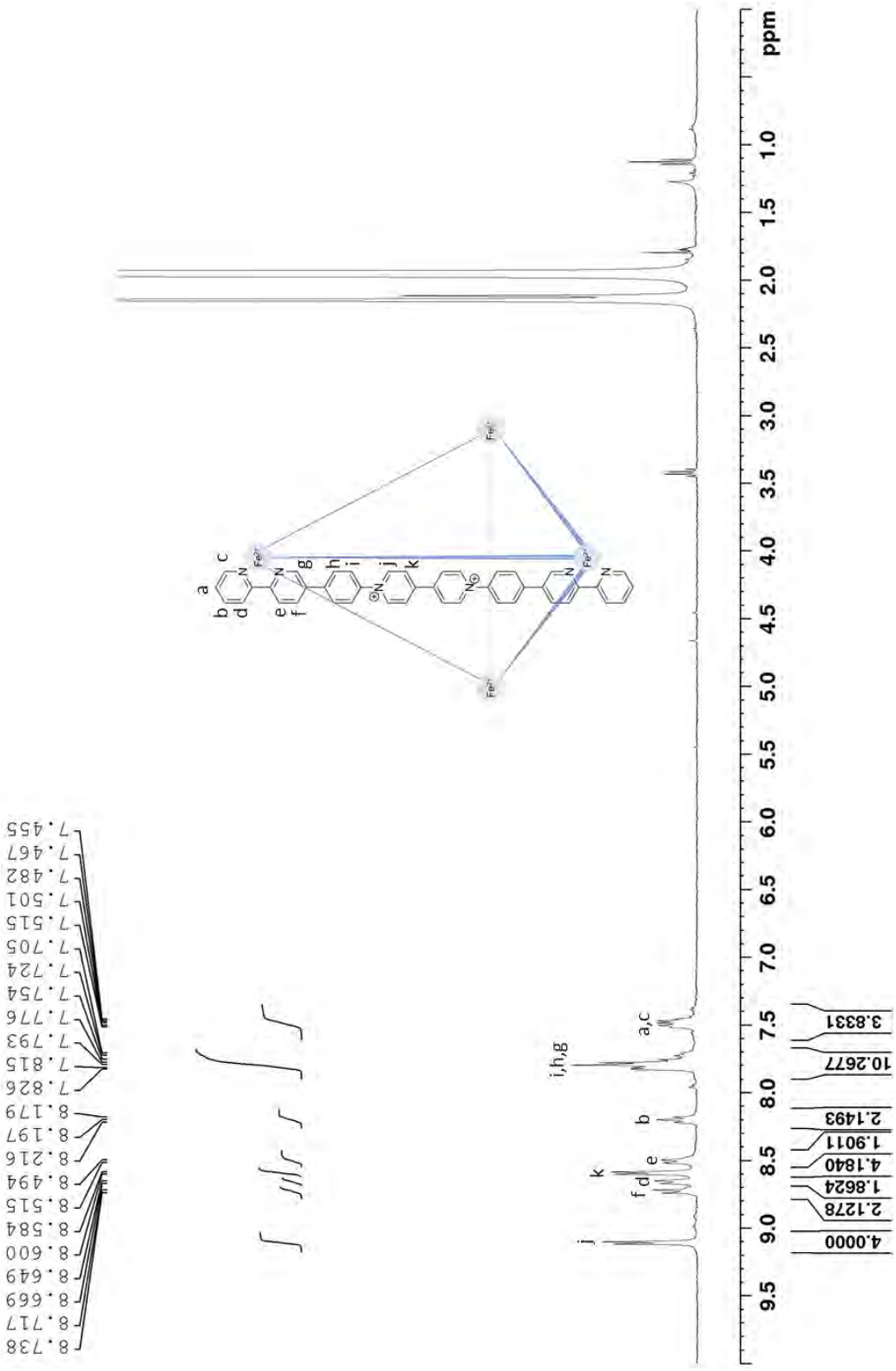

Figure IV-S51. ^{1}H NMR (600 MHz, CD_3CN, RT) recorded for **IV-12**·20NTf_2.

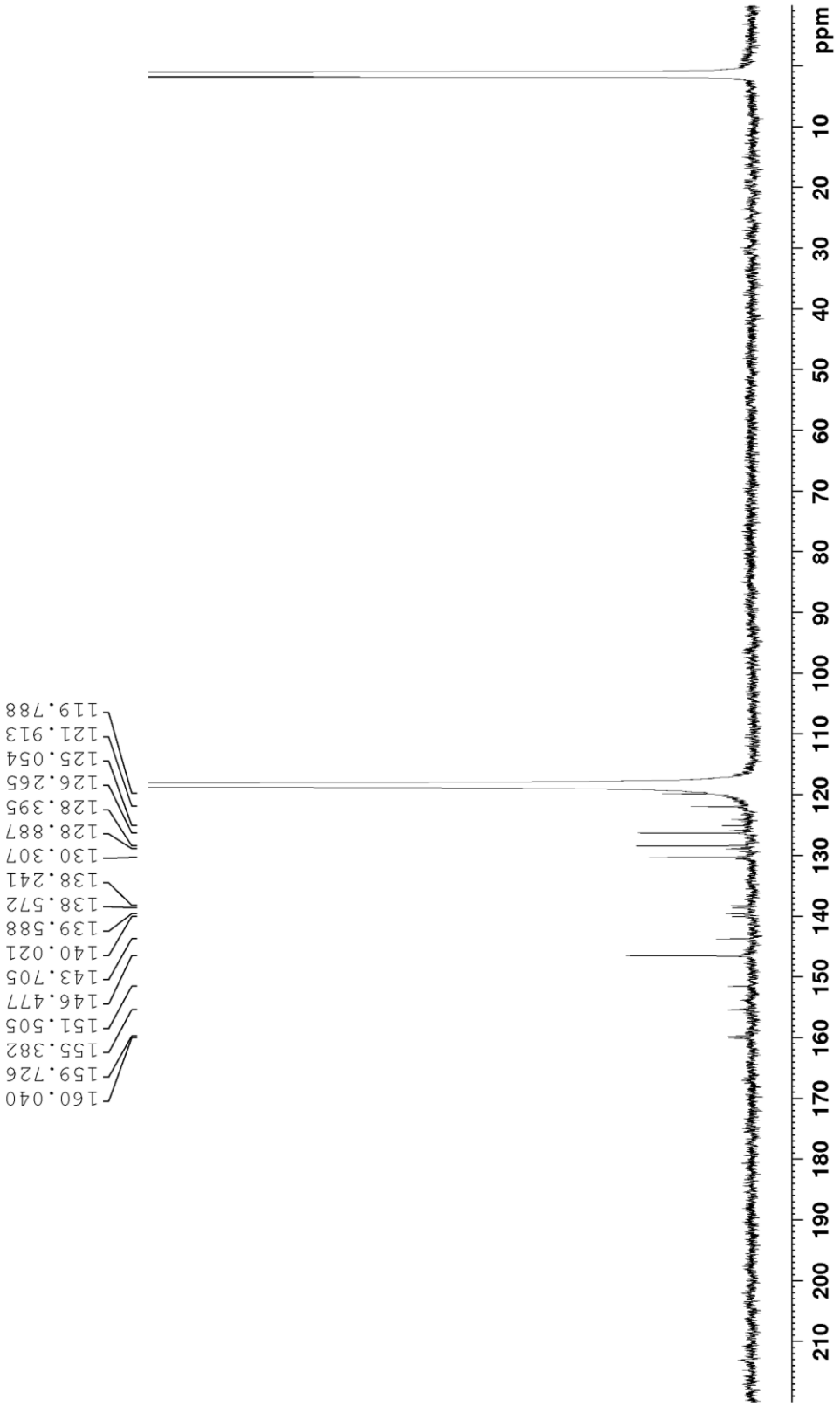

Figure IV-S52. ^{13}C NMR (126 MHz, CD_3CN, RT) recorded for cage **IV-12**·20NTf_2.

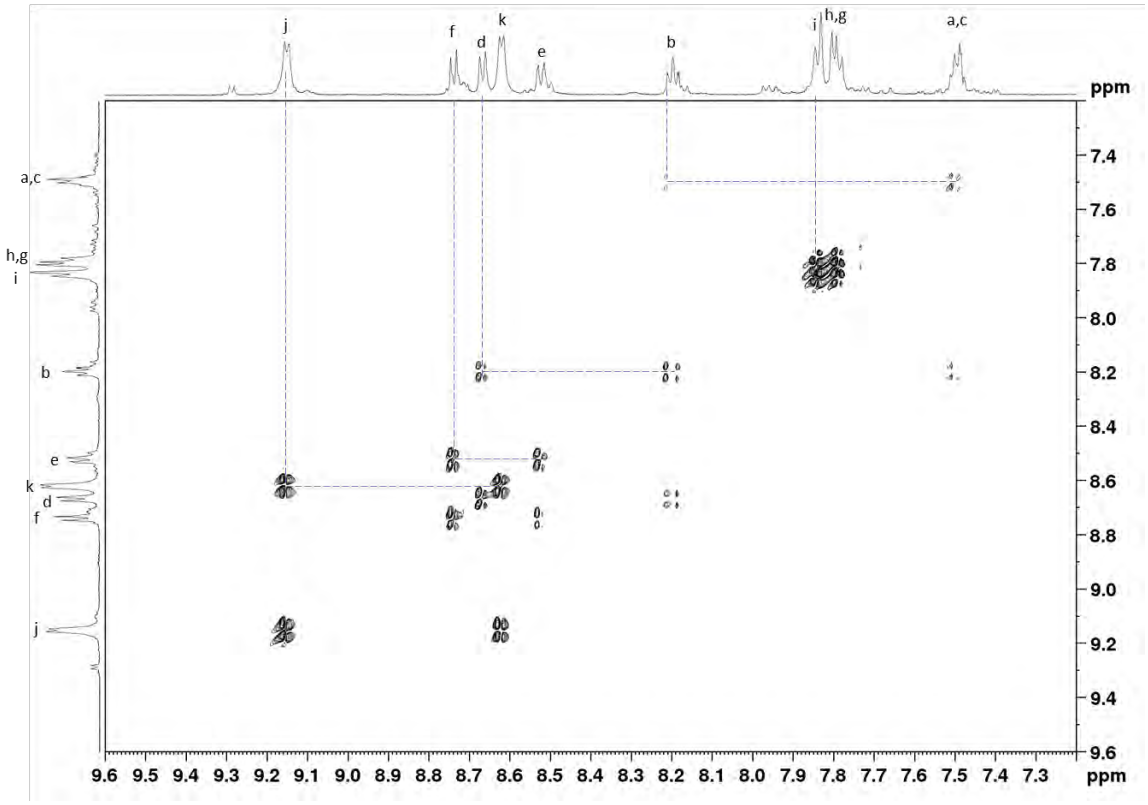

Figure IV-S53. COSY NMR (600 MHz, CD_3CN, RT) recorded for cage **IV-12**·$20PF_6$.

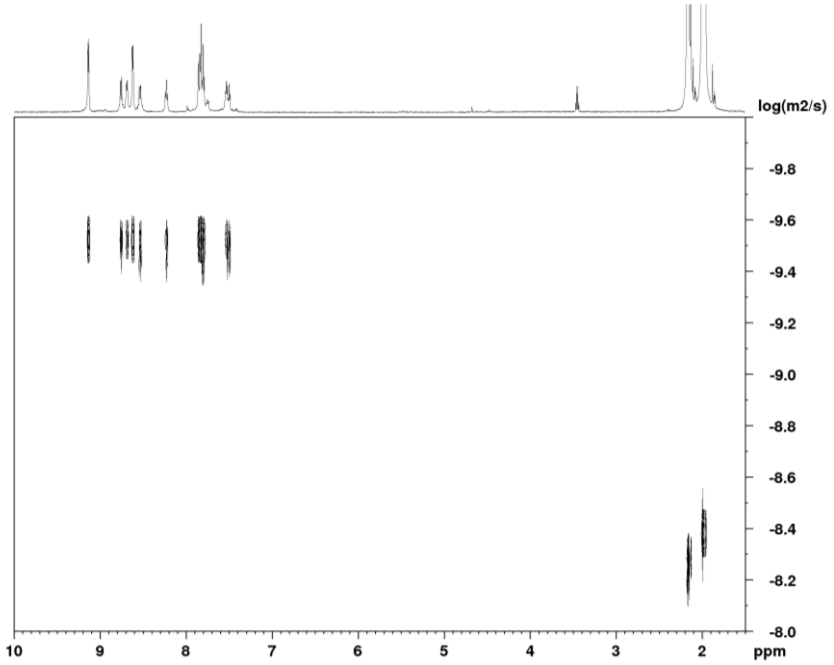

Figure IV-S54. DOSY NMR (600 MHz, CD_3CN, RT) recorded for cage **IV-12**·$20PF_6$ (D = 3.08 x 10^{-10} m^2/s).

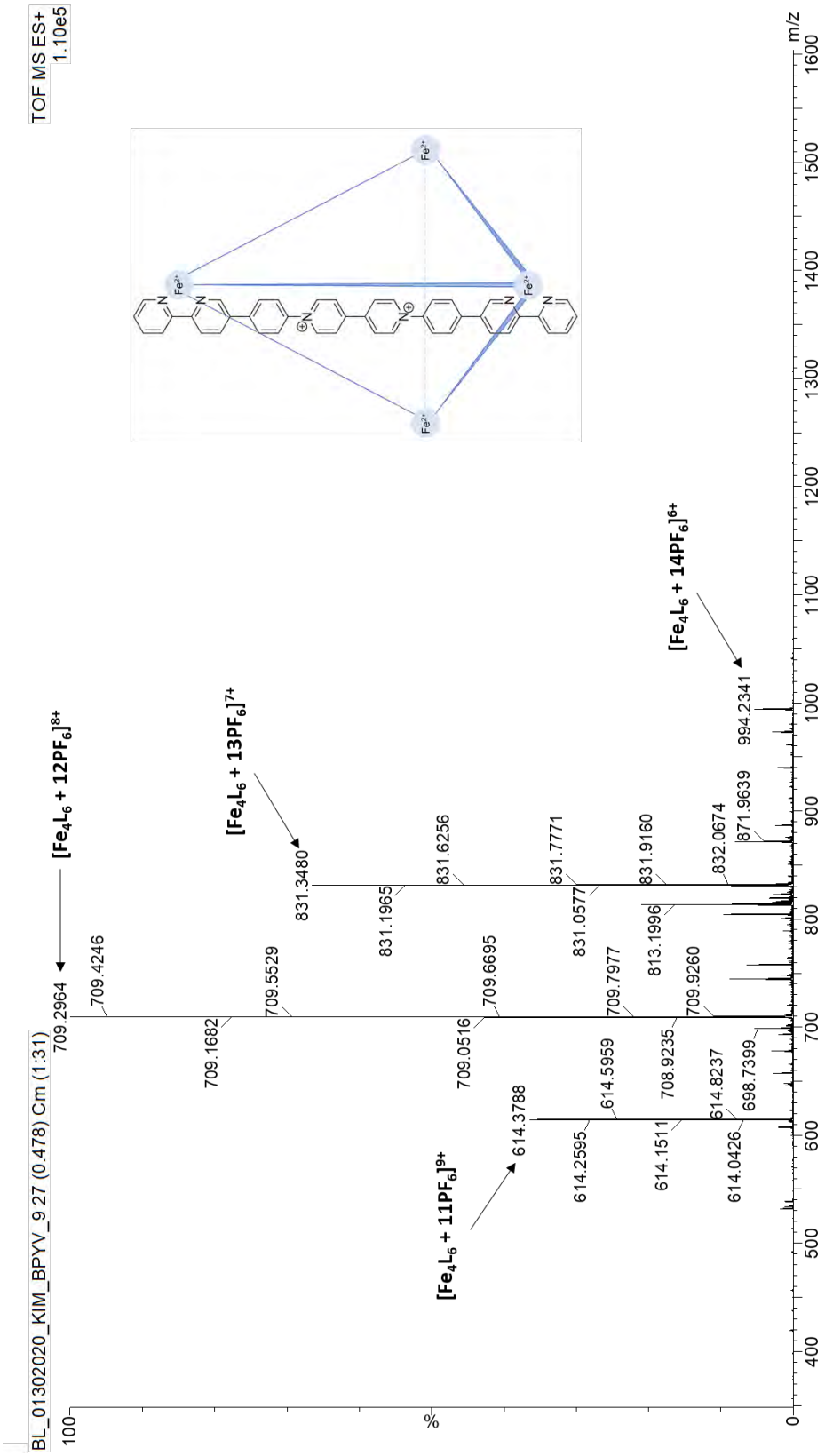

Figure IV-S55. ESI-TOF mass spectra (positive mode) for **IV-12**·20PF_6 where L = **IV-11**.

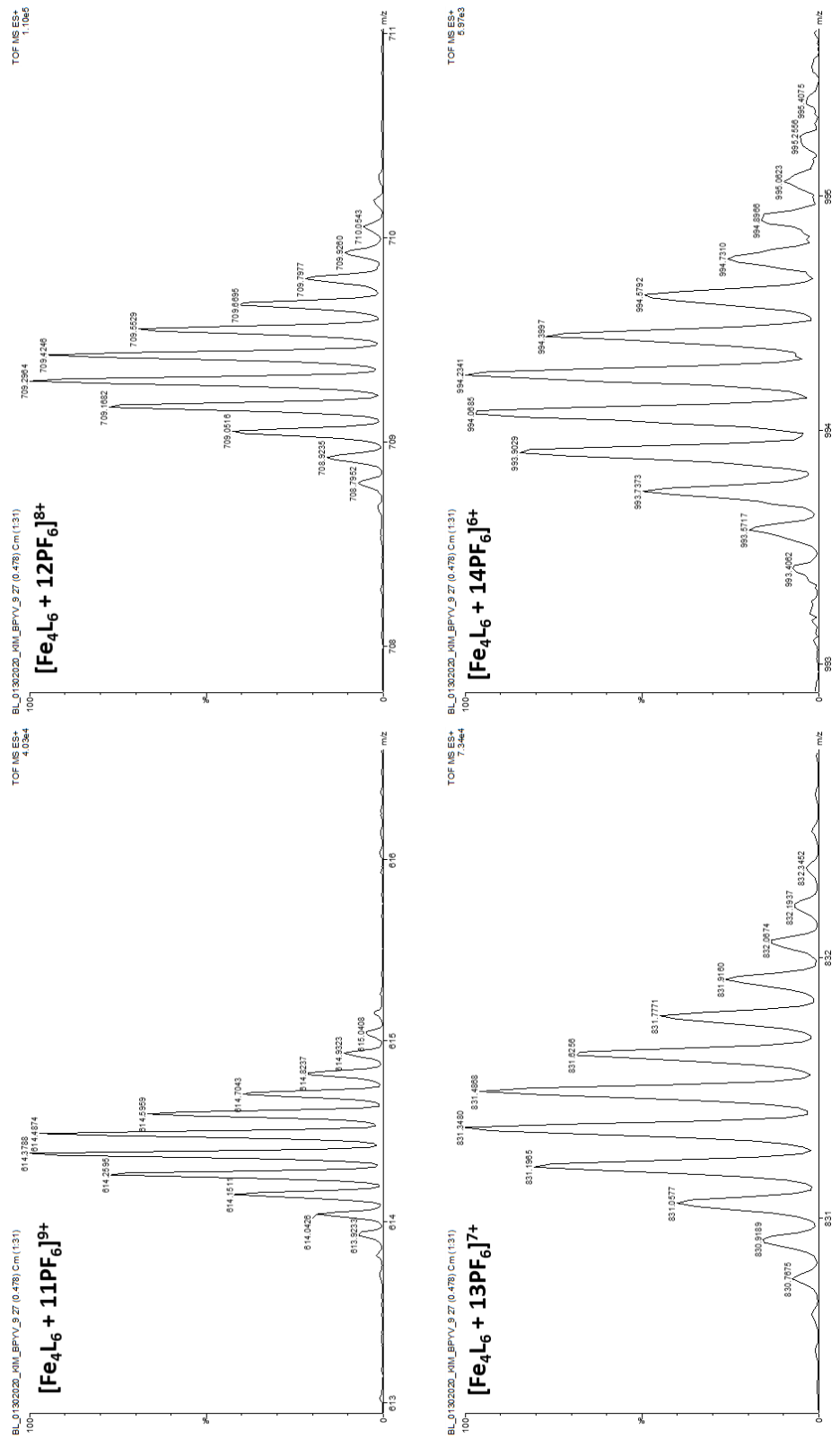

Figure IV-S56. Zoomed in ESI-TOF mass spectra (positive mode) for **IV-12**·20PF_6, where L = **IV-11**.

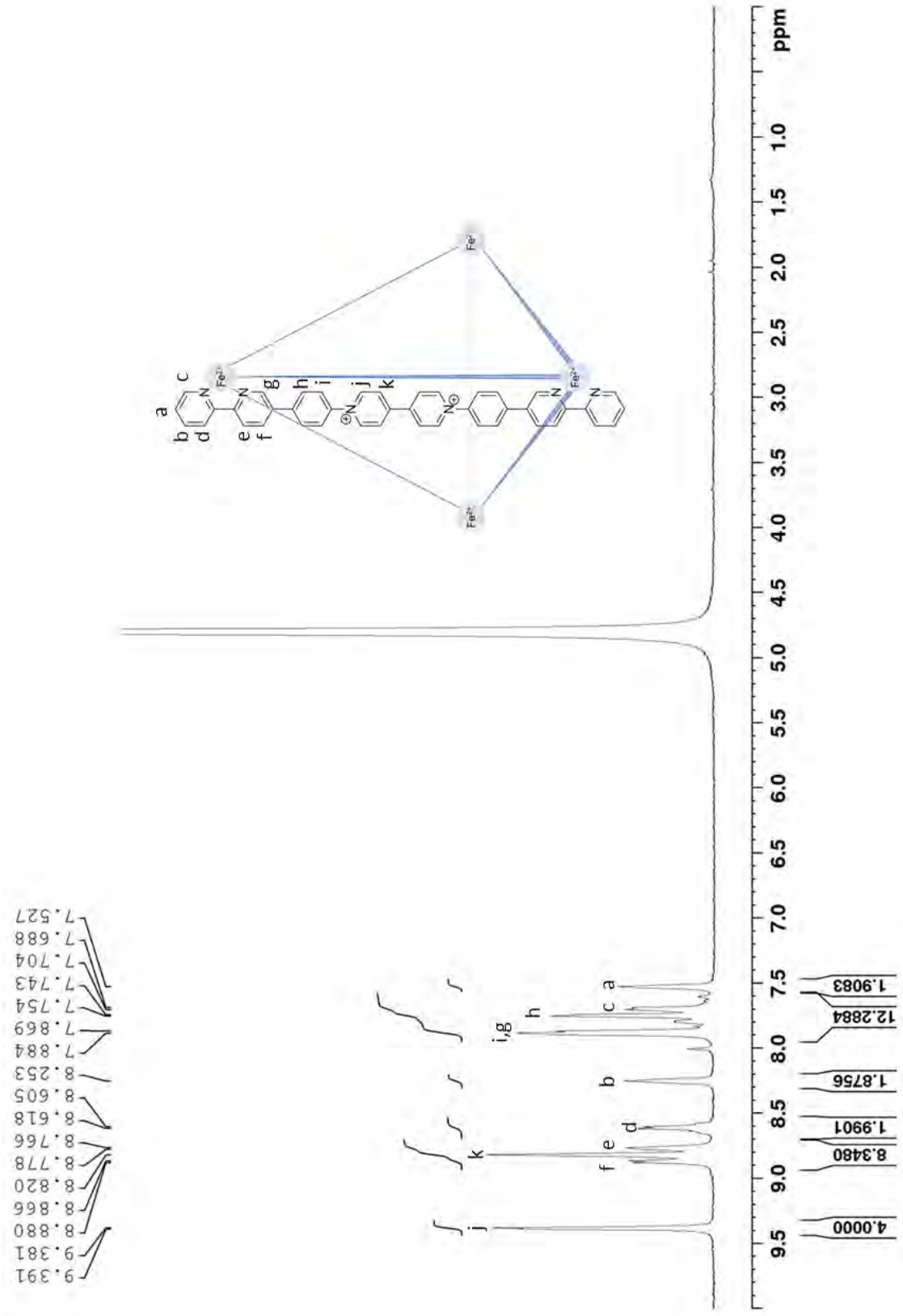

Figure IV-S57. ^{1}H NMR (600 MHz, D_2O, RT) recorded for cage **IV-12**·10(SO_4).

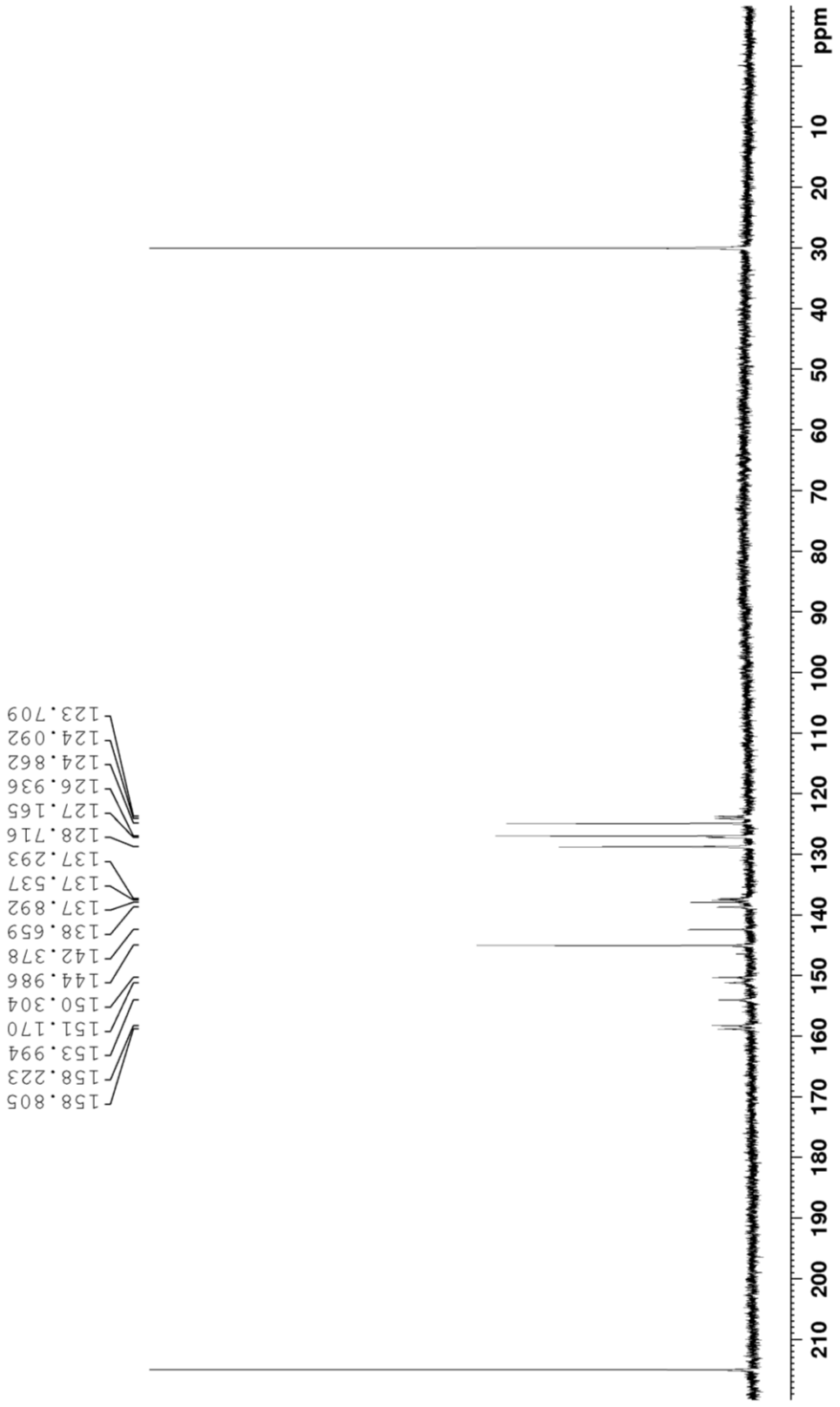

Figure IV-S58. ^{13}C NMR (126 MHz, D_2O, RT, Acetone as reference) recorded for cage **IV-12**·10(SO_4).

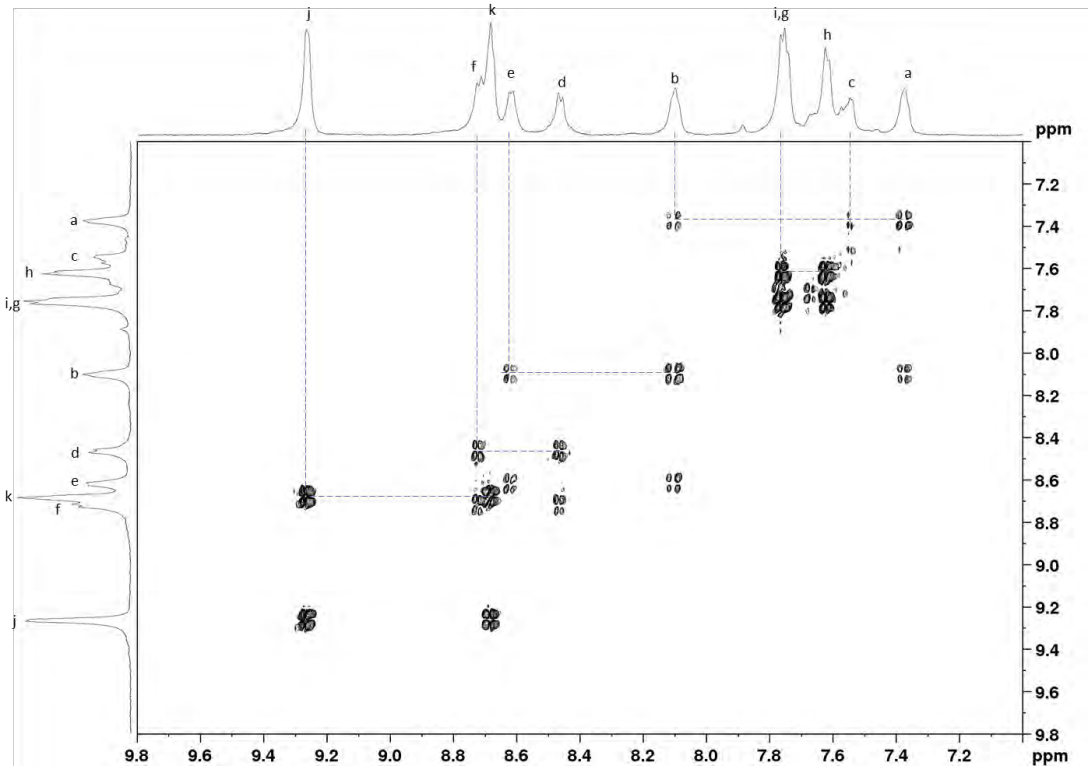

Figure IV-S59. COSY NMR (600 MHz, D_2O, RT) recorded for cage **IV-12**·10(SO_4).

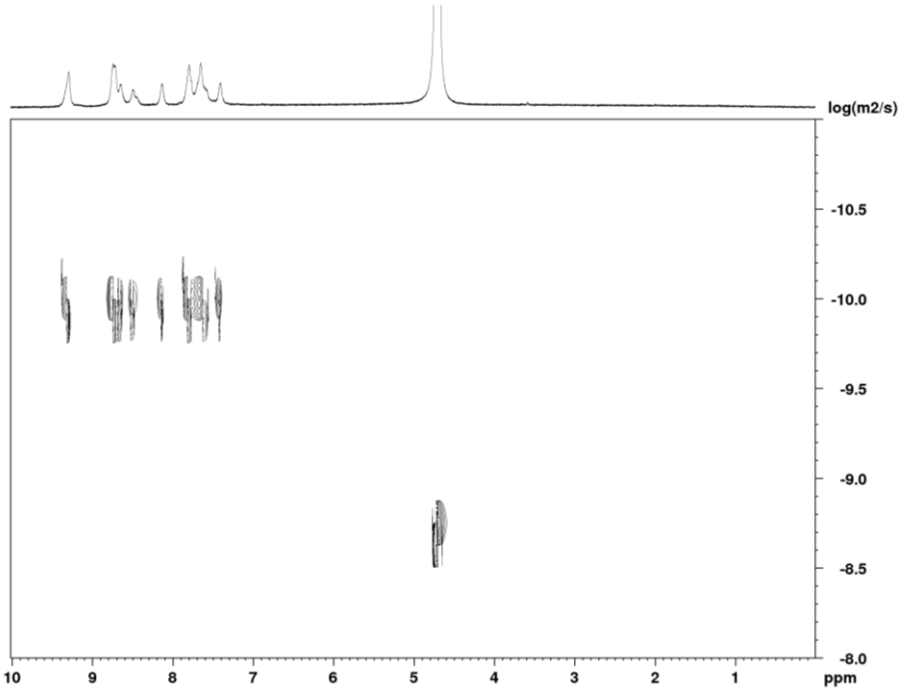

Figure IV-S60. DOSY NMR (600 MHz, D_2O, RT) recorded for cage **IV-12**·10(SO_4) (D = 8.01 x 10^{-11} m^2/s).

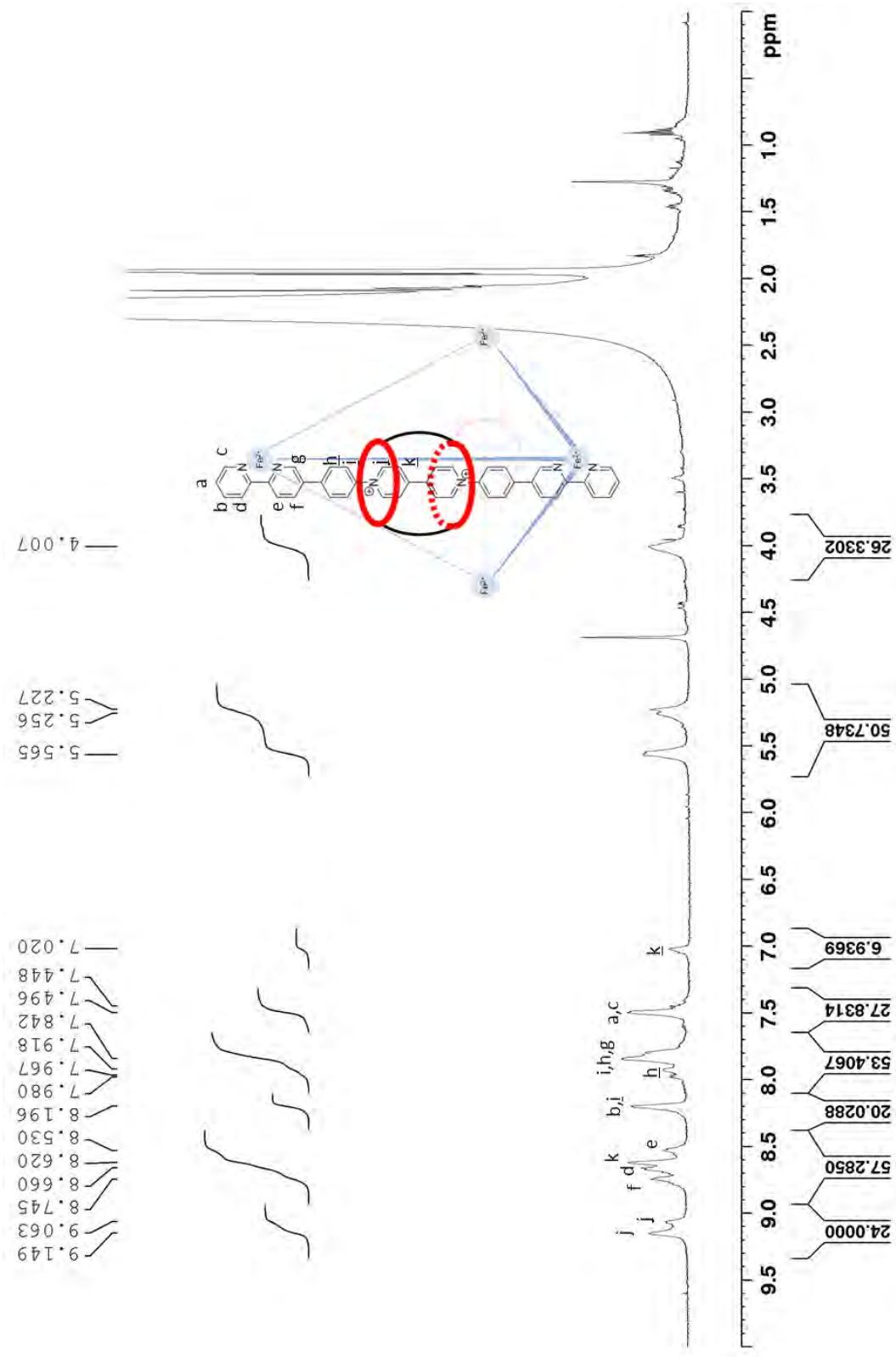

Figure IV-S61. ^{1}H NMR (600 MHz, CD_3CN, RT) recorded for cage **IV-13**·20PF_6. Underline represents resonances complexed with CB[7].

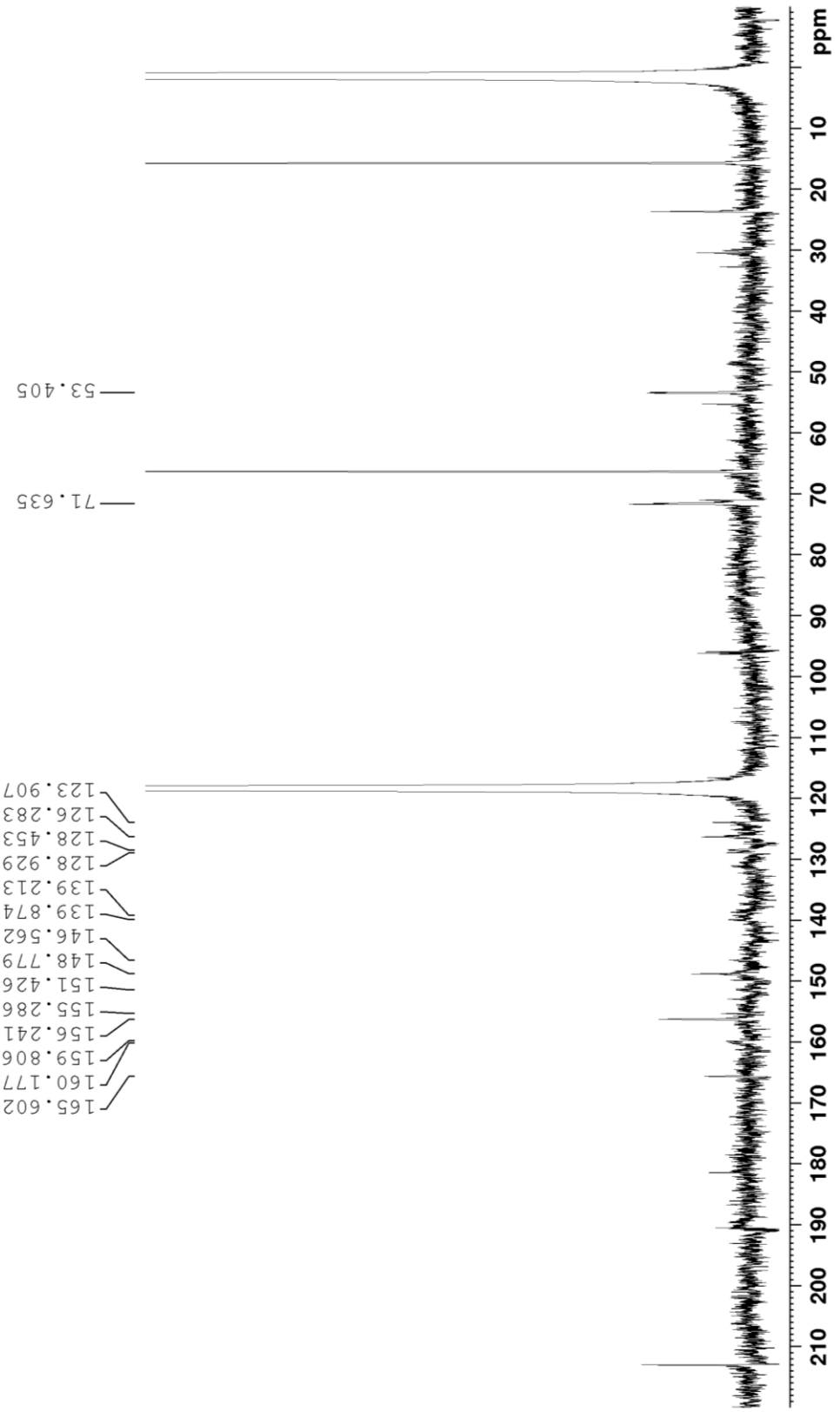

Figure IV-S62. ^{13}C NMR (200 MHz, CD_3CN, RT) recorded for cage **IV-13**·20PF_6.

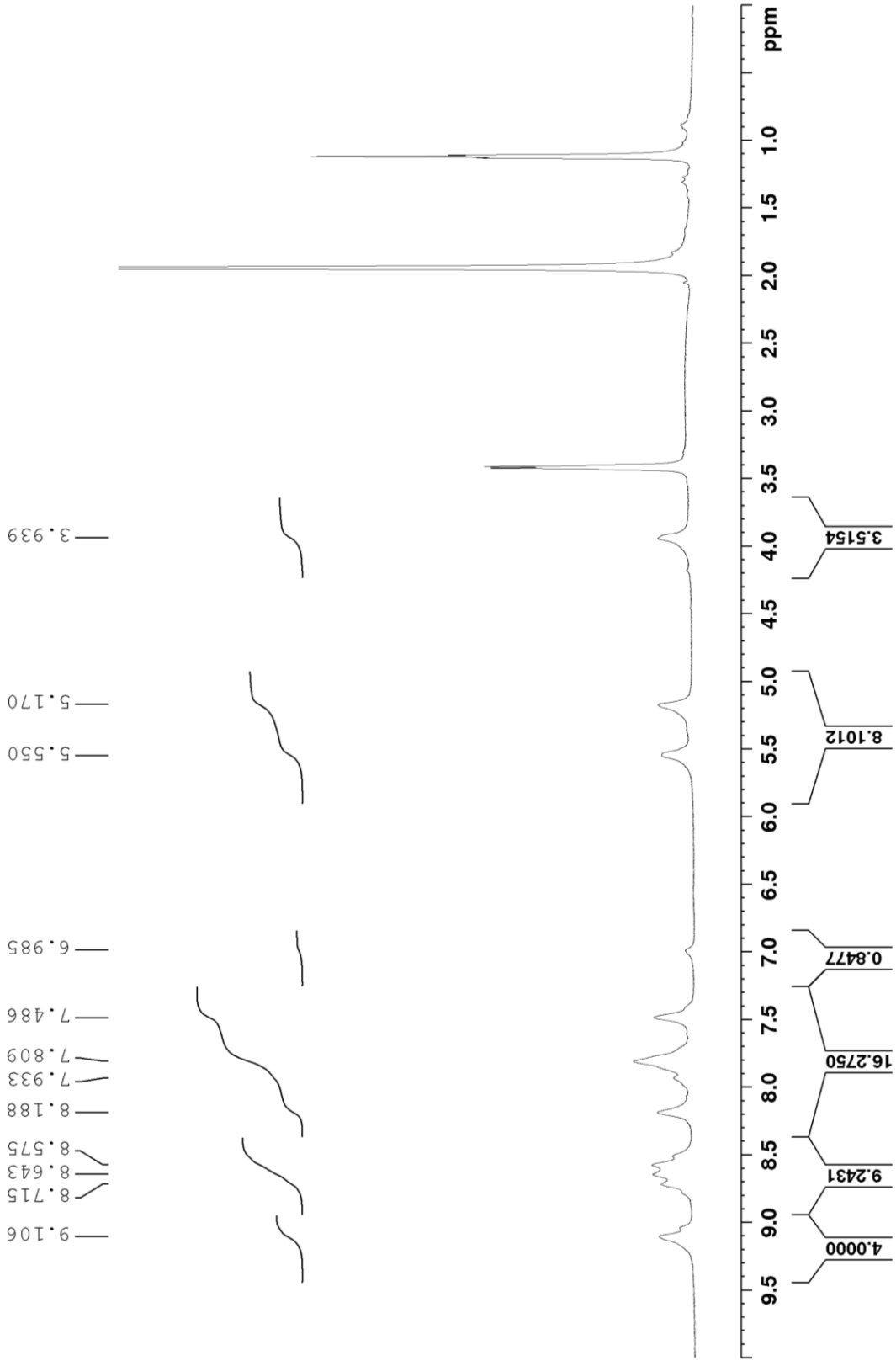

Figure IV-S63. ^{1}H NMR (400 MHz, CD_3CN, RT) recorded for cage **IV-13**·20NTf_2.

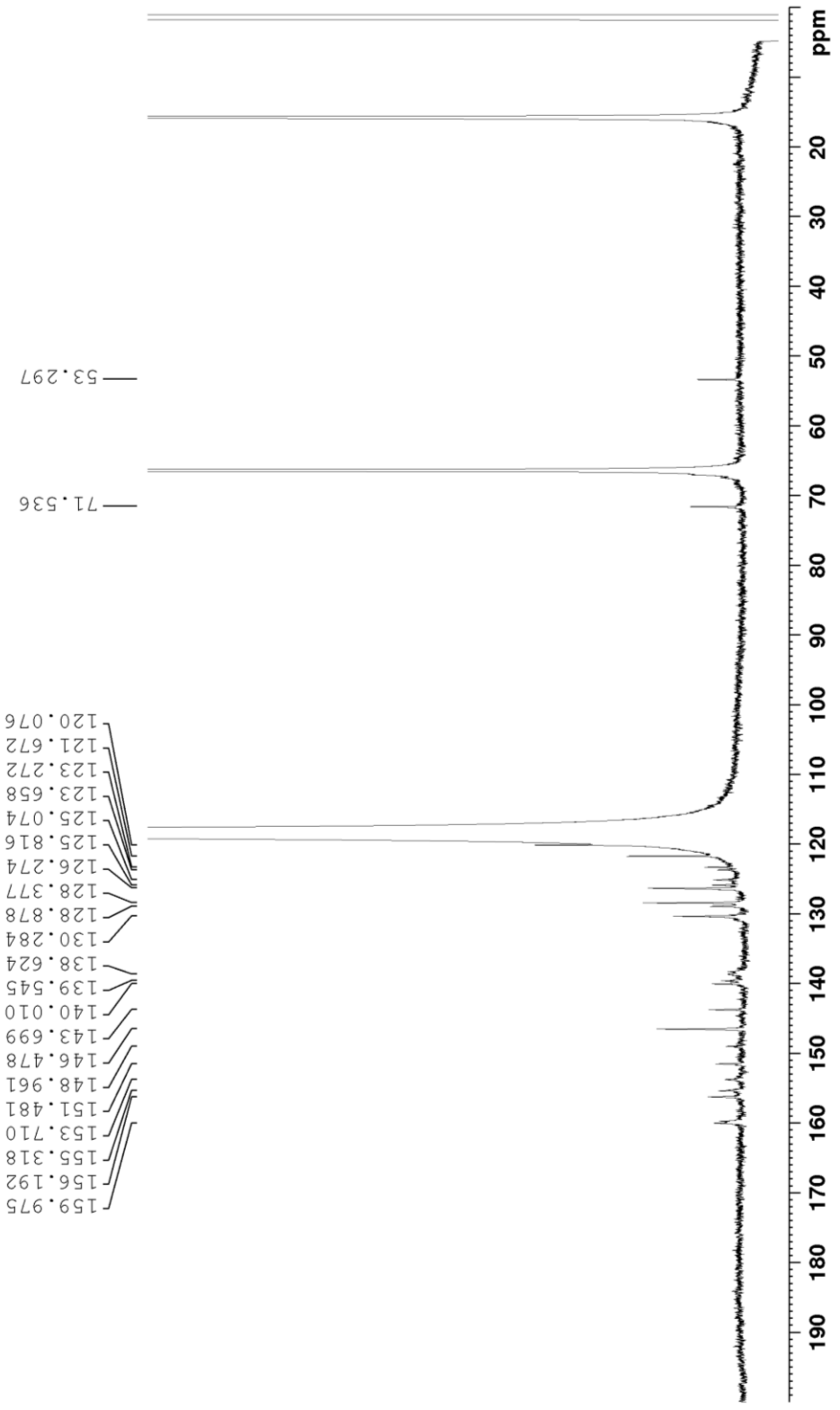

Figure IV-S64. ^{13}C NMR (200 MHz, CD_3CN, RT) recorded for cage **IV-13**·20NTf_2.

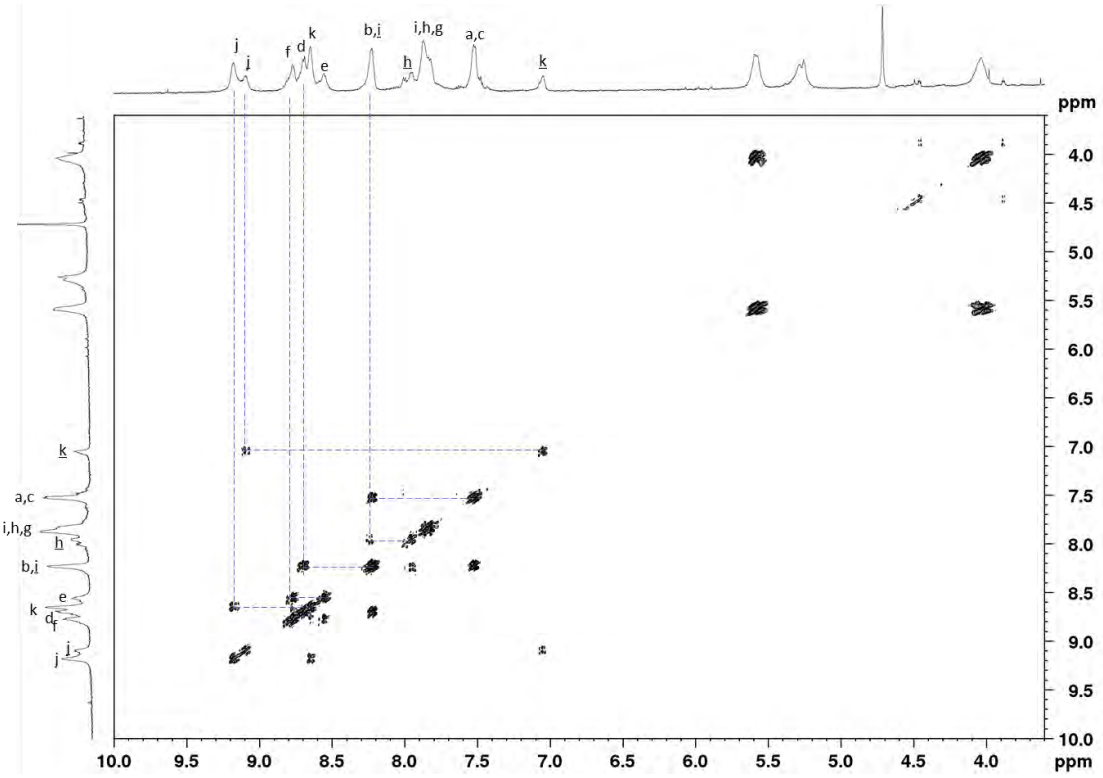

Figure IV-S65. COSY NMR (600 MHz, CD_3CN, RT) recorded for cage **IV-13**·$20PF_6$. Underline represents resonances complexed with CB[7].

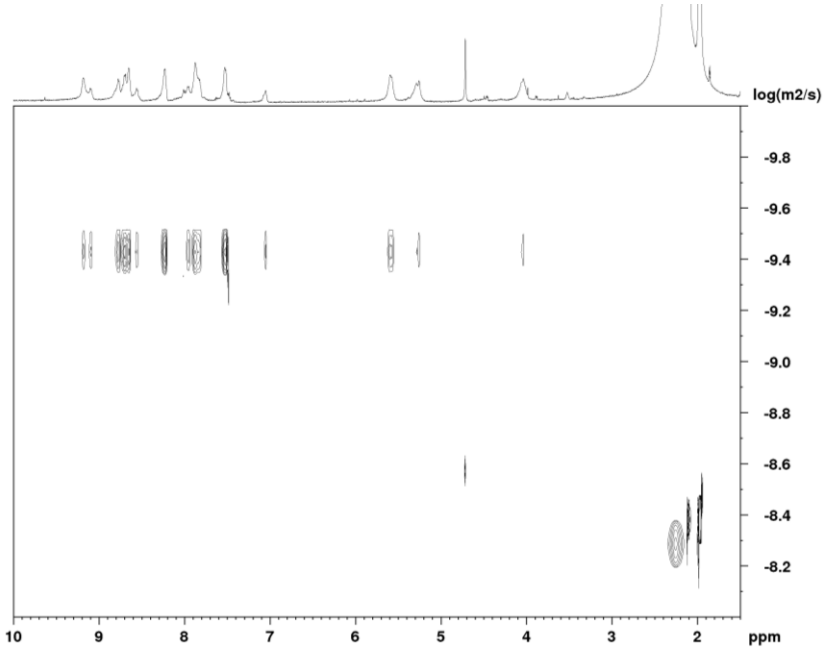

Figure IV-S66. DOSY NMR (600 MHz, CD_3CN, RT) recorded for cage **IV-13**·$20PF_6$. (D = 3.06 x 10^{-10} m^2/s).

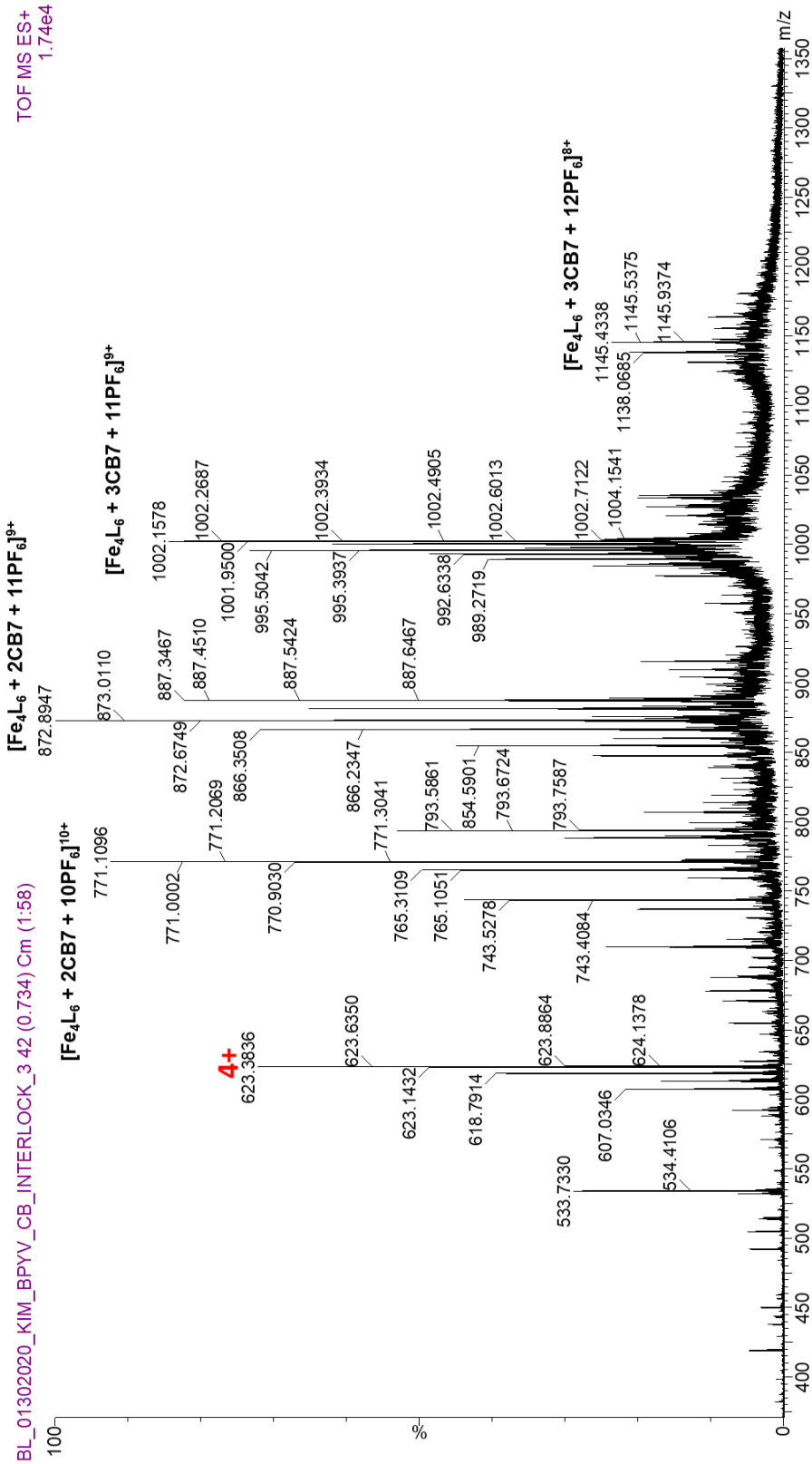

Figure IV-S67. ESI-TOF mass spectra (positive mode) of cage **IV-13**·20PF_6, where L = **IV-11**.

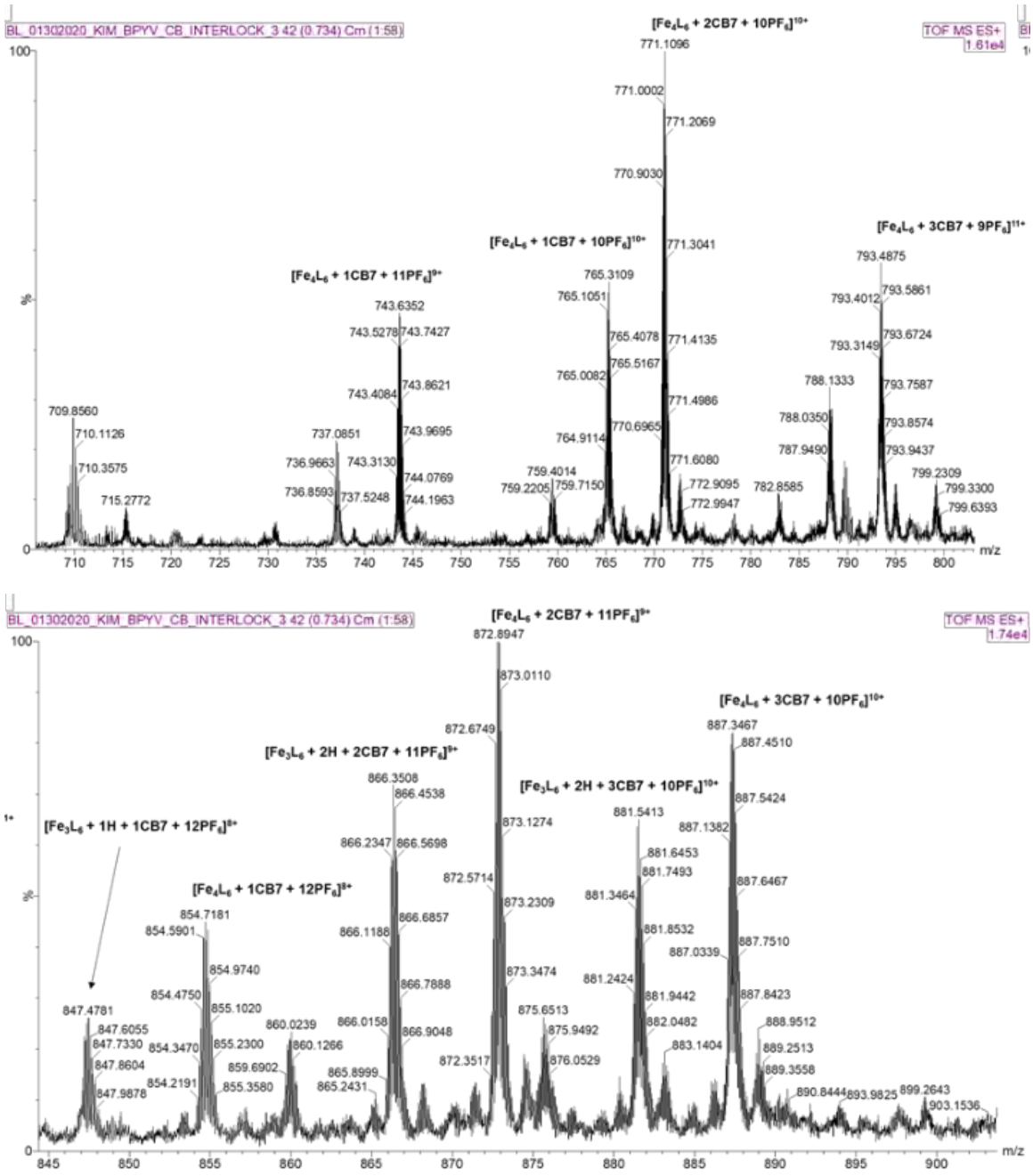

Figure IV-S68. Zoomed in ESI-TOF mass spectra of cage **IV-13**·20PF_6, where L = **IV-11**. *Top*: m/z = 700 – 810; *Bottom*: m/z = 845 – 905.

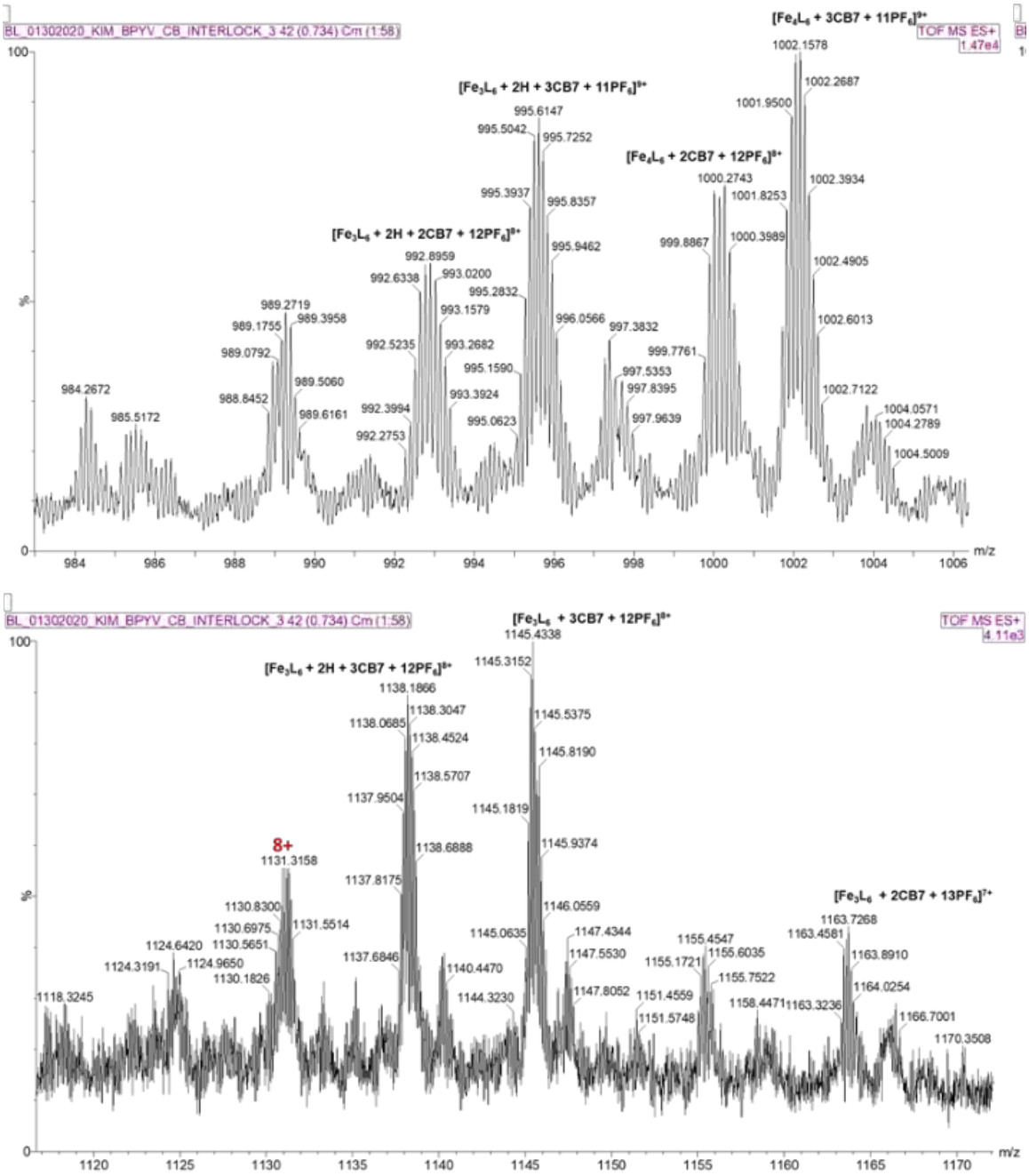

Figure IV-S69. Zoomed in ESI-TOF mass spectra of cage **IV-13**·20PF_6, where L = **IV-11**. *Top*: m/z = 982 – 1006; *Bottom*: m/z = 1115 – 1172.

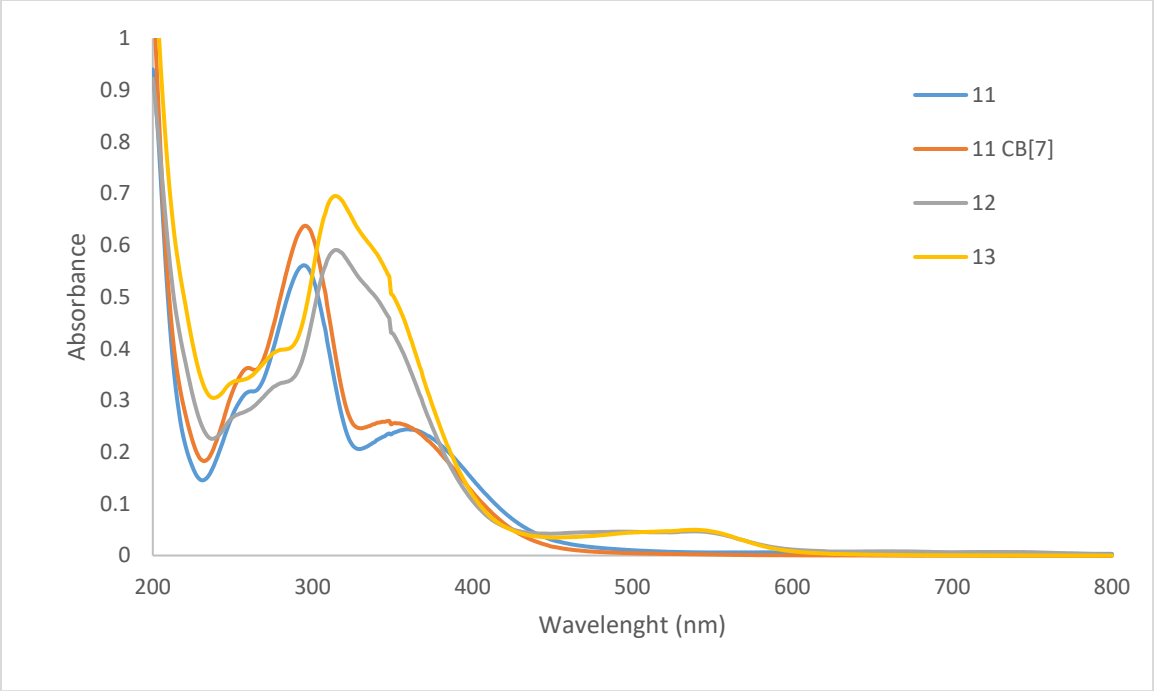

Figure IV-S70. UV VIS recorded for **IV-11**, **IV-11**·CB[7], Self-assembly **IV-12**, and Self-assembly **IV-13** in CH_3CN at room temperature.

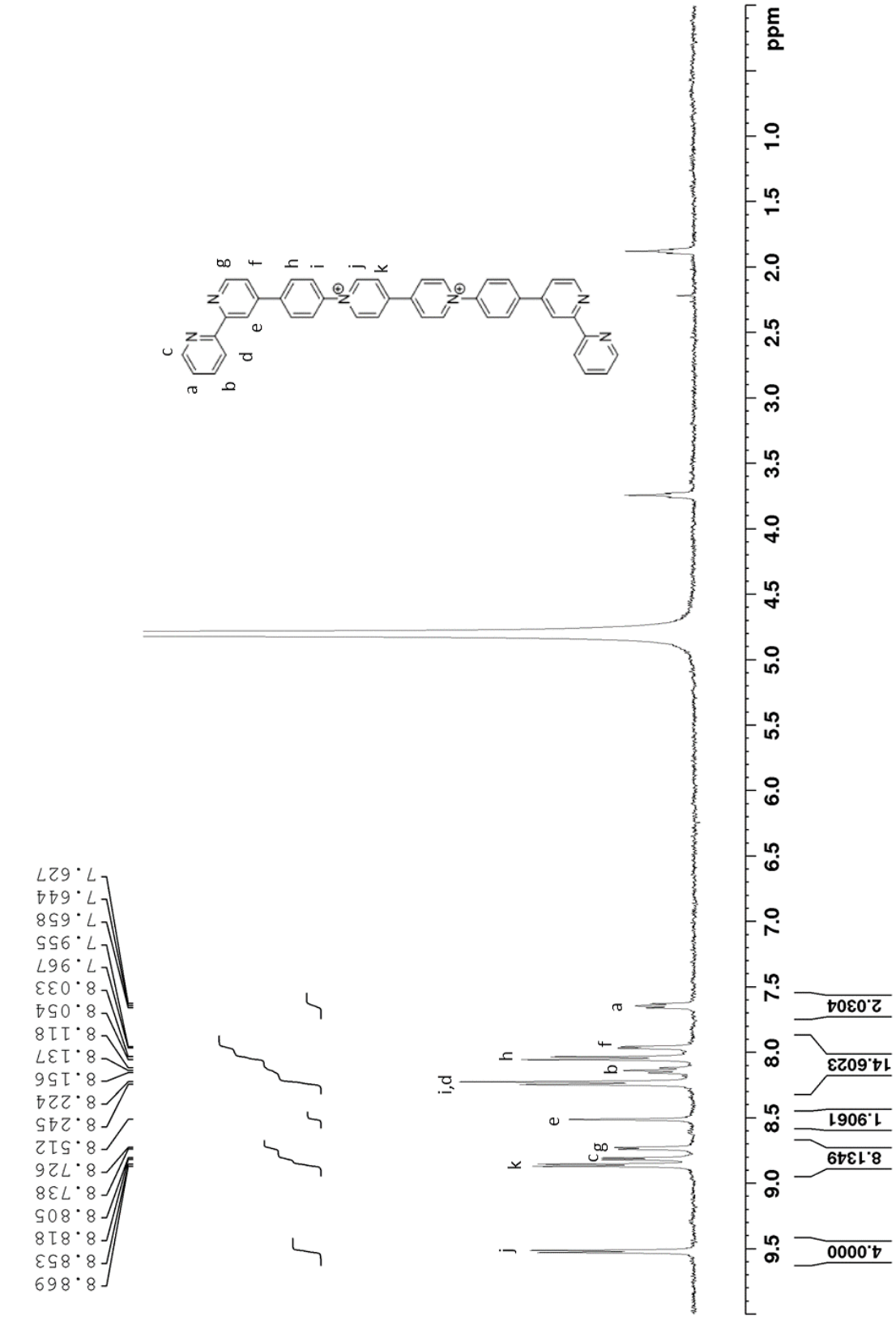

Figure IV-S71. ^{1}H NMR (400 MHz, D_2O, RT) recorded for **IV-16**·2Cl.

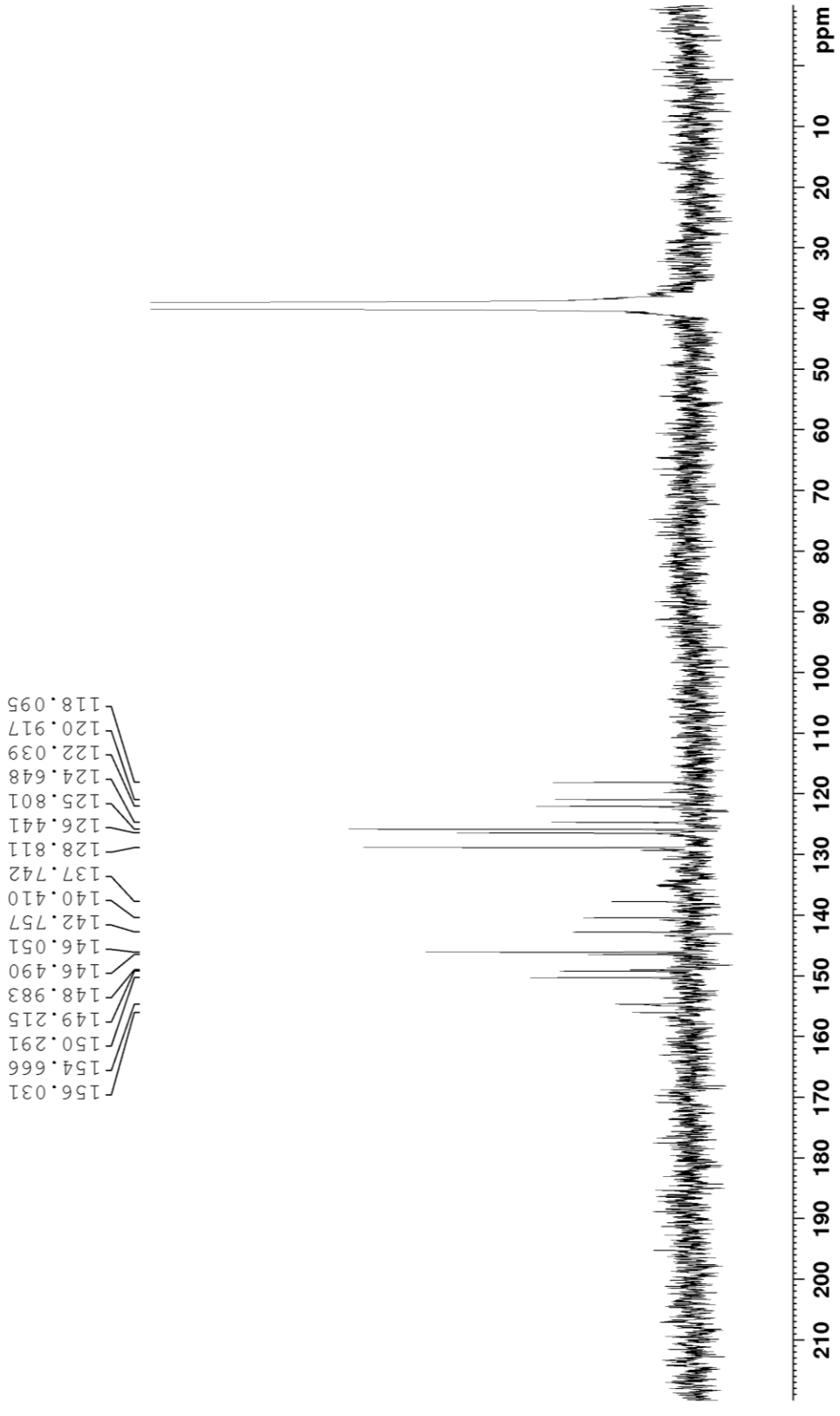

Figure IV-S72. ^{13}C NMR (126 MHz, DMSO-d_6, RT) recorded for **IV-16**·2Cl.

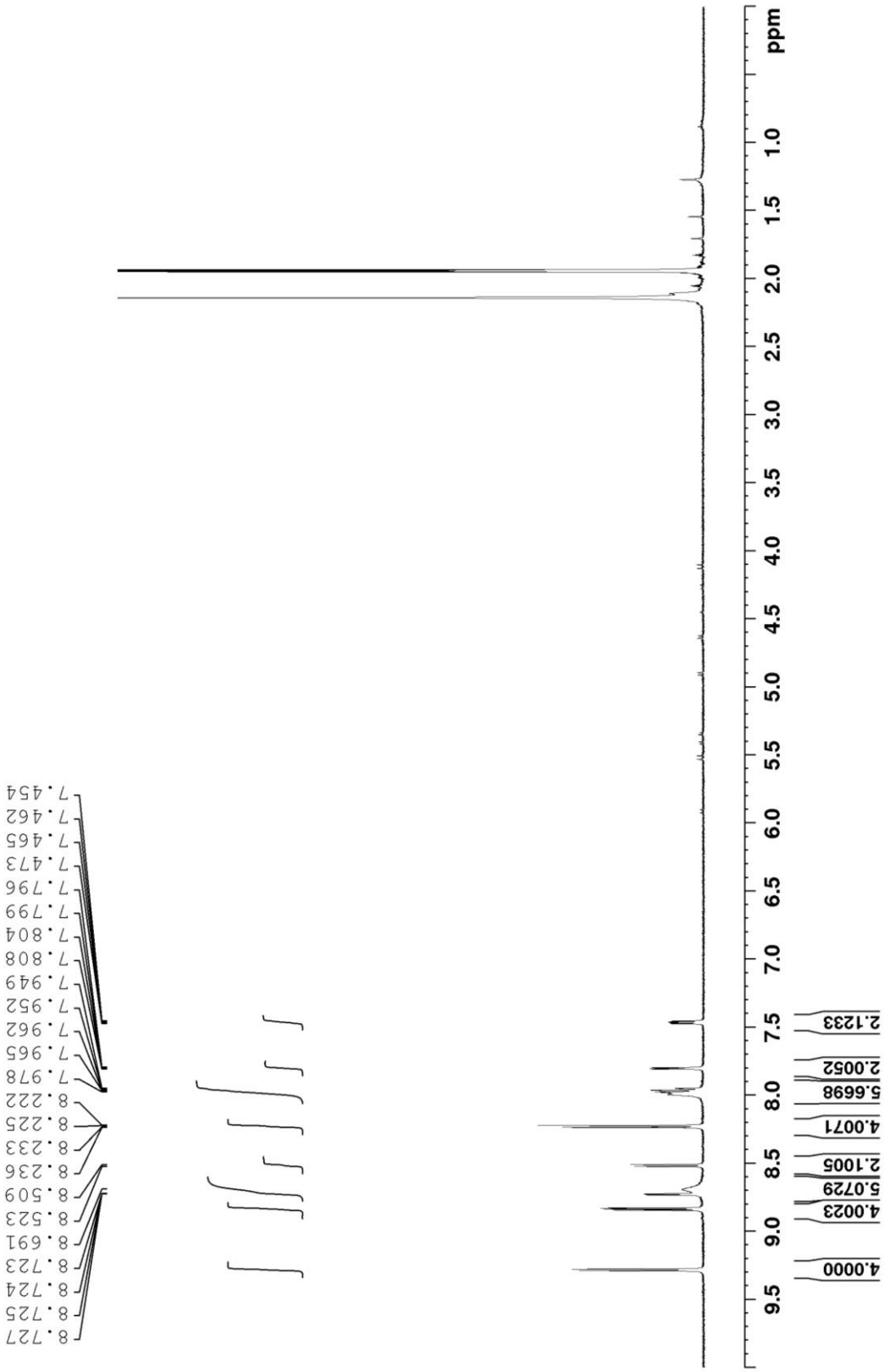

***Figure* IV-S73.** ^{1}H NMR (600 MHz, CD_3CN, RT) recorded for **IV-16**·$2PF_6$.

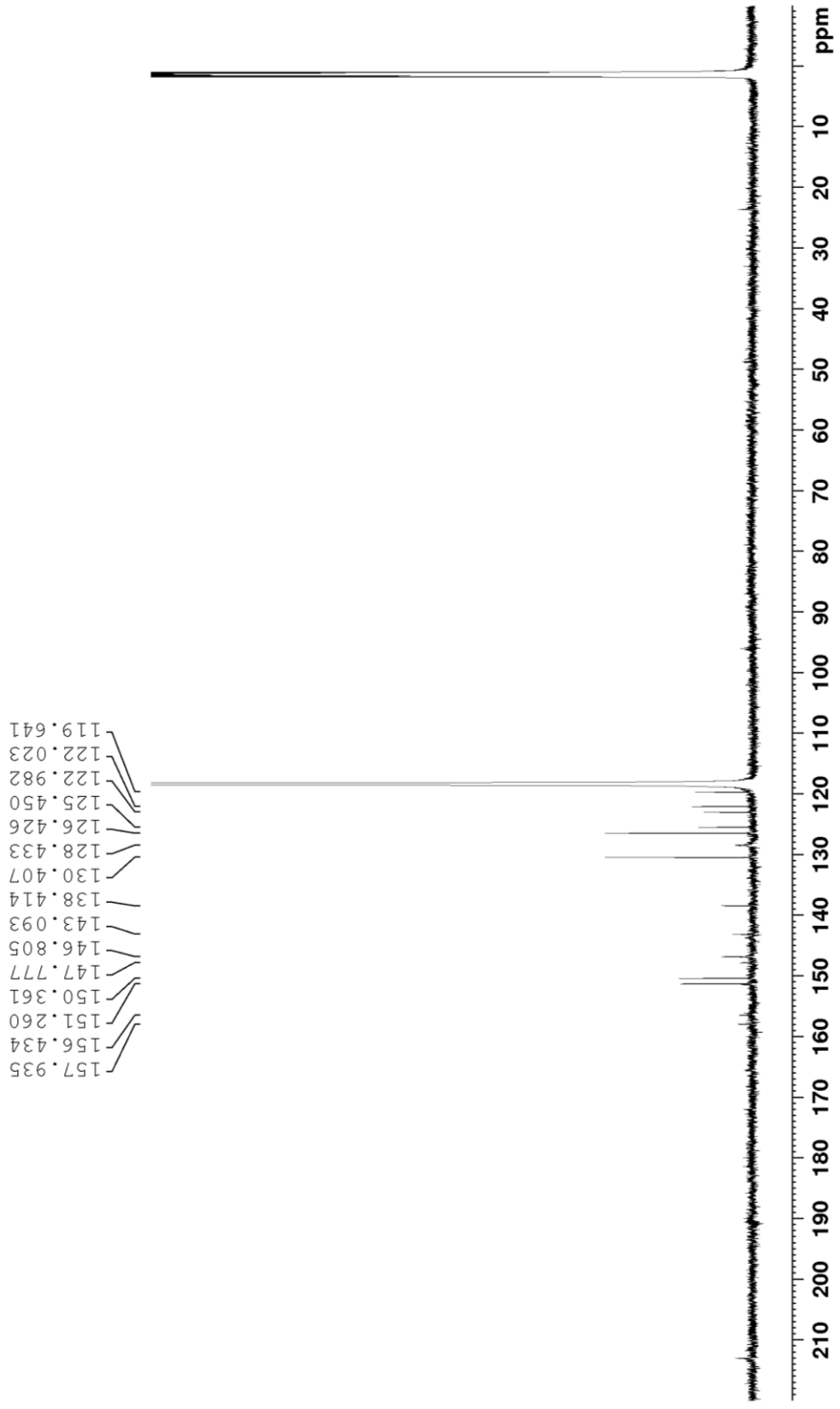

Figure IV-S74. ^{13}C NMR (126 MHz, CD_3CN, RT) recorded for **IV-16**·$2PF_6$.

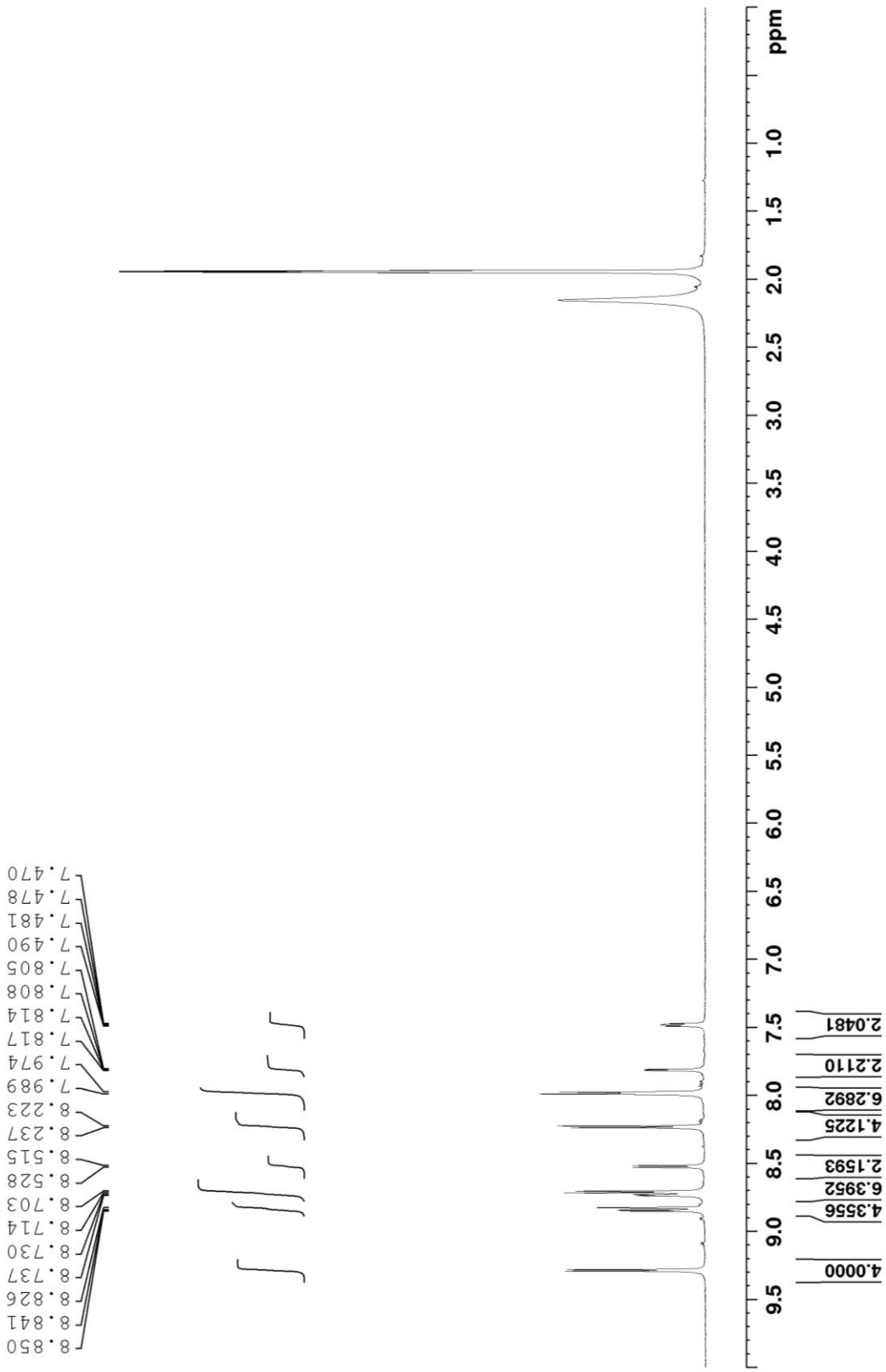

Figure IV-S75. ^{1}H NMR (600 MHz, CD_3CN, RT) recorded for **IV-16**·2NTf_2.

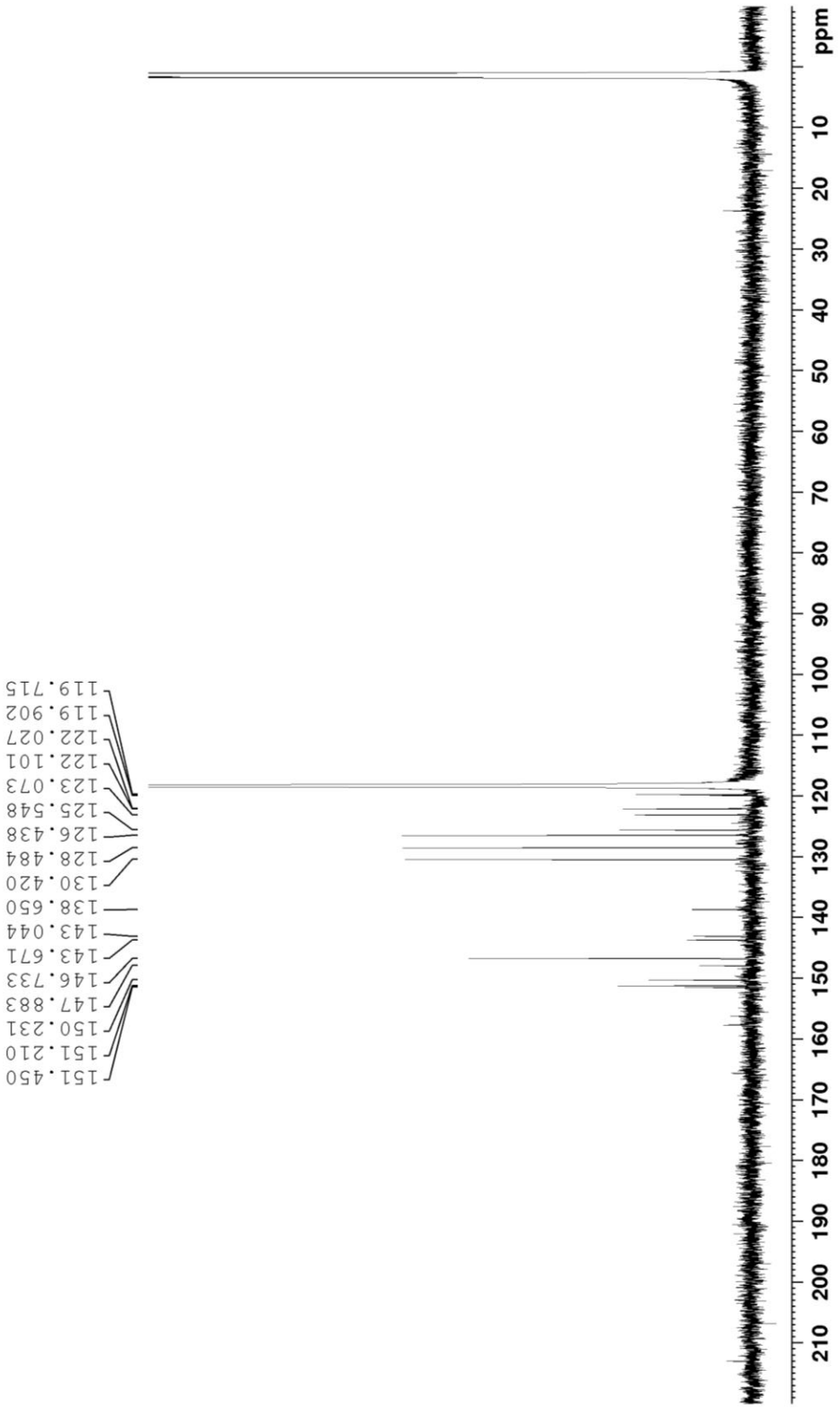

Figure IV-S76. ^{13}C NMR (126 MHz, CD_3CN, RT) recorded for **IV-16**·2NTf_2.

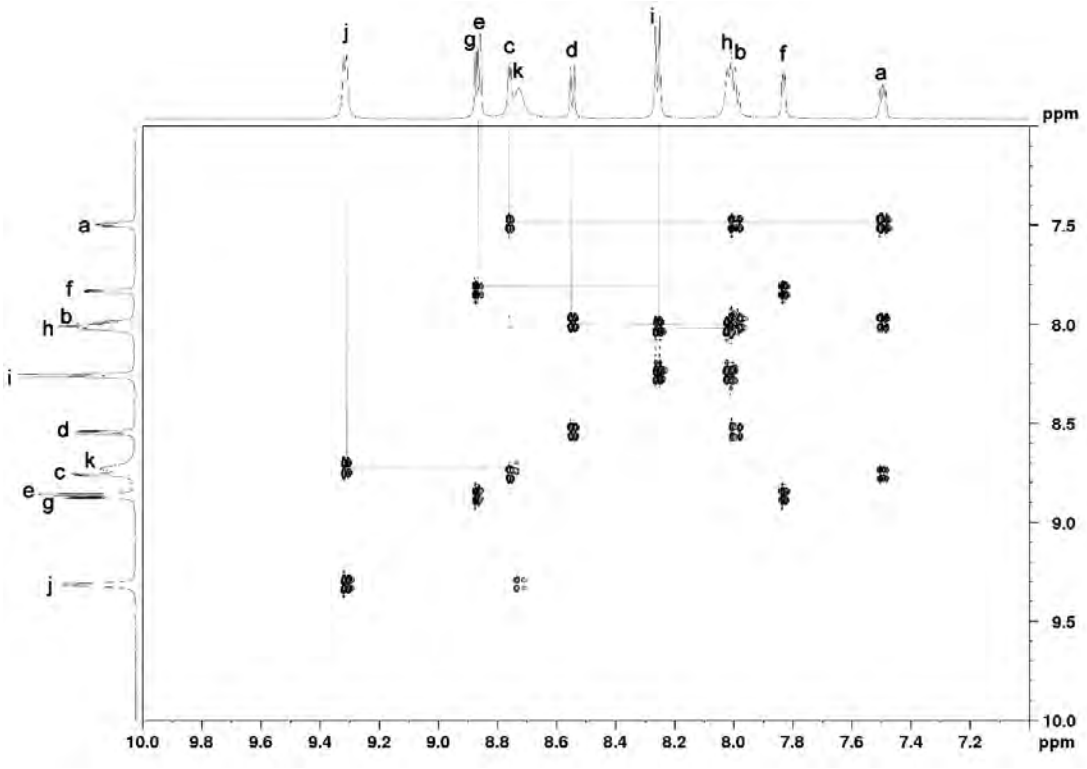

Figure IV-S77. COSY NMR (600 MHz, RT, 287 K) recorded for **IV-16**·2PF_6.

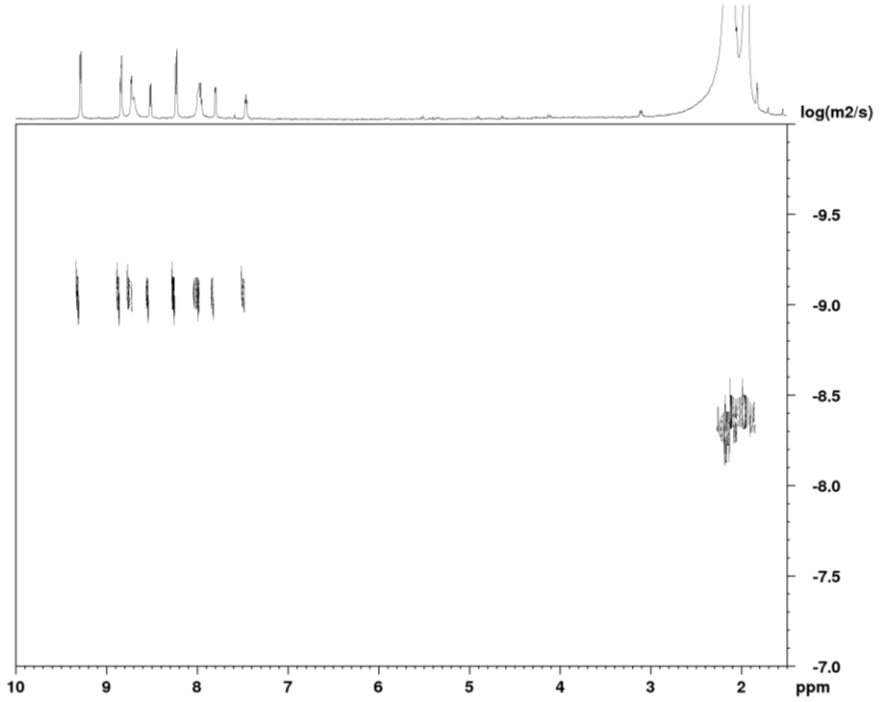

Figure IV-S78. DOSY NMR (600 MHz, CD_3CN, RT) recorded for **IV-16**·2PF_6 (D = 7.71 x 10^{-10} m^2/s).

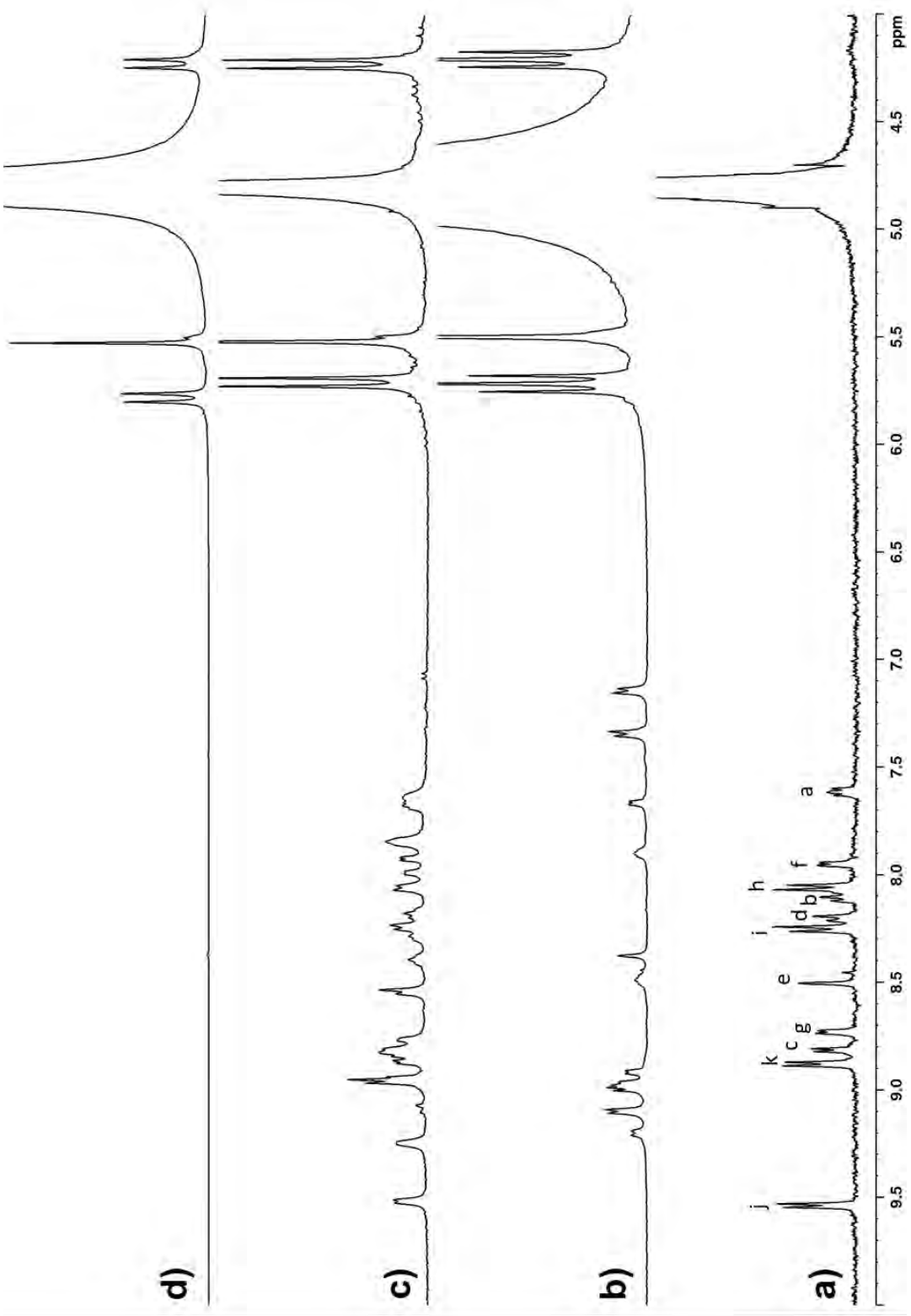

Figure IV-S79. ^{1}H NMR (400 MHz, D_2O, RT) titration of **IV-16**·2Cl with CB[7] (a) 0 equiv., (b) 0.7 equiv., (c) 2.3 equiv., (d) CB[7] alone.

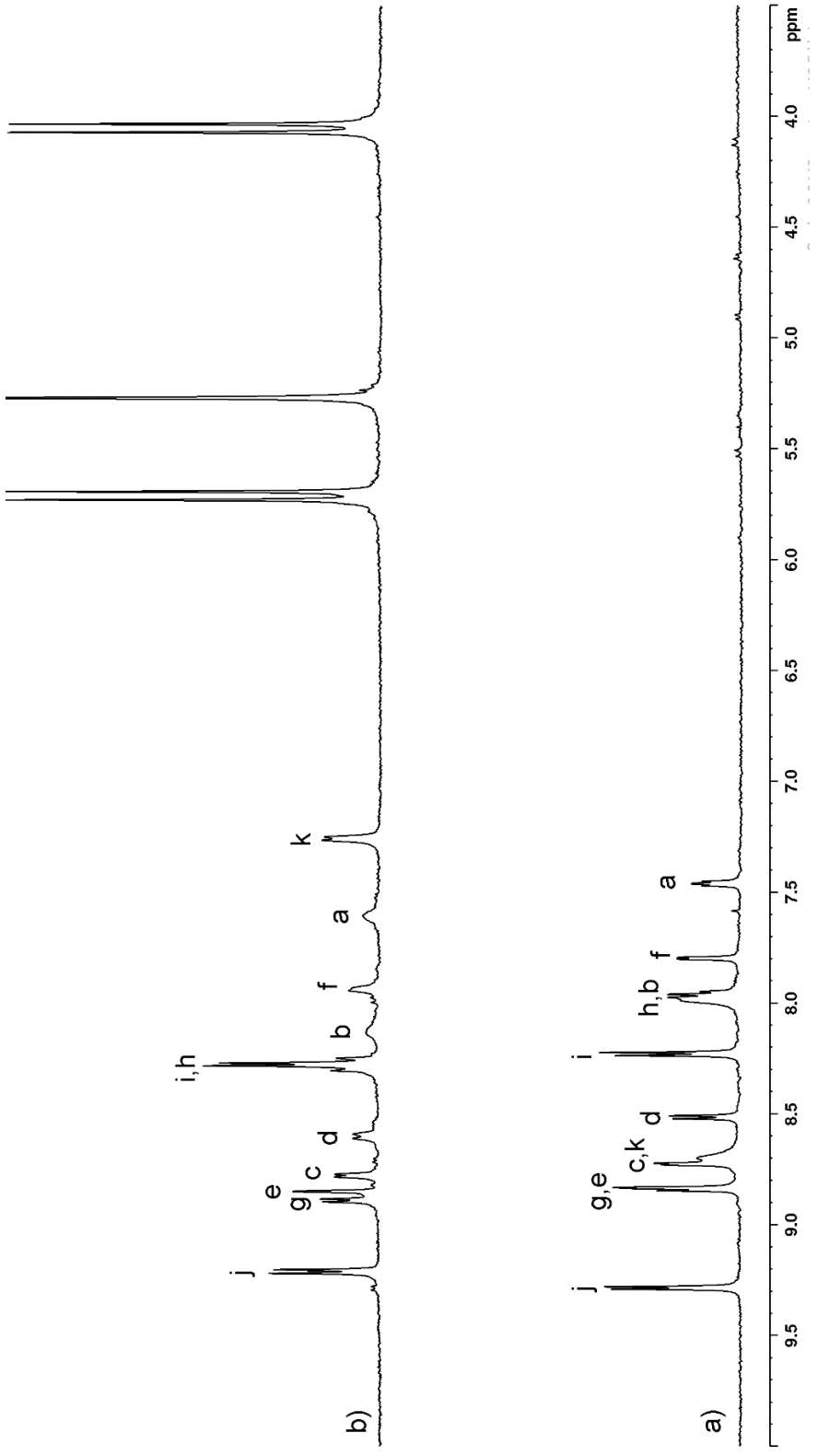

Figure IV-S80. ^{1}H NMR (600 MHz, CD_3CN, RT) recorded for **IV-16**·$2PF_6$ (a) alone, (b) with 1 equivalent of CB[7].

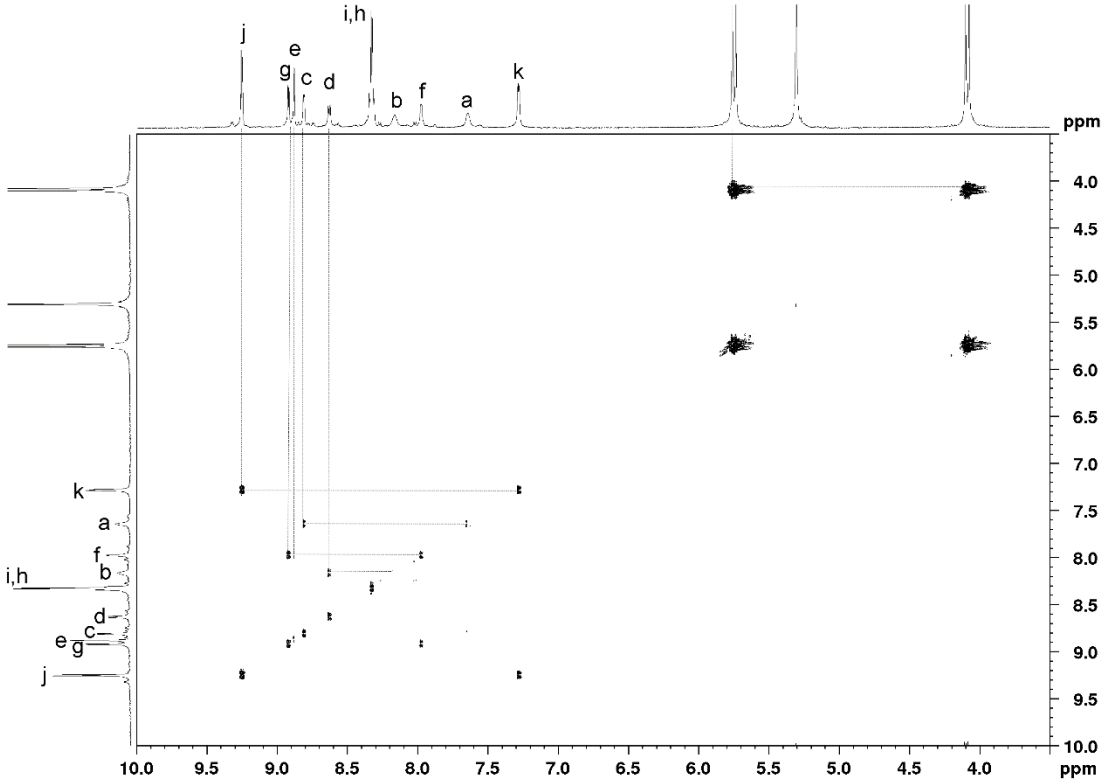

Figure IV-S81. COSY NMR (600 MHz, CD_3CN, 287 K) recorded for **IV-16**·CB[7].

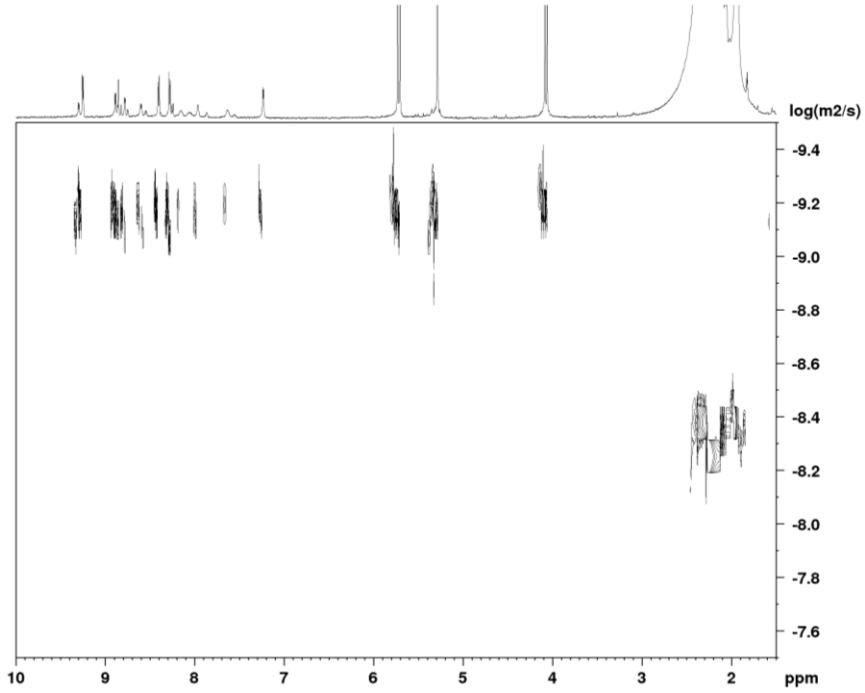

Figure IV-S82. DOSY NMR (600 MHz, CD_3CN, 287 K) recorded for **IV-16**·CB[7]·$2PF_6$ ($D = 5.66 \times 10^{-10}$ m^2/s).

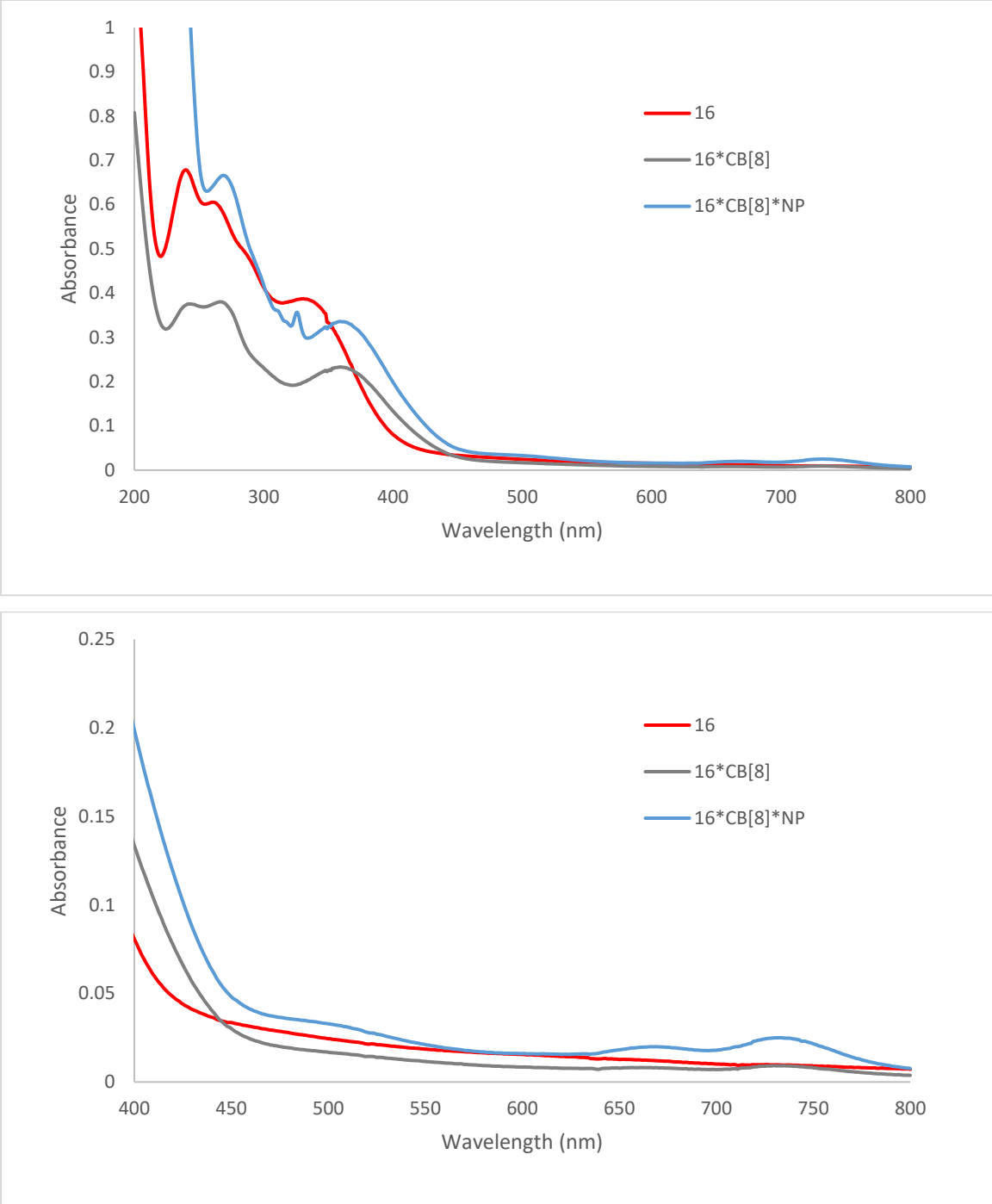

Figure IV-S83. UV/vis spectra recorded illustrating charge transfer complex formed when a 1:1:1 CB[8]:**IV-16**·2Cl:NP heteroternary complex occurs in water. *Top: full spectra; Bottom: zoomed in region from 400 nm – 800 nm.*

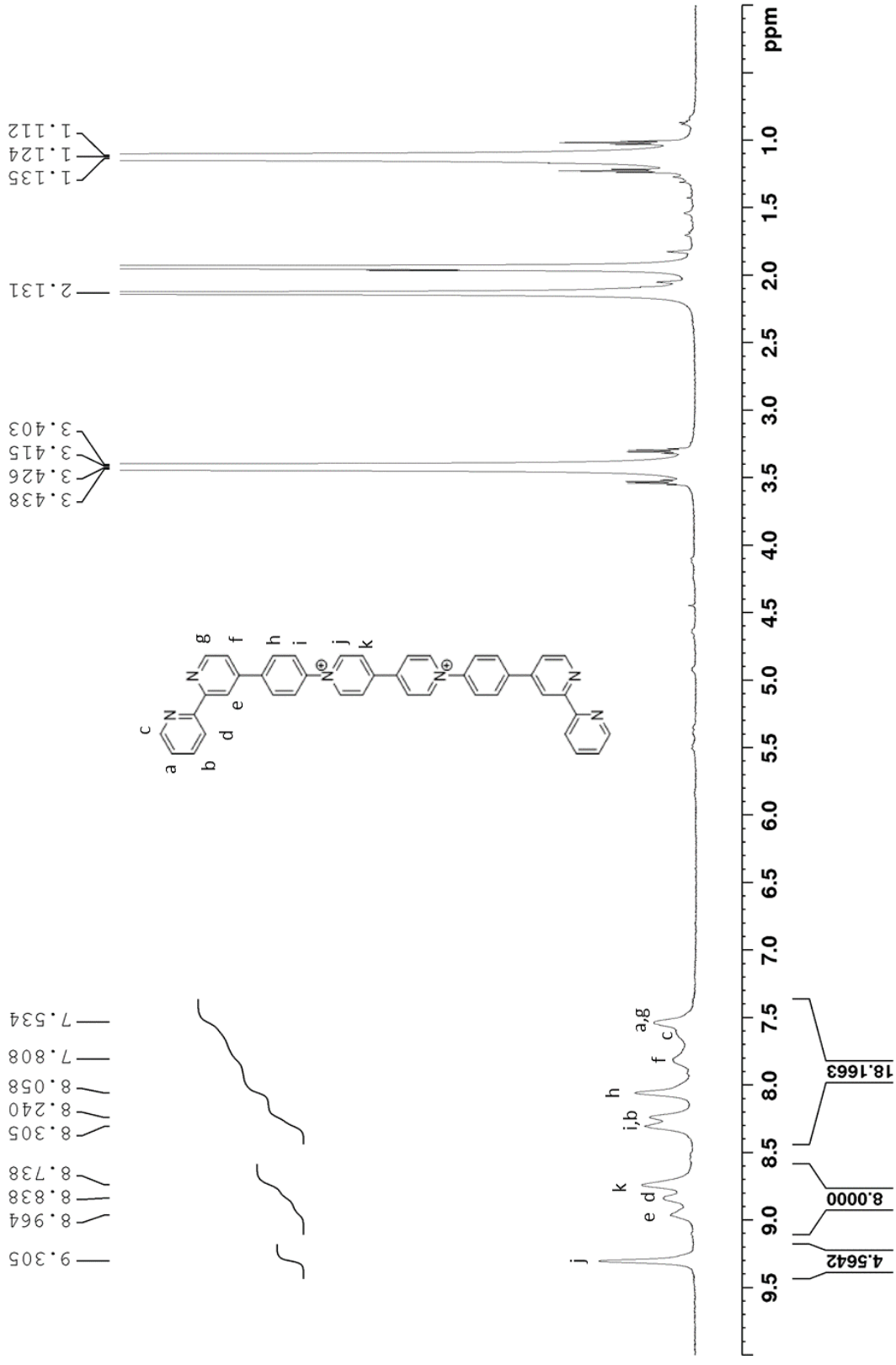

Figure IV-S84. ^{1}H NMR (600 MHz, CD_3CN, RT) recorded for cage **IV-17**·40PF_6.

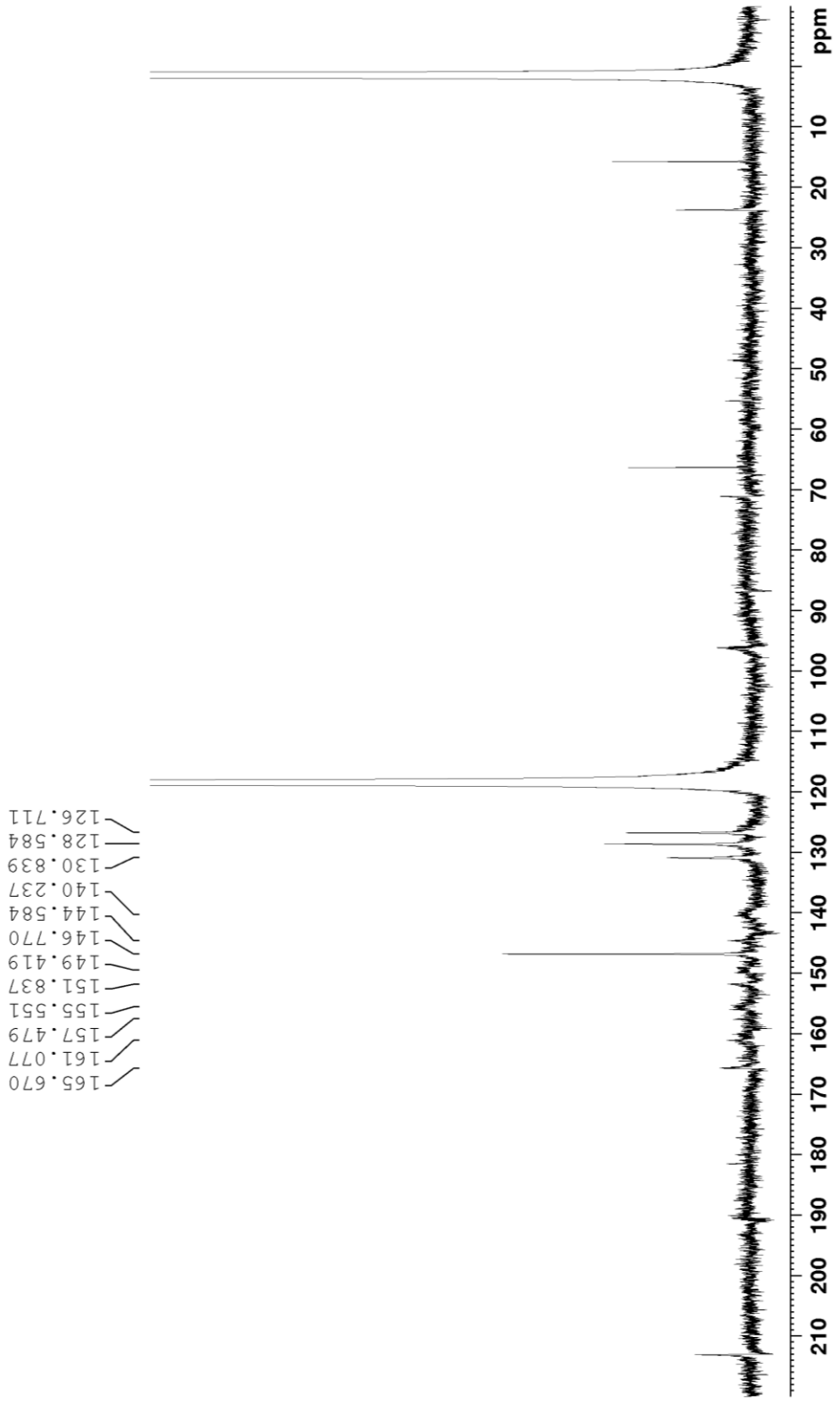

Figure IV-S85. ^{13}C NMR (126 MHz, CD_3CN, RT) recorded for cage **IV-17**·$40PF_6$.

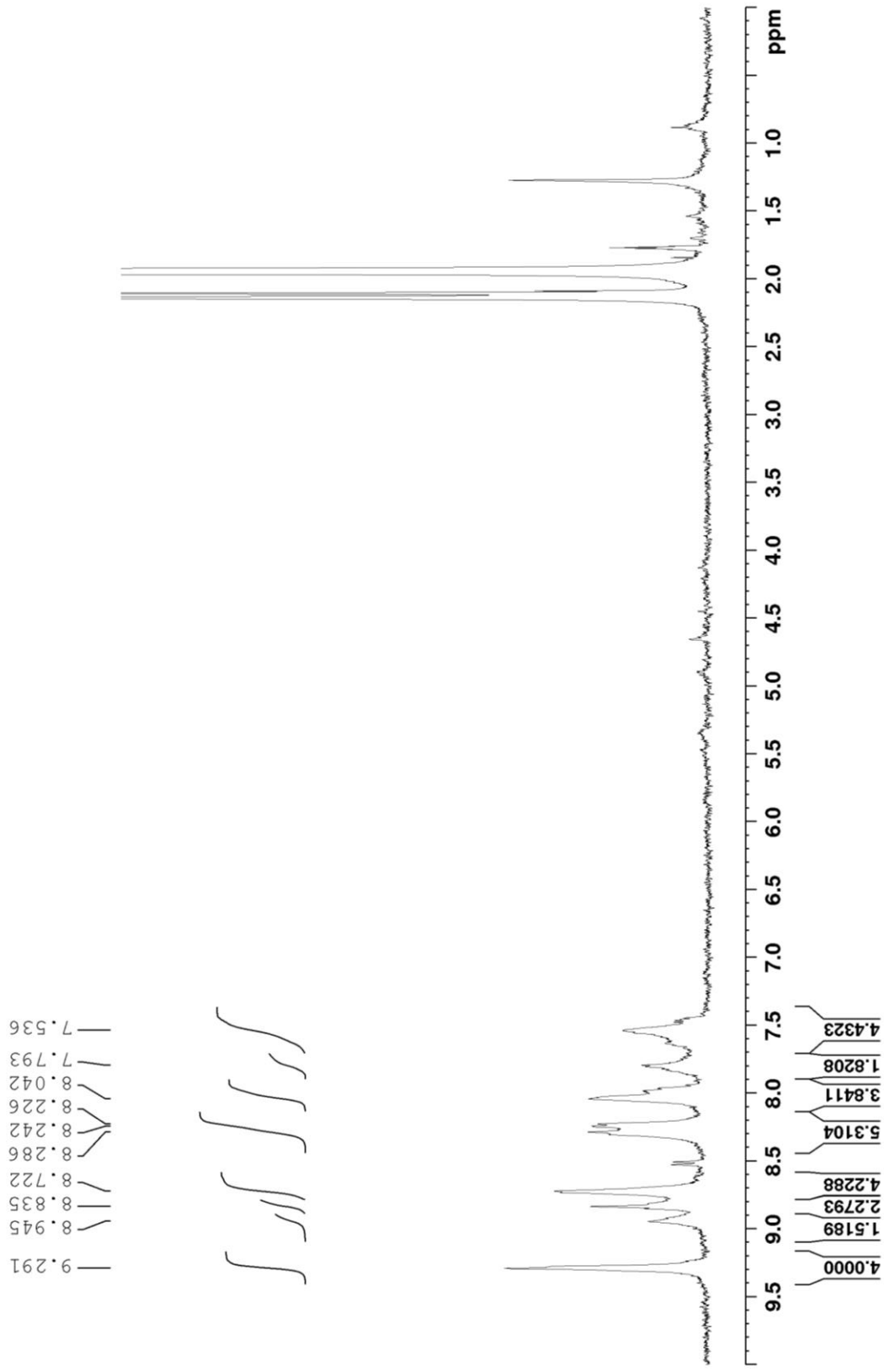

Figure IV-S86. ^{1}H NMR (600 MHz, CD_3CN, RT) recorded for cage **IV-17**·40NTf_2.

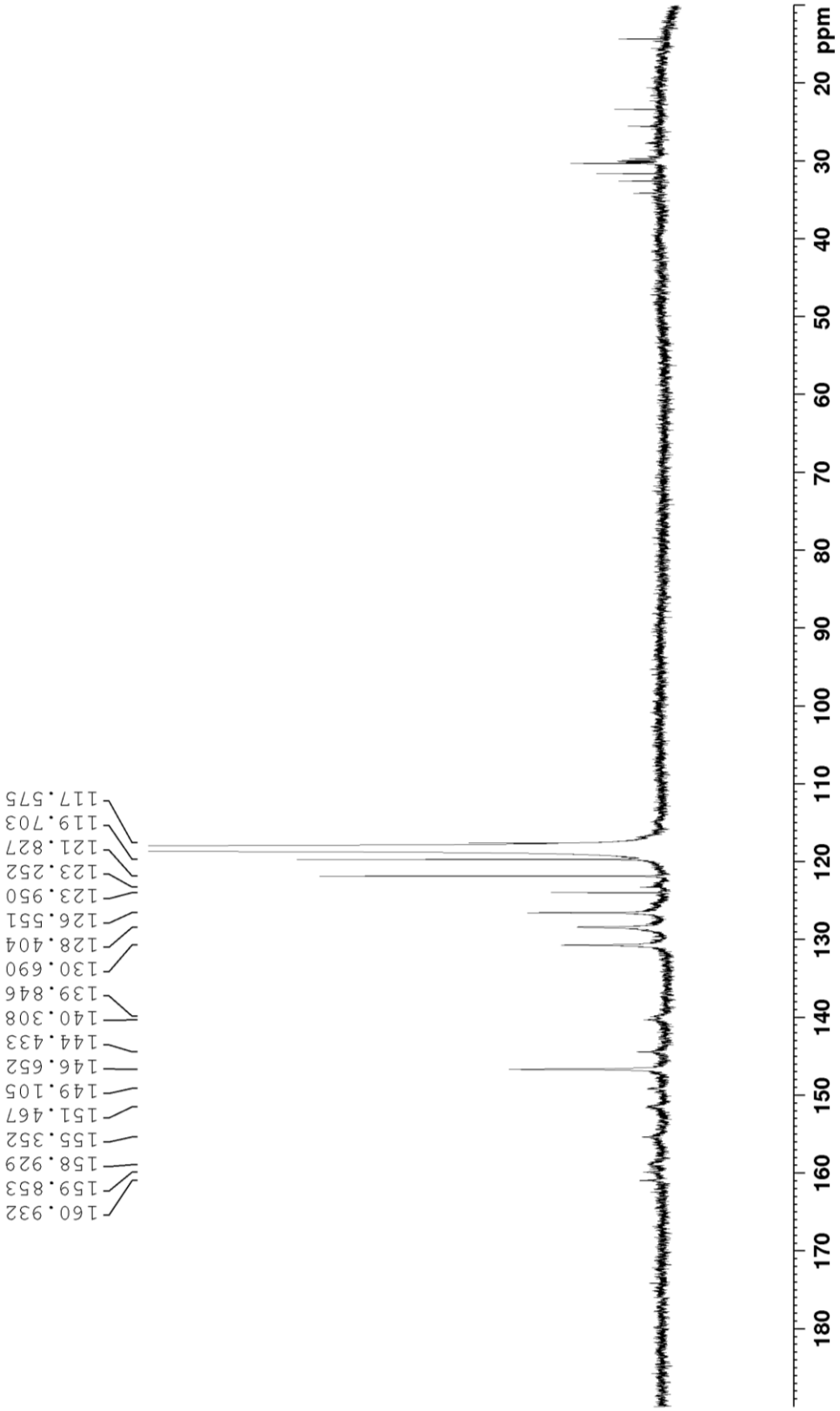

Figure IV-S87. ^{13}H NMR (600 MHz, CD_3CN, RT) recorded for cage **IV-17**·40NTf_2.

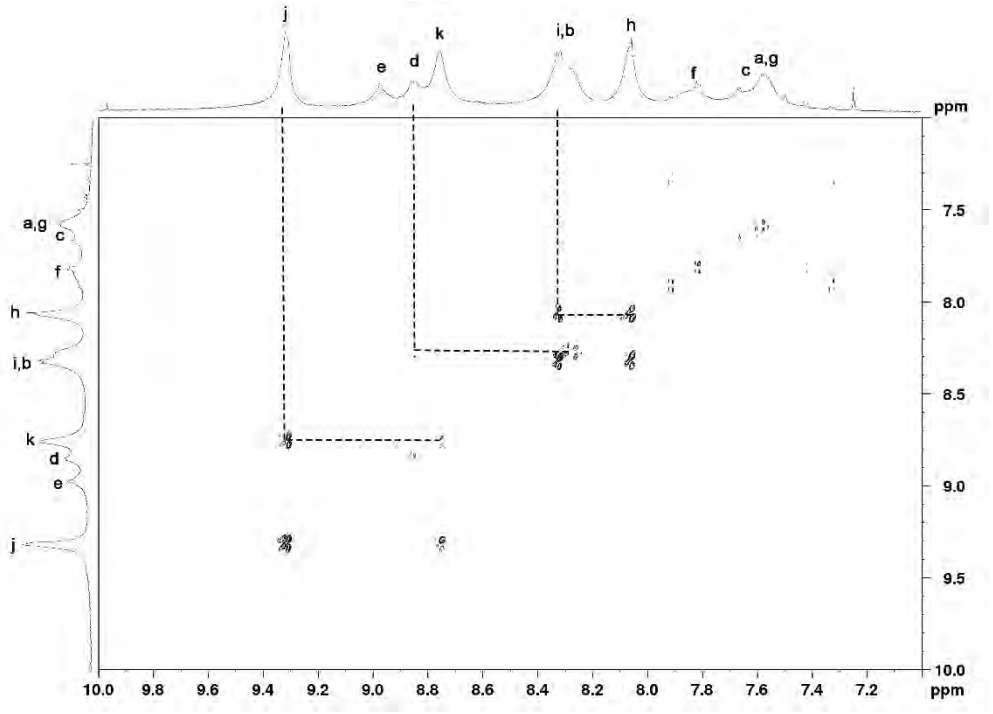

Figure IV-S88. COSY NMR (600 MHz, CD_3CN, RT) recorded for cage **IV-17**·$40PF_6$.

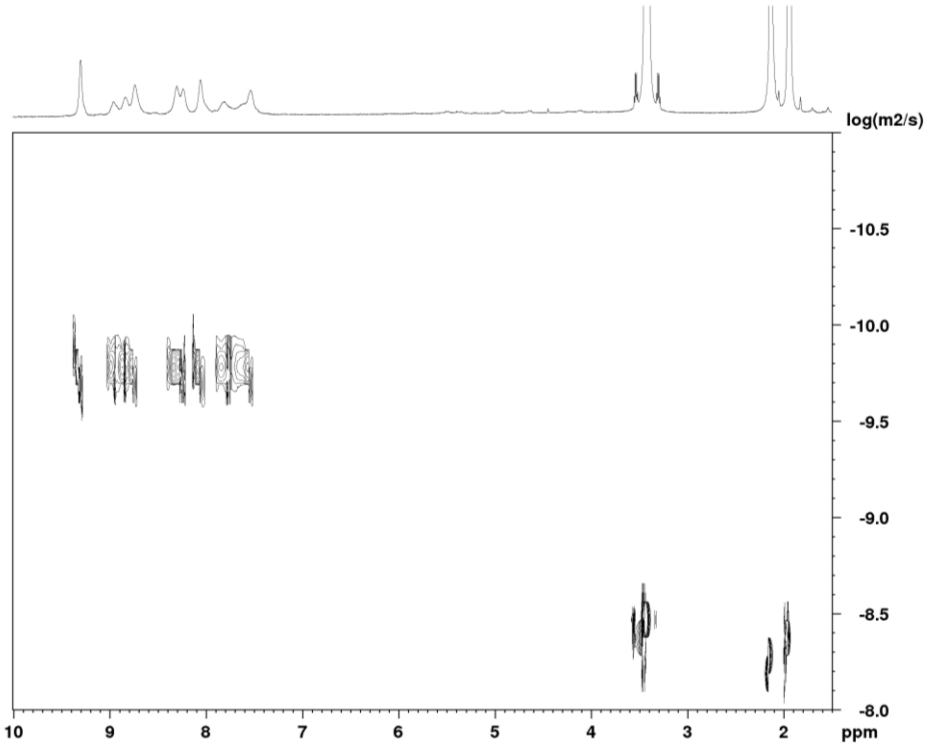

Figure IV-S89. DOSY NMR (600 MHz, CD_3CN, RT) recorded for cage **IV-17**·$40PF_6$ (D = 1.40 x 10^{-10} m^2/s).

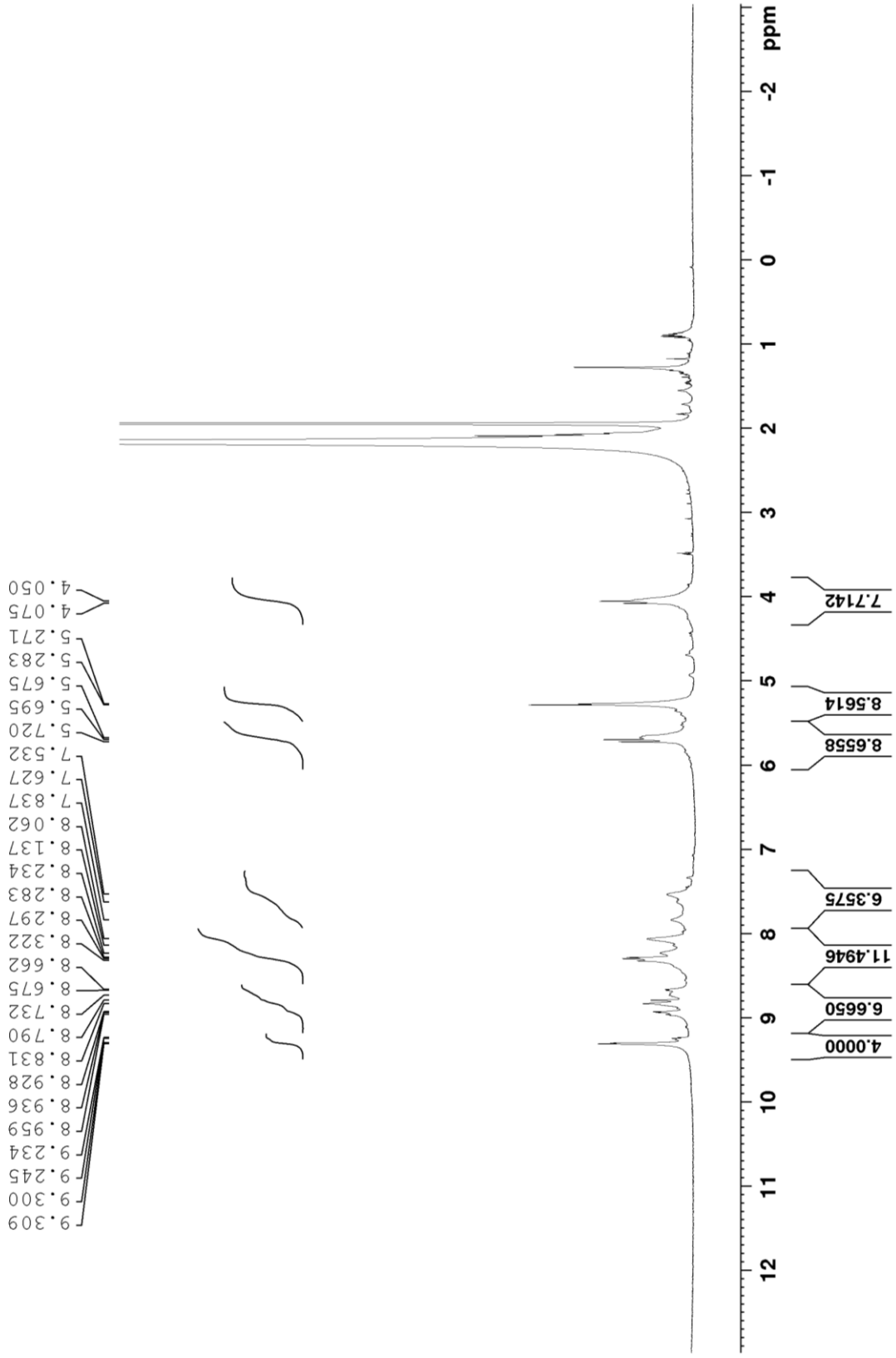

Figure IV-S90. ^{1}H NMR (400 MHz, CD_3CN, RT) recorded for cage **IV-18**·$40PF_6$.

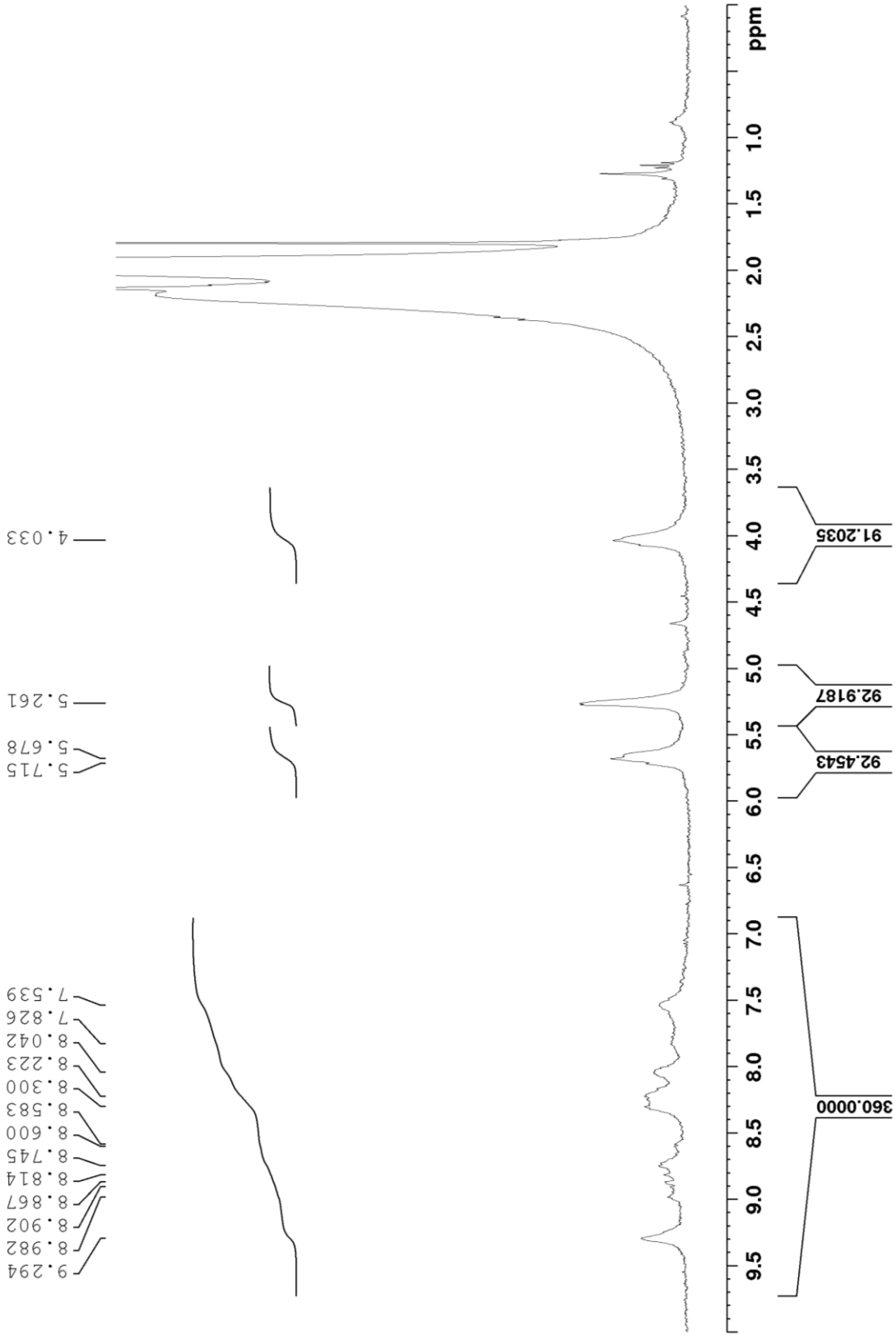

Figure IV-S91. ^{1}H NMR (400 MHz, CD_3CN, RT) recorded for cage **IV-18**·40NTf_2.

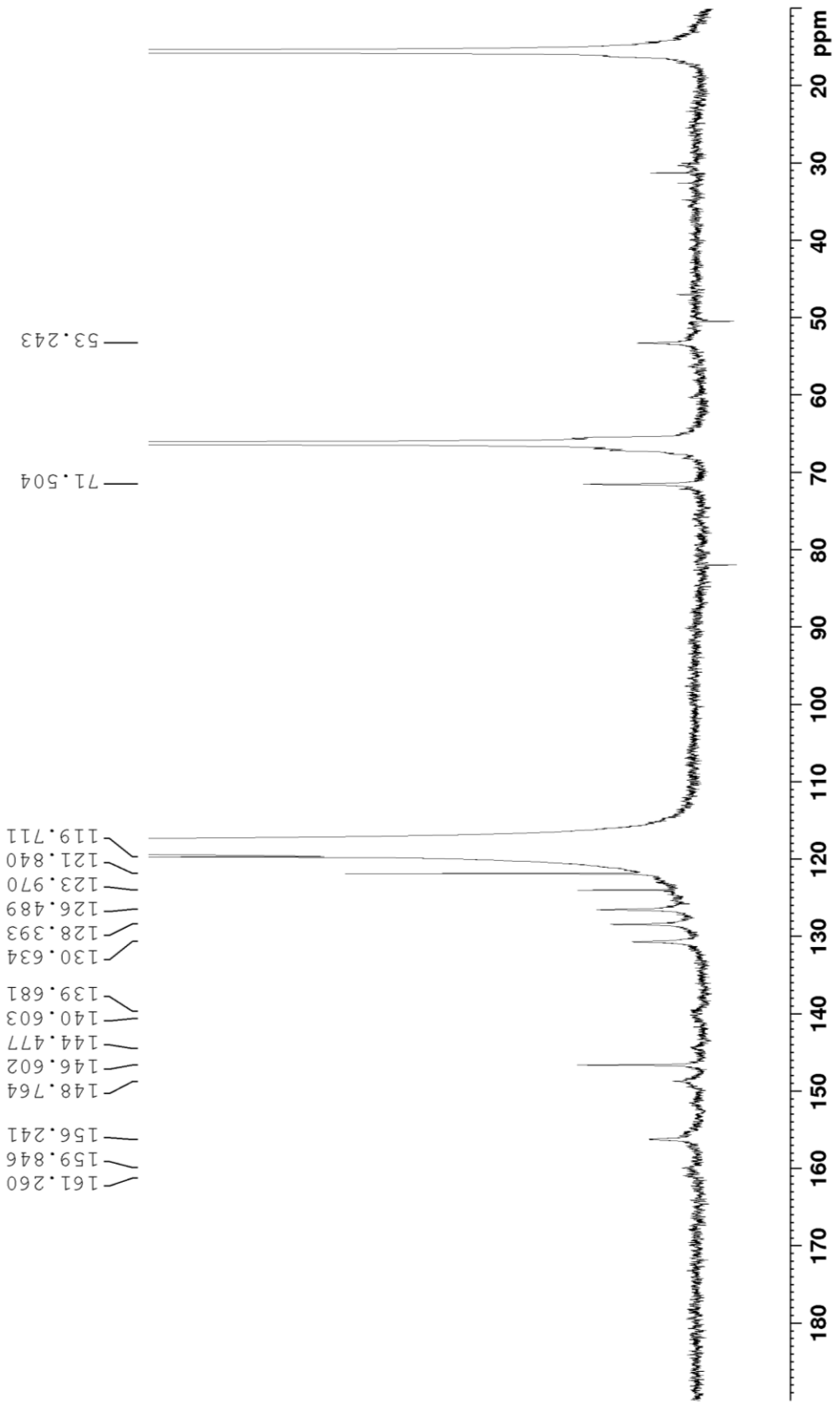

Figure IV-S92. ^{13}C NMR (200 MHz, CD_3CN, RT) recorded for cage **IV-18**·40NTf_2.

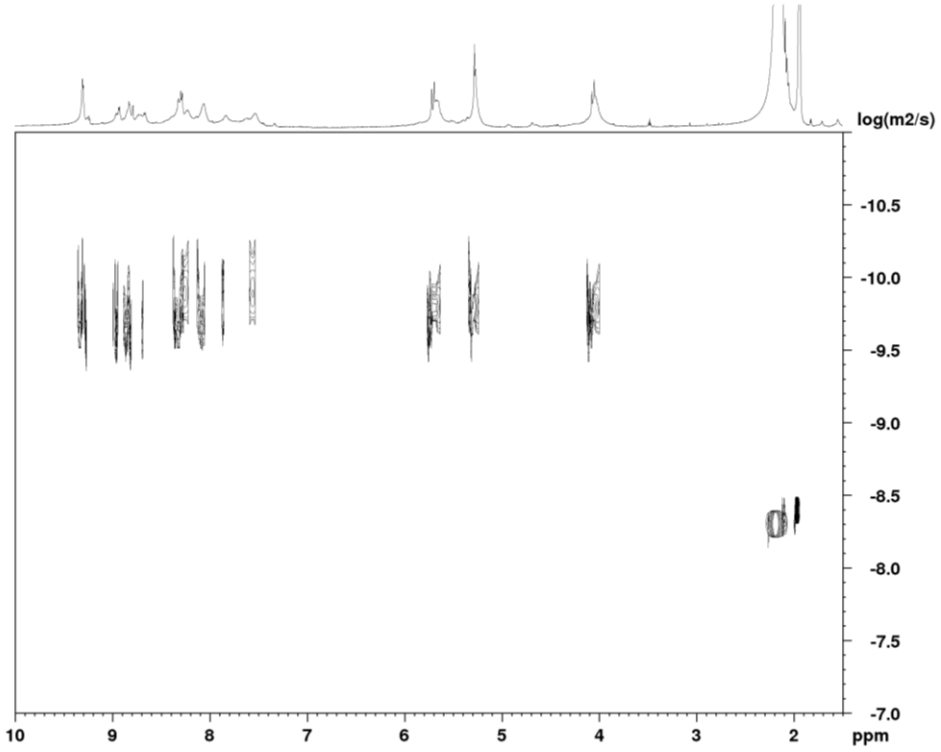

Figure IV-S93. DOSY NMR (600 MHz, CD_3CN, RT) recorded for cage **IV-18**·$40PF_6$ (D = 1.25 x 10^{-10} m^2/s).

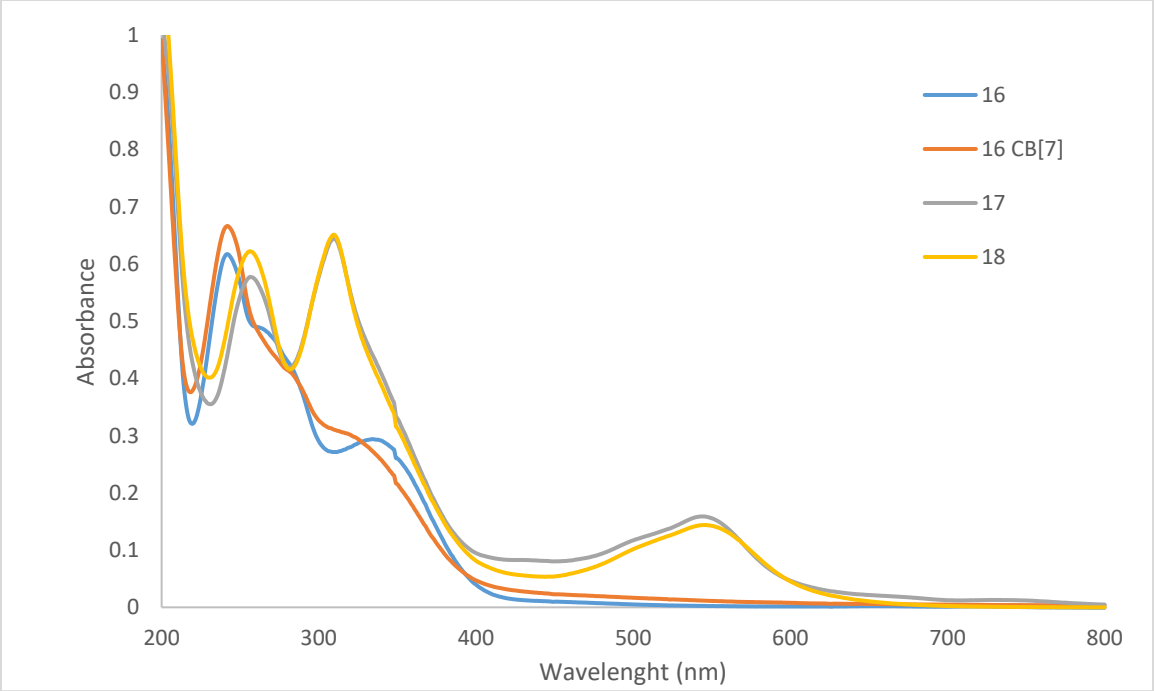

Figure IV-S94. UV-Vis spectra recorded for **IV-16**, **IV-16·CB[7]**, **IV-17**, and **IV-18**.

Hydrodynamic Diameter Determination:

Hydrodynamic radius (r) were calculated using Stokes-Einstein Equation:

$$D = \frac{k_B T}{6\pi\eta r};$$

Where k_B is Boltzmann's constant (1.381 x 10^{-23} m^2 kg s^{-2} K^{-1}), T is the temperature, η is viscosity of the solution (η_{MeCN} = 3.43 x 10^{-4} kg m^{-1} s^{-1}, η_{H2O}= 8.90 x 10^{-4} kg m^{-1} s^{-1}), and D is the diffusion coefficient determined through DOSY NMR.

Diameter calculations were determined by doubling the hydrodynamic radius which was found.

Bibliography

1. Pedersen, C. J. *Angew. Chem. Int. Ed.* **1988**, *27*, 1021-1027.
2. Lehn, J.-M. *Angew. Chem. Int. Ed.* **1988**, *27*, 89-112.
3. Cram, D. J. *Angew. Chem. Int. Ed.* **1988**, *27*, 1009-1020.
4. Lehn, J.-M. *Chem. Soc. Rev.* **2017**, *46*, 2378-2379.
5. Chakrabarty, R.; Mukherjee, P. S.; Stang, P. J., *Chem. Rev.* **2011**, *111*, 6810-6918.
6. Safont-Sempere, M. M.; Fernández, G.; Würthner, F. *Chem. Rev.* **2011**, *111*, 5784-5814.
7. Rebek, J. *Acc. Chem. Res.* **2009**, *42*, 1660-1668.
8. Jordan, J. H.; Gibb, B. C. *Chem. Soc. Rev.* **2015**, *44*, 547-585.
9. Yoshizawa, M.; Klosterman, J. K.; Fujita, M. *Angew. Chem. Int. Ed.* **2009**, *48*, 3418-3438.
10. Brown, C. J.; Toste, F. D.; Bergman, R. G.; Raymond, K. N. *Chem. Rev.* **2015**, *115*, 3012-3035.
11. Furukawa, H.; Cordova, K. E.; O'Keeffe, M.; Yaghi, O. M. *Science* **2013**, *341*, 1230444.
12. Zarra, S.; Wood, D. M.; Roberts, D. A.; Nitschke, J. R. *Chem. Soc. Rev.* **2015**, *44*, 419-432.
13. Del Valle, E. M. M. *Process Biochemistry* **2004**, *39*, 1033-1046.
14. Ikeda, A.; Shinkai, S. *Chem. Rev.* **1997**, *97*, 1713-1734.
15. Strutt, N. L.; Zhang, H.; Schneebeli, S. T.; Stoddart, J. F. *Acc. Chem. Res.* **2014,** *47*, 2631-2642.

16. Dale, E. J.; Vermeulen, N. A.; Juricek, M.; Barnes, J. C.; Young, R. M.; Wasielewski, M. R.; Stoddart, J. F. *Acc. Chem. Res.* **2016,** *49*, 262-273.

17. Diederich, F. *Angew. Chem. Int. Ed.* **1988**, *27*, 362-386.

18. Stella, V. J.; Rao, V. M.; Zannou, E. A.; Zia, V. *Adv. Drug Delivery Rev.* **1999,** *36*, 3-16.

19. Ghale, G.; Nau, W. M. *Acc. Chem. Res.* **2014**, *47*, 2150-2159.

20. Yu, Y.; Rebek, J. *Acc. Chem. Res.* **2018**, *51*, 3031-3040.

21. Anslyn, E. V. *J. Org. Chem.* **2007**, *72*, 687-699.

22. Meadows, M. K.; Anslyn, E. V. *Macrocyclic Supramol. Chem.* **2016**, 92-126.

23. Walker, S.; Oun, R.; McInnes, F. J.; Wheate, N. J. *Isr. J. Chem.* **2011**, *51*, 616-624.

24. Ma, X.; Zhao, Y. *Chem. Rev.* **2015**, *115*, 7794-7839.

25. Zhang, H.; Liu, Z.; Zhao, Y. *Chem. Soc. Rev.* **2018**, *47*, 5491-5528.

26. Ogoshi, T.; Harada, A. *Sensors* **2008**, *8*, 4961-4982.

27. Shetty, D.; Khedkar, J. K.; Park, K. M.; Kim, K. *Chem. Soc. Rev.* **2015**, *44*, 8747-8761.

28. Border, S. E.; Pavlovic, R. Z.; Zhiquan, L.; Badjic, J. D. *J. Am. Chem. Soc.* **2017**, *139*, 18496-18499.

29. Wang, W.; Finnegan, T. J.; Lei, Z.; Zhu, X.; Moore, C. E.; Shi, K.; Badjic, J. D. *Chem. Commun.* **2020**, *56*, 1271-1274.

30. Zhou, J.; Yu, G.; Huang, F. *Chem. Soc. Rev.* **2017**, *46*, 7021-7053.

31. Zhang, X.; Cheng, Q.; Li, L.; Shangguan, L.; Li, C.; Li, S.; Huang, F.; Zhang, J.; Wang, R. *Theranostics* **2019**, *9*, 3107-3121.

32. Huang, Q.; Zhao, H.; Shui, M.; Guo, D.-S.; Wang, R. *Chem. Sci.* **2020**, *11*, 9623-9629.

33. Chang, Y.; Chen, J.-Y.; Yang, J.; Lin, T.; Zeng, L.; Xu, J.-F.; Hou, J.-L.; Zhang, X. *ACS Appl. Mater. Interfaces* **2019**, *11*, 38497-38502.

34. Kassem, S.; van Leeuwen, T.; Lubbe, A. S.; Wilson, M. R.; Feringa, B. L.; Leigh, D. A. *Chem. Soc. Rev.* **2017**, *46*, 2592-2621.

35. Rekharsky, M. V.; Inoue, Y. *Chem. Rev.* **1998**, *98*, 1875-1917.

36. Trinh, T.; Cappel, J. P.; Geis, P. A.; McCarty, M. L.; Pilosof, D.; Zwerdling, S. S. Uncomplexed cyclodextrin solutions for odor control on inanimate surfaces, especially fabrics. WO9605358A1, 1996.

37. Davis, M. E.; Brewster, M. E. *Nat. Rev. Drug Discovery* **2004**, *3*, 1023-1035.

38. Brady, K. G. Captisol Assessment page. https://www.captisol.com/assessment (accessed April 1, 2021).

39. Barrow, S. J.; Kasera, S.; Rowland, M. J.; del Barrio, J.; Scherman, O. A. *Chem. Rev.* **2015**, *115*, 12320-12406.

40. Gutsche, C. D. *Acc. Chem. Res.* **1983**, *16*, 161-170.

41. Ogoshi, T.; Yamagishi, T.-A.; Nakamoto, Y. *Chem. Rev.* **2016**, *116*, 7937-8002.

42. Xue, M.; Yang, Y.; Chi, X.; Zhang, Z.; Huang, F. *Acc. Chem. Res.* **2012**, *45*, 1294-1308.

43. Wu, J.-R.; Yang, Y.-W. *Chem. Commun.* **2019**, *55*, 1533-1543.

44. Behrend, R.; Meyer, E.; Rusche, F., I. *Justus Liebigs Annalen der Chemie* **1905**, *339*, 1-37.

45. Freeman, W. A.; Mock, W. L.; Shih, N. Y. *J. Am. Chem. Soc.* **1981**, *103*, 7367-7368.

46. Kim, J.; Jung, I.-S.; Kim, S.-Y.; Lee, E.; Kang, J.-K.; Sakamoto, S.; Yamaguchi, K.; Kim, K. *J. Am. Chem. Soc.* **2000**, *122*, 540-541.

47. Day, A. I.; Arnold, A. P.; Blanch, R. J.; Snushall, B. *J. Org. Chem.* **2001**, *66*, 8094-8100.

48. Day, A. I.; Blanch, R. J.; Arnold, A. P.; Lorenzo, S.; Lewis, G. R.; Dance, I. *Angew. Chem. Int. Ed.* **2002**, *41*, 275-277.

49. Cao, L.; Šekutor, M.; Zavalij, P. Y.; Mlinarić-Majerski, K.; Glaser, R.; Isaacs, L. *Angew. Chem. Int. Ed.* **2014**, *53*, 988-993.

50. Liu, S.; Ruspic, C.; Mukhopadhyay, P.; Chakrabarti, S.; Zavalij, P. Y.; Isaacs, L. *J. Am. Chem. Soc.* **2005**, *127*, 15959-15967.

51. Rekharsky, M. V.; Mori, T.; Yang, C.; Ko, Y. H.; Selvapalam, N.; Kim, H.; Sobransingh, D.; Kaifer, A. E.; Liu, S.; Isaacs, L.; Chen, W.; Moghaddam, S.; Gilson, M. K.; Kim, K.; Inoue, Y. *Proc. Natl. Acad. Sci. U. S. A.* **2007**, *104*, 20737-20742.

52. Jeon, W. S.; Moon, K.; Park, S. H.; Chun, H.; Ko, Y. H.; Lee, J. Y.; Lee, E. S.; Samal, S.; Selvapalam, N.; Rekharsky, M. V.; Sindelar, V.; Sobransingh, D.; Inoue, Y.; Kaifer, A. E.; Kim, K. *J. Am. Chem. Soc.* **2005**, *127*, 12984-12989.

53. Lagona, J.; Mukhopadhyay, P.; Chakrabarti, S.; Isaacs, L. *Angew. Chem. Int. Ed.* **2005**, *44*, 4844-70.

54. Lee, J. W.; Samal, S.; Selvapalam, N.; Kim, H.-J.; Kim, K. *Acc. Chem. Res.* **2003**, *36*, 621-630.

55. Nau, W. M.; Florea, M.; Assaf, K. I. *Isr. J. Chem.* **2011**, *51*, 559-577.

56. Mock, W. L.; Shih, N.-Y. *J. Org. Chem.* **1986**, *51*, 4440-4446.

57. Hur, M. Y.; Murray, J.; Kim, K., Chapter 2 Synthesis of the Cucurbituril Family. In *Cucurbiturils and Related Macrocycles*, The Royal Society of Chemistry: 2020; pp 15-30.

58. Li, S.; Macartney, D. H.; Wang, R., Chapter 3 Host–Guest Chemistry of the Cucurbituril Family. In *Cucurbiturils and Related Macrocycles*, The Royal Society of Chemistry: 2020; pp 31-53.

59. Masson, E.; Ling, X.; Joseph, R.; Kyeremeh-Mensah, L.; Lu, X. *RSC Adv.* **2012**, *2*, 1213-1247.

60. Bush, M. E.; Bouley, N. D.; Urbach, A. R. *J. Am. Chem. Soc.* **2005**, *127*, 14511-14517.

61. Tian, J.; Xu, Z.-Y.; Zhang, D.-W.; Wang, H.; Xie, S.-H.; Xu, D.-W.; Ren, Y.-H.; Wang, H.; Liu, Y.; Li, Z.-T. *Nat. Commun.* **2016**, *7*, 11580.

62. Bosmans, R. P. G.; Briels, J. M.; Milroy, L.-G.; de Greef, T. F. A.; Merkx, M.; Brunsveld, L. *Angew. Chem. Int. Ed.* **2016**, *55*, 8899-8903.

63. Ko, Y. H.; Kim, E.; Hwang, I.; Kim, K. *Chem. Commun.* **2007**, 1305-1315.

64. Gao, C.; Kwong, C. H. T.; Sun, C.; Li, Z.; Lu, S.; Yang, Y.-W.; Lee, S. M. Y.; Wang, R. *ACS Appl. Mater. Interfaces* **2020**, *12*, 25604-25615.

65. Ma, D.; Zhang, B.; Hoffmann, U.; Sundrup, M. G.; Eikermann, M.; Isaacs, L., *Angew. Chem. Int. Ed.* **2012**, *51*, 11358-62.

66. Yang, H.; Yuan, B.; Zhang, X.; Scherman, O. A. *Acc. Chem. Res.* **2014**, *47*, 2106-2115.

67. Liu, J.; Lan, Y.; Yu, Z.; Tan, C. S. Y.; Parker, R. M.; Abell, C.; Scherman, O. A. *Acc. Chem. Res.* **2017**, *50*, 208-217.

68. Flinn, A.; Hough, G. C.; Stoddart, J. F.; Williams, D. J. *Angew. Chem. Int. Ed.* **1992**, *31*, 1475-1477.

69. Zhao, J.; Kim, H.-J.; Oh, J.; Kim, S.-Y.; Lee, J. W.; Sakamoto, S.; Yamaguchi, K.; Kim, K. *Angew. Chem. Int. Edi.* **2001**, *40*, 4233-4235.

70. Liu, S.-M.; Xu, L.; Wu, C.-T.; Feng, Y.-Q. *Talanta* **2004**, *64*, 929-934.

71. Ayhan, M. M.; Karoui, H.; Hardy, M.; Rockenbauer, A.; Charles, L.; Rosas, R.; Udachin, K.; Tordo, P.; Bardelang, D.; Ouari, O. *J. Am. Chem. Soc.* **2015**, *137*, 10238-10245.

72. Lucas, D.; Isaacs, L. *Org. Lett.* **2011**, *13*, 4112-4115.

73. Gilberg, L.; Zhang, B.; Zavalij, P. Y.; Sindelar, V.; Isaacs, L. *Org. & Biomol. Chem.* **2015**, *13*, 4041-4050.

74. Lucas, D.; Minami, T.; Iannuzzi, G.; Cao, L.; Wittenberg, J. B.; Anzenbacher, P.; Isaacs, L. *J. Am. Chem. Soc.* **2011**, *133*, 17966-17976.

75. Vinciguerra, B.; Cao, L.; Cannon, J. R.; Zavalij, P. Y.; Fenselau, C.; Isaacs, L., *J. Am. Chem. Soc.* **2012**, *134*, 13133-13140.

76. Vinciguerra, B.; Zavalij, P. Y.; Isaacs, L. *Org. Lett.* **2015**, *17*, 5068-5071.

77. Murkli, S.; Klemm, J.; Brockett, A. T.; Shuster, M.; Briken, V.; Roesch, M. R.; Isaacs, L. *Chem. Euro. J.* **2021**, *27*, 3098-3105.

78. Bockus, A. T.; Smith, L. C.; Grice, A. G.; Ali, O. A.; Young, C. C.; Mobley, W.; Leek, A.; Roberts, J. L.; Vinciguerra, B.; Isaacs, L.; Urbach, A. R. *J. Am. Chem. Soc.* **2016**, *138*, 16549-16552.

79. Zhou, X.; Su, X.; Pathak, P.; Vik, R.; Vinciguerra, B.; Isaacs, L.; Jayawickramarajah, J. *J. Am. Chem. Soc.* **2017**, *139*, 13916-13921.

80. Šindelář, V.; Lízal, T., Chapter 20 Hemicucurbiturils. In *Cucurbiturils and Related Macrocycles*, The Royal Society of Chemistry: 2020; pp 527-545.

81. Cova, T. F. G. G.; Nunes, S. C. C.; Valente, A. J. M.; Pinho e. Melo, T. M. V. D.; Pais, A. A. C. C. *J. Mol. Liq.* **2017**, *242*, 640-652.

82. Ma, D.; Hettiarachchi, G.; Nguyen, D.; Zhang, B.; Wittenberg, J. B.; Zavalij, P. Y.; Briken, V.; Isaacs, L. *Nat. Chem.* **2012**, *4*, 503-510.

83. Ganapati, S.; Isaacs, L. *Isr. J. Chem.* **2018**, *58*, 250-263.

84. Lu, X.; Samanta, S. K.; Zavalij, P. Y.; Isaacs, L. *Angew. Chem. Int. Ed.* **2018**, *57*, 8073-8078.

85. Mao, D.; Liang, Y.; Liu, Y.; Zhou, X.; Ma, J.; Jiang, B.; Liu, J.; Ma, D. *Angew. Chem. Int. Ed.* **2017**, *41*, 12614-12618.

86. Jiang, S.; Lan, S.; Mao, D.; Yang, X.; Shi, K.; Ma, D. *Chem. Commun.* **2018**, *54*, 9486-9489.

87. Mao, W.; Mao, D.; Yang, F.; Ma, D. *Chem. - Eur. J.* **2019**, *25*, 2272-2280.

88. Bauer, D.; Andrae, B.; Gass, P.; Trenz, D.; Becker, S.; Kubik, S. *Org. Chem. Front.* **2019**, Ahead of Print.

89. Hoffmann, U.; Grosse-Sundrup, M.; Eikermann-Haerter, K.; Zaremba, S.; Ayata, C.; Zhang, B.; Ma, D.; Isaacs, L.; Eikermann, M. *Anesthesiology* **2013**, *119*, 317-325.

90. Haerter, F.; Simons, J. C. P.; Foerster, U.; Moreno Duarte, I.; Diaz-Gil, D.; Ganapati, S.; Eikermann-Haerter, K.; Ayata, C.; Zhang, B.; Blobner, M.; Isaacs, L.; Eikermann, M. *Anesthesiology* **2015**, *123*, 1337-1349.

91. Ganapati, S.; Grabitz, S. D.; Murkli, S.; Scheffenbichler, F.; Rudolph, M. I.; Zavalij, P. Y.; Eikermann, M.; Isaacs, L. *Chem. Biochem.* **2017**, *18*, 1583-1588.

92. Xue, W.; Zavalij, P. Y.; Isaacs, L. *Org. Biomol. Chem.* **2019**, *17*, 5561-5569.

93. Ganapati, S.; Zavalij, P. Y.; Eikermann, M.; Isaacs, L. *Org. Biomol. Chem.* **2016**, *14*, 1277-1287.

94. Ndendjio, S. Z.; Liu, W.; Yvanez, N.; Meng, Z.; Zavalij, P. Y.; Isaacs, L. *New J. Chem.* **2020**, *44*, 338-345.

95. Tranchemontagne, D. J.; Mendoza-Cortés, J. L.; O'Keeffe, M.; Yaghi, O. M. *Chem. Soc. Rev.* **2009**, *38*, 1257-1283.

96. Mal, P.; Breiner, B.; Rissanen, K.; Nitschke, J. R. *Science* **2009**, *324*, 1697.

97. Cullen, W.; Misuraca, M. C.; Hunter, C. A.; Williams, N. H.; Ward, M. D. *Nat. Chem.* **2016**, *8*, 231-236.

98. Kumari, H.; Deakyne, C. A.; Atwood, J. L. *Acc. Chem. Res.* **2014**, *47*, 3080-3088.

99. Wang, Q.-Q.; Gonell, S.; Leenders, S. H. A. M.; Dürr, M.; Ivanović-Burmazović, I.; Reek, J. N. H. *Nat. Chem.* **2016**, *8*, 225-230.

100. Cook, T. R.; Stang, P. J. *Chem. Rev.* **2015**, *115*, 7001-7045.

101. Percástegui, E. G.; Ronson, T. K.; Nitschke, J. R. *Chem. Rev.* **2020**, *120*, 13480-13544.

102. Crawley, M. R.; Cook, T. R., CHAPTER 7 Coordination-driven Self-assembly of Functionalized Self-assembled Metallomacrocycles. In *Metallomacrocycles: From Structures to Applications*, The Royal Society of Chemistry: 2019; pp 152-194.

103. Grishagin, I. V.; Pollock, J. B.; Kushal, S.; Cook, T. R.; Stang, P. J.; Olenyuk, B. Z. *Proc. Nat. Acad. Sci.* **2014**, *111*, 18448.

104. Yan, X.; Cook, T. R.; Wang, P.; Huang, F.; Stang, P. J. *Nat. Chem.* **2015**, *7*, 342-348.

105. Olenyuk, B.; Whiteford, J. A.; Fechtenkötter, A.; Stang, P. J. *Nature* **1999**, *398*, 796-799.

106. Fujita, M.; Tominaga, M.; Hori, A.; Therrien, B. *Acc. Chem. Res.* **2005**, *38*, 369-378.

107. Harris, K.; Fujita, D.; Fujita, M. *Chem. Commun.* **2013**, *49*, 6703-6712.

108. Tominaga, M.; Suzuki, K.; Kawano, M.; Kusukawa, T.; Ozeki, T.; Sakamoto, S.; Yamaguchi, K.; Fujita, M. *Angew. Chem. Int. Ed.* **2004**, *43*, 5621-5625.

109. Hastings, C. J.; Pluth, M. D.; Bergman, R. G.; Raymond, K. N. *J. Am. Chem. Soc.* **2010**, *132*, 6938-6940.

110. Caulder, D. L.; Brückner, C.; Powers, R. E.; König, S.; Parac, T. N.; Leary, J. A.; Raymond, K. N. *J. Am. Chem. Soc.* **2001**, *123*, 8923-8938.

111. Leininger, S.; Olenyuk, B.; Stang, P. J. *Chem. Rev.* **2000**, *100*, 853-908.

112. Fujita, M.; Yazaki, J.; Ogura, K. *J. Am. Chem. Soc.* **1990**, *112*, 5645-7.

113. Jiang, B.; Ou, B.; Yang, H.-B., CHAPTER 2 Design Principles of Self-assembled Metallomacrocycles. In *Metallomacrocycles: From Structures to Applications*, The Royal Society of Chemistry: 2019; pp 20-46.

114. Mal, P.; Schultz, D.; Beyeh, K.; Rissanen, K.; Nitschke, J. R. *Angew. Chem. Int. Ed.* **2008**, *47*, 8297-8301.

115. Bolliger, J. L.; Belenguer, A. M.; Nitschke, J. R. *Angew. Chem. Int. Ed.* **2013**, *52*, 7958-7962.

116. Clegg, J. K.; Cremers, J.; Hogben, A. J.; Breiner, B.; Smulders, M. M. J.; Thoburn, J. D.; Nitschke, J. R. *Chem. Sci.* **2013**, *4*, 68-76.

117. Foster, J. A.; Parker, R. M.; Belenguer, A. M.; Kishi, N.; Sutton, S.; Abell, C.; Nitschke, J. R. *J. Am. Chem. Soc.* **2015**, *137*, 9722-9729.

118. Percástegui, E. G.; Mosquera, J.; Nitschke, J. R. *Angew. Chem. Int. Ed.* **2017**, *56*, 9136-9140.

119. Zarra, S.; Clegg, J. K.; Nitschke, J. R. *Angew. Chem. Int. Ed.* **2013**, *52*, 4837-4840.

120. Neelakandan, P. P.; Jiménez, A.; Nitschke, J. R. *Chem. Sci.* **2014**, *5*, 908-915.

121. Della Rocca, J.; Liu, D.; Lin, W. *Acc. Chem. Res.* **2011**, *44*, 957-968.

122. Sumida, K.; Rogow, D. L.; Mason, J. A.; McDonald, T. M.; Bloch, E. D.; Herm, Z. R.; Bae, T.-H.; Long, J. R. *Chem. Rev.* **2012**, *112*, 724-781.

123. Benyettou, F.; Prakasam, T.; Ramdas Nair, A.; Witzel, I.-I.; Alhashimi, M.; Skorjanc, T.; Olsen, J.-C.; Sadler, K. C.; Trabolsi, A. *Chem. Sci.* **2019**, *10*, 5884-5892.

124. Zheng, Y.-R.; Suntharalingam, K.; Johnstone, T. C.; Lippard, S. J., *Chem. Sci.* **2015**, *6*, 1189-1193.

125. Qiao, Y.; Zhang, L.; Li, J.; Lin, W.; Wang, Z. *Angew. Chem. Int. Ed.* **2016**, *55*, 12778-12782.

126. Sauvage, J.-P. *Angew. Chem. Int. Ed.* **2017**, *56*, 11080-11093.

127. Stoddart, J. F. *Angew. Chem. Int. Ed.* **2017**, *56*, 11094-11125.

128. Feringa, B. L. *Angew. Chem. Int. Ed.* **2017**, *56*, 11060-11078.

129. Vives, G.; Tour, J. M. *Acc. Chem. Res.* **2009**, *42*, 473-487.

130. De Bo, G.; Kuschel, S.; Leigh, D. A.; Lewandowski, B. *J. Am. Chem. Soc.* **2014**, *136*, 5811-5814.

131. Sun, T.; Zhang, Y. S.; Pang, B.; Hyun, D. C.; Yang, M.; Xia, Y. *Angew. Chem. Int. Ed.* **2014**, *53*, 12320-12364.

132. Wolinsky, J. B.; Grinstaff, M. W. *Adv. Drug Delivery Rev.* **2008**, *60*, 1037-1055.

133. Elsabahy, M.; Heo, G. S.; Lim, S.-M.; Sun, G.; Wooley, K. L. *Chem. Rev.* **2015**, *115*, 10967-11011.

134. Sengupta, S.; Eavarone, D.; Capila, I.; Zhao, G.; Watson, N.; Kiziltepe, T.; Sasisekharan, R. *Nature* **2005**, *436*, 568-572.

135. Kierstead, P. H.; Okochi, H.; Venditto, V. J.; Chuong, T. C.; Kivimae, S.; Fréchet, J. M. J.; Szoka, F. C. *J. Controlled Release* **2015,** *213*, 1-9.

136. Dreaden, E. C.; Austin, L. A.; Mackey, M. A.; El-Sayed, M. A. *Ther. Delivery* **2012,** *3*, 457-478.

137. Fang, J.; Nakamura, H.; Maeda, H. *Adv. Drug Delivery Rev.* **2011**, *63*, 136-151.

138. Longmire, M.; Choyke, P. L.; Kobayashi, H. *Nanomedicine* **2008**, *3*, 703-717.

139. Samanta, S. K.; Moncelet, D.; Briken, V.; Isaacs, L. *J. Am. Chem. Soc.* **2016**, *138*, 14488-14496.

140. Samanta, S. K.; Quigley, J.; Vinciguerra, B.; Briken, V.; Isaacs, L. *J. Am. Chem. Soc.* **2017**, *139*, 9066-9074.

141. Liu, S.; Zavalij, P. Y.; Isaacs, L., Cucurbit[10]uril. *J. Am. Chem. Soc.* **2005,** *127*, 16798-16799.

142. Cheng, X.-J.; Liang, L.-L.; Chen, K.; Ji, N.-N.; Xiao, X.; Zhang, J.-X.; Zhang, Y.-Q.; Xue, S.-F.; Zhu, Q.-J.; Ni, X.-L.; Tao, Z. *Angew. Chem. Int. Ed.* **2013**, *52*, 7252-7255.

143. Mock, W. L.; Shih, N. Y. *J. Org. Chem.* **1986**, *51*, 4440-4446.

144. Cao, L.; Sekutor, M.; Zavalij, P. Y.; Mlinaric-Majerski, K.; Glaser, R.; Isaacs, L. *Angew. Chem. Int. Ed.* **2014**, *53*, 988-993.

145. Biedermann, F.; Uzunova, V. D.; Scherman, O. A.; Nau, W. M.; De Simone, A. *J. Am. Chem. Soc.* **2012**, *134*, 15318-15323.

146. Biedermann, F.; Nau, W. M.; Schneider, H.-J. *Angew. Chem. Int. Ed.* **2014**, *53*, 11158-11171.

147. Isaacs, L. *Acc. Chem. Res.* **2014**, *47*, 2052-2062.

148. Del Barrio, J.; Horton, P.; Lairez, D.; Lloyd, G.; Toprakcioglu, C.; Scherman, O. *J. Am. Chem. Soc.* **2013**, *135*, 11760-11763.

149. del Barrio, J.; Ryan, S. T. J.; Jambrina, P. G.; Rosta, E.; Scherman, O. A. *J. Am. Chem. Soc.* **2016,** *138*, 5745-5748.

150. Wheate, N. J.; Limantoro, C. *Supramol. Chem.* **2016**, *28*, 849-856.

151. Park, K. M.; Murray, J.; Kim, K. *Acc. Chem. Res.* **2017**, *50*, 644-646.

152. Kim, E.; Kim, D.; Jung, H.; Lee, J.; Paul, S.; Selvapalam, N.; Yang, Y.; Lim, N.; Park, C. G.; Kim, K. *Angew. Chem., Int. Ed.* **2010**, *49*, 4405-4408.

153. Cao, L.; Hettiarachchi, G.; Briken, V.; Isaacs, L. *Angew. Chem. Int. Ed.* **2013**, *52*, 12033-12037.

154. Chen, H.; Ma, H.; Tan, Y. *J. Polym. Sci., Part A: Polym. Chem.* **2015**, *53*, 1748-1752.

155. Yeom, J.; Kim, S. J.; Jung, H.; Namkoong, H.; Yang, J.; Hwang, B. W.; Oh, K.; Kim, K.; Sung, Y. C.; Hahn, S. K. *Adv. Healthcare Mater.* **2015**, *4*, 237-244.

156. Webber, M. J.; Appel, E. A.; Vinciguerra, B.; Cortinas, A. B.; Thapa, L. S.; Jhunjhunwala, S.; Isaacs, L.; Langer, R.; Anderson, D. G. *Proc. Natl. Acad. Sci. U. S. A.* **2016**, *113*, 14189-14194.

157. Zou, L.; Braegelman, A. S.; Webber, M. J. *ACS Cent. Sci.* **2019**, *5*, 1035-1043.

158. Chen, H.; Huang, Z.; Wu, H.; Xu, J.-F.; Zhang, X. *Angew. Chem. Int. Ed.* **2017**, *56*, 16575-16578.

159. Sasmal, R.; Das Saha, N.; Pahwa, M.; Rao, S.; Joshi, D.; Inamdar, M. S.; Sheeba, V.; Agasti, S. S. *Anal. Chem.* **2018**, *90*, 11305-11314.

160. Sun, C.; Zhang, H.; Li, S.; Zhang, X.; Cheng, Q.; Ding, Y.; Wang, L.-H.; Wang, R. *ACS Appl. Mater. Interfaces* **2018**, *10*, 25090-25098.

161. Witt, D.; Lagona, J.; Damkaci, F.; Fettinger, J. C.; Isaacs, L. *Org. Lett.* **2000,** *2*, 755-758.

162. Chakraborty, A.; Wu, A.; Witt, D.; Lagona, J.; Fettinger, J. C.; Isaacs, L., *J. Am. Chem. Soc.* **2002,** *124*, 8297-8306.

163. Lagona, J.; Fettinger, J. C.; Isaacs, L. *Org. Lett.* **2003,** *5*, 3745-3747.

164. Stancl, M.; Hodan, M.; Sindelar, V. *Org. Lett.* **2009**, *11*, 4184-4187.

165. Stancl, M.; Gargulakova, Z.; Sindelar, V. *J. Org. Chem.* **2012**, *77*, 10945-10948.

166. Huang, W.-H.; Zavalij, P. Y.; Isaacs, L. *J. Am. Chem. Soc.* **2008**, *130*, 8446-8454.

167. Isaacs, L.; Park, S.-K.; Liu, S.; Ko, Y. H.; Selvapalam, N.; Kim, Y.; Kim, H.; Zavalij, P. Y.; Kim, G.-H.; Lee, H.-S.; Kim, K. *J. Am. Chem. Soc.* **2005**, *127*, 18000-18001.

168. Stancl, M.; Gilberg, L.; Ustrnul, L.; Necas, M.; Sindelar, V. *Supramol. Chem.* **2014**, *26*, 168-172.

169. Ma, D.; Zhang, B.; Hoffmann, U.; Sundrup, M. G.; Eikermann, M.; Isaacs, L. *Angew. Chem. Int. Ed.* **2012**, *51*, 11358-11362.

170. Zhang, X.; Xu, X.; Li, S.; Li, L.; Zhang, J.; Wang, R. *Theranostics* **2019**, *9*, 633.

171. Wu, A.; Chakraborty, A.; Witt, D.; Lagona, J.; Damkaci, F.; Ofori, M. A.; Chiles, J. K.; Fettinger, J. C.; Isaacs, L. *J. Org. Chem.* **2002**, *67*, 5817-5830.

172. Sijbesma, R. P.; Kentgens, A. P. M.; Lutz, E. T. G.; van der Maas, J. H.; Nolte, R. J. M. *J. Am. Chem. Soc.* **1993**, *115*, 8999-9005.

173. Rowan, A. E.; Elemans, J. A. A. W.; Nolte, R. J. M. *Acc. Chem. Res.* **1999**, *32*, 995-1006.

174. Wu, A.; Chakraborty, A.; Fettinger, J. C.; Flowers, R. A., II; Isaacs, L. *Angew. Chem. Int. Ed.* **2002**, *41*, 4028-4031.

175. Burnett, C. A.; Witt, D.; Fettinger, J. C.; Isaacs, L. *J. Org. Chem.* **2003**, *68*, 6184-6191.

176. Wu, F.; Wu, L.-H.; Xiao, X.; Zhang, Y.-Q.; Xue, S.-F.; Tao, Z.; Day, A. I. *J. Org. Chem.* **2012**, *77*, 606-611.

177. Zhao, Y.; Mandadapu, V.; Iranmanesh, H.; Beves, J. E.; Day, A. I. *Org. Lett.* **2017**, *19*, 4034-4037.

178. Isaacs, L.; Witt, D.; Fettinger, J. C. *Chem. Commun.* **1999**, 2549-2550.

179. Wu, A.; Mukhopadhyay, P.; Chakraborty, A.; Fettinger, J. C.; Isaacs, L. *J. Am. Chem. Soc.* **2004**, *126*, 10035-10043.

180. Zhang, B.; Isaacs, L. *J. Med. Chem.* **2014**, *57*, 9554-9563.

181. Hibbert, D. B.; Thordarson, P. *Chem. Commun.* **2016**, *52*, 12792-12805.

182. Wiseman, T.; Williston, S.; Brandts, J. F.; Lin, L.-N. *Anal. Biochem.* **1989**, *179*, 131-137.

183. Broecker, J.; Vargas, C.; Keller, S. *Anal. Biochem.* **2011**, *418*, 307-309.

184. Velazquez-Campoy, A.; Freire, E. *Nat. Protocols* **2006**, *1*, 186-191.

185. Jimenez, M. C.; Dietrich-Buchecker, C.; Sauvage, J.-P. *Angew. Chem. Int. Ed.* **2000**, *39*, 3284-3287.

186. Coskun, A.; Spruell, J. M.; Barin, G.; Dichtel, W. R.; Flood, A. H.; Botros, Y. Y.; Stoddart, J. F. *Chem. Soc. Rev.* **2012**, *41*, 4827-4859.

187. Marcos, V.; Stephens, A. J.; Jaramillo-Garcia, J.; Nussbaumer, A. L.; Woltering, S. L.; Valero, A.; Lemonnier, J.-F.; Vitorica-Yrezabal, I. J.; Leigh, D. A. *Science* **2016**, *352*, 1555-1559.

188. Vukotic, V. N.; Loeb, S. J. *Chem. Soc. Rev.* **2012**, *41*, 5896-5906.

189. Goujon, A.; Du, G.; Moulin, E.; Fuks, G.; Maaloum, M.; Buhler, E.; Giuseppone, N. *Angew. Chem. Int. Ed.* **2016**, *55*, 703-707.

190. Li, Z.; Barnes, J. C.; Bosoy, A.; Stoddart, J. F.; Zink, J. I. *Chem. Soc. Rev.* **2012**, *41*, 2590-2605.

191. Gassensmith, J. J.; Baumes, J. M.; Smith, B. D. *Chem. Commun.* **2009**, 6329-6338.

192. Bitsch, F.; Dietrich-Buchecker, C. O.; Khemiss, A. K.; Sauvage, J. P.; Van Dorsselaer, A. *J. Am. Chem. Soc.* **1991**, *113*, 4023-4025.

193. Amabilino, D. B.; Ashton, P. R.; Stoddart, J. F.; White, A. J. P.; Williams, D. J., *Chem. - Eur. J.* **1998**, *4*, 460-468.

194. Whang, D.; Park, K.-M.; Heo, J.; Ashton, P.; Kim, K. *J. Am. Chem. Soc.* **1998**, *120*, 4899-4900.

195. Black, S. P.; Stefankiewicz, A. R.; Smulders, M. M. J.; Sattler, D.; Schalley, C. A.; Nitschke, J. R.; Sanders, J. K. M. *Angew. Chem. Int. Ed.* **2013**, *52*, 5749-5752.

196. Li, Z.-Y.; Zhang, Y.; Zhang, C.-W.; Chen, L.-J.; Wang, C.; Tan, H.; Yu, Y.; Li, X.; Yang, H.-B. *J. Am. Chem. Soc.* **2014**, *136*, 8577-8589.

197. Fujita, M.; Ibukuro, F.; Hagihara, H.; Ogura, K. *Nature* **1994**, *367*, 720-3.

198. Kaifer, A. E. *Acc. Chem. Res.* **2014**, *47*, 2160-2167.

199. Yawer, M. A.; Havel, V.; Sindelar, V. *Angew. Chem. Int. Ed.* **2015**, *54*, 276-279.

200. Kaabel, S.; Adamson, J.; Topic, F.; Kiesila, A.; Kalenius, E.; Oreren, M.; Reimund, M.; Prigorchenko, E.; Lookene, A.; Reich, H. J.; Rissanen, K.; Aav, R. *Chem. Sci.* **2017**, *8*, 10.1039/C6SC05058A.

201. Joseph, R.; Nkrumah, A.; Clark, R. J.; Masson, E. *J. Am. Chem. Soc.* **2014**, *136*, 6602-6607.

202. Benyettou, F.; Zheng, X.; Elacqua, E.; Wang, Y.; Dalvand, P.; Asfari, Z.; Olsen, J.-C.; Han, D. S.; Saleh, N. i.; Elhabiri, M.; Weck, M.; Trabolsi, A. *Langmuir* **2016**, *32*, 7144-7150.

203. Cavatorta, E.; Verheijden, M. L.; van Roosmalen, W.; Voskuhl, J.; Huskens, J.; Jonkheijm, P., *Chem. Commun.* **2016**, *52*, 7146-7149.

204. Holloway, L. R.; McGarraugh, H. H.; Young, M. C.; Sontising, W.; Beran, G. J. O.; Hooley, R. J. *Chem. Sci.* **2016**, *7*, 4423-4427.

205. Wang, W.; Wang, Y.-X.; Yang, H.-B. *Chem. Soc. Rev.* **2016**, *45*, 2656-2693.

206. Kim, K. *Chem. Soc. Rev.* **2002**, *31*, 96-107.

207. Song, Y.; Huang, X.; Hua, H.; Wang, Q. *Dyes Pigm.* **2017**, *137*, 229-235.

208. Yamaguchi, I.; Higashi, H.; Shigesue, S.; Shingai, S.; Sato, M. *Tetrahedron Lett.* **2007**, *48*, 7778-7781.

209. Freitag, M.; Gundlach, L.; Piotrowiak, P.; Galoppini, E., *J. Am. Chem. Soc.* **2012**, *134*, 3358-3366.

210. Li, J.; Yu, Y.; Luo, L.; Li, Y.; Wang, P.; Cao, L.; Wu, B. *Tetrahedron Lett.* **2016**, *57*, 2306-2310.

211. Zhang, K.-D.; Tian, J.; Hanifi, D.; Zhang, Y.; Sue, A. C.-H.; Zhou, T.-Y.; Zhang, L.; Zhao, X.; Liu, Y.; Li, Z.-T. *J. Am. Chem. Soc.* **2013**, *135*, 17913-17918.

212. Huang, Z.; Yang, L.; Liu, Y.; Wang, Z.; Scherman, O. A.; Zhang, X. *Angew. Chem. Int. Ed.* **2014**, *53*, 5351-5355.

213. Bloch, W. M.; Abe, Y.; Holstein, J. J.; Wandtke, C. M.; Dittrich, B.; Clever, G. H. *J. Am. Chem. Soc.* **2016**, *138*, 13750-13755.

214. Howlader, P.; Das, P.; Zangrando, E.; Mukherjee, P. S. *J. Am. Chem. Soc.* **2016**, *138*, 1668-1676.

215. Klaerner, F.-G.; Schrader, T. *Acc. Chem. Res.* **2013**, *46*, 967-978.

216. Biedermann, F.; Elmalem, E.; Ghosh, I.; Nau, W. M.; Scherman, O. A., *Angew. Chem. Int. Ed.* **2012**, *51*, 7739-7743.

217. Ni, X.-L.; Chen, S.; Yang, Y.; Tao, Z. *J. Am. Chem. Soc.* **2016**, *138*, 6177-6183.

218. Lu, K.; He, C.; Lin, W. *J. Am. Chem. Soc.* **2014**, *136*, 16712-16715.

219. Pollock, J. B.; Cook, T. R.; Schneider, G. L.; Lutterman, D. A.; Davies, A. S.; Stang, P. J., *Inorg. Chem.* **2013**, *52*, 9254-9265.

220. Pollock, J. B.; Schneider, G. L.; Cook, T. R.; Davies, A. S.; Stang, P. J. *J. Am. Chem. Soc.* **2013**, *135*, 13676-13679.

221. Adam, J. M.; Bennett, D. J.; Bom, A.; Clark, J. K.; Feilden, H.; Hutchinson, E. J.; Palin, R.; Prosser, A.; Rees, D. C.; Rosair, G. M.; Stevenson, D.; Tarver, G. J.; Zhang, M.-Q. *J. Med. Chem.* **2002**, *45*, 1806-1816.

222. Bom, A.; Bradley, M.; Cameron, K.; Clark, J. K.; Van Egmond, J.; Feilden, H.; MacLean, E. J.; Muir, A. W.; Palin, R.; Rees, D. C.; Zhang, M.-Q. *Angew. Chem. Int. Ed.* **2002**, *41*, 265-270.

223. Stella, V. J.; Rajewski, R. A. *Pharm. Res.* **1997**, *14*, 556-567.

224. Smith, L. C.; Leach, D. G.; Blaylock, B. E.; Ali, O. A.; Urbach, A. R. *J. Am. Chem. Soc.* **2015**, *137*, 3663-3669.

225. Dsouza, R. N.; Pischel, U.; Nau, W. M. *Chem. Rev.* **2011,** *111*, 7941-7980.

226. Macartney, D. H. *Isr. J. Chem.* **2011**, *51*, 600-615.

227. Gamal-Eldin, M. A.; Macartney, D. H. *Can. J. Chem.* **2014**, *92*, 243-249.

228. Zhang, X.; Xu, X.; Li, S.; Wang, L.-H.; Zhang, J.; Wang, R. *Sci. Rep.* **2018**, *8*, 1-7.

229. Isaacs, L. Aqdot Home Page. https://aqdot.com (accessed May 6, 2020).

230. Wilson, B. H.; Loeb, S. J. *Chem.* **2020**, *6*, 1604-1612.

231. Roy, I.; Limketkai, B.; Botros, Y. Y.; Stoddart, J. F. *Acc. Chem. Res.* **2020**, *53*, 2762.

232. Li, Q.; Zhang, W.; Miljanic, O. S.; Sue, C.-H.; Zhao, Y.-L.; Liu, L.; Knobler, C. B.; Stoddart, J. F.; Yaghi, O. M. *Science* **2009**, *325*, 855-859.

233. Li, Q.; Sue, C.-H.; Basu, S.; Shveyd, A. K.; Zhang, W.; Barin, G.; Fang, L.; Sarjeant, A. A.; Stoddart, J. F.; Yaghi, O. M. *Angew. Chem. Int. Ed.* **2010**, *49*, 6751-6755, S6751/1-S6751/19.

234. Tian, J.; Zhou, T.-Y.; Zhang, S.-C.; Aloni, S.; Altoe, M. V.; Xie, S.-H.; Wang, H.; Zhang, D.-W.; Zhao, X.; Liu, Y.; Li, Z.-T. *Nat. Commun.* **2014**, *5*, 5574.

235. Zhang, Y.-C.; Xu, Z.-Y.; Wang, Z.-K.; Wang, H.; Zhang, D.-W.; Liu, Y.; Li, Z.-T. *ChemPlusChem* **2020**, *85*, 1498-1503.

236. Das, G.; Sharma, S. K.; Prakasam, T.; Gandara, F.; Mathew, R.; Alkhatib, N.; Saleh, N. i.; Pasricha, R.; Olsen, J.-C.; Baias, M.; Kirmizialtin, S.; Jagannathan, R.; Trabolsi, A. *Commun. Chem.* **2019**, *2*, 1-9.

237. Samanta, S. K.; Moncelet, D.; Vinciguerra, B.; Briken, V.; Isaacs, L. *Helv. Chim. Acta.* **2018**, *101*, e1800057.

238. Nitschke, J. R. *Acc. Chem. Res.* **2007**, *40*, 103-112.

239. Castilla, A. M.; Ramsay, W. J.; Nitschke, J. R. *Acc. Chem. Res.* **2014,** *47*, 2063-2073.

240. Rodríguez, J.; Mosquera, J.; Couceiro, J. R.; Nitschke, J. R.; Vázquez, M. E.; Mascareñas, J. L. *J. Am. Chem. Soc.* **2017**, *139*, 55-58.

241. Riddell, I. A.; Smulders, M. M. J.; Clegg, J. K.; Nitschke, J. R. *Chem. Commun.* **2011**, *47*, 457-459.

242. Kamogawa, H.; Sato, S. *Bull. Chem. Soc. Japan* **1991**, *64*, 321-323.

243. Fischer-Durand, N.; Rejeb, S. B.; Le Goffic, F. *Synth. Commun.* **1998**, *28*, 963-970.

244. Cheng, W.-C.; Kurth, M. J. *Org. Prep. Proced. Int.* **2002**, *34*, 585,587-608.

245. Schultz, D.; Nitschke, J. R. *Angew. Chem. Int. Ed.* **2006**, *45*, 2453-2456.

246. Meng, W.; Clegg, J. K.; Thoburn, J. D.; Nitschke, J. R. *J. Am. Chem. Soc.* **2011,** *133*, 13652-13660.

247. Ronson, T. K.; Meng, W.; Nitschke, J. R. *J. Am. Chem. Soc.* **2017**, *139*, 9698-9707.

248. Avram, L.; Cohen, Y. *Chem. Soc. Rev.* **2015**, *44*, 586-602.

249. Einstein, A. *Annalen der Physik* **1905**, *322*, 549-560.

250. Liu, Y.; Yu, Y.; Gao, J.; Wang, Z.; Zhang, X. *Angew. Chem. Int. Ed.* **2010**, *49*, 6576-6579.

251. Biedermann, F.; Scherman, O. A. *J. Phys. Chem. B* **2012**, *116*, 2842-2849.

252. Wang, W.; Kaifer, A. E. *Supramol. Chem.* **2010**, *22*, 710-716.

253. Amabilino, D. B.; Stoddart, J. F. *Chem. Rev.* **1995**, *95*, 2725-2828.

254. Mahata, K.; Frischmann, P. D.; Würthner, F. *J. Am. Chem. Soc.* **2013**, *135*, 15656-15661.

255. Glasson, C. R. K.; Meehan, G. V.; Clegg, J. K.; Lindoy, L. F.; Turner, P.; Duriska, M. B.; Willis, R. *Chem. Commun.* **2008**, 1190-1192.

256. Zhang, Y.; Crawley, M. R.; Hauke, C. E.; Friedman, A. E.; Cook, T. R. *Inorg. Chem.* **2017**, *56*, 4258-4262.

257. Hauser, A.; Vef, A.; Adler, P. *J. Chem. Phys.* **1991**, *95*, 8710-8717.

258. Browne, C.; Brenet, S.; Clegg, J. K.; Nitschke, J. R. *Angew. Chem. Int. Ed.* **2013**, *52*, 1944-1948.

259. Brandenburg, J. G.; Bannwarth, C.; Hansen, A.; Grimme, S. *J. Chem. Phys.* **2018**, *148*, 064104.

260. Marenich, A. V.; Cramer, C. J.; Truhlar, D. G. *J. Phys. Chem. B* **2009**, *113*, 6378-6396.

261. Adamo, C.; Barone, V. *J. Chem. Phys.* **1999**, *110*, 6158-6170.

262. Weigend, F.; Ahlrichs, R. *PhysChemChemPhys* **2005**, *7*, 3297-3305.

263. Grimme, S.; Ehrlich, S.; Goerigk, L. *J. Comput. Chem.* **2011**, *32*, 1456-1465.

264. Neese, F. *WIREs Comput. Mol. Sci* **2012**, *2*, 73-78.

265. Case, D. A.; Babin, V.; Berryman, J. T.; Betz, R. M.; Cai, Q.; Cerutti, D. S.; Cheatham III, T. E.; Darden, T. A.; Duke, R. E.; Gohlke, H.; Goetz, A. W.; Gusarov, S.; Homeyer, N.; Janowski, P.; Kaus, J.; Kolossváry, I.; Kovalenko, A.; Lee, T. S.; LeGrand, S.; Luchko, T.; Luo, R.; Madej, B.; Merz, K. M.; Paesani, F.; Roe, D. R.; Roitberg, A.; Sagui, C.; Salomon-Ferrer, R.; Seabra, G.; Simmerling, C. L.; Smith, W.; Swails, J.; Walker, R. C.; Wang, J.; Wolf, R. M.; Wu, X.; Kollman, P. A. *AMBER 16*, University of California: 2016.

266. Wang, J. M.; Wolf, R. M.; Caldwell, J. W.; Kollman, P. A.; Case, D. A. *J. Comput. Chem.* **2004**, *25*, 1157-1174.

267. Elmes, R. B. P.; Erby, M.; Bright, S. A.; Williams, D. C.; Gunnlaugsson, T. *Chem. Commun.* **2012**, *48*, 2588-2590.